IMPERIAL

وزارة التعليم العالي والبحث العلمي
MINISTRY OF HIGHER EDUCATION AND SCIENTIFIC RESEARCH

From Genesis to Demise: Investigating The Stratigraphic Evolution, Island Dolomitisation, and Drowning of The Cretaceous Mid-Pacific Isolated Carbonate Platforms

Mahmoud Nourelyamani

Imperial College London
Department of Earth science and Engineering
Faculty of Engineering

Submitted in part fulfilment of the requirements for the degree of Doctor of Philosophy

Supervised by Professor Cédric M. John and Dr Rebecca E. Bell

April 2024

DECLARATIONS

Declaration of originality

I declare that this thesis, submitted for the degree of Doctor of Philosophy at Imperial College London and Associateship of the Royal School of Mines, is original research that has been completed by me, and carried out under the supervision of Professor Cédric M. John and Dr Rebecca E. Bell. All published and unpublished material used in this thesis has been appropriately referenced. None of this work has previously been submitted to Imperial College London or any other academic institution for a degree or diploma, or for any other qualification.

Mahmoud Samir El-Yamani

29th April 2024



Copyright declaration

The copyright of this thesis rests with the author and is made available under a Creative Commons Attribution-NonCommercial-NoDerivatives Licence (CC BY-NC-ND 4.0). Researchers are free to copy and redistribute the material in any medium or format on the condition that; they credit the author, do not use it for commercial purposes and do not distribute modified versions of the work.

When reusing or sharing this work, researchers should ensure they make the licence terms clear to others by naming the licence and linking to the licence text.

Please seek permission from the copyright holder for uses of this work that are not included in this licence or permitted under UK Copyright Law.

© Mahmoud S. El-Yamani 2024

ACKNOWLEDGEMENT

I extend my sincere gratitude to the Governmental mission of the Ministry of Higher Education and Scientific Research in Egypt (MOHESR) for their generous funding, covering my tuition fees, bench fees, and stipend throughout my Ph.D. studies. Additionally, I deeply appreciate the support from the Egyptian Bureau for Cultural and Educational Affairs in London (ECEB), which guided me through my Ph.D. journey. Special thanks go to Dr. Rasha Kamal, Cultural Attaché, Prof. Rasha Hussein, Cultural Attaché, Ms. Norhan Kandil, The Counsellor's Personal Assistant, Mrs. Doaa Sharaky, the Administrative & Financial Attaché, Mr. Khaled, Mais Al-Utaibi, and all the staff of ECEB for their assistance. I acknowledge with gratitude the significant bench fees funding from MOHESR, which not only facilitated my Ph.D. studies, research expenses, and attending conferences but also supported other members, research projects, and the lab facilities in the Carbonate Research Group at Imperial College. My thanks also extend to the Faculty Members of the Geology Department, Faculty of Science, Ain Shams University, for their support in securing my scholarship and academic leave.

I am immensely thankful to my supervisors, Becky and Cédric, for their invaluable guidance and endless support throughout my Ph.D. journey. Becky, your inspiration and guidance have been invaluable to me. Thank you for your continued guidance, advice, attention to detail, and enthusiasm. You have always been there for me professionally and personally, providing critical insights while balancing patience and kindness. I hope to implement everything I have learnt from you in the future. Cédric, I appreciate the time you spent on our long discussions, especially during the downtimes. Thank you for highlighting the importance of maintaining a healthy work-life balance. Your support, and encouragement have been invaluable. The supervision of both of you has been pivotal in building my research skills in the academia.

I would like to thank my friends in the Carbonate Research Group and the LBRG Group. Special thanks to Harriet, Saira, and Sarah for being there over the past four years and for being good friends. Thanks Waleed for the constructive feedback and encouragement to step outside. Thanks Qi, for your help in setting up the CL microscope and for Eid Cookies.

To my dear friends Ahmed Alghuraybi and Nihal Darraj, I am deeply grateful for your support and willingness to lend an ear to my complaints, rants, and vents. Thank you for everything - for your feedback, for the shared moments, and for your care. I consider myself incredibly fortunate to have you as friends. Wish you all the best in your life.

To my close buddies Amr and Belal, the countless cups of tea we've shared are a testament to the time we've spent together. I am grateful for the warmth and companionship you've offered, which has truly made wherever we are feel like home. Your presence has enriched every moment, and I'm deeply thankful for the bond of friendship we share.

This thesis would not have been possible without the support, guidance and pray of my family. My Mother, a remarkable individual unlike any other. The person who feels what I am thinking of without talking. She gave me life, taught me, held me, shouted at me but most importantly loved me unconditionally. My Father, the person who spent days and nights to facilitate everything to me. The person who gave me the greatest gift anyone could ever give another person. He believed in me! I dearly wish he were here to witness the fulfilment of his dream for my Ph.D. May Allah grant him the highest levels of Jannah. To my dear sister Reem and my brother-in-law Almostafa, whose presence have transformed London into a home away from home, thank you for your unwavering love and support. And to my niece Koki, whose infectious smile has been a constant source of joy and optimism, I'm endlessly grateful. To my sister Soha and my brother Mostafa, your support, encouragement, and prayers have been a source of strength throughout this journey. Your kindness knows no bounds, and I am blessed to have you all.

Finally, I want to deeply thank my beloved country Egypt for supporting my study.

ABSTRACT

The Cretaceous period witnessed widespread neritic carbonate development, including isolated carbonate platforms (ICPs) which are geologically complex and economically significant for hydrocarbon exploration, as in Egypt's Zohr Field. Despite extensive research, many questions remain about how these platforms formed, evolved, and ultimately declined. This thesis explores these gaps by focusing on Cretaceous ICPs in the Mid-Pacific (Resolution and Allison guyots), integrating core, logging, seismic reflection, and geochemical data, and tectonic reconstruction to derive broader implications.

I elucidated the sequence stratigraphic evolution of these platforms, revealing a more dynamic interplay of factors—including eustasy, subsidence, carbonate production, ocean chemistry, and magmatism—than traditional models suggest. The high-resolution 3D depositional model developed here can be applied to other Cretaceous ICPs worldwide. Karst features on these platforms show two patterns: vertically stacked flank-margin caves along steep windward margins and laterally extensive karst-horizons in the interior with sinkholes and intermittent intervals of brecciation and solution-vugs.

The dolomitisation of these platforms, long attributed to seawater circulation, appears to be driven by magmatism instead. I propose a hydrothermal model where heat flow, seawater circulation, and slight mixing with magmatic fluids altered seawater chemistry, increasing magnesium and enabling dolomite formation. A global database of Cretaceous dolostones supports my reinterpretation, challenging older models of widespread dolomitisation by the Cretaceous normal seawater.

These platforms were demised in the late-Albian to early-Cenomanian, when magmatism caused uplift and subaerial exposure, halting carbonate production. Rapid subsidence from hotspot migration and eustatic rise deepened platform tops, pushing them beyond depths suitable for carbonate growth. My findings challenge the hypothesis of "death-by-excessive-warmth-in-peri-equatorial-waters"—suggesting the heat tolerance of Cretaceous carbonate-secreting organisms.

This work provides new insights into the evolution, diagenesis, and decline of Cretaceous ICPs, improving our understanding of ancient carbonate systems and their significance for analogous platforms in frontier hydrocarbon exploration, like East Mediterranean.

TABLE OF CONTENTS

DECLARATIONS 2

ACKNOWLEDGEMENT 3

ABSTRACT 4

TABLE OF CONTENTS 5

LIST OF FIGURES 10

CHAPTER ONE INTRODUCTION & LITERATURE REVIEW 19

1.1 Research Problems and Rationale 19
1.1.1 Stratigraphic Evolution of the Cretaceous Isolated Carbonate Platforms 19
1.1.2 Dolomitisation in the Cretaceous Isolated Carbonate Platforms 26
1.1.3 The Demise of the Cretaceous Isolated Carbonate Platforms 28
1.1.4 Thesis Broad Aim 30

1.2 The West Pacific Cretaceous Isolated Carbonate Platforms 31
1.2.1 The Formation of the Mid-Pacific Mountains Volcanic Plateau 34
1.2.2 Sedimentological and Stratigraphic Evolution of the Cretaceous Shallow-Marine Carbonates on the Mid-Pacific Seamounts 36
1.2.3 Diagenetic Evolution of the Cretaceous Shallow-Marine Carbonates on the Mid-Pacific Seamounts 40
1.2.4 The Demise of Cretaceous Shallow-Marine Carbonates on the Pacific Seamounts 41
1.2.5 Gaps in Knowledge 43
1.2.5.1 The depositional settings and stratigraphic evolution of the Cretaceous Pacific ICPs 43
1.2.5.2 The subaerial exposure and karstification complex history of the Cretaceous Pacific ICPs 44
1.2.5.3 Scarcity of dolomites in the Cretaceous Pacific ICPs 44
1.2.5.4 The mysterious demise of the Cretaceous Pacific ICPs 45

1.3 Specific Research Aims and Objectives 47
1.3.1 What are the controlling factors on the stratigraphic evolution and large-scale karstification in the Cretaceous Pacific ICPs? 47
1.3.2 How did the scarce dolomitisation occur during the Cretaceous Calcitic ocean just in a few Pacific ICPs? 48
1.3.3 What Controlled the Demise of the Pacific Cretaceous ICPs? Are They suitable analogues for thermal-stress intolerant or tolerant modern tropical atolls under the human-induced future climate changes? 48

1.4 Research Data 49

1.5 Thesis Structure 50

CHAPTER TWO STRATIGRAPHIC EVOLUTION AND KARSTIFICATION OF A CRETACEOUS MID-PACIFIC ATOLL (RESOLUTION GUYOT) RESOLVED FROM CORE-LOG-SEISMIC INTEGRATION AND COMPARISON WITH MODERN AND ANCIENT ANALOGUES* 53

2.1 Abstract 55

2.2 Highlights 55

2.3 Introduction 56

2.4 Geological Setting 58

2.5 Data and Methods 60
2.5.1 Dataset 60
2.5.2 Revised Age Model 61
2.5.3 Seismic and Log Interpretation 61

2.6 Results and Interpretation 63
2.6.1 Revised age model 63
2.6.2 Seismic Facies Analysis 66
2.6.3 Seismic-Stratigraphic Units 75
2.6.3.1 Seismic Unit-1: Hauterivian (132 ± 1 Ma–130.8 ± 1 Ma) 76
2.6.3.2 Seismic Unit-2: Early Barremian to early Aptian (130.8 ± 1 Ma–125.5 ± 1 Ma) 76
2.6.3.3 Seismic Unit-3: Early Aptian to early mid Aptian (125.5 ± 1 Ma–122.8 ± 1 Ma) 76
2.6.3.4 Seismic Unit-4: Mid Aptian to Mid Albian (122.8 ± 1 Ma–105.15 ± 1 Ma) 77
2.6.3.5 Seismic Unit-5: Mid Albian to late Albian (105.15 ± 1 Ma–100.45 ± 1 Ma) 77
2.6.3.6 Seismic Unit-6: age uncertain, Maastrichtian (?) to late Pliocene (?) 77

2.7 Discussion 81
2.7.1 From seismic facies to depositional model 81
2.7.2 Controls on the Sequence-Stratigraphic Evolution of Resolution Guyot and Links to the Cretaceous Eustasy 84
2.7.3 Controls on the Distribution of Karstification 87
2.7.4 Fluid Vents in the Mid-Pacific Atolls 90

2.8 Conclusion 91

CHAPTER THREE MECHANISM OF ISLAND DOLOSTONES FORMATION IN THE CRETACEOUS CALCITIC OCEAN: INSIGHTS FROM THE CRETACEOUS MID-PACIFIC GUYOTS* 93

3.1 Abstract 95

3.2 Highlights 95

3.3 Introduction 96

3.4 Geological settings 102

3.5 Data and Methods 102

3.6 Results and Interpretation 108
3.6.1 Seismic interpretation and seismic facies forward modelling 108
3.6.2 Dolostone Core and Petrographic Observations 114
3.6.2.1 Macroscale dolostone textures 114
3.6.2.2 Microscale dolomite textures 114
3.6.3 Dolomite Geochemistry 115

3.7 Discussion 124
3.7.1 The Link Between Magmatism and Hydrothermal Venting 124
3.7.2 Magmatically Driven Hydrothermal Dolomitisation 125
3.7.2.1 Controls on Dolomitisation Distribution 129
3.7.3 Implications on Island Dolomitisation and Normal Marine Dolomitisation by the Cretaceous Calcitic Seawater 133

3.8 Conclusion 134

CHAPTER FOUR BEYOND THERMAL STRESSES: MAGMATISM, KARSTIFICATION, AND HOTSPOT MIGRATION DICTATED THE DEMISE OF THE MID-PACIFIC CRETACEOUS ATOLLS 136

4.1 Abstract 137

4.2 Highlights 138

4.3 Introduction 138

4.4 Geologic Settings 142

4.5 Data and Methods 147

4.6 Results and Interpretation 151
4.6.1 Age model of Allison Guyot 151
4.6.2 Seismic interpretation 151
4.6.2.1 Seismic Facies and Magmatic Intrusion Related Structures 151
4.6.2.2 Timing of magmatism in the Mid-Pacific Mountains 153

4.7 Discussion 160
4.7.1 The Demise Mechanism of the Mid-Pacific Cretaceous Atolls 160
4.7.1.1 Magmatism, Karstification and Cessation of Shallow-Marine Carbonate Sedimentation 161
4.7.1.2 Inhibition of Shallow-Marine Carbonate Production Resurgence on Re-Submerged Mid-Pacific Atolls 165
4.7.1.2.1 Migration off the Hotspot Swell 165
4.7.1.2.2 Paleoenvironmental Conditions after Re-submergence 167
4.7.2 Comparing the Proposed Demise Mechanism with other Western Pacific Cretaceous Atolls 171
4.7.3 The Role of Excess Warmth in Peri-equatorial Oceans in Cretaceous Atolls Demise: Lessons to the Future Global Warming 171

4.8 Conclusion 176

CHAPTER FIVE DISCUSSION, FUTURE WORK, AND CONCLUSION 177

5.1 General Synthesis 179
5.1.1 What are the controlling factors on the stratigraphic evolution and large-scale karstification in the Pacific Cretaceous ICPs? 179
5.1.2 How did the scarce dolomitisation occur during the Cretaceous Calcitic ocean just in a few Pacific ICPs? 185
5.1.3 What controlled the demise of the Cretaceous Pacific ICPs? Are they suitable analogues for thermal-stress intolerant or tolerant modern tropical atolls under the human-induced future climate changes? 187

5.2 Future Work 190
5.2.1 Quantitative sequence stratigraphy and forward stratigraphic modelling 190
5.2.2 Understanding dolomitisation during the Cretaceous calcitic sea through reactive transport modelling 191
5.2.3 Hydrothermal fluid flow vents: the history of intraplate volcanic activities in the Pacific and fluid flow pathways reutilisation in carbonate successions 191
5.2.4 Quantitative analyses of the factors controlling the demise of the Pacific Cretaceous isolated carbonate platforms 192

5.3 Conclusions 193

BIBLIOGRAPHY 199

APPENDIX A: *SUPPLEMENT* TO STRATIGRAPHIC EVOLUTION AND KARSTIFICATION OF A CRETACEOUS MID-PACIFIC ATOLL (RESOLUTION GUYOT) RESOLVED FROM CORE-LOG-SEISMIC INTEGRATION AND COMPARISON WITH MODERN AND ANCIENT ANALOGUES[1] 228

Table A1: Depositional Age Dating Methodology at Site 866 229

Table A2: Time-Depth Relationship at Site 866 (Resolution Guyot) 236

APPENDIX B: *SUPPLEMENT* TO MECHANISM OF ISLAND DOLOSTONES FORMATION IN THE CRETACEOUS CALCITIC OCEAN: INSIGHTS FROM THE MID-PACIFIC GUYOTS[2] 238

Table B1: Cenozoic Island Dolostone Database 239

Table B2: Cretaceous Island Dolostone Database 243

Table B3: Logging Data at Site 866 247

Table B4: Dolomite Isotope Data at Site 866 247

Table B5: Elemental Composition at Site 866, 867, & 868 247

Table B6: XRF major, minor, and trace elements at Site 866 249

Table B7: Time-Depth Relationship at Site 866 (Resolution Guyot) 251

Table B8: Summary of Index Properties at Site 866 251

Table B9: Palaeoclimate Maps of Mid-Pacific Atolls During Dolomitisation 259

Material B1: Dolomitisation Age Determination Methodology 260

Material B2: Dolomitisation Temperature Calculation Methodology 263

Material B3: Burial & Thermal History Modelling Methodology 264

Table B10: Depositional Age Dating Methodology at Site 866 267

Table B11: Geothermal Gradient of Enwetak Atoll 267

Table B12: Dolomitisation Temperature Calculation Results Using Nine Different Fractionation Equation 268

Table B13: Calculation of Estimated Duration Spent by the Shallow Marine Carbonates of the Cretaceous Pacific Atolls Below 1000 m 269

Table B14: Summary of Interparticle Porosities at Site 866 269

APPENDIX C: *SUPPLEMENT* TO BEYOND THERMAL STRESSES: MAGMATISM, KARSTIFICATION, AND HOTSPOT MIGRATION DICTATED DEMISE OF THE MID-PACIFIC CRETACEOUS ATOLLS 270

Figure C1: Potential Areal Extent and Diameters of the Interpreted Sills at Allison Guyot _____271

Figure C2: Potential Areal Extent and Diameters of the Interpreted Sills At Resolution Guyot_____ 273

Figure C3: Hurricane Index at the Mid-Pacific Mountains (highlighted by red box) at 97 Ma (Valdes et al., 2021) _____ 274

Figure C4: Tropical cyclogenesis (dark shade) during the Mid-Cretaceous (Agustsdottir et al., 1999) and the corresponding location of the Mid-Pacific Mountains (highlighted by red box)_____ 275

Figure C5: Ocean surface currents at the Mid-Pacific Mountains (highlighted by red box) at 97 Ma (Valdes et al., 2021) _____ 276

Figure C6: Ocean surface current at Wodejebato Guyot (highlighted by red dot) at demise age (Valdes et al., 2021) _____ 277

Figure C7: Ocean temperature and ocean surface current at MIT Guyot (highlighted by red dot) at demise age (Valdes et al., 2021)_____ 277

Figure C8: The age progression track of the Japanese Seamount Trail (highlighted by transparent red box and an arrow of the hotspot migration direction) revealing a singular hotspot origin (Modified after Koppers et al., 2003)_____ 278

Figure C9: Ocean surface temperature at the Mid-Pacific Mountains (highlighted by red box) at 97 Ma (Valdes et al., 2021) _____ 279

Figure C10: Ocean surface temperature at Takuyo-Daisan Guyot (highlighted by red dot) at 111 Ma (Valdes et al., 2021) _____ 280

Figure C11: Sea surface temperature at MIT Guyot (highlighted by red dot) at 102.6 Ma (Valdes et al., 2021) _____ 280

Figure C12: Ocean surface temperature at Wodejebato Guyot (highlighted by red dot) at 69 Ma (Valdes et al., 2021) _____281

LIST OF FIGURES

Figure 1.1 (A) The relative proportion of the Phanerozoic isolated carbonate platforms of each age in the compiled database by Rankey (2023). Relative size of boxes in the plots are proportional to the number of data points. Note the significant difference between Cretaceous and Miocene and Plio-Pleistocene. (B) Graph of the relative proportion of different growth patterns for each geologic age (Rankey, 2023) overlain by long-term sea level curve of Hallam (1984). Note the significant difference between the growth patterns of the Cretaceous and Miocene and Plio-Pleistocene isolated carbonate platforms. _____ 22

Figure 1.2 Examples of the global distribution of the isolated carbonate platforms of (A) the Cenozoic age in SE Asia (Mathew et al., 2020) and (B) the Cretaceous age in the Mediterranean and Mesozoic Tethys and their possible analogues (GEPLAN CONSULTING, n.d.). _____ 23

Figure 1.3 The differences between the Cretaceous and the Oligocene-Holocene long- and short-term eustasy. (A) Phanerozoic long-term sea level reconstructions from plate tectonic models (Karlsen et al., 2020; Vérard et al., 2015; Wright et al., 2020; Young et al., 2022), strontium isotopes as a proxy for ridge spreading (van der Meer et al., 2017), 'modern land' flooding (Marcilly et al., 2022), a compilation of stratigraphically derived curves of Haq et al. (Haq, 2018a, 2018b, 2014; Haq and Al-Qahtani, 2005; Haq and Schutter, 2008) and from a Late Cenozoic ice/sea level paleo-climate model, 1 Myr averaged (Stap et al., 2017). Adapted from van der Meer et al. (2022). The highlighted pink and blue boxes show the difference between the Cretaceous and the Oligocene-Holocene long-term sea level, respectively. (B) Long- and short-term curve of the Cretaceous eustasy (Haq, 2014). (C) Cenozoic sea-level curves of Miller et al. (2005) in cyan and Miller et al. (2020) in black, adapted from Burton et al. (2023). _____ 24

Figure 1.4 The figure shows the pronounced difference in seismic characteristics between (A) the layered, parallel, high-amplitude, continuous seismic facies that characterises the Miocene and Oligo-Miocene isolated carbonate platforms (Sarawak, Malaysia; modified from Gartner et al., 2004) and (B) the often homogeneous, seismically transparent internal characteristics, and or poor seismic imaging of many of the Cretaceous isolated carbonate platforms (Zohr discovery in the East Mediterranean; modified Lottaroli and Meciani, 2022). _____ 25

Figure 1.5 Various models of unmodified seawater dolomitisation. The figure shows that the dolomitising fluid (connate) is pumped through porous limestones at depths ranging from at surface to moderate burial (~2 km). Adapted from Warren (2000). _____ 27

Figure 1.6 (A) Phanerozoic CO_2 fluctuations [ppm] from COPSE Model (Lenton et al., 2018) along with CO_2 emissions under the shared socio-economic (SSP) and representative concentration pathways (RCP) from the pre-industrial society, 1750, to 2300 (Meinshausen et al., 2020). The grey bar highlights the overlap between the predicted CO_2 levels between 2080-2170 (~900-1300 ppm) under the different pathways and the Phanerozoic CO_2 fluctuations. The dashed lines show the Mid-Late Cretaceous ages of the overlap. (B) The Phanerozoic global temperature curve (red curve) showing the main warming and cooling events (adapted from Scotese et al., 2015) including: PETM = Paleocene-Eocene Thermal Maximum, EEOC = Early Eocene Climatic Optimum, MECO = Mid-Eocene Climatic Optimum, EOT = Eocene-Oligocene Transition, MMCO = Mid-Miocene Climatic Optimum, LGM = Last Glacial Maximum, PAW = Post-Anthropogenic Warming. Panel (B) also shows the rates of extinction through the Phanerozoic (black curve) highlighting mass extinction (dashed black line) and reef crises (grey bands) events (modified after Harnik et al., 2012). The purple stars in panel (B) highlight the ages of ocean anoxic events and ocean acidification. _____ 29

Figure 1.7 (A) The vertical gravity gradient map of the Pacific Plate (Sandwell et al., 2014; https://portal.gplates.org/portal/vertical_gravity_gradient/) showing the fracture zones, the West Pacific Seamount Province (WPSP) and its' seamount trails (Ratak, Ralik, Anewetak, Ujlan, Magellan, Northern and Southern Wake, Typhoon, and Japanese Seamount Trails), the location of five Cretaceous Pacific isolated carbonate platforms. (B) The vertical gravity gradient map of the Mid-Pacific Mountains showing the location of Sio (1), Heezen (2), Resolution (3), Jacqueline (4), Allison (5), Cape Johnson (6), Renard (7), and Horizon (8) guyots. _____ 32

Figure 1.8 Bathymetry maps of Resolution and Allison guyots (Keizer et al., 2001; https://earthref.org/SC/#top) showing the drilling sites of Ocean Drilling Program Leg 143 sites (Sites 865-868) and Deep Sea Drilling Project Leg 62 Site 463, and 2D seismic surveys. 33

Figure 1.9 Palaeogeographical reconstruction and evolution models of the Mid-Pacific Mountains. (A) The single hotspot hypothesis (Henderson, 1985; Duncan and Clague, 1985) of the evolution of the Mid-Pacific Mountains depicting the present-day (filled square and triangles) and original (open square and triangles) locations of Sites 865, 866, and 869 (adapted from Pringle and Duncan, 1995). Ages of volcanism for each site are sourced from Pringle and Duncan (1995). Geochemical anomaly zones corresponding to the modern SOPITA (Staudigel et al., 1991) and DUPAL (Hart, 1984) are shown. The filled circles indicating modern active hotspots (Pringle and Duncan, 1995). (B) Time series palaeotectonic reconstruction by Pockalny et al. (2021) showing the melt sources and the timing of various eruptions associated with the hotspots. The figure shows the motion paths of the Larson melt region (yellow lines) and previously identified hotspots (blue lines; Pockalny et al., 2021). Pink circles represent the locations of mantle plume sources of each identified hotspot (Pockalny et al., 2021) 35

Figure 1.10 Lithostratigraphic columns of Allison Guyot Site 865 and Resolution Guyot site 866-868 and the basinal deposits close to Resolution Guyot DSDP Site 463 (reproduced from Timofeev et al., 1981; Sager et al., 1993a, b, c; El-Yamani et al., 2022, 2024). The figure summarises the main lithological and fossil content of the different lithostratigraphic units at the drilling sites. Check figure 1.8 for the drilling sites' locations. 39

Figure 1.11 Demise hypotheses of the Cretaceous Pacific isolated carbonate platforms. (A) The crisis zones, identified by Larson et al. (1995) in the death-in-the-tropics hypothesis, for ODP Leg 143/144 Cretaceous atolls based on the age and palaeolatitudes of their demise (adapted from Larson et al., 1995). (B) Palaeolatitudes of the Cretaceous Pacific atolls at the time of platform initiation (not filled circle) and drowning (red filled circle), along with the palaeotemperature trends (adapted from Jenkyns and Wilson, 1999). Panel (B) shows the relative position of drowned platform to the equator on which Jenkyns and Wilson (1999) proposed death-by-excess-warmth-in-shallow-peri-equatorial-waters hypothesis and the black bold line resembles the paleotemperature trends from northern Europe. 42

Figure 1.12 The speculative and less reliable identification of system tracts in shallow marine carbonate successions using a single section or wellbore. (A) Flow chart depicting the process of identifying system tracts using a cross section of the carbonate platform, with a focus on determining the platform margin's position where dA/dt is the rate of change in the accommodation space and dG/dt is the rate of change in the growth potential. (B) Flow chart depicting identifying system tracts within a single section or borehole. It involves a more speculative approach compared to using cross-sections, relying on proxy indicators like trends in deepening and shoaling. Figure adapted from Schlager (2005). 46

Figure 2.1. (a) Map of the Pacific Ocean showing guyots (blue dots) targeted during ODP Legs 143 and 144 (adapted from Wilson et al., 1998). (b) Bathymetry map (mbsl; meter below sea level) showing the location of Resolution Guyot and the location of ODP and DSDP Sites, seismic data and figures in this study. The bathymetry map (b) of Resolution Guyot reveals the typical alternating scalloped-promontory shape of isolated carbonate platforms. 58

Figure 2.2. Lithostratigraphic description of ODP Sites 866, 867 and 868 and DSDP Site 463 (adapted from Timofeev et al., 1981; Sager et al., 1993a, 1993b). The figure shows a summary of the lithological and fossil content of the different lithostratigraphic units at different drill sites along with a correlation between seismic data, logging data (SGR; Spectral Gamma Ray and U; Uranium log) and lithostratigraphic description at Site 866, showing the identified seismic-stratigraphic surfaces (SS) and units (SU) and seismic facies (SF). 60

Figure 2.3. (a) The low-latitude calibrated composite $\delta^{13}C_{carb}$ curve (reproduced from Herrle et al., 2015, using published data from Tethyan sections of Erba et al., 1999; Gale et al., 2011; Herrle et al., 2004) correlated with (b) the $\delta^{13}C_{carb}$ curve of Resolution Guyot (correlation lines highlighted in black) using carbon isotope data from Jenkyns (1995). Dark and light blue zones represent nine correlative intervals in-between ten excursion tie points. (c) The strontium isotope age model at ODP Site 866 based on using strontium isotope data from

Jenkyns et al. (1995) and the values in the reference curve of McArthur et al. (2012, version 5B). (d) Age-depth plot of Resolution Guyot at Site 866 using the calculations from the strontium isotope age model. Please refer to APPENDIX A Table A1 in the supplementary materials showing the detailed steps and calculations for the revised age model. 65

Figure 2.4. Main seismic facies and their reflection characteristics (internal geometries, continuity amplitude and shape) along with the corresponding well zone, if available. Their identification and interpretation are based on comparing the observed characteristics with similar examples from the literature. 74

Figure 2.5. Seismic profiles along with logging data wherever available (SGR; Spectral Gamma Ray and U; Uranium log) showing the palaeogeographic distribution of the different seismic facies and seismic stratigraphic units in the isolated carbonate platform of Resolution Guyot. See Figure 2.1 for the location of these figures. 75

Figure 2.6. FMS images from the upper 450 m (a–c) at Site 866 showing brecciated and disrupted carbonates associated with extensive development of vugs. The relatively dark colours in the FMS image log indicate resistivity lower than the host rock, which may represent open vugs or fractures or filling material different from the host rock. (a,b) FMS images show extensive presence of solution vugs. (c) FMS image shows the possible presence of cave breccia appearing by the same colour of the host rock (bright) and surrounded by sediment fills of dark colour. 75

Figure 2.7. Integration of seismic and core data reveals the characteristics of each seismic-stratigraphic surface (SS1–SS5). (a) The figure shows examples of similar characteristics from the literature along with how the seismic-stratigraphic surface would appear in the seismic data. (b) Core images at site 866 showing the corresponding characteristics of seismic-stratigraphic surface. The vertical scale (black bar) of core images is 10 cm. 79

Figure 2.8. Seismic-stratigraphic interpretation of the different seismic-stratigraphic units in Resolution Guyot showing the trajectory of the platform margin complex and the interpreted seismic-stratigraphic units (from seismic Unit-1 to Unit-6) on top of the basement along with (1) the age of each stratigraphic surface interpreted from the revised age model, (2) a table highlighting their age and stacking pattern and (3) interpretation of their evolution in comparison with the eustatic curve of the Cretaceous by Haq (2014). 80

Figure 2.9. Palaeogeographic reconstruction of the different depositional environments in Resolution Guyot carbonate atoll by integrating the interpreted seismic facies with satellite images from the Glorieuses archipelago. (a) 3D conceptual depositional model showing the different seismic facies and the corresponding facies belts. (b) Satellite image from Glorieuses archipelago (using the descriptions by Jorry et al., 2016 and Prat et al., 2016) used to guide the palaeogeographic interpolation of the different facies belts in Resolution Guyot carbonate atoll. 83

Figure 2.10. (a) E–W seismic profile showing pervasive discontinuous seismic reflection (SF3) at two different levels reflecting two different episodes of karstification, (b) interpreted carton showing the different karstification episodes, each of which is located below seismic-stratigraphic surfaces 4 and 5 which separate them from more continuous reflections, (c) seismic profile showing potential sinkholes at the seismic-stratigraphic surfaces 4 and 5, (d) seismic profile showing potential sinkholes at the seismic-stratigraphic surface 4, (e) seismic profile from Browse Basin in Australia (adapted from Van Tuyl et al., 2018), showing similar characteristics where karst horizon is highlighted by discontinuous broken chaotic reflections. 89

Figure 2.11. (a) Seismic amplitude profile along with root-mean-square and signal envelope amplitude profiles from Resolution Guyot showing the string of beads features along the platform margin interpreted as flank-margin fracture-cave system (highlighted in dashed boxes), (b) seismic amplitude profile from Tarim basin showing similar vertical stack of string of beads controlled by the fault system (adapted from Yang et al., 2012) and seismic attribute analysis showing the bright spot associated with string of beads in Tarim basin (adapted from Zhao et al., 2014). 90

Figure 2.12. Fluid venting system in Resolution Guyot. The figure shows seismic amplitude profile and the corresponding variance attribute showing large fluid vents (SF12) with disrupted reflections, and upward bending reflections. The variance attribute shows the places affected by fluid flow pipes appearing as zones of dim to chaotic reflections relative to the well-bedded, high–medium-amplitude facies of the host-rock strata. 91

Figure 3.1. The compiled geo-dataset of Cenozoic and Cretaceous islands and atolls (see APPENDIX B Table B1 and B2). (A) World map of the distribution of the Cretaceous and the Cenozoic carbonate islands and atolls. (B) The percentage of dolomitised and not dolomitised carbonate islands and atolls of Cretaceous and Cenozoic ages. The compiled dataset might not be quantitatively representative of all the formed islands and atolls in the earth during the Cretaceous and the Cenozoic as not all of them were drilled or are outcropping. Therefore, the presented dataset might not represent a complete rock record. Although, it can provide, at least, a source of relative comparison to show the difficulty of unmodified seawater dolomitisation in the Cretaceous islands in comparison with the Late Cenozoic islands and atolls. 98

Figure 3.2. Secular variations in molar Mg/Ca ratio (A) and Mg^{2+} concentration (B) in seawater throughout the Phanerozoic (Hardie, 1996; Horita et al., 2002; Demicco et al., 2005). 99

Figure 3.3. A. The Pacific Ocean map showing the location of the Mid-Pacific Mountains and Resolution and Allison guyots (Bai et al., 2019). B. Bathymetry maps of Resolution and Allison guyots (Keizer et al., 2001) showing the locations of drilling sites 865 and 866 and the 2D seismic data. 100

Figure 3.4. Lithostratigraphic descriptions of Resolution (Site 866) and Allison (Site 865) guyots adapted from (Sager et al., 1993a, 1993b; El-Yamani et al., 2022). The figure shows a summary of the lithological and fossil content of the different lithostratigraphic units, and their porosity measurements (Sager et al., 1993a, 1993b) at different drill sites along with the identified seismic facies. The mineralogy profile of each drilling site was retrieved by integrating core scans, core descriptions (ODP Initial Reports, 1993a, 1993b), facies and petrographic descriptions (Arnaud et al., 1995). The red dots in the porosity profile of 865 represents the location of the identified dense beds that act as permeability barriers. 101

Figure 3.5. A. The interpreted seismic facies at Resolution and Allison guyots showing an example of each seismic facies, summaries of their characteristics, and interpretation sketch of seismic facies. B. The Figure also shows analogue seismic profiles with similar seismic facies from Okinawa Trough 2D seismic data (Chen et al., 2020) and Vøring Basin 3D seismic data (Jamtveit et al., 2004) to provide a source of comparison with the displayed characteristics of the seismic facies at the guyots. 110

Figure 3.6. Seismic facies forward modelling of the interpreted magmatic sill-intrusion. A. A schematic representation of the intruding sill across the sedimentary succession at Site 865 along with their corresponding petrophysical properties. B. and C. Dominant frequency attribute seismic profiles along with spectral analysis data from Resolution and Allison guyots, respectively. A comparison between seismic profiles (D.) displaying the interpreted sills at Resolution and Allison guyots against the results of the seismic facies forward modelling of the conceptual geologic model from core descriptions (E.) at Site 865 using 65 and 75 Hz frequencies, both D. and E. have the same vertical scale. The dashed box in E. highlights the area displayed in the synthetic seismic facies forward models. 111

Figure 3.7. Seismic interpretation of the magmatic and hydrothermal system in Resolution Guyot. The seismic profile shows the seismic features of SF1: magmatic sill-intrusions (i.e. high amplitude, concordant to locally crosscut relationships within the host-rock strata, sheet-like shape, and abrupt terminations) and their associated SF2: hydrothermal vents and smaller scale fluid flow pipes (i.e. eye-, crater-, mounded-, or dome-shaped geometry of their upper parts, upward bending of surrounding seismic reflections, disrupted reflections within SF2, and their intimate association with underlying magmatic sill-intrusion). The highlighted part with transparent green box represents the approximate depths of the dolomite body(ies) projected away from Site 866. 112

Figure 3.8. Seismic interpretation of the magmatic and hydrothermal system in Allison Guyot. The seismic profile shows the seismic features of SF1: magmatic sill-intrusions (i.e. high amplitude, concordant to locally crosscut relationships within the host-rock strata, sheet-like shape, and abrupt terminations) and their associated SF2: hydrothermal vents and smaller scale fluid flow pipes (i.e. eye-, crater-, mounded-, or dome-shaped geometry of their upper parts, upward bending of surrounding seismic reflections, disrupted reflections within SF2, and their intimate association with underlying magmatic sill-intrusion). The highlighted part with transparent green box represents the approximate depths of the dolomite body(ies) projected away from Site 865. _____ 113

Figure 3.9. Core photographs of the dolomitised succession at Site 866, Resolution Guyot. The scale bar represents 30 cm. The naming of the cores is as follows: core number, core type (R: rotary coring), and section number. A. Core photo showing the beige and cream hues of limestone (LST) oolitic grainstone (738 mbsf). B. Core photo showing light brown partially dolomitised limestone (LST) of peloidal bioclastic grainstone (1174 mbsf). C. Core photo of beige colour of patchy dolomitised limestone of peloidal wacke-to pack-stone with few replacive dolomites (RD) (1309 mbsf). D. Core photo showing in the upper part non-dolomitised limestone (peloidal and oolitic grainstone) while the lower part is dolomitised with replacive dolomites and dolomite cement (1358 mbsf). E. Core photo of dark brown dolostone with preserved calcitic grains, dolomite cements, and replacive dolomites. The lower part of the photo shows non-dolomitised limestone (1457 mbsf). F. Core photo of light brown colour of peloidal grainstone of partially dolomitised limestone (1468 mbsf). D, E, and F represent partially-totally dolomitised intervals alternating with limestones. G. Massive dolostone of oncoidal and oolitic pack- and grain-stone (1550 mbsf). The photo shows calcitic grains, replaced grains with dolomites, and mouldic porosities of dissolved ooids and onocolites which are filled totally or partially with dolomite cements. H. Core photo of massive dolostone of oncoidal and oolitic grain- to rud-stone. (1592 mbsf). The photo shows calcitic grains, replaced grains with dolomites, and mouldic porosities of dissolved ooids and onocolites which are partially or totally filled with dolomite cements. _____ 117

Figure 3.10 Dolomite distribution versus depth at Site 866 based on integrating core descriptions, MgO%, and dolomite% using grain density along with measured porosities (Sager et al., 1993a) and facies templates (Arnaud et al., 1995). The green boxes highlight the dolomitised intervals. Facies numbers, based on (Arnaud et al., 1995), are: Facies 0: Fine-grained Pelsparites, Facies 1: Peloosparites and Oopelsparites with Reworked Ooids, Facies 2: Well-sorted Oosparites to Oomicrites, Facies 3: Peloosparites and Peloomicrites, Facies 4: Oo-oncosparites with Rounded Micritic Oncoids, Facies 5: Pelsparite and Pelmicrite with Echinoderm Plates and Small Benthic Foraminifers, Facies 6: Coarse-grained Biosparites with Rounded Elements, Facies 7: Coarse-grained Biosparites with Rudist and Gastropod Shells, Facies 8: Pelbiomicrites and Pelbiosparites with Benthic Foraminifers, Facies 9: Micrites and Pelmicrites with Sponge Spicules and Large Benthic Foraminifers, Facies 10: Micrites and Biomicrites with Large Foraminifers, Facies 11: Micrite and Pelmicrite with Rudists and Gastropods, Facies 12: Micrite and Pelmicrite with Green Algae, Facies 13: Micrite with Ostracodes and Small Benthic Foraminifers, Facies 14: Micrite and Pelmicrite with Bird's Eyes, Facies 15: Micrite and Pelmicrite with Oncolites, Facies 16: Micrite-Pelmicrite and Dolomicrite-Dolopelmicrite with Algal-Microbial Mats, Facies 17: Micrite and Dolomicrite with Thin Sedimentary Laminations, Facies 18: Micrite with Desiccation Cracks. 118

Figure 3.11. Thin-section photomicrographs showing plane polarised light (PPL) and crossed polarised light (XPL). A. and B. Photomicrographs from totally dolomitised intervals showing replacive dolomites (RD) and dolomite cement (DC) with fabric preservation of ooids (Oo), oncoids (Oc) and peloids (Pl), from samples at depths 1551 and 1594, respectively. C. Photomicrograph from partially dolomitised interval showing outlines of original fabric and partially dolomitisation of muddy matrix (Mc), from a sample at depth 1446 mbsf. D. Patchy dolomitised limestone, from a sample at depth 1175 mbsf. E. Pervasively dolomitised limestone with fabric preservation, from a sample at depth 1165 mbsf. F. Partially filled vug with dolomite cement in a wackestone, from a sample at depth 1137 mbsf._____ 120

Figure 3.12. Thin-section photomicrographs showing plane polarised light (PPL) and cathodoluminescence (CL). Concentric to oscillatory zoned luminescence of dark to bright orange, dark to light brown (A–D) and bright yellow zones (D). E. Concentric to oscillatory zoned luminescence of dull to bright red and reddish orange. Thin section photomicrographs from A to E are from samples at depths 1446, 1551, 1591, 1594, 1467 mbsf, respectively. _____ 121

Figure 3.13. Geochemical analyses of the dolomite at Site 866. A. Mn and Fe plot showing a cluster of the host rock and low Fe and Mn dolomites within values of island dolomites by Budd (1997) and presence of Fe-enriched dolomites. B. Fe and Mn plot with depth showing Fe-enrichment of the dolomite close to the basement. The dashed line in panel (B) shows the location of the potential terrigenous input (T.I). C. Depositional age model of the host rock (El-Yamani et al., 2022) and the $^{87}Sr/^{86}Sr$ ages of the dolomite and $^{40}Ar/^{39}Ar$ ages of the basement and K/Ar whole-rock ages of the basement (Baker et al., 1995; Pringle and Duncan, 1995). D. $\delta^{18}O_{Dol}$ vs depth showing temperature increase with depth which is different from the expected thermal history of host rock at 1572 and 1224 mbsf between 125 and 110 Ma. 122

Figure 3.14. Geochemical analysis plot at Site 866 showing the presence of dolomites between 1620 and 1100 with absence of dolomite above that level. It also shows the peak of SiO_2% above the dolomites with no correlation with TiO_2%, Al_2O_3%, Fe_2O_3%, and Cr ppm. The figure shows the frequency analysis on log interpretation showing that the interval between 110 and 1010 mbsf is characterised by (1) 77% of RHOB is ~2.15–2.35 gm/cm^3, (2) 58% of NPHI is ~30–39 pu, and (3) 62% of DTLN is ~80–100 us/ft. 123

Figure 3.15. Conceptual model of the sills emplacement, hydrothermal vents and the released magmatic fluids interacting with the basement leaching Fe and Mg to the circulating seawater causing a slight modification of its metal content, increasing the Mg^{2+} budget, Mg/Ca ratio, and temperature which facilitated dolomitisation. The dispersed intervals rich with volcanic ash acting as an aquiclude to the upflow of the dolomitising fluids. The model shows the expected dolomite distribution away from the drilling site based on the presence of preferentially dolomitised intervals at the drilling site. 132

Figure 4.1. Phanerozoic CO_2 fluctuations [ppm] from Valdes et al. (2021). Foster CO_2 curve is the modelled CO_2 curve from Valdes et al. (2021) by removing much of the shorter-term variability in the Foster et al. (2017) Phanerozoic CO_2 curve. Smoothed CO_2 curve is an alternative curve by Valdes et al. (2021) that pass through the cloud of individual CO_2 proxy-based reconstructions and hence represents one possible reality. The figure shows global CO_2 emissions [ppm] under the shared socio-economic (SSP) and representative concentration pathways (RCP) from the pre-industrial society, 1750, to 2300 (Meinshausen et al., 2020). The grey bar highlights the overlap between the predicted CO_2 levels between 2065-2150 (~700-1250 ppm) under the different pathways and the Phanerozoic CO_2 fluctuations. The dashed lines show the Cretaceous ages of the overlap. 141

Figure 4.2. (A) The vertical gravity gradient map of the Pacific Plate (Sandwell et al., 2014; https://portal.gplates.org/portal/vertical_gravity_gradient/) showing the fracture zones, the West Pacific Seamount Province (WPSP) and its' seamount trails (Ratak, Ralik, Anewetak, Ujlan, Magellan, Northern and Southern Wake, Typhoon, and Japanese Seamount Trails), and the location of five Cretaceous Pacific isolated carbonate platforms. (B) Bathymetry maps of Resolution and Allison guyots (Keizer et al., 2001; https://earthref.org/SC/#top) showing the Ocean Drilling Program Leg 143 sites (Site 865 and Site 866), 2D seismic surveys, and locations of figures in this study. 144

Figure 4.3. (A) Maps of the central Pacific Basin illustrating volcanic features of the Pacific Ocean including Line Islands, the Mid-Pacific Mountains, Necker Ridge, Northern Volcanic Province, and the Pukapuka and Boudeuse Ridges. The map A.2 shows the age progression of the "hotspot" tracks for the proposed Larson melt region. Triangles denote locations of dated seamounts. Colours of seamounts and hotspot tracks indicate age of feature. The red arrow in map A.2 shows the age when Larson Melt Region left the Mid-Pacific Mountains (after 100 Ma) (B) Series of tectonic reconstructions of the Pacific plate illustrating the melt source and timing of various eruptive events related to the Line Islands system. Motion paths of the Larson melt region (yellow lines) and previously identified hotspots potentially contributing to the Line Islands system (blue lines) are shown. Pink circles are locations of selected upward-projected shear-wave anomaly isosurfaces representing the melt sources of mantle plumes and hotspots (French and Romanowicz, 2015). Maps are adapted from Pockalny et al. (2021). 145

Figure 4.4. Lithostratigraphic columns of Allison Guyot Site 865 and Resolution Guyot Site 866 (reproduced from El-Yamani et al., 2022a; Sager et al., 1993a, b). The figure summarises the main lithological and fossil content

of the different lithostratigraphic units at the drill-sites. It shows the distribution of the different seismic facies (SF), seismic units (SU), and seismic horizons (e.g. H1-AG) tied with the drill-sites. SGR; Spectral Gamma Ray, U; Uranium log. At Site 866, the interpreted horizons by El-Yamani et al. (2022) are displayed with the adapted naming (refer to the text for the naming convention). 146

Figure 4.5. Criteria for determining apparent age of magmatic intrusions based on stratigraphic stratal terminations. (A) Schematic sketch of a hydrothermal vent complex illustrating the palaeo-seabed at time of venting on which a dome is down-lapping (modified from Manton et al., 2022). (B) Seismic profile showing the apparent age of the Paleocene-Eocene transition magmatic emplacement in the Møre Basin (modified from Kjoberg et al., 2017) based on interpreting the palaeo-seabed at time of venting on which a dome is down-lapping. (C and D) Schematic sketches of intrusion-related surface uplift and forced folding and the consequent reflection configurations (modified from Magee et al., 2014). (D) Schematic sketch showing the apparent age of magmatic emplacement as the age range between palaeo-surface at time of intrusion and the onlapping strata. 150

Figure 4.6. Correlation between the low latitude calibrated composite reference $\delta^{13}C_{carb}$ curve (reproduced from Herrle et al., 2015, using published data from Tethyan sections of Erba et al., 1999; Gale et al., 2011; Herrle et al., 2004) and the $\delta^{13}Cc_{arb}$ curve of Resolution Guyot (correlation lines highlighted in green; El-Yamani et al., 2022) and $\delta^{13}C_{carb}$ curve of Allison Guyot (correlation lines highlighted in red) using carbon isotope data from Jenkyns (1995). The figure shows strontium isotope ($^{87}Sr/^{86}Sr$) age model at both guyots based on using strontium isotope data from Jenkyns et al. (1995) and the values in the reference curve of McArthur et al. (2012, version 5B). Tying points in strontium isotope ($^{87}Sr/^{86}Sr$) age model of Allison Guyot are filled with pink. 155

Figure 4.7. Seismic interpretation of the different magmatism related structures at Resolution Guyot in relation to the identified seismic horizons. (A and B) Seismic amplitude profiles from Resolution Guyot showing the interpreted sills and the associated hydrothermal vents with crater upper termini onlapped and filled by vent fill and pelagic deposits. 156

Figure 4.8. (A) Seismic amplitude profile from Allison Guyot showing the interpreted sills and the associated hydrothermal vents with dome upper termini onlapped by pelagic deposits. (B) Seismic amplitude profile from Allison Guyot showing the interpreted sills and the associated suprasill forced folds onlapped by pelagic deposits. 157

Figure 4.9. Timing of magmatism in the Mid-Pacific guyots by interpreting magma associated structures in closer-look of uninterpreted and closer look seismic profiles along with schematic representations of the interpretations. 158

Figure 4.10. Seismic amplitude and root-mean-square-amplitude profiles in Allison (A) and Resolution (B) guyots showing their sills intrusions and the interpreted thicknesses. Seismic profiles are in two-way time milliseconds. The horizontal scale is 1,250 m. 159

Figure 4.11. Timing of (1) deposition of shallow marine Cretaceous carbonates at Allison and Resolution guyot, (2) the radiometric age dating of the different basement samples at Resolution, Allison, and Jacqueline guyots using data from Winterer et al. (1993), Pringle and Duncan (1995), and Clouard and Bonneville (2005), (3) the apparent ages of the magmatic episodes interpreted in this study based on seismic stratigraphic principles of interpreting timing of magmatism based on the associated magmatic structures, (4) qualitative representation of Larson Melt Region migration within and outside the Mid-Pacific Mountains, and (5) five time steps of the new tectonic reconstruction of the Pacific Plate (Pockalny et al., 2021) showing the different hotspot migration pathways in relation to the Mid-Pacific Mountains. The figure highlights the overlap, by light transparent purple box, between the cessation of the shallow marine carbonate sedimentation and subaerial exposure at Allison and Resolution guyots, the radiometric ages of some basement samples at Allison and Jacqueline guyots, and the apparent age range of the interpreted magmatic events in this study in Allison and Resolution guyot. 163

Figure 4.12. Forced folding and surface uplift associated with the magmatic emplacement in Allison Guyot. (A) Seismic amplitude profile from Allison Guyot showing the broad doming and surface uplift related to the magmatic

emplacement within the Cretaceous sedimentary succession. The interpretation of the magmatic sills between H1-AG and H2-AG and the broad doming of H4-AG shows spatial alignment. Horizon H3-AG was used to interpret the forced surface uplift amplitude displaying a range of ~100 m using interval velocity of 2,650 m/s (Sager et al., 1993b). (b) TWT map of Horizon H4-AG (topmost surface of the shallow-marine Cretaceous atoll at Allison Guyot) showing the spatial alignment between interpreted sills (highlighted by lemon green lines) with the interpreted surface uplift and forced folding (highlighted by white dashed line). _____ 164

Figure 4.13. The growth potential of the different carbonate grains in the Mid-Pacific atolls versus the possible rates of relative sea level rise during the Cenomanian eustatic rise and the dynamic subsidence induced from the migration of the Mid-Pacific atolls away off the Larson Melt Region hotspot swell. Carbonate grains and their associated production rates are: Ooid (Harris, 1979), Lagoonal Muds (Broecker and Takahashi, 1966; Robbins et al., 1997), Algal Mats (Chivas et al. 1990; Reid and Browne, 1991; Planavsky and Ginsburg, 2009; Jahnert and Collins, 2012), Corals (Gischler et al., 2023), Individual Rudists (Steuber et al., 1998), Calci-sponge (proifera) (Fallon and Guilderson, 2005), carbonate production for intervals of 10^2–10^5 yr (Schlager 1999), Requieniid vertical accumulation rate over 10^4-10^5 yr (Masse and Fenerci-Masse, 2006). _____ 167

Figure 4.14. The demise mechanism of the Cretaceous Pacific atolls showing the journey of the Mid-Pacific guyots from (1) thermal subsidence of the basement and (2) carbonate deposition to (3) the magmatic emplacement, the associated uplift, and (4) the cessation of the shallow marine carbonate deposition to (5) the rapid subsidence of the basement after cooling of magma, degassing of the associated hydrothermal system, and moving of the Mid-Pacific guyots away from the hotspot swell. The black dashed line shows the associated hotspot swell dynamic uplift. _____ 170

Figure 5.1 Cycle of the birth, rise, caldera-formation, emergence, subsidence, and the collapse of a seamount, ending with fragmentation of the seamounts in subduction zones (modified from Staudigel and Clague, 2010). The Pacific Cretaceous isolated carbonate platforms are represented by stage 5 (volcanically extinct seamounts) which is prior to the destructive subduction tectonism in stage 6. _____ 178

Figure 5.2 Comparison between (A) the sedimentological model of the isolated carbonate platform Dunquin South in Porcupine Basin, Ireland (modified after Gomez et al., 2022) and the 3D depositional model of Resolution Guyot carbonate atoll showing the palaeogeographic reconstruction of the different depositional environments and their corresponding seismic facies. The depositional model was generated by integrating the interpreted seismic facies with satellite images from the Glorieuses archipelago. Note that the legend of panel (A) is labelled from a to i which were used to link the highlight the similar facies in panel (B), appearing in red bold font. 182

Figure 5.3 Map view of the isolated carbonate platforms of (A) Resolution Guyot and (B) Kashagan (adapted from Ronchi et al., 2010). The figure illustrates similarities in the distribution of different karstification geomorphologic features between the two platforms. In Resolution Guyot (A), laterally extensive karst horizons predominantly occur in the platform interior, matching the cyclic meteoric diagenesis zones observed in the Kashagan platform (B). The palaeocaves in Resolution Guyot are primarily located along the platform margin, influenced by flank margin fractures, a pattern closely resembling the distribution of flank-margin karst features in the Kashagan platform (B). _____ 183

Figure 5.4 Seismic amplitude profiles from (A, B) Resolution Guyot and (C) the Middle Miocene Mega Platform, Luconia Province, Offshore Sarawak, Malaysia (modified after Vahrenkamp et al., 2004). The figure highlights the difference between the thicknesses of karstified intervals in Cretaceous isolated carbonate platforms (A, B) and Miocene counterparts (C; highlighted by cyan square bracket). The comparison reflects development of thicker karstified intervals in Cretaceous isolated carbonate platforms. _____ 184

Figure 5.5 (A) The predicted global distribution of *Porites lobata* where red, green, and blue colours mean lost, gained and retained habitat, respectively under a 'business as usual' Representative Concentration Pathway 8.5 climate-change scenario in 2100 (Cacciapaglia and van Woesik, 2015). (B) The simulated annual sea surface temperature variability over Tropical Indo-Pacific region under RCP 8.5 conditions in year 2100 (Zhang et al., 2020b). (C) Modelled global sea surface temperatures during the Cretaceous (111, 102.6, 97.2, 69 Ma) at the locations of the

Pacific Cretaceous isolated carbonate platforms (starting from the top left with Takuyo-Daisan then MIT then Resolution and Allison, and finally Wodejebato. Maps were retrieved using the Earth Systems Modelling Result website from the following URL https://www.paleo.bristol.ac.uk/ummodel/users/Valdes_et_al_2021/new2/; Valdes et al., 2021). 189

Figure 5.6 The Pacific Atolls to be investigated as part of the CARAPACE Project (Adapted from John et al., 2021). 195

Figure 5.7 Seismic interpretation of multiple intraplate volcanisms in the Mid-Pacific Mountains Cretaceous isolated carbonate platforms. (A) Seismic amplitude profiles showing the apparent ages of multiple volcanisms in Resolution Guyot based on stratal terminations of the upper vent associated with the emplacement. (B) Seismic amplitude profiles showing the apparent age of intraplate volcanisms in Allison Guyot based on stratal terminations of the volcanic cone with the surrounding sediments. (C) Timelines of eruption timing and melt delivery style for each of melt sources and their effect on the Mid-Pacific Mountains (adapted from Pockalny et al., 2021). 197

Figure 5.8 A preliminary seismic interpretation of a seismic amplitude profile from Resolution Guyot. The interpretation tentatively reveals a potential mounded structure situated in the middle of the hydrothermal vent, surrounded by amplitude anomalies. This observation may suggest the occurrence of multiple episodes of hydrothermal venting along the same fluid flow pathway, indicating a phenomenon known as hydrothermal vent reutilisation. 198

Figure A1.1 Correlation and tie-points between the data from Resolution Guyot (ODP Site 866) and Reference curve (reproduced from Herrle et al., 2015, using published data from Tethyan sections of Erba et al., 1999; Herrle et al., 2004; Gale et al., 2011, and calibrated using Gradstein et al., 2012; GTS2012). 230

Figure A1.2 Tie-points and strontium isotope stratigraphy for Resolution Guyot using reference curves of McArthur et al. (2012, version 5B) and Bodin et al. (2015). Some of the points have values different than their tie-points in the reference curve(s). These points were selected as they show similar trend in the values before and after it. Regardless this shift in the values of some points, the plotted data points with depth has similar trends (highlighted by arrows) to the reference curves (McArthur et al., 2012; Bodin et al., 2015). 231

Figure A1.3 The calculation of the sedimentation rate between every 2 successive tie-points to calculate the ages for the succession in between through linear interpolation. 235

Figure B.1 Possible ages of the dolomites spanning from ~125.6 Ma to ~107.5 Ma. 262

CHAPTER ONE

INTRODUCTION & LITERATURE REVIEW

1.1 Research Problems and Rationale

Shallow-marine carbonate sediments constitute one of the most abundant and widely used archives recording Earth's evolution, spanning over 3 billion years. These biochemical sediments, primarily composed of precipitated metals (e.g. Ca^{2+}, Mg^{2+}) and carbonate ions (CO_3^{2-}) in equilibrium with ancient seawater with minimal detrital influence, offer insights into palaeo-environmental conditions. In contemporary ecosystems, modern carbonate systems host ≥25% of marine life (Knowlton et al., 2010) and play a crucial role as carbon sinks, sequestering a quarter of the global CO_2 emissions within marine sediments (Jones et al., 2015). Beyond their ecological and environmental significance, shallow-water carbonate rocks hold substantial economic value, serving as vital reservoirs for water and hydrocarbon resources (e.g. Gregg et al., 2015), while also presenting opportunities for CO_2 storage (e.g. Seyyedi et al., 2020).

Among the Phanerozoic carbonate rock-record, the Cretaceous (145–66 Ma) stands out as an exceptional period characterised by high average sea-surface temperatures (SSTs; O'Brien et al., 2017; Valdes et al., 2021), short intervals of extreme warmth (Foster et al., 2018), and the highest sea level in the Phanerozoic (75–250 m higher than the present day mean sea level, Haq, 2014). These conditions coincided with widespread carbonate deposition in both pelagic and neritic environments (Steuber et al., 2023), making the Cretaceous one of the most prolific periods of neritic carbonate platforms development (Kiessling et al., 2003). The Cretaceous carbonate rock-record has global significance, hosting ~28% of major reservoirs and ~16% of the world's hydrocarbon reserves (Ulmishek and Klemme, 1990; Simo et al., 1993; Kendall et al., 2009). In addition, Cretaceous carbonate deposits also contain valuable resources such as bauxite, sedimentary iron, phosphate ores, and building materials (Scott et al., 1993). This shows the great importance to understand factors controlling initiation, configuration, development, and mechanisms involved in the demise of Cretaceous rudist-bearing shallow marine carbonates. Despite being the focus of many studies, there are still unknowns and challenges associated with unravelling these complexities (e.g. Bialik et al., 2021a).

1.1.1 Stratigraphic Evolution of the Cretaceous Isolated Carbonate Platforms

Across the diverse spectrum of T-factory carbonate depositional systems (T stands for "tropical" and "top-of-the-water-column"; sensu Schlager, 2005), isolated carbonate platforms (ICPs) stand

as one of the most striking constructional edifices on Earth as they are "imposing and complex" (Rankey, 2023). Since the Archean era, thousands of ICPs have undergone phases of initiation, expansion, contraction, and eventual termination, offering unique records of Phanerozoic changes encompassing sea level fluctuations, palaeoceanographic shifts, palaeogeographic reconfigurations, marine ecology, and evolution (e.g. Schlanger and Premoli Silva, 1986; Robinson, 2011; Rankey, 2020, 2023). Our current understanding about stratigraphic evolution and economic potentials of ICPs predominantly comes from previous studies on the Miocene and Oligo-Miocene ICPs due to their commercial significance (Greenlee and Lehmann, 1993; Bachtel et al., 2004; Burgess et al., 2013; Courgeon et al., 2016a; Paumard et al., 2017; Rankey et al., 2019). Rankey (2023) in his compiled database of the Phanerozoic ICPs (n= 850) showed that ICPs are unevenly distributed through geologic time, 70% are of Cenozoic age, 11% are Mesozoic, and 19% are Palaeozoic. This was reflected on the author's compiled database as ~80% of the studies were on Miocene and Oligocene-Miocene ICPs (Figure 1.1; Rankey, 2023). The database acknowledges limitations in its coverage of Phanerozoic ICPs, as it does not provide a comprehensive description of each platform on Earth (Rankey, 2023). Notably, it lacks equitable representation of platforms across both temporal and spatial dimensions. This bias partly mirrors genuine, long-term fluctuations in the prevalence of isolated carbonate platforms, similar to changes observed in reef abundance (Kiessling, 2002; Rankey, 2023). Nevertheless, the discovery of the Cretaceous ICP of Zohr Field represented a pivotal moment in the global exploration efforts for similar platforms in the Eastern Mediterranean (Figure 1.2; Ghalayini et al., 2018; Papadimitriou et al., 2018; El-Oribi et al., 2022; Nader et al., 2023). Interests in exploring Cretaceous ICPs extend to other regions such as the Atlantic margins of Namibia and South Africa and the Porcupine Basin in Ireland (Lambregts et al., 2014; McDermott et al., 2015; Intawong et al., 2019; Loma-Villacorta et al., 2022; Rochelle-Bates et al., 2024). The promising economic importance of the Cretaceous ICPs has reignited efforts to understand the factors controlling their stratigraphic evolution, diagenesis, and termination as highlighted in the study by Bialik et al. (2021a) on the early Cenomanian volcanic atolls along the eastern Levant margin.

The extensive knowledge acquired from studying Miocene and Oligo-Miocene ICPs (Figure 1.1; Rankey, 2023) cannot be directly applied to their Cretaceous counterparts due to the significant differences between them (Rusciadelli and Shiner, 2018). Notably, Miocene and Oligo-Miocene ICPs (a) were developed on land-attached shelves, (b) were associated closely with clastic systems, (c) have various geometrical growth patterns (backstepping, aggrading, and prograding) and simpler tectonic environments, while the Cretaceous ICPs (a) were formed on isolated microcontinents or volcanic islands, (b) experienced complex tectonic settings, (c) have mainly

prograding and aggrading geometrical growth patterns and (d) differ in carbonate factory characteristics and sea level variations (Figure 1.1; Pritchard, 2014; Rusciadelli and Shiner, 2018; Saqab et al., 2021; Rankey, 2023; Rochelle-Bates et al., 2024). For instance, differences in large-scale meteoric diagenesis and karstification highlight distinctions between Miocene and Oligo-Miocene ICPs and Cretaceous ICPs (e.g. Rusciadelli and Shiner, 2018). Miocene and Oligo-Miocene ICPs in SE Asia were emerged due to relatively short-term (100s Kyr), low-amplitude (10s m) 3rd order glacio-eustatic relative sea level changes (Figure 1.3) which led to intense meteoric diagenesis, creating widespread vuggy-mouldic porosity by leaching skeletal grains in highstand system tracts (Sun and Esteban, 1994). Finer-grained transgressive system tracts typically lack meteoric diagenesis, accentuating differences in the original depositional fabric. This contributes to the distinctive layered, parallel, high-amplitude, continuous seismic facies of these systems (e.g. Gartner et al., 2004; Neuhaus et al., 2004; Figure 1.3). In contrast, the Cretaceous ICPs have generally experienced exposure associated with long-term (≥1-10s My), high-amplitude (>100 m; Figure 1.3) relative sea level changes, often involving extensive karstification that crosscuts depositional facies boundaries (Cozzi et al., 2018; Rusciadelli and Shiner, 2018; El-Oribi et al., 2022; Burchette et al., 2023). The crosscutting nature of these diagenetic events means that diagenesis tends to reduce the already subtle and gradual differences in depositional fabric and so contributes to the often homogeneous and seismically transparent internal character of the ICPs (e.g. Eberli et al., 2004a; Rusciadelli and Shiner, 2018; Figure 1.4).

Therefore, finding archetypes of the Cretaceous ICPs is pivotal to address (a) how they developed, (b) what later diagenetic impacts affected them, (c) how they demised, and (d) how their seismic-reflection expressions differ from those of their Miocene and Oligo-Miocene counterparts.

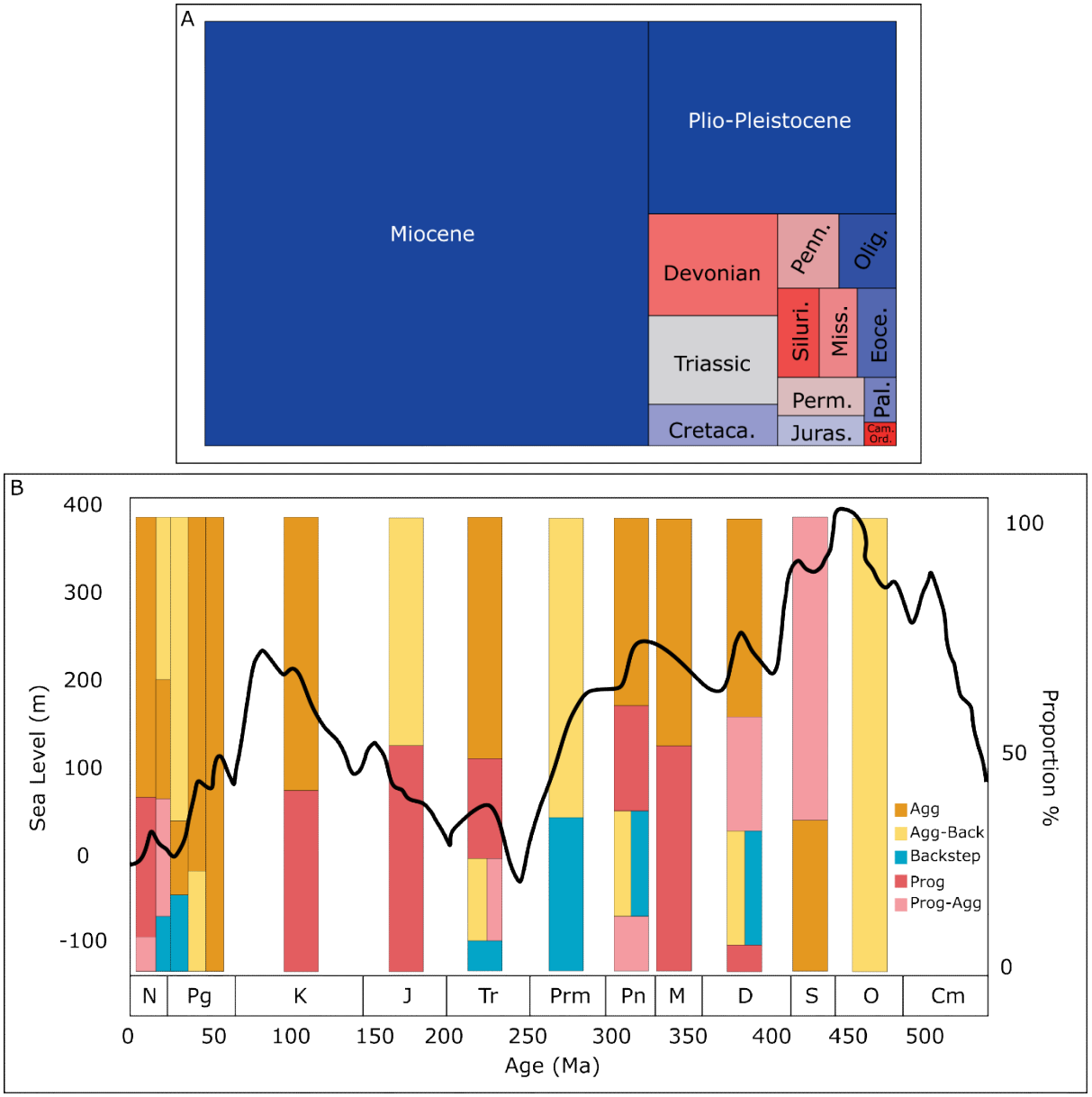


Figure 1.1 (A) The relative proportion of the Phanerozoic isolated carbonate platforms of each age in the compiled database by Rankey (2023). Relative size of boxes in the plots are proportional to the number of data points. Note the significant difference between Cretaceous and Miocene and Plio-Pleistocene. (B) Graph of the relative proportion of different growth patterns for each geologic age (Rankey, 2023) overlain by long-term sea level curve of Hallam (1984). Note the significant difference between the growth patterns of the Cretaceous and Miocene and Plio-Pleistocene isolated carbonate platforms.

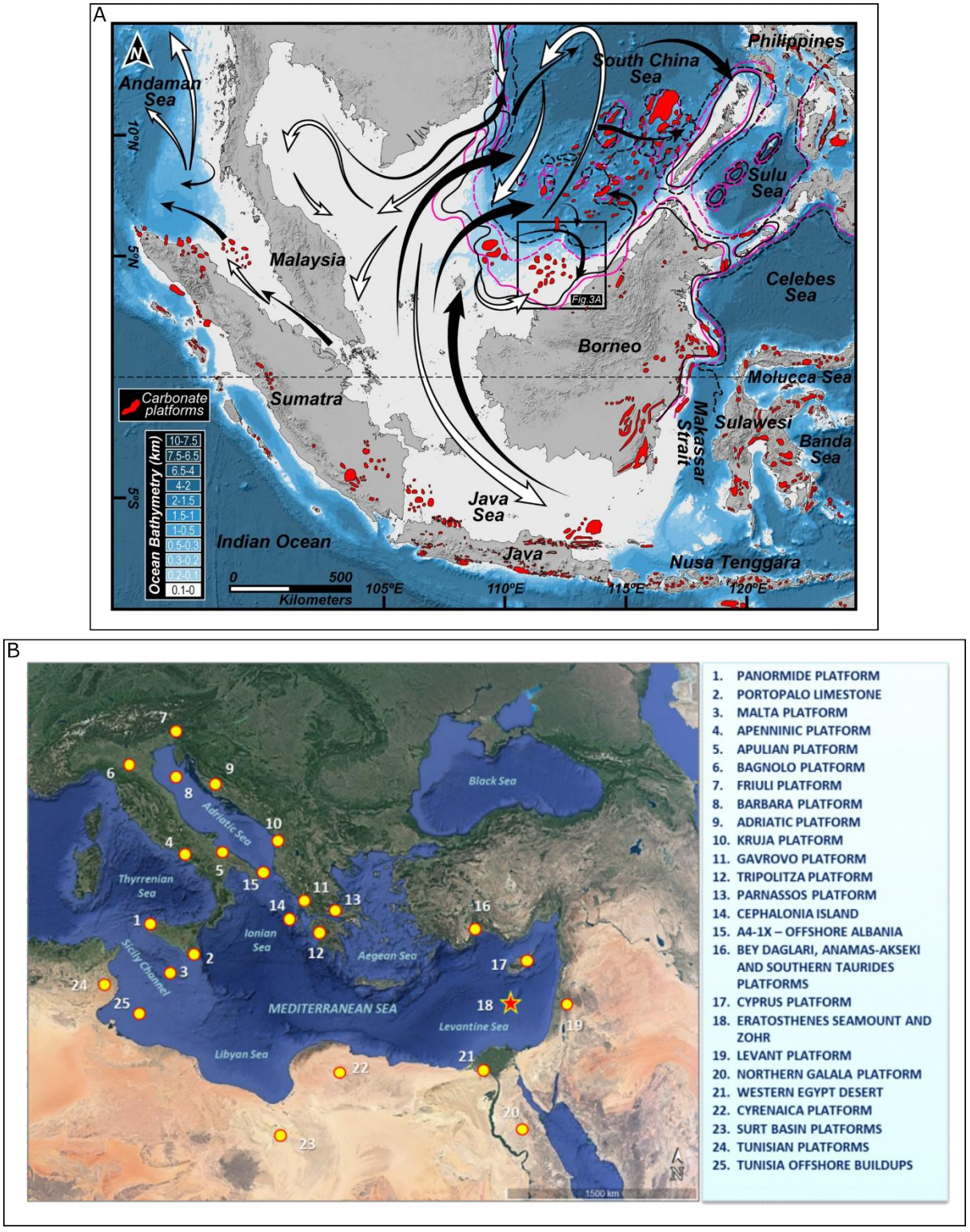


Figure 1.2 Examples of the global distribution of the isolated carbonate platforms of (A) the Cenozoic age in SE Asia (Mathew et al., 2020) and (B) the Cretaceous age in the Mediterranean and Mesozoic Tethys and their possible analogues (GEPLAN CONSULTING, n.d.).

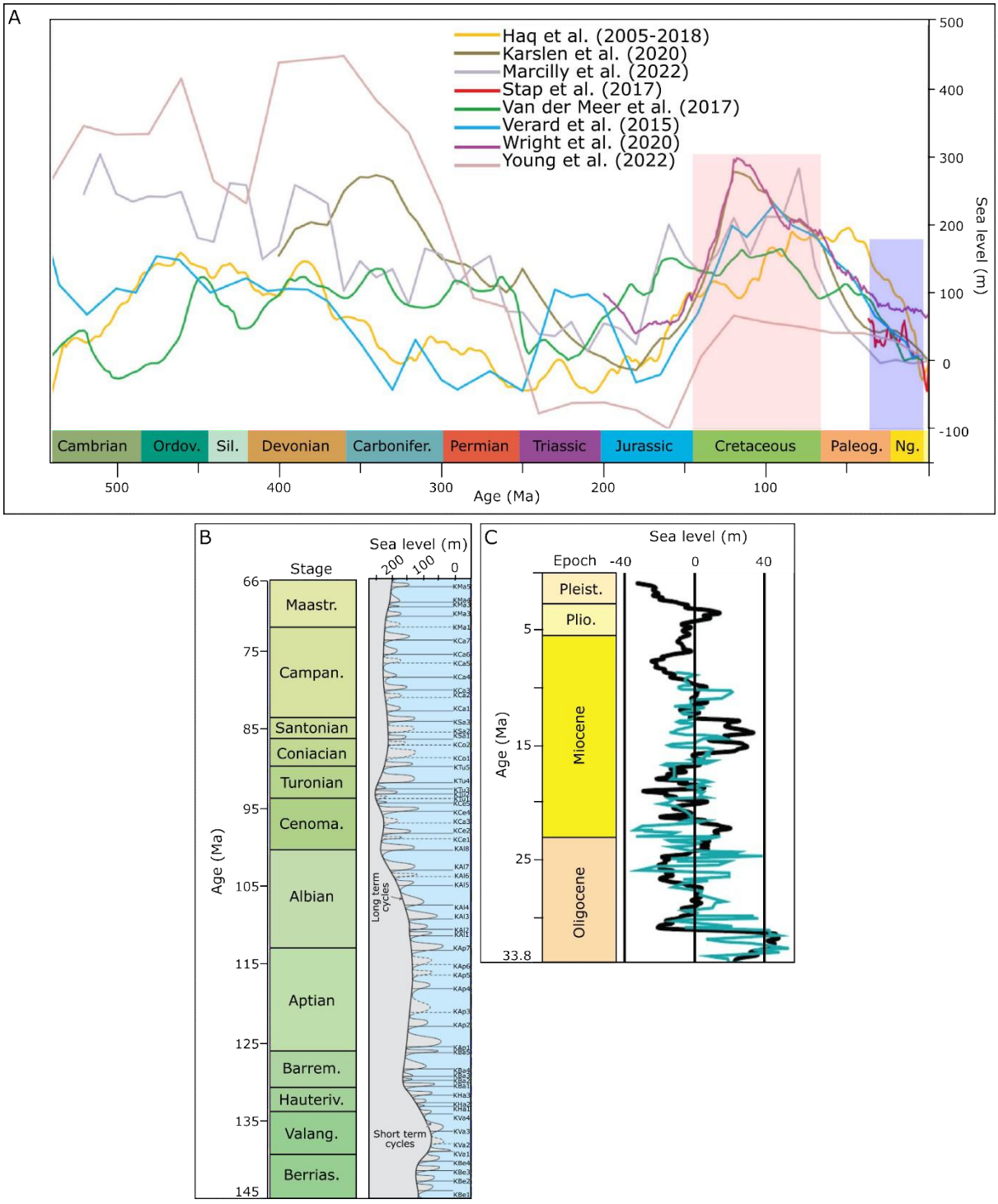


Figure 1.3 The differences between the Cretaceous and the Oligocene-Holocene long- and short-term eustasy. (A) Phanerozoic long-term sea level reconstructions from plate tectonic models (Karlsen et al., 2020; Vérard et al., 2015; Wright et al., 2020; Young et al., 2022), strontium isotopes as a proxy for ridge spreading (van der Meer et al., 2017), 'modern land' flooding (Marcilly et al., 2022), a compilation of stratigraphically derived curves of Haq et al. (Haq, 2018a, 2018b, 2014; Haq and Al-Qahtani, 2005; Haq and Schutter, 2008) and from a Late Cenozoic ice/sea level paleo-climate model, 1 Myr averaged (Stap et al., 2017). Adapted from van der Meer et al. (2022). The highlighted pink and blue boxes show the difference between the Cretaceous and the Oligocene-Holocene long-term sea level, respectively. (B) Long- and short-term curve of the Cretaceous eustasy (Haq, 2014). (C) Cenozoic sea-level curves of Miller et al. (2005) in cyan and Miller et al. (2020) in black, adapted from Burton et al. (2023).

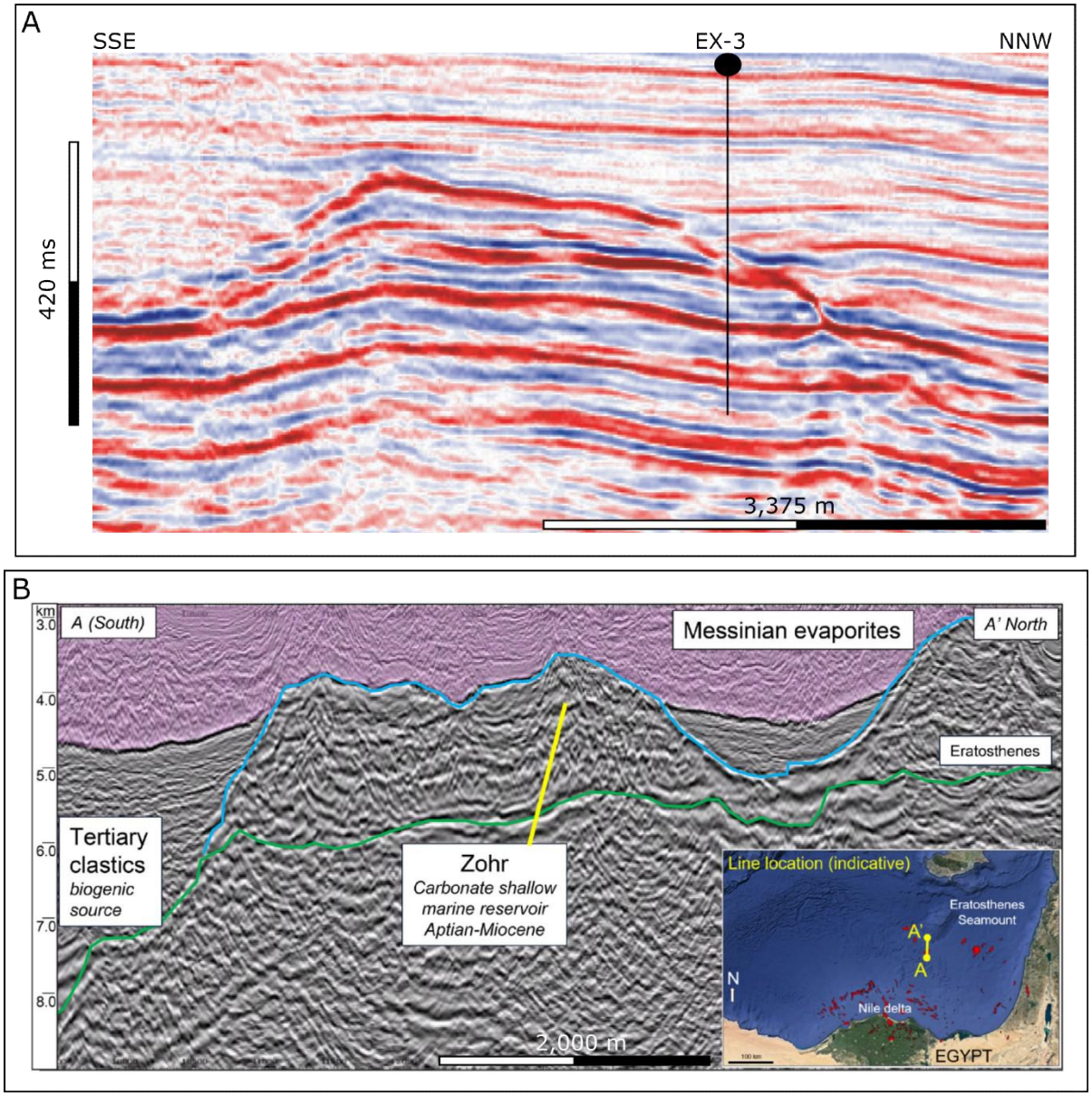


Figure 1.4 The figure shows the pronounced difference in seismic characteristics between (A) the layered, parallel, high-amplitude, continuous seismic facies that characterises the Miocene and Oligo-Miocene isolated carbonate platforms (Sarawak, Malaysia; modified from Gartner et al., 2004) and (B) the often homogeneous, seismically transparent internal characteristics, and or poor seismic imaging of many of the Cretaceous isolated carbonate platforms (Zohr discovery in the East Mediterranean; modified Lottaroli and Meciani, 2022).

1.1.2 Dolomitisation in the Cretaceous Isolated Carbonate Platforms

Shallow-marine carbonates are extremely susceptible to mineralogical and textural post-depositional alterations which occur at any time from initial deposition to deep burial and exhumation. Approximately half of the Earth's carbonate rock-record is dolomitised (Zenger et al., 1980). Dolomite ($CaMg[CO_3]_2$) is very important as a reservoir for hydrocarbons, a building material, a metallurgical flux, a host for Mississippi Valley-type base metal deposits, and freshwater aquifers (Braithwaite et al., 2004). The origin of dolomite has been a puzzling research topic for over two centuries, known as the "Dolomite Problem", owing to the challenges in synthesising dolomite under laboratory conditions resembling Earth's surface temperature and its abundance in the rock-record versus scarcity in modern sedimentary environments (e.g. Land, 1985; Gregg et al., 2015). However, recent studies challenge this view suggesting significant dolomite formation in the Neogene (e.g. Shalev et al., 2019).

Recently, studies suggested that syn-depositional and near-surface early-burial dolomitisation by marine fluids, both normal and near-normal, is more widespread than previously believed in the rock-record (Newport et al., 2017, 2020; Manche and Kaczmarek, 2019; Ryan et al., 2020), and even in modern deep ocean sediments (e.g. Shalev et al., 2019). Normal and near-normal seawater, as defined here, includes normal marine to slightly evaporated mesohaline fluids that have not reached gypsum saturation (e.g. Ryan et al., 2020). Evidence supporting this widespread dolomitisation by such marine fluids can be observed in the prevalence of dolomitised Cenozoic ICPs (e.g. Grand Cayman, Cayman Brac, Little Bahama Bank, Great Bahama Bank, Niue, Enewetak, Jamaica, and Kita-daito-jima, Schlanger et al., 1963; Land, 1973; Jones, 1989; Pleydell et al., 1990; Land, 1991; Whitaker et al., 1994; Vahrenkamp and Swart, 1994; Budd, 1997; Wheeler et al., 1999; Jones et al., 2001; Jones and Luth, 2002; Melim et al., 2002; MacNeil and Jones, 2003; Jones, 2005; Suzuki et al., 2006; Zhao and Jones, 2012a, b). These dolomites were formed via (Figure 1.5) deep cold seawater pumping below calcite saturation depth (e.g. Enewetak atoll deep-seated dolomites; Saller, 1984), reflux of slightly concentrated seawater (e.g. Machel and Burton, 1994; Wang et al., 2022), tidal pumping (e.g. Carballo et al., 1987), and Kohout convection (e.g. Aharon et al., 1987; Wheeler et al., 1999; Swart and Melim, 2000). The dolomitisation of most Cenozoic islands occurred during the Late Miocene to Late Pleistocene (~10-0.5 Ma) when seawater had high Mg^{2+} concentrations (~49-55.1 mmol) and Mg:Ca (~5.2) and was highly supersaturated with respect to dolomite (Brennan et al., 2013). In contrast, Cretaceous calcitic seawater (Horita et al., 2002; Timofeeff et al., 2006) had lower Mg^{2+} concentrations (30-42 mmol) and Mg:Ca (0.6-1.3), resulting in lower dolomite saturation (e.g. Arvidson et al., 2011). Such conditions favoured calcite precipitation over aragonite or high Mg-calcite, impacting

dolomitisation potential of seawater (Steuber and Rauch, 2005) and potentially hindering large-scale massive dolomitisation (e.g. Newport et al., 2017, 2020).

Therefore, investigating dolomitisation conditions during the Cretaceous is crucial to understand the scarcity of Cretaceous dolostones and to evaluate the effectiveness of syndepositional and near-surface early-burial dolomitisation by Cretaceous calcitic (low-Mg) seawater. Dolomitised carbonate islands and atolls (i.e. not deeply buried) offer promising targets for elucidating the origins of dolomite, as (a) the hydrological systems and fluid chemistries responsible for dolomitisation are either still operational or can be readily reconstructed, (b) the relatively limited range of dolomitisation temperatures to surface or near-surface conditions, and (d) the absence of deep burial diagenesis reduces the chemical or textural overprinting that obscures the initial origin of dolomites (Budd, 1997; Ren and Jones, 2018). Hence, investigating dolomitised ICPs of Cretaceous age would facilitate answering the aforementioned questions.

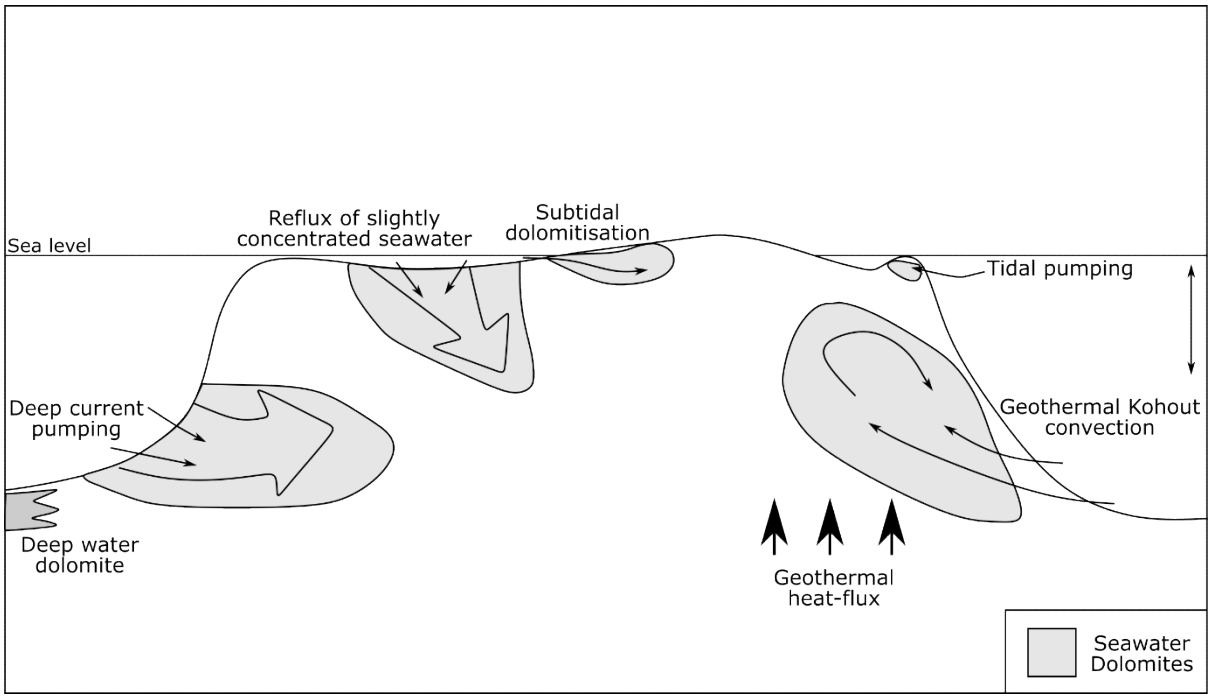


Figure 1.5 Various models of unmodified seawater dolomitisation. The figure shows that the dolomitising fluid (connate) is pumped through porous limestones at depths ranging from at surface to moderate burial (~2 km). Adapted from Warren (2000).

1.1.3 The Demise of the Cretaceous Isolated Carbonate Platforms

Throughout both modern times and geological history, climate fluctuations have exerted significant influence on Earth's surface processes. The sedimentary record of shallow-marine carbonates serves as a repository of secular palaeo-environmental changes, including atmospheric CO_2, sea-level fluctuations, occurrences of oceanic anoxic events (OAEs), ocean acidification, and variations in salinity, temperature, turbidity, and light penetration, all of which influence marine life (Figure 1.6; Hallock and Schlager, 1986; Erlich et al., 1990, 1993; Schlager, 1991; Thorne, 1992; Lenton et al., 2018). Global warming, a recurrent theme in many extinction events throughout Earth's history (Harnik et al., 2012), may arise from perturbation of the carbon cycle, triggering ocean acidification and anoxia (Figure 1.6). However, it remains uncertain whether such warming events acted as triggers or consequences of other environmental changes that ultimately led to mass extinctions (Steuber et al., 2023).

The future projections under fossil-fuel intensive SSP5-8.5 scenario suggest that CO_2 concentrations could reach or surpass Eocene and mid-Cretaceous levels (Figure 1.6; Hay, 2011; Tierney et al., 2020). These ancient analogues provide benchmarks for evaluating the increasingly sophisticated climate models utilised in forecasting future scenarios (Tierney et al., 2020). Investigating the biogeodynamics of Cretaceous shallow-marine carbonate systems may offer valuable insights for understanding (a) potential extinction risks faced by modern biota and (b) proxies for recovery and demise of modern biota under global warming (e.g. Bryers et al., 2022; Steuber et al., 2023), keeping in mind the difference between modern organisms and Cretaceous counterparts (e.g. modern corals versus Cretaceous rudists). While many modern organisms cannot survive when seawater temperatures exceed 30°C (e.g., Garrabou et al., 2009), laboratory and field studies on modern molluscs, foraminifera, and shallow-marine corals have shown that some species can tolerate temperatures as high as ~40°C (Song et al., 2014; Cacciapaglia and van Woesik, 2015; Schmidt et al., 2016; Seuront et al., 2019). Given the high susceptibility of carbonate islands and atolls to future global warming trends and the potential resemblance of future CO_2 levels to those of the Eocene and mid-Cretaceous, it is important to investigate how the Cretaceous ICPs were demised and determine whether warming events were the primary cause of their demise. This assessment may help establish whether Cretaceous ICPs can serve as analogues for modern carbonate islands intolerant to thermal stress, or if other factors influenced their demise, rendering them analogues for thermally tolerant modern counterparts.

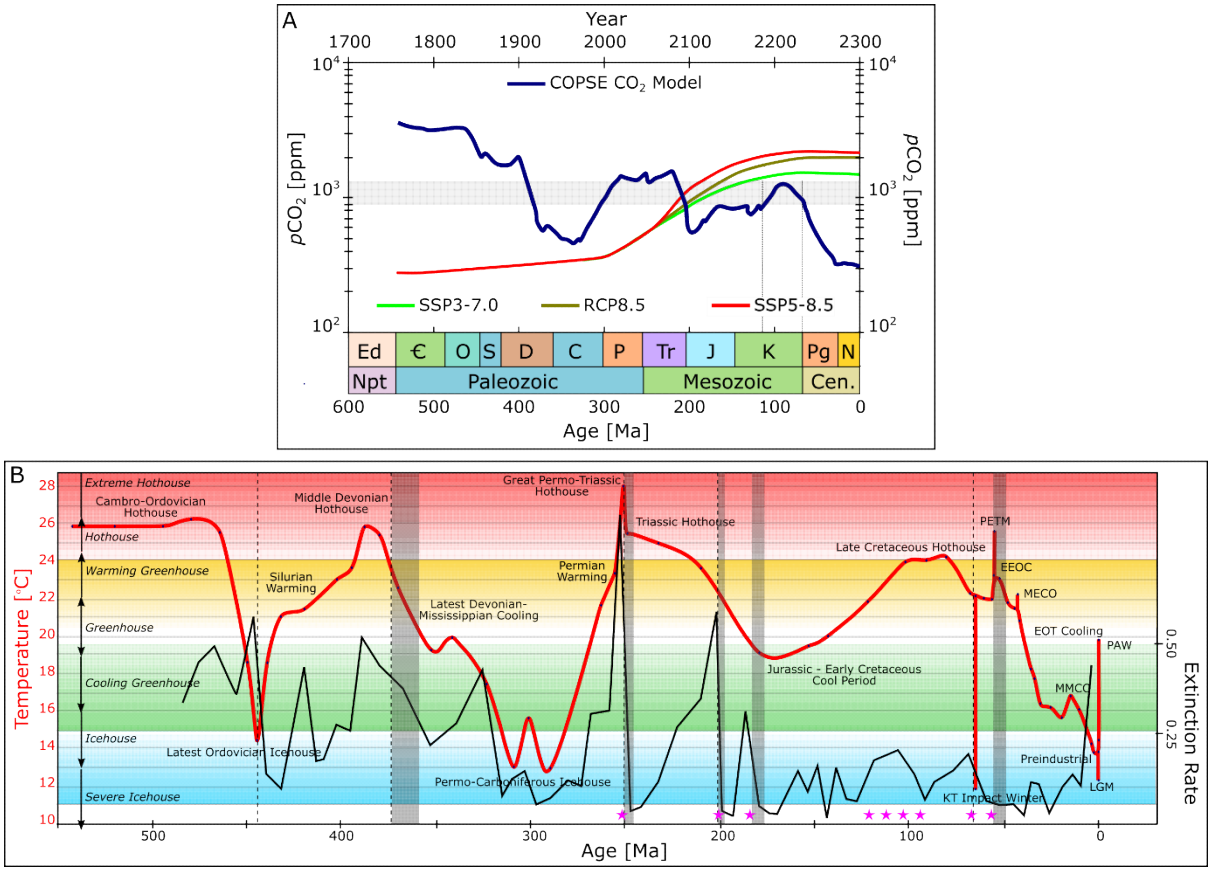


Figure 1.6 (A) Phanerozoic CO_2 fluctuations [ppm] from COPSE Model (Lenton et al., 2018) along with CO_2 emissions under the shared socio-economic (SSP) and representative concentration pathways (RCP) from the pre-industrial society, 1750, to 2300 (Meinshausen et al., 2020). The grey bar highlights the overlap between the predicted CO_2 levels between 2080-2170 (~900-1300 ppm) under the different pathways and the Phanerozoic CO_2 fluctuations. The dashed lines show the Mid-Late Cretaceous ages of the overlap. (B) The Phanerozoic global temperature curve (red curve) showing the main warming and cooling events (adapted from Scotese et al., 2015) including: PETM = Paleocene-Eocene Thermal Maximum, EEOC = Early Eocene Climatic Optimum, MECO = Mid-Eocene Climatic Optimum, EOT = Eocene-Oligocene Transition, MMCO = Mid-Miocene Climatic Optimum, LGM = Last Glacial Maximum, PAW = Post-Anthropogenic Warming. Panel (B) also shows the rates of extinction through the Phanerozoic (black curve) highlighting mass extinction (dashed black line) and reef crises (grey bands) events (modified after Harnik et al., 2012). The purple stars in panel (B) highlight the ages of ocean anoxic events and ocean acidification.

1.1.4 Thesis Broad Aim

The aim of this research is to answer several broad sedimentologic questions: what controlled the stratigraphic evolution, subaerial exposure and related karstification, island dolomitisation, and drowning of the Cretaceous ICPs? To answer these broad questions, I study the Cretaceous Mid-Pacific ICPs. The geological settings of the Mid-Pacific Cretaceous ICPs were very suitable to do this study because they (1) were not exposed to terrigenous inputs, (2) haven't been deeply buried, and (3) haven't suffered from destructive tectonism. In this chapter, I will introduce the Mid-Pacific Cretaceous ICPs and take a brief dive into the literature to describe our current understanding and identify the gaps in our knowledge. Subsequently, I will provide the detailed aims and objectives of this study followed by a review of the available research data. At the end of this chapter, I will explain the thesis structure. The subsequent three chapters contain three stand-alone scientific papers. Some of the work has already been peer-reviewed and published, and some of it is in preparation to be submitted in the near-future. The final chapter will integrate the findings of all three chapters, to address withstanding gaps in knowledge and look to future work in the field.

1.2 The West Pacific Cretaceous Isolated Carbonate Platforms

Within the western Pacific Ocean, numerous flat-topped Cretaceous seamounts occupy the ocean floor, exhibiting distinctive organisational patterns (Figure 1.7A; Matthews et al., 1974; Winterer and Metzler, 1984; McNutt et al., 1990). These geological features are organised (a) in groups to form larger complexes, (b) along a preferential direction to form a chain, or (c) as isolated features (Figure 1.7A; Haggerty and Premoli Silva, 1995). These features were termed "guyots" by Hess (1946), and their distribution, as originally mapped, was primarily between latitudes 8°30'-27°N and longitudes 165°W-146°E. However, scattered guyots were located up to 45°N and 165°W (Jenkyns and. Wilson, 1999). Since the Early Cretaceous, volcanic activities created the West Pacific Seamount Province (WPSP; Figure 1.7A) extending from the Mid-Pacific Mountains (MPM; Figure 1.7B) to the Mariana Trench. The WPSP consists of MPM, Shatsky Rise, and Ontong Java oceanic plateaus and nine seamount trails (Ratak, Ralik, Anewetak, Ujlan, Magellan, Northern and Southern Wake, Typhoon, and Japanese Seamount Trails; Figure 1.7A; Larson, 1991; Koppers et al., 2003). The MPM is a volcanic plateau formed in a region of intense hotspot volcanism referred to as the South Pacific isotopic and thermal anomaly (SOPITA; Staudigel et al., 1991). It consists of flat-topped seamounts with shallow-marine limestone cover below pelagic caps, including Sio, Heezen, Resolution, Jacqueline, Allison, Cape Johnson, Renard, and Horizon atolls (Figure 1.7B; Winterer and Sager, 1995).

The Cretaceous Pacific seamounts have attracted significant scientific interest, particularly through the Ocean Drilling Program (ODP) Leg 143/144 conducted during 1992-1993. The aims of ODP Leg 143/144 were to address the following research questions: (a) timing and causes of platform drowning, (b) timing and amplitude of relative changes in sea level and their relation to regional tectonics and to sea-level changes recorded in other parts of the globe, (c) seamount latitude changes, as recorded in the palaeomagnetism of lagoon sediments as well as in the underlying volcanics, (d) ages of the volcanic edifices, as clues to the direction and rates of age progression, (e) longevity of the mantle source, (f) bio-provinciality of the Cretaceous reefal organisms and post-reefal palaeoceanographic reconstruction (Sager et al., 1992). During the ODP Leg 143 expedition, Resolution and Allison guyots were the main targets for the drilling campaign (Figure 1.8; Sager et al., 1993 a, b, and c). Resolution Guyot was drilled at three discrete sites (sites 866-868; Sager et al., 1993 a, b), facilitating a radial transect from the periphery of the platform to its interior, while Allison Guyot underwent drilling at only one site, providing access to its platform interior (Site 865; Sager et al., 1993c). ODP Leg 144 drilled Limalok (Site 871), Lo-En (Site 872), and Wodejebato (Sites 873-877) guyots in the Marshall Islands chain, MIT Guyot (Site 878), a

drowned atoll midway between the Marshall Islands and Japan, and Takuyo-Daisan Guyot (Sites 879-880) in the Japanese Seamount Province (Figure 1.7A; Haggerty and Premoli Silva, 1995). Deep Sea Drilling Project (DSDP) Leg 62 was targeting the basinal deposits of MPM (DSDP Site 463), Northern Hess Rise (DSDP Site 464), and Southern Hess Rise (DSDP 465 and 466) in the North Central Pacific Ocean (Thiede et al., 1981).

In this thesis, I focus on the MPM, studying Resolution and Allison guyots due to their extensive coverage of the Cretaceous period (i.e. Hauterivian to latest Albian; Winterer and Sager, 1995) within the Pacific ICPs.

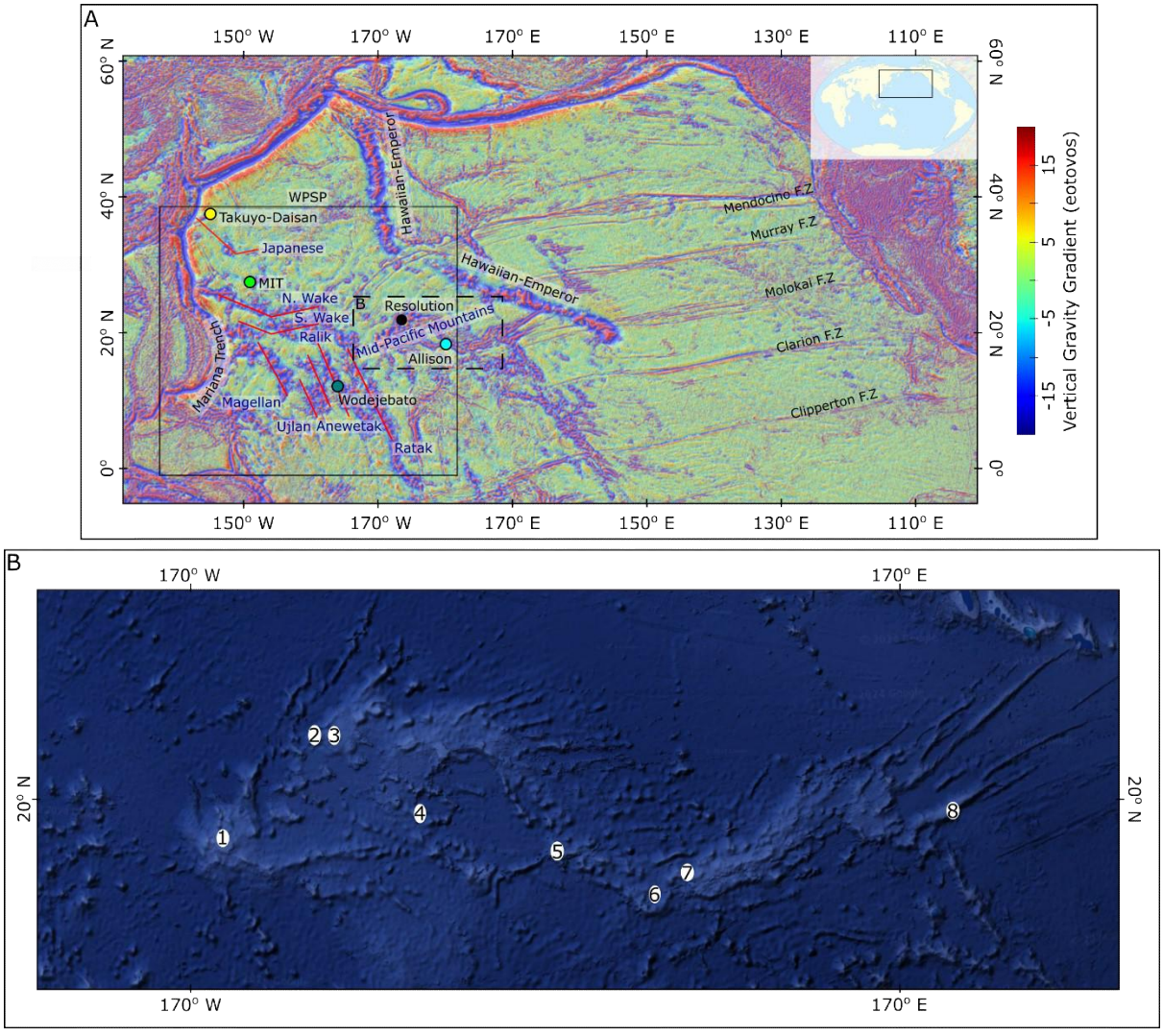


Figure 1.7 (A) The vertical gravity gradient map of the Pacific Plate (Sandwell et al., 2014; https://portal.gplates.org/portal/vertical_gravity_gradient/) showing the fracture zones, the West Pacific Seamount Province (WPSP) and its' seamount trails (Ratak, Ralik, Anewetak, Ujlan, Magellan, Northern and Southern Wake, Typhoon, and Japanese Seamount Trails), the location of five Cretaceous Pacific isolated carbonate platforms. (B) The vertical gravity gradient map of the Mid-Pacific Mountains showing the location of Sio (1), Heezen (2), Resolution (3), Jacqueline (4), Allison (5), Cape Johnson (6), Renard (7), and Horizon (8) guyots.

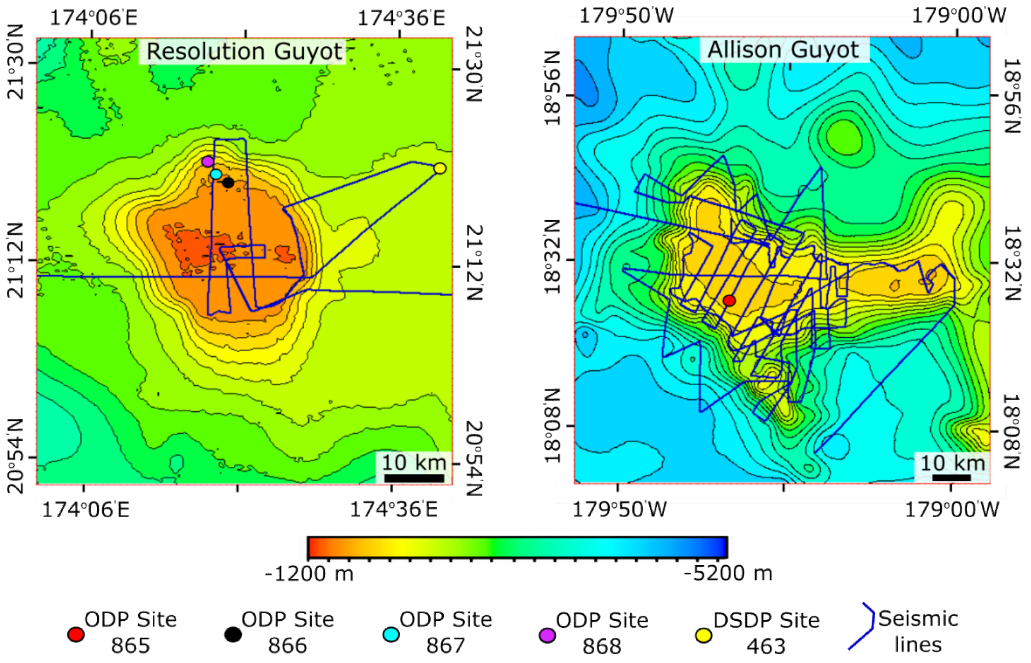


Figure 1.8 Bathymetry maps of Resolution and Allison guyots (Keizer et al., 2001; https://earthref.org/SC/#top) showing the drilling sites of Ocean Drilling Program Leg 143 sites (Sites 865-868) and Deep Sea Drilling Project Leg 62 Site 463, and 2D seismic surveys.

1.2.1 The Formation of the Mid-Pacific Mountains Volcanic Plateau

The MPM is one of the most distinctive morphologies within the context of western Pacific seamount chains, but the origin and evolution of their volcanic foundations is poorly understood owing to a paucity of igneous rock samples (Figure 1.7; Winterer and Sager, 1995). Unlike the typical linear arrangement of discrete seamounts, the MPM exhibits characteristics similar to a plateau with large areas elevated above the regional seafloor depths (Winterer and Sager, 1995). The origin of the MPM has been a subject of considerable debate within the scientific community. Some hypotheses propose that the MPM formed as the Pacific Plate traversed over a relatively stationary hotspot (Figure 1.9A), a notion supported by studies such as those by Henderson (1985) and Duncan and Clague (1985). These models suggested that the MPM was formed between 150 to 100 Ma (Winterer and Sager et al., 1995). In general, age data from the MPM broadly support the hotspot hypothesis, showing a trend of progressively younger ages towards the east and falling within the expected age range (Winterer and Sager, 1995). However, Winterer and Sager (1995) highlighted two issues in the hotspot hypothesis (Figure 1.9A): (a) these models are fraught with uncertainties due to limited age constraints resulting from sparse age data availability (Winterer and Sager, 1995), (b) the MPM plateau cannot be directly traced to a present-day hotspot.

Recent tectonic reconstructions of the Pacific Plate by Pockalny et al. (2021) have introduced an alternative perspective. The authors identified a newly proposed melt source region, termed the Larson melt region, situated along an arc between 16°S, 129°W and 22°S, 124°W. This region, named in honour of Roger Larson, is positioned between the Crough and Marquesas hotspots near the eastern boundary of the Pukapuka Ridge. The authors proposed the following framework (Figure 1.9B): (a) the western extent of the MPM likely formed between 130 to 110 Ma through a plume-ridge interaction with the Larson melt region; (b) during this epoch, the melt region likely represented a plume head situated within proximity of the Pacific-Farallon spreading axis; (c) the eastern portion of the MPM appears to be younger than the western portion and overlays an inferred trace of a precursor of the Molokai Fracture Zone; and (d) subsequent phases of distributed volcanism across the MPM could be attributed to the transit of the Tahiti hotspot during the interval spanning 110 to 85 Ma.

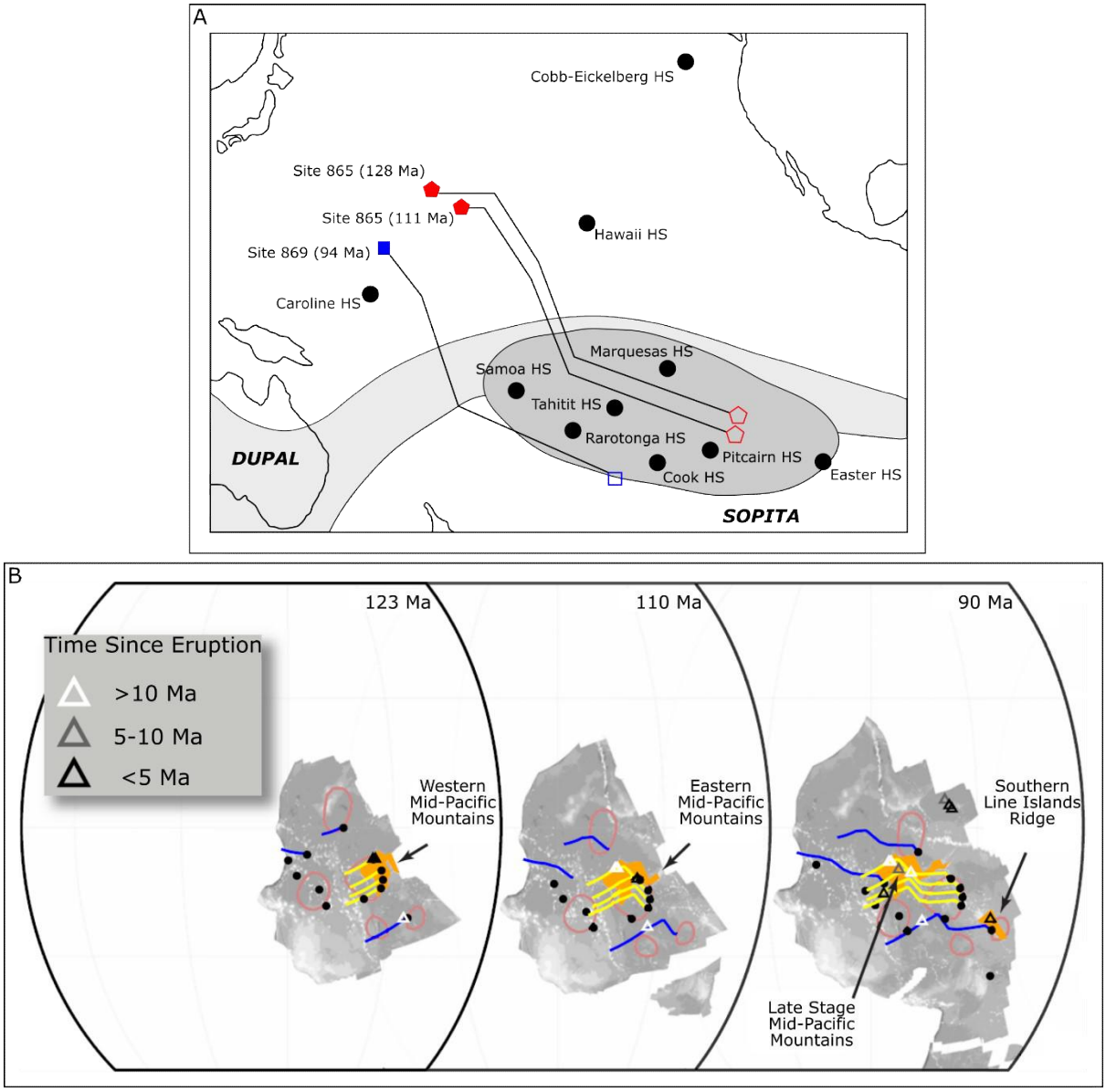


Figure 1.9 Palaeogeographical reconstruction and evolution models of the Mid-Pacific Mountains. (A) The single hotspot hypothesis (Henderson, 1985; Duncan and Clague, 1985) of the evolution of the Mid-Pacific Mountains depicting the present-day (filled square and triangles) and original (open square and triangles) locations of Sites 865, 866, and 869 (adapted from Pringle and Duncan, 1995). Ages of volcanism for each site are sourced from Pringle and Duncan (1995). Geochemical anomaly zones corresponding to the modern SOPITA (Staudigel et al., 1991) and DUPAL (Hart, 1984) are shown. The filled circles indicating modern active hotspots (Pringle and Duncan, 1995). (B) Time series palaeotectonic reconstruction by Pockalny et al. (2021) showing the melt sources and the timing of various eruptions associated with the hotspots. The figure shows the motion paths of the Larson melt region (yellow lines) and previously identified hotspots (blue lines; Pockalny et al., 2021). Pink circles represent the locations of mantle plume sources of each identified hotspot (Pockalny et al., 2021)

1.2.2 Sedimentological and Stratigraphic Evolution of the Cretaceous Shallow-Marine Carbonates on the Mid-Pacific Seamounts

When the volcanic substrates at MPM underwent subsidence, they were situated within the equatorial belt conducive to the proliferation of shallow-marine T-Factory carbonates (Winterer and Sager, 1995). Starting with the sedimentary sequence at Resolution Guyot, owing to its extensive temporal span, the shallow-marine carbonate succession at Site 866 has a thickness of ~1,620 metres with an age spanning from the Hauterivian to the late Albian (Figure 1.10; Sager et al., 1993a). Sedimentation rates initially ranged from approximately 175 to 200 m/Myr during the Hauterivian, gradually decelerating to 40 to 50 m/Myr during the late Aptian to Albian (Arnaud et al., 1995; Strasser et al., 1995). The sedimentary succession at Resolution Guyot is divided into eight lithostratigraphic units, consisting of six major and two minor units (Sager et al., 1993a; Strasser et al., 1995; Winterer and Sager, 1995). Lithostratigraphic Unit VIII (Figure 1.10; 1,620-1,400 meters below seafloor; mbsf) represents the basal lithostratigraphic unit characterised by ooilitic/oncoidal grainstone, indicative of transgressive processes over the volcanic edifice. Successive lithostratigraphic units VII and VI (1,400-1,203 mbsf and 1,203-792 mbsf, respectively) depict a transition to fine-grained wackestone/packstone with algal mats and erosional facies, reflective of lagoonal-peritidal restricted conditions. The depositional setting shifts again towards more open marine conditions in lithostratigraphic Unit V (792-677 mbsf), consisting of oolitic grainstones, before transitioning back to finer-grained wackestone/packstone with terrestrial plant debris in lithostratigraphic Unit IV (677-434 mbsf), indicative of restricted lagoonal-peritidal conditions. Lithostratigraphic Unit III (434-20 mbsf) represents the uppermost portion of the Cretaceous succession, characterised by mudstone/wackestone with low faunal diversity, suggesting progressively restricted lagoonal conditions. Lithostratigraphic Unit II comprises poorly defined manganese-encrusted shallow-marine limestone. By the late Albian, shallow-marine carbonate production ceased. The depositional dynamics shifted towards pelagic deposition (lithostratigraphic Unit I) from Maastrichtian to Pliocene times. ODP sites 867 and 868 intersect the uppermost portion of lithostratigraphic Unit II, with sites 867 and 868 located at the edge and the slope break of Resolution Guyot, respectively. Below a thin crust of phosphatised nannofossil limestone, the succession at Site 867 comprises interbedded coarse- and fine-grained layers, showing a transition from shallow lagoonal facies with some rudists at the base into ooid sands and subsequently into storm-dominated and high-energy intertidal facies at the top (Figure 1.10; drilled section; 77m; Sager et al., 1993b; Strasser et al., 1995). The sedimentary succession at Site 868 is characterised by sponge-rudist calcareous sponges in upright growth positions, and floatstone and minor grainstone rich in requieniid and caprinid rudists, gastropods, and sponge

fragments, indicative of an open-marine environment near fair-weather wave base (Figure 1.10; drilled section; 20 m; Sager et al., 1993b; Strasser et al., 1995). The facies relationships between drilling sites at Resolution Guyot were utilised to interpret the depositional settings (Strasser et al., 1995; Winterer and Sager et al., 1995). The authors suggested that the platform rim was composed of storm-dominated beach ridges, protecting the lagoon behind them. In front of the beach rim, the sponge-rudist bioherms lived and produced carbonate deposits that were washed onto the beaches and farther into the lagoon.

At Allison Guyot, lithostratigraphic Subunit IVD of the sedimentary sequence (871-838 mbsf) is formed of clayey limestone with intrusions of three alkali basalt sills (Figure 1.10; Sager et al., 1993c). Between these sills, the limestone shows layers of heavily burrowed clayey and dolomitic limestone. Moving above the basaltic sills, from lithostratigraphic Subunits IVC to IVA (838-622 mbsf), the composition shifts to limestone, clayey limestone, and clayey dolomitic limestone (Sager et al., 1993c). The succession is mostly composed of bioturbated wackestone and packstone, with some claystone layers and reworked claystone pebbles. Pyrite is often found in the burrowed limestone, which is commonly dolomitised. The clayey limestone transitions into a section primarily composed of bioturbated wackestone (207-622 mbsf; lithostratigraphic Unit III), with some packstone, peloidal mudstone, and occasional grainstone intervals likely due to wackestone winnowing. Additionally, a few beds of requieniid rudists, with articulated valves, are scattered throughout the wackestone. The upper part of the shallow-marine limestone sequence (207-140 mbsf; lithostratigraphic Unit II), located below the unconformity separating the limestones from the overlying Upper Cretaceous and Cenozoic pelagic cap, is made up of phosphatised limestone. This section shares similarities with the underlying strata (i.e. lithostratigraphic Unit III) but shows increasing phosphatisation towards the top (Sager et al., 1993c). The shallow-marine carbonate deposition at Site 865 was dominated by lagoonal environment protected behind a platform edge barrier (Sager et al., 1993c). Above this, the oldest overlying pelagic cap deposits date from early to mid-Turonian and were found in cavities and cracks on the platform's uppermost surface. These are followed by Maastrichtian-age pebbles of pelagic limestone, and a thick pelagic cap spanning from the Paleocene to Quaternary (lithostratigraphic Unit I; Sager et al., 1993c; Sliter et al., 1995).

Our current comprehension of the stratigraphic evolution of the MPM Cretaceous atolls comes from sparse well data (e.g. Arnaud et al., 1995; Jenkyns and Wilson, 1999; Wilson et al., 1998). The vintage 2D seismic reflection data, which has lower quality compared to modern standards (e.g. Sager et al., 1993a; Kenter and Ivanov, 1995), has not been used in studying sedimentological and stratigraphic evolution of the MPM Cretaceous ICPs. The sequence stratigraphic analyses of Resolution Guyot have primarily relied upon data derived solely from Site 866, including (a) facies

identification, (b) geophysical log examination, (c) recognition of sequence boundaries indicated by palaeosols or a change in stacking pattern of parasequences, (d) recognition of maximum flooding surfaces or intervals based on microfauna and macrofauna, and (e) identification of the vertical evolution of stacked parasequences that show a shallowing-upward (progradational trend), a constant water depth (aggradational trend), or that display a deepening-upward facies evolution (retrogradational trend; Arnaud et al., 1995; Strasser et al., 1995). The Hauterivian to Albian sequence at Site 866 comprises 19 depositional sequences, each marked by distinct transgressive systems tracts, maximum flooding events, and highstand systems tracts (Arnaud et al., 1995). These sequences are organized into four depositional sequence sets. The first set (Hauterivian transgressions) encompasses Hauterivian sequences 1 through 4, characterised by the presence of oolitic and oncoidal open-marine sediments. Following an emersion horizon, possibly associated with local uplift, the second set comprises eight Hauterivian to Barremian depositional sequences (sequences 5 through 12). These sequences are composed of restricted subtidal to intertidal facies transitioning from progradation to aggradation, with a thickening-upward trend likely linked to increased subsidence rates towards the top. The third sequence set comprises four Aptian sequences (sequences 13 through 16) characterised by open-marine facies and a general deepening trend up to the lower/upper Aptian boundary. Two major maximum flooding surfaces are identified, with the upper one correlating with the Goguel level in southeastern France and the Selli level in central Italy. The fourth sequence set includes upper Aptian to Albian sequences 17 through 19, marked by a sudden shift to restricted facies, indicating continuous aggradation of swamp, marsh, and shallow-lagoonal sediments.

Arnaud et al. (1995) and Strasser et al. (1995) highlighted that sedimentation processes and facies distribution on Resolution Guyot were modulated by low-amplitude, high-frequency sea-level fluctuations that created small-scale cycles. To decipher whether those relative sea level cycles were of global signature, Arnaud et al. (1995) compared the stratigraphic framework at Site 866 with stable areas, such as eastern Venezuela on the northern part of the Guyana shield, and regions of minor instability, such as carbonate platforms from the European (southeastern France) and Apulian (central Italy) margin of the Ligurian Tethys. This comparative analysis showed similarities between the stratigraphic framework at Site 866 and the analogous stable areas and consequently the authors suggested that sedimentation at Site 866 was primarily influenced by sea-level fluctuations rather than subsidence variations.

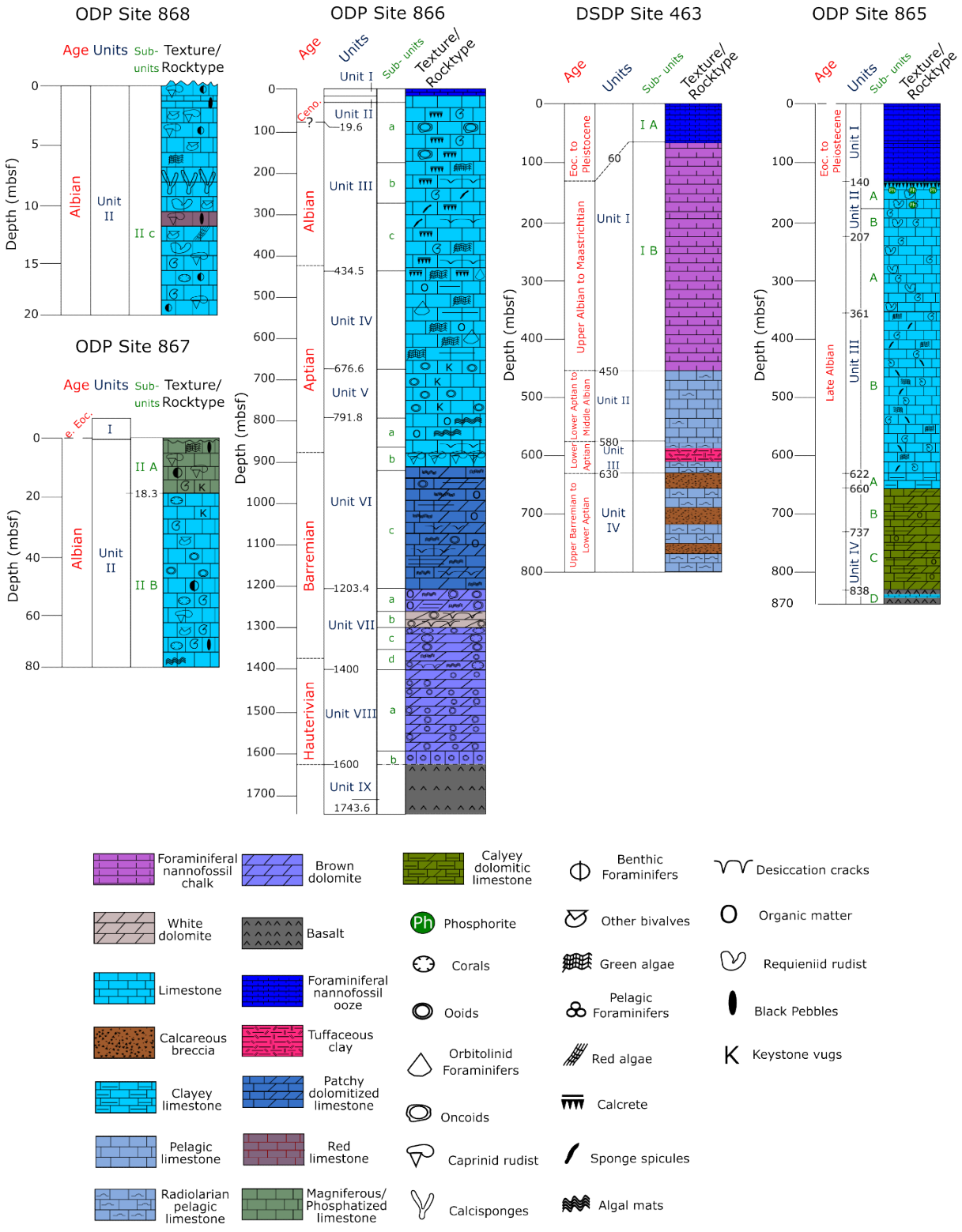


Figure 1.10 Lithostratigraphic columns of Allison Guyot Site 865 and Resolution Guyot site 866-868 and the basinal deposits close to Resolution Guyot DSDP Site 463 (reproduced from Timofeev et al., 1981; Sager et al., 1993a, b, c; El-Yamani et al., 2022, 2024). The figure summarises the main lithological and fossil content of the different lithostratigraphic units at the drilling sites. Check figure 1.8 for the drilling sites' locations.

1.2.3 Diagenetic Evolution of the Cretaceous Shallow-Marine Carbonates on the Mid-Pacific Seamounts

The diagenetic evolution of Resolution and Allison guyots, as inferred from core data, manifests a relatively simple history, encompassing marine-phreatic, meteoric-phreatic, and meteoric-vadose, alongside early and late diagenetic dolomitisation (Sager et al., 1993a, c; Flood and Chivas, 1995; Röhl and Strasser, 1995; Strasser et al., 1995). Subaerial exposure and karstification of the Albian succession of the MPM Cretaceous ICPs has been a subject of debate among researchers (van Waasbergen and Winterer, 1993; Winterer et al., 1995; Wilson et al., 1998; Winterer, 1998; Jenkyns and Wilson, 1999). Observations of irregular surfaces on the upper Albian carbonates beneath the pelagic cap, discerned through 3.5-kHz echo-soundings and seismic-reflection data, suggest evidence of subaerial exposure in both guyots (Winterer, 1998; Winterer et al., 1995). In line with that, petrographic analyses of samples retrieved from the Allison and Resolution guyots reveal dissolution cavities, stalagmite-like calcite structures, and calcite cements (e.g. dogteeth) indicative of meteoric vadose diagenesis (Winterer et al., 1995). On the contrary, the oxygen and carbon isotope analyses by Wilson et al. (1998) and Jenkyns and Wilson (1999) suggest that the signatures of the bulk carbonates and calcite cements fail to provide any evidence of meteoric diagenesis and so the authors suggested that the irregular topographies might have resulted from submarine dissolution rather than subaerial exposure and karstification. Consequently, it was proposed that both the drilled Pacific Cretaceous guyots in Leg 143/144 have never been uplifted or deformed (e.g. Lechler et al., 2015).

Dolomite occurrence at Resolution Guyot is notable commencing at ~500 mbsf and recurring around 900 mbsf (Sager et al., 1993a). Further downhole, dolomite persists continuously below 1000 mbsf, with brown dolomite prevalent in Barremian-age sediments from 1200 to 1620 mbsf in lithostratigraphic Units VII and VIII (Site 866; Flood and Chivas, 1995; Winterer and Sager, 1995). Within the brown dolomite, there is a distinct white dolomite layer, spanning a 30-meter-thick interval from 1250 to 1280 mbsf (Flood, 1998). Some researchers propose that dolomite formation at Resolution Guyot might have occurred during early diagenesis, potentially facilitated by evaporative pumping within sequences bounded by clayey, organic-rich algal laminates (Sager et al., 1993a, c; Strasser et al., 1995). A different origin was proposed by Flood and Chivas (1995). The authors presented $^{87}Sr/^{86}Sr$ isotope data from the brown dolomites, suggesting an age of either 90 or 105-120 Ma. Thereby, the authors hypothesised that the Late Cretaceous deep (>1000 m) cold seawater below calcite and aragonite saturation depths bathed the permeable interior of the carbonate pile. The inward and upward circulation of seawater through the platform was driven by kohout geothermal convection in a similar fashion to the dolomitisation processes proposed

for Late Cenozoic Enewetak and Niue islands' dolostones (Saller, 1984; Aharon et al., 1987). The $^{87}Sr/^{86}Sr$ isotope signature of the white dolomite indicates a significant time delay of approximately 100 Myr between carbonate deposition and dolomitisation (Flood et al., 1996). The white dolomites at Resolution Guyot were suggested to be formed by normal marine dolomitisation via kohout geothermal convection, similar to the brown dolomites, but significantly later (Flood et al., 1996; Flood, 1998). At Allison Guyot, dolomite is also present where it is found in some layers between 660 and 837 mbsf at Site 865 (Sager et al., 1993c). Burrows exhibit preferential dolomitisation at Allison Guyot owing to their higher permeability (Sager et al., 1993c). XRD analysis by Murdmaa et al. (1995) between 670-836 mbsf reveals varying degrees of dolomite abundance, ranging from abundant to rare. Sager et al. (1993c) suggested that seasonally evaporative conditions have facilitated dolomitisation at Allison Guyot.

1.2.4 The Demise of Cretaceous Shallow-Marine Carbonates on the Pacific Seamounts

Three distinct hypotheses have been proposed to explain the demise of the Cretaceous Pacific ICPs of ODP Leg 143/144 guyots: the death-by-emergence-and-submergence hypothesis, the death-in-the-tropics hypothesis, and the death-by-excess-warmth-in-shallow-peri-equatorial-waters hypothesis. The first hypothesis, articulated by van Waasbergen and Winterer (1993), Winterer et al. (1993), Winterer and Sager (1995), and Winterer (1998), postulates simultaneous platform karstification and drowning events across a broad latitudinal range. The underlying cause of emergence, whether tectonic or eustatic, remains enigmatic (e.g. Winterer et al., 1993; Winterer and Sager, 1995). The first hypothesis also fails to explain why shallow-marine carbonate platforms did not re-establish on subsiding karstified limestone topography, while they initially flourished on volcanic pedestals, presumably subject to more rapid subsidence (Jenkyns and Wilson, 1999). The second hypothesis, introduced by Larson et al. (1995), suggests that the demise of the Cretaceous Pacific ICPs was driven by the palaeo-equatorial upwelling belt of high productivity (Figure 1.11; Hallock and Schlager, 1986; Vogt, 1989). However, the demise ages of the Pacific Cretaceous ICPs do not align with any of the Cretaceous Oceanic Anoxic Events (OAEs), with some of the platforms were even thriving during OAE1a (e.g. Resolution and MIT guyots; Jenkyns and Wilson, 1999). The third hypothesis posits that platform drowning occurred nearer to the equator during cooler intervals, such as the early Albian and Maastrichtian (Takuyo Daisan and Wodejebato guyots), and farther south during warmer periods, like the Albian-Cenomanian boundary and the mid-Eocene (MIT, Resolution, Allison, Limalok guyots). The third hypothesis (Figure 1.11) proposed a correlation between these findings and the elevated temperatures in shallow peri-equatorial waters which was suggested to be detrimental to carbonate-secreting organisms inhabiting the platforms by drawing a parallel with modern bleaching of coral and foraminifera,

when exposed to prolonged high temperatures (>30°C). Such conditions were suggested to enable subsidence or eustatic rise to surpass sedimentation rates, thereby facilitating platform drowning.

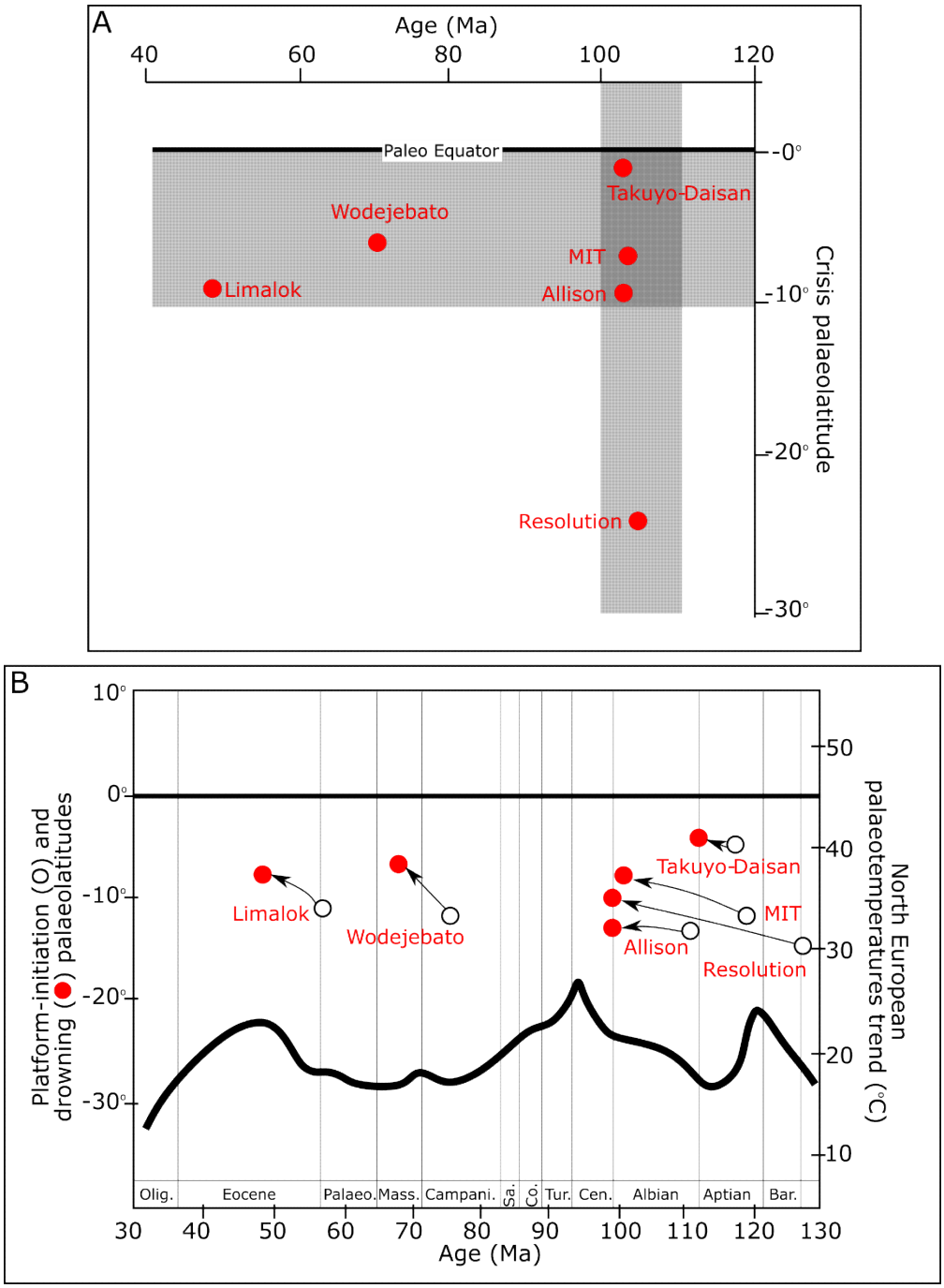


Figure 1.11 Demise hypotheses of the Cretaceous Pacific isolated carbonate platforms. (A) The crisis zones, identified by Larson et al. (1995) in the death-in-the-tropics hypothesis, for ODP Leg 143/144 Cretaceous atolls based on the age and palaeolatitudes of their demise (adapted from Larson et al., 1995). (B) Palaeolatitudes of the Cretaceous Pacific atolls at the time of platform initiation (not filled circle) and drowning (red filled circle), along with the palaeotemperature trends (adapted from Jenkyns and Wilson, 1999). Panel (B) shows the relative position of drowned platform to the equator on which Jenkyns and Wilson (1999) proposed death-by-excess-warmth-in-shallow-peri-equatorial-waters hypothesis and the black bold line resembles the paleotemperature trends from northern Europe.

1.2.5 Gaps in Knowledge

The previous section (Subsection: 1.2) presented the latest research findings of the Cretaceous Pacific ICPs, illuminating the current state of knowledge in this field. These findings serve as a foundation upon which I discern areas lacking comprehensive understanding, thereby identifying crucial research gaps. Understanding these gaps is paramount for guiding future investigations, facilitating advancements, and addressing unanswered questions within the broader realm of the Cretaceous ICPs.

1.2.5.1 The depositional settings and stratigraphic evolution of the Cretaceous Pacific ICPs

To decipher the sequence stratigraphic evolution of a shallow-marine T-factory carbonate platform, insights into the shore-to-basin cross-section of the platform and the position of the platform edge are necessary (Figure 1.12; Schlager, 2005). Seismic profiles, outcrops, or well-correlated series of boreholes can adequately provide such information (Figure 1.12; Schlager, 2005). In case of their absence, sequences and systems tracts can be identified within single boreholes, relying on proxy indicators like deepening and shoaling trends (Figure 1.12; Schlager, 2005). Nonetheless, identifying sequences and systems tracts using a single section or single borehole is more speculative and less reliable compared to the cross-section method due to potentially non-unique or autocyclic deepening and shoaling trends (e.g. Schlager, 2005; Burgess and Prince, 2014; Xiao and Waltham, 2019). In addition, carbonate platforms exhibit high internal spatial complexity, often resembling mosaics rather than the classical linear belts of depositional environments that are parallel or sub-parallel to a coastline or platform edge (Wright and Burgess, 2005). Given these issues, uncertainties surround our understanding of the depositional settings and stratigraphic evolution of the Pacific Cretaceous ICPs, primarily stemming from sparse well data only (e.g., Arnaud et al., 1995; Jenkyns and Wilson, 1999; Wilson et al., 1998). The available seismic-reflection data from the MPM Cretaceous ICPs haven't been used, judging by its low quality (Kenter and Stafleu, 1995). The authors suggested that interpreting reflections related to changes in sea level or oceanographic events, as well as distinct stratigraphic features such as erosional surfaces, sedimentary packages, facies changes, or diagenetic boundaries, is not feasible on the seismic profiles. The recent advancements in our understanding of carbonate systems, facilitated by satellite imaging and facies analyses on modern isolated carbonate platforms (e.g. Gischler, 2006; Harris et al., 2015; Jorry et al., 2016; Prat et al., 2016; Rankey, 2016; Utami et al., 2018; Wu et al., 2020) and seismic imaging of carbonates (e.g. Saller and Vijaya, 2002; Eberli et al., 2004b; Zampetti et al., 2004; Fournier et al., 2005; Burgess et al., 2013; Paumard et al., 2017; Clark et al., 2018; Van Tuyl et al., 2018; Huang et al., 2020; Cross et al., 2021; Hendry et al., 2021; Ma et al., 2021), offer promising avenues for revisiting vintage seismic and well data of the MPM

Cretaceous ICPs. Revisiting the MPM Cretaceous ICPs offers the potential to enhance our comprehension of these complex systems, in terms of their depositional settings and stratigraphic evolution.

1.2.5.2 The subaerial exposure and karstification complex history of the Cretaceous Pacific ICPs

Wilson et al. (1998) and Jenkyns and Wilson (1999) proposed that the irregular topographies observed in the uppermost shallow-marine carbonates at Resolution and Allison guyots could have arisen from submarine dissolution rather than subaerial exposure and karstification. This interpretation was based on the absence of any evidence for meteoric diagenesis on the $\delta^{13}C_{carb}$ and $\delta^{18}O_{carb}$ data. Consequently, it was proposed that both guyots have never been uplifted (Lechler et al., 2015). In both guyots, there is clear evidence of active exchange between pore waters and the surrounding modern seawater, indicating that seawater freely circulates through the islands (i.e. fluid-buffered system; Sager et al., 1993a, 1993c; Paull et al., 1995). In fluid-buffered systems, subsequent diagenesis can reset the isotopic composition of the preceding diagenetic products to match the circulating fluid (e.g. Hoffman and Lamothe, 2019; Lau and Hardisty, 2022). This phenomenon was observed in carbonate sediments of nonglacial Cryogenian and early Ediacaran age in northern Namibia, where large positive and negative $\delta^{13}C_{carb}$ excursions in shallow-water marine platforms occurred while coeval carbonates in the upper fore-slope of the Namibian platform exhibited a uniform $\delta^{13}C_{carb}$ composition compatible with dissolved inorganic carbon in the modern ocean (Hoffman and Lamothe, 2019). This was explained by seawater-buffered diagenesis that circulated modern seawater into the sediments through geothermal convection (Hoffman and Lamothe, 2019). Considering that the MPM Cretaceous ICPs are seawater-buffered systems, such a use of carbon and oxygen isotopes by Wilson et al. (1998) and Jenkyns and Wilson (1999) may raise questions. Hence, the question whether subaerial exposure and karstification took place in the MPM Cretaceous ICPs, along with the potential consequences of answering this question for the uplift, subsidence, and ultimately the demise hypotheses of both ICPs, persists as an area requiring further investigation.

1.2.5.3 Scarcity of dolomites in the Cretaceous Pacific ICPs

During the Cretaceous period, marked by humid global climate, calcitic seas (Mg:Ca ≤1) and high relative sea levels, widespread dolomitisation was largely hindered in many carbonate successions (e.g. Steuber and Rauch, 2005; Newport et al., 2017, 2020). In accordance, Gabellone and Whitaker (2016), employing reactive transport modelling, demonstrated the limited dolomitisation potential and very low dolomitisation rates of normal Aptian seawater (~1-2% dolomite fraction) and derived brines, in stark contrast to modern seawater (~62% dolomite after 500 kyr) and derived brines. Within the drilled Cretaceous Pacific ICPs of ODP Leg 143/144, dolomites are found

exclusively in Resolution and Allison guyots, while they are notably absent in others (i.e. Wodejebato, MIT, and Takuyo-Daisan Guyots; Haggerty and Premoli Silva, 1995). This raises some questions about the selective dolomitisation observed in Resolution and Allison guyots. If only the Cretaceous normal seawater and/or derived brines were capable of dolomitising parts of the Cretaceous succession in Resolution and Allison guyots, why did similar dolomitisation not occur in the other Cretaceous Pacific ICPs? What factors facilitated overcoming the limited dolomitisation potential of the Cretaceous seawater exclusively in Resolution and Allison guyots? Consequently, substantial uncertainty persists regarding the dolomitisation mechanism of the Pacific Cretaceous ICPs and its implications for evaluating the efficacy of syndepositional and near-surface early-burial dolomitisation by Cretaceous calcitic seawater. Further investigations are needed to unravel these complexities and enhance our comprehension of dolomitisation processes in Cretaceous carbonate platforms.

1.2.5.4 The mysterious demise of the Cretaceous Pacific ICPs

The mechanisms governing the demise of the Cretaceous Pacific ICPs are still surrounded by several questions. In the death-by-emergence-and-submergence hypothesis, if fluctuations in relative sea level drove the submergence of these platforms, the reasons behind such fluctuations remain elusive. Additionally, why carbonate platforms failed to re-establish after submergence is still unknown. In the death-in-the-tropics hypothesis, if equatorial upwelling of nutrients and CO_2 played a significant role in platform demise, the absence of corresponding organic-rich intervals atop the drowned platforms, and the fact that none of the Cretaceous Pacific ICPs were demised during any of the Cretaceous OAEs (Wilson et al., 1998), raises questions. In the death-by-excess-warmth-in-shallow-peri-equatorial-waters hypothesis, if hot equatorial waters were the primary factor in platform demise, it's puzzling why other shallow-marine carbonate platforms thrived in similarly warm equatorial temperatures, ranging from 30-37°C (Steuber et al., 2005; Walliser and Schöne, 2020; Schmitt et al., 2022) to even much higher temperatures of ~41-48°C (El-Shazly et al., 2011; Torres de la Cruz et al., 2020). As a result, there are still a lot of unknowns about why the Pacific Cretaceous ICPs drowned and how it connects to modern coral bleaching. This area remains open for further investigation.

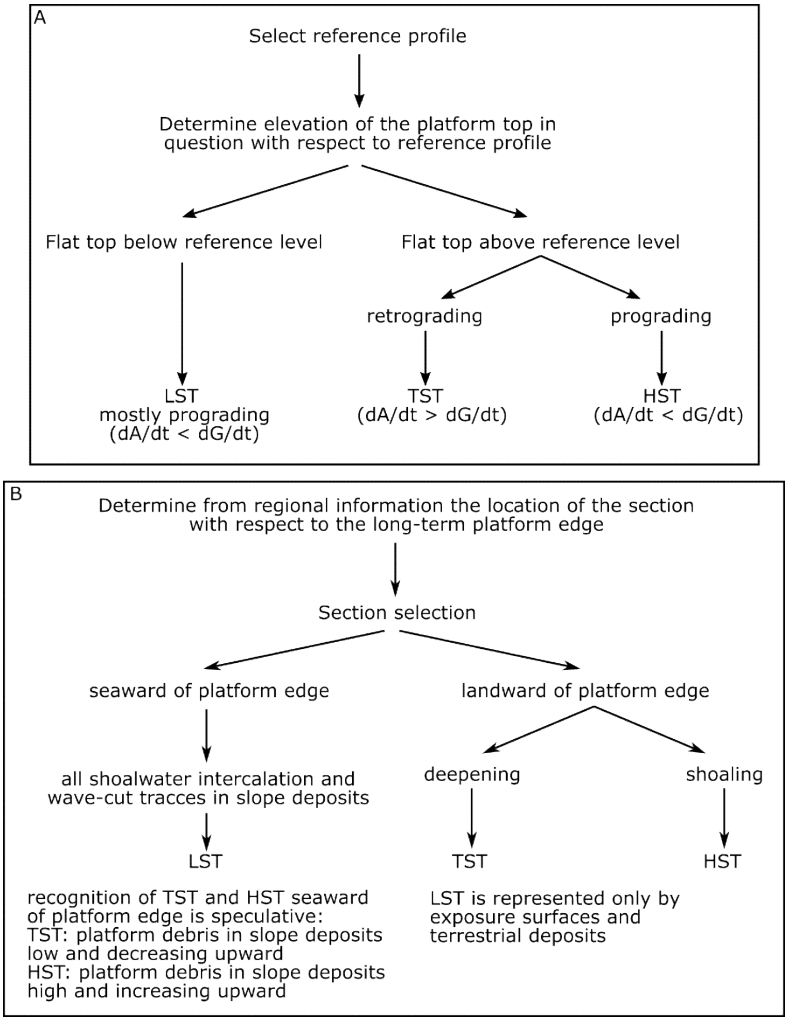


Figure 1.12 The speculative and less reliable identification of system tracts in shallow marine carbonate successions using a single section or wellbore. (A) Flow chart depicting the process of identifying system tracts using a cross section of the carbonate platform, with a focus on determining the platform margin's position where dA/dt is the rate of change in the accommodation space and dG/dt is the rate of change in the growth potential. (B) Flow chart depicting identifying system tracts within a single section or borehole. It involves a more speculative approach compared to using cross-sections, relying on proxy indicators like trends in deepening and shoaling. Figure adapted from Schlager (2005).

1.3 Specific Research Aims and Objectives

The overall aim of this research is to understand how the Cretaceous ICPs grew from genesis to demise passing through the large-scale meteoric diagenesis (i.e. karstification) and dolomitisation stage. Considering the aforementioned gaps in knowledge, in this thesis I aim to answer the following questions:

1. What are the controlling factors on the stratigraphic evolution and karstification in the Pacific Cretaceous ICPs?
2. How did the scarce dolomitisation during the Cretaceous occur in just a few Pacific ICPs?
3. What controlled the demise of the Cretaceous Pacific ICPs? Are they suitable analogues for thermal-stress intolerant or tolerant modern tropical atolls under the human-induced future climate changes?

To answer these questions, I utilised a multi-faceted approach combining core-log-seismic data from the Mid-Pacific Mountains. Here, I detail the specific aims of this dissertation and the general objectives of each of them.

1.3.1 What are the controlling factors on the stratigraphic evolution and large-scale karstification in the Cretaceous Pacific ICPs?

- Integrate the core-log-seismic data of the MPM Cretaceous ICPs to build a detailed description of their seismic characteristics, considering their spatial distribution, which can serve as an analogue for the seismic characteristics of the Cretaceous ICPs.
- Build a 3D depositional model of the Cretaceous ICPs.
- Trace the platform margin trajectory in consideration to the available core and log data.
- Interpret seismic stratigraphic architecture of the MPM Cretaceous ICPs
- Build a clearer image on the evolution of the MPM Cretaceous ICPs by unthreading the interplay between eustasy, changes in carbonate production rates, subsidence rate and magmatism during the Cretaceous.
- Unravel the factors influencing karstification and the spatial and temporal distribution of karst-related features in the MPM Cretaceous ICPs.
- Interpret the distribution of fractures, fracture corridors, fluid conduits in the MPM Cretaceous ICPs and their implications on seawater circulation in the guyots.

1.3.2 How did the scarce dolomitisation occur during the Cretaceous Calcitic ocean in just a few Pacific ICPs?

- Compile a global geo-dataset of dolomitised and non-dolomitised carbonate island and atolls of Late Cenozoic and Cretaceous ages.
- Interpret the seismic data around the dolomitised successions at the tied wells to understand their temporal and spatial geological settings.
- Perform synthetic seismic facies forward modelling to groundtruth my interpretation.
- Integrate core-log-seismic data with the geochemical data of the limestones and dolostones in the MPM Cretaceous ICPs to understand factors that favoured dolomitisation in just a few exceptions in the Cretaceous ICPs.
- Assess the effectiveness of syndepositional and near-surface early-burial dolomitisation by Cretaceous calcitic seawater.
- Emphasise the importance of distinguishing true syndepositional and near-surface early-burial normal seawater dolomites from other types of dolomites.

1.3.3 What controlled the demise of the Pacific Cretaceous ICPs? Are they suitable analogues for thermal-stress intolerant or tolerant modern tropical atolls under the human-induced future climate changes?

- Integrate core-log-seismic data with the latest palaeo-tectonic reconstruction of the Pacific Plate to decipher the history of the MPM Cretaceous ICPs from the cessation of shallow-marine sedimentation to the onset of the drowning.
- Use published articles on the Cretaceous palaeoclimatic conditions (i.e. temperature, tropical cyclones, storms, hurricanes, and ocean surface currents) with the palaeogeographic reconstructions of the Cretaceous Mid-Pacific ICPs to understand their potential effects on carbonate production.
- Evaluate the plausibility of my proposed model by considering our understanding of the favourable ecological conditions for shallow-marine carbonate-secreting organisms within the depositional systems of the MPM Cretaceous ICPs.
- Test the applicability of my newly proposed model on other Pacific Cretaceous ICPs.
- Compare my newly proposed model with the previously proposed hypotheses.
- Suggest whether the Pacific Cretaceous ICPs can act as analogues for thermal-stress intolerant or tolerant modern tropical atolls under the human-induced future climate changes.

1.4 Research Data

To answer the current gaps of knowledge about the Pacific Cretaceous ICPs and the specific aims and objectives, this research study uses the core-log-seismic data collected during ODP Leg 143/144, DSDP Leg 62, and the Roundabout Expedition Leg 10 at Resolution and Allison guyots. Seismic data were collected by cruise 'Roundabout Expedition Leg 10' (RNDB10WT; Nov–Dec 1988) aboard the R/V Thomas Washington which was a dedicated program to image the Mesozoic Guyots in the western Pacific. This survey consisted of single-channel, 2D seismic profiles acquired using an 80-in^3 water gun, processed by the University of Texas Institute for Geophysics. Processing involved filtering (50–200), mixing (1:1:1), and automatic gain control (Marine Geoscience Data System, n.d.). Seismic reflection datasets were visualised using Petrel® software. The seismic data is displayed in the American polarity convention, where a downward increase in acoustic impedance (e.g. seabed) is represented by trough-peak-trough with red-blue-red reflections. The bathymetry data of the drowned ICPs used in this study come from Earthref website (Keizer et al., 2001). The wireline-logging data used in this study includes Calliper (CALI), spectral gamma ray (SGR) including potassium (K), thorium (Th), and uranium (U), sonic (DTLN), formation density (RHOB), formation microscanner (FMS), photoelectric absorption factor (PEF), and neutron porosity (NPHI) (Division of Marine and Large Program, n.d.). The wireline-logging data were visualised using Interactive-Petrophysics® Software. High-resolution core images were accessed from the International Ocean Discovery Program JOIDES Resolution Science Operator website (JOIDES Resolution Science Operator, n.d.). Physical properties measurements of the shallow-marine carbonates at Resolution and Allison guyots (sites 865 and 866), acquired by the shipboard party, are used, including porosity, grain density, and compressional wave velocity (Sager et al., 1993a; Kenter and Ivanov, 1995). Satellite images from modern examples of ICPs were accessed using Google Earth® Software. The geochemical aspects of this study are based on doing my own interpretations of the geochemical data that were generated by the Ocean Drilling Program in the Proceedings of the Scientific Results of Leg 143. The geochemical data encompasses Mn, Sr, and Fe content, $\delta^{18}O$, $\delta^{13}C$, and $^{87}Sr/^{86}Sr$ isotope, major, minor, and trace elements of dolostone and limestone and radiometric age data of basaltic basements in Leg 143 (Baker et al., 1995; Flood and Chivas, 1995; Jenkyns, 1995; Jenkyns et al., 1995; Pringle and Duncan, 1995; Sager, 1995; Röhl and Strasser, 1995). Published core and facies descriptions by the shipboard scientific party are utilised in this study (e.g. Timofeev et al., 1981; ODP Initial Reports, 1993a, b; Sager et al., 1993a, b, c; Arnaud et al., 1995).

1.5 Thesis Structure

The subsequent three chapters are structured as stand-alone scientific papers, each containing relevant literature and descriptions of datasets, methods, and geological settings. Some of the work has already been peer-reviewed and published, while other parts are at various stages of peer review for publication. The inclusion of published and submitted papers may lead to some repetition, especially in the introduction, geologic settings, and data and methods sections. The final chapter will review my work, address withstanding gaps in knowledge, and look to future work in the field.

The research chapters in this thesis (Chapters 2-4) use 'we'/'our' pronouns to acknowledge the work of the co-authors included in my published and/or submitted work. However, I confirm that I conceptualised the projects, carried out all the research work and analyses, wrote all the manuscripts, created all the figures, and edited all the manuscripts. Professor Cédric M. John and Dr Rebecca E. Bell supervised my Ph.D., helped in conceptualisation, and reviewed my manuscripts. Acknowledgements are included at the beginning of each scientific chapter. The following chapters of the thesis are organised as follows:

Chapter 2: Stratigraphic Evolution and Karstification of a Cretaceous Mid-Pacific Atoll (Resolution Guyot) Resolved from Core-Log-Seismic Integration and Comparison with Modern and Ancient Analogues.

In Chapter 2, I address ***"Aim 1"***, focusing on investigating the factors influencing depositional setting, stratigraphic evolution, and karstification of the Cretaceous Mid-Pacific atoll, Resolution Guyot. Employing a comprehensive approach integrating core-log-seismic data analyses, I identify seismic facies and their distribution, delineating depositional facies and seismic-sequence stratigraphic units. I refine the age model using $\delta^{13}C_{carb}$ and $^{87}Sr/^{86}Sr$ isotopes. Through palaeogeographic reconstruction, I create a 3D depositional model illustrating the heterogeneous nature of seismic facies and their corresponding depositional facies. The developed seismic sequence-stratigraphic framework elucidates the influence of eustasy, subsidence rate, production rate, and magmatism. Results reveal extensive karstified intervals, including sinkholes and fracture-cave systems along the flank margin. The vertically stacked fracture-cave systems suggest syndepositional platform margin fractures' significant contribution. Seismic interpretation identifies large-scale fluid venting systems across the platform, facilitating active seawater ventilation and dynamic pore water-seawater exchange within Mid-Pacific atolls.

Chapter 2 was published in ***Basin Research*** in April 2022. All this published work was conceptualised, completed, written, edited, and submitted by myself, with supervision, review and

editing by my supervisors Professor Cédric M. John and Dr Rebecca E. Bell. https://doi.org/10.1111/bre.12670

Chapter 3: Mechanism of Island Dolostones Formation in the Cretaceous Calcitic Ocean: Insights from the Cretaceous Mid-Pacific Guyots.

In Chapter 3, I investigate ***"Aim 2"*** to understand the primary factors governing island dolomitisation during the Cretaceous and its implications on seawater dolomitisation in calcitic ocean. A global geo-dataset comparing dolomitised versus non-dolomitised carbonate islands, atolls, and isolated platforms of Late Cenozoic and Cretaceous age is compiled to examine the prevalence of early-burial seawater dolomitisation. My dataset highlights a scarcity of dolomitised Cretaceous islands compared to Cenozoic counterparts, prompting examination on dolomite exceptions in the Cretaceous Resolution and Allison guyots. Seismic interpretation reveals (a) magmatic sills intrusion associated with hydrothermal vent complexes within the sedimentary succession of both guyots and (b) a spatial overlap between dolomites in the tied well and sills on the seismic data. Using $^{87}Sr/^{86}Sr$ isotopes, the ages of dolomitisation are overlapping with magmatism in the MPM and volcanism in the western Pacific. I determine the host-rock temperatures during dolomitisation through burial and thermal modelling, utilising the age-depth relation from Chapter 2. $\delta^{18}O_{dol}$ derived dolomitisation temperatures exceed concurrent host-rock temperatures. Fe levels in dolomites near the basement are significantly higher than normal seawater dolomites. Consequently, I propose a magmatically driven hydrothermal dolomitisation, showing that deep-seated island dolostones do not only form from pumping cold deep seawater below calcite saturation depth but are influenced by magmatism. The lack of dolostones in other Cretaceous islands challenges interpretations of platform-scale syndepositional near-surface early-burial dolomitisation by Cretaceous normal seawater, highlighting the necessity to consider factors like dolomite geometry, geological settings, and dolomitisation age in interpreting their origin.

Chapter 3 was published in ***Marine and Petroleum Geology*** in January 2024. This published work was conceptualised, completed, written, edited, and submitted by me, with supervision, review, and editing by my supervisors Professor Cédric M. John and Dr Rebecca E. Bell. https://doi.org/10.1016/j.marpetgeo.2024.106741

Chapter 4: Beyond Thermal Stresses: Magmatism, Karstification, and Hotspot Migration Dictated the Demise of the Mid-Pacific Cretaceous Atolls

In Chapter 4, focusing on Resolution and Allison guyots, I tackle **"Aim 3"** through core-log-seismic integration to understand their demise mechanisms. Seismic interpretation reveals

extensive late Albian-early Cenomanian magmatism across the MPM guyots, which uplifted the carbonate tops through magmatic-underplating, causing subaerial exposure and thus halting shallow-marine carbonate production. Using the latest published palaeotectonic reconstructions of the Pacific Plate suggests that between 98-95 Ma the MPM migrated off the Larson Melt Region which caused rapid subsidence, combined with Cenomanian eustatic rise, resulting in rapid relative sea level rise. I test the possible ranges of the relative sea level rise against the maximum vertical production rates of the different carbonate grains in the MPM Cretaceous ICPs. Most of these rates exceed the maximum vertical production rates of carbonate components but fall below the short-term maximum vertical production rates of individual rudists. By integrating recently published global palaeogeographic reconstructions and palaeoclimatic modelling results, I illustrate that Resolution and Allison guyots were likely affected by tropical cyclones, storms, ocean currents, and waves during early-Cenomanian to early-Turonian times. This environmental influence might have added additional negative feedback for vertical accumulation rates during the relative sea level rise. In addition, I utilise recent palaeoclimatic modelling results to determine SSTs throughout the lifespan of the atolls. The comparison reveals that (a) the SSTs overlap with the temperature range of thriving rudist-bearing carbonates, and (b) the SSTs remained relatively constant throughout the lifespan and demise of the atolls. Thus, I refute the hypothesis that warm waters lead or even contributed to the demise of the Pacific Cretaceous ICPs in a similar fashion to modern coral bleaching. My findings support the "death-by-emergence-and-submergence" hypothesis, which was challenged by later studies, by unveiling its main unknowns (a) the factor governing subaerial exposure, and (b) why shallow-marine sedimentation didn't revive after re-submergence. An implication of my study is the suggestion that Pacific Cretaceous ICPs were thermally resilient. This resilience may parallel that of modern stress tolerant counterparts, offering valuable insights into the potential effects of human-induced greenhouse climate on contemporary tropical biota.

This chapter is to be submitted to ***Global and Planetary Changes*** soon.

Chapter 5: Discussion, Conclusion, and Future Work

In the conclusion and future work chapter, I analyse the findings from my three scientific studies and critically evaluate path of the MPM Cretaceous ICPs from initiation to demise, examining the geological factors that influenced their evolution. In each aspect I show the potential wider implications on other ICPs of different age and in different geological settings. I then list how I will continue to develop this research after the completion of my PhD and discuss future areas of work.

CHAPTER TWO

STRATIGRAPHIC EVOLUTION AND KARSTIFICATION OF A CRETACEOUS MID-PACIFIC ATOLL (RESOLUTION GUYOT) RESOLVED FROM CORE-LOG-SEISMIC INTEGRATION AND COMPARISON WITH MODERN AND ANCIENT ANALOGUES*

* A version of this chapter is published in ***Basin Research***:

El-Yamani, M. S., John, C. M., & Bell, R. (2022). Stratigraphic evolution and karstification of a Cretaceous Mid-Pacific atoll (Resolution Guyot) resolved from core-log-seismic integration and comparison with modern and ancient analogues. ***Basin Research***, 34(5), 1536-1566.

The work presented in this chapter has been published in Basin Research:

El-Yamani, M. S., John, C. M., & Bell, R. (2022). Stratigraphic evolution and karstification of a Cretaceous Mid-Pacific atoll (Resolution Guyot) resolved from core-log-seismic integration and comparison with modern and ancient analogues. Basin Research, 34(5), 1536-1566. https://doi.org/10.1111/bre.12670.

Acknowledgements

The results presented here are part of Mahmoud Samir El-Yamani's PhD research at Imperial College London, funded by a full scholarship (MM21/19) from the Ministry of Higher Education and Scientific Research of Egypt. This study benefited from samples and data from the International Ocean Discovery Program (IODP) and its predecessors (ODP and DSDP). We thank Schlumberger and Lloyd's Register for providing access to Petrel software 2020 and Interactive Petrophysics 4.6 respectively. The authors thank Or M. Bialik and the second anonymous reviewer for their constructive reviews that helped to improve the initial version of this paper. The Associate Editor Peter Burgess is thanked for the editorial handling and the constructive reviews that helped to improve the initial version of this paper.

Data availability statement

The data that support the findings of this study are openly available in:

The Marine Geoscience Data System repository at https://www.marine-geo.org/tools/search/Files.php?data_set_uid=29456 (Seismic Data).

The Division of Marine and Large Programs at https://mlp.ldeo.columbia.edu/logdb/scientific_ocean_drilling/ by searching for Leg 143 (Logging Data).

International Ocean Discovery Program, JOIDES Resolution Science Operator at https://web.iodp.tamu.edu/OVERVIEW/?&exp=143 (Core Images and Description).

Proceedings of the Ocean Drilling Program at http://www-odp.tamu.edu/publications/leg_ndx/143index.htm (Drilling Reports, Geochemical data, Core Description).

2.1 Abstract

Atolls are faithful recorders helping us understand eustatic variations, the evolution of carbonate production through time, and changes in magmatic hotspots activity. Several early Cretaceous Mid-Pacific atolls were previously investigated through ocean drilling, but due to the low quality of vintage seismic data available, few spatial constraints exist on their stratigraphic evolution and large-scale diagenesis. Here, we present results from an integrated core-log-seismic study at Resolution Guyot and comparison with modern and ancient analogues. We identify six seismic-stratigraphic units: (1) platform initiation with aggradation and backstepping through the Hauterivian which ended by platform emersion; (2) reflooding of the platform with progradation and aggradation through the Barremian till the early-Aptian when ocean anoxic event 1a resulted in incipient drowning; (3) platform backstepping till the mid-Aptian when the platform shifted to progradation and aggradation till the mid-Albian; (4) platform emersion; (5) reflooding with backstepping ending at the latest-Albian by platform emersion; and (6) final drowning. The stratigraphic surfaces bounding these units are coeval with some of the Cretaceous eustatic events, which suggest an eustatic control on the evolution of this atoll and confirm that several previously reported sea-level variations in the early Cretaceous are driven by eustasy. Changes in subsidence and carbonate production rates and suspected later magmatism have also impacted the stratigraphic evolution. The suspected later magmatism could lead to environmental perturbations and potentially platform demise. Contrary to previous studies, we identify two emersion events during the mid- and late-Albian which resulted in intensive meteoric dissolution and karstification. The platform margin syndepositional fractures interacted with the subaerial exposure events by focusing the dissolution which formed vertically stacked flank-margin fracture-cave system. The study gives a unique insight into the interplay between eustasy, subsidence, and volcanic activity(ies) on long-term evolution of early Cretaceous shallow-marine carbonates. It also documents the impact and distribution of hypogenic and epigenic fluid-flow in atolls serving as an analogue for isolated carbonate platforms.

2.2 Highlights

- Reappraisal of the seismic stratigraphy of the Hauterivian to the latest Albian Mid-Pacific carbonate atoll.
- The stratigraphic evolution comprises three transgressive phases separated by two highstand phases before final drowning.
- Eustasy is a primary controlling factor on the Mid-Pacific early Cretaceous carbonate evolution.

- Changes in subsidence and carbonate production rates and magmatism also impacted platform evolution.
- Two eustatically driven emersion events are interpreted in the Albian leading to intensive karstification.
- Karstification along syndepositional fractures led to fracture-cave system at the rims.

2.3 Introduction

Isolated carbonate platforms and atolls are faithful recorders of the evolution of life on Earth, of palaeoceanographic changes, and of base-level changes (e.g. Schlanger and Premoli Silva, 1986; Robinson, 2011; Harris et al., 2015; Wu et al., 2020; Bialik et al., 2021a,b). They occur throughout the geologic record, from the Archean to the present. The low latitudes of all oceans host isolated carbonate platforms including, but not limited to, the Maldives, Chagos and the Mascarene in the Indian Ocean, the Great and Little Bahama Banks in the Atlantic, Funafuti, Bikini and Tuamotu Islands in the Pacific Ocean and Macclesfield Bank in the South China Sea. They are of particular interest because their internal architecture, onset, growth, diagenetic alterations, and demise tend to be largely controlled by biotic evolution, eustasy, volcanism, subsidence and environmental conditions. Therefore, they offer better assessment of the factors controlling carbonate evolution, as they are away from clastic input (Courgeon et al., 2017).

Several drowned Cretaceous atolls are scattered throughout the Pacific Ocean, thanks to the abundance of hotspot volcanism in the region. The Mid- and Western-Pacific have been investigated by several seismic and drilling campaigns (Ocean Drilling Program (ODP) Leg 144 and 143; Figure 2.1; Winterer and Sager, 1995), thus offering some existing data to understand carbonate production, stratigraphic development and possible ties to eustasy in this region. In addition, these atolls are prone to subaerial exposure and karstification (e.g. Wodejebato and Limalok guyots; Arnaud-Vanneau et al., 1995), dolomitization (e.g. Resolution and Allison guyots; Röhl and Strasser, 1995) and later magmatic activity(ies) (e.g. Allison guyots; Pringle and Duncan, 1995), thus offering good natural laboratories to understand spatial and temporal evolution of diagenetic alterations such as meteoric, burial and hydrothermally induced diagenesis and island dolomite.

Despite the complex heterogeneity of carbonate platforms, our understanding of the Pacific Cretaceous atolls mostly comes from sparse well data (e.g. Arnaud et al., 1995; Wilson et al., 1998; Jenkyns and Wilson, 1999) with rare use of vintage 2D seismic reflection data (e.g. Wodejebato and Limalok guyots; Arnaud-Vanneau et al., 1995) of lower quality than modern standards (e.g.

Sager et al., 1993a; Strasser et al., 1995). Hence, largely due to a lack of good seismic coverage of reasonable quality, the seismic-stratigraphic framework of the Pacific drowned Cretaceous atolls, their evolution, depositional architecture, karstification geomorphic features and potential presence of fluid venting systems are poorly resolved. Our paper presents a core-log-seismic integration study on Resolution Guyot in the Mid-Pacific Mountains and comparison with modern and ancient carbonate system analogues to shed new light on these unknowns.

Seismic imaging of carbonate rocks has developed tremendously in the last two decades. This is reflected in the increasing number of special publications focusing on seismic imaging of carbonates (e.g. Eberli et al., 2004b; Hendry et al., 2021) and seismic-based research articles (e.g. Saller and Vijaya, 2002; Zampetti et al., 2004; Fournier et al., 2005; Burgess et al., 2013; Paumard et al., 2017; Clark et al., 2018; Van Tuyl et al., 2018; Bialik et al., 2021a,b; Huang et al., 2020; Cross et al., 2021; Ma et al., 2021). Moreover, our conceptual understanding of carbonate systems has improved recently, thanks to satellite image and facies analyses on modern isolated carbonate platforms (e.g. Gischler, 2006; Harris et al., 2015; Jorry et al., 2016; Prat et al., 2016; Rankey, 2016; Utami et al., 2018; Wu et al., 2020). The developments in our understanding of carbonate systems and seismic imaging over the last two decades offer an opportunity to revisit the vintage seismic and well data of the early Cretaceous Mid-Pacific atolls to better understand these systems.

Deciphering the controls on the carbonate platform evolution is an ongoing question (e.g. Wilson et al., 1998; Jenkyns and Wilson, 1999; Pomar et al., 2004; Westphal et al., 2010; Hönig et al., 2017; Droxler and Jorry, 2021). Considering: (1) the Cretaceous as one of the most prolific periods of carbonate sedimentation (Kiessling et al., 2003), (2) the presence of significantly different eustatic curves for the Cretaceous (Sahagian et al., 1996; Miller et al., 2005; Haq, 2014) and (3) the isolated carbonate platforms as prime targets for subsurface energy applications (e.g. Burgess et al., 2013; Esestime et al., 2016; Rusciadelli and Shiner, 2018), there is a need to better understand how the Mid-Pacific atolls functioned during the Cretaceous. This work applies seismic-stratigraphic methods to the Resolution Guyot carbonate atoll as a prime example of a Mid-Pacific early Cretaceous (Hauterivian to Albian) atoll. We integrate drilling and seismic data with examples from recently published literature of modern and ancient carbonate analogues using high-resolution seismic data and satellite images. Our objectives were to understand the following: (1) the stratigraphic evolution of the early Cretaceous (Hauterivian to Albian) carbonate atoll of Resolution Guyot to give insights into the response of Cretaceous reef builders to eustasy and global anoxia, (2) the potential karstification events as direct evidence of eustatic lowstands in the Cretaceous affecting the Mid-Pacific guyots and how the karst seismic geomorphic features are

distributed and controlled, and (3) constraints on the distribution of fractures, fracture corridors and any evidence for the presence of fluid conduits.

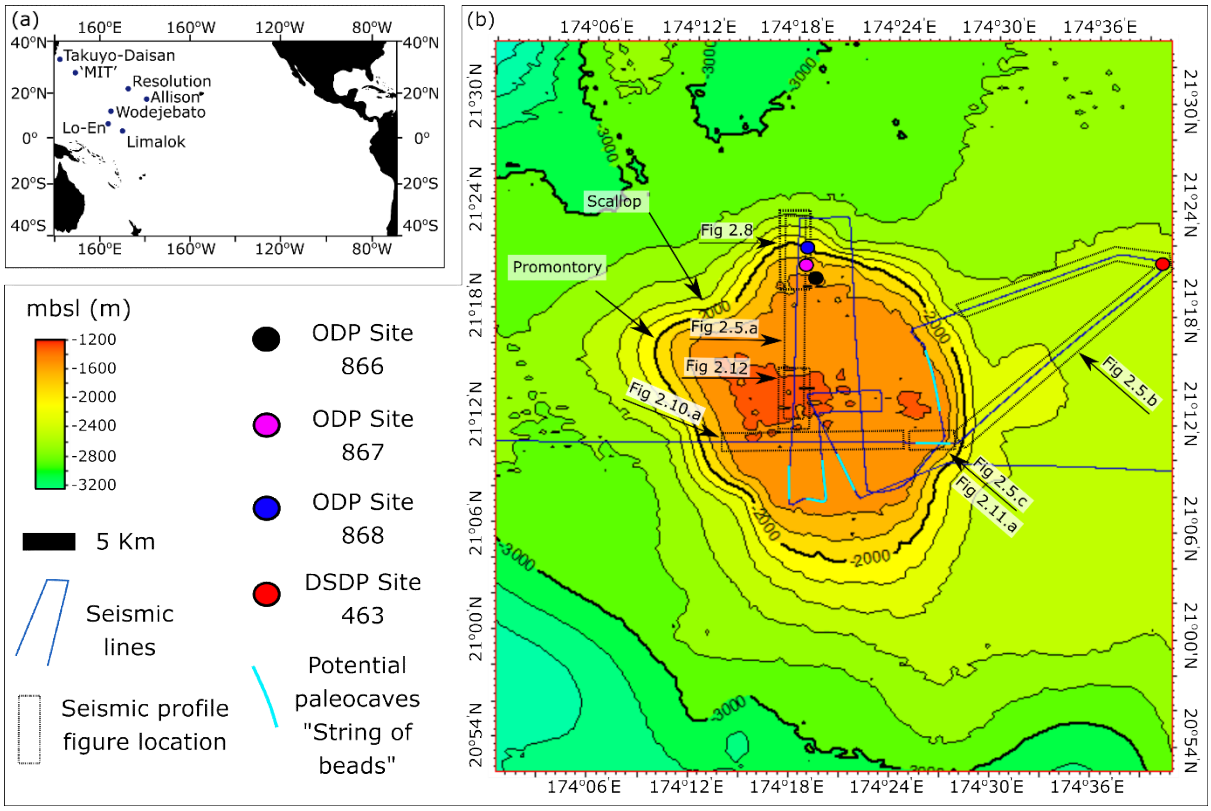


Figure 2.1. (a) Map of the Pacific Ocean showing guyots (blue dots) targeted during ODP Legs 143 and 144 (adapted from Wilson et al., 1998). (b) Bathymetry map (mbsl; meter below sea level) showing the location of Resolution Guyot and the location of ODP and DSDP Sites, seismic data and figures in this study. The bathymetry map (b) of Resolution Guyot reveals the typical alternating scalloped-promontory shape of isolated carbonate platforms.

2.4 Geological Setting

Resolution Guyot is a drowned atoll in the Mid-Pacific Mountains, one of the most prominent seamount chains in the Pacific Ocean (Winterer and Sager, 1995). This isolated carbonate platform is 25 × 35 km wide (Figure 2.1; a radius of ca. 15 km) and was originally formed at sea level, but is currently drowned and the platform top sits ca. 1200–1400 m below sea level. It has a sedimentary cover (Figure 2.2; Hauterivian-Albian; ca. 1620 m thickness; Winterer and Sager, 1995) resting on a volcanic edifice: it can be classified as a guyot which was originally deposited as an atoll (sensu Scott and Rotondo, 1983). It is capped by a thin pelagic cap deposited after the drowning (Winterer and Sager, 1995). Almost all our understanding of Resolution Guyot comes from ODP Site 866 near the platform margin (Figure 2.1), as the other two sites (i.e. 867 and 868) are very shallow.

Extensive intraplate volcanic features characterize the Pacific seafloor (Hamilton, 1956). The radiometric age of the oldest volcanic samples at Site 866 is 127.6 ± 2.1 Ma, with younger ages at

121.3 ± 1.6 Ma (Pringle and Duncan, 1995). In addition to its importance in understanding the Earth's history, magmatic activity and associated fluid flow make major contributions to seep locations (e.g. Feng and Chen, 2015), deformation (e.g. Omosanya et al., 2017) and diagenetic alterations (e.g. carbonate dissolution, Sun et al., 2013; dolomitization, Breislin et al., 2020; silicification, Fiordalisi et al., 2021).

Based on only 1D data from Site 866 (very low average recovery of ca. 15.4%; Arnaud et al., 1995), the sequence stratigraphy of Resolution Guyot atoll can be summarized as follows: (1) Hauterivian transgression; (2) very restricted aggrading shallow marine Barremian regression sequences; (3) progressive deepening during the early-Aptian with the appearance of shallow, open-marine sediments; (4) early-Aptian transgression characterized by open-marine deposits; (5) return to shallow-marine-restricted deposits during the late-Aptian; and (6) new transgressive period during the Albian, with the development of a shallow, open-marine environment. Arnaud et al. (1995) and Strasser et al. (1995) both highlighted that the vertical facies evolution that was used to build this stratigraphic evolution model is only applicable at the drill site and the sequence stratigraphy away from the well is unknown.

The diagenetic history of the Resolution Guyot carbonates based on core data is relatively simple including marine and meteoric diagenesis and late diagenetic dolomitization (Flood and Chivas, 1995; Röhl and Strasser, 1995). The presence of meteoric diagenesis is still debated: the irregular surface of the upper Albian carbonates below the pelagic cap observed in 3.5-kHz echo-soundings and seismic profiles is interpreted as evidence for subaerial exposure (Winterer et al., 1995; Winterer, 1998), but the oxygen and carbon isotope signature of bulk carbonates and calcitic cements do not offer any supporting evidence of meteoric diagenesis (Wilson et al., 1998; Jenkyns and Wilson, 1999). This observation has raised the debate of whether the Pacific Cretaceous atolls have ever experienced subaerial exposure and karstification before their demise. This debate was reflected on the hypotheses for the demise of the Mid-Pacific atolls, which are: (1) 'death-by-emergence-and-submergence' (Winterer et al., 1995; Winterer, 1998) and (2) 'death-in-tropics' (Larson, 1991; Wilson et al., 1998; Jenkyns and Wilson, 1999).

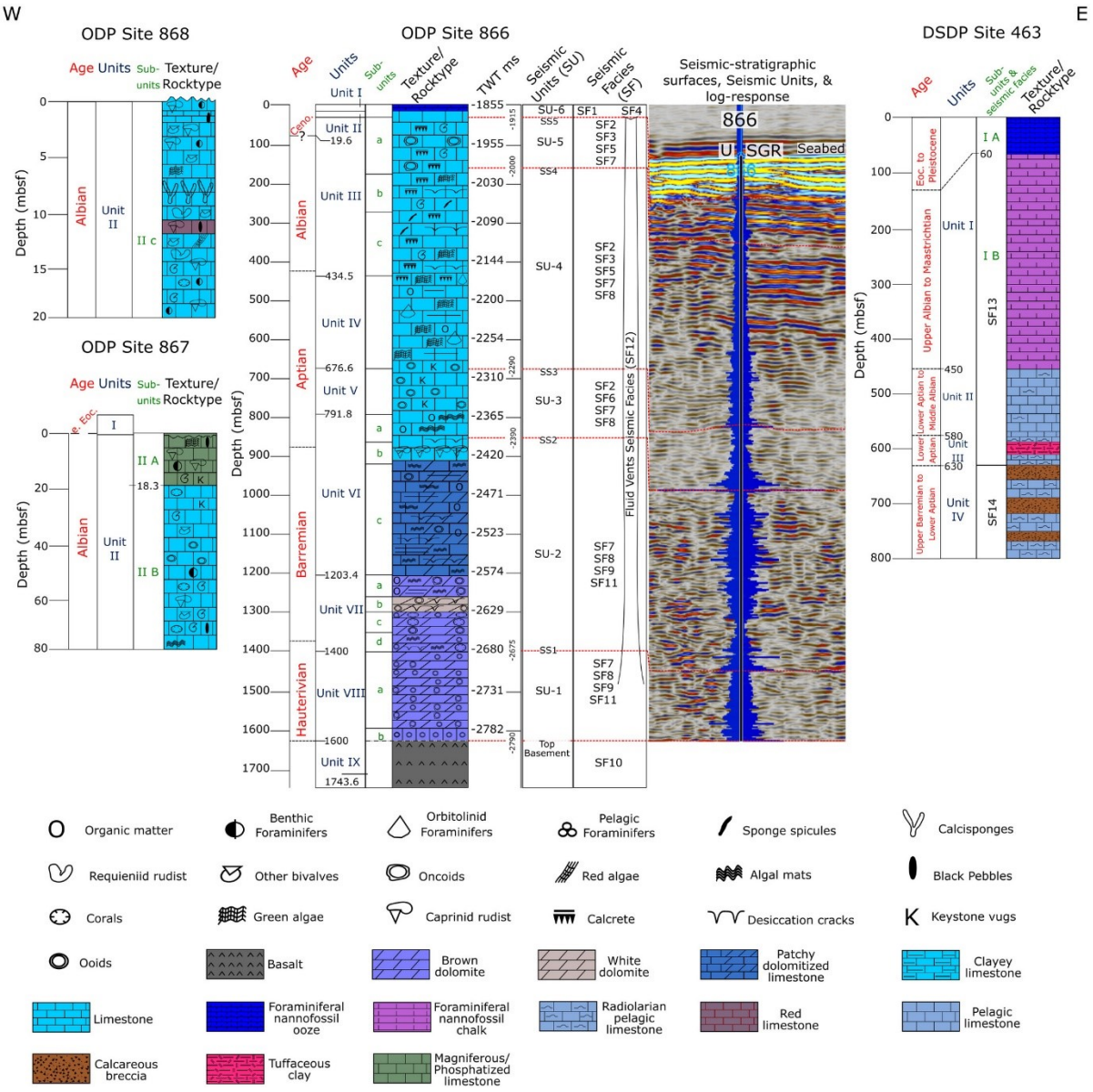


Figure 2.2. Lithostratigraphic description of ODP Sites 866, 867 and 868 and DSDP Site 463 (adapted from Timofeev et al., 1981; Sager et al., 1993a, 1993b). The figure shows a summary of the lithological and fossil content of the different lithostratigraphic units at different drill sites along with a correlation between seismic data, logging data (SGR; Spectral Gamma Ray and U; Uranium log) and lithostratigraphic description at Site 866, showing the identified seismic-stratigraphic surfaces (SS) and units (SU) and seismic facies (SF).

2.5 Data and Methods

2.5.1 Dataset

This study uses bathymetry, well and seismic reflection data (Figure 2.1). Bathymetry comes from Earthref website (Keizer et al., 2001) and well data come from ODP sites 866, 867 and 868 (Sager et al., 1993a,b) and Deep-Sea Drilling Program (DSDP) Site 463 (Timofeev et al., 1981) (Figures 2.1 and 2.2). Site 866 penetrated 1620 m of platform interior sediments followed by 143 m of the basaltic basement. Sites 867 and 868, respectively, penetrated ca. 80 and 20 m of the platform

margin. Site 463 penetrated ca. 822 m of peri-platform sediments. Well data used in this study include core images, published core descriptions (e.g. Timofeev et al., 1981; Sager et al., 1993a,b; Arnaud et al., 1995) and logging data including calliper, spectral gamma ray (SGR), potassium (K), thorium (Th), uranium (U), sonic, and Formation MicroScanner (FMS).

The seismic data (Figure 2.1) were collected during cruise 'Roundabout Expedition Leg 10' (RNDB10WT; Nov–Dec 1988) by the R/V Thomas Washington, a programme dedicated to seismic imaging of the Mesozoic Guyots of the western Pacific. The data are single channel, 2D seismic acquired using an 80-in.3 water gun, which was processed by the Institute for Geophysics at the University of Texas including filtering (50–200), mixing (1:1:1) and automatic gain control (Marine Geoscience Data System, n.d.).

2.5.2 Revised Age Model

Age constraints in this study are achieved by combining existing carbon- and strontium-isotope data from Jenkyns (1995) and Jenkyns et al. (1995) at Site 866. Details of our correlation methodology and calculations are provided in APPENDIX A Table A1. Briefly, we match the $\delta^{13}C$ data from Jenkyns et al. (1995) with the low-latitude calibrated composite $\delta^{13}C_{carb}$ curve (reproduced from Herrle et al., 2015, using published data from Tethyan sections of Erba et al. (1999), Gale et al. (2011), Herrle et al. (2004), and calibrated using Gradstein et al. (2012; GTS2012)). The carbon-isotope stratigraphy approach is similar to age dating of the Cretaceous Sverdrup Basin Arctic sediments by Herrle et al. (2015). Subsequently, we use the strontium-isotope data from Jenkyns (1995) and correlate their values with a recent global $^{87}Sr/^{86}Sr$ curve (McArthur et al., 2012, version 5B) anchored on GTS2012 (Gradstein et al., 2012) as the eustatic chart for the Cretaceous by Haq (2014) is also anchored on the same geologic time scale. The best model was obtained by iteratively moving tie points until both strontium isotope and $\delta^{13}C$ constraints were honoured.

2.5.3 Seismic and Log Interpretation

Our Seismic to well tie is achieved by revising the proposed depth to seismic reflectors from Sager et al. (1993a) with integration of sonic logs at Site 866 to obtain a continuous time-depth relationship (APPENDIX A Table A2; Figure 2.2). The same velocity of the first 100 m at Site 866 is applied to sites 867 and 868 to convert geological horizon depths to time so they could be identified in the seismic data. Seismic interpretation and FMS data plotting are performed using Petrel® and Interactive-Petrophysics® Software, respectively.

We have conducted our seismic interpretation using seismic-stratigraphic principles (Mitchum et al., 1977; Courgeon et al., 2016a), that include (1) defining the seismic facies based on interpreting reflection geometries (internal and external), continuity, amplitude and their location within the platform; (2) tracking the key seismic-stratigraphic surfaces and associated reflection (stratal) terminations, if available. In many cases, key horizons identified within the wells (e.g. the dolomite-basement boundary; Figure 2.2) are not identified as distinct single reflections in the seismic data, but as boundaries between zones with differing seismic facies. Our seismic facies analysis is therefore critical to developing a seismic-stratigraphic framework for the atoll and the two interpretation steps: (i) mapping seismic facies and (ii) mapping seismic-stratigraphic surfaces are intimately linked. To groundtruth our seismic facies analysis and to overcome the issue of the low quality of the data, each seismic facies is compared with well data wherever possible and with several high-quality analogous seismic data sets from other carbonate platforms. This resulted in better understanding of what our seismic facies interpreted within these vintage data may represent away from drill sites. Seismic attributes are used to assist the interpretation including root-mean-square-amplitude (RMSA) and signal-envelope and variance amplitudes. Seismic-stratigraphic trends of progradation, aggradation and retrogradation are interpreted through tracing the trajectory of the platform margin using break-of-slope or mounded seismic facies features (Burgess et al., 2013). The interpretation of different seismic-stratigraphic surfaces is guided by integrating several inputs, including; (1) seismic reflection (stratal) terminations (if available); (2) marker reflections coinciding with distinct changes in reflection characteristics (e.g. sharp change across the entire atoll from chaotic to continuous reflections or high-amplitude to low-amplitude reflections); (3) core data (e.g. brecciated intervals resembling subaerial exposure and karstification); and (4) logging data (e.g. sharp peaks in SGR and U resembling flooding surface). Maximum flooding surfaces (MFS) are identified at the base of the last backstepping margin on which reflections of subsequent units downlap (e.g. Yose et al., 2006). *Type-1 sequence-boundaries* (Schlager, 2005) are interpreted at the top of pervasively discontinuous seismic reflections showing a rugged surface offering potential evidence of subaerial exposure (e.g. Howarth and Alves, 2016; Paumard et al., 2017; Van Tuyl et al., 2018) where sinkholes can be observed to delineate a sequence boundary (e.g. Paumard et al., 2017). Sinkhole characteristics can be summarized as (1) having V- or U-shape (e.g. Heubeck et al., 2004; Howarth and Alves, 2016), (2) showing drape or collapse of the overlying sediments (Bachtel et al., 2004) and (3) appearing as dim areas within continuous reflections and associated with bright-spot anomalies underneath (Yang et al., 2018). *Type-3 sequence-boundaries* are interpreted on prominent reflection surfaces representing a depositional hiatus between the highstand system tract (HST) and the immediately overlying

transgressive system tract (TST) with no evidence of exposure (Schlager, 2005). These stratigraphic surfaces are interspersed with seismic-stratigraphic units each of which has certain internal seismic facies and stacking pattern revealed by tracing platform margin seismic facies (Burgess et al., 2013).

2.6 Results and Interpretation

2.6.1 Revised age model

Ten excursion points and nine correlative intervals in between were matched (highlighted by correlation lines with the low latitude calibrated composite $\delta^{13}C_{carb}$ curve; Figure 2.3, APPENDIX A Table A1) based on similar $\delta^{13}C$ trends. In addition, 7 tie points (inflection and plateaus) were identified in Sr isotopes (APPENDIX A Table A1):

- At ca. 1328 mbsf (0.707449 ± σ 0.00002) corresponding to trends during the early Barremian (ca. 130.5 Ma; McArthur et al., 2012; Bodin et al., 2015)
- At ca. 1040 mbsf (0.707595 ± σ 0.00002) corresponding to the late early-Barremian (ca. 129 Ma; McArthur et al., 2012; Bodin et al., 2015)
- At ca. 591 mbsf (0.707334 ± σ 0.00002) corresponding to the late Aptian (ca. 121.4 Ma; McArthur et al., 2012)
- At ca. 434 mbsf (0.707229 ± σ 0.00002) corresponding to the latest Aptian (ca. 114.8 Ma; Bodin et al., 2015; McArthur et al., 2012)
- At ca. 250 mbsf (0.707436 ± σ 0.000031) corresponding to the mid-Albian (ca. 107.75–106.8 Ma; McArthur et al., 2012)
- Between ca. 165 and 125 mbsf (0.707421 ± σ 0.00002, 0.707421 ± σ 0.000021, and 0.707414 ± σ 0.00002) corresponding to the late-Albian (ca. 103.6–105.15 Ma; McArthur et al., 2012)
- At ca. 48 mbsf (0.707458 ± σ 0.000024) corresponding to the latest Albian (ca. 101.3 Ma; McArthur et al., 2012).

The revised age model (Figure 2.3; APPENDIX A Table A2) suggests that (1) sedimentation started above the basement at Site 866 at ca. 132 ± 1 Ma based on the projected age of the first recovered sample at 1620 mbsf, (2) the Hauterivian/Barremian boundary lies at ca. 1400 mbsf, (3) the Barremian/Aptian boundary lies at ca. 880 mbsf, (4) the Aptian/Albian boundary lies at ca. 390 mbsf and (5) neritic carbonate production ceased in the latest Albian/early Cenomanian (ca. 100.45 Ma) based on the projected age of the last shallow marine carbonate sample recovered below the pelagic cap at ca. 19.6 mbsf.

This revised age model is anchored on the geologic time scale of Gradstein et al. (2012) giving a timespan from ca. 132 ± 1 and ca. 100.5 ± 1 Ma between onset and drowning of the carbonate platform. In Section 5.2, the updated age-model is used to compare our record with the Haq (2014) revised eustatic record and Pohl et al. (2020) carbonate production trends as they are all anchored on the same geologic time scale (Gradstein et al., 2012).

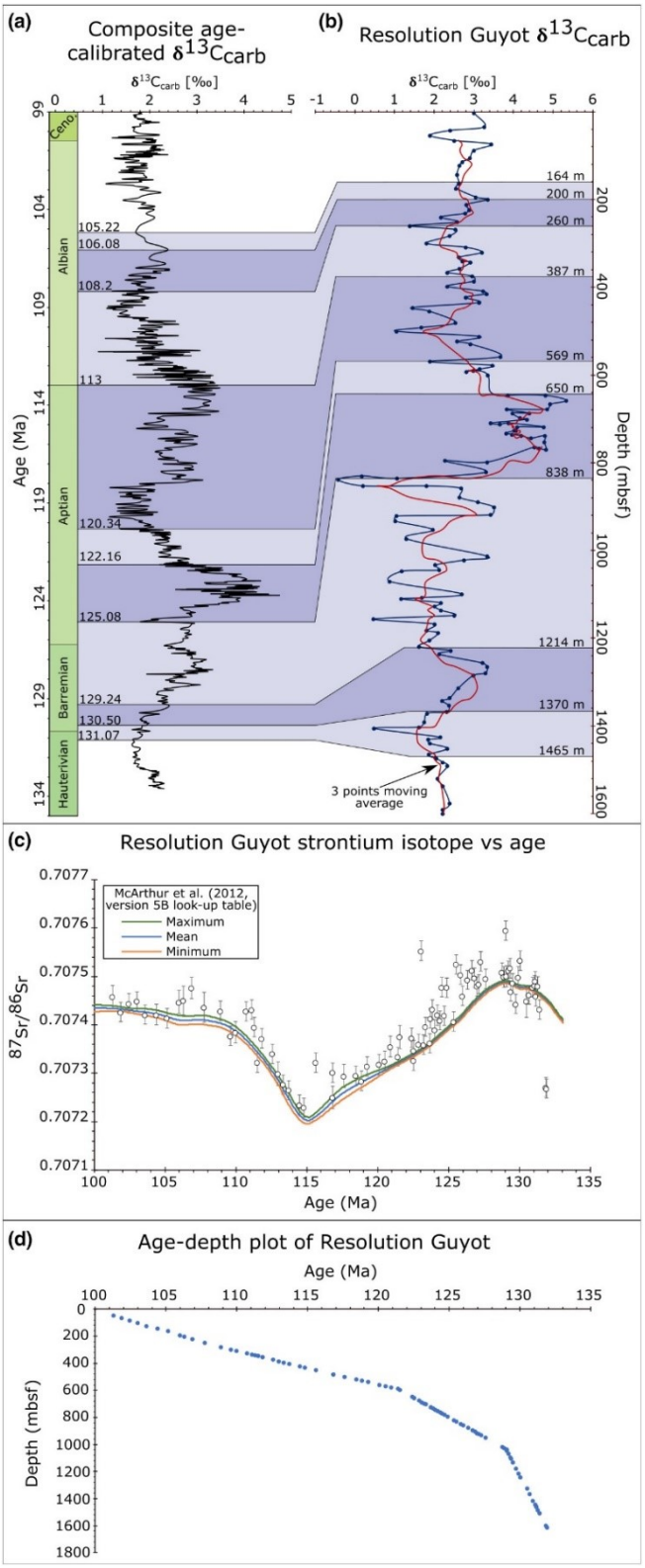


Figure 2.3. (a) The low-latitude calibrated composite $\delta^{13}C_{carb}$ curve (reproduced from Herrle et al., 2015, using published data from Tethyan sections of Erba et al., 1999; Gale et al., 2011; Herrle et al., 2004) correlated with (b) the $\delta^{13}C_{carb}$ curve of Resolution Guyot (correlation lines highlighted in black) using carbon isotope data from Jenkyns (1995). Dark and light blue zones represent nine correlative intervals in-between ten excursion tie points. (c) The strontium isotope age model at ODP Site 866 based on using strontium isotope data from Jenkyns et al. (1995) and the values in the reference curve of McArthur et al. (2012, version 5B). (d) Age-depth plot of Resolution Guyot at Site 866 using the calculations from the strontium isotope age model. Please refer to APPENDIX A Table A1 in the supplementary materials showing the detailed steps and calculations for the revised age model.

2.6.2 Seismic Facies Analysis

We identified fourteen seismic facies (Figure 2.4) and their palaeogeographic distributions within the atoll (Figure 2.5) based on seismic reflection properties including reflection patterns, continuity, amplitude and external and internal geometry. Detailed characteristics of these seismic facies are explained below along with their interpretation integrating drilling and logging data and comparison with modern examples from high-resolution seismic data sets.

Seismic facies 1 (SF1) consists of horizontal, parallel and continuous reflections of very high amplitude (Figures 2.4 and 2.5). It is found forming a tabular sheet ca. 20–60 ms TWT thick covering the upper most part of the guyot (ca. 30–90 m given our time–depth relationship, APPENDIX A Table A2). It is also observed basinward of the toe of the slope where it onlaps the platform margin and extends for tens of kilometres (Figures 2.4 and 2.5).

Interpretation: SF1 (Figure 2.4) is interpreted as pelagic deposits covering the carbonate platform. This is supported by core data from Site 866 that encounter nannofossil ooze (i.e. lithostratigraphic Unit I; Figure 2.2). The seismic character of SF1 matches basinal deposits identified by Van Tuyl et al. (2018) in the Miocene carbonate build-ups in northwest Australia. The very high amplitude of SF1 could be explained by the underlying iron-manganese encrusted limestone (lithostratigraphic Unit II; Figure 2.2) representing a drowning succession similar to those identified by Eberli et al. (2010) on the Marion Plateau. Similar seismic facies was described by Mitchell et al. (2015) in other Pacific guyots.

Seismic facies 2 (SF2) consists of sub-horizontal to horizontal parallel and continuous reflections of high-to-moderate amplitude (Figure 2.4). It is ca. 250 ms TWT thick (ca. 420 m). SF2 is found throughout the platform interior extending for tens of kilometres. Laterally, SF2 transitions to SF6, 7 and 8 at the platform margin where the reflections become more chaotic (Figures 2.4 and 2.5).

Interpretation: SF2 (Figure 2.4) is interpreted as the platform interior, as it corresponds to cyclic packstone–wackestone and mudstone lithofacies (i.e. lithostratigraphic Unit III at Site 866; Figure 2.2). The seismic character of SF2 matches the lagoon facies identified by Van Tuyl et al. (2018) at the Miocene carbonate build-ups in northwest Australia. In our data, lagoon deposits (Figures 2.2 and 2.4) appear sometimes as transparent (ca. −2150 to ca. −2400 ms TWT) or chaotic (ca. −2400 to ca. −2800 ms TWT) which correlates to similar seismic facies observed on the Great Bahama Bank (GBB) and the synthetic seismic section of the Maiella Platform by Eberli et al. (2004a).

Seismic facies 3 (SF3) is characterized by pervasively discontinuous subparallel to chaotic reflections of high to low amplitude (Figure 2.4). SF3 extends laterally throughout the platform (Figures 2.4 and 2.5).

Interpretation: SF3 (Figure 2.4) is interpreted as karst horizons. It shares similar seismic characteristics as karst horizons formed by subaerial exposure in the South Malé Atoll in the Maldives (Betzler et al., 2015), the Browse Basin, Northwest Australia (Howarth and Alves, 2016; Van Tuyl et al., 2018) and Macclesfield Bank in the South China Sea (Huang et al., 2020). Observations from cores also support karstification including (1) core recovery at Site 866 above 500 mbsf (within SF3) is ca. 8%, which decreases to ca. 1.5% above 300 mbsf (within SF3) suggesting brecciation of the limestone (2) FMS Images at Site 866 (ca. 250–450 mbsf; within SF3) show intensive brecciation and abundance of vuggy porosities (Swiss cheese-like vugs; Figure 2.6), (3) several yellow, reddish, and brown stained calcrete horizons are found at ca. 60 and ca. 220–420 mbsf (Sager et al., 1993a), (4) the drill bit at Site 867 dropped freely for 8 m interpreted as entering a cave (Sager et al., 1993b).

Seismic facies 4 (SF4) is a discrete, concave feature (a topographic depression) ca. 30 ms TWT deep (ca. 45 m) with a diameter of 1500–1750 m (Figure 2.4) filled with onlapping sediments. Layers below the depression are chaotic and highly discontinuous. This facies is encountered only at the seabed in the middle of the platform (Figure 2.5).

Interpretation: Based on observations of crater-like depressions with onlapping reflections, SF4 (Figure 2.4) could be interpreted as a pockmark or crater formed by sediment removal through fluid venting which is similar to category 5 pockmarks identified by Betzler et al. (2011) in the Maldives carbonate platform. Alternatively, it could be a sag structure similar to karst collapse sags discussed by McDonnell et al. (2007) in the Cambrian–Ordovician Ellenburger Group in Texas.

Seismic facies 5 (SF5) is a vertical anomalous feature appearing as beads of high-amplitude reflections compared with the host rock. These vertical bodies have a height of ca. 15–50 ms TWT (ca. 25–90 m; mainly ca. 50 m) and a width of ca. 100–150 m (Figures 2.4 and 2.5).

Interpretation: The anomalous appearance of SF5 (Figure 2.4) is interpreted as "paleocaves" as they match the string-of-beads "paleocaves" reflections identified by numerous authors in Tahe oilfield (e.g. Zeng et al., 2020) and Tarim Basin (e.g. Yang et al., 2012) in China and many other places (Basso et al., 2018; Van Tuyl et al., 2018). The bit drop at Site 867 (at the platform margin) was interpreted as a sign of entering a cave (Sager et al., 1993b): this occurred at a drilling depth close to where we interpret "paleocaves" in seismic data. The high acoustic impedance contrast between

the host rock and the "paleocaves" is due to the cave filling material which could be sedimentary deposits, collapse breccia or empty space filled with seawater (Campos Basin, Brazil; Basso et al., 2018).

Seismic facies 6 (SF6) has a broadly mounded external morphology and involves chaotic to wavy semi-continuous bidirectionally dipping low-amplitude reflections, which form bodies of ca. 60 ms TWT thick (ca. 130 m). It is found at the platform margin between SF2 and 7 (Figures 2.4 and 5).

Interpretation: SF6 (Figure 2.4) is interpreted as a part of the platform margin representing shoal deposits; it corresponds to lithostratigraphic Unit V at Site 866 which is formed of planar and cross-laminated well-sorted oolitic grainstones with keystone vugs (Figure 2.2). SF6 seismic characteristics match shoals identified by Bachtel et al. (2004), Handford and Baria (2007), Paumard et al. (2017) and Zhang et al. (2020a).

Seismic facies 7 (SF7) has convex up mounded semi continuous to discontinuous reflections of moderate-to-high amplitude, which show bidirectional downlaps (Figure 2.4). SF7 is located within the platform interior, forming ca. 30 ms TWT thick (ca. 60 m) bodies with lateral extent of ca. 500 m. At the platform margin, it forms bodies of ca. 30–60 ms TWT thickness (ca. 60–90 m) with lateral extent of ca. 600–1600 m (Figures 2.4 and 2.5). Associated onlapping geometries can be observed around the mounded bodies (Figure 2.4).

Interpretation: SF7 (Figure 2.4) is interpreted as platform margin facies. This interpretation is supported by lithofacies at Sites 867 and 868 (Figures 2.2 and 2.5) which are located closely to SF7. Site 867 comprises peloidal and oolitic grainstones and coarse-grained rudist shell debris representing beach deposits (Sager et al., 1993a). Site 868 comprises sponges and requieniid rudists bafflestones and framestones interpreted as sponge, rudists and corals (subordinate) bioherms under wave and storm action alternating with coarse shell rubble layers (Strasser et al., 1995). According to Bover-Arnal et al. (2015), Özer et al. (2017), and Gili and Götz (2018), requieniid rudists are dominant in the platform margin and upper-slope settings. Therefore, SF7 likely represents a sand beach barrier with sponge and rudist build-ups that extend to the upper slope, which appear as the onlapping seismic reflections at the front of SF7. The mounded reflections with bidirectional downlaps in SF7 are similar to the shelf-margin defined by Bachtel et al. (2004). The onlapping seismic reflections behind SF7 are interpreted as a back-margin apron which matches the backreefs identified by Masaferro et al. (2004) in the Miocene build-ups of the Luconia province. This is supported by the lithology of the uppermost part of the lithostratigraphic Unit

III at Site 866, which is formed of coarse-grained floatstones and rudstones with shell debris and rip-up clasts representing washover deposits.

Seismic facies 8 (SF8) consists of moderate- to high-amplitude semi-continuous to discontinuous reflections which exhibit sigmoid to sigmoid-oblique clinoformal geometries. They are located only at the platform margin (Figures 2.4 and 2.5) and are onlapped by parallel and climbing reflections.

Interpretation: SF8 (Figure 2.4) is interpreted as platform margin clinoforms, as it matches the described character of marginal clinoforms by Bachtel et al. (2004) and Van Tuyl et al. (2018). No well-based lithological controls exist but our interpretation of SF8 is supported by the exclusive location of this facies at the margin (Figure 2.5).

Seismic facies 9 (SF9) presents high-amplitude reflections with abrupt terminations and local transgressions exhibiting planar shapes and of distinct lateral extent (Figures 2.4 and 2.5). SF9 extends laterally from ca. 500 to 2500 m and vertically from ca. 25 to 55 ms TWT (ca. 50–120 m).

Interpretation: SF9's (Figure 2.4) characteristics of high-amplitude reflections with limited lateral extent and abrupt terminations match described magmatic sills in numerous studies (e.g. Planke et al., 2005; Magee et al., 2015, 2016; Chen et al., 2020; Geng et al., 2020). We therefore tentatively suggest that SF9 are intruded magmatic sills, but SF9 has not been drilled at Resolution Guyot.

Seismic facies 10 (SF10) consists of highly disrupted chaotic reflections of generally low amplitude with some zones of high amplitude (Figure 2.4). Gentle clinoforms (?), seaward dipping (?), and faint layered reflections were observed in some localities. This facies is only found in the deepest imaged part of the guyot (Figure 2.5).

Interpretation: SF10 (Figure 2.4) is interpreted as the volcanic basement, as it corresponds to basalts at Site 866 (Lithostratigraphic Unit IX; Figure 2.2). Its seismic characteristics are similar to the seamount on the Saurashtra Volcanic Platform described by Corfield et al. (2010) in terms of (1) chaotic, uneven and discontinues reflections, (2) some reflections around the margins show geometries similar to seaward dipping reflectors and volcanic clinoforms which correlates well with the suggested subaerial lava flow of the studied samples at Site 866 by Baker et al. (1995). Delineating the top volcanic basement is complicated by the similar density and seismic velocity of the volcanic basement and the overlying dolomitized limestone leading to similar acoustic impedances (Kenter and Ivanov, 1995; Figure 2.2).

Seismic facies 11 (SF11) consists of discontinuous, chaotic reflection zones, which are located immediately above SF10 (Figures 2.4 and 2.5). High-amplitude reflections of SF9 (intruded

magmatic sills) can be observed within the chaotic zone. This facies extends laterally throughout the platform within the sedimentary succession from ca. −2400 to −2800 ms TWT (ca. 830–1620 mbsf). Qualitatively, at ca. −2675 to −2650 ms TWT (ca. 1400 mbsf), SF11 can be divided into two parts with more layered high-amplitude reflections above and less layered high-amplitude reflections and more chaotic low-amplitude reflections below.

Interpretation: SF11 (Figure 2.4) is interpreted as chaotic zones associated with fluid escape pipes similar to those described by Huang et al. (2020) in Macclesfield Bank in the South China Sea. At the same horizontal level of this seismic facies, the lithology at Site 866 is formed of a range of lithofacies from dolomitized oncoidal/oolitic grainstones in lithostratigraphic Unit VIII to lagoonal wacke/pack-stones in lithostratigraphic Units VII–VI.

Seismic facies 12 (SF12) presents vertical zones of disrupted and reduced reflection continuity (Figure 2.4). Within SF12, reflections range from upward convex or concave to more complex geometries. In some cases, SF12 is surrounded by tilted and enhanced reflection amplitudes (Figures 2.4 and 2.5). It is closely associated with SF11 in its lower part and extends vertically for a height of ca. 500–700 ms TWT (900–1300 m).

Interpretation: SF12 (Figure 2.4) is interpreted as fluid vents which (Figure 2.2) present vertical zones of disrupted reflectivity and reduced reflection continuity cutting through layered successions similar to fluid flow pipes described in numerous studies (e.g. Hustoft et al., 2007; Moss and Cartwright, 2010; Cartwright and Santamarina, 2015). The variance attribute helps in discriminating the places affected by fluid flow pipes appearing as zones of dim to chaotic reflections relative to the well-bedded, high-medium amplitude facies of the host-rock strata (e.g. Jamtveit et al., 2004; Omosanya et al., 2018; Hendry et al., 2021). The interpreted fluid vents are surrounded by upward bending reflections potentially indicating deflection by upward fluid flow similar to fluid conduits described by Omosanya et al. (2018) in the Vøring Basin Offshore Norway and Wang et al. (2018a) in the South China Sea.

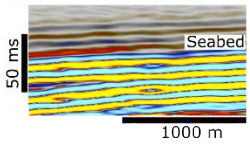
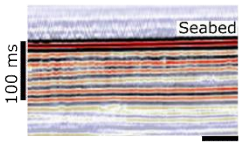
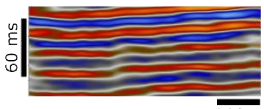
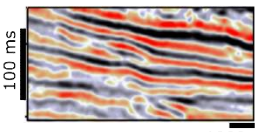
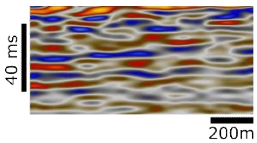
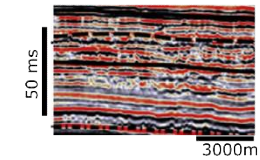
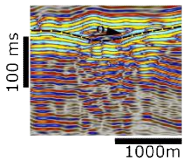
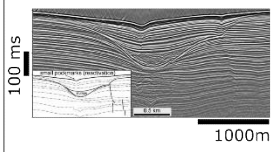
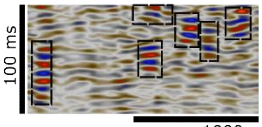
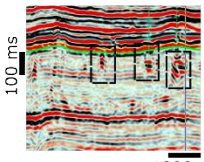
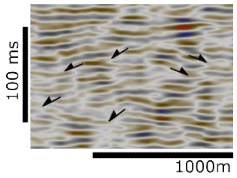
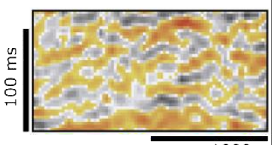
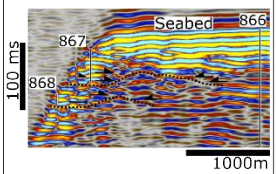
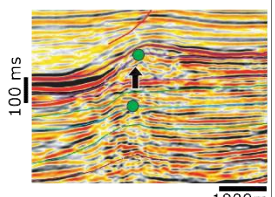
Seismic facies 13 (SF13) is characterized by mounded chaotic, hummocky, subparallel and discontinuous reflections of varying amplitudes (Figure 2.4). It is found in basinal regions and forms lenticular bodies ca. 200–450 ms TWT thick that pinch out towards the toe of the platform edge (Figure 2.5).

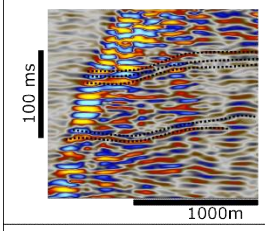
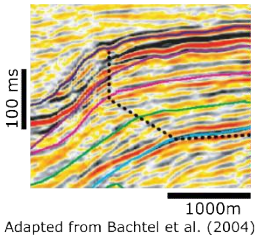
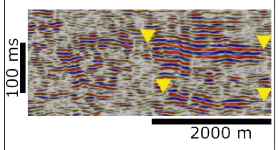
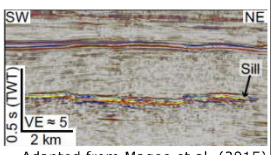
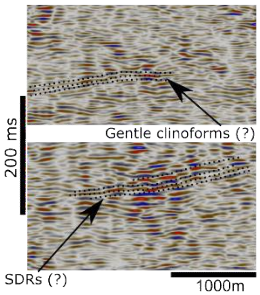
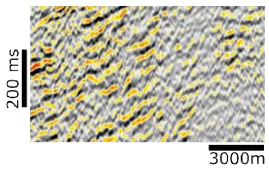
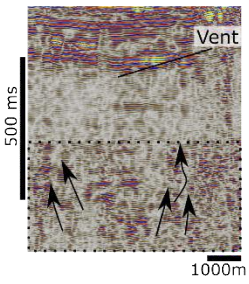
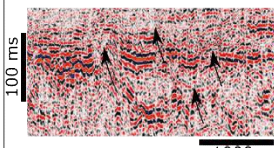
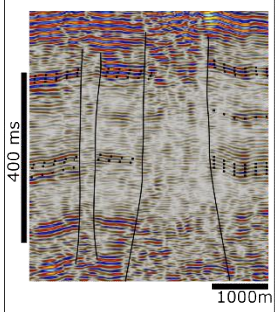
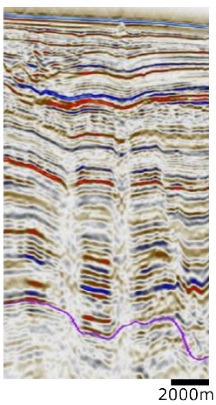
Interpretation: SF13 (Figure 2.4) is interpreted as mass-transport deposits (MTDs) as the cores recovered at Site 463 (lithostratigraphic Unit IV; Figure 2.2) comprise clastic rubbles of limestones and radiolarian limestones (Timofeev et al., 1981) with slump structures. This matches both the

lithostratigraphic descriptions (Wunsch et al., 2018) and seismic characteristics (Principaud et al., 2015) of MTDs along the slope of the Great Barrier Reef.

Seismic facies 14 (SF14) is characterized by continuous parallel reflections with amplitudes varying from low to high. It forms sheet-like bodies ca. 600–750 ms TWT thick that covers tens of kilometres in the basinal region and onlaps on the toe of the platform edge (Figures 2.4 and 2.5).

Interpretation: SF14 (Figure 2.4) is interpreted as contourite drifts formed of nannofossil ooze (lithostratigraphic Unit I-III at Site 463) as the seismic character matches the sheet-like drift deposits within the Inner Sea in the Maldives (Lüdmann et al., 2013).

Seismic Facies (− +)	Reflection Characteristics	Lithology & characteristics	Well Zone	Interpretation(s)	Example of Similar Seismic Facies from literature
SF1 Parallel seismic reflections (Cap) 	Sub-horizontal to horizontal, parallel, and continues reflections of highest amplitude Sheet like ~25-40 ms TWT thick package	Nannofossil ooze heavily replaced and impregnated with phosphate and covered with manganese dendrites	*ODP Site 866 Unit I*	Hemipelagic deposits	 Adapted from Van Tuyl et al. (2018)
SF2 Parallel seismic reflections (Interior) 	Sub-horizontal to horizontal parallel and continues reflections of high amplitude Thick package of ~200-300 ms TWT It covers the whole platform interior for tens of kilometres	Platform interior mudstones, wackestones, & packstones	*ODP Site 866 Unit III*	Platform interior Lagoonal deposits	 Adapted from Van Tuyl et al. (2018)
SF3 Broken horizontal reflections 	Zones of horizontal to sub- horizontal parallel highly broken reflections of high to moderate amplitude	No core or well data available encountered this facies but laterally calcrete zones were reported at ODP Site 866 in Unit III	—	Karst horizons	 Adapted from Van Tuyl et al. (2018)
SF4 Depression 	Depression feature of ~50 ms TWT deep & diameter of 1500-2000 m. Layers below the depression are chaotic, disrupted and highly broken.	———	—	Crater like depression Pockmark (?)	 Adapted from Betzler et al. (2011)
SF5 Vertical shafts of bright reflections 	Bright spot anomalous feature of parallel reflections forming features called string of beads	———	—	Paleocaves	 Adapted from Zeng et al. (2020)
SF6 Wavy seismic reflections 	Mounded bodies of chaotic to wavy semi continues bidirectional downlap reflections of low amplitude Found at the platform margin	Well sorted oolitic grainstone with keystone vugs and corss-lamination	*ODP Site 866 Unit V*	Oolitic shoals and beaches at the platform margin complex	 Adapted from Paurmard et al. (2017)
SF7 Mounded seismic reflections 	Convex up mounded shape bodies of semi continues to discontinuous moderate to high amplitude reflections with bidirectional downlap	Site 867: peloidal & ooiltic grainstones with low-angle planar lamination & keystone vugs, and coarse grained sediments of rudists shell debris Site 868: interbedded succession of baffestone & framestone of calcareous sponges, requeiniid rudists, & subordinate corals & floatstone & grainstone rich in requeiniid & caprinid rudists	*ODP Site 867 & 868 Subunits IIB & IIC*	Mounded facies: Platform margin complex (oolitic shoal, beach, storm deposits) Onlapping facies at the edge: uppermost part of the slope very close to the platform margin (sponge-requeiniid rudist bioherms)	 Adapted from Bachtel et al. (2004)

Seismic Facies - +	Reflection Characteristics	Lithology & characteristics	Well Zone	Interpretation(s)	Example of Similar Seismic Facies from literature
SF8 sigmoidal to sigmoid oblique reflections 	Medium to high amplitude, semi continuous to discontinuous, gently inclined seismic reflections. Sigmoid to sigmoid-oblique geometries Located at the platform margin and dipping toward it	———	—	Platform margin clinoforms	 Adapted from Bachtel et al. (2004)
SF9 Planar high amplitude reflections with abrupt terminations 	Laterally limited high amplitude reflections with abrupt terminations (highlighted by yellow triangles) and local transgression through the host rock Planar shaped in the seismic sections	———	—	Potential concordant magmatic sills	 Adapted from Magee et al. (2015)
SF10 Disrupted chaotic zone with faint layering 	Disrupted chaotic reflections Low to moderate & some times high amplitude Gentle clinoforms, seaward-dipping-reflections & faint layering	Some soils, minor volcaniclastic rocks, brecciated & fresh basalt	*ODP Site 866 Unit IX*	Volcanic Basement	 Adapted from Shahzad et al. (2019)
SF11 Chaotic variable amplitude reflections 	Disrupted reflection zones characterized by chaotic reflectors form which fluid flow vent system originate	It is found within the zones from -2400 to -2800 TWT ms where oolitic grainstone shifts upward to inner platform cyclic wacke/packstone	*ODP Site 866 Unit VIII to subunit VIB*	Chaotic seismic facies with fluid flow seismic pipes	 Adapted from Huang et al. (2020)
SF12 Vertical zones of disrupted reflectivity & reduced reflection continuity 	Vertical zones with disrupted reflectivity & reduced reflection continuity Surrounded by: Tilted reflectors (marked by dashed lines) Vertical extent ~500-700 ms	———	—	Fluid flow vents	 Adapted from Hendry et al. (2021)

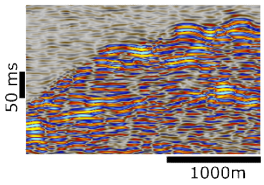
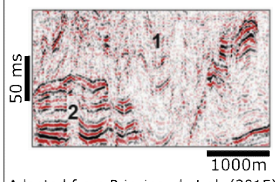
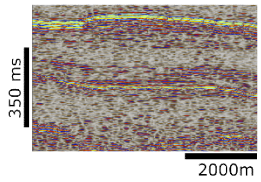
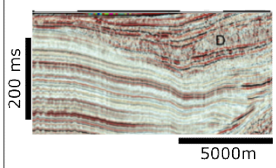
Seismic Facies - +	Reflection Characteristics	Lithology & characteristics	Well Zone	Interpretation(s)	Example of Similar Seismic Facies from literature
SF13 Basinal highly chaotic reflectors 	Mounded chaotic, hummocky, subparallel, & discontinues reflections of varying amplitude from low to high. Lenticular bodies of around 200-450 ms TWT thickness that pinches out toward the toe of the platform edge.	succession of alternating deposits of clastic rubbles of oolitic and organic-detrital limestones and radiolarian limestone with slump structures	*DSDP Site 463 Unit IV*	Mass Transport Deposits (MTDs)	 Adapted from Principaud et al. (2015)
SF14 Basinal Sheets 	Continues parallel reflections of verifying amplitudes from low to high forming sheet-like bodies It covers tens of kilometres in the basinal part It onlaps on the toe of the platform edge	Foraminiferal nannofossil chalk & chert	*DSDP Site 463 Unit I & II*	Contourite drifts	 Adapted from Eberli and Betzler (2019)

Figure 2.4. Main seismic facies and their reflection characteristics (internal geometries, continuity amplitude and shape) along with the corresponding well zone, if available. Their identification and interpretation are based on comparing the observed characteristics with similar examples from the literature.

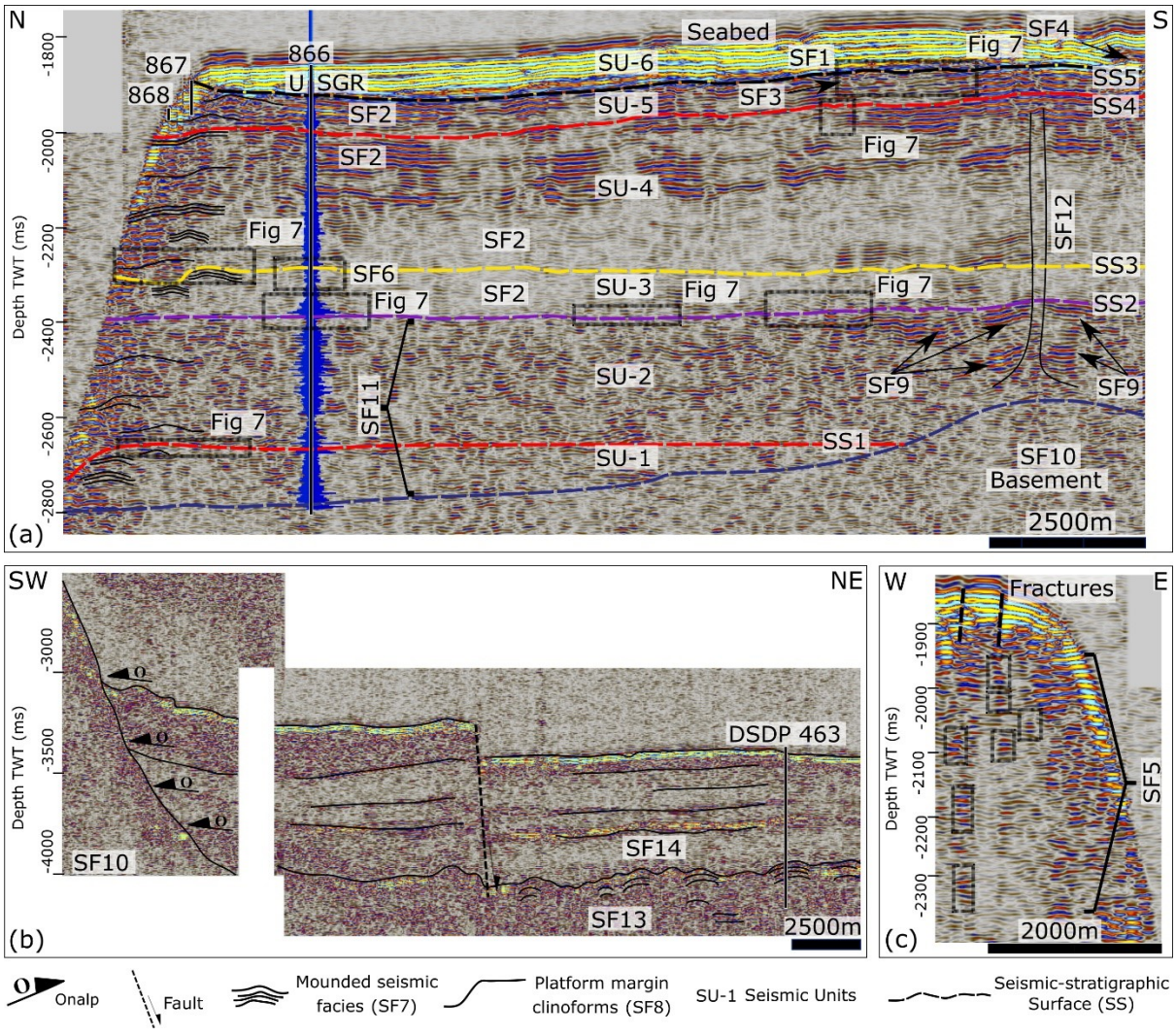


Figure 2.5. Seismic profiles along with logging data wherever available (SGR; Spectral Gamma Ray and U; Uranium log) showing the palaeogeographic distribution of the different seismic facies and seismic stratigraphic units in the isolated carbonate platform of Resolution Guyot. See Figure 2.1 for the location of these figures.

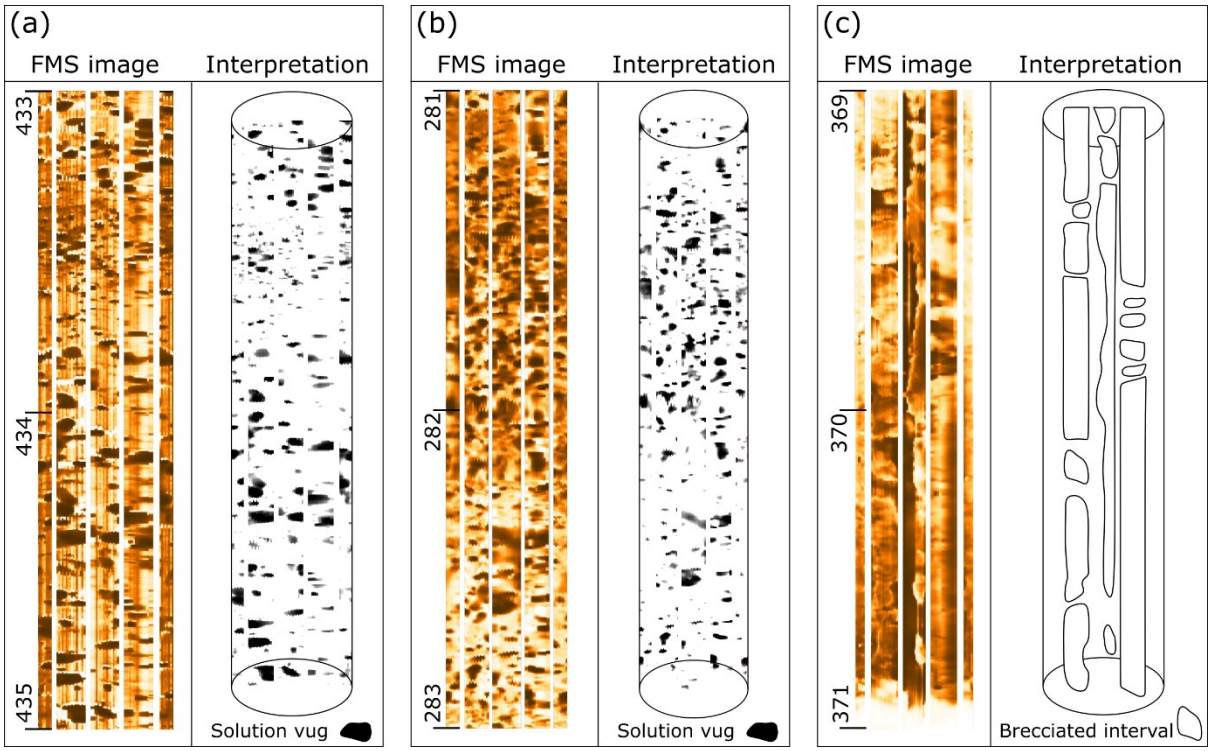


Figure 2.6. FMS images from the upper 450 m (a–c) at Site 866 showing brecciated and disrupted carbonates associated with extensive development of vugs. The relatively dark colours in the FMS image log indicate resistivity lower than the host rock, which may represent open vugs or fractures or filling material different from the host rock. (a,b) FMS images show extensive presence of solution vugs. (c) FMS image shows the possible presence of cave breccia appearing by the same colour of the host rock (bright) and surrounded by sediment fills of dark colour.

2.6.3 Seismic-Stratigraphic Units

Based on the detailed analysis of seismic facies above and guided by the core and well-log data (SGR, U, Th, K, FMS), the sedimentary succession from the seafloor down to the basement is divided into six seismic-stratigraphic units (Figure 2.5) each of which has certain seismic reflection geometries, stratal stacking patterns, and bounding seismic-stratigraphic surfaces. The timespan of each seismic unit is identified using the age of the bounding seismic-stratigraphic surfaces at the corresponding depths in the revised age model at Site 866 (Figure 2.3; APPENDIX A Table A1).

The top of the acoustic basement, as constrained at Site 866, appears in seismic data as the boundary between more chaotic, less layered reflections below the top basement (constrained by core data) and less chaotic, more layered reflections above (Figure 2.5). However, these different seismic facies (SF 10 and 11) are subtly different and are not bounded by a single reflection event, making the boundary between them difficult to constrain. Consequently, two possible interpretations of the top basement are mapped, which are (1) a flat-topped basement and (2) a flat-topped basement on the edges with doming in the centre of the guyot.

2.6.3.1 Seismic Unit-1: Hauterivian (132 ± 1 Ma–130.8 ± 1 Ma)

Seismic Unit-1 occurs immediately on top of the basement. It is capped by seismic-stratigraphic surface 1 (SS1) appearing at ca. −2675 to −2650 ms TWT separating more chaotic and less layered reflections below from less chaotic and more layered reflections of SF11 above. SS1 (Figure 2.7) includes (1) a sinkhole which is visible in the seismic data as a V-shaped depression; (2) sharp peaks in SGR, K, U, Th logs at Site 866; (3) a brecciated and reworked interval in the cores at ca. 1400 mbsf. Seismic Unit-1 (Figure 2.5) is characterized by chaotic reflections of SF11, and platform margin mounded seismic facies (SF7). SF7 can be seen to first aggrade and then backstep to the south (Figure 2.8). At Site 866, Seismic Unit-1 includes a ca. 200 m thick zone of dolomitized oolitic/oncoidal grainstone (lithostratigraphic Unit VIII; Figure 2.2).

2.6.3.2 Seismic Unit-2: Early Barremian to early Aptian (130.8 ± 1 Ma–125.5 ± 1 Ma)

Seismic Unit-2 is capped by SS2 (Figure 2.7), a surface marked by a sharp change in reflection amplitude from moderate to high (SF11) below to low and transparent (SF2) above at ca. −2377 to −2388 ms TWT. In addition, SS2 appears as a surface on which internal geometries of the subsequent Seismic Unit-3 downlap (Figure 2.7). At Site 866, SS2 (Figure 2.7) is characterized by dramatic sharp peaks in SGR, U, Th, and K logs associated with organic and clay-rich limestones and black shale layers between ca. 850 and 830 mbsf. Seismic Unit-2 (Figure 2.5) is characterized by chaotic reflections of SF11, and platform margin clinoforms and mounded seismic facies (SF7 and SF8). The platform margin (SF7 and SF8) shows first progradation from its former location in Seismic Unit-1, followed by aggradation (Figure 2.8). In the middle of the platform, potential magmatic sills (SF9) start to appear (Figures 2.5 and 2.8). At Site 866, Seismic Unit-2 is ca. 550–570 m thick and consist of peritidal lagoonal lithofacies of lithostratigraphic Unit-VII to within subunit-VIA (Figure 2.2).

2.6.3.3 Seismic Unit-3: Early Aptian to early mid Aptian (125.5 ± 1 Ma–122.8 ± 1 Ma)

Seismic Unit-3 is capped by SS3 (Figure 2.7) which is constrained by clinoforms near the platform edge downlapping onto the surface at ca. −2300 ms TWT. At Site 866 (ca. 670 mbsf), SS3 coincides with sharp increase in SGR, k, Th and U logs (Figures 2.5 and 2.7) and the cores show clay-rich layers. Behind the platform margin (SF7), the seismic facies (Figure 2.8) transitions from interpreted shoal deposits (SF6) to transparent platform interior seismic facies (SF2). Above SS2, the platform margin (SF7) is backstepping. At site 866, Seismic Unit-3 is ca. 160–180 m thick and consist of lithofacies shifting from lagoonal cyclic pack/wacke-stone and algal laminates of lithostratigraphic subunit VIA to oolitic shoal grainstone of lithostratigraphic Unit V.

2.6.3.4 Seismic Unit-4: Mid Aptian to Mid Albian (122.8 ± 1 Ma–105.15 ± 1 Ma)

The uppermost part of Unit-4 is characterized by pervasive discontinuous seismic reflections (i.e. karstification; SF3) and SS4 separates these (Figure 2.7) from more continuous less chaotic reflections above (at ca. −2000 to 1920 ms TWT). Some potential sinkholes are observed (V-shaped depressions; Figure 2.7) along SS4. At Site 866, the recovery is too low at that level, but FMS data show intermittent intervals of intensively brecciated and disrupted carbonates associated with extensive vugs at ca. 270 to 430 mbsf (Figure 2.6). Above SS3 (Figure 2.8), the trajectory of the platform margin (SF7 and SF8) within Unit-4 starts with progradation followed by aggradation. Behind the platform margin (Figure 2.5), seismic facies transitions from onlapping back-margin to transparent and high-amplitude platform interior reflections (SF2) with abundance of karstification facies (SF3) between ca. −2130 and ca. −1920 ms TWT. At Site 866, Seismic Unit-4 is ca. 500–510 m thick and consist of restricted platform interior peritidal lithofacies of lithostratigraphic Unit IV to lowermost part of lithostratigraphic subunit IIIA (Figure 2.2).

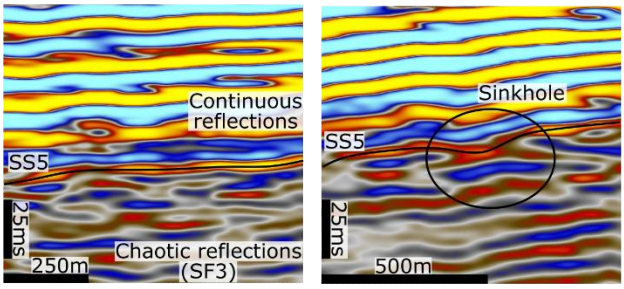
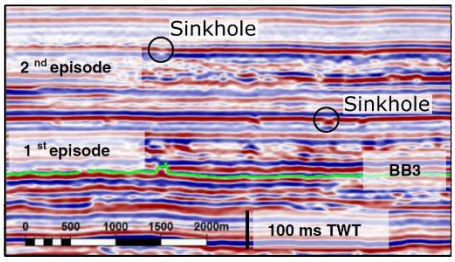
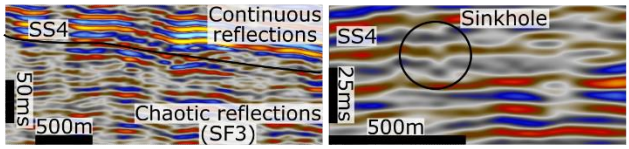
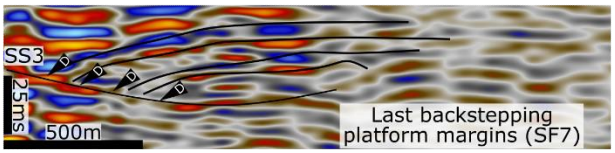
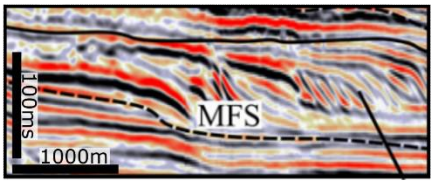
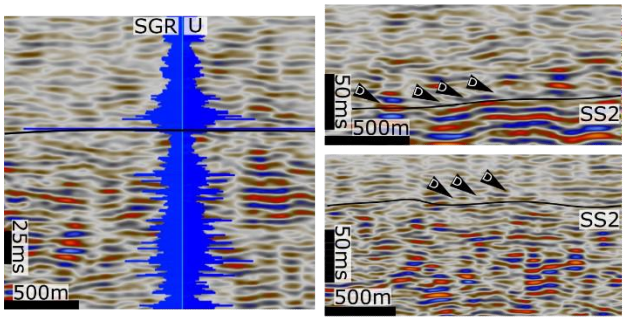
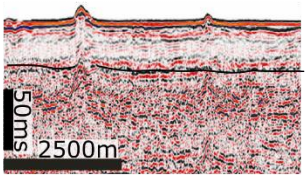
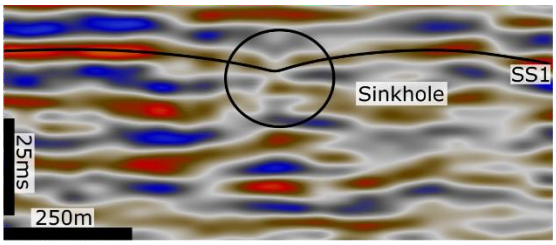
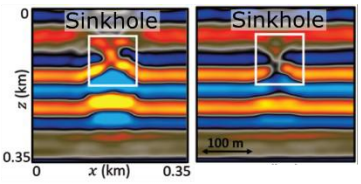
2.6.3.5 Seismic Unit-5: Mid Albian to late Albian (105.15 ± 1 Ma–100.45 ± 1 Ma)

The uppermost part of Seismic Unit-5 is characterized by pervasive discontinuous seismic reflections. SS5 separates them from continuous parallel reflections above (at ca. −1920 to −1850 ms TWT; SF1; Figure 2.7) and in the same way as SS4 some potential sinkholes were observed (V-shaped depressions) along SS5. Like Seismic Unit-4, the recovery here is low, but SS5 corresponds to a level at Site 866 above which manganese-encrusted and phosphatic limestone layers at the base of lithostratigraphic Unit-II are found. Above SS4 (Figure 2.8), the trajectory of the platform margin (SF7) is backstepping and behind SF7, seismic facies transitions from back-margin to platform interior (SF2) with abundance of karstification (SF3). At Site 866, Seismic Unit-5 is ca. 140–150 m thick and consist of platform interior gastropod/dasyclad wackestone of lithostratigraphic subunit IIIA (Figure 2.2).

2.6.3.6 Seismic Unit-6: age uncertain, Maastrichtian (?) to late Pliocene (?)

Seismic Unit-6 represents the last seismic-stratigraphic unit in the sedimentary succession. It is formed of aggrading laterally continuous sheets of pelagic sediments (SF1) bounded by the seabed (Figures 2.5 and 2.8). At Site 866, it is ca. 20–32 m thick composed of manganiferous limestone and foraminiferal nannofossil ooze of lithostratigraphic Units II and I (Figure 2.2).

(a)

	Seismic characteristics at the stratigraphic surfaces	Examples of similar seismic characteristics from literature
Seismic stratigraphic surface 5 (SS5)		 Adapted from Howarth and Alves (2016)
Seismic stratigraphic surface 4 (SS4)		Seismic section from Browse Basin showing: 1) characteristic discontinuous chaotic broken reflections of karst intervals; 2) sinkholes formed above the karsts in the more continuous horizons
Seismic stratigraphic surface 3 (SS3)		 Adapted from Van Tuyl et al. (2019) Seismic section from Browse Basin showing downlap stratal termination of the prograding clinoforms on the MFS
Seismic stratigraphic surface 2 (SS2)		 Adapted from Huang et al. (2020) Seismic section from Zhongsha atoll showing using the abrupt change in amplitude in delineating the bounding seismic-stratigraphic surface
Seismic stratigraphic surface 2 (SS1)		 Adapted from Jensen et al. (2021) The seismic signature of paleokarst sinkholes generated by synthetic seismic modelling

(b)

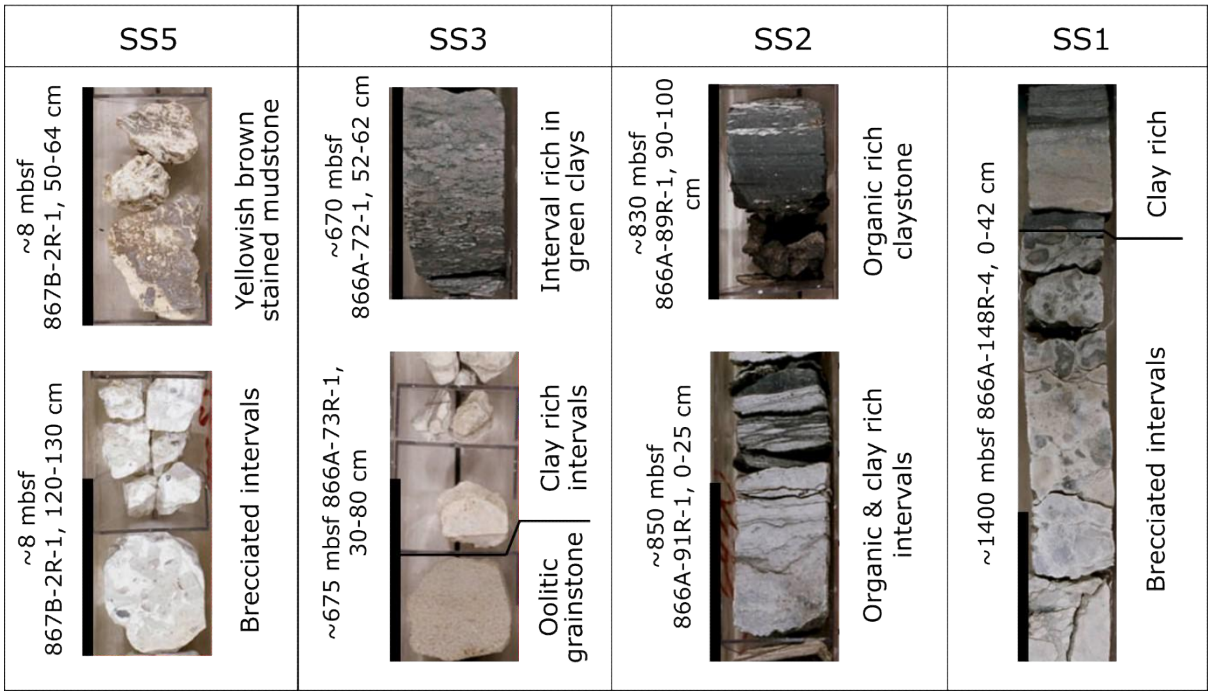


Figure 2.7. Integration of seismic and core data reveals the characteristics of each seismic-stratigraphic surface (SS1–SS5). (a) The figure shows examples of similar characteristics from the literature along with how the seismic-stratigraphic surface would appear in the seismic data. (b) Core images at site 866 showing the corresponding characteristics of seismic-stratigraphic surface. The vertical scale (black bar) of core images is 10 cm.

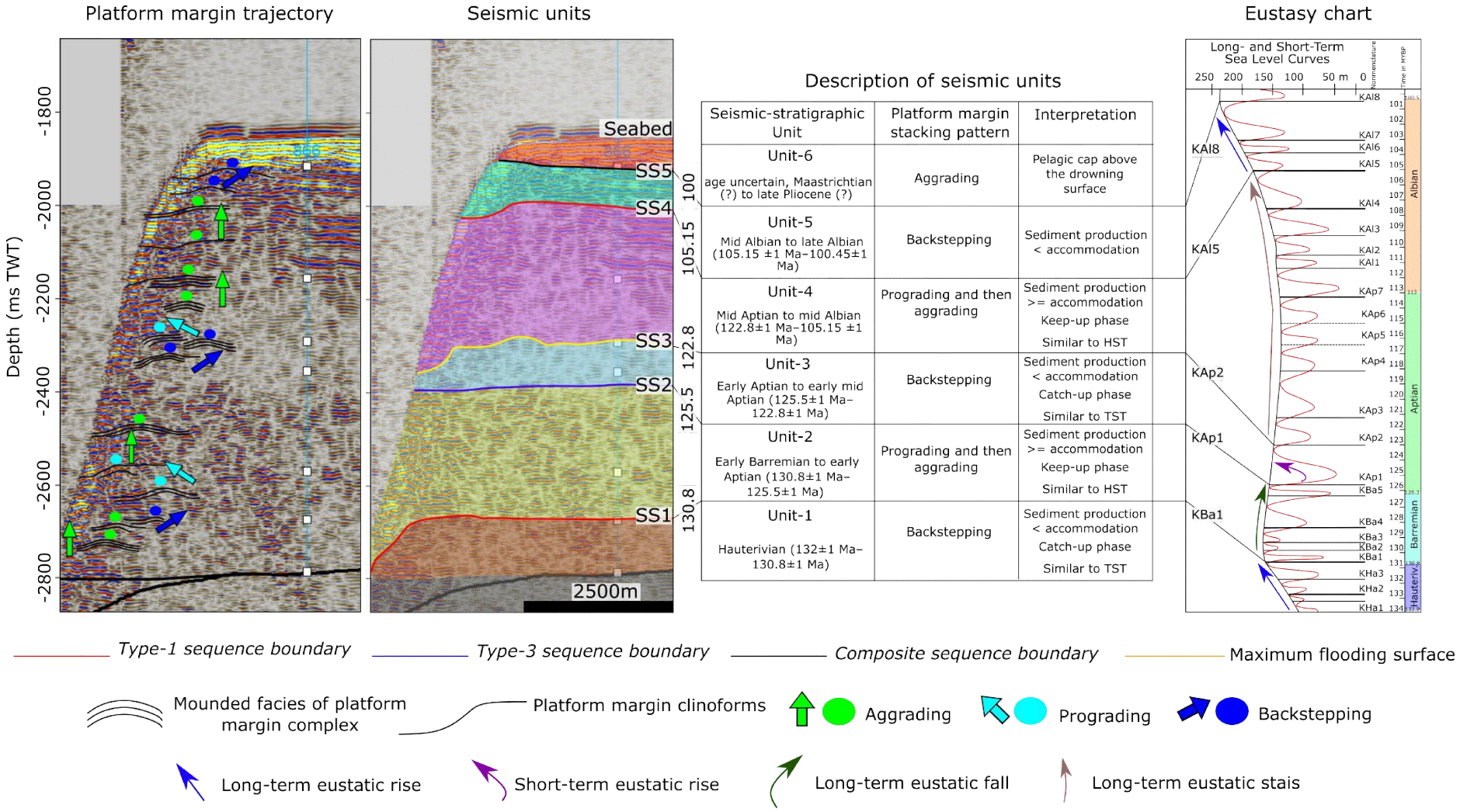


Figure 2.8. Seismic-stratigraphic interpretation of the different seismic-stratigraphic units in Resolution Guyot showing the trajectory of the platform margin complex and the interpreted seismic-stratigraphic units (from seismic Unit-1 to Unit-6) on top of the basement along with (1) the age of each stratigraphic surface interpreted from the revised age model, (2) a table highlighting their age and stacking pattern and (3) interpretation of their evolution in comparison with the eustatic curve of the Cretaceous by Haq (2014).

2.7 Discussion

2.7.1 From seismic facies to depositional model

The distribution of the identified seismic facies and the depositional environments we propose they represent are interpolated regionally using information from modern analogues (e.g. satellite images from the Glorieuses archipelago by Jorry et al., 2016 and Prat et al., 2016, Figure 2.9) to build a 3D conceptual depositional model of Resolution Guyot (Figure 2.9). Despite that, corals as organisms are not comparable to rudists, the depositional geometry of the Cretaceous carbonate platforms is characterized by: (1) small accommodation spaces typical of Cretaceous eustasy, (2) high rates of carbonate production under wave action promoting lateral progradation (i.e. prograding clinoforms), (3) dominance of autotrophic organisms (i.e. rudists), (4) backstepping during increasing accommodation and (5) rubble swept towards the inner platform and down into surrounding deeper waters (Skelton, 2003; Gili and Götz, 2018). Consequently, they tend to develop flat-topped profiles that can be compared with modern carbonate platforms. Several studies compared the depositional environments of the Cretaceous outcrop deposits and subsurface reservoirs with modern carbonate platforms (Yose et al., 2006; Homewood et al., 2007; Droste et al., 2010; Sena and John, 2013).

The distribution of seismic facies representing key depositional elements is as follows: (1) the platform margin mounded facies (SF7) extends laterally for ca. 700–2000 m, (2) the back-margin apron (onlapping reflection in the back of SF7) is at least 650 m wide, based on the distance between SF7 and Site 866 where back-margin facies were encountered in the uppermost part of Unit III (Figures 2.4 and 2.5), (3) the upper-slope facies (onlapping reflection in front of SF7) is ca. 400–800 m wide, (4) the platform interior (SF2) is ca. 20,000 m with patch reefs (SF7) of width ca. 500 m, (5) the platform margin facies (SF7) can have back shoals (SF6) which could be part of the platform margin or a back-margin apron, (6) platform slopes of the Resolution Guyot and other atolls surrounding it are prone to producing MTDs (SF13) extending for 10s of kilometres and (7) down-slope contourite drifts (SF14) are surrounding the platform and extending for 10s of km.

The uncertainties in our model can be summarized in the following: (1) taking modern carbonate platforms as an analogue, the platform margin could either be a continuous margin (e.g. Pigeon Atoll in South China Sea; Rankey, 2016) or a discontinuous margin cut by channels and formed of faroes (e.g. Felidhoo Atoll in Maldives; Gischler et al., 2014), (2) the mounded seismic facies of the platform margin (SF7) could exhibit different facies in other sides of our platform, but no other drilling data are available to test that and (3) the platform interior patch reefs and rudist

meadows could be scattered (e.g. Felidhoo Atoll in Maldives; Gischler et al., 2014) or attached together forming ridge-and-pond morphology (e.g. Alacranes Reef, Mexico; Purkis et al., 2015).

We can infer other depositional environments at a finer scale which are below the resolution of our seismic data by comparing well data with satellite images from the Glorieuses archipelago. Within the platform interior, drilling reports (Figure 2.2; Sager et al., 1993a,b) mentioned the presence of floatstone and rudstone intervals comprising reworked shell debris, ooids and intraclasts with blackened material interpreted as delivered to the platform interior by storm and wave action. This could represent washover fans (i.e. part of the back-margin apron) similar to what is observed in the back-reef apron and sandwaves of the Glorieuses archipelago (Figure 2.9; Jorry et al., 2016 and Prat et al., 2016). Moreover, lithostratigraphic subunit VIB at Site 866 (Figure 2.2) consists of caprinid rudists in living position in a peloidal pack/wackestone matrix which is overlain by well-washed grainstones to rudstone containing carpinid rudists debris. The ODP party (e.g. Sager et al., 1993a) interpreted this succession as part of the outer bank and shoal deposits. We suggest an alternative interpretation for this subunit: rudist meadows within the platform interior with shell debris formed by storm events. Our interpretation is supported by: (1) the described caprinid rudists in the drilling reports (Figure 2.2; Sager et al., 1993a,b) are in living position, suggesting that one of the valves was implanted in the wacke/packstone substrate. This is similar to elevator rudists described by Gili and Götz (2018) and interpreted as living in relatively quiet environments. Also (2) an inner platform depositional environment was suggested based on the presence of caprinid rudists at other locations (e.g. Maestrat Basin; Bover-Arnal et al., 2015; the Lycian Nappes; Özer et al., 2017).

The ODP party (Strasser et al., 1995; Winterer and Sager, 1995) depositional model was based solely on the facies description at Sites 866, 867, 868 and the 3.5-kHz echo-sounder profile passing through them. They suggested that the platform rim was composed of storm beach deposits, with a lagoon and sponge-rudist bioherms behind and in front of them, respectively. As highlighted by Strasser et al. (1995), this is valid only for the location of the echo-sounder profile and the wells. Our new conceptual model overcomes this limitation by integrating the drilling data with the seismic facies interpretation and modern analogues which helps in defining a detailed depositional model for the entire guyot.

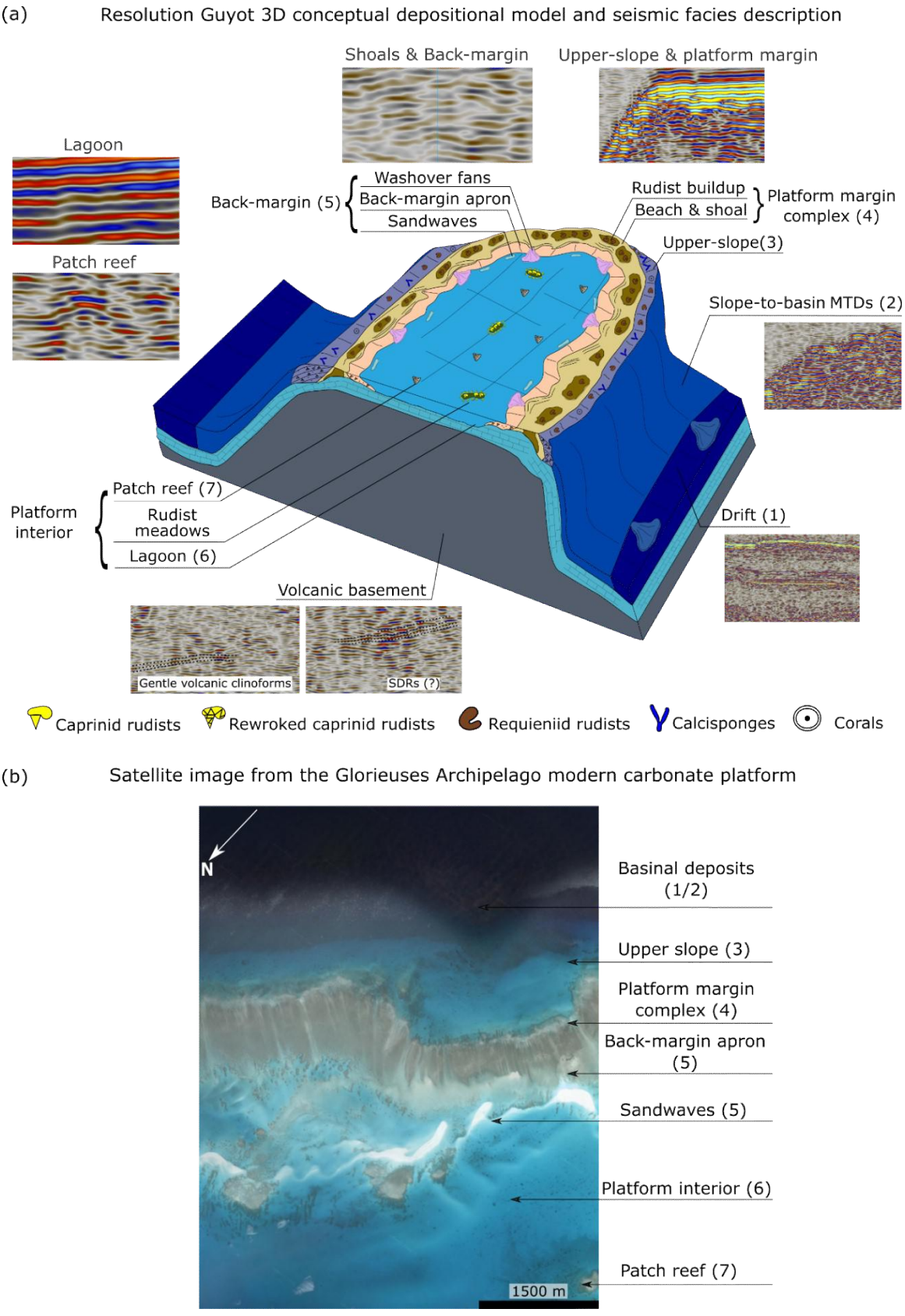


Figure 2.9. Palaeogeographic reconstruction of the different depositional environments in Resolution Guyot carbonate atoll by integrating the interpreted seismic facies with satellite images from the Glorieuses archipelago. (a) 3D conceptual depositional model showing the different seismic facies and the corresponding facies belts. (b) Satellite image from Glorieuses archipelago (using the descriptions by Jorry et al., 2016 and Prat et al., 2016) used to guide the palaeogeographic interpolation of the different facies belts in Resolution Guyot carbonate atoll.

2.7.2 Controls on the Sequence-Stratigraphic Evolution of Resolution Guyot and Links to the Cretaceous Eustasy

The initial aggradation followed by backstepping of the platform margin immediately above the basement (Seismic Unit-1) reflects a catch-up phase characteristic of the TST (Figure 2.8). The lithology of Seismic Unit-1 at Site 866 (lithofacies Unit VIII; oolitic/oncoidal grainstone; Figures 2.2 and 2.8) reflects similar conditions to the current widespread oolitic shoals in the Bahamas as a response to rising sea level. This phase (Hauterivian; 132 ± 1 Ma–130.8 ± 1 Ma) ended by subaerial exposure judging by the presence of (1) brecciated intervals at Site 866, (2) a sinkhole above the last backstepping platform margin and (3) sharp peak of SGR, K, U logs reflecting organic/clay-rich layer, which is thought to be deposited during exposure and subsequent reflooding.

Above SS1, the prograding and then aggrading platform margin of Seismic Unit-2 reflects a keep-up phase similar to an HST (Figure 2.8). This is reflected by (1) the lateral expansion of the platform, filling all the available accommodation and (2) the restricted lagoonal deposits at Site 866 with increased supratidal, sabkha, tidal flats and algal mats (lithostratigraphic Unit VII-Subunit VIA; Figures 2.2 and 2.8). Thus, we interpret SS1 as a composite surface representing both the sequence stratigraphic boundary (exposure) and a maximum flooding surface (high gamma-ray values and progradation on top of the surface). Seismic Unit-2 (early Barremian to early Aptian; 130.8 ± 1 Ma–125.5 ± 1 Ma) is capped by SS2, which represents a series of organic-rich clay layers and a 10-cm-thick black shale. These layers were interpreted by Jenkyns (1995) as OAE 1a. The previous studies showed that the carbonate factory did not shut down completely during the OAE 1a as the clay-rich and organic rich facies are alternating with lagoonal deposits reflecting peritidal settings (water depth ⩽10 m; Jenkyns and Wilson, 1999). Therefore, we suggest that this interval represents an incipient drowning surface.

Above SS2, carbonate production was less than accommodation creation as the platform margin is backstepping (Figure 2.8). Hence, Seismic Unit-3 (early Aptian to early mid Aptian; 125.5 ± 1 Ma–122.8 ± 1 Ma) is similar to Seismic Unit-1 and is interpreted as an overall TST, while SS2 is a flooding surface (Figure 2.8). Above SS2, The lithofacies at site 866 shift from restricted lagoonal deposits to oolitic beach-shoals (lithostratigraphic Subunit VIA-Unit V; Figures 2.2 and 2.8). The base of Seismic Unit-4 is marked by a switch to prograding platform margin downlapping onto SS3 (interpreted as a maximum flooding surface, Figures 2.7 and 2.8). Lithofacies of the MFS (SS3) at Site 866 include a clay-rich layer with a sharp peak in SGR, K, U and Th logs.

The initial progradation of Seismic Unit-4 (Mid Aptian to Mid Albian; 122.8 ± 1 Ma–105.15 ± 1 Ma) changes to aggradation of the platform margin, reflecting a keep-up phase and this unit is interpreted as an HST (Figure 2.8). At Site 866, lithofacies shift from oolitic beach-shoals below SS3 to restricted lagoon pack/wacke-stone above SS3 (lithostratigraphic Unit IV-Unit III; Figures 2.2 and 2.8). SS4 is marked at the top of the pervasive discontinuous seismic reflections, suggesting a subaerial exposure and karstification event (supported by the intermittent intervals of brecciated and vuggy carbonates below; Figure 2.6). SS4 is thus interpreted as a sequence boundary (Figures 2.7 and 2.8).

Seismic Unit-5 represents the last phase of carbonate sedimentation (Mid-Albian to late-Albian; 105.15 ± 1 Ma–100.45 ± 1 Ma). The platform margin is backstepping (Figure 2.8), reflecting a catch-up phase and Seismic Unit-5 is interpreted as a TST. Apart from the very low recovery at Site 866, lithofacies from Site 868 to 866 suggest a southward shift of the platform margin (Strasser et al., 1995) supporting the interpretation of a TST. Seismic Unit-5 is capped by SS5 showing similar characteristics of karstification and potential sinkholes: hence, SS5 shows evidence for subaerial exposure (Figures 2.7 and 2.8). Following reflooding of the guyot above SS5, a thin (30 m; at Site 866B; Sager et al., 1993a) pelagic sediment cap is deposited with no record of shallow marine carbonate sedimentation. This is reflected on SS5 by manganese oxyhydroxides and phosphatized material which represents a drowning succession (Sager et al., 1993a). Therefore, SS5 may be a sequence boundary (exposure) followed by a flooding surface (drowning), or a combined type-1 and type-3 sequence boundary (Figure 2.8).

The stratigraphic evolution of the carbonate sequences is a consequence of several controlling factors including, but not limited to, the interplay of changes in accommodation and sediment supply, sediment transport rates and basin-margin topography. Here, an important observation is that key seismic-stratigraphic surfaces mostly match the timing of known eustatic inflections in the Cretaceous (Haq, 2014; Figure 2.8):

- Sequence boundary SS1 (130.84 ± 1 Ma) and KBa1 (130.6 Ma; Haq, 2014) appear to be of similar age. KBa1 is considered a major sequence boundary with medium-amplitude eustatic changes (25–75 m, Haq, 2014).
- Interpreted flooding surface SS2 (125.5 ± 1 Ma) and KAp1 (125.6 Ma; Haq, 2014) appear to be of similar age. KAp1 is a major sequence boundary with large amplitude of eustatic changes (>75 m, Haq, 2014). It is possible that SS2 is in fact a composite surface (sequence boundary and flooding surface), but we lack evidence in seismic to support that.

- Interpreted maximum flooding surface SS3 (122.8 ± 1 Ma) and KAp2 (123 Ma; Haq, 2014) are of similar age. According to Haq (2014), KAp2 is a sequence boundary with a moderate amplitude of eustatic changes (25–75 m). It is thus possible that SS3 is a composite surface (sequence boundary and MFS), but we do not see seismic evidence for this.
- Interpreted sequence boundary SS4 (105.15 ± 1 Ma) and KAl5 (105 Ma; Haq, 2014) are of similar age. Kal5 is a relatively small (<25 m) amplitude eustatic event (Haq, 2014).
- The ages of interpreted sequence boundary SS5 (100.45 ± 1 Ma) and KAl8 (100.6 Ma; Haq, 2014) appear to be close. KAl8 is considered a major (>75 m) eustatic lowering event (Haq, 2014).

Another observation is that the trend of small- and large-scale eustatic variations in Haq (2014) may have impacted the development of the different seismic units (Figure 2.8):

- The three periods of development of transgressive Seismic Units-1, -3, and -5 appear to be formed during the long-term Hauterivian rise, the short-term early-Aptian rise (between KAp1 and KAp2) and the long-term late-Albian rise (Haq, 2014), respectively.
- The two periods of development of highstand Seismic Units-2 and -4 appear to be formed during the long-term Barremian fall and the long-term period of stasis through Aptian and early Albian (Haq, 2014), respectively.

The fact that some of the Cretaceous eustatic events (2nd and 3rd order fluctuations; from the Hauterivian to latest Albian) above match those in Haq (2014) suggests that (1) the Cretaceous eustasy plays a key role in the stratigraphic evolution of the Mid-Pacific atolls and (2) they are indeed driven by eustasy and not regional tectonics of the Arabian plate, as most of the data used in building the eustatic chart in Haq (2014) come from there.

In addition, other factors impacted the stratigraphic evolution of the atoll. Age-depth plot (Figure 2.3) shows rapid initial subsidence decreasing with time. The rapid initial subsidence combined with the Hauterivian long-term sea-level rise (Haq, 2014) resulted in rapid creation of accommodation facilitating the deposition of transgressive Seismic Unit-1. The study by Pohl et al. (2020; anchored on GTS2012) showed that neritic carbonates production reached the maximum between ca. 120 Ma and 80 Ma preceded by an increase in the production between ca. 130 Ma and 120 Ma. Putting this in consideration with (1) the Barremian long-term sea-level fall and the long period stasis to the late Albian and (2) the gradual decrease of subsidence with time, the available accommodation space would be limited which was reflected in thick highstand Seismic Unit-2 and Unit-4. Both transgressive Seismic Unit-3 and Unit-5 can be explained by the

outpacing of the early-Aptian short-term and late-Albian long-term rises, respectively (Haq, 2014). The dominance of oolitic beach-shoals in the transgressive Seismic Unit-3 above the OAE 1a is similar to the Cupido platform in Mexico, which may suggest similar impact from recovery of marine alkalinity following the acidification phase during OAE 1a (Núñez-Useche et al., 2015). Our paper shows the potential presence of later magmatic activity(ies) intruding through the sedimentary succession (SF9; Figure 2.5). The interpreted potential sills have no age controls, as they have not been drilled (Figure 2.2). In general, volcanic activities could possibly impact the evolution and demise of the atoll through changing subsidence rates and causing environmental perturbations (e.g. the Neogene isolated carbonate platforms in Mozambique Channel; Courgeon et al., 2016b; Courgeon et al., 2017).

2.7.3 Controls on the Distribution of Karstification

Our work sheds new light on the debated subaerial exposure and karstification of the Albian succession of the Mid-Pacific Mountains atolls (Winterer et al., 1995; Wilson et al., 1998; Winterer, 1998; Jenkyns and Wilson, 1999). Here, we present detailed subsurface geomorphological evidence for two karstification episodes during the Albian (Figures 2.6 and 2.10). The distribution of karst horizon seismic facies (SF3) at and directly below sequence boundaries SS4 and SS5 (Figure 2.10) strongly support subaerial exposure of Resolution Guyot at ca. 105.15 ± 1 Ma (marked by SS4) and ca. 100.45 ± 1 Ma (marked by SS5). Our findings of two major karstification events before the demise may support the hypothesis of 'death-by-emergence-and-submergence' by Winterer et al. (1995) and Winterer (1998).

The interpreted "paleocaves" (SF5; Figures 2.4, 2.5, and 2.11) are observed in Resolution Guyot by tracing anomalous bright spots with limited lateral extent described as "string-of-beads" by other publications (e.g. Yang et al., 2012; Yu et al., 2016; Basso et al., 2018; Zeng et al., 2020). As RMSA and signal envelope attributes are sensitive to extreme amplitude variations, they were used in delineating the lateral and vertical extension of the "string-of-beads" (Figure 2.11). It could be argued that these high-amplitude seismic features could also be related to non-karstic features associated with other high-amplitude seismic events and can mislead the interpretation (e.g. Basso et al., 2018); however, in our case, majority of the depths of the interpreted "paleocaves" correlate well to depths of (1) low core recovery at Site 866 along with free drop of the drill pit at Site 867 for ca. 8 m, (2) intensive brecciation and solution vugs in the FMS images (Figure 2.6) at Site 866 and (3) karst horizon seismic facies (Figure 2.10). The karst features in FMS images (i.e. intermittent zones of intensive brecciation and solution vugs) have a height of few meters up to 20 m. This vertical extension can be regarded as thin beds producing a constructive tuning effect

and result in high amplitudes. Multiple cave-systems will ultimately form "string-of-beads" know by Loucks (1999) as coalesced palaeocave complexes (e.g. Yu et al., 2016).

The "paleocaves" are mostly encountered along the steep windward margin (Figure 2.11). They are stacked vertically between ca. −1950 and −2300 ms TWT. Following the "string of beads" upwards on the seismic profiles, it becomes clear that the surface expressions of these features are fractures cutting through the pelagic cap (Figure 2.11). We propose that these fractures are bank margin cave-fracture systems (Smart et al., 1988; Mylroie et al., 1995; Whitaker and Smart, 1997a, b; Frost and Kerans, 2009). The coexistence of fractures and "paleocaves" (Figure 2.11) offers a potential mechanism for the formation and control of "paleocaves" (SF5) at Resolution Guyot. In addition, we suggest that the correspondence of the high-amplitude anomalies and fractures likely mean that the interpreted "string of beads" are real geological features rather than geophysical artefacts. Carbonate platform margins are prone to syndepositional collapse, faulting and fracturing with reactivation during and post burial (Nolting et al., 2018; Nolting and Fernández-Ibáñez, 2021). Consequently, fractures can act as long-lived fluid conduits (Budd et al., 2013). At Resolution guyot, the vertically stacked "paleocaves" associated with fractures (Figure 2.11) may suggest that meteoric dissolution was focused on platform margin syndepositional fractures, ultimately leading to fracture-cave formation. Subsequent exposures would lead to multiple episodes of cave development and either reactivation of existing fractures and karst (e.g. in shallow subsurface of Florida; Evans et al., 1994), or formation of new platform margin fractures and caves. The maximum vertical extent of all the stacked flank margin caves at Resolution Guyot is ca. 520–700 m. Syndepositional platform margin fractures can exceed that extent (e.g. >1000 m in the isolated carbonate platform of the Tengiz field; Narr and Flodin, 2012). The bathymetry map of Resolution Guyot shows the presence of alternating scallops and promontories (Figure 2.1) on the margins which may cause preferential concentration of stresses and become sweet spots for fracturing (Figure 2.11).

We have attempted to estimate the duration of each subaerial exposure event. As highlighted by Loucks (1999), multiple cave systems reflect either a long-term exposure or multiple exposures represented by composite unconformity(ies). Due to (1) the absence of any obvious time gaps in the Sr-isotope curve (Figure 2.3), (2) the intermittent appearance of the brecciated and vuggy intervals in FMS between ca. 270 and 430 mbsf (Figure 2.6) and (3) the presence of several calcrete horizons at Site 866 (ca. 60 mbsf; below SS5 and 220–420 mbsf; below SS4; Sager et al., 1993a), we suggest that the karst horizons were formed by multiple exposures represented by composite unconformities (SS4 and SS5). In addition to the proposed multiple exposures, contribution from other freshwater fluids (e.g. the gradient from island freshwater lens and mixing zone flank margin

caves; Mylroie and Carew, 1990; Mylroie et al., 1995; Micallef et al., 2021a,b) and hypogenic fluids (e.g. Zhu et al., 2017) to the dissolution features is also possible.

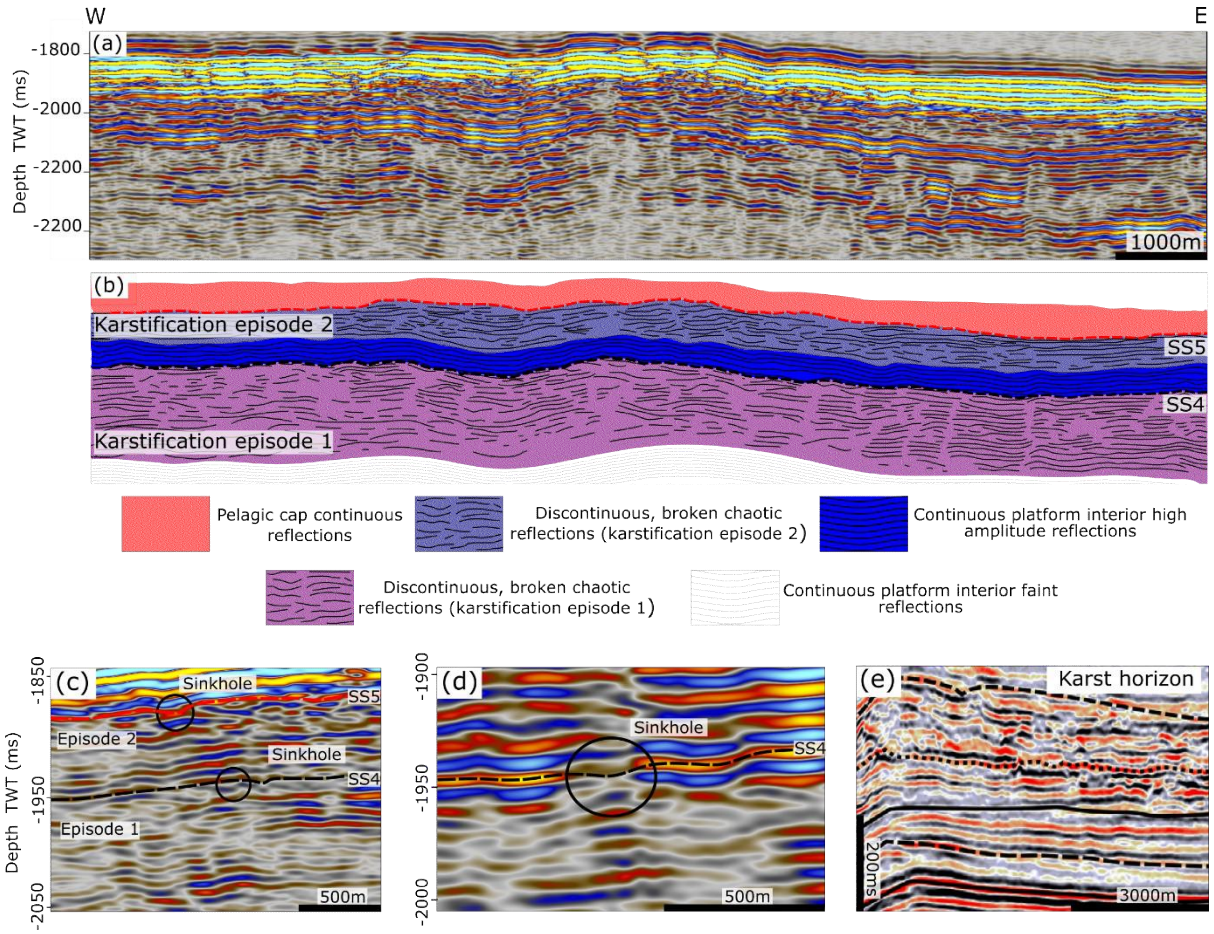


Figure 2.10. (a) E–W seismic profile showing pervasive discontinuous seismic reflection (SF3) at two different levels reflecting two different episodes of karstification, (b) interpreted carton showing the different karstification episodes, each of which is located below seismic-stratigraphic surfaces 4 and 5 which separate them from more continuous reflections, (c) seismic profile showing potential sinkholes at the seismic-stratigraphic surfaces 4 and 5, (d) seismic profile showing potential sinkholes at the seismic-stratigraphic surface 4, (e) seismic profile from Browse Basin in Australia (adapted from Van Tuyl et al., 2018), showing similar characteristics where karst horizon is highlighted by discontinuous broken chaotic reflections.

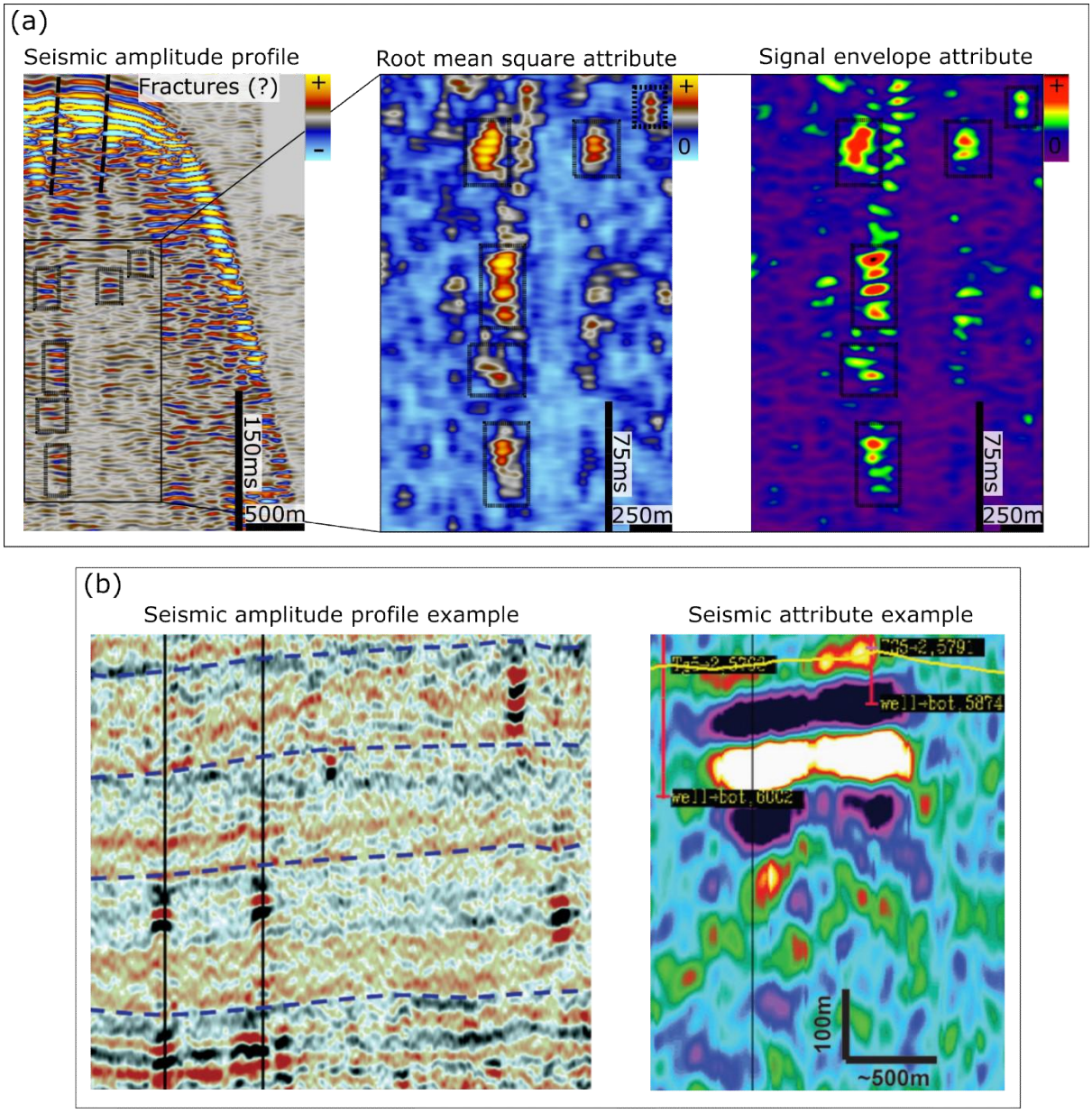


Figure 2.11. (a) Seismic amplitude profile along with root-mean-square and signal envelope amplitude profiles from Resolution Guyot showing the string of beads features along the platform margin interpreted as flank-margin fracture-cave system (highlighted in dashed boxes), (b) seismic amplitude profile from Tarim basin showing similar vertical stack of string of beads controlled by the fault system (adapted from Yang et al., 2012) and seismic attribute analysis showing the bright spot associated with string of beads in Tarim basin (adapted from Zhao et al., 2014).

2.7.4 Fluid Vents in the Mid-Pacific Atolls

Vents for cross-stratal fluids are recognizable on seismic by (1) vertical zones of disturbed reflection continuity and (2) association with amplitude anomalies and seismic artefacts (Hustoft et al., 2007; Moss and Cartwright, 2010; Cartwright and Santamarina, 2015). At Resolution Guyot, we observed extensive areas (ca. 900–1300 m length; SF12) of disturbed chaotic reflections (Figure 2.12) cutting through almost the entire sedimentary succession associated with amplitude anomalies (e.g. sharp amplitude cut-off; Figure 2.12). Sharing similar characteristics, we suggest

that these features represent fluid vents (SF12) for cross-stratal fluids through the Cretaceous atoll of Resolution Guyot.

Upward bending and tilted reflections surrounding the fluid vents may indicate an upward fluid flow (Wall et al., 2010; Omosanya et al., 2018; Wang et al., 2018a; Behbehani et al., 2019; Niyazi et al., 2021a,b). Fundamentally, pipes are conduits for cross-stratal magma (e.g. Huang and Jokat, 2016), hydrocarbon migration (Berndt, 2005; Cartwright et al., 2007; Maestrelli et al., 2017), fluids from overpressured layers (compaction of clays and mud rich sediments) and methane (Berndt et al., 2003; Netzeband et al., 2010). Deciphering the origin of these potential fluid venting systems requires further investigations bearing in mind the quality of the seismic data and absence of drilling data close to the vents.

Fluid venting system and karstification features (e.g. flank-margin fracture-cave system, karst horizons, sinkholes) might have contributed to seawater ventilating of the Mid-Pacific atolls. These features could support geochemical analysis (Paull et al., 1995), suggesting active exchange between the atoll pore-waters and surrounding seawater.

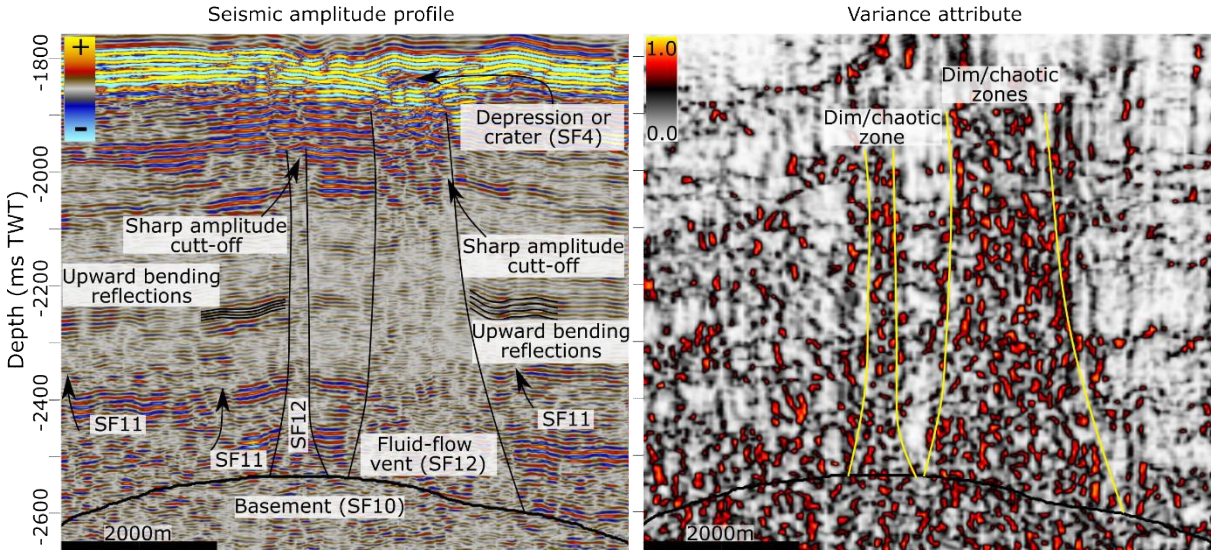


Figure 2.12. Fluid venting system in Resolution Guyot. The figure shows seismic amplitude profile and the corresponding variance attribute showing large fluid vents (SF12) with disrupted reflections, and upward bending reflections. The variance attribute shows the places affected by fluid flow pipes appearing as zones of dim to chaotic reflections relative to the well-bedded, high–medium-amplitude facies of the host-rock strata.

2.8 Conclusion

Our detailed study succeeded in identifying the carbonate system of the Cretaceous Mid-Pacific atolls including deep shelf basin (including drift deposits), slope-to-basin (including MTDs), upper-slope (including sponge and requieniid rudists build-up and reworked material from the platform margin and interior), platform margin complex (including beaches, shoals, requieniid rudists build-

up, and storm deposits), back-margin (including back-margin apron, washover fans, sandwaves and shoals) and platform interior (including lagoon deposits, patch reefs and rudist meadows).

The platform evolution was controlled by the interplay between eustasy, changes in carbonate production rates and subsidence rates, and magmatism. The stratigraphic succession in Resolution Guyot is divided into two highstand units (early-Barremian to early-Aptian and mid-Aptian to mid-Albian) and three transgressive units (Hauterivian, early-Aptian to early mid-Aptian and Mid- to late-Albian). These units and their bounding surfaces are coeval with some of the Cretaceous eustatic events (major upward surge through the Hauterivian, KBa1, KAp1, KAp2, KAl5, KAl8; Haq, 2014) which may potentially suggest an impact from second- and third-order eustatic fluctuations on the evolution of Resolution Guyot. The initial subsidence rate was rapid with a gradual decrease with time. This facilitated the Hauterivian transgression along with the Hauterivian eustatic rise. The worldwide carbonate production reached the maximum between 125 and 95 Ma. This may have acted with (1) the long-term sea-level fall through the Barremian and the long period stasis to the late Albian and (2) the gradual decrease in subsidence, which ultimately developed highstand units during the Barremian and the Albian. The recovery of marine alkalinity following the acidification phase during OAE 1a might have contributed to the short-term early-Aptian sea-level rise in developing the transgressive oolitic shoals. The long-term late-Albian rise might have outpaced the slow subsidence and high production rates facilitating the development of the transgressive unit before the demise.

The study has revealed clear evidence of two subaerial exposure events in the mid (105.15 ± 1 Ma) and late Albian (100.45 ± 1 Ma), which may support the hypothesis of 'death-by-emergence-and-submergence' by Winterer et al. (1995) and Winterer (1998). Syndepositional fractures at the rims interacted with the subaerial exposure events by focusing the dissolution which formed vertically stacked flank-margin fracture-cave system. In addition to karstification features, fluid vents were interpreted and both might contribute to the seawater ventilating of Mid-Pacific atolls.

Revisiting the Mid-Pacific carbonates allows us to build a much clearer image of the interplay between eustasy, changes in carbonate production rates, subsidence rate and magmatism during the early Cretaceous and their large-scale impact on evolution, demise and diagenesis in carbonate systems which can serve as an analogue for isolated carbonate platforms.

CHAPTER THREE

MECHANISM OF ISLAND DOLOSTONES FORMATION IN THE CRETACEOUS CALCITIC OCEAN: INSIGHTS FROM THE CRETACEOUS MID-PACIFIC GUYOTS*

* The work presented in this chapter has been published in ***Marine and Petroleum Geology***:

El-Yamani, M. S., John, C. M., & Bell, R. (2024). Mechanism of island dolostones formation in the Cretaceous calcitic ocean: Insights from the Mid-Pacific Guyots. ***Marine and Petroleum Geology***, 106741. https://doi.org/10.1016/j.marpetgeo.2024.106741.

Acknowledgements

The results presented here are part of Mahmoud Samir El-Yamani's PhD research at Imperial College London, funded by a full scholarship (MM21/19) from the Ministry of Higher Education and Scientific Research of Egypt under support from the Egyptian Bureau for Cultural and Educational Affairs. This study benefited from samples and data from the International Ocean Discovery Program (IODP) and its predecessors (ODP and DSDP). We thank Schlumberger, Ikon Science, and Lloyd's Register for providing access to Petrel®, RokDoc®, and Interactive Petrophysics® software, respectively. The authors would like to thank Carl Jaquemyn and Qi Adlan for helping in setting up the polarised light and cathodoluminescence microscopes. The Associate Editor Marco Brandano is thanked for the editorial handling and the constructive reviews that helped to improve the initial version of this paper. The authors thank the reviewers (Cathy Hollis and Luca Martire) for their thorough and constructive reviews and comments that helped to improve the initial version of this paper. David Budd is thanked for the useful discussion on the earlier versions of the manuscript.

Data availability statement

The data that support the findings of this study are openly available in:

The Marine Geoscience Data System repository at https://www.marine-geo.org/tools/search/Files.php?data_set_uid=29456 (Seismic Data).

The Division of Marine and Large Programs at https://mlp.ldeo.columbia.edu/logdb/scientific_ocean_drilling/ by searching for Leg 143 (Logging Data).

International Ocean Discovery Program, JOIDES Resolution Science Operator at https://web.iodp.tamu.edu/OVERVIEW/?&exp=143 (Core Images and Description).

Proceedings of the Ocean Drilling Program at http://www-odp.tamu.edu/publications/leg_ndx/143index.htm (Drilling Reports, Geochemical data, Core Description).

3.1 Abstract

Dolomite is common in carbonate successions. There is an ongoing debate about the origin of ancient massive dolostones. Recent studies suggest widespread syndepositional and early-burial dolomitisation by normal and near-normal seawater, in the rock record, than previously recognised. Seawater dolomitisation is ubiquitous in Cenozoic islands but Cretaceous counterparts are rare, except for Resolution and Allison guyots, Mid-Pacific Mountains. We explored their dolomitisation conditions and the implications on our understanding of Cretaceous normal seawater syndepositional and near-surface dolomitisation. Integrating geochemical and borehole data reveals temporal overlap between $^{87}Sr/^{86}Sr$ ages of dolomites, and K/Ar and $^{40}Ar/^{39}Ar$ ages of the basement. Dolomites near basaltic basement exhibit 42-times Fe-enrichment compared to normal seawater dolomites. Host-rock thermal modelling suggested that $\delta^{18}O_{dol}$ temperatures are ~18–29 °C higher than concurrent temperatures. Seismic interpretation and seismic facies forward modelling demonstrate a spatial overlap between dolomites and magmatic sills in both guyots. Accordingly, magmatically driven hydrothermal dolomitisation is proposed, which promoted dolomitisation by providing high heat flow, increasing seawater circulation, and overcoming limited dolomitisation potential of Cretaceous seawater. The H_2O–CO_2–SO_2–HCl-rich magmatic-hydrothermal acidic fluids would mix with seawater causing slight modification by leaching Mg and Fe from basaltic basement. Consequently, magmatically active Cretaceous islands had greater potential for seawater dolomitisation than counterparts with ceased magmatism, due to increased heat flux and slight increase in Mg:Ca of dolomitising fluids. Our findings imply that deep-seated island dolostones don't only form by deep cold seawater below calcite saturation depth. Instead, magmatism appears crucial in this study and potentially other locations (e.g. Xisha Islands). The absence of dolostones in other Cretaceous islands supports previous models of reduced effectiveness of massive dolomitisation by Cretaceous normal seawater, questioning interpretations of syndepositional and near-surface dolomitisation. Thus, caution is advised when interpreting these dolomites by considering additional factors (dolomite geometry, geological settings, and dolomitisation age), as they may share characteristics with syndepositional and near-surface normal seawater dolomites.

3.2 Highlights

- Magmatically driven hydrothermal dolomitisation is suggested for the Cretaceous atolls in the Mid-Pacific Mountains.
- Magmatically active Cretaceous islands had greater potentiality for seawater dolomitisation than their inactive counterparts.

- The model gives an alternative explanation to deep-seated island dolostones in this study and potentially other locations.
- The Cretaceous normal seawater dolomitisation appears of reduced effectiveness, supporting previous reactive transport modelling and field studies.
- Caution is advised in interpreting these dolomites as they may share characteristics with syndepositional and near-surface early-burial normal marine dolomites.

3.3 Introduction

Dolomite ($CaMg(CO_3)_2$) is abundant in the rock record and scarce in modern sedimentary environments (e.g. Land, 1985). However, some challenge this view suggesting significant dolomite formation in the Neogene (e.g. Shalev et al., 2019). The origin of dolomite has been a puzzling topic for over two centuries, known as the "Dolomite Problem", due to the challenge of synthesising dolomite at laboratory conditions resembling the Earth's surface temperature (e.g. Gregg et al., 2015). Recent studies propose that early syndepositional dolomitisation by marine fluids (normal and near-normal) is more widespread than previously believed (Newport et al., 2017, 2020; Manche and Kaczmarek, 2019; Ryan et al., 2020), even in modern deep ocean sediments (e.g. Shalev et al., 2019). Seawater dolomites are ubiquitous in Cenozoic islands and atolls (e.g. Grand Cayman, Cayman Brac, Little Bahama Bank, Great Bahama Bank, Niue, Enewetak, Jamaica, and Kita-daito-jima, Schlanger et al., 1963; Land, 1973; Jones, 1989; Pleydell et al., 1990; Land, 1991; Whitaker et al., 1994; Vahrenkamp and Swart, 1994; Budd, 1997; Wheeler et al., 1999; Jones et al., 2001; Jones and Luth, 2002; Melim et al., 2002; MacNeil and Jones, 2003; Jones, 2005; Suzuki et al., 2006; Zhao and Jones, 2012a, b). These dolomites were formed from unmodified seawater (Warren, 2000; his Figure 10) via deep cold seawater pumping below calcite saturation depth (e.g. Enewetak atoll deep-seated dolomites; Saller, 1984), reflux of slightly concentrated seawater (e.g. Machel and Burton, 1994; Wang et al., 2022), tidal pumping (e.g. Carballo et al., 1987), and Kohout convection (e.g. Aharon et al., 1987; Wheeler et al., 1999; Swart and Melim, 2000). Approximately 80% of Cenozoic islands and atolls yield dolostones from normal seawater origin, while ~40% of Cretaceous islands and atolls are dolomitised with ~11% of them suggested to be from normal seawater origin (Figure 3.1; check APPENDIX B Table B1 and B2 for the criteria of compiling and analysing the geo-dataset of drilled and/or outcropped Cenozoic and Cretaceous carbonate islands and atolls).

Most Cenozoic islands were dolomitised during the Late Miocene to Late Pleistocene (~10–0.5 Ma; Wang et al., 2019a) when Cenozoic aragonitic seawater (Figure 3.2) had high

Mg^{2+} concentrations (~49–55.1 mmol) and Mg:Ca (~5.2) and were highly supersaturated with respect to dolomite (Brennan et al., 2013). In stark contrast, Cretaceous calcitic seawater (Figure 3.2; Horita et al., 2002; Timofeeff et al., 2006) had lower Mg^{2+} concentrations (30–42 mmol) and Mg:Ca (0.6–1.3). Consequently, dolomite saturation was lower than during the Late Cenozoic (e.g. Arvidson et al., 2011). These conditions favoured calcite precipitation over aragonite or high Mg-calcite which might have impacted dolomitisation potential of seawater (Steuber and Rauch, 2005) and likely hindered large-scale dolomitisation (e.g. Newport et al., 2017, 2020). In line with this, Gabellone and Whitaker (2016) using reactive transport modelling showed very limited dolomitisation potential and very low dolomitisation rates of normal Aptian seawater (~1–2% dolomite fraction), in contrast to modern seawater (~62% dolomite after 500 kyr). Despite the above, two notable exceptions to the scarcity of Cretaceous island dolostones, in the Pacific Cretaceous atolls, are Resolution and Allison guyots, both drowned atolls on volcanic basement (Figure 3.3 and 3.4; Sager et al., 1993a, b). In both guyots, Sager et al. (1993b) and Strasser et al. (1995) suggested early syndepositional dolomitisation in intertidal and subtidal facies by seasonally evaporative pumping. In Resolution Guyot, Flood and Chivas (1995) suggested that the thick dolomitic limestone and dolostones were formed by normal seawater dolomitisation through deep cold seawater pumping at depths below calcite saturation depth by Kohout convection (e.g. Enewetak atoll; Saller, 1984).

In light of the above, this paper investigates dolomitisation conditions in Cretaceous islands and atolls, Resolution and Allison guyots, compared to Late Cenozoic counterparts to (a) understand the reasons behind the scarcity of dolostones in Cretaceous islands, (b) evaluate the effectiveness of syndepositional and near-surface early-burial dolomitisation by Cretaceous calcitic seawater, (c) emphasise the importance of distinguishing true syndepositional and near-surface early-burial normal seawater dolomites from other types of dolomites. Hence, the study (a) integrated seismic interpretation and seismic facies forward modelling, (b) utilised published geochemical and stable isotope data of dolomite, limestone, and basement from the Ocean Drilling Program (ODP), and (c) conducted burial and thermal modelling of the limestone host rock, in order to fully evaluate the controls on dolomitisation.

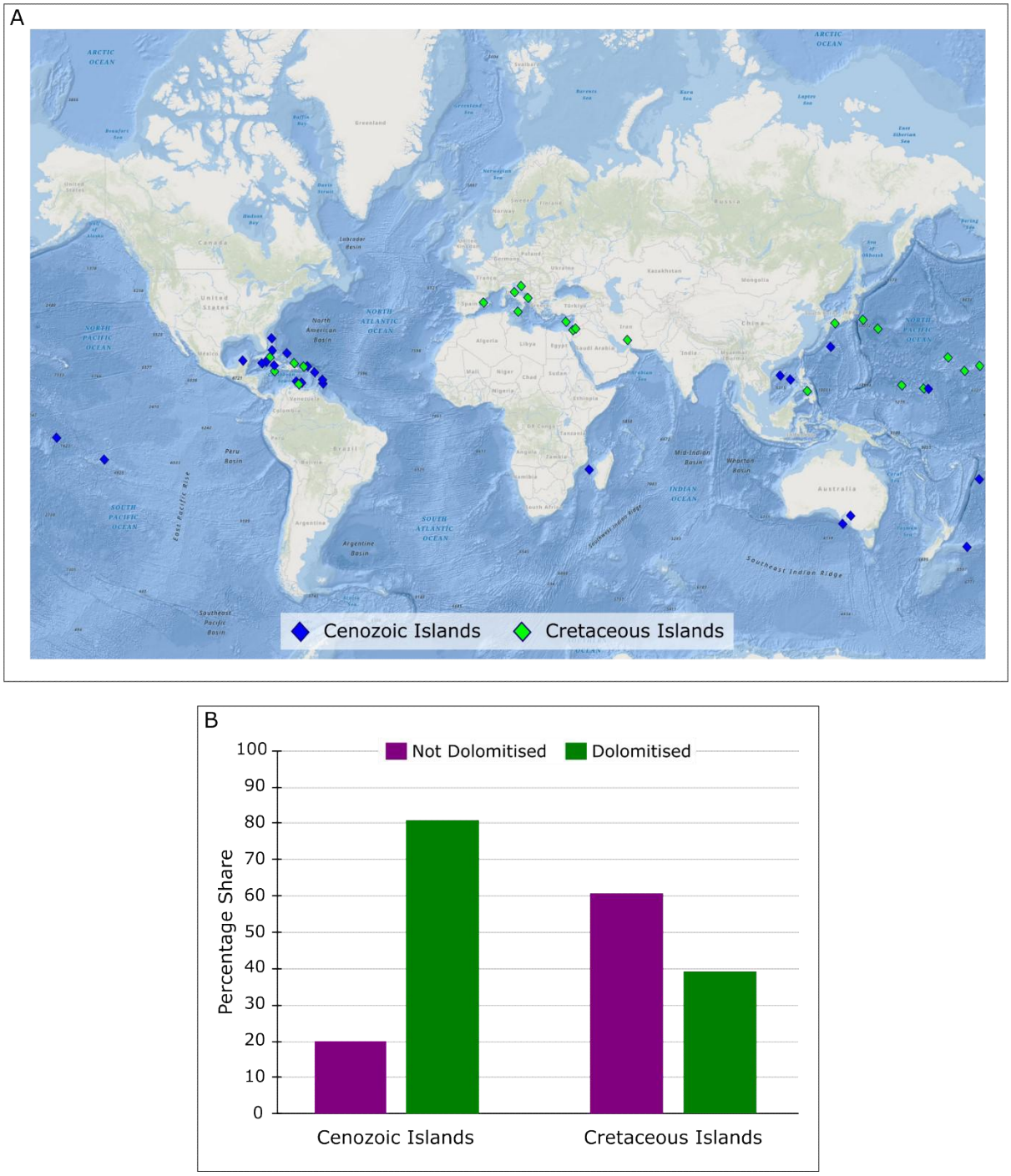


Figure 3.1. The compiled geo-dataset of Cenozoic and Cretaceous islands and atolls (see APPENDIX B Table B1 and B2). (A) World map of the distribution of the Cretaceous and the Cenozoic carbonate islands and atolls. (B) The percentage of dolomitised and not dolomitised carbonate islands and atolls of Cretaceous and Cenozoic ages. The compiled dataset might not be quantitatively representative of all the formed islands and atolls in the earth during the Cretaceous and the Cenozoic as not all of them were drilled or are outcropping. Therefore, the presented dataset might not represent a complete rock record. Although, it can provide, at least, a source of relative comparison to show the difficulty of unmodified seawater dolomitisation in the Cretaceous islands in comparison with the Late Cenozoic islands and atolls.

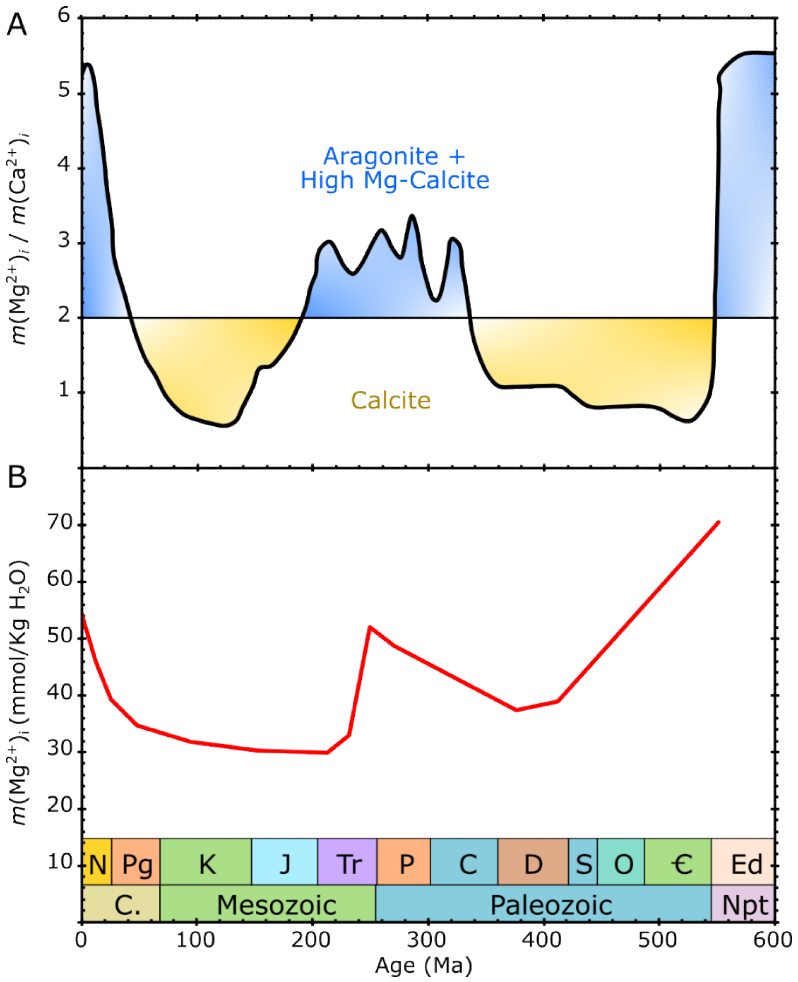


Figure 3.2. Secular variations in molar Mg/Ca ratio (A) and Mg^{2+} concentration (B) in seawater throughout the Phanerozoic (Hardie, 1996; Horita et al., 2002; Demicco et al., 2005).

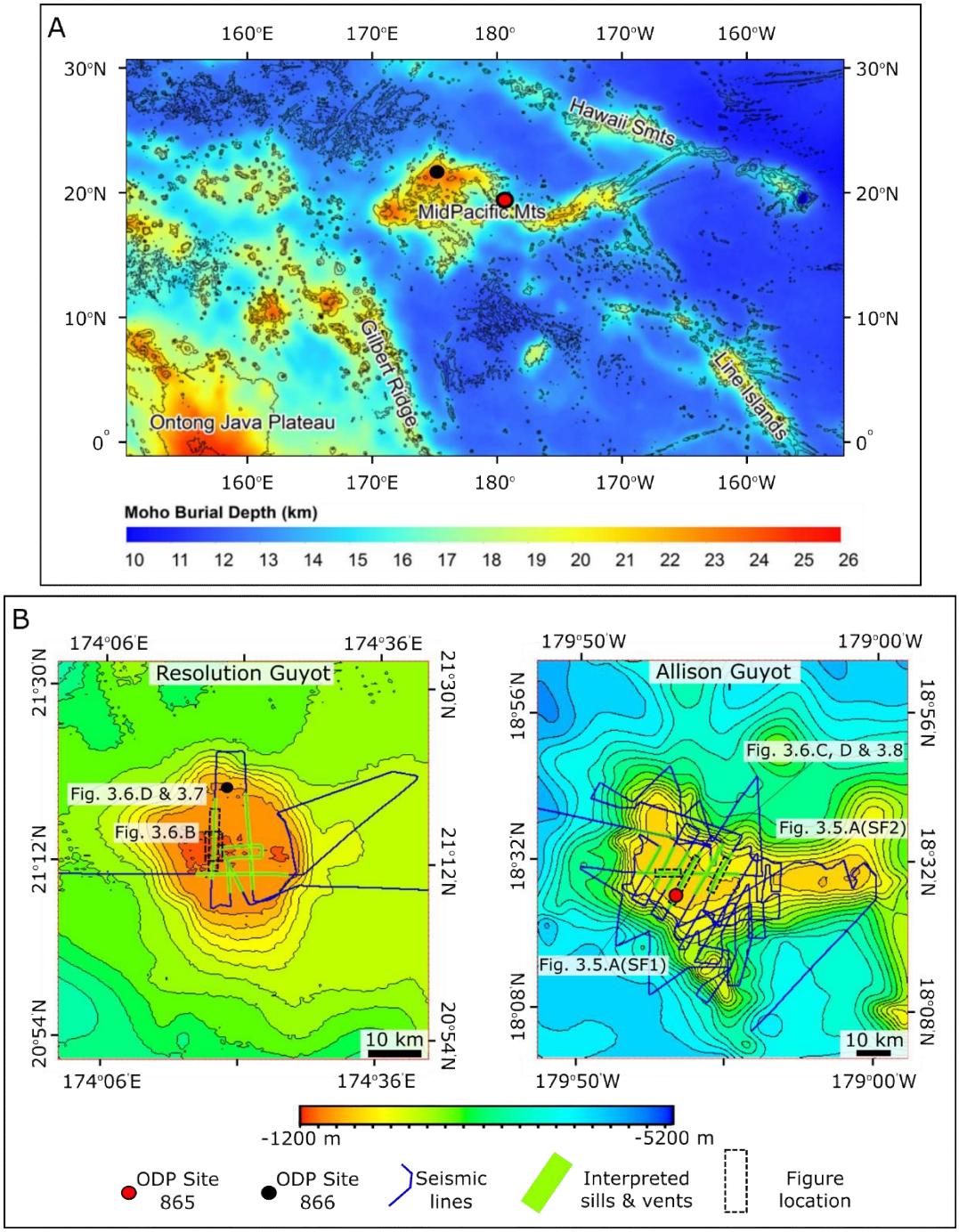


Figure 3.3. A. The Pacific Ocean map showing the location of the Mid-Pacific Mountains and Resolution and Allison guyots (Bai et al., 2019). B. Bathymetry maps of Resolution and Allison guyots (Keizer et al., 2001) showing the locations of drilling sites 865 and 866 and the 2D seismic data.

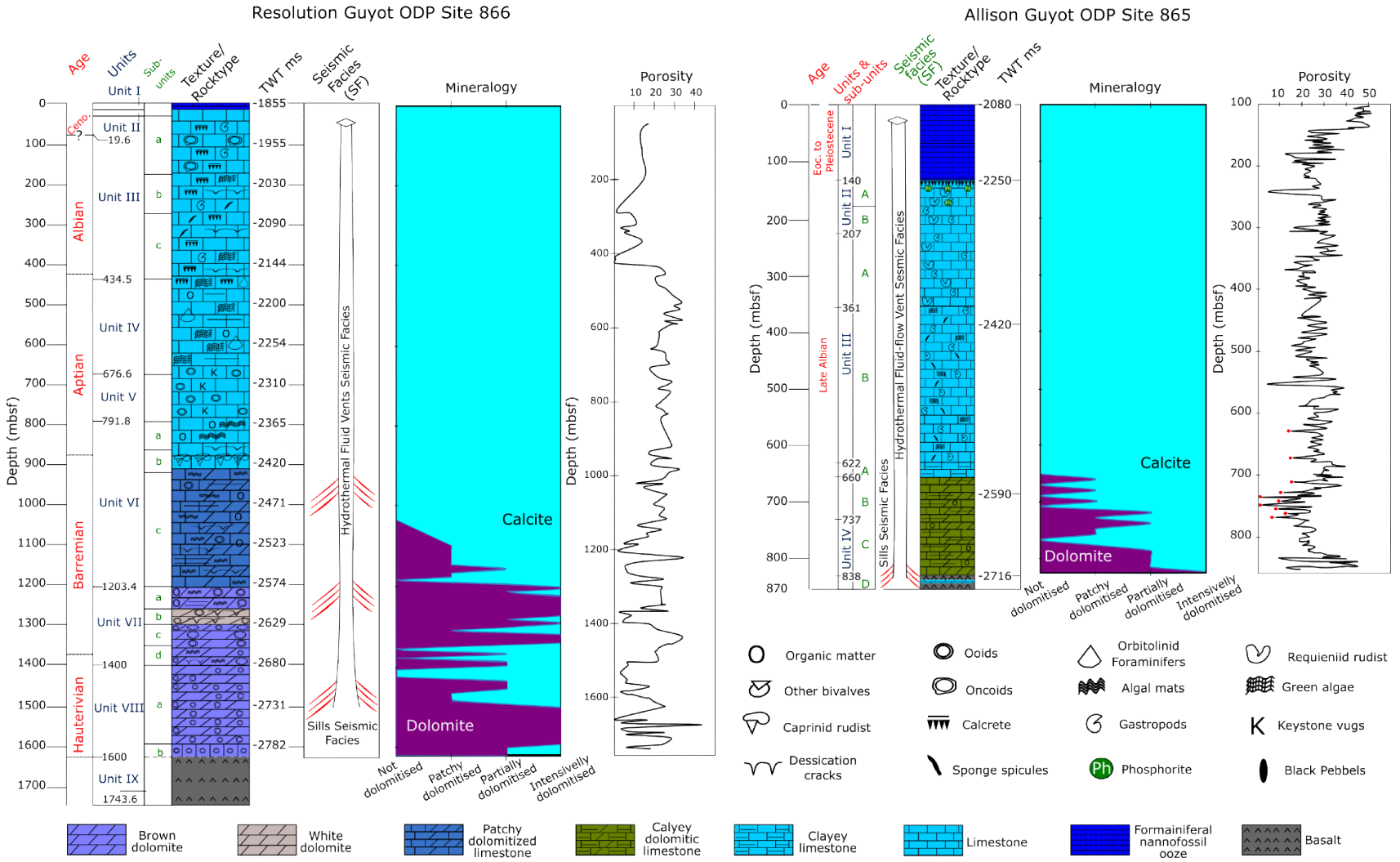


Figure 3.4. Lithostratigraphic descriptions of Resolution (Site 866) and Allison (Site 865) guyots adapted from (Sager et al., 1993a, 1993b; El-Yamani et al., 2022). The figure shows a summary of the lithological and fossil content of the different lithostratigraphic units, and their porosity measurements (Sager et al., 1993a, 1993b) at different drill sites along with the identified seismic facies. The mineralogy profile of each drilling site was retrieved by integrating core scans, core descriptions (ODP Initial Reports, 1993a, 1993b), facies and petrographic descriptions (Arnaud et al., 1995). The red dots in the porosity profile of 865 represents the location of the identified dense beds that act as permeability barriers.

3.4 Geological settings

This study focuses on Resolution and Allison guyots which are parts of the Mid-Pacific Mountains, a volcanic plateau formed within the region of intense hotspot volcanism known as the South Pacific isotopic and thermal anomaly (Figure 3.3; Staudigel et al., 1991). It is characterised by flat-topped seamounts with shallow marine limestone cover and pelagic cap, including Sio, Heezen, Resolution, Jacqueline, Allison, Cape Johnson, Renard, and Horizon atolls (Winterer and Sager, 1995). These were targeted with other Mesozoic Pacific Guyots by ODP Leg 143/144 and Roundabout Expedition Leg 10 cruise. Resolution (Site 866) and Allison (Site 865) guyots have a ~570-600 m thick unit of dolostone and dolomitic limestone on top of basaltic basement and a ~180 m thick unit of clayey dolomitic limestone sitting on top of drilled magmatic sills, respectively (Figure 3.3 and 3.4; Sager et al., 1993a, 1993b). At Allison Guyot, early diagenetic dolomite occurrences are documented in some layers between 660 and 837 metres below seafloor (mbsf) at Site 865 (Sager et al., 1993b). Burrows exhibit preferential dolomitisation owing to their higher permeability (Sager et al., 1993b). XRD analysis by Murdmaa et al. (1995) between 670-836 mbsf reveals varying degrees of dolomite abundance, ranging from abundant to rare. Dolomite occurrences within Resolution Guyot are notable, commencing at ~500 mbsf and recurring ~900 mbsf (Sager et al., 1993a). Further downhole, dolomite persists continuously below ~1000 mbsf, with brown dolomite prevalent in sediments from ~1200 to ~1620 mbsf in lithostratigraphic Units VII and VIII (Site 866; Flood and Chivas, 1995). The dolomitised succession at Site 866 contains a distinct white dolomite interval spanning 30 m (1250–1280 mbsf; Flood, 1998) within the broader brown dolomite context. This white dolomite interval exhibits a markedly different $^{87}Sr/^{86}Sr$ ratio of 0.70822, consistent with an Oligo-Miocene age, contrasting with the $^{87}Sr/^{86}Sr$ of the surrounding brown dolomites of ~0.70735, which aligns with the Cretaceous Age (Flood and Chivas, 1995; Flood et al., 1996; Flood, 1998). Given the focus of the paper on Cretaceous island dolomitisation, we exclude the 30-m interval of the Cenozoic white dolomite from our analyses. In both guyots, Resolution and Allison, an active exchange between pore-waters and surrounding modern seawater is evident based on similar $^{87}Sr/^{86}Sr$, major-element composition, and $\delta^{18}O$ (Sager et al., 1993a, 1993b; Paull et al., 1995; Flood, 1998) indicating that open ocean water freely circulates through the islands.

3.5 Data and Methods

This paper utilises core-log-seismic data collected during ODP Leg 143/144 and the Roundabout Expedition Leg 10 at Resolution and Allison guyots. Seismic data (Figure 3.3) were collected by

cruise 'Roundabout Expedition Leg 10' (RNDB10WT; Nov–Dec 1988) aboard the R/V Thomas Washington which was a dedicated program to image the Mesozoic Guyots in the western Pacific. This survey consisted of single-channel, 2D seismic profiles acquired using an 80-in^3 water gun, processed by the University of Texas Institute for Geophysics. Processing involved filtering (50–200), mixing (1:1:1), and automatic gain control (Marine Geoscience Data System, n.d.). This study used wireline-logging data including sonic (DTLN), formation density (RHOB), photoelectric absorption factor (PEF), and neutron porosity (NPHI) (Division of Marine and Large Program, n. d.; APPENDIX B Table B3). High-resolution core images were accessed from the International Ocean Discovery Program JOIDES Resolution Science Operator website (JOIDES Resolution Science Operator, n.d.). The geochemical aspects of this study are based on doing our own interpretations of the geochemical data that were generated by the Ocean Drilling Program in the Proceedings of the Scientific Results of Leg 143. These geochemical data encompass Mn, Sr, and Fe content, $\delta^{18}O$, $\delta^{13}C$, and $^{87}Sr/^{86}Sr$ isotopes, and major, minor, and trace elements of dolostone and limestone at Site 866 and radiometric age data of basaltic basements in Leg 143 (Baker et al., 1995; Flood and Chivas, 1995; Jenkyns, 1995; Jenkyns et al., 1995; Pringle and Duncan, 1995; Sager, 1995; Röhl and Strasser, 1995; APPENDIX B Table B4-6). Table 3.1 summarises depth intervals of samples, standard sample, laboratory, device, techniques, data source, and corresponding supplemental sheet displaying the geochemical data values. Resolution Guyot offers a comprehensive dataset of geochemical, seismic reflection, and wireline-logging data, while Allison Guyot provides seismic reflection and wireline-logging data. Our analysis primarily focuses on Resolution Guyot but includes comparisons with Allison Guyot whenever data permits.

Constraining the spatial geological settings around the dolomites in the tied wells of Resolution and Allison guyots was achieved through doing seismic interpretation on the processed seismic data (as processed by University of Texas Institute for Geophysics). Seismic reflection datasets were interpreted and visualised using Petrel® software. The seismic data is displayed in the American polarity convention, where a downward increase in acoustic impedance (e.g. seabed) is represented by trough-peak-trough with red-blue-red reflections. Seismic to well tie at sites 865 and 866 was performed using the time-depth relation of El-Yamani et al. (2022; APPENDIX B Table B7) and Sager et al. (1993b). Seismic facies and their corresponding depths and palaeogeographic distributions in atolls were categorised by interpreting reflection internal configuration and geometries, distribution of seismic reflections, and their signal properties (continuity, frequency, and amplitude; Mitchum et al., 1977). The interpreted seismic facies were constrained through making a 1D convolution forward seismic model where drilling data were available in one guyot and missing in the other, using RokDoc® software. Synthetic seismic facies

forward modelling requires five inputs which are (a) a conceptual geologic model, (b) bulk densities ϱ and compressional wave velocities V_p of the rock units in the conceptual model, (c) simulating a zero-offset survey using the Zoeppritz equations, (d) a zero-phase Ricker wavelet, (e) wavelet frequency (Magee et al., 2015). A suitable conceptual model to the seismic facies was built using the core descriptions (i.e. defining the different rock units and their thicknesses) and ϱ and V_p of each rock unit. These petrophysical properties (ϱ and V_p) were extracted from the wireline-logging data and the physical properties measurements (Sager et al., 1993a, 1993b). Wireline-log interpretation was performed using Interactive Petrophysics® software. The wavelet frequencies were extracted from the seismic data using dominant frequency attribute and the spectral analysis tool using Petrel® software.

One hundred and eleven thin sections, across the whole sedimentary section at Site 866, were utilised in this study on the dolomite from Resolution Guyot. Optical and cathodoluminescence microscopes at Imperial College London were used for analysis. Thin sections were studied using a transmitted light Zeiss Axioskop 40 with an AxioCam ICc1 camera. Cathodoluminescence (CL) microscopy was conducted on a Nikon Eclipse 50i luminoscope equipped with a CITL cathodoluminescence MK5-2 stage and an AxioCam ICc1 camera. The CL microscope operated at a current of 315 μA, an accelerating voltage of 15 kV, and a vacuum of 0.003 mBar. Dolomite crystal textures were described based on the classifications of Flügel (2010) and Gregg (1987), while crystal sizes were defined according to the classification of Chatalov (1971) and James and Jones (2015). Cathodoluminescence crystal zonation were described using the classification of Machel and Burton (1991). The occurrence of dolomite at Resolution Guyot was identified by integrating core images, MgO% plot, grain density plot, and RHOB, NPHI, and PEF wireline-logs due to the low core recovery (15% average) which were all checked with core descriptions and thin sections (APPENDIX B Table B8). Qualitative lithological interpretation from wireline-logs was based on (a) defining a dolomite dominated interval where PEF is 3.14–4.11 b/e and limestone dominated interval where PEF is > 4.11–5 b/e (Glover, 2000; Wang et al., 2015; Szabó et al., 2023) and (b) defining a dolomite dominated interval where RHOB is positively separated from PEF and vice versa for limestone dominated intervals (Wang et al., 2015). The grain density of samples from Site 866 (Sager et al., 1993a; Kenter and Ivanov, 1995) was used as a proxy for mineralogy (Zenger, 1968; Kenter and Ivanov, 1995) using the following equation:

$$\%\boldsymbol{dol} = \frac{\boldsymbol{\rho_{sample} - \rho_{calcite}}}{\mathbf{0.148}} \times \mathbf{100}$$

where ϱ_{sample} is the grain density of the sample considering grain densities for calcite and dolomite are 2.71 and 2.87 gm/cm^3, respectively (Carmichael, 1989).

We utilise Fe, Sr, and Mn concentrations in dolomites to trace their potential sources in the dolomitising fluids (Budd, 1997). Dolomite age constraints at Site 866 were established by correlating dolomites' $^{87}Sr/^{86}Sr$ data with the Phanerozoic $^{87}Sr/^{86}Sr$ seawater compositions using LOWESS LOOK-UP TABLE 5B regressions (McArthur et al., 2012; check APPENDIX B Material B1). Calculating temperatures of the dolomitisation fluids at Site 866 involved employing Horita's (2014) oxygen isotope fractionation equation, dolomites' $\delta^{18}O_{dol}$, and a $\delta^{18}O_{sw}$ value of Mid-Cretaceous seawater (~0.2‰ VSMOW, the Mid-Cretaceous zonal $\delta^{18}O_{sw}$ at the guyots' paleogeographic location; Zhou et al., 2008; check APPENDIX B Table B9 for the reasoning for choosing the corresponding $\delta^{18}O_{sw}$). Detailed calculation steps and results are discussed in APPENDIX B Material B2. Burial and thermal modelling aimed to reconstruct the concurrent host-rock temperatures during dolomitisation periods (detailed calculation steps and results are discussed in APPENDIX B Material B3). This involved integrating (a) the depositional age model at Site 866 of El-Yamani et al. (2022) to reconstruct stratigraphic accumulation over time (APPENDIX B Table B10), (b) the new dolomitisation age model from this study, (c) the average sea surface temperature during Mid-Cretaceous (~33 °C) at the guyots' paleogeographic locations (using Scotese and Wright's, 2018 palaeogeographic reconstruction and Valdes's et al., 2021 palaeoclimatic simulations; detailed maps of the ocean surface temperatures are provided in APPENDIX B Table B9), and (d) geothermal gradient. Geothermal gradients in atolls and carbonate islands differ from continental areas as they have a negative gradient due to the active exchange between pore-water and surrounding seawater. Therefore, pore-water temperature profiles in carbonate islands and atolls should mimic those of the open marine profile (Warren, 2000). Instances from various locations such as Enewetak, Bikini, Kita-daito-jima, Fangataufa, Mururoa atolls, Reed Bank, Tahiti, Grand Cayman Islands, Florida Platform, and Yucatán Peninsula have been documented, showcasing gradients ranging from −2.2 °C/100 m in Reed bank and Mururoa atoll (Rougerie and Wauthy, 1993; Guille, 1996; Henry et al., 1996; Wang et al., 2020) to −2.5 to −3.2 °C/100 m in Mururoa atoll and Grand Cayman Island (Ren and Jones, 2017) up to −4.6 °C/100 in Tahiti Island (Steinmann and Déjardin, 2004). Considering the similarity in the dimensions and thickness of sedimentary cover between Enewetak atoll and Resolution guyot, the geothermal gradient of Enewetak atoll was employed (Swartz, 1958; detailed ranges are provided in APPENDIX B Table B11). Additionally, concentrations of major, minor, and trace elements at Site 866 were integrated with wireline-logging data (DTLN, RHOB, and NPHI). Frequency analysis and histograms were conducted on the wireline-logging data.

Rock Type	Geochemical Analysis	Number of Samples	Depth Ranges	Techniques & Laboratory	Data Sources	Standard Samples	Corresponding Supplemental Sheet of the Data
Dolostone	Sr isotope	9	1572-1224	Finnigan MAT 261 multicollector mass spectrometer at the Precise Radiogenic Isotope Services, Australian National University, Canberra	Flood and Chivas (1995)	SRM 987 and EN-1	B4
	$\delta^{18}O$	9	1572-1224	isotopic measurements were performed at the Research School of Earth Sciences, Canberra	Flood and Chivas (1995)	NBS-18 and NBS-19	
	$\delta^{13}C$	9	1572-1224				
	Elemental analysis (Fe & Mn)	12	1611-1175	Microprobe analyses inductively coupled plasma atomic emission spectroscopy, Queensland University of Technology, Brisbane atomic. Microprobe analyses with absorption analysis by a Philips PU 9400X and inductively coupled plasma spectrometry by a sequential spectrometer Philips PU 7000.	Flood and Chivas (1995) & Röhl and Strasser (1995)		B5
	Elemental analysis (Sr)	6	1593-1252				
Limestone	Sr isotope	86	48-1611	VG Sector 54 thermal ionization mass spectrometer (TIMS) at the Department of Geology, University of North Carolina at Chapel Hill.	Jenkyns (1995) & Jenkyns et al. (1995)	NBS 987	B10
	$\delta^{18}O$	86	48-1611	VG Isocarb device and Prism mass spectrometer at Oxford University		NBS 19 and Cambridge Carrara marble	
	$\delta^{13}C$	86	48-1611				
	Elemental analysis (Fe & Mn)	13	10-1593	Microprobe analyses with absorption analysis by a Philips PU 9400X and inductively coupled plasma	Röhl and Strasser (1995)		B5

	Elemental analysis (Sr)	18	10-1593	spectrometry by a sequential spectrometer Philips PU 7000.			
Bulk chemistry of the whole sedimentary succession		77	1591-39	X-ray-fluorescence analysis	Röhl and Strasser (1995)		B6

Table 3.1 Summary table of all the geochemical data used in this paper. The table shows types of data, number of samples, depths of samples, the techniques used and the laboratories, data source, standard samples, and the corresponding Supplemental Sheet of the data.

3.6 Results and Interpretation

3.6.1 Seismic interpretation and seismic facies forward modelling

Seismic facies and their corresponding depths and palaeogeographic distributions in the atolls were categorised by analysing seismic properties like reflection pattern, continuity, amplitude, and internal and external geometry. Detailed characteristics of these seismic facies are explained with integrating drilling and wireline-logging data and comparing them with examples from high-resolution seismic data sets.

Seismic Facies 1 (SF1; Figure 3.5): It displays a distinct seismic stratigraphic expression within the host-rock strata as it comprises localised, anomalous, high-amplitude, parallel reflections with limited lateral continuity and abrupt terminations. SF1 exhibits a sheet-like shape with predominantly concordant to locally crosscut relationships within the host-rock strata. At Resolution Guyot, SF1 is found between depths of −2725 and −2400 TWT-ms (two-way time millisecond; ~900–1500 mbsf), while at Allison Guyot, SF1 occurs at depths of −2775 to −2600 TWT-ms (~650->870 mbsf).

Interpretation: The seismic features of SF1 (i.e. high amplitude, concordant to locally crosscut relationships within the host-rock strata, sheet-like shape, and abrupt terminations) closely resemble magmatic sill-intrusions observed in various 2D and 3D seismic data across different geological settings (Planke et al., 2000, 2005; Magee et al., 2015; Chen et al., 2020; Niyazi et al., 2021a,b; Figure 3.5). At Resolution Guyot, Site 866 did not encounter any drilled magmatic sill intruding through the sedimentary succession. Conversely, at Allison Guyot (Site 865), magmatic sill-intrusions penetrating limestones were found between depths of 830–871 mbsf. To validate our interpretation of SF1, seismic facies forward modelling was conducted. Utilising the drilling report from Allison Guyot (Sager et al., 1993b), detailing the thicknesses of drilled sills and the limestone they intruded, an input model was created (Figure 3.6A). The drilling reports indicated compressional wave velocity and density of drilled sills at 4854 m/s and 2.7 kg/m^3, and for limestones, 3406 m/s and 2.4 kg/m^3, respectively. Dominant frequency attribute and spectral analysis tools revealed the seismic data's dominant frequency at both atolls to be ~65–75 Hz (Figure 3.6B-C). The input model was transformed into a synthetic seismic facies forward model by simulating a zero-offset survey using Zoeppritz equations and a zero-phase Ricker wavelet (Magee et al., 2015). The resulting seismic facies forward modelling demonstrated that the thickness and stacking pattern of magmatic sill-intrusions at Allison Guyot would produce six alternating troughs and peaks, characterised by localised, abrupt brightening of high amplitude

reflections (Figure 3.6D). This aligned with observations within the area of drilled sills at Allison Guyot and the seismic characteristics of interpreted bright reflection packages in Resolution Guyot (Figure 3.6D). Consequently, we interpret SF1 as magmatic sills-intrusion intruding through sedimentary succession of Resolution Guyot between depths of −2700 to −2400 TWT ms (~900–1500 mbsf; Figure 3.3 and 3.6D) and Allison Guyot between depths of −2775 to −2600 TWT-ms (~650->870 mbsf).

Seismic Facies 2 (SF2; Figure 3.5): The interpreted magmatic sill-intrusions in both guyots are associated with vertical zones of disrupted and reduced reflection continuity which are surrounded by tilted and enhanced reflection amplitudes. SF2 bases consistently align with the tips of interpreted magmatic sill-intrusions (Figure 3.5). The upper part of SF2 exhibits eye-, crater-, mounded-, or dome-shaped geometry with a width of ~700-1700 m. The vertical disrupted zones of SF2 have inward-dipping reflections. Variance attribute highlights SF2 as zones of dim to chaotic reflections relative to the well-bedded reflections of the host-rock strata. Adjacent to SF2, localised areas show small-scale chaotic reflections and vertical discontinuities.

Interpretation: The interpreted seismic characteristics of SF2 (i.e. eye-, crater-, mounded-, or dome-shaped geometry of their upper parts, upward bending of surrounding seismic reflections, disrupted reflections within SF2, their inward-dipping reflections, and their intimate association with underlying magmatic sill-intrusion) strongly resemble hydrothermal vent complexes associated with magmatic intrusions as identified in 2D and 3D seismic data across various geological settings (Jamtveit et al., 2004; Planke et al., 2005; Chen et al., 2020, Figure 3.5). The smaller-scale zones of chaotic reflections and vertical discontinuities surrounding SF2 (Figure 3.5, 3.7, and 3.8) are interpreted as fluid escape pipes (Huang et al., 2020). SF2 spans a width of 300–1500 m in both guyots, up to 5000–6000 m at their centres (Figure 3.7 and 3.8). The interpreted sills and associated hydrothermal vents extend across both guyots' widths (Figure 3.3) but are primarily concentrated in the middle. The horizontal distance of the closest hydrothermal vent complexes to the dolomites at Resolution and Allison guyots drilling sites is ~2600 to 2000 m, respectively.

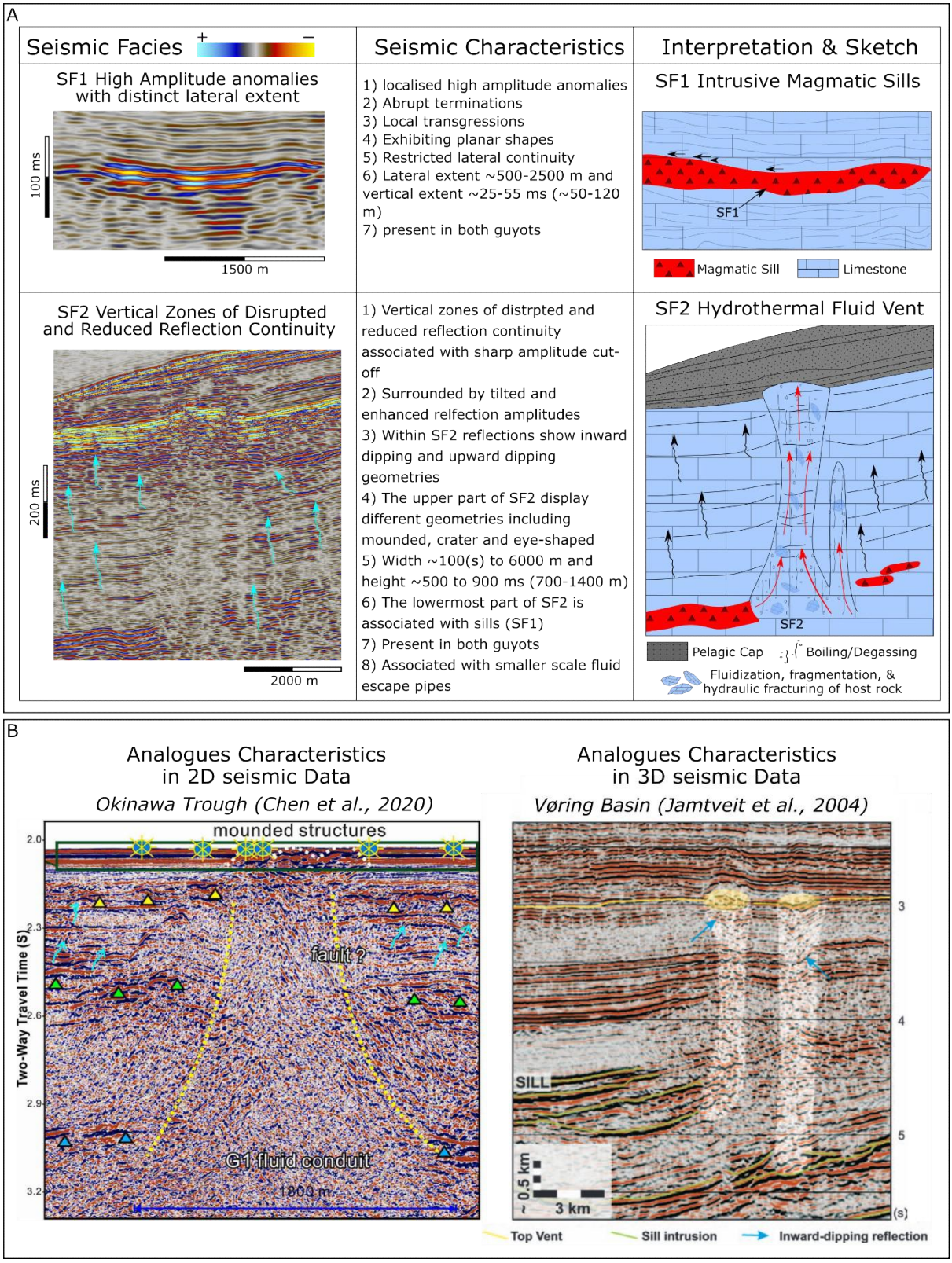


Figure 3.5. A. The interpreted seismic facies at Resolution and Allison guyots showing an example of each seismic facies, summaries of their characteristics, and interpretation sketch of seismic facies. B. The Figure also shows analogue seismic profiles with similar seismic facies from Okinawa Trough 2D seismic data (Chen et al., 2020) and Vøring Basin 3D seismic data (Jamtveit et al., 2004) to provide a source of comparison with the displayed characteristics of the seismic facies at the guyots.

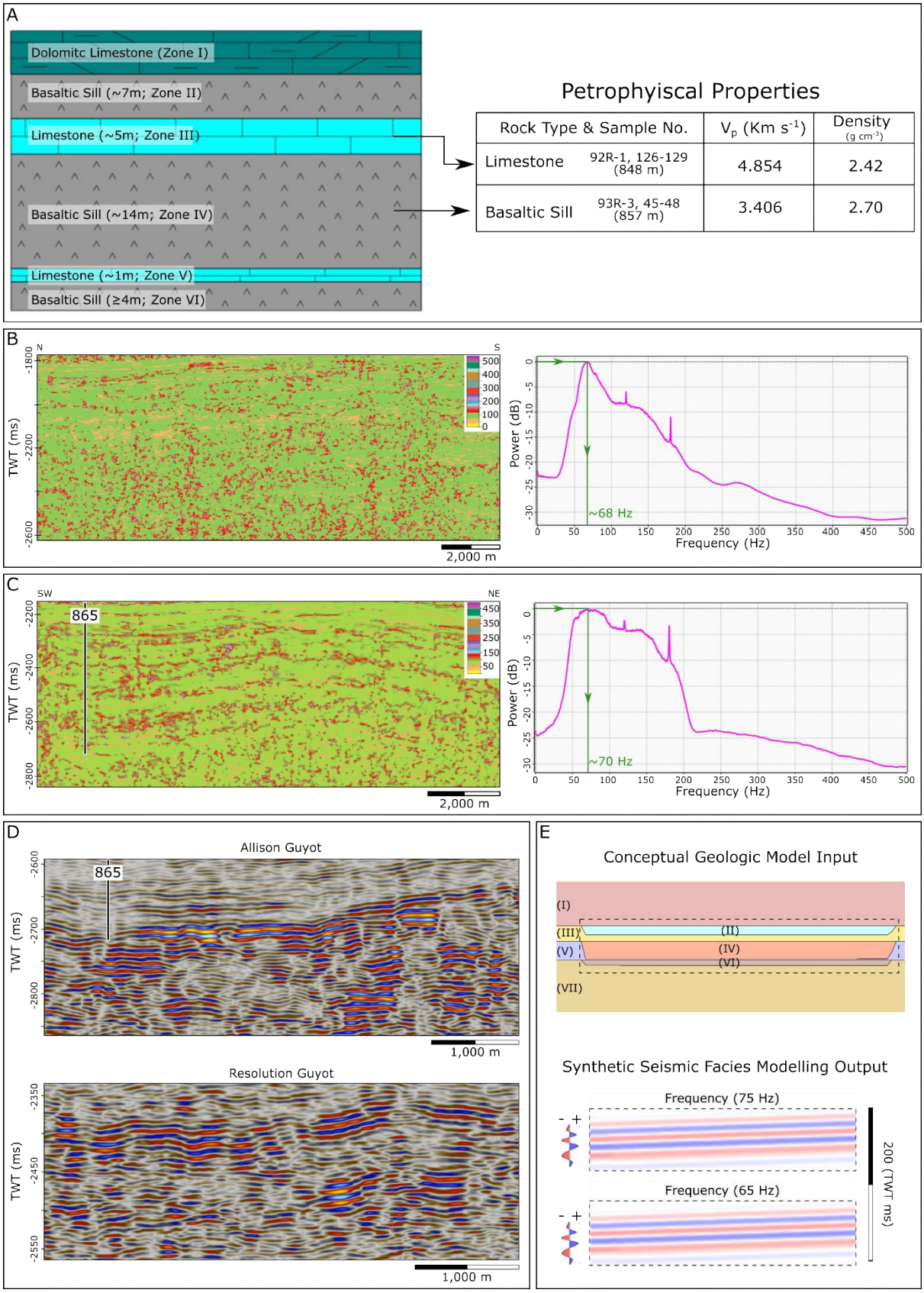


Figure 3.6. Seismic facies forward modelling of the interpreted magmatic sill-intrusion. A. A schematic representation of the intruding sill across the sedimentary succession at Site 865 along with their corresponding petrophysical properties. B. and C. Dominant frequency attribute seismic profiles along with spectral analysis data from Resolution and Allison guyots, respectively. A comparison between seismic profiles (D.) displaying the interpreted sills at

Resolution and Allison guyots against the results of the seismic facies forward modelling of the conceptual geologic model from core descriptions (E.) at Site 865 using 65 and 75 Hz frequencies, both D. and E. have the same vertical scale. The dashed box in E. highlights the area displayed in the synthetic seismic facies forward models.

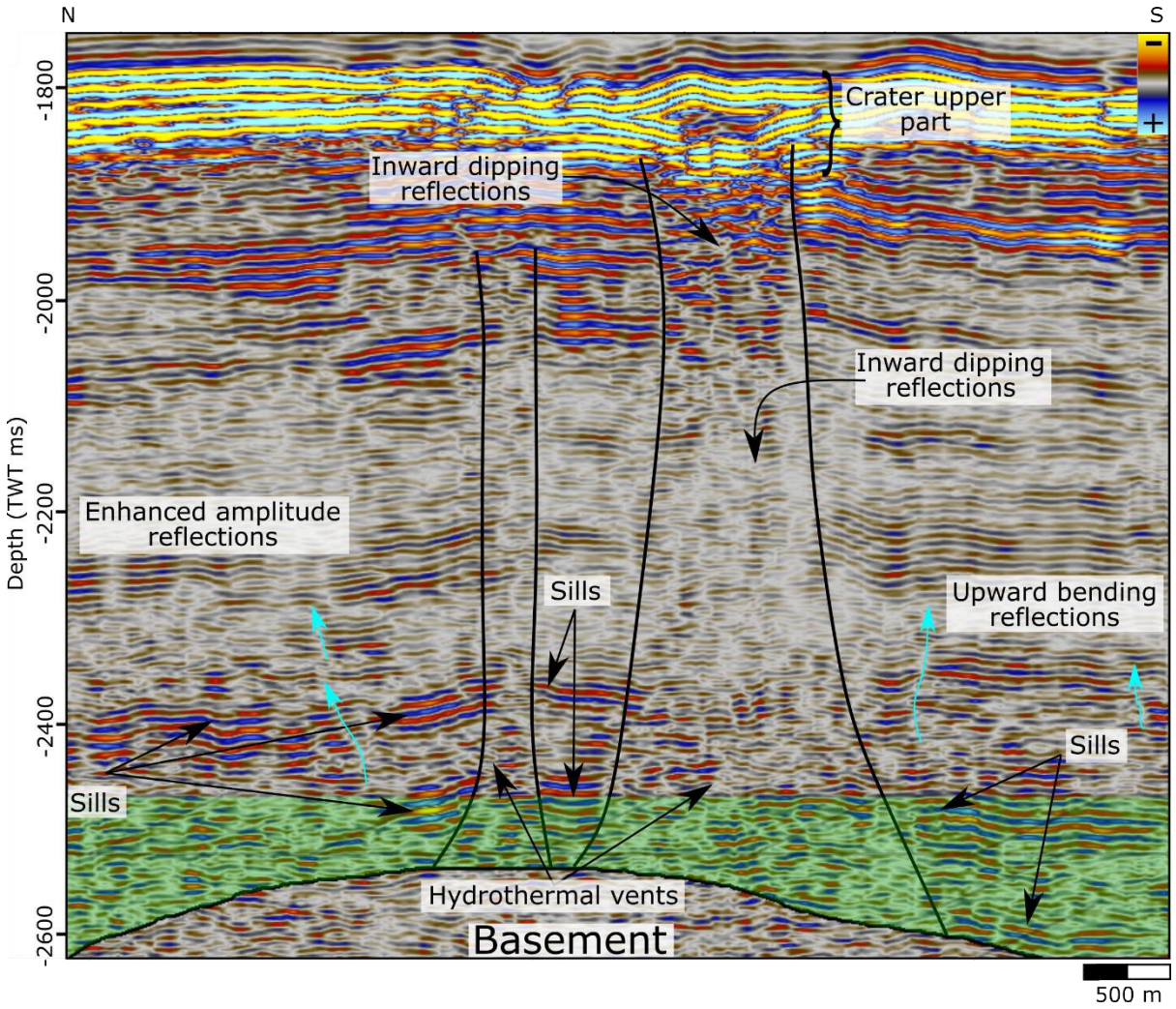


Figure 3.7. Seismic interpretation of the magmatic and hydrothermal system in Resolution Guyot. The seismic profile shows the seismic features of SF1: magmatic sill-intrusions (i.e. high amplitude, concordant to locally crosscut relationships within the host-rock strata, sheet-like shape, and abrupt terminations) and their associated SF2: hydrothermal vents and smaller scale fluid flow pipes (i.e. eye-, crater-, mounded-, or dome-shaped geometry of their upper parts, upward bending of surrounding seismic reflections, disrupted reflections within SF2, and their intimate association with underlying magmatic sill-intrusion). The highlighted part with transparent green box represents the approximate depths of the dolomite body(ies) projected away from Site 866.

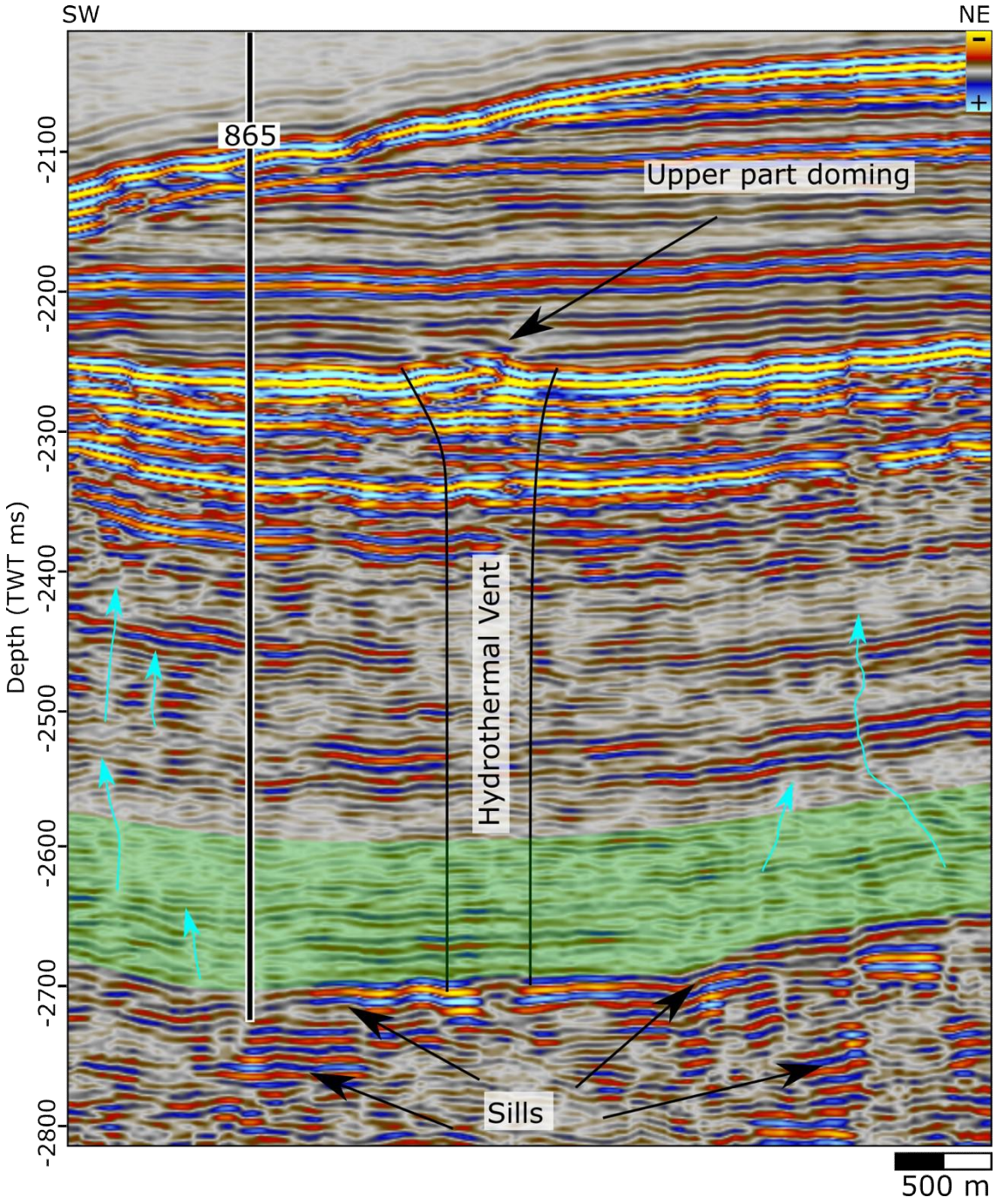


Figure 3.8. Seismic interpretation of the magmatic and hydrothermal system in Allison Guyot. The seismic profile shows the seismic features of SF1: magmatic sill-intrusions (i.e. high amplitude, concordant to locally crosscut relationships within the host-rock strata, sheet-like shape, and abrupt terminations) and their associated SF2: hydrothermal vents and smaller scale fluid flow pipes (i.e. eye-, crater-, mounded-, or dome-shaped geometry of their upper parts, upward bending of surrounding seismic reflections, disrupted reflections within SF2, and their intimate association with underlying magmatic sill-intrusion). The highlighted part with transparent green box represents the approximate depths of the dolomite body(ies) projected away from Site 865.

3.6.2 Dolostone Core and Petrographic Observations

3.6.2.1 Macroscale dolostone textures

The sedimentary sequence at Resolution Guyot comprises non-dolomitised limestones, partially/patchy dolomitised limestones, and dolostones (Figure 3.9). Dolostones are distinguished by their dark brown colour (Figure 3.9G, H) compared to the beige, cream, and light brown hues of limestone and dolomitic limestone (Figure 3.9A-F). Identifying dolomite at Resolution Guyot involved integrating core images, MgO% and grain density plots, and wireline-logs due to low core recovery. The integrated approach delineates (Figure 3.10): (a) complete dolomitisation at 1620-1500 mbsf, (b) intervals partially dolomitised alternating with limestones at 1500-1360 mbsf, (c) partially to completely dolomitised succession at 1360-1160 mbsf, (d) patchy dolostones intercalating with limestones above 1160 and below 1000 mbsf. Dolomite is almost absent in cores, thin sections, and smear slides descriptions above this level (ODP Initial Reports, 1993a) which suggest that the interpreted intervals in wireline-logs above that are mistakenly identified possibly due to (a) the bad conditions of the borehole (note wireline-logs spikiness; check APPENDIX B Table B8), and (b) presences of clays in the limestone which can have overlapping densities (2.6–3.3 gm/cm^3; Deer et al., 1966) with dolomite.

In pervasively dolomitised sections, fine to medium crystalline dark brown replacive dolomite matrix exists, with molds and vugs filled by medium to coarse crystalline golden-light brown dolomite cements (Figure 3.9G, H). Precursor limestone fabrics are mostly well preserved, showing carbonate grains and mouldic pores (Figure 3.9G, H). The calcitic carbonate grains (e.g. ooids, oncoids, pisoids, bivalves) show different preservation levels from unaltered to partially or totally dolomitised (Figure 3.9G, H). Partially and patchy dolomitised sections display lighter brown to cream colours, with mainly fine to medium crystalline replacive dolomite, replacing matrix and grains (Figure 3.9B-D, F).

3.6.2.2 Microscale dolomite textures

Replacive dolomites (RD) show finely to medium crystalline (100–300 μm) planar-e and planar-s textures (Figure 3.11). The Pervasively dolomitised sections have a densely interlocked mosaic (Figure 3.11A-C), while partially to patchy dolomitised sections are less dense (Figure 3.11D-F). Dolomite cements (DC) are present throughout the whole section with finely to medium crystalline (150–350 μm up to 400–500 μm) planar-s to non-planar textures (Figure 3.11). Dolomite cements partially to fully occlude mouldic, vuggy, interparticle and intercrystalline porosities (Figure 3.11F). In some cases, dolomite cements have finer crystals lining vugs and coarser crystals in the centre. Original limestone fabrics are mostly preserved with varying degrees

from totally to partially retentive to ghost structures of preexisting carbonate grains (e.g. ooid, peloids, oncoids, bioclasts; Figure 3.11A-C, E). In few cases, the original fabrics are preserved just in few relics of ghost structures. Dolomite crystals typically exhibit concentric to oscillatory zoned luminescence of dark to bright orange, dark to light brown and bright yellow zones (Figure 3.12A-D). Some show similar luminescence but of dull to bright red and reddish orange (Figure 3.12E). Unzoned, mottled, or blotchy luminescence are almost absent across the succession.

3.6.3 Dolomite Geochemistry

Dolomites have $\delta^{18}O_{dol}$ values from −1.6 to +0.7 and $\delta^{13}C_{dol}$ values from +2.1 to +2.8. While host-rock Limestones have $\delta^{18}O_{lmst}$ values from −3.44 to −0.53 (average: 2.01) and $\delta^{13}C_{lmst}$ values from −0.42 to +5.34 (average: +2.67). Dolostones at Site 866 exhibit $^{87}Sr/^{86}Sr$ ratios between 0.7072880 and 0.7073970 (Figure 3.13). The corresponding representative limestone at the same depth range shows $^{87}Sr/^{86}Sr$ ratios between 0.7074490 and 0.7075330. Dolostones have Sr content ranging from 106 to 239 ppm (average: 148 ppm), while limestones Sr content range from 56 to 368 ppm (average: 179 ppm). Dolomite Fe and Mn contents (Figure 3.13A-B) range from 70 to 3172 ppm (average: 860 ppm) and 2–49 ppm (average: 17 ppm), respectively. Limestone exhibits Fe and Mn contents (Figure 3.13A-B) from 9 to 388 ppm (average: 105 ppm) and 1–28 ppm (average: 11 ppm), respectively. The MgO% plot at Site 866 indicates a lack of partially to fully dolomitised limestone above 1100–1000 mbsf, with a noticeable SiO_2% peak (~68%) at approximately 1075 mbsf (Figure 3.14).

Interpretation: To explore the age ranges of dolomitisation processes that occurred at Site 866, dolomite $^{87}Sr/^{86}Sr$ isotope ratios were utilised. This involved applying the validation approach outlined by Budd (1997) and Wang et al. (2019a), which includes verifying whether these ratios accurately represent the seawater primarily involved in dolomitisation and confirming that no subsequent alterations in the Sr composition occurred within the system. Dolomite Sr content (106–239 ppm; mean 148 ppm) falls below 300 ppm, suggesting an open seawater-buffered diagenetic system. The dolomite $^{87}Sr/^{86}Sr$ ratios generally increase from bottom to top of the dolostone succession, resembling patterns seen in seawater-mediated Cenozoic island dolostones. Their $^{87}Sr/^{86}Sr$ ratios overlap with Mid-Cretaceous Sr-isotope stratigraphy (McArthur et al., 2012). Based on the $^{87}Sr/^{86}Sr$ ages, derived from McArthur et al.'s LOWESS LOOK-UP TABLE 5B, dolomitisation of Early-Cretaceous limestone (depositional age ~132-130 Ma) occurred during the Mid-Cretaceous (125 ± 0.5 to 119.3 ± 1 Ma and/or 112.9 ± 0.35 to 109.5 ± 1.1 Ma; Figure 3.13C), indicating ages of at least 5–12 million years younger than the host-rock and 8–15 million years younger than the initiation of sedimentation at Site 866. The possibility of dolostone

recrystallisation following the initial dolomitisation phase could reset $^{87}Sr/^{86}Sr$ values and other geochemical aspects as well ($\delta^{18}O_{dol}$, $\delta^{13}C_{dol}$, major and minor elemental composition) which would invalidate dating (Budd, 1997; Wang et al., 2019a). However, the following evidence suggests replacement rather than recrystallisation: (a) preservation of depositional fabric and allochem ghosts (Figure 3.11), (b) absence of dolomites with markedly different geochemical signatures ($\delta^{18}O_{dol}$, Sr content), and (c) retention of crystal zonation under CL (e.g. Gregg and Sibley, 1984; Lee and Friedman, 1987; Mazzullo, 1992; Machel, 2000a; Figure 3.12). Based on integrating dolomitisation age of the shallowest (1224 mbsf) and deepest (1572 mbsf) samples with dolomite $^{87}Sr/^{86}Sr$ values with their depositional age (El-Yamani et al., 2022), the overburden thickness during dolomitisation (125 ± 0.5 to 119.3 ± 1 Ma and/or 112.9 ± 0.35 to 109.5 ± 1.1 Ma) ranged from 425 to 920 and 771–1262 mbsl (metre below sea-level), respectively. Burial and thermal history calculations of the host rock at depths 1224 and 1572 mbsf from initial deposition to 110 Ma are provided in APPENDIX B Material B3, showing the overburden thicknesses.

By applying Horita's (2014) equation, the lightest and heaviest $\delta^{18}O_{dol}$ of dolomites at Site 866 indicate that the calculated dolomitisation temperatures are rising from 30.4 °C (1224 mbsf: shallowest sample) to 41.2 °C (1572 mbsf: deepest sample). This gradual temperature increase with depth (Figure 3.13D) contrasts with typical seawater-mediated island dolostones (e.g. Budd, 1997; Suzuki et al., 2006; Ren and Jones, 2016; Wang et al., 2019a; Li et al., 2023a). Burial and thermal modelling of the limestone host rock suggests that the concurrent pore-fluid ambient temperatures during dolomitisation (125 ± 0.5 to 119.3 ± 1 Ma and/or 112.9 ± 0.35 to 109.5 ± 1.1 Ma; Figure 3.13D; APPENDIX B Material B1) should have been approximately 14.5–11 °C (Figure 3.13D). Elemental data from Resolution Guyot depict host limestone and low Mn, Fe dolomites (Figure 3.13A) aligning within the range of seawater island dolomites (Budd, 1997), but with some Fe-rich dolomites concentrated only near the basement (1620–1398 mbsf; ~50% of dolomites with 1536–3172 ppm Fe; mean 2204 ppm; Figure 3.13B).

The termination of the dolomitised section aligns with an abrupt peak in SiO_2% (~68%; Figure 3.14). This peak could indicate terrigenous input and/or volcanic ashes, given the geological context. However, the lack of correlation between the SiO_2% peak and TiO_2%, Al_2O_3%, or Fe_2O_3% at that level dismisses clastic input (Röhl and Strasser, 1995; Śliwiński et al., 2012). Evidence suggesting that the interval above the pervasive dolomite (1100–1010 mbsf) includes dispersed volcanic ash-rich intervals is: (a) frequency analysis of wireline-logs matches characteristics of volcanic ashes (Watson et al., 2017) with 77% of RHOB log falling between 2.15

and 2.35 gm/cm^3, 58% of NPHI log between 30 and 39 pu, and 62% of DTLN between 80 and 100 us/ft; (b) silica content at ~1080 mbsf (~69%) fits within the suggested range for volcanic ashes (45–75 wt%; Heiken, 1972); (c) fragments of volcanic glass are observed at 1010–1040 mbsf (Röhl and Strasser, 1995); (d) low Cr concentration (≤1 ppm) matches values of discrete ash layers (<3 ppm; Sigurdsson et al., 1997); (e) the presence of varicolored (green–grey) smectitic, illitic, and I/S mixed-layer clays (Baudin et al., 1995); (f) their host-rock limestone has mid-late Barremian age which overlaps with the proposed volcanic ash origin of the Barremian and Aptian clays at Site 463 (25 km east of Resolution Guyot; the Barremian-Aptian volcanism in the western Pacific; Vallier and Jefferson, 1981).

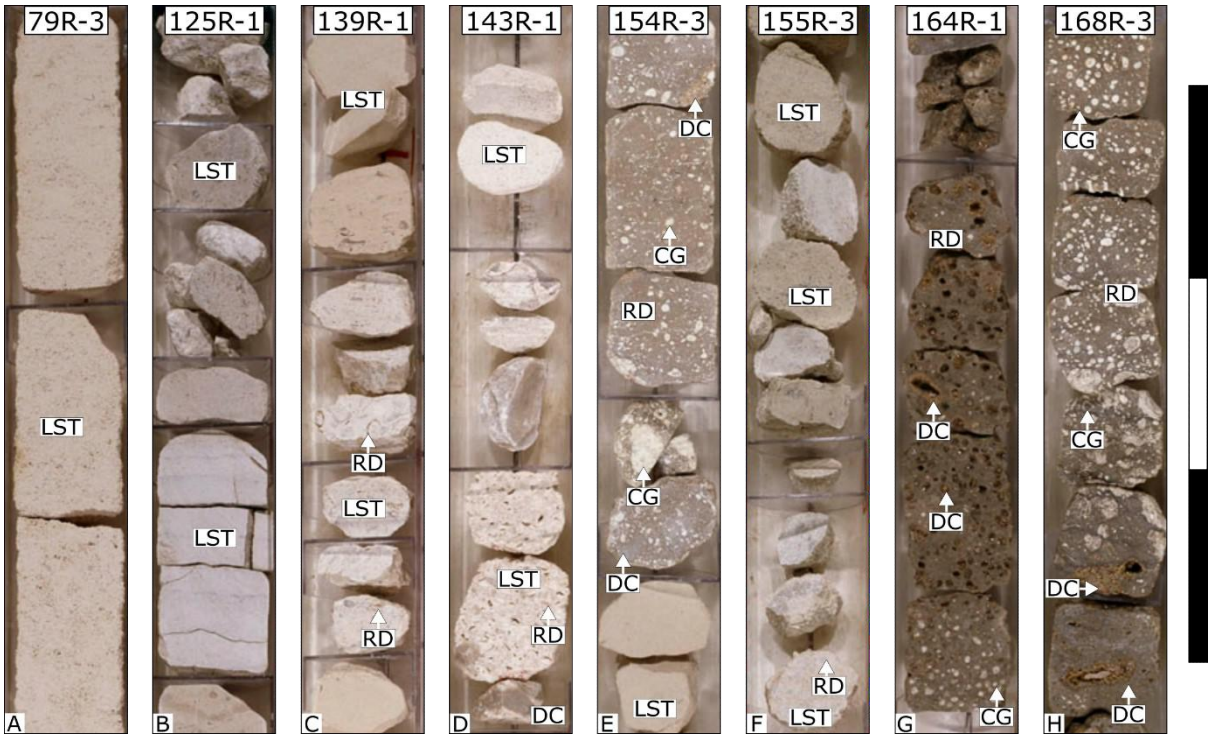


Figure 3.9. Core photographs of the dolomitised succession at Site 866, Resolution Guyot. The scale bar represents 30 cm. The naming of the cores is as follows: core number, core type (R: rotary coring), and section number. A. Core photo showing the beige and cream hues of limestone (LST) oolitic grainstone (738 mbsf). B. Core photo showing light brown partially dolomitised limestone (LST) of peloidal bioclastic grainstone (1174 mbsf). C. Core photo of beige colour of patchy dolomitised limestone of peloidal wacke-to pack-stone with few replacive dolomites (RD) (1309 mbsf). D. Core photo showing in the upper part non-dolomitised limestone (peloidal and oolitic grainstone) while the lower part is dolomitised with replacive dolomites and dolomite cement (1358 mbsf). E. Core photo of dark brown dolostone with preserved calcitic grains, dolomite cements, and replacive dolomites. The lower part of the photo shows non-dolomitised limestone (1457 mbsf). F. Core photo of light brown colour of peloidal grainstone of partially dolomitised limestone (1468 mbsf). D, E, and F represent partially-totally dolomitised intervals alternating with limestones. G. Massive dolostone of oncoidal and oolitic pack- and grain-stone (1550 mbsf). The photo shows calcitic grains, replaced grains with dolomites, and mouldic porosities of dissolved ooids and onocolites which are filled totally or partially with dolomite cements. H. Core photo of massive dolostone of oncoidal and oolitic grain- to rud-stone. (1592 mbsf). The photo shows calcitic grains, replaced grains with dolomites, and mouldic porosities of dissolved ooids and onocolites which are partially or totally filled with dolomite cements.

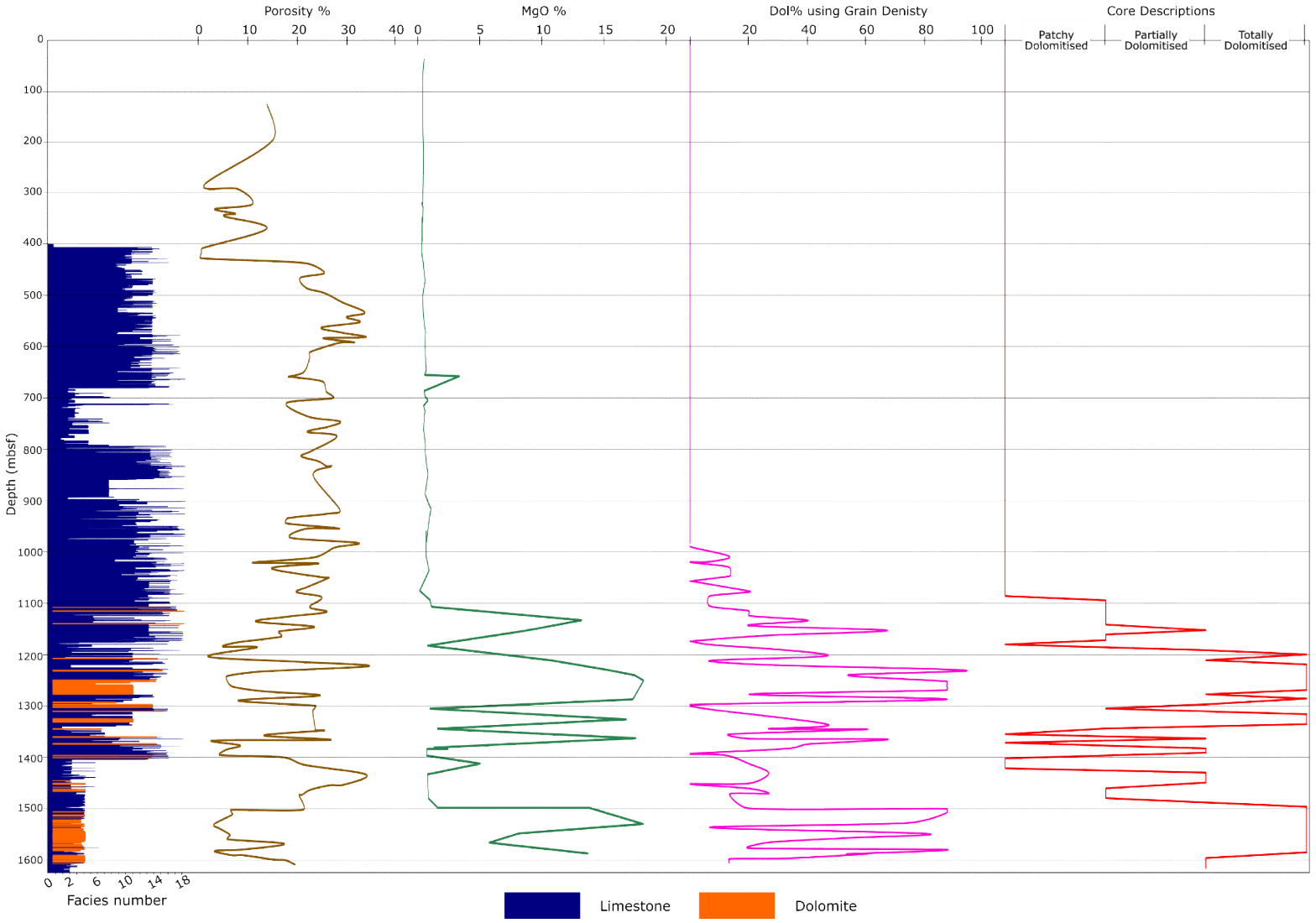


Figure 3.10 Dolomite distribution versus depth at Site 866 based on integrating core descriptions, MgO%, and dolomite% using grain density along with measured porosities (Sager et al., 1993a) and facies templates (Arnaud et al., 1995). The green boxes highlight the dolomitised intervals. Facies numbers, based on (Arnaud et al., 1995), are: Facies 0: Fine-grained

Pelsparites, Facies 1: Peloosparites and Oopelsparites with Reworked Ooids, Facies 2: Well-sorted Oosparites to Oomicrites, Facies 3: Peloosparites and Peloomicrites, Facies 4: Oo-oncosparites with Rounded Micritic Oncoids, Facies 5: Pelsparite and Pelmicrite with Echinoderm Plates and Small Benthic Foraminifers, Facies 6: Coarse-grained Biosparites with Rounded Elements, Facies 7: Coarse-grained Biosparites with Rudist and Gastropod Shells, Facies 8: Pelbiomicrites and Pelbiosparites with Benthic Foraminifers, Facies 9: Micrites and Pelmicrites with Sponge Spicules and Large Benthic Foraminifers, Facies 10: Micrites and Biomicrites with Large Foraminifers, Facies 11: Micrite and Pelmicrite with Rudists and Gastropods, Facies 12: Micrite and Pelmicrite with Green Algae, Facies 13: Micrite with Ostracodes and Small Benthic Foraminifers, Facies 14: Micrite and Pelmicrite with Bird's Eyes, Facies 15: Micrite and Pelmicrite with Oncolites, Facies 16: Micrite-Pelmicrite and Dolomicrite-Dolopelmicrite with Algal-Microbial Mats, Facies 17: Micrite and Dolomicrite with Thin Sedimentary Laminations, Facies 18: Micrite with Desiccation Cracks.

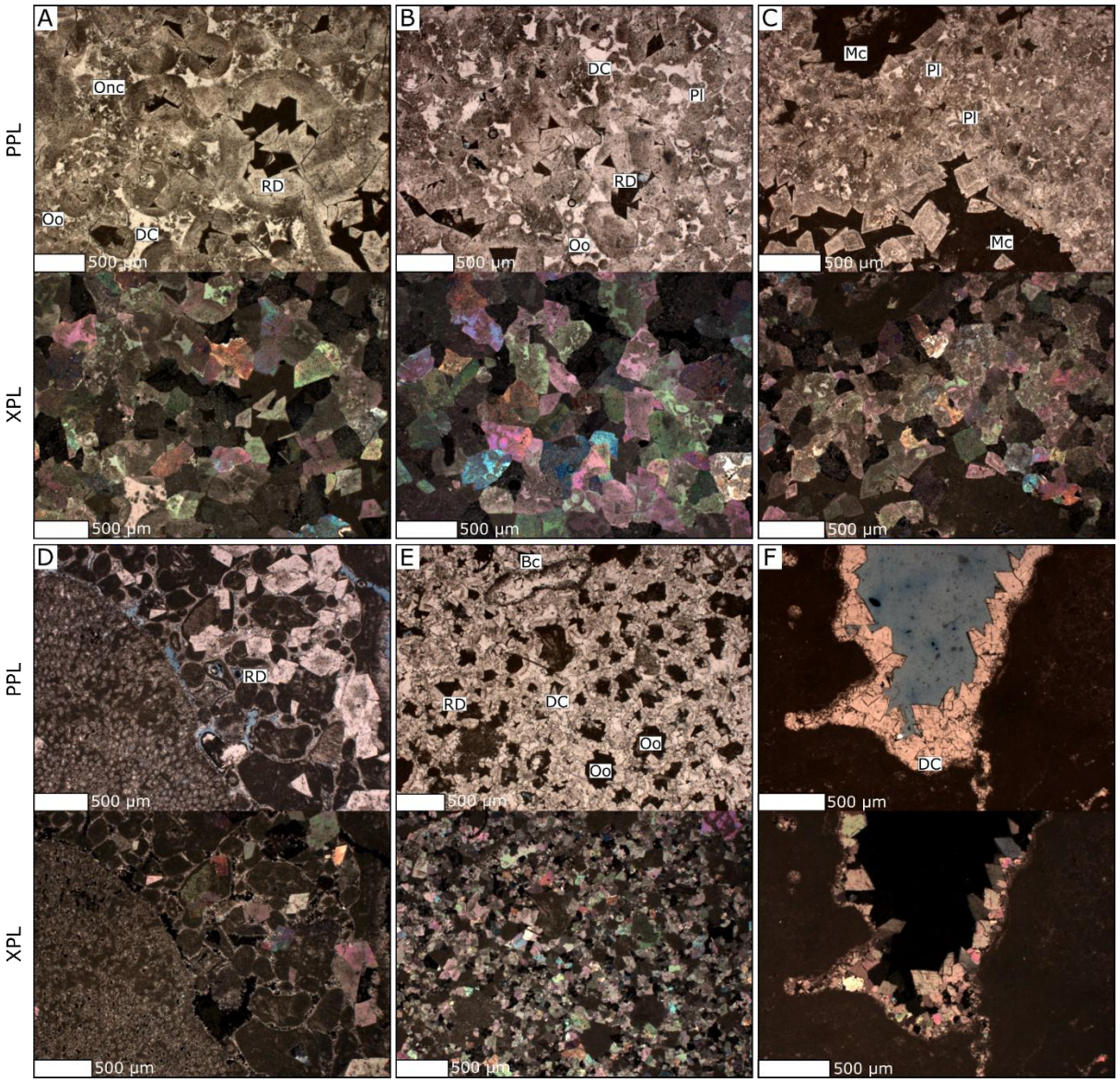


Figure 3.11. Thin-section photomicrographs showing plane polarised light (PPL) and crossed polarised light (XPL). A. and B. Photomicrographs from totally dolomitised intervals showing replacive dolomites (RD) and dolomite cement (DC) with fabric preservation of ooids (Oo), oncoids (Oc) and peloids (Pl), from samples at depths 1551 and 1594, respectively. C. Photomicrograph from partially dolomitised interval showing outlines of original fabric and partially dolomitisation of muddy matrix (Mc), from a sample at depth 1446 mbsf. D. Patchy dolomitised limestone, from a sample at depth 1175 mbsf. E. Pervasively dolomitised limestone with fabric preservation, from a sample at depth 1165 mbsf. F. Partially filled vug with dolomite cement in a wackestone, from a sample at depth 1137 mbsf.

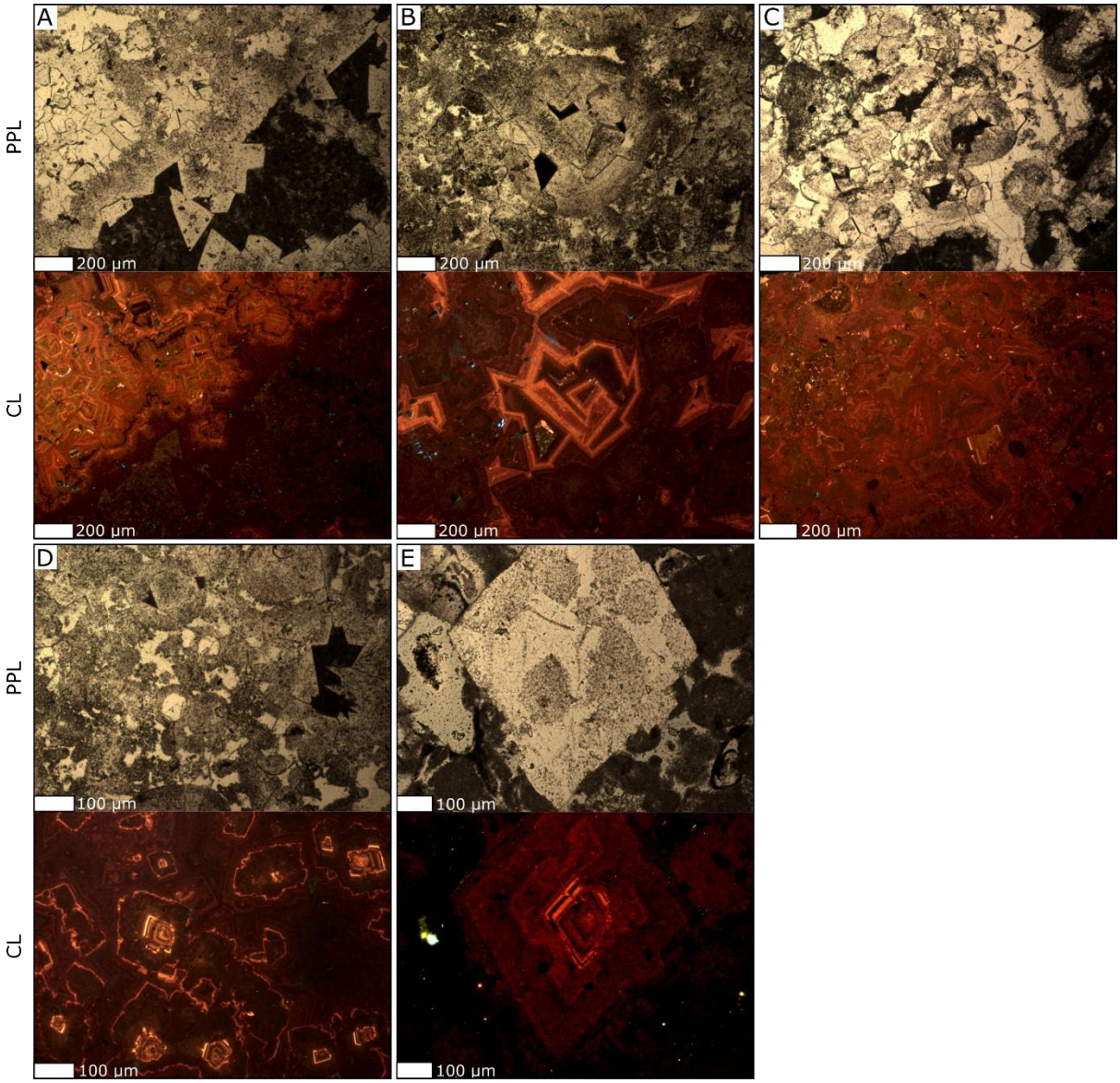


Figure 3.12. Thin-section photomicrographs showing plane polarised light (PPL) and cathodoluminescence (CL). Concentric to oscillatory zoned luminescence of dark to bright orange, dark to light brown (A–D) and bright yellow zones (D). E. Concentric to oscillatory zoned luminescence of dull to bright red and reddish orange. Thin section photomicrographs from A to E are from samples at depths 1446, 1551, 1591, 1594, 1467 mbsf, respectively.

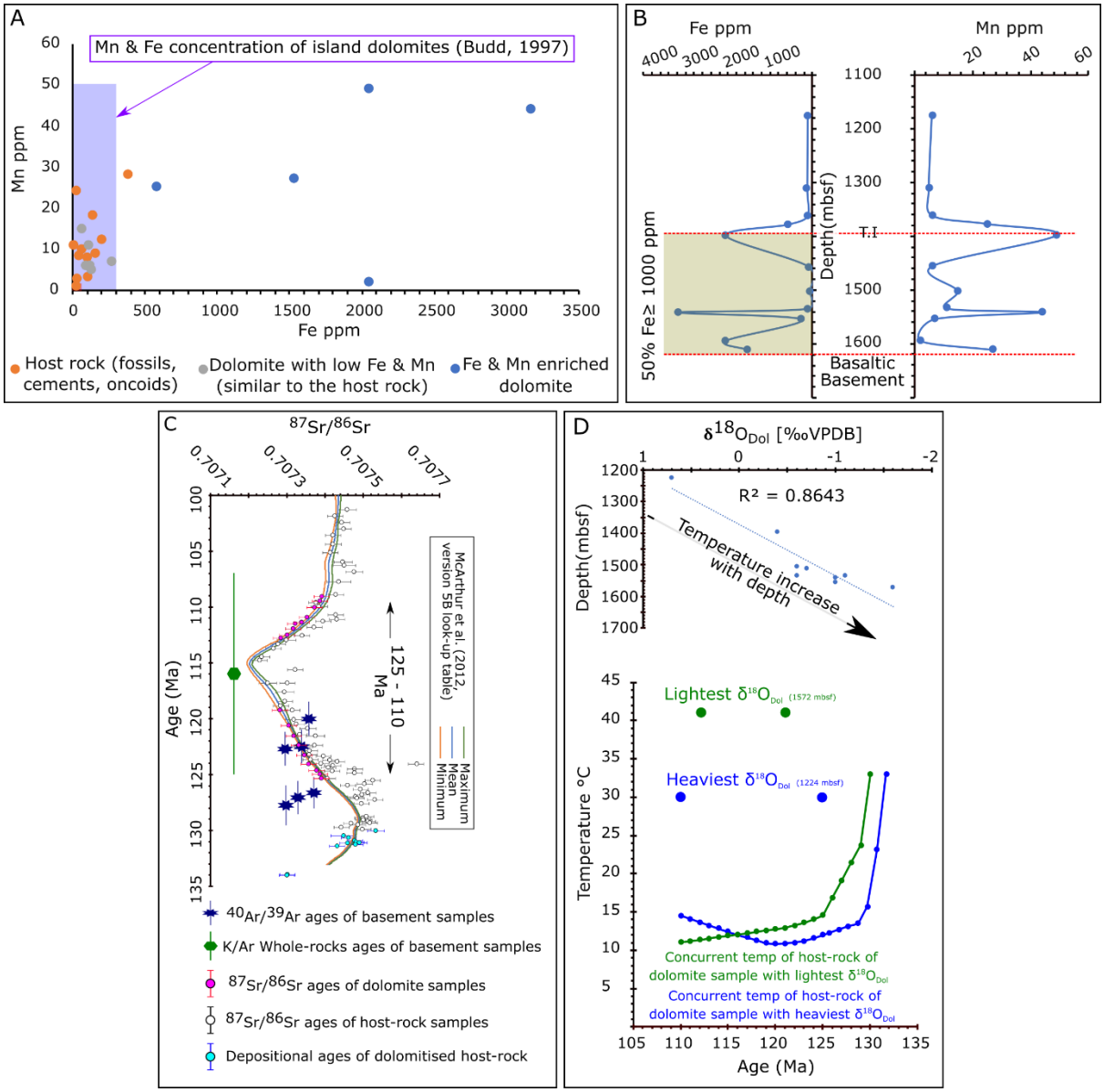


Figure 3.13. Geochemical analyses of the dolomite at Site 866. A. Mn and Fe plot showing a cluster of the host rock and low Fe and Mn dolomites within values of island dolomites by Budd (1997) and presence of Fe-enriched dolomites. B. Fe and Mn plot with depth showing Fe-enrichment of the dolomite close to the basement. The dashed line in panel (B) shows the location of the potential terrigenous input (T.I). C. Depositional age model of the host rock (El-Yamani et al., 2022) and the $^{87}Sr/^{86}Sr$ ages of the dolomite and $^{40}Ar/^{39}Ar$ ages of the basement and K/Ar whole-rock ages of the basement (Baker et al., 1995; Pringle and Duncan, 1995). D. $\delta^{18}O_{Dol}$ vs depth showing temperature increase with depth which is different from the expected thermal history of host rock at 1572 and 1224 mbsf between 125 and 110 Ma.

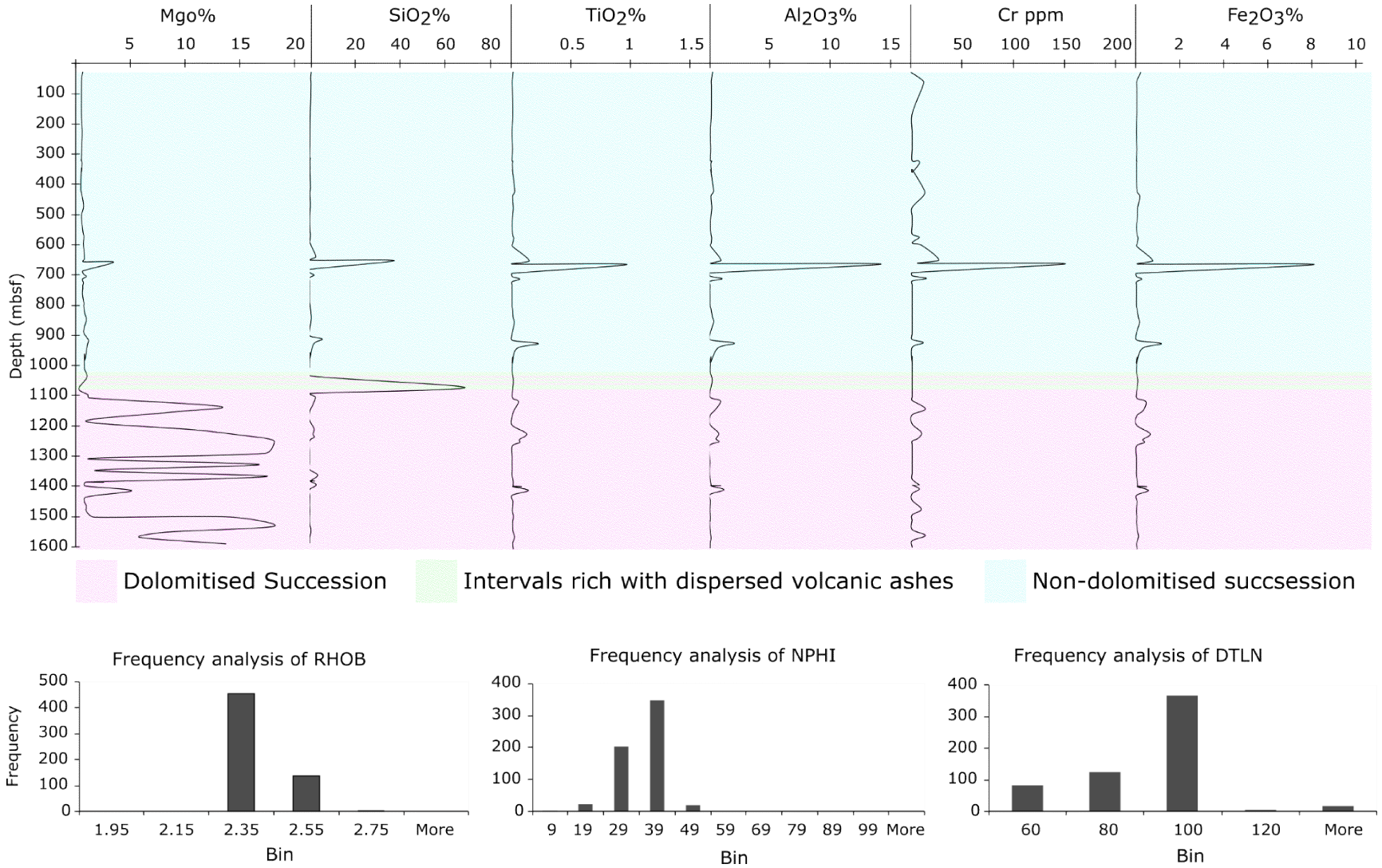


Figure 3.14. Geochemical analysis plot at Site 866 showing the presence of dolomites between 1620 and 1100 with absence of dolomite above that level. It also shows the peak of SiO_2% above the dolomites with no correlation with TiO_2%, Al_2O_3%, Fe_2O_3%, and Cr ppm. The figure shows the frequency analysis on log interpretation showing that the interval between 110 and 1010 mbsf is characterised by (1) 77% of RHOB is ~2.15–2.35 gm/cm^3, (2) 58% of NPHI is ~30–39 pu, and (3) 62% of DTLN is ~80–100 us/ft.

3.7 Discussion

3.7.1 The Link Between Magmatism and Hydrothermal Venting

Previous studies on different types of hydrothermal vents complexes across different types of sedimentary basins interpreted their origin as 'volcanic features' (Skogseid et al., 1992; Davies et al., 2002). However, subsequent studies, based on integrating wireline-logging data and 3D seismic data, suggested that hydrothermal vents above sills are formed predominantly through hydrothermal fluid circulation and subsurface remobilisation of sediments rather than extrusive seafloor volcanism (Bell and Butcher, 2002; Planke et al., 2005). The origin of hydrothermal vent complexes (SF2) in this study is deduced through seismic facies analyses, exhibiting distinct characteristics compared to the host-rock (Figure 3.5, 3.7, and 3.8): (a) cylindrical low amplitude conduits, (b) eye-, crater-, mounded- or dome-shaped upper parts, (c) internal inward-dipping reflections, (d) preferred locations of hydrothermal vents at the tips of magmatic sills. These seismic features resemble hydrothermal vent complexes in other settings linked with magmatic intrusions that mobilise fluids, leading to fracturing of overlying strata (e.g. Jamtveit et al., 2004; Planke et al., 2005; Hansen, 2006). To form these complexes, local fluid pressure must exceed hydrostatic pressure, generated through the following factors (Judd and Hovland, 2007; Planke et al., 2005; Aarnes et al., 2012; Iyer et al., 2017; Omosanya et al., 2018; Wang et al., 2018a): (a) temperature increase by the magmatic sill-intrusions would rapidly heat the surrounding rocks causing boiling of pore-fluids, (b) magmatic release of H_2O–CO_2–SO_2–HCl-rich hydrothermal fluids from the intruded magma would cause overpressure, (c) metamorphic dehydration reactions between magmatic intrusions and host-rock would release various gases (e.g. CO_2 and SO_2), (d) generation of large quantities of other gaseous such as CH_4 could result in large overpressures. As pressure cannot be dissipated quickly, areas around the magmatic sill-intrusions would become overpressured and hydraulic fracture networks would form hydrothermal vent complexes and associated smaller scale fluid escape pipes along which gas, water, magmatic fluids, and volatiles would escape to the seafloor (Roelofse et al., 2021). The previously described factors were seen at Resolution and Allison guyots. At Site 865, the contact between sills and overlying carbonates reveals decarbonated, metasomatised, lignite-bearing sedimentary layers that contain fragments of very highly to completely altered basalts due to high intrusion temperatures (Sager et al., 1993b). Site 866 displays a negative $\delta^{34}S_{CAS}$ shift (125-110 Ma), suggesting increased volcanism, hydrothermal activities, and magmatic sulphur release (Mills et al., 2017; Paytan et al., 2004). Relatively high T_{max} values at Site 865 and charcoal content at Site 866 (Baudin et al., 1995) imply thermal anomalies caused by basaltic sills. In addition, our interpretation of the seismic data

revealed the absence of any volcanic cones or lava flows (e.g. Infante-Paez and Marfurt, 2018) related to the interpreted hydrothermal vents at both guyots. Hence, hydrothermal vent complexes above the sills in both guyots resulted from hydrothermal fluid circulation and hydraulic fracturing of sediments rather than extrusive seafloor volcanism.

3.7.2 Magmatically Driven Hydrothermal Dolomitisation

Fe and Mn concentrations can provide one of the most useful types of information regarding interpretations of dolomite genesis (James and Jones, 2015). Modern seawater typically contains low Mn (0.2 ppb) and Fe (2 ppb; Drever, 1997). According to Veizer (1983), dolomites formed in seawater should exhibit low Mn (1 ppm) and Fe (3–50 ppm). Seawater-mediated island dolomites are known for low Fe (<300 ppm) and Mn (<50 ppm) concentrations (Budd, 1997). However, the lowermost 220 m of Cretaceous dolomitic limestones and dolostones at Resolution Guyot exhibit notably high Fe content (range: 1536–3172 ppm; mean: 2204 ppm), suggesting external metal sources like overlying soil, underlying volcanics, or detrital siliciclastics (Budd, 1997). Soil horizons and exposure surfaces are not likely the source here as the observed Fe-enrichment cannot be explained by Fe-stained exposure surfaces (e.g. Fe of few hundreds of ppm in dolomites around soil horizons and exposure surfaces in Grand Bahama Island and the Xisha islands; Budd, 1997; Li et al., 2023a). The correlation between terrigenous input proxies (SiO_2%, TiO_2%, Al_2O_3%, Fe_2O_3%; Figure 3.14) around ~1400-1380 mbsf suggests terrigenous input, supported by dispersed clay seams in cores. Therefore, this might suggest terrigenous input as the source of Fe-enrichment at that level. However, this cannot explain the Fe-enrichment below 1400 mbsf (Figure 3.14) because (a) there is no correlation between terrigenous input proxies below that level except at ~1552 mbsf which corresponds to a very small, millimetres-thick, clay seam, (b) clay seams are very rare in the cores with millimetre-centimetre scale, and (c) XRD analyses at Site 866 suggest absence of any clayey interbeds between 1400 and 1601 mbsf (Murdmaa et al., 1995). Thus, this rules out terrigenous input as a source of Fe-enrichment below 1400 mbsf. Therefore, the volcanic basement is the only plausible source left for Fe-enrichment at ~1620-1540 mbsf. The depths of dolomites (Figure 3.4 and 3.7C, D) at Allison (−2707 to −2596 TWT ms; 660–837 mbsf) and Resolution (−2790 to −2490 TWT ms; 1620–1050 mbsf) guyots and the depths of the interpreted sills on seismic data are laterally overlapping which suggests spatial coexistence. Moreover, there is a strong temporal overlap between (a) the $^{87}Sr/^{86}Sr$ ages of dolomites, (b) the ages of basalt samples at Site 866 (107–125 Ma using K/Ar whole-rocks age dating and an average of 126 Ma using $^{40}Ar/^{39}Ar$ age dating, Baker et al., 1995; Pringle and Duncan, 1995; Sager, 1995), (c) the negative $\delta^{34}S_{CAS}$ shift at Site 866 (110–125 Ma; Mills et al., 2017), and (d) the proven magmatism

at the Mid-Pacific Mountains (130-110 Ma; Pockalny et al., 2021) which may suggest a causality relationship (Figure 3.13C). Based on the dolomitisation age of the shallowest (1224 mbsf) and deepest (1572 mbsf) samples with dolomite $^{87}Sr/^{86}Sr$ values, the range of the overburden thickness during dolomitisation was 425–920 and 771–1262 m, respectively. Such an overburden thickness suggests post-depositional dolomitisation within depths of shallow to intermediate burial diagenetic settings (sensu Machel, 1999). This does not support syndepositional or near-surface early-burial dolomitisation by normal to seasonally evaporative seawater as suggested earlier (Sager et al., 1993b; Röhl and Strasser, 1995; Strasser et al., 1995). The $\delta^{18}O_{dol}$ calculated temperatures are ~18–29 °C hotter than the concurrent temperatures of the host rock (Figure 3.13D) given that the proven active exchange between pore-water and surrounding seawater at the Pacific guyots (Paull et al., 1995) should have driven the temperatures within the guyots towards the surrounding seawater temperatures (i.e. negative geothermal gradient in oceanic islands and atolls mimicking those of the open marine profile as observed in Enewetak, Bikini, Kita-daito-jima, Fangataufa, and Mururoa atolls, Reed Bank, Tahiti, and Grand Cayman Islands, Florida Platform, and Yucatán Peninsula; Swartz, 1958 ; Kohout et al., 1977; Rougerie and Wauthy, 1993; Guille, 1996; Henry et al., 1996; Andrié et al., 1998; Fairhurst et al., 1999; Leclerc et al., 1999; Jean-Baptiste and Leclerc, 2000; Jones et al., 2000; Warren, 2000; Stoessell et al., 2002; Steinmann and Déjardin, 2004; Montaggioni and Braithwaite, 2009; Ren and Jones, 2017; Wang et al., 2020). Using other published equations of oxygen isotope fractionation during dolomitisation to compute $\delta^{18}O_{dol}$ temperatures (Northrop and Clayton, 1966; O'Neil and Epstein, 1966; Fritz and Smith, 1970; Sheppard and Schwarcz, 1970; Matthews and Katz, 1977; Land, 1985; Woronick and Land, 1985; Vasconcelos et al., 2005; Müller et al., 2019; APPENDIX B Table B12) would change the absolute values of $\delta^{18}O_{dol}$ derived temperatures but it does not change the conclusion that dolomitisation temperatures are hotter than concurrent temperatures of the host-rock with at least 12–25 °C. Our calculations are conservative considering that if the $\delta^{18}O_{water}$ was changed by the interaction of normal Cretaceous seawater (0.2‰ SMOW; Zhou et al., 2008) with magmatic fluids (5.3–10‰ SMOW; Sahlström et al., 2019), then the temperature of dolomitisation could be significantly higher than estimated. Therefore, this suggests the presence of an external heat source (sensu hydrothermal dolomite; Machel and Lonnee, 2002).

Accordingly, our integration of geochemical, seismic, and wireline-logging data at Resolution Guyot led us to propose a magmatically driven hydrothermal dolomitisation model (Figure 3.15) which is suggested to be applicable as well in Allison Guyot based on the similar geologic setting and the association between sills and dolomites (Figure 3.7 and 3.8). Three main contributions of magmatic emplacement to facilitate dolomitisation have been inferred from our study. Firstly,

magmatic activities, including sill emplacement, and the resultant magmatic-hydrothermal fluids, have contributed significantly to boosting thermal energy, driving increased seawater circulation through the atolls, thereby acting as a high heat flux source. In general, the average basal heat flux of magmatically passive oceanic island crusts have a range of ~60–101 mW/m^2 (Henry et al., 1996; Leclerc et al., 1999; Jean-Baptiste and Leclerc, 2000; Turcotte and Schubert, 2001; Wilson et al., 2001). To estimate the basal heat flow at Resolution Guyot, we used the compiled dataset by Stein and Stein (1992) which relate the heat flow to the age of the oceanic crust. Considering the deposition began at Site 866 at ~132–133 Ma (El-Yamani et al., 2022), indicating the volcanic pedestal's age beneath the atoll is at least that old. This corresponds with the magnetostratigraphic zonation observed in the sedimentary layers at Site 866 (Tarduno et al., 1995), where the base of the sedimentary sequence is placed within Chron M7 (around 132-132.55 million years ago, according to the geological time scale 2012 by Ogg, 2012). This suggests that the basement must be of at least that age or older. As the age of basalts at the same site is average ~126 Ma (Pringle and Duncan, 1995; Sager, 1995), the minimum quiescence time before magmatism recommenced and the youngest possible age of the volcanic pedestal during subsequent magmatism would be ~6–7 million years. Consequently, the highest possible basal heat flux from the pedestal, before magmatic rejuvenation at ~126 Ma, would be at most ≤ 100 mW/m^2 (using Stein and Stein, 1992 database; check their Figure 1), falling within the known ranges of basal heat flux in magmatically passive oceanic island crusts. This is much lower than the heat flux at regions where magma ascends and hydrothermal circulation occurs (e.g. >800–2000 mW/m^2; Leroy et al., 2010; Pearson-Grant et al., 2022). Such surge occurs because the emplacement of magmatic intrusions and basaltic lavas generates temperatures ≥1000–1350 °C (Parfitt and Wilson, 2009; Clague et al., 2018; Shea et al., 2022), significantly influencing the local heat flow dynamics. This explains the higher temperatures of the dolomites at Site 866 compared to the concurrent temperatures of the host rock, and the strong temporal overlap between the dolomitisation $^{87}Sr/^{86}Sr$ ages and $^{40}Ar/^{39}Ar$ and K/Ar ages of basement samples. Numerical modelling by Jean-Baptiste and Leclerc (2000) and Frazer et al. (2023) emphasised the positive impact of the increase in the basal heat flow on the fluid flux velocities across the carbonate platforms. Similarly, reactive transport modelling of early-burial island dolomitisation by geothermal convection showed that the increase of basal heat flux from 40 to 100 mW/m^2 would double the dolomitisation rate (Whitaker and Xiao, 2010). Accordingly, the magmatism in Resolution Guyot had important impacts on the fluid flux and the temperature to overcome the very limited dolomitisation potential and dolomitisation rates of normal Cretaceous seawater (Gabellone and Whitaker, 2016).

Secondly, the ongoing discussion showed that the seismically interpreted hydrothermal vents, and smaller scale fluid flow pipes in both atolls were magmatically originated through hydraulic fracturing. They have width ranges of few to tens of hundreds of metres (Figure 3.3, 3.7, and 3.8). However, previous modelling and field-based studies suggested that individual active hydrothermal vents widths are significantly narrower (5–10 m) than what is observed in seismic data (Collignon et al., 2018; Manton et al., 2022). Therefore, what appears on seismic data to be relatively wide conduits with width of hundreds of metres was suggested to represent amalgamated vent structure of highly fractured rock masses (Huuse et al., 2010; Manton et al., 2022). This would suggest that the widespread presence of hydrothermal vents and smaller scale fluid pipes in both atolls would reflect the presence of highly fractured rock masses across the atolls. This fracturing would enhance the fluid flux across the atolls and so the dolomitisation reactivity as observed in (a) the reactive transport modelling results showing that the presence of a permeable platform margin fault zone enhances dolomitisation on the upper slope and margin, and to a lesser but significant extent, across platform interior (Frazer et al., 2023) and (b) field-studies (e.g. Hammam Faraun stratabound dolostone bodies, Gulf of Suez; Hirani et al., 2018).

Thirdly, our study suggests that the underlying volcanic basement is likely the source for Fe-enriched dolostones at ~1620-1540 mbsf. Fe solubility in seawater from basaltic rocks depends on pH, oxygen, redox potential, temperature, and organic ligands (Hemley et al., 1992; Heinrich and Candela, 2014). Mg and Fe are contained in pyroxene and olivine minerals whose dissolution rates decrease with increasing pH (Gudbrandsson et al., 2011). Neutral pH keeps Fe as insoluble oxyhydroxides (Stranghoener et al., 2018). Therefore, injection of acidic CO_2-charged fluids into crystalline basalts would favour metals mobility (e.g. Mg and Fe; Caruso et al., 2021). During magmatism, highly acidic magmatic H_2O–CO_2–SO_2–HCl-rich fluids discharge and mix with seawater during upflow (Seewald et al., 2015; Wilckens et al., 2019). Even mixing a small volume of magmatic-hydrothermal fluids with predominantly normal seawater would lower the fluid's pH (Breislin et al., 2020). This promotes mafic mineral alteration in basalts, leaching metals like Mg and Fe (Gamo et al., 1997; Gudbrandsson et al., 2011; Caruso et al., 2021), enriching seawater. Considering that, the temporal overlap between dolomitisation age, basaltic basement ages, and the negative $\delta^{34}S_{CAS}$ shift at Site 866 and the presence of Fe-rich dolomites just close to the basement (~1620-1540 mbsf) may suggest that seawater underwent slight modification by slight mixing with magmatic-hydrothermal fluids, facilitating leaching metals (Fe and Mg) from the basement. This slight modification of seawater by mixing with magmatic-hydrothermal fluids would promote dolomitisation at both atolls because (a) localised seawater acidification was proposed to promote dolomitisation (Rivers et al., 2021; Rivers, 2023) and (b) leaching of Mg from

mafic minerals in basalts would locally elevate the Mg^{2+} concentration and Mg:Ca ratio of the dolomitising fluid (Robertson et al., 2019; Breislin et al., 2020; Koeshidayatullah et al., 2020). These, coupled with higher water temperature (e.g. Benjakul et al., 2020) and pCO_2 (e.g. Sibley, 1990) would counteract three significant kinetic inhibitors: cold seawater and the low Cretaceous seawater Mg^{2+} concentration and Mg:Ca ratio.

Basalts in Resolution Guyot are highly altered (average MgO wt% of 4.8 and FeO wt% of 1.5; Kurnosov et al., 1995). Appropriate fresh analogues for the West Pacific Guyots are the Hawaiian ocean island basalts (Kurnosov et al., 2007) which have average MgO wt% of 12.3 and FeO wt% of 11.9 (Dasgupta et al., 2010). This alteration of the basaltic rocks of the West Pacific Guyots was attributed to hydrothermal processes and subaerial weathering (Kurnosov et al., 1995, 2007). In Allison Guyot, although the basaltic basement was not drilled, intensive hydrothermal alteration is observed in magmatic sills with an average MgO wt% of 5.5 and an average FeO wt% of 2.2 (Kurnosov et al., 1995, 2007). The porous nature of the basement, characterised by vesicular and fractured lavas (Sager et al., 1993a), supports the potential of circulation of slightly modified seawater.

3.7.2.1 Controls on Dolomitisation Distribution

Our integrated approach of delineating the distribution of dolomitised intervals at Resolution Guyot (Figure 3.10) appears to reflect that their distribution seems to be controlled on both local and large scales. On large scale, during the dolomitisation period(s) at Resolution Guyot, our burial history calculations reflect that at least ~220–720 m of limestone above the dolomitised succession did not undergo dolomitisation (APPENDIX B Material B3). This raises a question about why the overlying succession wasn't dolomitised, especially that geothermal convection dolomitisation operates across the entire thickness during the dolomitisation period, as observed in field (e.g. Aharon et al., 1987; Vahrenkamp and Swart, 1994) and reactive transport modelling (e.g. Whitaker and Xiao, 2010; Frazer et al., 2023) studies. Two potential explanations arise for this distribution. The first possibility is that the dolomites at Resolution Guyot might exhibit mushroom-shaped structures as in (a) the Latemar Platform (Wilson et al., 1990) and (b) the modelling results of dolomitisation by geothermal circulation of brines (Pal et al., 2015) or it might be controlled by igneous intrusions, their associated brecciated contacts, and fractures (Jacquemyn et al., 2014). However, the absence of additional drilling sites across the platform prevents the verification of this hypothesis. The second possibility is that there could be an aquitard which might have impeded fluid flow above this level and focused the fluid flow within the dolomitised part. This hypothesis appears more plausible considering the correlation we observe between the

termination of dolomitisation (~1100-1010 mbsf) and the identified dispersed volcanic ash-rich intervals (Figure 3.14). Volcanic ashes and their altered clays can occlude pore spaces, creating a baffle, as seen in the diagenetic fronts in the Tengiz Field (Kenter et al., 2006; Dickson and Kenter, 2014).

At a local scale, dolomitisation is seen within a ~570-600 m section of dolomitic limestone and dolostone, occurring at specific levels rather than uniformly throughout (Figure 3.3 and 3.10; APPENDIX B Table B8). In general, preferential dolomitisation is often controlled by permeability pathways: (a) certain intervals with higher permeability that focus fluid movement (e.g. karstified or fractured intervals; Li et al., 2023a; Hirani et al., 2018), or (b) variations in the mineralogy and texture of sediment types (e.g. Saller et al., 2001; Whitaker and Xiao, 2010). Our examination of dolomite distribution with the sedimentary facies template at Site 866 (Arnaud et al., 1995) shows no correlation which suggests that textural or facies controls are less likely. Dolomites are found across various lithofacies, from wacke- and pack-stone to grain- and rud-stone (Figure 3.10), and the same in the non-dolomitised sections. Additionally, measurements of porosity reveal no link between tight zones and non-dolomitised sequences. The non-dolomitised sections between dolomitised intervals at Resolution Guyot exhibit a wide range of interparticle porosities (4.5–27.25%; mean: 18.7%; Kenter and Ivanov, 1995). Permeability can be derived from interparticle porosity in nonvuggy carbonate rocks based on Lucia's (1995) equations. By using the three different equations of Lucia's (1995) for the different rock classes, the non-dolomitised grainstone-dominated intervals have estimated permeability of $1.2 - 68 \times 10^3\ mD$ (median: $7.2 \times 10^3\ mD$; average: $16.5 \times 10^3\ mD$), non-dolomitised packstone-dominated intervals have estimated permeability of $5 \times 10^{-3} - 3.9 \times 10^2\ mD$ (median: $1.7 \times 10^2\ mD$; average: $1.8 \times 10^2\ mD$), and wacke- and mud-stone dominated intervals have estimated permeability of $\leq 1\ mD$ (APPENDIX B Table B14). Results from reactive transport modelling by Whitaker and Xiao (2010) on early-burial geothermal convection dolomitisation indicate that permeabilities ranging from tens to tens of thousands of millidarcies are sufficient for convective fluid flow and suitable for geothermal convection dolomitisation. Accordingly, the non-dolomitised pack- and grain-stone-dominated intervals at Resolution Guyot possess permeability ranges suitable for this process, as opposed to the wacke- and mud-stone dominated intervals. However, despite adequate permeability, these intervals remain non-dolomitised. Therefore, the control through fractures becomes the most probable scenario. Our earlier discussions suggested the formation of hydrothermal vents through hydraulic fracturing. Consequently, the distribution and density of fracture networks around and away from vents may have governed fluid movement,

creating pathways for fluid flow and leading to the observed dolomitised bodies at specific levels in Resolution Guyot.

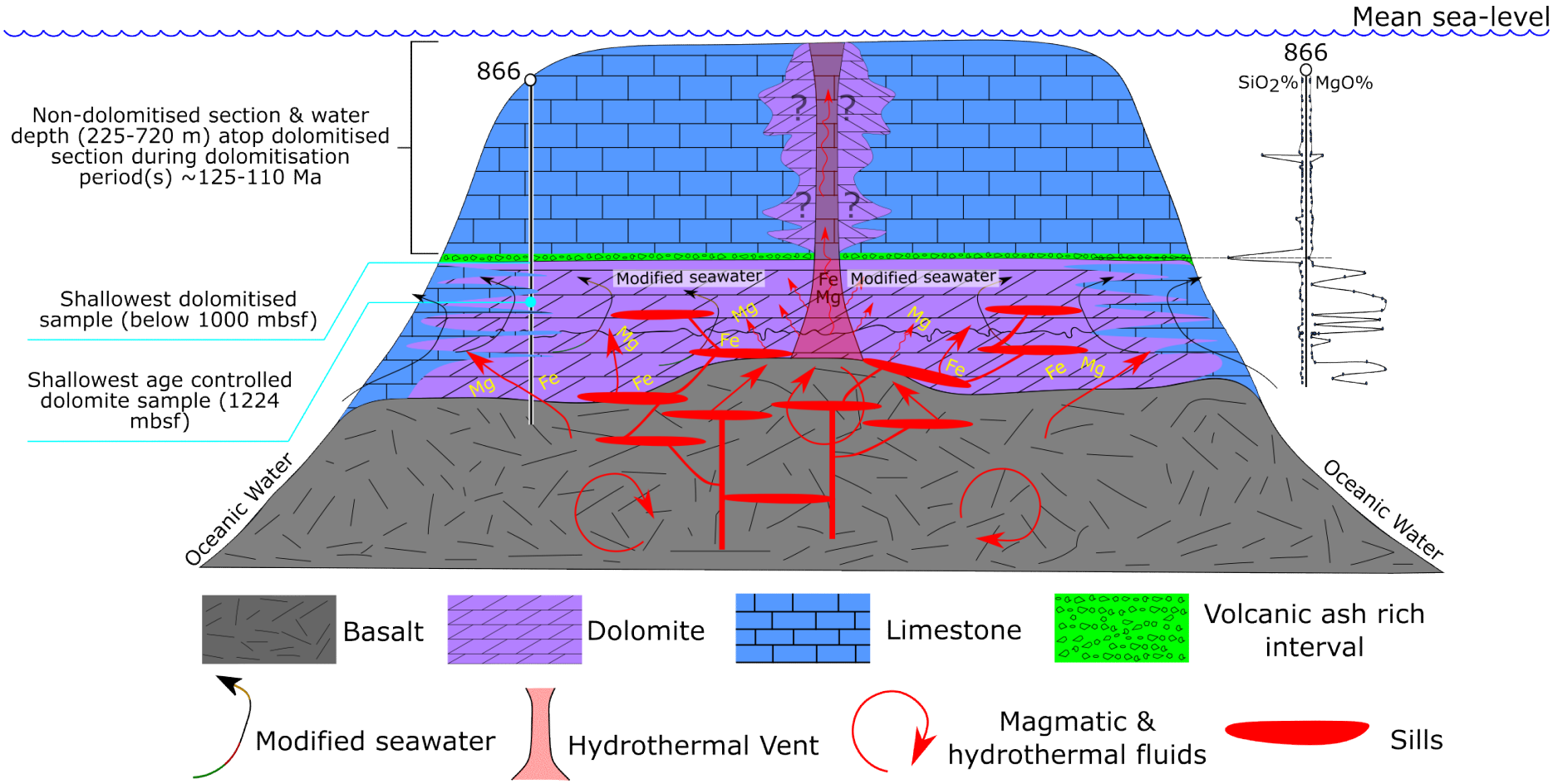


Figure 3.15. Conceptual model of the sills emplacement, hydrothermal vents and the released magmatic fluids interacting with the basement leaching Fe and Mg to the circulating seawater causing a slight modification of its metal content, increasing the Mg^{2+} budget, Mg/Ca ratio, and temperature which facilitated dolomitisation. The dispersed intervals rich with volcanic ash acting as an aquiclude to the upflow of the dolomitising fluids. The model shows the expected dolomite distribution away from the drilling site based on the presence of preferentially dolomitised intervals at the drilling site.

3.7.3 Implications on Island Dolomitisation and Normal Marine Dolomitisation by the Cretaceous Calcitic Seawater

The findings of this study exhibit both differences and similarities with dolomitisation models for Cenozoic island dolostones. Most studies on Cenozoic island dolostones propose dolomitisation by normal seawater (e.g. Budd, 1997; Warren, 2000; Ren and Jones, 2018). However, Machel (2000b) introduced an alternative concept for Cenozoic island dolomitisation involving plate tectonics-induced convection of seawater that was enriched by magmatic-hydrothermal solutions. Our proposed model overlaps with Machel (2000b). However, in contrast to the Neogene, Cretaceous normal seawater appears insufficient for syndepositional and early-burial near-surface island dolomitisation. Several factors may have hindered unmodified early-burial near-surface seawater dolomitisation during the Cretaceous compared to Late Cenozoic (e.g. dolomite saturation levels, Mg-budget, and Mg:Ca of dolomitising fluids; Arvidson and Mackenzie, 1997, 1999; Kaczmarek and Sibley, 2011; Al-Disi et al., 2019). Our proposed model may have overcome these primary kinetic barriers only through the previously discussed contributions from magmatism. Therefore, magmatism appears essential for extensive island dolomitisation by Cretaceous normal salinity seawater, rather than serving as an alternative as in Late Cenozoic islands (Machel, 2000b).

Cold deep seawater below calcite saturation depth (>1000 m; James and Choquette, 1983; Saller, 1986; Flood and Chivas, 1995) may not solely explain deep-seated island dolomites in various locations. We conducted an analysis using two main factors: (a) the current depths of Cretaceous islands and atolls (Wodejebato, Ita-Mai-Tai, Horizon, MIT, Allison, and Resolution), and (b) the age of the oldest pelagic cap on each atoll, to roughly estimate how long these drowned atolls stayed below 1000 mbsl. This calculation considered that pelagic caps accumulate at depths >200 mbsl (James and Jones, 2015) and assumed that the subsidence rates were constant. The analysis suggests that these islands were exposed to deep marine water below 1000 m for a prolonged period, ~20–56 Ma (Heezen et al., 1973; Winterer et al., 1973; Larson et al., 1995; Pearson, 1995; detailed calculations are available in APPENDIX B Table B13). However, dolomites were only seen to be associated with magmatic emplacements (e.g. Resolution and Allison guyots). Notably, deep Cenozoic samples from Hawaii (Saller and Winterbottom, 2022) and the Cenozoic Limalok atoll lacked dolomites (Ogg et al., 1995). Our study implies that magmatically driven hydrothermal dolomitisation through sill emplacement explains the depth of deep-seated dolomites in Resolution and potentially Allison guyots. This mechanism might also elucidate deep-seated dolomites in other atolls and islands during the Cretaceous and other periods with significant

magmatism. For instance, in Xisha Islands, Miocene-Pliocene magmatism(s) were proposed to influence dolomitisation and dolomite transformation (Wei et al., 2006, 2008; Wang et al., 2018b; Li et al., 2023b; Liu et al., 2023) while other studies suggest normal to near-normal seawater dolomitisation without a significant impact from Miocene-Pliocene magmatism(s) (e.g. Bi et al., 2018; Wang et al., 2018c, 2022; Li et al., 2023a).

Our findings and the absence of early dolomites in other Cretaceous islands indicate that Cretaceous normal seawater alone might not suffice for widespread syndepositional and early-burial near-surface massive dolomitisation on various carbonate platforms. The Phanerozoic early near-surface dolomites dataset (Manche and Kaczmarek, 2021) shows that ≥70% of Cretaceous dolomites were formed in restricted depositional settings with elevated evaporation, temperature, and Mg:Ca. In contrast, Neogene dolomites are mainly associated with open-marine settings, indicative of normal seawater dolomitisation. This is reflected in our dataset where only few Cretaceous large isolated carbonate platforms were dolomitised by evaporated seawater (Malta, Adriatic, Apenninic, and Apulian platforms; Gatt, 2012; Read et al., 2016; Vinci et al., 2017; Torrieri et al., 2021; APPENDIX B Table B2). Hence, modification of Cretaceous seawater appears necessary. Some geochemical and petrographic characteristics of dolomites in our study and other examples of large-scale Cretaceous platform dolomitisation (e.g. mesohaline reflux dolomitisation of Zebbag Formation, Newport et al., 2017) highlight the need for cautious interpretation as they might overlap with near-surface early-burial and syndepositional normal (i.e. unmodified) seawater dolomites. Similarly, geochemistry and petrography of Derbyshire Platform's dolomites would reflect predominantly seawater origin with low dolomitisation temperature (<50 °C), while the new findings suggest influence of high volcanism heat and mixing with magmatic fluids (Breislin et al., 2020; Frazer et al., 2023). Therefore, comprehensive interpretation should consider additional factors like dolomite geometry, geological settings, and timing of dolomitisation (e.g. Budd, 1997).

3.8 Conclusion

This study provides insights into the formation of two rare examples of shallow-burial seawater-like Cretaceous island dolomitisation. Integrating geochemical observations, burial and thermal modelling of the limestone host rock, and core-log-seismic data indicates a magmatically driven hydrothermal dolomitisation origin. The magmatic emplacement facilitated dolomitisation by maintaining a high heat flow which would substantially increase the flux of circulating seawater and overcome the very limited dolomitisation potential and rate of Cretaceous seawater. The presence of Fe-rich dolomites suggests slight modification of the dolomitising seawater by mixing

with the released H_2O–CO_2–SO_2–HCl-rich magmatic-hydrothermal fluids during upward flow. Acidic conditions might have facilitated leaching of metals (Mg and Fe) from basaltic basement and sills, resulting in enrichment of circulating dolomitising seawater. Our model might have overcome significant kinetic barriers such as low ambient temperature and Mg:Ca of seawater through magmatically associated vigorous heat flux and slight modification of seawater. Therefore, magmatically active Cretaceous islands had greater potentiality for seawater dolomitisation than passive counterparts. This mechanism may have broader applicability to other "island dolostones", particularly in explaining deep-seated post-depositional dolomites (e.g. Xisha Islands). It presents an alternative explanation to the interpretation of deep-seated dolomites, which is often attributed to dolomitisation by deep marine waters below calcite saturation depth. The absence of near-surface early-burial and syndepositional massive dolostones formed by unmodified seawater in any of the other Cretaceous islands and atolls implies reduced effectiveness of syndepositional and near-surface early-burial massive dolomitisation by Cretaceous normal (i.e. unmodified) seawater, questioning some of the previous interpretations. Therefore, we recommend that caution should be exercised in interpreting these dolomites as they may share certain characteristics with syndepositional and early-burial near-surface seawater dolomites, making it necessary to consider additional aspects (dolomite geometry, geological settings, and timing of dolomitisation).

CHAPTER FOUR

BEYOND THERMAL STRESSES: MAGMATISM, KARSTIFICATION, AND HOTSPOT MIGRATION DICTATED THE DEMISE OF THE MID-PACIFIC CRETACEOUS ATOLLS

4.1 Abstract

Understanding past environmental changes is crucial for anticipating future climate scenarios. Projections indicate that CO_2 levels could resemble those of the Mid-Late Cretaceous by 2065-2150, making it a potential analogue for future climates. Shallow-marine carbonate ecosystems, sensitive to environmental shifts, offer insights into how ecosystems responded to such changes. By studying how ancient carbonate systems coped with environmental challenges, we can better anticipate the fate of modern counterparts which support ≥25% of marine life. Previous research linked the demise of Cretaceous atolls in the Mid-Pacific Mountains (MPM; Resolution and Allison guyots) to excessive warmth in peri-equatorial waters, as in modern corals bleaching under high temperatures (>30°C). The study integrates core-log-seismic data and tectonic reconstructions of the Pacific Plate, to investigate the demise mechanism of the MPM atolls and evaluate their potential as analogues for modern reefs. Seismic interpretation revealed that during the late Albian-early Cenomanian, extensive magmatism affected the MPM causing uplift and subaerial exposure, ceasing shallow-marine carbonate production. later, migration of the MPM away from the Larson Melt Region caused rapid subsidence, and along with the rising Cenomanian eustatic sea-level, collectively caused rapid relative sea level rise. Following submergence of the platform top, carbonate accumulation rates atop the platforms were likely reduced due to production lag time. This was aggravated by off-bank sediment transport due to the lack of bioconstructed reefal margins, and the exposure of platform tops to tropical cyclones, storms, hurricanes, and surface currents. These factors supported relative sea-level rise to outpace carbonate accumulation through introducing continuous negative feedbacks to accumulation rates, deepening platform tops beyond critical depths for shallow-water carbonate production, despite their maximum production rates. Furthermore, the role of Cretaceous warmth in harming carbonate production and the demise of the Pacific atolls was analysed using published palaeo-climatic modelling data, reconstructions of sea-surface temperature, and palaeogeographic reconstructions. Temperatures fluctuated between 30-34°C, occasionally reaching ≤36°C, and generally remained constant or decreasing over the atolls' lifespans and demise, consistent with thriving conditions for Cretaceous carbonate platforms. This challenges the hypothesis that excessive warmth in peri-equatorial Cretaceous seawater harmed carbonate production as in modern heat-intolerant corals, proposing instead a more feasible analogue, with caution, to modern heat-tolerant species. The findings support the "death-by-emergence-and-submergence" hypothesis for the MPM atolls' demise by addressing longstanding unknowns about the cause of emergence and the absence of sediment accumulation after re-submergence. Moreover, it adds to recent research suggesting rapid

subsidence of islands moving away from mantle swell uplift may resolve the carbonate platforms drowning paradox.

4.2 Highlights

- The study explores the demise mechanism of Mid-Pacific Cretaceous atolls, uncovering a complex interaction of magmatism, tectonic movements, and environmental factors.
- The study reveals how magmatic events during the late Albian to early Cenomanian caused uplift and cessation of shallow-marine carbonate deposition on atolls, highlighting temporal overlap and potential causal relationships with volcanic activity.
- Rapid subsidence following hotspot migration, combined with eustatic sea-level rise implicated in the drowning of these atolls.
- The vertical accumulation rates at MPM atolls after re-submergence appeared to be brought down by off-bank sediment transport through equatorial hurricanes, ocean-surface currents, production lag time and the lack of true reefal bioconstructed margins.
- The findings challenge the prevailing notion that high sea surface temperatures were detrimental to Cretaceous carbonate-secreting organisms, suggesting their potential resilience.
- Cretaceous carbonate-secreting organisms on the Pacific atolls appear to be heat-tolerant, suggesting a more plausible analogue to modern heat-tolerant species on tropical atolls and banks.

4.3 Introduction

Shallow-marine carbonate systems play a crucial role in marine biosphere by hosting >25% of marine life and accounting for ~25% of the global CO_2 sink into marine sediments (Knowlton et al., 2010; Jones et al., 2015). Environmental fluctuations throughout both modern and geological times have significantly impacted Earth's biosphere (e.g. Strasser et al., 2022). Modern and ancient shallow-marine carbonate systems retain records of environmental changes in their sediments, including sea-level variations, oceanic anoxic events (OAEs), ocean acidification, and shifts in salinity, nutrient supply, temperature, turbidity, and light penetration (e.g. Hallock and Schlager 1986; Erlich et al. 1990, 1993; Schlager, 1991; Thorne, 1992; Dechnik et al., 2017; Pratte et al., 2018). Tropical neritic carbonate factories face drowning when the rate of accommodation creation exceeds sediment accumulation or when growth rate is impacted by ecological disturbances (Schlager, 1981). Various factors can cause drowning, including rapid relative sea level rise (Webster et al., 2009; Paumard et al., 2017), migration of oceanic atolls away off hotspot swells

(Huppert et al., 2020), subaerial exposure followed by sea-level rise (e.g. Camoin et al., 1998), high subsidence rates (e.g. DiCaprio et al., 2010; Minzoni et al., 2015), platform margin collapse (e.g. Petrovic et al., 2023), climate change (e.g. Betzler et al., 1995), high nutrient influx (e.g. Hallock and Schlager, 1986), siliciclastic influx (e.g. Seard et al., 2013), global environmental perturbations (e.g. OAE 1a; Huck et al., 2010), and combinations of different factors such as intense monsoon winds and nutrient excess (e.g. Eberli et al., 2010; Reolid et al., 2020; Betzler et al., 2021, 2023). By comparing the patterns and drivers of shallow-marine carbonate inception, development, demise and drowning in the past, researchers can identify parallels with predicted future scenarios, despite differences in environmental conditions across various periods (Harnik et al., 2012).

Continued anthropogenic CO_2 emissions are projected to approach or even exceed levels of the Eocene and Mid-Late Cretaceous periods (Hay, 2011; Tierney et al., 2020). By 2065-2150, under Regional Rivalry (SSP3-7.0) and Fossil-Fuel Development (SSP5-8.5) scenarios, atmospheric CO_2 levels may rise to ~700-1,250 ppm (Figure 4.1; Meinshausen et al., 2020), comparable to Mid-Late Cretaceous levels (~1,150-700 ppm; Foster et al., 2017; Valdes et al., 2021). These elevated CO_2 levels may lead to more frequent and severe heatwaves in tropical oceans, potentially resulting in mass mortalities of marine life (White et al., 2023). Considering the valuable insights gained from understanding past responses of carbonate platforms and reefs to rapid climate changes (Pandolfi et al., 2011), studying the demise of the Cretaceous atolls may provide useful insights into understanding potential future risks under climate changes on shallow-marine modern biota in tropical atolls, especially given potentially similar climate conditions. The biogeodynamics of Cretaceous shallow-marine carbonate systems may offer valuable information for assessing future extinction risks for modern biota under global warming, despite differences in organisms (Bryers et al., 2022; Steuber et al., 2023).

During the Cretaceous, from the Hauterivian to the Mid-Maastrichtian, the western Pacific Ocean hosted many Cretaceous atolls (Figure 4.2). These atolls drowned between early Albian and mid-Maastrichtian times near the equator (0-10° S; Resolution, Allison, MIT, Wodejebato, Takuyo-Daisan guyots; Wilson et al., 1998). Three main hypotheses explain their demise. Hypothesis 1, "death-by-emergence-and-submergence" suggests that atolls were exposed, then submerged without re-establishing a carbonate factory (van Waasbergen and Winterer, 1993; Winterer et al., 1993; Winterer and Sager, 1995; Winterer, 1998). As stated by the authors, the causes of emergence (whether eustatic or tectonic) and drowning (whether blocked migration routes for larvae or slowly moving equatorial currents inhibiting larval survival to Pacific islands) were speculated or stated as unknown. In addition, Hypothesis 1 fails to explain why carbonate platforms did not re-establish on subsiding karstified platforms below sea level, despite initially forming on volcanic pedestals

with presumably greater subsidence rates (Jenkyns and Wilson, 1999). Hypothesis 2, "death-in-the-topics" posits that the palaeoequatorial upwelling belt of high productivity caused atoll demise (Larson et al., 1995). However, a $^{87}Sr/^{86}Sr$ stratigraphy study by Wilson et al. (1998) showed that none of the atolls drowned during any OAEs, and some atolls even thrived during OAE1a (e.g. Resolution and MIT guyots). Jenkyns and Wilson (1999) criticised previous hypotheses, observing that platform drowning took place closer to the equator during cooler intervals (e.g. Albian and Maastrichtian), and farther from the equator during warmer intervals (e.g. mid-Eocene). Thus, the authors proposed Hypothesis 3, "death-by-superheated-peri-equatorial-waters," suggesting that during the Cretaceous, the peri-equatorial warm waters (>30°C) were inhospitable to carbonate-secreting organisms like modern corals bleaching under high temperatures. This scenario allowed subsidence or eustatic rise to outpace sedimentation, leading to drowning. Hypothesis 3 is built on the suggestion that some rudists may have possessed zooxanthellae (Jenkyns and Wilson, 1999), which is potentially erroneous as indicated by many researchers (e.g. Gili et al., 1995; Skelton and Gili, 2012; Skelton et al., 2013). In addition, the global distribution of Cretaceous carbonates shows extensive development of shallow-marine carbonates in equatorial and sub-equatorial zones (Kiessling et al., 2003; Bromhead et al., 2022; Wohlwend et al., 2016; Gertsch et al., 2010) which may suggest that peri-equatorial warm waters were not hostile to carbonate-secreting organisms. Considering that, the drowning of the Pacific Cretaceous atolls is still an open question, requiring further investigation (Iba and Sano, 2007; Skelton et al., 2013) and so is their significance as analogues for biota response in a warming world.

To address this, the present study primarily examines Resolution and Allison Guyots in the Mid-Pacific Mountains (MPM), while also considering other Pacific Cretaceous guyots. The focus on the MPM Cretaceous atolls is driven by the availability of recently published data, including new age models and comprehensive seismic interpretations incorporating core and logging data (El-Yamani et al., 2022, 2024). The main objective of this study is to uncover the mechanisms behind the demise of the Pacific Cretaceous atolls and ascertain the role of climate. The findings of the study are then compared with recently published projections of future thermal-stress refugia for modern tropical shallow-marine carbonate producers by 2100 to identify differences and similarities.

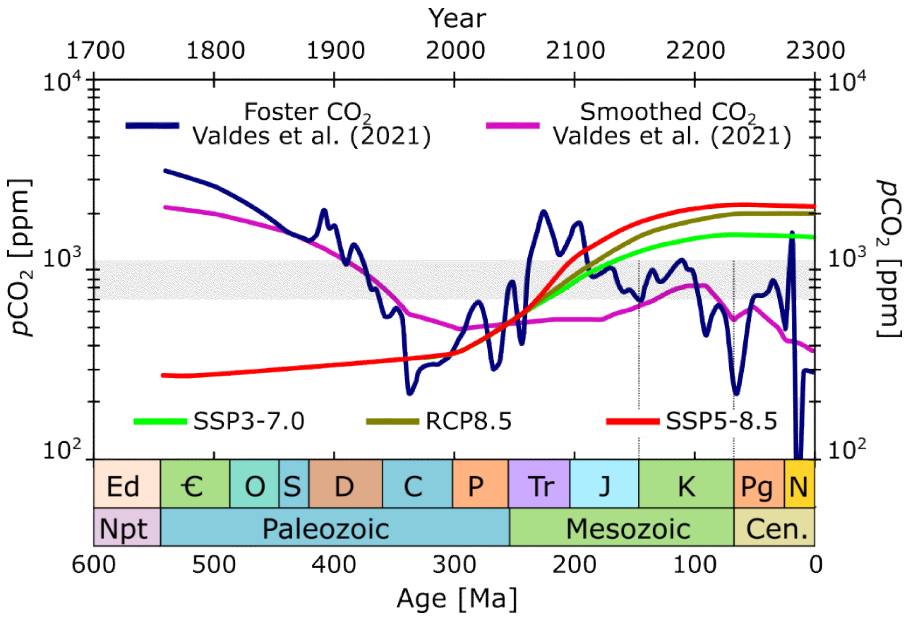


Figure 4.1. Phanerozoic CO_2 fluctuations [ppm] from Valdes et al. (2021). Foster CO_2 curve is the modelled CO_2 curve from Valdes et al. (2021) by removing much of the shorter-term variability in the Foster et al. (2017) Phanerozoic CO_2 curve. Smoothed CO_2 curve is an alternative curve by Valdes et al. (2021) that pass through the cloud of individual CO_2 proxy-based reconstructions and hence represents one possible reality. The figure shows global CO_2 emissions [ppm] under the shared socio-economic (SSP) and representative concentration pathways (RCP) from the pre-industrial society, 1750, to 2300 (Meinshausen et al., 2020). The grey bar highlights the overlap between the predicted CO_2 levels between 2065-2150 (~700-1250 ppm) under the different pathways and the Phanerozoic CO_2 fluctuations. The dashed lines show the Cretaceous ages of the overlap.

4.4 Geologic Settings

Since the Early Cretaceous, volcanic activities created the West Pacific Seamount Province (WPSP; Figure 4.2) which extends from the MPM to the Mariana Trench (e.g. Koppers et al., 2003). The WPSP consists of MPM, Shatsky Rise, and Ontong Java oceanic plateaus and nine seamount trails (Figure 4.2; Ratak, Ralik, Anewetak, Ujlan, Magellan, Northern and Southern Wake, Typhoon, and Japanese Seamount Trails; Larson, 1991; Koppers et al., 2003). The MPM is one of the most distinctive morphologies within the context of WPSP as the MPM exhibits characteristics similar to a plateau with large areas elevated above the regional seafloor depths rather than the typical linear arrangement of discrete seamounts (Winterer and Sager, 1995). The latest tectonic reconstructions of the Pacific Plate have introduced a newly proposed melt source region, the Larson melt region, situated between the Crough and Marquesas hotspots (Figure 4.3; Pockalny et al., 2021). The authors proposed the following framework: (a) the western part of the MPM likely formed between 130 to 110 Ma through a plume-ridge interaction with the Larson melt region; (b) during that, the melt region represented a plume head situated close to the Pacific-Farallon spreading axis; (c) the eastern portion of the MPM is younger than the western portion and overlays an inferred trace of the Molokai Fracture Zone; and (d) the transit of the Tahiti hotspot between 110 and 85 Ma caused subsequent phases of distributed volcanism across the MPM.

The Cretaceous Pacific seamounts were targeted by the Ocean Drilling Program (ODP) Leg 143/144 during 1992-1993. During ODP Leg 143 expedition, Resolution and Allison guyots were the main drilling targets (Figure 4.2; Sager et al., 1993a). Resolution Guyot was drilled at three sites (sites 866-868; Sager et al., 1993a), facilitating a radial transect from the periphery to the interior of the platform, while Allison Guyot underwent drilling at only one site, providing access to platform interior (Site 865; Sager et al., 1993b). ODP Leg 144 drilled Limalok (Site 871), Lo-En (Site 872), and Wodejebato (Sites 873-877) guyots in the Marshall Islands chain, MIT Guyot (Site 878), a drowned atoll midway between the Marshall Islands and Japan, and Takuyo-Daisan Guyot (Sites 879-880) in the Japanese Seamount Province (Haggerty and Premoli Silva, 1995). Deep Sea Drilling Project (DSDP) Leg 62, at Site 463, was targeting the basinal deposits of MPM (Timofeev et al., 1981).

Resolution Guyot is a volcanic pedestal covered with a 1620 m thick sequence of Hauterivian to latest Albian shallow-marine carbonates under a thin pelagic cap formed after drowning (Figure 4.4; Sager et al., 1993a; El-Yamani et al., 2022). Similarly, Allison Guyot includes a ~740-metre-thick layer of Late Albian shallow-marine carbonates, topped with a thick pelagic cap (~140 m) formed after drowning (Figure 4.4; Sager et al., 1993b). The exact cessation time of shallow-marine

carbonate production on both guyots is uncertain but estimated around the late Albian (~98-99±2 Ma; Winterer, 1998; Wilson et al., 1998). The ages of the overlying pelagic deposits differ between the two guyots (Sager et al., 1993a, b; Sliter, 1995; Winterer and Sager, 1995). On Allison Guyot, the oldest overlying pelagic deposits are from early to mid-Turonian and were found on cavities and cracks on the platform's uppermost surface (Sliter, 1995; Winterer and Sager, 1995). These are followed by Maastrichtian-age pebbles of pelagic limestone, and a thick pelagic cap spanning from the Paleocene to Quaternary (Winterer and Sager, 1995). On Resolution Guyot, the shallow-marine carbonate sequence is covered by manganese-encrusted pelagic limestone, overlain by Maastrichtian-late Pliocene nannofossil ooze (Winterer and Sager, 1995).

Wodejebato guyot is linked to the Ralik Seamount Trails, associated with the Macdonald, Rarotonga, and Society hot spots (Koppers et al., 2003). The volcanic pedestal of Wodejebato has an age of ~83.2 ±1.1 Ma, serving as a foundation for shallow-marine carbonate sedimentation from ~75 Ma to 67 Ma (Arnaud-Vanneau et al., 1995; Pringle and Duncan, 1995). The earliest pelagic sedimentation is of early Paleocene age, indicated by pelagic limestone clasts atop the youngest late Maastrichtian shallow-water carbonates (Larson et al., 1995). Takuyo-Daisan Guyot is a part of the Japanese Seamount Trail with a volcanic pedestal of an age ~117.5±1.1 Ma (Pringle, 1993; Koppers et al., 2003). Carbonate platform deposition spanned from late Aptian to Albian age (Larson et al., 1995). Unlike other guyots in this study, the onset of pelagic sedimentation couldn't be determined from drilling data of ODP Leg 144 (Larson et al., 1995). MIT guyot is a volcanic island that is not associated with any of the nine WPSP seamount trails (Koppers et al., 2003) where shallow-marine deposition spanned through early Aptian-late Albian, transitioning to pelagic sedimentation during the latest Albian (Larson et al., 1995).

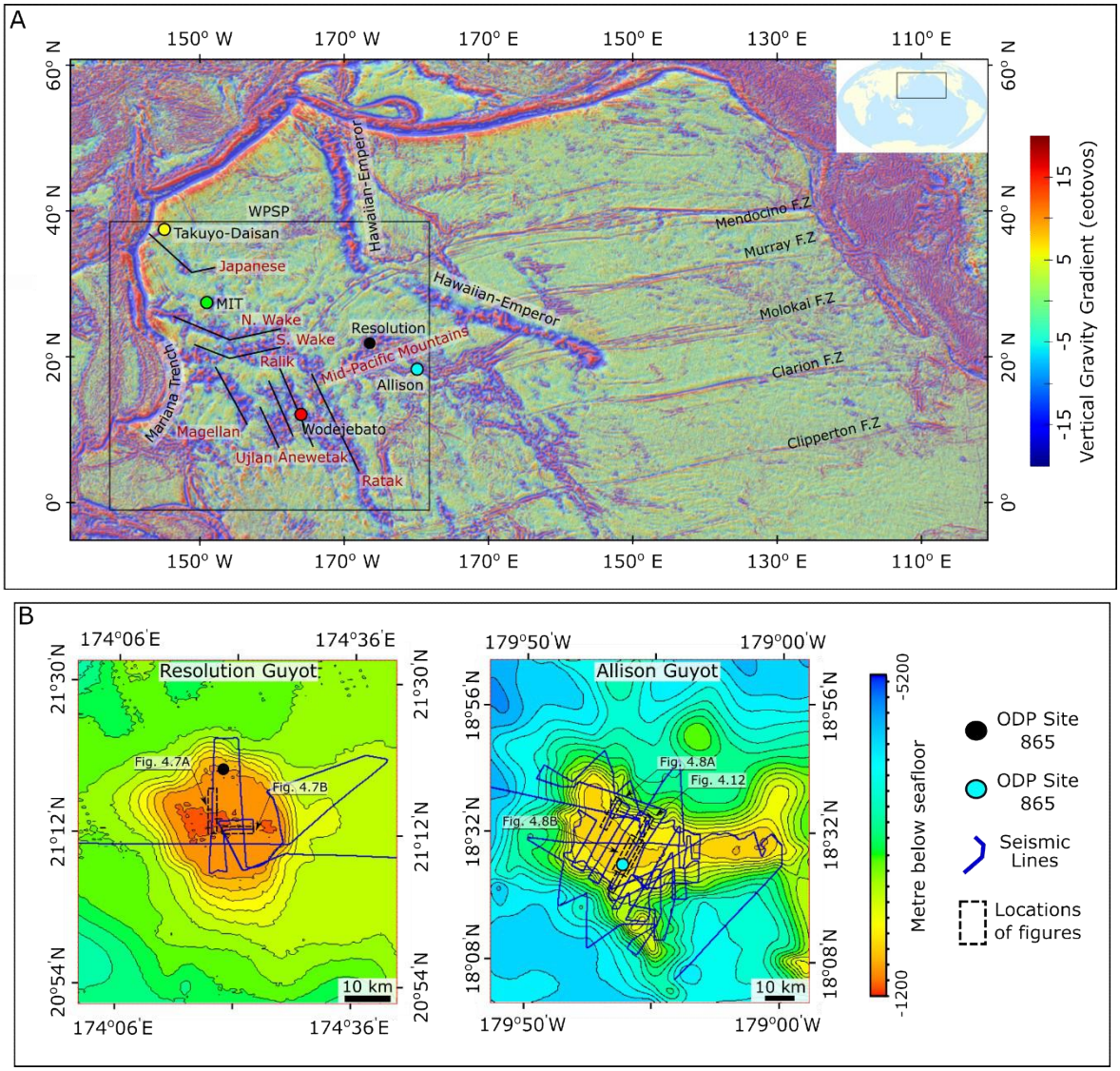


Figure 4.2. (A) The vertical gravity gradient map of the Pacific Plate (Sandwell et al., 2014; https://portal.gplates.org/portal/vertical_gravity_gradient/) showing the fracture zones, the West Pacific Seamount Province (WPSP) and its' seamount trails (Ratak, Ralik, Anewetak, Ujlan, Magellan, Northern and Southern Wake, Typhoon, and Japanese Seamount Trails), and the location of five Cretaceous Pacific isolated carbonate platforms. (B) Bathymetry maps of Resolution and Allison guyots (Keizer et al., 2001; https://earthref.org/SC/#top) showing the Ocean Drilling Program Leg 143 sites (Site 865 and Site 866), 2D seismic surveys, and locations of figures in this study.

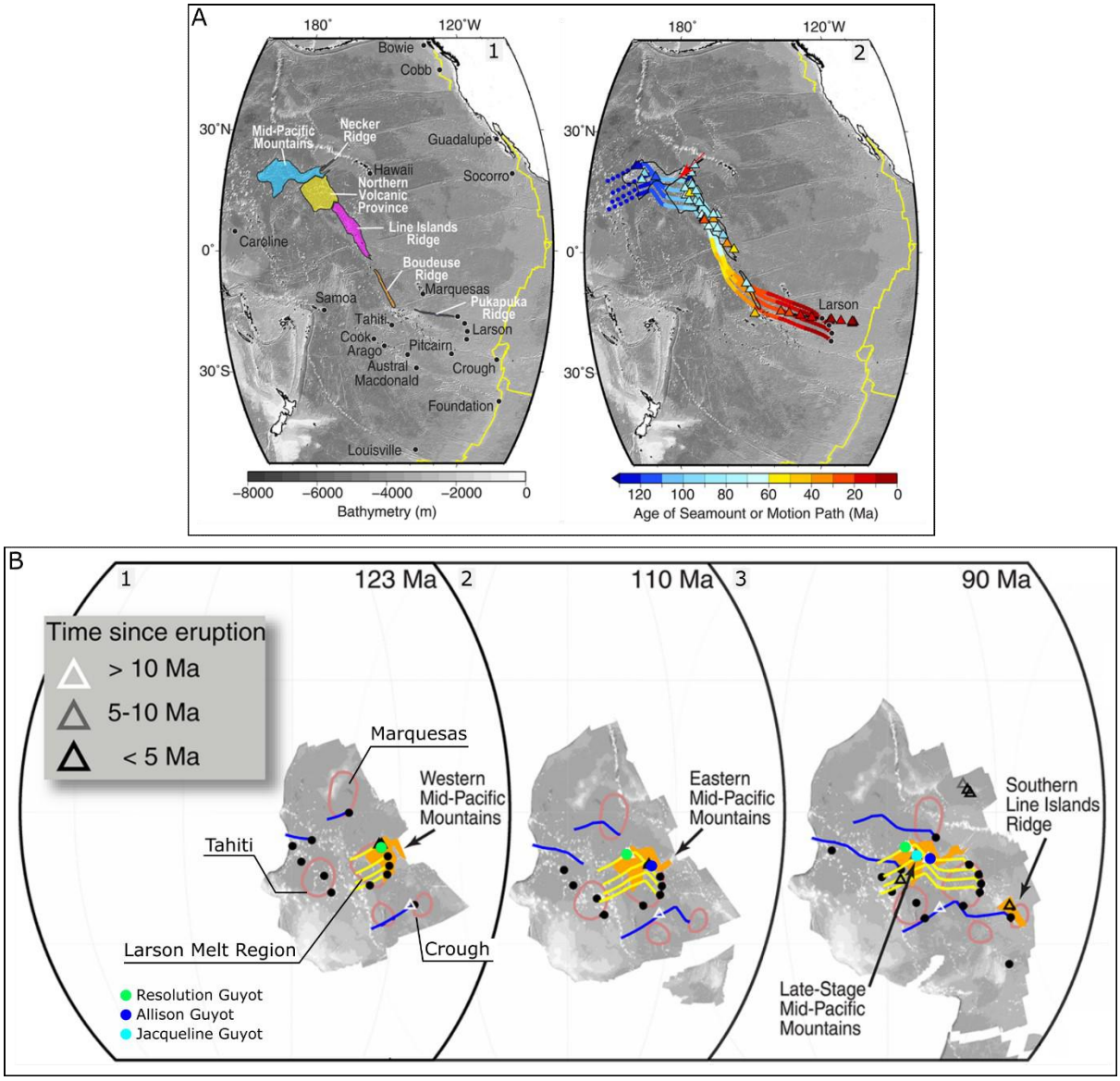


Figure 4.3. (A) Maps of the central Pacific Basin illustrating volcanic features of the Pacific Ocean including Line Islands, the Mid-Pacific Mountains, Necker Ridge, Northern Volcanic Province, and the Pukapuka and Boudeuse Ridges. The map A.2 shows the age progression of the "hotspot" tracks for the proposed Larson melt region. Triangles denote locations of dated seamounts. Colours of seamounts and hotspot tracks indicate age of feature. The red arrow in map A.2 shows the age when Larson Melt Region left the Mid-Pacific Mountains (after 100 Ma) (B) Series of tectonic reconstructions of the Pacific plate illustrating the melt source and timing of various eruptive events related to the Line Islands system. Motion paths of the Larson melt region (yellow lines) and previously identified hotspots potentially contributing to the Line Islands system (blue lines) are shown. Pink circles are locations of selected upward-projected shear-wave anomaly isosurfaces representing the melt sources of mantle plumes and hotspots (French and Romanowicz, 2015). Maps are adapted from Pockalny et al. (2021).

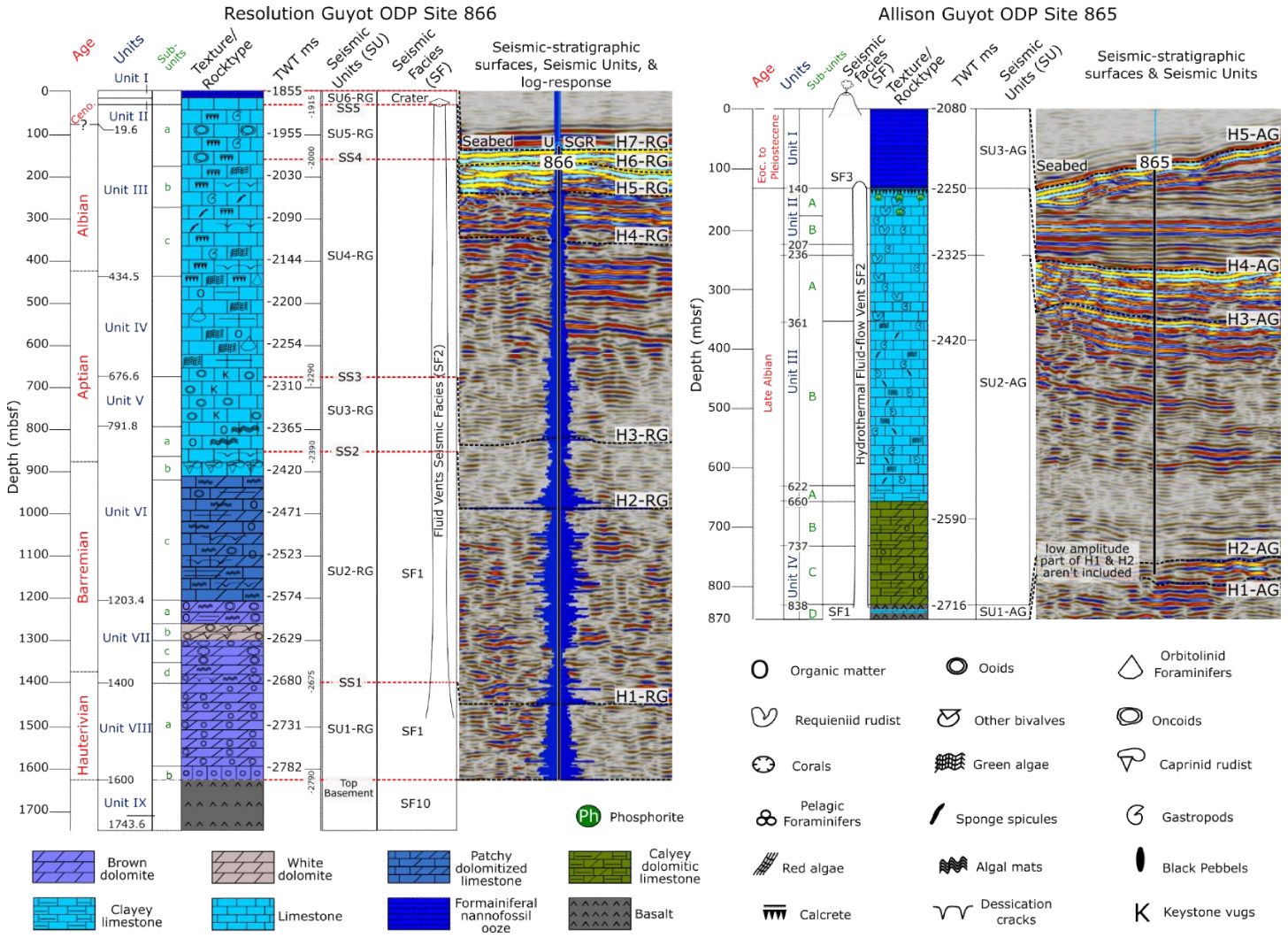


Figure 4.4. Lithostratigraphic columns of Allison Guyot Site 865 and Resolution Guyot Site 866 (reproduced from El-Yamani et al., 2022a; Sager et al., 1993a, b). The figure summarises the main lithological and fossil content of the different lithostratigraphic units at the drill-sites. It shows the distribution of the different seismic facies (SF), seismic units (SU), and seismic horizons (e.g. H1-AG) tied with the drill-sites. SGR; Spectral Gamma Ray, U; Uranium log. At Site 866, the interpreted horizons by El-Yamani et al. (2022) are displayed with the adapted naming (refer to the text for the naming convention).

4.5 Data and Methods

This paper utilises core-log-seismic data collected during ODP Leg 143/144 and the Roundabout Expedition Leg 10 at Resolution and Allison guyots to understand the demise history of their atolls. Seismic data were collected by cruise 'Roundabout Expedition Leg 10' (RNDB10WT; Nov–Dec 1988) aboard the R/V Thomas Washington which was a dedicated program to image the Mesozoic Guyots in the western Pacific (Figure 4.2). This survey consisted of single-channel, 2D seismic profiles acquired using an 80-in^3 water gun, processed by the University of Texas Institute for Geophysics. Processing involved filtering (50–200), mixing (1:1:1), and automatic gain control (Marine Geoscience Data System, n.d.). We also use wireline-logging data including sonic (DTLN) and formation density (RHOB) (Division of Marine and Large Program, n.d.).

Seismic reflection datasets are visualised and interpreted using Petrel® software. The seismic data is displayed in the American polarity convention, where a downward increase in acoustic impedance (e.g. seabed) is represented by trough-peak-trough with red-blue-red reflections. To establish time-depth relationships, we utilise previous seismic-to-well ties by El-Yamani et al. (2022, 2024) in both guyots and the proposed prominent reflections at Site 865 by Sager et al. (1993b). The study uses the revised age model of Resolution Guyot by El-Yamani et al. (2022) to integrate the age-depth model with the seismic data at the tied well (Sites 866). To establish the age-depth model with the seismic data at the tied well at Allison Guyot (Site 865), we first established a revised age-depth model by correlating the strontium-isotope values from Jenkyns (1995) at Site 865 with the global $^{87}Sr/^{86}Sr$ curve (McArthur et al., 2012, version 5B). The $\delta^{13}C_{carb}$ data at Site 865 (Jenkyns et al., 1995) are correlated with the global low-latitude calibrated composite $\delta^{13}C_{carb}$ reference curve (Herrle et al., 2015). The best age model for shallow-marine carbonates at Allison Guyot is obtained by iteratively adjusting tie points to match both isotopes, with an assigned error estimate of ± 1.0 Myr.

The seismic interpretation methodology employed in this study follows the seismic-stratigraphic principles outlined by Mitchum et al. (1977) and Courgeon et al. (2016a). This approach involves defining seismic facies, tracing key seismic-stratigraphic surfaces and associated reflection terminations and describing the geometries of seismic reflections within the depositional units bounded by these seismic discontinuities and key surfaces. For Resolution Guyot, we adopt the seismic-sequence stratigraphic framework established by El-Yamani et al. (2022), utilising the following horizons (Figure 4.3): H1-RG (SS1; Top of Seismic Unit-1, ~130.8 ± 1 Ma), H2-RG (SS2; Top of Seismic Unit-2, ~125.5 ± 1 Ma), H3-RG (SS3; Top of Seismic Unit-3, ~122.8 ± 1 Ma), H4-RG (SS4; Top of Seismic Unit-4, ~105.15 ± 1 Ma), H5-RG (SS5; Top of Seismic Unit-

5, ~100.5 ± 1 Ma; representing the karstification surface at the topmost part of the shallow-marine carbonate succession), H6-RG representing the boundary between shallow-marine carbonate succession and the pelagic cap, and H7-RG representing the seabed. At Allison Guyot, we interpreted five horizons: H1-AG (Base of basaltic sills), H2-AG (Top of basaltic sills), H3-AG (prominent mostly continuous reflections within the shallow marine sedimentary succession), H4-AG (Top of the Cretaceous shallow-marine carbonates below the pelagic cap), H5-AG (seabed). El-Yamani et al. (2024) identified magmatic sills intrusions and associated hydrothermal vents on seismic data from both guyots. The interpreted magmatic intrusions were groundtruthed by developing synthetic seismic facies forward modelling supported by drilling data at Allison Guyot (Site 865; El-Yamani et al., 2024). Here, this work is extended by mapping and correlating magmatic sills intrusions on 2D seismic data through tracing the high amplitude anomalous reflections that are onlapped by the overlying and surrounding strata assuming intrusions are broadly sub-circular in map view (Trude, 2004; Hansen et al., 2008; Jackson et al., 2013; Magee et al., 2017). Consequently, the observed parts of sills on the 2D seismic lines are treated as representative of sills diameters to measure intrusion diameter-to-depth ratio (Hansen and Cartwright, 2006). In addition, Root-mean-square amplitude (RMSA) attribute is used in delineating the top and base of sills from seismic data in order to calculate their thicknesses as RMSA is sensitive to extreme amplitude variations (Wang et al., 2019b). Two interval velocity of sills are used to measure the thicknesses. First, we use an interval velocity (V_1) of ~4,854 m/s, based on measured compressional wave velocity by the shipboard scientific party of a basaltic samples of sills at Site 865 (Sager et al., 1993b). Second, we use an interval velocity (V_2) of 5,550 m/s, which is widely used for basaltic rocks (e.g. Skogly, 1998). The apparent ages of magmatic events in both guyots are determined by examining their stratal terminations which involves: (1) utilising age-constrained sedimentary reflections through a depth-age model at drilling sites, (2) considering the base vent surface (Figure 4.5A, B), which corresponds to the palaeo-seabed at the time of venting, and (3) assessing unconformities between forced folding and onlapping sedimentary reflections of known age (Figure 4.5C, D). This approach has been effectively used in previous studies to determine the ages of magmatic intrusions (e.g. Trude et al., 2003; Planke et al., 2005; Hansen and Cartwright, 2006; Manton et al., 2022).

The study incorporates the latest tectonic reconstruction of the Pacific Plate (Pockalny et al., 2021). This reconstruction includes a series of maps illustrating the motion paths and mantle sources of various hotspots in the Pacific, including the Larson melt region, Tahiti, and Marquesas hotspots. Additionally, it outlines the timing of various eruptive events, shedding light on the formation of geological features such as the Mid-Pacific Mountains (MPM), Necker Ridge, Northern Volcanic

Province, Lines Islands Ridge, Boudeuse Ridge, and Pukapuka Ridge. To account for the palaeoclimatic conditions of the Pacific Cretaceous atolls from their rise to demise, the study utilises paleogeographic reconstructions by Winterer and Sager (1995), Torsvik et al. (2012), and Scotese and Wright (2018). These reconstructions provide insights into the past positions of the atolls and their paleolatitudes. The paleolatitudes derived from these reconstructions are determined using online resources such as https://paleolatitude.org/ (Van Hinsbergen et al., 2015) and https://climatearchive.org/# (Steinig et al., 2022). Subsequently, these paleolatitudes are utilised in global palaeoclimate models provided by Valdes et al. (2021), Poulsen et al. (1998), and Agustsdottir et al. (1999). These models help identify the corresponding environmental parameters at different time steps, including sea surface temperatures (SSTs), ocean surface currents, wind speed, and the location of the equatorial hurricane belt and tropical cyclones. This comprehensive approach allows for a detailed examination of the environmental conditions experienced by the Cretaceous atolls throughout their history.

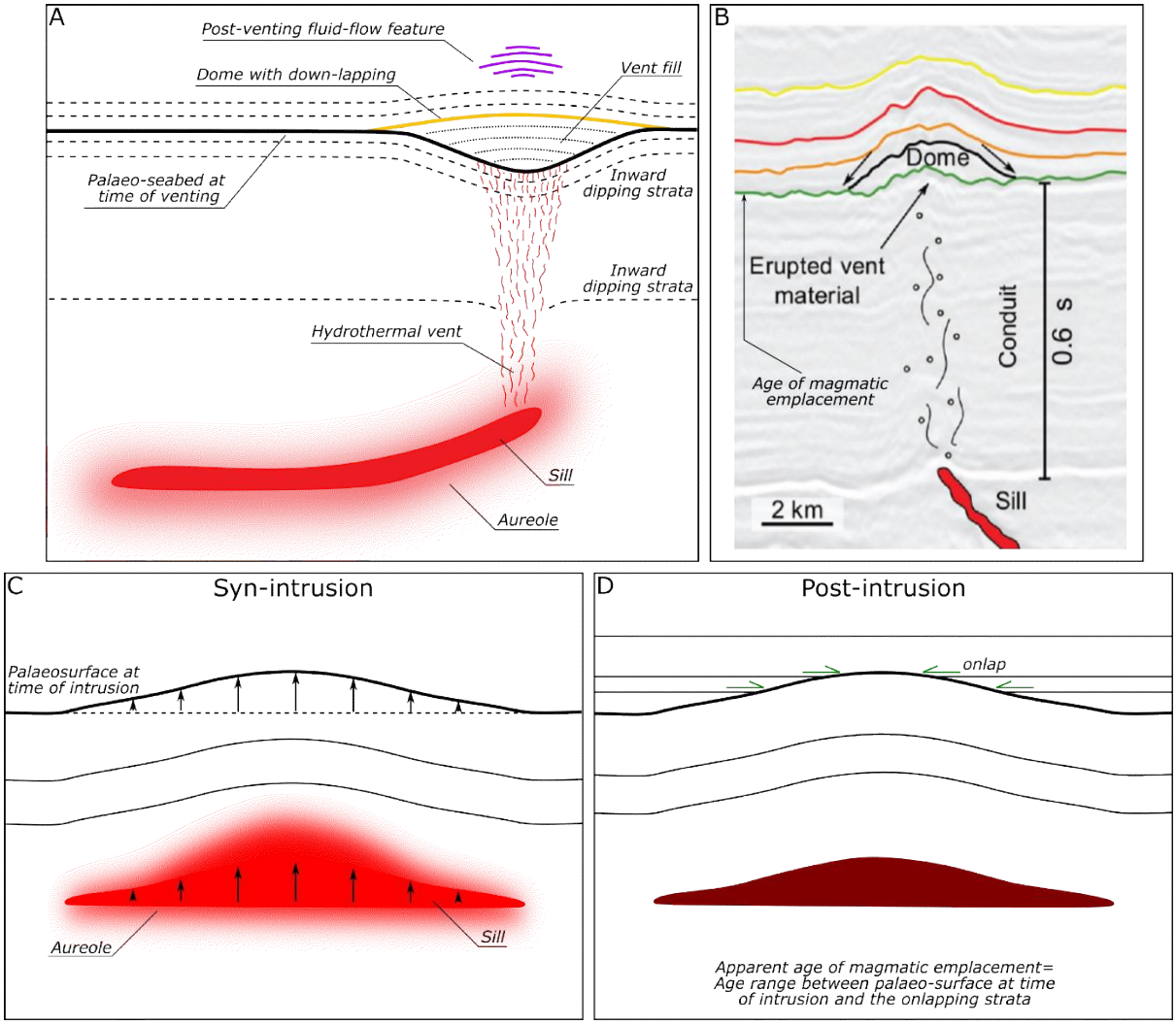


Figure 4.5. Criteria for determining apparent age of magmatic intrusions based on stratigraphic stratal terminations. (A) Schematic sketch of a hydrothermal vent complex illustrating the palaeo-seabed at time of venting on which a dome is down-lapping (modified from Manton et al., 2022). (B) Seismic profile showing the apparent age of the Paleocene-Eocene transition magmatic emplacement in the Møre Basin (modified from Kjoberg et al., 2017) based on interpreting the palaeo-seabed at time of venting on which a dome is down-lapping. (C and D) Schematic sketches of intrusion-related surface uplift and forced folding and the consequent reflection configurations (modified from Magee et al., 2014). (D) Schematic sketch showing the apparent age of magmatic emplacement as the age range between palaeo-surface at time of intrusion and the onlapping strata.

4.6 Results and Interpretation

4.6.1 Age model of Allison Guyot

Ten excursion points and nine correlative intervals between excursions were identified and matched based on similar $\delta^{13}C_{carb}$ trends, as highlighted by correlation lines with the low latitude age calibrated composite $\delta^{13}C_{carb}$ curve. In the Sr isotope data at Site 865, four inflection tie points and plateaus were identified, allowing for correlation to the reference curve of McArthur et al. (2012). The revised age model at Site 865, integrating both $\delta^{13}C_{carb}$ and Sr isotope data, suggests the following sedimentation history for Allison Guyot (Figure 4.6): (a) sedimentation began at late Aptian ~114.4±1.0 Ma, based on the projected age of the first recovered sample at 846 mbsf, and (b) neritic carbonate production continued until the latest Albian/earliest Cenomanian (~100.12±1.0 Ma), as evidenced by the first shallow-marine carbonate sample recovered below the pelagic cap at ~140 mbsf. This history at Allison Guyot is different from shallow-marine carbonate sedimentation history in Resolution Guyot (Figure 4.6; El-Yamani et al., 2022) where: (a) sedimentation began around ~132±1.0 Ma, based on the projected age of the first recovered sample at 1620 mbsf, and (b) neritic carbonate production continued until the latest Albian/earliest Cenomanian (~100.4±1.0 Ma), with the cessation of neritic carbonate production indicated by the age of the first shallow marine carbonate sample recovered below the pelagic cap at ~20 mbsf.

4.6.2 Seismic interpretation

4.6.2.1 Seismic Facies and Magmatic Intrusion Related Structures

El-Yamani et al. (2022, 2024) demonstrated that the sedimentary successions in both guyots are intruded with magmatic sills, as indicated by Seismic Facies 1 (Figure 4.3, 4.7, and 4.8). These sills appear as localised and abrupt high-amplitude reflections with sudden terminations that cut across stratigraphic levels and exhibit limited lateral continuity. This interpretation was validated through synthetic seismic facies forward modelling using drilling data of basaltic sills in Allison Guyot (Site 865; El-Yamani et al., 2024). The authors also showed that these sills, in both guyots, are associated with vertical zones of disrupted and reduced reflection continuity that are interpreted as hydrothermal fluid vents (Seismic Facies 2; Figure 4.3, 4.7, and 4.8) associated with the magmatic emplacement (Planke et al., 2005) based on the following seismic characteristic: (a) originating at the tips of the magmatic sills, (b) the inward dipping reflections within the vents, and (c) their upper termini have shapes of craters (Figure 4.3, 4.7, and 4.9), dome-shaped, eye-shaped, and pock-shaped. In addition, the present study interprets the presence of wide, flat-topped, periclinal antiforms with subtle onlap and truncation relation (Seismic Facies 3; Figure 4.8 and 4.9). These structures, observed in both guyots, are closely associated with the magmatic sills. Comparison

with high-resolution seismic data suggests that these structures represent supra-sill forced folds (e.g. Magee et al., 2014). The interpreted supra-sill forced folds indicate that the emplacement of sills in the sedimentary successions of Resolution and Allison Guyots was accompanied by uplift (e.g. Magee et al., 2014).

In the present study, the interpretation of hydrothermal vents in Allison Guyot shows that the base and top vent boundaries have domal and crater geometries (Figure 4.8 and 4.9). The high density of seismic data at Allison Guyot allowed us to map the potential areal distribution of the interpreted magmatic sills complexes, which extend almost across the whole guyot, covering an area of ~460 km^2 (APPENDIX C Figure C1 and C2). The sills have a 'planar transgressive' inclined sheet morphology (cutting through different stratigraphic levels; sensu Planke et al., 2005), intruding across depths ranging from >650 mbsf to levels deeper than bottom hole depth at 870 mbsf (~3000 TWT ms). In Allison Guyot, sills were encountered at the base of Site 865 having a thickness of ~40 m (Sager et al., 1993b). On seismic data, the stacked thicknesses of interpreted sill range from 70-80 m up to ~150 m, using V_1 and 90 up to ~170 m, using V_2 (Figure 4.10).

In Resolution Guyot, the base and top vent boundaries of the interpreted hydrothermal vents exhibit crater-like, eye-shaped, and pock-shaped geometries (Figure 4.7 and 4.9). Unlike Allison Guyot, the areal extent of the interpreted magmatic sills cannot be precisely mapped due to the sparse distribution of seismic data at Resolution Guyot. However, based on the distribution of the interpreted sill in map view, three different interpolation scenarios suggest an areal extent of approximately ~78-200 km^2 assuming intrusions are broadly sub-circular in map view (Trude, 2004; Hansen et al., 2008; Jackson et al., 2013). The sills in Resolution Guyot also exhibit a 'planar transgressive' inclined sheet morphology, intruding mainly through the sedimentary succession from ~900 to 1500 mbsf (Figure 4.6C, D). Although sills were not drilled in Resolution Guyot, their stacked thicknesses on seismic data range from ~80 up to ~160 m using V_1 and 90 up to 185, using V_2 (Figure 4.10).

The mapped sills are used for a relative comparison between their diameters and depths. We acknowledge the uncertainties surrounding our mapping due to the spacing between 2D seismic lines and the lack of drilling sites across platform widths. Therefore, measured diametres, at best, would give rough estimates. The measured diametres in Resolution and Allison guyots range from 800-6,800 m (average: 3,631; mode: 3,800; APPENDIX C Figure C1 and C2) and 1,000-15,600 m (average: 4008; mode: 2900; APPENDIX C Figure C1 and C2), respectively. As sills intrude the sedimentary succession at depths of 900-1500 mbsf in Resolution Guyot and ~650->870 mbsf in

Allison Guyot, the diameter-to-depth ratios have on average a range of 2.4-4 and 4.6-6.2, respectively.

4.6.2.2 Timing of magmatism in the Mid-Pacific Mountains

In Resolution Guyot, the interpreted seismic-horizons divide the stratigraphic succession into six seismic-stratigraphic units (SU1-RG to SU6-RG). Magmatic sills are concentrated across the middle of the platform intruding through the lower part of the sedimentary succession (SU1-RG and SU2-RG) which is formed of lithostratigraphic Unit VIII to subunit-VIA at Site 866 (Figure 4.3 and 4.7). Large hydrothermal vents and magma conduits are associated with these sills, cutting through horizon from H1-RG and terminating just above H5-RG, which represents the karstification surface at the uppermost part of shallow-marine Cretaceous carbonates (Figure 4.7). This is covered by SU6-RG which represents the pelagic cap, characterised by continuous seismic reflections, below seabed (H7-RG).

In Allison Guyot, the interpreted seismic-horizons divide the stratigraphic succession into three seismic-stratigraphic units (SU1-AG to SU3-AG). Magmatic sills are observed across the whole width of the guyot intruding through SU1-AG. The associated large hydrothermal vents and magma conduits cut through the whole shallow-marine carbonate succession in Allison Guyot and terminate just at seismic horizon H4-AG (upper boundary of SU2-AG; Figure 4.8). The interpreted supra-sill forced folds coincide with H4-AG. Between H4-AG and H5-AG, the seismic unit SU3-AG representing the pelagic cap of Allison Guyot, is characterised by continuous seismic reflections (Figure 4.8) with no hydrothermal vents piercing through it.

Our seismic interpretations imply that both guyots experienced subsequent episode(s) of intraplate magmatism (i.e. after initiation of shallow-marine carbonate sedimentation; Figure 4.7 and 4.9). In Allison Guyot, an episode of magmatism (Episode-AG) is inferred from a forced folding in the northwestern part of the guyot, corresponding to seismic horizon H4-AG (the topmost of the shallow marine carbonates beneath the pelagic cap; ~100.15 ± 1 Ma). The dome-shaped and crater-shaped termini of hydrothermal vents across Allison Guyot are also onlapped by the pelagic cap sediments (Figure 4.8 and 4.9C, D). The oldest overlying pelagic sediments recovered from cracks and cavities at the uppermost part of Allison Guyot shallow-marine have an assemblage of planktonic foraminifers that represents *Helvetoglobotruncana helvetica* Taxon-Range Zone (Sager et al., 1993b; Sliter, 1995). This taxon-range zone yields an age of early to middle Turonian (93.5-92.6 Ma; Huber and Petrizzo, 2014). Thus, the stratal termination relationship between the hydrothermal vents' termini and the suprasill forced fold with the pelagic cap suggests that the

magmatic Episode-AG could potentially possess an apparent age falling within the range of 100.15±1 Ma and 93.5-92.6 Ma (Figure 4.11).

In Resolution Guyot, evidence of magmatism (Episode-RG) is apparent from interpreted hydrothermal vents cutting through the entire shallow-marine sedimentary sequence (Figure 4.7). The vents have crater shapes and are positioned near the seabed horizon H7-RG. Tracing the base vent allows for the estimation of the apparent age of the palaeo-seabed at the time of venting (Manton et al., 2022). Moreover, the palaeosurface, where crater-shaped vent termini are interpreted and down-lapping domes are observed, can serve as a significant indicator for inferring the age of emplacement (e.g. Kjoberg et al., 2017). The base vent corresponding to Episode-RG aligns with horizon H6-RG. According to well data from Site 866, horizon H6-RG marks the boundary between the uppermost section of the shallow-marine carbonates (~ 100.5 Ma) and the subsequent overlying pelagic cap. The onlapping intra-vent reflections represent the vent fill and pelagic deposits. This is overlain by the pelagic deposits where few examples of downlapping are observed (Figure 4.7 and 4.9A, B). The oldest pelagic deposits recovered above the shallow-marine carbonates at Resolution Guyot contain a nannofossil assemblage zone CC24 (Sager et al., 1993a) which corresponds to the late Campanian/early Maastrichtian age (~73.8-72 Ma; Ogg and Hinnov, 2012). Consequently, the stratal termination relationship between the base vent and the overlying pelagic cap suggests that the magmatic event at Resolution Guyot (Episode-RG) potentially has an apparent age between ~100.5±1 Ma and ~73.8-72 Ma (Figure 4.9A, B and 4.11). This apparent age is supported by the observation that all reflections below H6-RG (i.e. drowning surface) display upward bending related to venting (Figure 4.7B) while the continuous reflections on top (i.e. pelagic cap) are not affected, meaning that magmatism and venting happened before pelagic sedimentation.

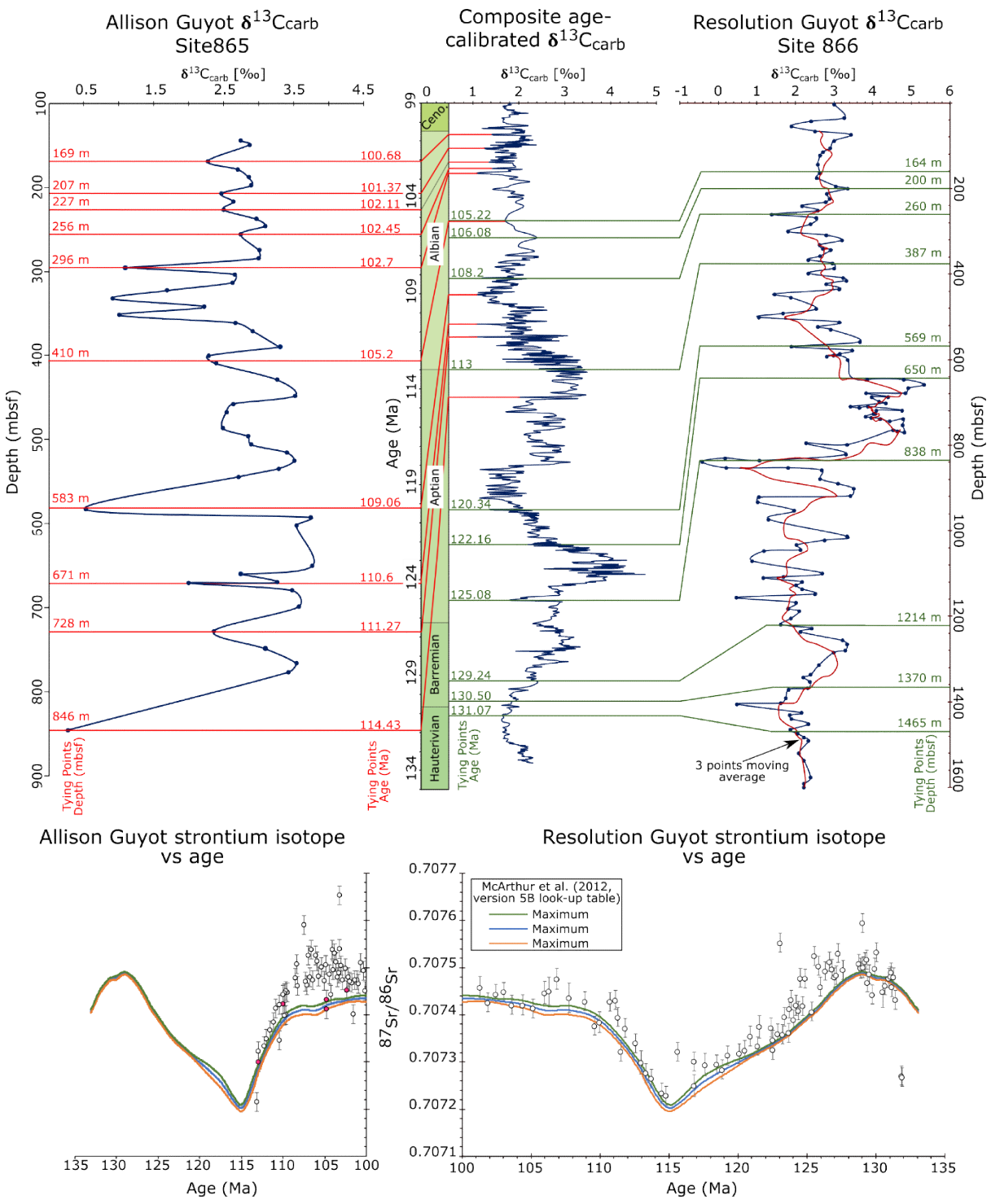


Figure 4.6. Correlation between the low latitude calibrated composite reference $\delta^{13}C_{carb}$ curve (reproduced from Herrle et al., 2015, using published data from Tethyan sections of Erba et al., 1999; Gale et al., 2011; Herrle et al., 2004) and the $\delta^{13}Cc_{arb}$ curve of Resolution Guyot (correlation lines highlighted in green; El-Yamani et al., 2022) and $\delta^{13}C_{carb}$ curve of Allison Guyot (correlation lines highlighted in red) using carbon isotope data from Jenkyns (1995). The figure shows strontium isotope ($^{87}Sr/^{86}Sr$) age model at both guyots based on using strontium isotope data from Jenkyns et al. (1995) and the values in the reference curve of McArthur et al. (2012, version 5B). Tying points in strontium isotope ($^{87}Sr/^{86}Sr$) age model of Allison Guyot are filled with pink.

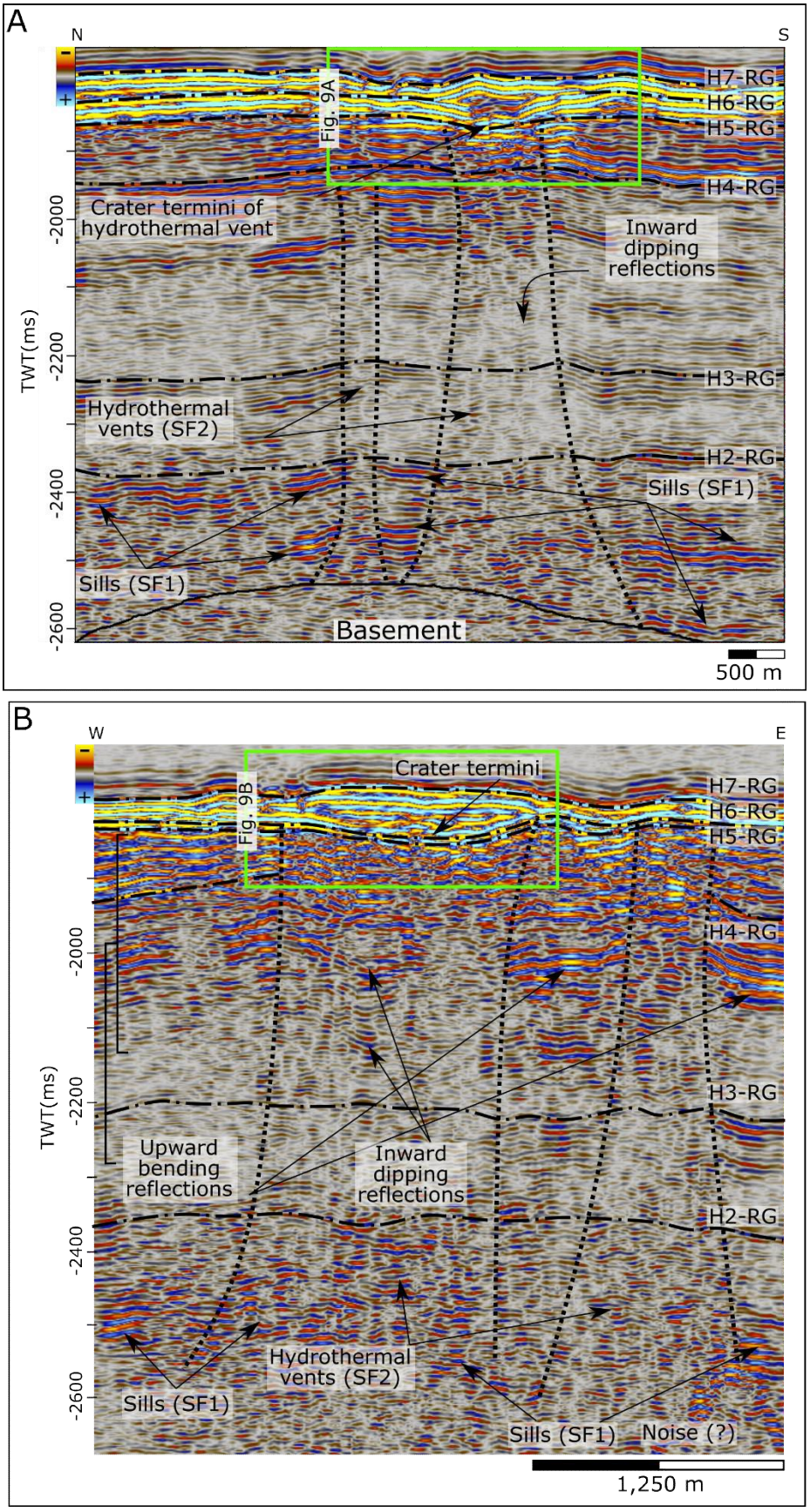


Figure 4.7. Seismic interpretation of the different magmatism related structures at Resolution Guyot in relation to the identified seismic horizons. (A and B) Seismic amplitude profiles from Resolution Guyot showing the interpreted sills and the associated hydrothermal vents with crater upper termini onlapped and filled by vent fill and pelagic deposits.

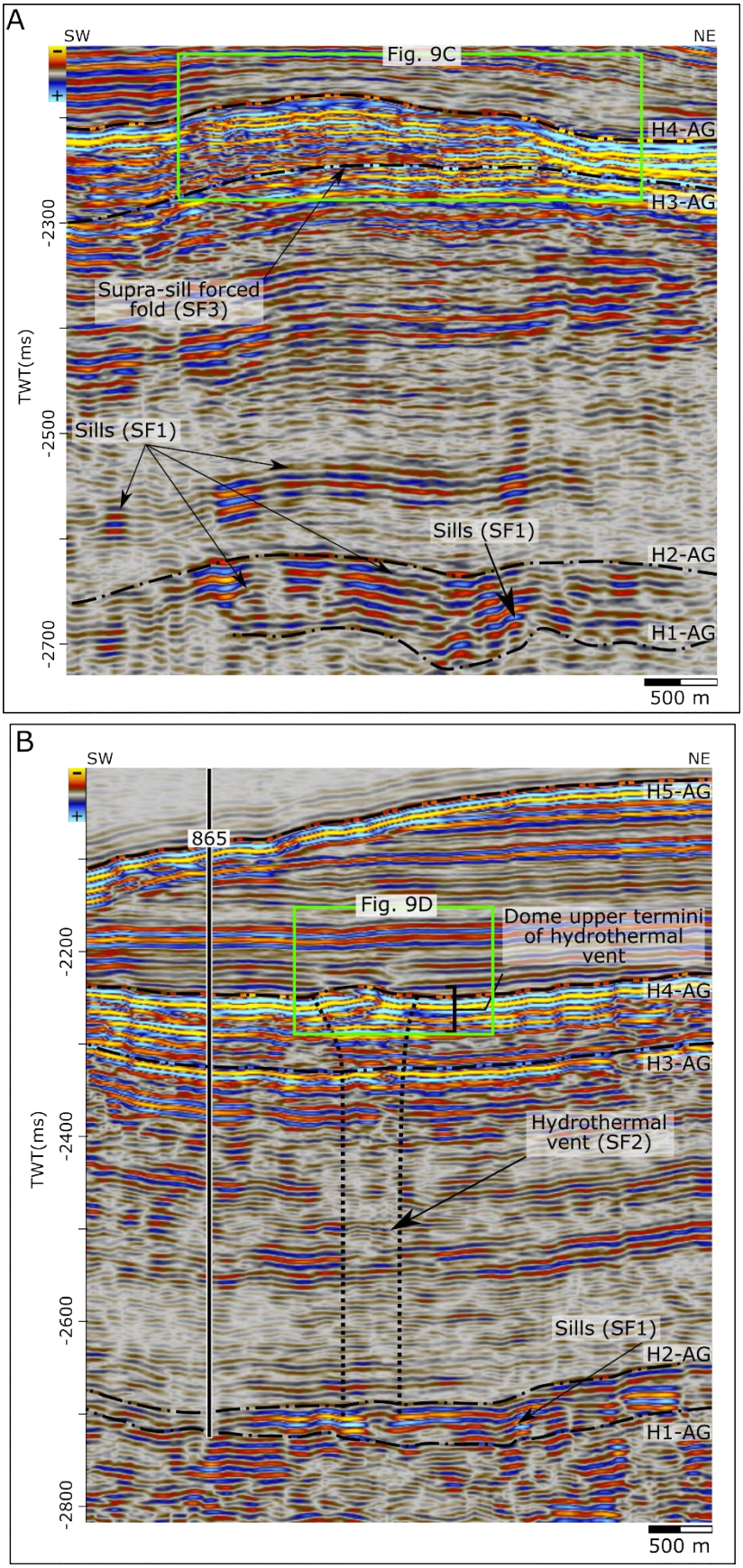


Figure 4.8. (A) Seismic amplitude profile from Allison Guyot showing the interpreted sills and the associated hydrothermal vents with dome upper termini onlapped by pelagic deposits. (B) Seismic amplitude profile from Allison Guyot showing the interpreted sills and the associated suprasill forced folds onlapped by pelagic deposits.

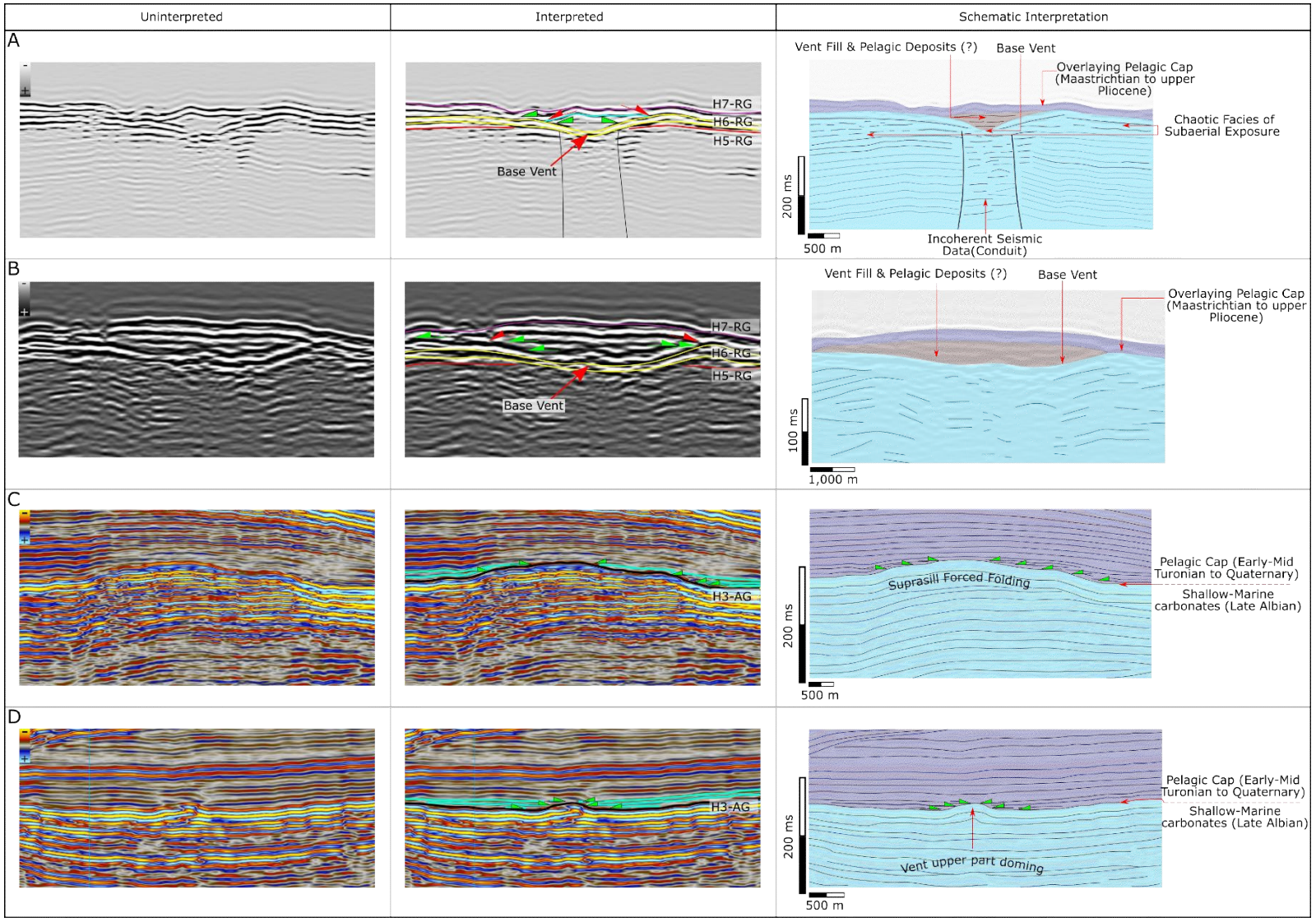


Figure 4.9. Timing of magmatism in the Mid-Pacific guyots by interpreting magma associated structures in closer-look of uninterpreted and closer look seismic profiles along with schematic representations of the interpretations.

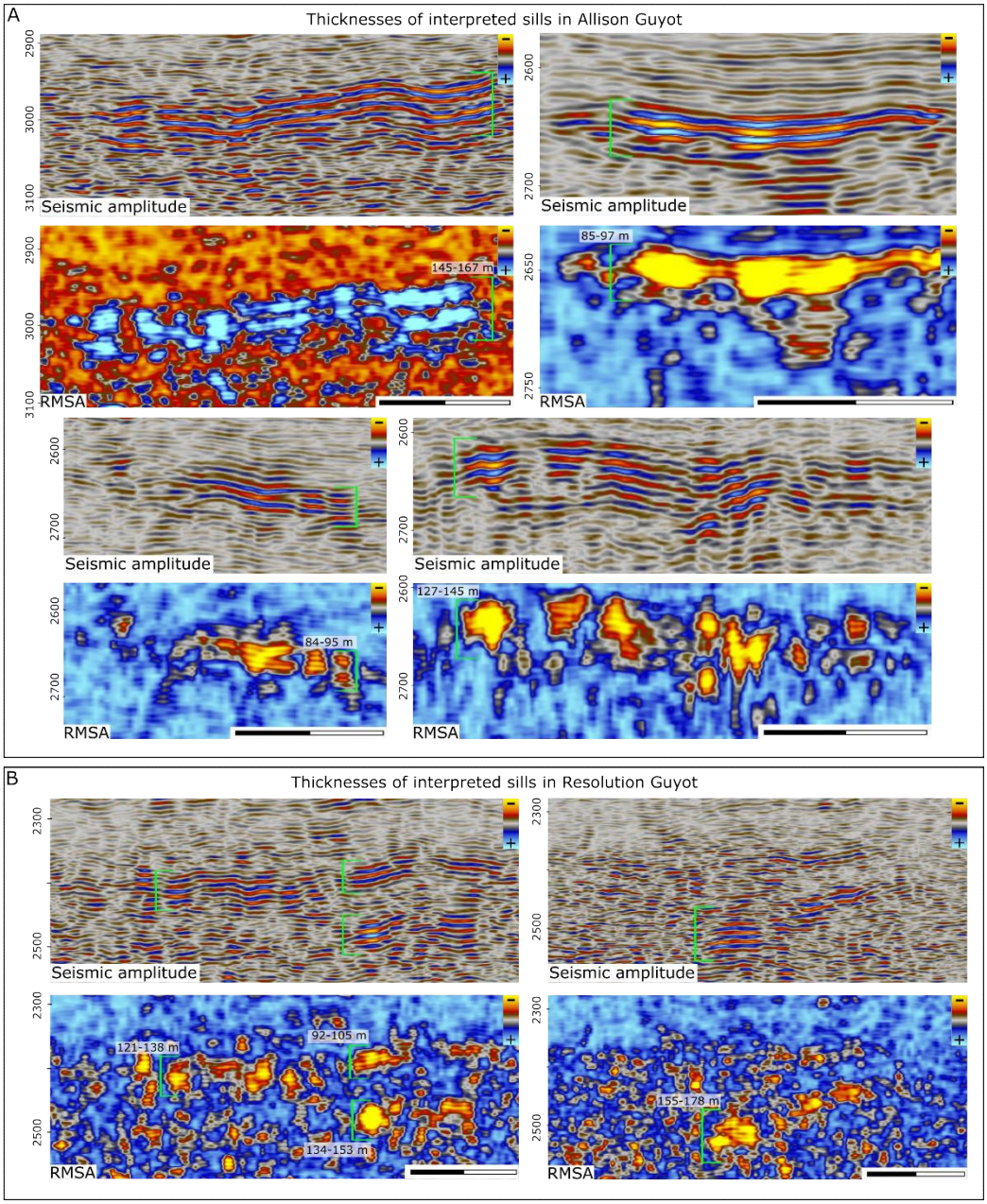


Figure 4.10. Seismic amplitude and root-mean-square-amplitude profiles in Allison (A) and Resolution (B) guyots showing their sills intrusions and the interpreted thicknesses. Seismic profiles are in two-way time milliseconds. The horizontal scale is 1,250 m.

4.7 Discussion

4.7.1 The Demise Mechanism of the Mid-Pacific Cretaceous Atolls

As observed, the interpreted magmatic events (Episode-AG and -RG) cut through the shallow-marine carbonate layers in both guyots but appear not to impact the overlying pelagic caps (Figure 4.7 and 4.9). Although we cannot precisely pinpoint their exact ages, their apparent age ranges overlap with each other (Figure 4.11), as Episode-RG has apparent age between ~100.5 ± 1 Ma to ~73.8-72 Ma and Episode-AG has apparent age between ~100.15 ± 1 Ma to ~93.5 Ma. Putting these magmatic age ranges into context with the Pacific Plate's tectonic history may help to better constrain their age. During late Albian to early Cenomanian (102-98 Ma), extensive volcanic activity from plumelets originating from the South Pacific mantle superplume affected the WPSP (Magellan, Anewetak, and Wake Seamount Trails, Hemler guyot, and seamounts near Necker Ridge, Koppers et al., 2003; Liu et al., 2022). This volcanic activity appears to be affecting the MPM within the same time range, as it is observed in Jacqueline Guyot, a midway MPM guyot between Resolution and Allison, where basaltic samples have ages of ~98.5±1.4 Ma (Figure 4.8; Winterer et al., 1993; Clouard and Bonneville, 2005). At Allison Guyot, some of the basaltic samples yield ages of 101.2±0.8 and 102.70±2.70 Ma (Winterer et al., 1993; Clouard and Bonneville, 2005). Moreover, widespread volcanism in the Central and West Pacific is indicated by significant volcanogenic sediments in the Nuru Basin, Central Pacific Basin, Hess Rise, and Magellan Rise, to the north and south of the MPM, with an age of upper Albian-lower Cenomanian (Thiede et al., 1981; Vallier and Jefferson, 1981). Around the same age, shallow-marine carbonate production ceased simultaneously in both Allison and Resolution guyots (Figure 4.11), with evidence of subaerial exposure affecting the topmost part of the shallow-marine carbonates on both guyots (Winterer et al., 1995; El-Yamani et al., 2022). Considering this information, it appears there is a temporal overlap and potentially a causal relationship (Figure 4.11) between (a) the confirmed magmatic activities in the MPM (101.2 ± 0.8 and 102.70 ± 2.70 Ma, Allison Guyot; 98.5 ± 1.4 Ma, Jacqueline Guyot), (b) the interpreted magmatic activities in the MPM in this study (i.e. Episode-AG and -RG), (c) the documented widespread volcanism in the western Pacific plate during the late Albian-early Cenomanian age, and (d) the end of shallow marine carbonate deposition and the subaerial exposure of the MPM guyots (~100.15 and ~100.5 ± 1 Ma, Allison and Resolution guyots; El-Yamani et al., 2022). Consequently, we suggest that during late Albian-early Cenomanian, extensive magmatic activity impacted the MPM (Episode-AG and -RG; Figure 4.11), causing uplift and cessation of shallow-marine carbonate deposition on the platform tops at

Resolution and Allison guyots. This age of magmatism is plausible as the MPM was still in the vicinity of the Larson Melt Region (Pockalny et al., 2021).

4.7.1.1 Magmatism, Karstification and Cessation of Shallow-Marine Carbonate Sedimentation

Igneous intrusions into pre-existing sedimentary successions can cause magmatic underplating, involving shallow emplacement of sheet-like intrusions connecting to deeper intrusions and magma reservoirs within the lower oceanic plate, resulting in magma accumulation and uplift (Klügel et al., 2015). This uplift is often significant and can cause substantial changes in the overlying terrain. Various seamounts, such as those found in the Hawaiian Islands, Marquesas Islands, La Réunion, Ninetyeast Ridge, and Canary Islands, have demonstrated this phenomenon, with observed uplift reaching 100(s) m (Watts et al., 1985, 1989; Caress et al., 1995; Charvis et al., 1999; Dañobeitia and Canales, 2000; Marques et al., 2020).

In the MPM, the magmatic events Episode-AG and -RG (Figure 4.11) seem to have had a significant regional impact, affecting Allison, Resolution, and Jacqueline guyots simultaneously. Evaluation of the interpreted areal dimensions and thicknesses of magmatic-sill intrusions within Resolution and Allison guyots indicates the accumulation of a considerable volume of intruding magma (Figure 4.10; APPENDIX C Figure C1 and C2). Such a significant influx of magma would likely trigger magmatic underplating across the MPM, leading to simultaneous uplift. This uplift would result in subaerial exposure and the cessation of shallow-marine carbonate sedimentation atop the Allison and Resolution platforms. Seismic interpretation reveals a broad doming in Allison Guyot spanning from horizon H1-AG up to H4-AG. The broad doming of the mapped horizon H4-AG and the interpreted sills exhibit a spatial correlation, suggesting a genetic association (Figure 4.8; Hansen and Cartwright, 2006; Jackson et al., 2013; Magee et al., 2014). Considering the potential diameter-to-depth ratios of the interpreted sill intrusions ranging from 2.4-4 and 4.6-6.2 (i.e., >1.5), the associated surface uplift and forced folding would mirror the thicknesses of the underlying sill (Hansen and Cartwright, 2006). Based on the interpreted sill thicknesses in Allison Guyot (~70-170 m), and Resolution Guyot (~80-185 m), alongside the exclusion of deeper magmatic-sill intrusions beyond those detected in the seismic data analyses conducted in this investigation, the anticipated surface uplift would exceed >70-80 m up to ~170-185 m (Figure 4.10). These estimations are considered conservative due to the usual association of shallow intrusions in volcanic islands with deeper intrusions and magma reservoirs within the lower oceanic plate, leading to further magma accumulation and uplift (Klügel et al., 2015). The ranges of sill thicknesses overlap with the inferred surface uplift amplitude (~100 m; Figure 4.12; 75 TWT ms), derived by tracing H3-AG and utilising an average interval velocity of 2,650 m/s (Sager et al., 1993b). The thicknesses of the karstified uppermost parts of the shallow-marine

carbonates in Resolution (~150 m; El-Yamani et al., 2022) and Allison (150-200 m; Winterer et al., 1995) guyots align with both the anticipated surface uplift ranges based on our measured sill thicknesses and the interpreted surface uplift amplitude derived from our mapping of H3-AG (Figure 4.12). Such exposure heights and uplift are likely attributable to magmatic intrusions-associated uplift, rather than eustasy (Maclennan and Lovell, 2002).

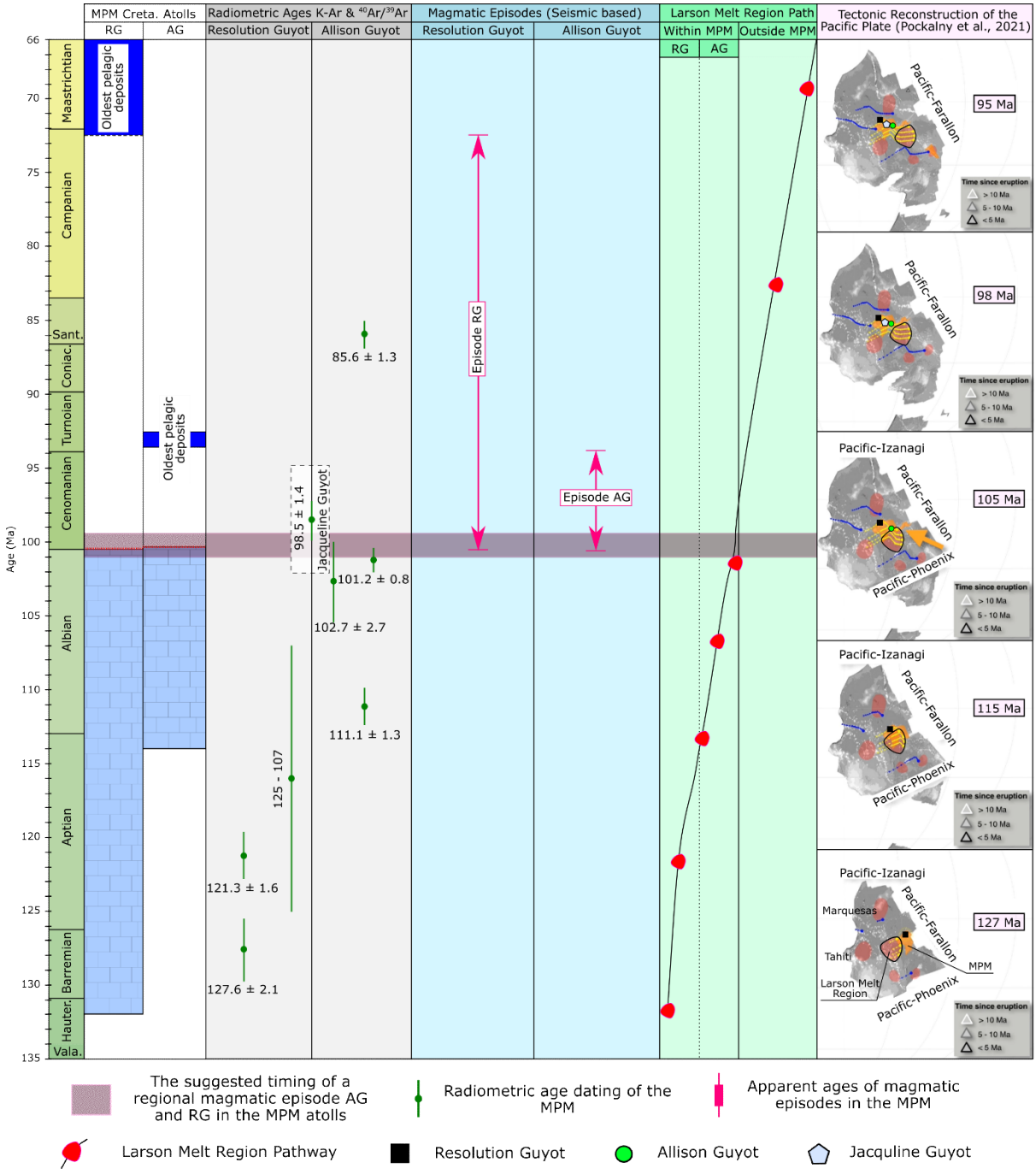


Figure 4.11. Timing of (1) deposition of shallow marine Cretaceous carbonates at Allison and Resolution guyot, (2) the radiometric age dating of the different basement samples at Resolution, Allison, and Jacqueline guyots using data from Winterer et al. (1993), Pringle and Duncan (1995), and Clouard and Bonneville (2005), (3) the apparent ages of the magmatic episodes interpreted in this study based on seismic stratigraphic principles of interpreting timing of magmatism based on the associated magmatic structures, (4) qualitative representation of Larson Melt Region migration within and outside the Mid-Pacific Mountains, and (5) five time steps of the new tectonic reconstruction of the Pacific Plate (Pockalny et al., 2021) showing the different hotspot migration pathways in relation to the Mid-Pacific Mountains. The figure highlights the overlap, by light transparent purple box, between the cessation of the shallow marine carbonate sedimentation and subaerial exposure at Allison and Resolution guyots, the radiometric ages of some basement samples at Allison and Jacqueline guyots, and the apparent age range of the interpreted magmatic events in this study in Allison and Resolution guyot.

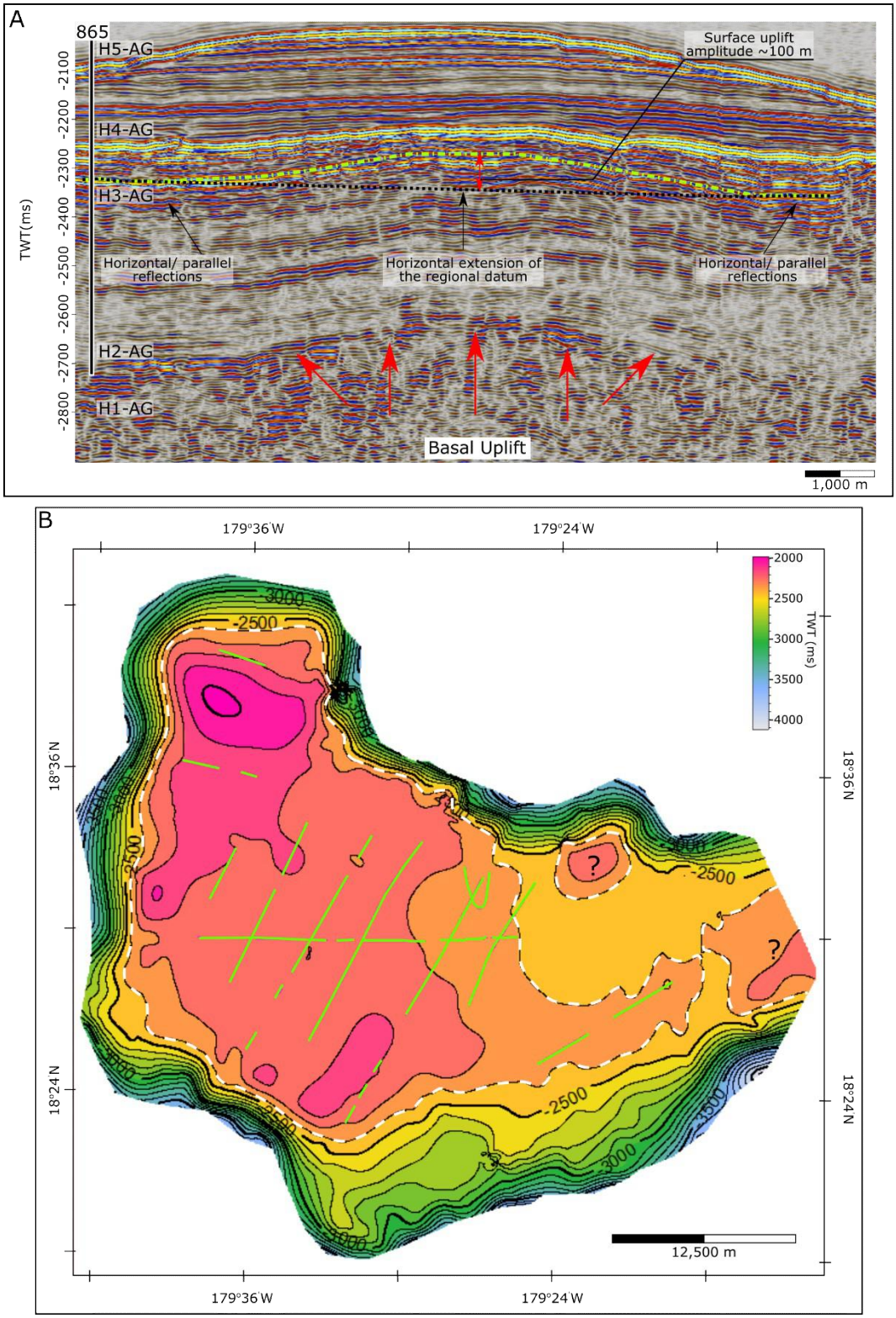


Figure 4.12. Forced folding and surface uplift associated with the magmatic emplacement in Allison Guyot. (A) Seismic amplitude profile from Allison Guyot showing the broad doming and surface uplift related to the magmatic emplacement within the Cretaceous sedimentary succession. The interpretation of the magmatic sills between H1-AG and H2-AG and the broad doming of H4-AG shows spatial alignment. Horizon H3-AG was used to interpret the forced surface uplift amplitude displaying a range of ~100 m using interval velocity of 2,650 m/s (Sager et al., 1993b). (b) TWT map of Horizon H4-AG (topmost surface of the shallow-marine Cretaceous atoll at Allison Guyot) showing the spatial alignment between interpreted sills (highlighted by lemon green lines) with the interpreted surface uplift and forced folding (highlighted by white dashed line).

4.7.1.2 Inhibition of Shallow-Marine Carbonate Production Resurgence on Re-Submerged Mid-Pacific Atolls

4.7.1.2.1 Migration off the Hotspot Swell

Tropical carbonate factories face drowning when rate of accommodation creation exceeds sediment accumulation or when growth rate is impacted by ecological disturbances (Schlager, 1981). The latest tectonic reconstruction of the Pacific Plate Line Islands system identified a new melt source region, the Larson Melt Region, responsible for the formation of the MPM (Pockalny et al., 2021). The reconstruction unveiled that, after 100 Ma (roughly ~98-95 Ma; Figure 4.3 and 4.11), the MPM began moving away from the Larson Melt Region mantle plume source where the Larson Melt Region started to enter the Northern Province. Generally, hotspot swells form as ascending mantle plumes or hot, buoyant plume material accumulates beneath the lithosphere, causing active upwelling and increased thermal buoyancy beneath the swell (Crough, 1983). As volcanic islands migrate off mantle plume sources owing to plate motion, the seafloor undergoes rapid subsidence, with rates being influenced by various factors as the speed of plate motion, the size of swells, and dynamic pressure fluctuations beneath the swell (Huppert et al., 2015, 2020; Montaggioni et al., 2023). The exact subsidence rate of the swell tail in the Larson melt region remains undetermined. Nevertheless, on the Pacific Plate, swell tail subsidence rates are notably fast, averaging ~0.4 mm/year, with a maximum rate reaching ~1 mm/year, as evidenced in the Marquesas hotspot, situated adjacent to the Larson melt region (Huppert et al., 2020). Higher rates of ~3 mm/year have been documented in the Hawaiian Islands (e.g. Sharp and Renne, 2005; Puga-Bernabéu et al., 2016). Additionally, during the Cenomanian (100-93.9 Ma), which coincides with the potential demise age range of Resolution and Allison atolls, there is well-documented evidence of eustatic sea-level rise (van der Meer et al., 2022). The rate of eustatic rise for small-scale cycles during the Cenomanian varies between ~0.1 mm/year (Gale et al., 2002) and ~0.2 up to 0.3-0.37 mm/year (Haq, 2014) and reaching up to ≥1 mm/year during the Late Cenomanian (Voigt et al., 2006) from 94.9-94.4 Ma to 94.46-94.15 Ma (Lehmann e al., 2015; Jeans et al., 2021).

Considering potential ranges of relative sea-level rise induced by swell tail subsidence and small-scale cycles of the Cenomanian sea-level rise (Table 1), we question their role in hindering shallow-marine carbonate production after re-submergence. We compare them with the vertical production rates of the main components in the MPM atoll depositional systems (Figure 4.13; Arnaud et al., 1995; Strasser et al., 1995; van Waasbergen, 1995; El-Yamani et al., 2022). The potential range of relative sea-level rise spans from 0.5 to 4 mm/year. While the majority of these potential rates of relative sea-level rise exceed production rates of carbonate components (e.g. lagoonal muds, ooids, algal microbial mats, and calci-sponges), they all fall below the vertical

growth rates of individual rudists (>10 mm/yr; Steuber et al., 1998; Figure 4.14). However, the rapid vertical growth rates of rudists don't translate into the actual sediment accumulation rate because (a) in lagoonal settings, limited support of vertically growing shells by low rates of ambient sedimentation induced frequent toppling, and (b) the constant mechanical destruction of rudists by storms and migrating bioclastic bars in open marginal settings, resulting in short-term sedimentation rates that are considerably lower than the vertical growth rate (Gili and Skelton 1999; Steuber, 2000).

Almost all the inferred potential ranges of relative sea-level rise in the MPM appear to surpass the growth potential of reefs and carbonate platforms (0.6 mm/year for 10^2–10^5 years; Schlager, 1999; Table 1) which would offer a plausible explanation for prolonged carbonate platform weakening and drowning of the Cretaceous atolls in the MPM (Resolution and Allison guyots; Figure 4.14). A similar case was observed in the northeastern Australian margin where drowning was due to a >50 m/m.y relative sea-level rise (DiCaprio et al., 2010). Similar observations were made in the Hawaii-Emperor atolls, where the latitudinal overlap between swell subsidence and drowning indicated that the migration of atolls off the swell was the primary factor leading to drowning (Huppert et al., 2020).

Subsidence Induced by Hotspot Swell Migration	Small scale and 3rd order cycles during the Cenomanian			
	~0.1 mm/year (Gale et al., 2002)	~0.2 mm/year (Haq, 2014)	~0.3 mm/year (Haq, 2014)	~ 1 mm/year (Voigt et al., 2006)
The Pacific Plate swell tail average subsidence rates (~0.4 mm/yr; Huppert et al., 2020)	0.5	0.6	0.7	1.4
Marquesas hotspot swell tail maximum subsidence rate (~1 mm/yr; Huppert et al., 2020)	1.1	1.2	1.3	2
Hawaiian hotspot subsidence rate (~3 mm/yr; Ludwig et al., 1991; Sharp and Renne, 2005; Puga-Bernabéu et al., 2016)	3.1	3.2	3.3	4

Table 1. The twelve possible relative sea level rise rates during the Cenomanian Sea level rise and the dynamic subsidence induced from the migration of the Mid-Pacific Atolls away off the Larson Melt Region hotspot swell.

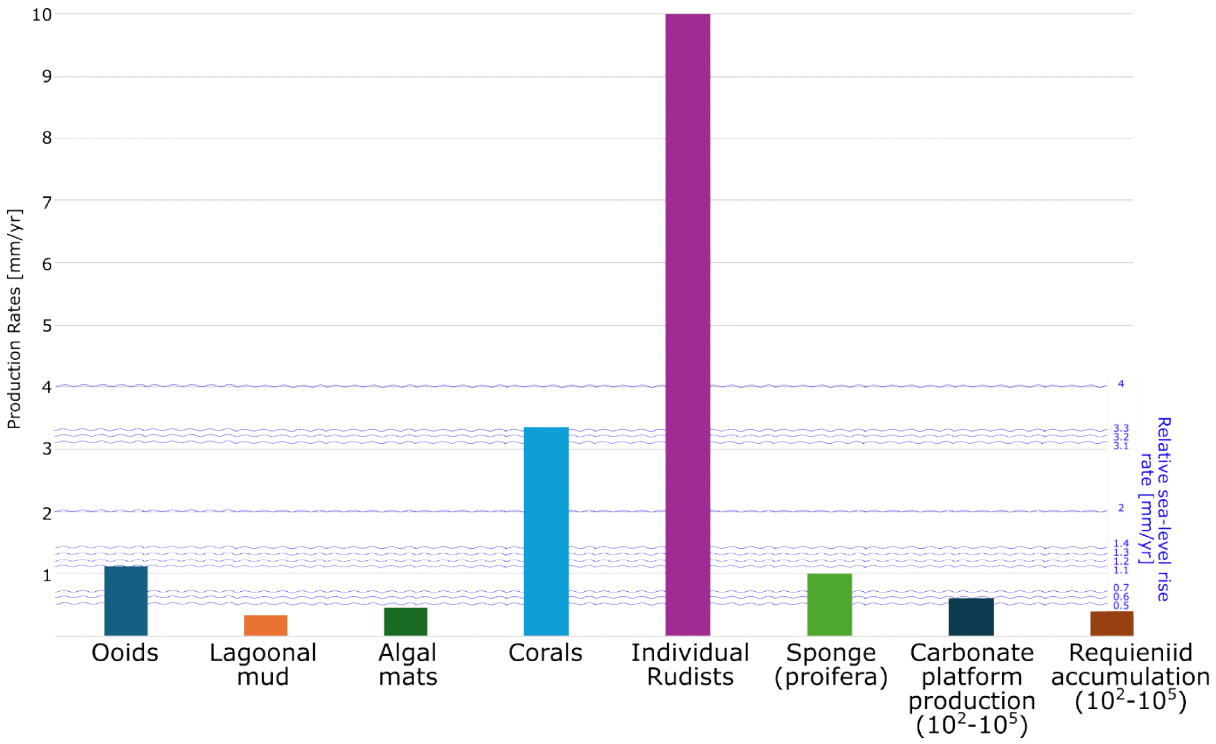


Figure 4.13. The growth potential of the different carbonate grains in the Mid-Pacific atolls versus the possible rates of relative sea level rise during the Cenomanian eustatic rise and the dynamic subsidence induced from the migration of the Mid-Pacific atolls away off the Larson Melt Region hotspot swell. Carbonate grains and their associated production rates are: Ooid (Harris, 1979), Lagoonal Muds (Broecker and Takahashi, 1966; Robbins et al., 1997), Algal Mats (Chivas et al. 1990; Reid and Browne, 1991; Planavsky and Ginsburg, 2009; Jahnert and Collins, 2012), Corals (Gischler et al., 2023), Individual Rudists (Steuber et al., 1998), Calci-sponge (proifera) (Fallon and Guilderson, 2005), carbonate production for intervals of 10^2–10^5 yr (Schlager 1999), Requieniid vertical accumulation rate over 10^4-10^5 yr (Masse and Fenerci-Masse, 2006).

4.7.1.2.2 Paleoenvironmental Conditions after Re-submergence

Shallow-marine carbonate platform demise only requires a rate of relative sea-level rise that is higher than the carbonate accumulation rate at the initial water depth which would cause continuous negative feedbacks to the sediment accumulation rates (Kim et al., 2012). In the MPM, alongside the aforementioned relative sea-level rise, the accumulation rates of shallow-marine carbonates on the atolls subsequent to re-submergence seemed to be affected by three suppressing factors: (a) production lag time, (b) equatorial hurricanes and tropical cyclones, and (c) ocean-surface currents. Firstly, when a carbonate factory is re-submerged after exposure, its gradual initiation is marked by slow growth succeeded by rapid expansion (Schlager, 2005), following a sigmoidal curve (Enrique, 1976; Schlager, 2005; Kim et al., 2012). This lag time is often estimated to be ~2->5 kyr (Montaggioni, 2005; Schlager, 2005; Kemp and Sadler, 2014), although variations exist, ranging from 10(s) kyr (Strasser, 2015) to millions of years (Hottinger, 1989).

Secondly, At the same age of the relative sea-level rise at the MPM, and between the Cenomanian to early Turonian (98-93.5 Ma), Allison and Resolution guyots were situated within the latitudinal

range of 11-8°S (Winterer and Sager, 1995) and 8.90-5.90°S (Torsvik et al., 2012), respectively. Plotting these locations onto global palaeo-climatic modelling maps (Agustsdottir et al., 1999; Valdes et al., 2021; APPENDIX C Figure C3 and C4), reveals that Resolution and Allison guyots were exposed to equatorial hurricanes and tropical cyclones year-round. Such conditions would induce off-bank sediment transport and reduction in sediment accumulation (e.g. Toomey et al., 2013), reefal cover destruction and reduction (e.g. Gardner et al., 2005), and ultimately, the demise of carbonate banks (e.g. Macintyre et al., 2007). The persistent rise in relative sea level in MPM atolls during the Cenomanian would have increased water depth, resulting in decreased energy dissipation from waves, currents, and storms. This would favour the formation of platform margin gravels over intact bioconstruction, leading to continuous platform margin retrogradation (Blanchon et al., 2017). Storm-induced reworking of Cretaceous rudists would redistribute much of them, forming thin lenticular rudist congregations, significantly reducing their vertical accumulation rates over geological time by orders of magnitude (Masse and Fenerci-Masse, 2006; Gili and Götz, 2018).

Thirdly, the MPM atolls were influenced by the circumglobal equatorial current system, evident through Tethyan planktonic and benthic foraminifera records (Gordon et al., 1973; Arnaud-Vanneau and Sliter, 1995). These ocean-surface currents closely resemble modern equatorial currents (Gordon et al., 1973). Global paleoclimate models for the Mid-Cretaceous (100-97 Ma; Poulsen et al., 1999; Valdes et al., 2021) indicate that equatorial ocean-surface currents over the MPM latitudes had an average velocity of 15-20 up to 25-30 cm/s (APPENDIX C Figure C5). However, simulations of the Late Cenomanian and Cenomanian-Turonian boundary (95-94 Ma) depicted intensified ocean-surface circulation and robust wind-driven circumglobal equatorial currents compared to today (Ladant et al., 2020; Laugié et al., 2020). Modern equatorial currents have an average velocity of ~20-50 to 50-60 cm/s (10°S to 3-4°N; Rougerie et al., 1997; Reddy, 2001). Considering the anticipated similarity or even increased strength of Cretaceous surface atmospheric winds and ocean currents compared to modern conditions (Hay and DeConto, 1999; Bush and Philander, 1997; Valdes et al., 2021), we suggest that MPM atolls encountered circumglobal equatorial ocean-surface currents with average velocities ~20-60 cm/s. Such velocities overlap with critical thresholds for entraining various-sized carbonate grains (Table. 2).

The platform tops of the MPM atolls were prone to disturbances caused by storms, hurricanes, and currents, resulting in sediment loss (Hughes, 2000; Skelton and Gili, 2012; Bover-Arnal et al., 2015). This vulnerability is attributed to the absence of well-defined bioconstructed reefal margins (Winterer and Sager, 1995; El-Yamani et al., 2022) because rudists are gregarious sediment-dwellers, lacking the ability to form reefal frameworks with any topographic relief (Gili et al., 1995).

Therefore, newly produced sediments, rudist larvae, and other sessile organisms may have been transported away from the platforms, impeding their settling and vertical accumulation (Stoner, 1990; Fraschetti et al., 2002; Reolid et al., 2020; Ling et al., 2021). This could explain the presence of off-bank transported shallow-water benthic foraminifers of Cenomanian age in basinal deposits at Site 463, ~25 km from Resolution Guyot (Winterer and Sager, 1995). The culmination of these factors (i.e. production lag time, equatorial hurricanes and storms, ocean-surface currents, absence of bioconstructed reefal margins) is proposed to contribute to the relative sea-level rise at the MPM atolls, surpassing the rate of carbonate accumulation by introducing continuous negative feedback (Figure 4.14). Consequently, their platform summits underwent gradual deepening, exceeding depths beyond the critical threshold for shallow-water carbonate producers (10-15 m; Schlager, 1981) such as rudists, benthic fossils inhabiting shallow marine waters (~10-15 m; Poulsen et al., 1999), despite their maximum growth potential (Kim et al., 2012).

The findings presented in this paper regarding the demise history of the MPM atolls (Resolution and Allison guyots) align with Hypothesis 1, "death-by-emergence-and-submergence" when compared to previously proposed demise hypotheses. The discussion tackles the key uncertainties within Hypothesis 1 (van Waasbergen and Winterer, 1993; Winterer et al., 1993; Winterer and Sager, 1995; Winterer, 1998) that were central in challenging the hypothesis (Jenkyns and Wilson, 1999). Firstly, the present paper clarified the cause of emergence, whether tectonic or eustatic. Secondly, it explained why further shallow-water sediments did not accumulate on the MPM atolls after re-submergence. The study showed evidence on (a) how magmatism primarily led to the subaerial exposure of the MPM, addressing the first question, and (b) how the migration away from the hotspot swell and the concurrent eustatic rise predominantly caused the drowning after re-submergence, answering the second question.

Grain types	Bivalve and gastropod shells Fick et al. (2020)	Calcareous Sand Smith and Cheung (2005)	Larger Benthic Foraminifera Yordanova and Hohenegger (2007)	Biogenic Sands Paphitis et al. (2002)	Carbonate Sands Prager et al. (1996)	Coral Reef Sediment Bian et al. (2023)
Critical threshold horizontal velocity	0.08-0.25 m/s	0.16-0.23 m/s	0.10-0.18 m/s	0.20-0.33 m/s	0.24-0.30 m/s	0.20-0.57 m/s
Size range	Sieve diameter ~2-16 mm	Median diameter ~0.2-0.76 mm	test width ~0.5-2 mm	Sieve Diameter 0.33-0.8 mm	Median grain 0.5-1.1 mm	Median sieve diameter 0.58-4.50 mm

Table 2. A summary of the critical threshold horizontal velocity of different carbonate grain types (to be entrained) and their corresponding size range.

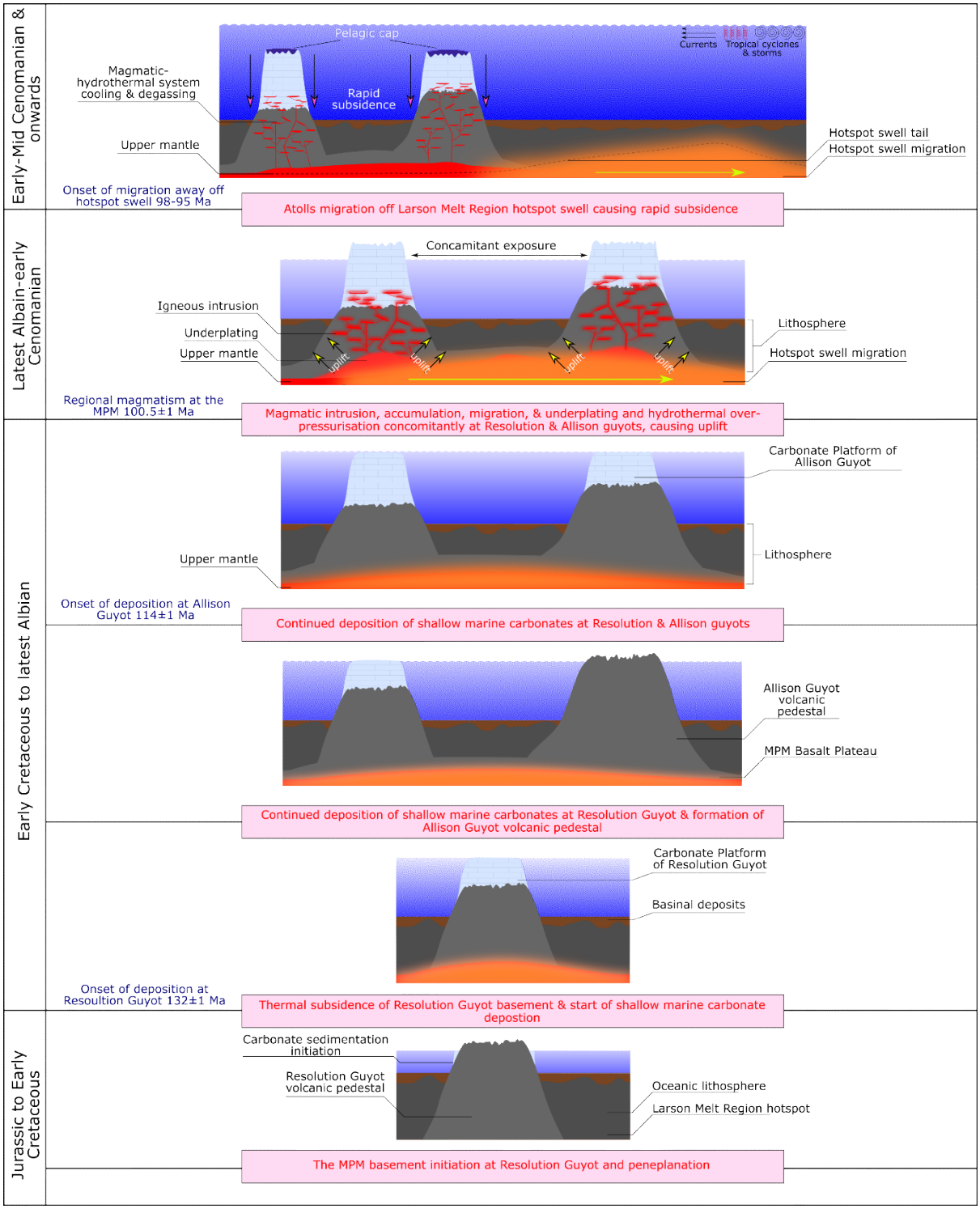


Figure 4.14. The demise mechanism of the Cretaceous Pacific atolls showing the journey of the Mid-Pacific guyots from (1) thermal subsidence of the basement and (2) carbonate deposition to (3) the magmatic emplacement, the associated uplift, and (4) the cessation of the shallow marine carbonate deposition to (5) the rapid subsidence of the basement after cooling of magma, degassing of the associated hydrothermal system, and moving of the Mid-Pacific guyots away from the hotspot swell. The black dashed line shows the associated hotspot swell dynamic uplift.

4.7.2 Comparing the Proposed Demise Mechanism with other Western Pacific Cretaceous Atolls

Here, we investigate the applicability of our proposed mechanism for demise through rapid subsidence following hotspot migration to other Cretaceous atolls in the West Pacific. Beginning with Wodejebato Guyot, palaeotectonic reconstructions indicate that between 75-65 Ma, the northern Marshall Islands moved away from hotspot swells of Tahiti, Macdonald, Rurutu, and Rarotonga, leading to rapid subsidence in the region (Turner and Jarrard, 1982; Duncan and Clague, 1985; Lincoln et al., 1993). This timeframe aligns with the demise ages of Wodejebato Guyot at ~69±1 Ma. During that time, a significant global sea-level rise is documented (the mid-Maastrichtian event eustatic rise: 69.5-67.5 Ma; Dubicka et al., 2024). Additionally, equatorial ocean-surface currents also influenced Wodejebato (40-70 cm/s: APPENDIX C Figure C6). In basinal deposits near Wodejebato, off-bank transported shallow-water carbonate sediments from the Late Campanian-early Maastrichtian are found (Site 869; Sager et al., 1993c; Sliter, 1995), overlapping with its demise age. Thus, similar to the MPM atolls, the rapid subsidence from hotspot migration, the mid-Maastrichtian eustatic rise, and equatorial ocean-surface currents may explain Wodejebato's drowning. In contrast, MIT Guyot may not be aligning with our model as it is a solitary seamount and unrelated to WPSP seamount trails and hotspots (Koppers et al., 2003). However, in the late Albian (~105-101 Ma) sea level began to rise rapidly (Haq, 2014; Bąk et al., 2016). Also, MIT atoll during its demise was influenced by strong equatorial currents (40-60 cm/s: APPENDIX C Figure C7).

Moving to Takuyo-Daisan Guyot, it is part of the Japanese Seamount Trail, displaying a hotspot track and age progression consistent with a singular origin (Koppers et al., 1995, 2003; APPENDIX C Figure C8). This age progression reflects the migration of Takuyo-Daisan atoll off the hotspot swell between 117.5±1.1 Ma and 108.3±2 Ma, evidenced from the age of the next volcanic island in the trail (Winterer Guyot; Koppers et al., 2003). This movement away from the hotspot swell coupled with the early Albian global sea-level rise (Haq et al., 1987; Föllmi, 2012; Haq, 2014; Jaillard et al., 2019) may result in rapid subsidence, as in MPM atolls, in this study and the Hawaii-Emperor chain in Huppert et al. (2020). Having said that, our proposed demise mechanism seems to demonstrate good relevance to other Cretaceous Western Pacific atolls.

4.7.3 The Role of Excess Warmth in Peri-equatorial Oceans in Cretaceous Atolls Demise: Lessons to the Future Global Warming

The aforementioned discussions have introduced an alternative explanation to the demise of Cretaceous Pacific Atolls. This raises questions regarding the potential role of Cretaceous excess

warmth in peri-equatorial oceans in reducing the carbonate production rates on the Pacific Atolls and ultimately leading to their demise. To test this, we utilise Cretaceous global paleoclimate modelling data from Valdes et al. (2021) and sea-surface temperature reconstructions from O'Brien et al. (2017). By integrating these datasets with palaeogeographic reconstructions of the Cretaceous Pacific atolls, several key observations emerge (Table. 3): (a) SSTs across lifespan and demise of the atolls typically range from ~30-34°C, occasionally reaching a maximum of ~35°C, (b) according to the estimates from Valdes et al. (2021) SSTs remain relatively constant throughout the lifespan and demise of the atolls, except for Wodejebato Guyot, where a decrease is observed, (c) there is a decrease in SSTs is consistent across all atolls according to the estimates from O'Brien et al. (2017), (d) the warmest 3-months SSTs based on the modelling results of Valdes et al. (2021) are not exceeding 36°C. Notably, all these SSTs ranges align with the optimal conditions for Cretaceous rudist-bearing carbonate platforms (~30-37°C; Steuber et al., 2005; Walliser and Schöne, 2020; Schmitt et al., 2022), indicating their potential adaptability to such temperatures. Other Cretaceous rudist-bearing carbonate platforms thrived even at much higher SSTs (e.g. the Cupidito unit in NE Mexico, ~31-48°C, Torres de la Cruz et al., 2020; the Cenomanian-Turonian rudist-bearing carbonates in Sinai, Egypt, ~35-41°C, El-Shazly et al., 2011).

The present study challenges the idea that the demise of Cretaceous Western Pacific atolls was due to excess warmth in shallow peri-equatorial waters. The assumption that Cretaceous organisms were similarly susceptible to thermal stress as modern coral bleaching considering that some Cretaceous rudists may have possessed zooxanthellae is refuted (Jenkyns and Wilson, 1999). Instead, the warm SSTs during the Mid-Late Cretaceous (~30-34°C up to 35-36°C) appear to be habitable for shallow-marine carbonate-secreting organisms on the Pacific atolls, indicating their thermal resilience. This resilience aligns with suggestions that episodic production of warm low-latitude SSTs >30°C favoured the proliferation of rudists and carbonate platform expansion during the Cretaceous (Johnson et al., 1996; Johnson, 2002). Similarly, palaeoecological modelling of the Cretaceous greenhouse highlighted the flourishing of T-factory carbonates around the equator at SSTs ~31-34°C (Michel et al., 2019; Pohl et al., 2019).

The findings prompt questions about the potential of Cretaceous organisms as analogues for future refugia of thermal-stress tolerant modern tropical counterparts This consideration is particularly pertinent given the projected rise in SSTs under the RCP8.5 scenario, which would resemble the Cretaceous levels (>30-32°C; Zhang et al., 2020b). Extrapolating ecological patterns and responses between Cretaceous and modern taxa remains poorly understood, however insights from their rise and demise can help assessing future extinction risks for modern biota under climate change (Bryers et al., 2022; Steuber et al., 2023). In the modern world, many carbonate-secreting

organisms struggle to thrive in temperatures >30°C, although studies have shown that some species can tolerate higher temperatures, up to ~40°C (Cacciapaglia and van Woesik, 2015; Schmidt et al., 2016; Weinmann and Langer, 2017). Understanding how ancient ecosystems coped with similar climate changes is crucial in predicting the fate of modern ecosystems. Therefore, it is important to consider how the Cretaceous organisms adapted to the Cretaceous green- and hot-house palaeo-climate when assessing the impacts of global warming on their modern counterparts. Additionally, evaluating how ecological responses of Cretaceous organisms can be extrapolated to modern thermally resilient biota, especially in equatorial banks and atolls with similar depositional settings, is essential.

Initiation Age [Ma]	Demise Age [Ma]	Time steps [Ma]	ODP Site	Modern Latitude	Modern Longitude	Palaeo Latitude	Palaeo Longitude	Palaeogeographic Reconstruction Reference	SST[1]	SST[2]	Warmest SST[3]	Warmest SST[4]
MIT Guyot												
119±2 (Wilson et al., 1998)	101±2 (Wilson et al., 1998)	102	878	27°N	152°E	2°S	166°W	Scotese and Wright (2018)	32-34°	27-28°	32-34°	34-36°
		107				3°S	167°W		〃	---------	〃	32-34°
		111				4°S	170°W		〃	30-31°	〃	34-36°
		115.8				7°S	170°W		〃	29-30°	〃	32-34°
		121.8				10°S	172°W		〃	31-32°	〃	34-36°
Wodejebato Guyot												
76±1 (Wilson et al., 1998)	69±1 (Wilson et al., 1998)	69	874-872	12°N	165°E	2°S	161°W	Scotese and Wright (2018)	30-32°	27-28°	30-32°	26-28
		75				5°S	156°W		32-34°	29-30°	32-34°	32-34°
Takuyo-Daisan Guyot												
118±2 (Wilson et al., 1998)	111±2 (Wilson et al., 1998)	111	879	34°N	144°E	5°N	174°W	Scotese and Wright (2018)	32-34°	30-31°	32-34°	34-36°
		115.8				2°N	176°W		30-32°	29-30°	30-32°	30-32°
		121.8				1°N	176°W		〃	31-32°	〃	〃
Resolution Guyot												
132±1 (El-Yamani et al., 2022)	100.4±1 (El-Yamani et al., 2022)	98-93.5	866-868	21.4°N	174.4°E	8-5.9°S	143°W	Winterer and Sager (1995), and Torsvik et al. (2012)	32-34°	≤35 °	32-34°	32-34°
		102				12°S	147°W	Scotese and Wright (2018)	〃	27-28°	〃	34-36°
		107				13°S	150°W		〃	---------	〃	〃
		111				14°S	151°W		〃	30-3°	〃	〃
		115				16°S	151°W		〃	29-30°	〃	32-34°
		121.8				18°S	151°W		〃	31-32°	〃	34-36°
		127.2				20°S	151°W		30-32°	34-35°	〃	32-34°
Allison Guyot												
114.4±1 (This study)	100.12±1 (This study)	98-93.5	865	18.5 N	179.5 W	11-8.9°S	140°W	Winterer and Sager (1995), and Torsvik et al. (2012)	32-34°	≤35°	32-34°	32-34°
		102				16°S	143°W	Scotese and Wright (2018)	〃	---------	32-34°	34-36°
		107				17°S	144°W		〃		32-34°	34-36°
		111				17°S	146°W		〃	30-31°	32-34°	34-36°

Table 3. A summary of the initiation and demise ages of five Pacific Cretaceous guyots. It shows their ODP sites, modern and palaeogeographical locations (based on paleogeographic reconstructions by Scotese and Wright, 2018, Winterer and Sager, 1995, and Torsvik et al., 2012), and the corresponding sea surface temperatures (SST[1] from Valdes et al., 2021 palaeo-climatic modelling; https://www.paleo.bristol.ac.uk/ummodel/users/Valdes_et_al_2021/new2/; SST[2] from O'Brien et al., 2017 from TEX_{86} and planktonic foraminiferal oxygen isotopes) at various time steps through their lifespan as atolls; Warmest SST[3] and Warmest SST[4] show the warmest 3-months SSTs from palaeo-climatic modelling of Valdes et al. (2021) using smoothed CO_2 and Foster et al. (2017) Phanerozoic CO_2 curves, respectively. Refer to APPENDIX C Figure C9 to C12 for the global SST[1] during age intervals across the lifespans of the different guyot.

4.8 Conclusion

The study investigated the demise of Mid-Pacific Cretaceous atolls to test whether climate-related demise scenarios are necessary, identifying several interconnected factors. During the late Albian to early Cenomanian, the cessation of carbonate sedimentation is linked to magmatic events and widespread volcanism in the Western Pacific. This extensive volcanism led to uplift and halted shallow-marine carbonate deposition on these atolls by causing subaerial exposure. After re-submergence, the atolls had been migrated away off Larson Melt Region Hotspot Swell which, in addition to the Cenomanian eustatic rise, led to rapid relative sea level rise. Concomitantly, vertical accumulation rates at MPM atolls after re-submergence appeared to be brought down by off-bank sediment transport through equatorial hurricanes, ocean-surface currents, production lag time and the lack of true reefal bioconstructed margins. The convergence of these factors supported making the rapid relative sea-level rise at Mid-Pacific Cretaceous atolls to outpace the rate of carbonate accumulation through introducing continuous negative feedback. As a result, the uppermost section of the carbonate platform gradually deepened, eventually reaching depths beyond the critical threshold for most shallow-water carbonate producers, despite the maximum growth potential of carbonate production. The present paper, using published global paleoclimate data, sea-surface temperature reconstructions, and palaeogeographic reconstructions, showed that the SSTs across lifespan and demise of the atolls typically remain relatively constant without changing ranging from ~30-34°C up to ~35-≤36°C. In some cases, there was a decrease in the SSTs across lifespan and demise of the atolls. These findings challenge the notion that the Cretaceous green- and hot-house equatorial SSTs were detrimental to the Cretaceous carbonate-secreting organisms, indicating their potential resilience to higher temperatures. As a result, the study proposes with caution that the Cretaceous Pacific atolls may serve as valuable analogues for assessing the potential impacts of future climate change on some of the heat-tolerant shallow-marine carbonate producers in the modern tropical carbonate platforms. This paper supports the hypothesis of "death-by-emergence-and-submergence," for the demise of MPM atolls. It addresses the main uncertainties within the hypothesis previously challenged by other researchers; the cause of emergence and why shallow-water sediments didn't accumulate after re-submergence. It presents clear evidence that magmatism primarily led to subaerial exposure, while migration away from the hotspot swell and eustatic rise caused drowning after re-submergence. The study adds to recent work suggesting that rapid subsidence resulting from islands migrating away from a mantle source of swell uplift (dynamic uplift) may provide a solution to the paradox of carbonate platform drowning and thus previous explanations, such as rapid pulses of eustatic rise or catastrophic palaeoenvironmental changes in equatorial regions, may not be necessary.

CHAPTER FIVE

DISCUSSION, FUTURE WORK, AND CONCLUSION

This study was motivated by the need to elucidate the processes governing the depositional settings, stratigraphic evolution, subaerial exposure, island dolomitisation, and drowning of the Cretaceous ICPs in order to understand how those systems were functioning during the Cretaceous green- and hot-house climate. The geological settings of the Pacific Cretaceous ICPs were very suitable to do this study because (a) they were not exposed to terrigenous inputs, (b) haven't been deeply buried, (c) haven't suffered from destructive tectonism (i.e. Figure 5.1). This context of completely drowned volcanically extinct seamounts (Staudigel and Clague, 2010), with minimised erosion, allowed for the observation and interpretation of primary depositional, diagenetic, and drowning processes with minimal masking by later destructive geological processes.

The research presented in my thesis provides new insights into the evolution of the MPM Cretaceous ICPs from their genesis to demise across their subaerial exposure and island dolomitisation. Employing an integrative approach, I utilised core-log-seismic data and comparison with both modern and ancient analogues to illuminate the depositional settings, stratigraphic evolution, and karstification at Resolution Guyot (Chapter 2). Subsequently, I presented a comprehensive database highlighting the scarcity of island dolomites in Cretaceous ICPs and a study investigating the formation of island dolostones in the Mid-Pacific Cretaceous ICPs through seismic-reflection and geochemical analyses (Chapter 3). Finally, In Chapter 4, I revealed the interplay between magmatism, karstification, and hotspot migration, along with the demise of the Pacific Cretaceous ICPs, through integration of core-log-seismic data, palaeotectonic reconstruction, and palaeoclimatic models.

The key implications derived from the studies presented in my thesis and their wider implications are presented in this chapter, with the objective of addressing the fundamental questions raised in this research (in Subsection 1.3), namely (a) What are the controlling factors on the stratigraphic evolution and large-scale karstification in the Cretaceous Pacific ICPs?, (b) How did scarce dolomitisation occur during the Cretaceous Calcitic ocean just in a few Pacific ICPs?, (c) What controlled the demise of the Cretaceous Pacific ICPs? Are they suitable analogues for thermal-stress intolerant or tolerant modern tropical atolls under the human-induced future climate changes? I end this chapter with possibilities for future work.

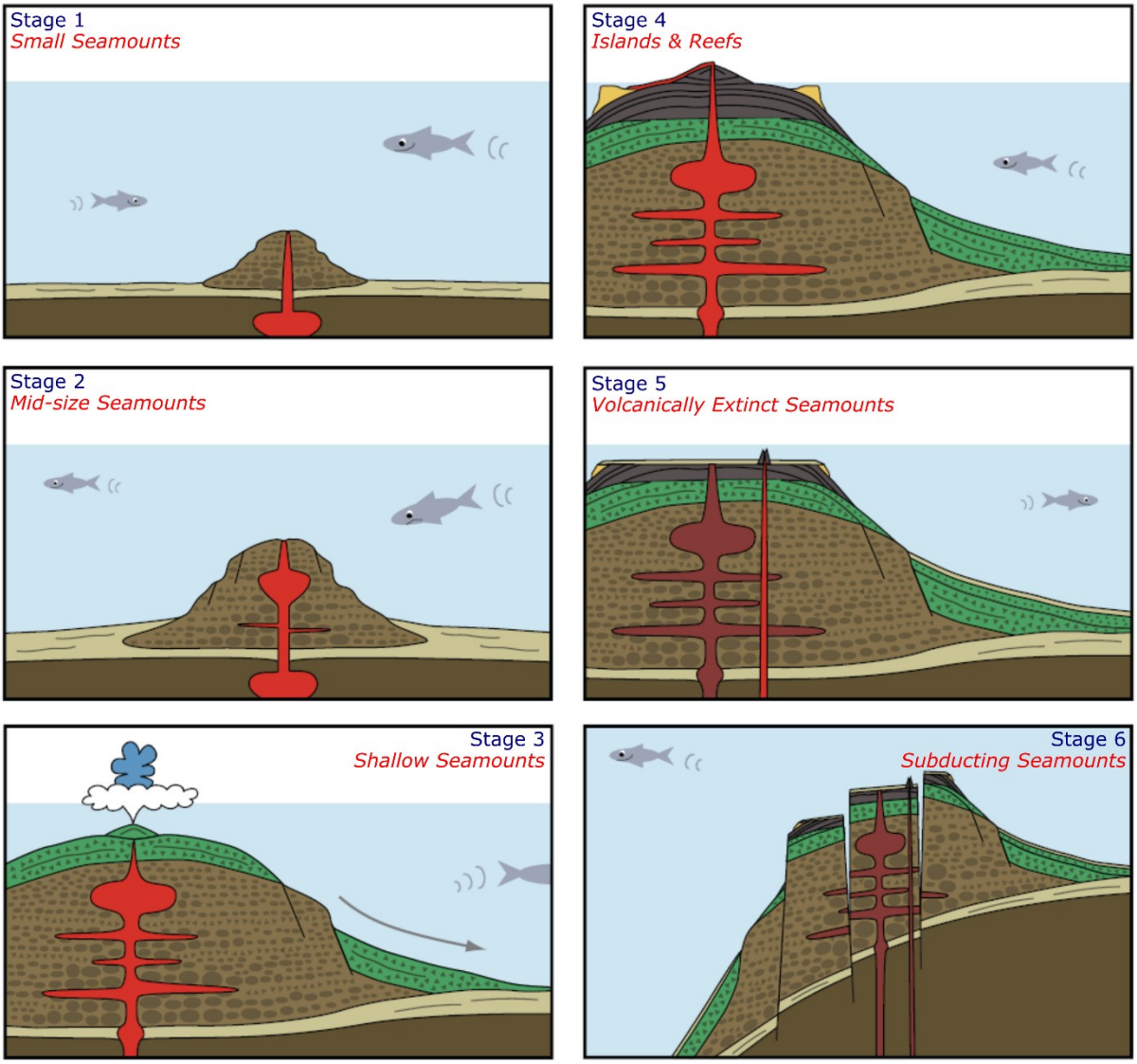


Figure 5.1 Cycle of the birth, rise, caldera-formation, emergence, subsidence, and the collapse of a seamount, ending with fragmentation of the seamounts in subduction zones (modified from Staudigel and Clague, 2010). The Pacific Cretaceous isolated carbonate platforms are represented by stage 5 (volcanically extinct seamounts) which is prior to the destructive subduction tectonism in stage 6.

5.1 General Synthesis

5.1.1 What are the controlling factors on the stratigraphic evolution and large-scale karstification in the Pacific Cretaceous ICPs?

In Chapter 2 (subsection 2.7.1), the interpolation of (a) the palaeogeographic distribution of the identified seismic facies and (b) their interpreted depositional environments from core and log data, using information from modern analogues, shows that the Cretaceous ICPs include key depositional elements which are as follows (Figure 2.9): (a) The platform margin mounded facies extend laterally for approximately 700–2,000 metres (sand beach barrier of peloidal and ooiltic grainstones and coarse-grained rudist shell debris with sponge and rudist build-ups). (b) Onlapping facies behind the margin, the back-margin apron spans at least 650 metres wide (wash-over deposits of coarse-grained floatstones and rudstones with shell debris and rip-up clasts). (c) Onlapping facies in front of the margin, the upper-slope fore-reef facies has a width of about 400–800 metres (sponge and rudist build-ups). (d) Inside the platform, a lagoon is encircled behind the margin covering around 20,000 metres width (cyclic packstone–wackestone and mudstone lagoonal lithofacies) with mounded patch reefs and rudist meadows facies ~500 metres wide. (e) Within the platform margin facies, back shoals may occur, either as part of the platform margin or a back-margin apron (cross-laminated well-sorted oolitic grainstones). (f) Platform slopes surrounding Resolution Guyot, were prone to producing MTDs extending for tens of kilometres (clastic rubbles of limestones and radiolarian limestones). (g) Down-slope contourite drifts encircle the platform and extend for tens of kilometres (nannofossil ooze). A significant implication is raised from my developed 3D depositional model of Resolution Guyot. In comparison with the detailed sedimentological model of Dunquin South Cretaceous ICP in the middle of the Porcupine Basin in the North Atlantic Ocean (Figure 5.2), which relies on a combination of three-dimensional time migrated seismic data and attribute blending (relative acoustic impedance, envelope, chaos, spectral decomposition, amplitude, and time maps; Gomez et al., 2022), the 3D model of Resolution Guyot seems almost identical to Dunquin South Cretaceous ICP, sharing similar facies and depositional settings. This would imply that my proposed depositional model has wide applicability to Cretaceous ICPs across different geological settings. The detailed seismic facies templet can offer guidance in interpreting other Cretaceous ICPs across different geological settings which would tackle the absence of appropriate analogues for Cretaceous ICPs in frontier areas such as (the East Mediterranean and the Atlantic margins of Namibia and South Africa).

The stacking pattern of the platform margin and the identified sequence boundaries and surfaces revealed that the stratigraphic evolution of the MPM Cretaceous ICPs was influenced by various

factors (Subsection 2.7.2; Figure 2.7 and 2.8), including (a) Cretaceous eustasy, (b) changes in the Cretaceous neritic carbonate production rates, (c) magmatism, (d) subsidence rate, and (e) ocean chemistry. This contrasts with previous suggestions that their stratigraphic evolution was solely controlled by global sea level changes (Arnaud et al., 1995). Evidence supporting this includes key seismic-stratigraphic surfaces aligning closely with known eustatic changes in the Cretaceous, as well as the timing of transgressive and highstand seismic units corresponding to specific periods of sea-level change. Furthermore, the rapid initial subsidence combined with the Hauterivian long-term sea-level rise facilitated the deposition of the initial transgressive seismic unit. Changes in the global neritic carbonate production rates also appear to have influenced the stratigraphic evolution in the MPM Cretaceous ICPs. The study by Pohl et al. (2020) indicates a peak between approximately 120 Ma and 80 Ma, preceded by a rise in production between about 130 Ma and 120 Ma. In combination with the Barremian long-term sea-level fall and subsequent stasis to the late Albian, and the gradual decrease in subsidence over time, the available accommodation space was limited which reflected in the formation of two thick highstand seismic units. Despite these conditions, two transgressive seismic units were formed during that time which can be attributed to the outpacing of the early-Aptian short-term and late-Albian long-term rises, respectively (Haq, 2014). The prevalence of oolitic beach-shoals in the transgressive seismic unit laying directly above the OAE 1a seems to be controlled by the changes in the ocean chemistry through the recovery of marine alkalinity following the acidification phase during OAE 1a similar to the Cupido platform in Mexico (Núñez-Useche et al., 2015). The interpreted subsequent magmatic activity(ies) intruding through the sedimentary succession might have impacted the evolution and demise of the atoll by altering subsidence rates and causing environmental perturbations. However, the interpreted magmatic events lack age controls as they have not been drilled, which hinders interpreting their impact on the stratigraphic evolution.

I provided novel insights into the subaerial exposure and karstification processes of the Cretaceous Pacific ICPs (in subsection 2.7.3). The detailed subsurface geomorphological evidence from seismic facies (karst horizons, flank-margin fracture-cave system, and sinkholes; Figure 2.10 and 2.11) and FMS logs (solution vugs and brecciated intervals; Figure 2.6) calibrated by core data suggests two distinct karstification episodes during the Albian period. Contrary to previous suggestions of submarine dissolution, the findings indicate subaerial exposure events around 105.15 ± 1 Ma and 100.45 ± 1 Ma, supported by the distribution of laterally extensive karst horizon seismic facies. The interpretation of a subaerial exposure event preceding the platform's drowning was crucial for subsequent discussions on the mechanism of the Pacific Cretaceous ICPs' demise. Syndepositional platform margin fractures played a significant role in facilitating fluid flow and the

development of flank-margin cave systems. Comparisons with karstification features in other ICPs of different ages suggest similarities in distribution patterns (Figure 5.3), however the karst horizons are thicker than their Miocene counterparts (Figure 5.4). This disparity could be attributed to the long-term, high-amplitude relative sea level changes during the Cretaceous compared to the relatively short-term, low-amplitude glacio-eustatic relative sea level changes during the Miocene. This information could be also beneficial for guiding further exploration activities in East Mediterranean plays where Cretaceous ICPs are suggested to be highly karstified (Burchette et al., 2023).

The study identifies a venting system for cross-stratal fluids in Resolution Guyot (in subsection 2.7.4). This venting system, along with karstification features, likely facilitated the ventilation of seawater across the MPM guyots. This could explain the geochemical analysis indicating active exchange between atoll pore-waters and surrounding seawater in wells located 4,000 to 6,000 m away from the platform margin (Paull et al., 1995). This underscores the dynamic interaction between subsurface fluids and the marine environment in atoll settings, with potential implications for understanding fluid flow dynamics and diagenetic processes in similar geological environment.

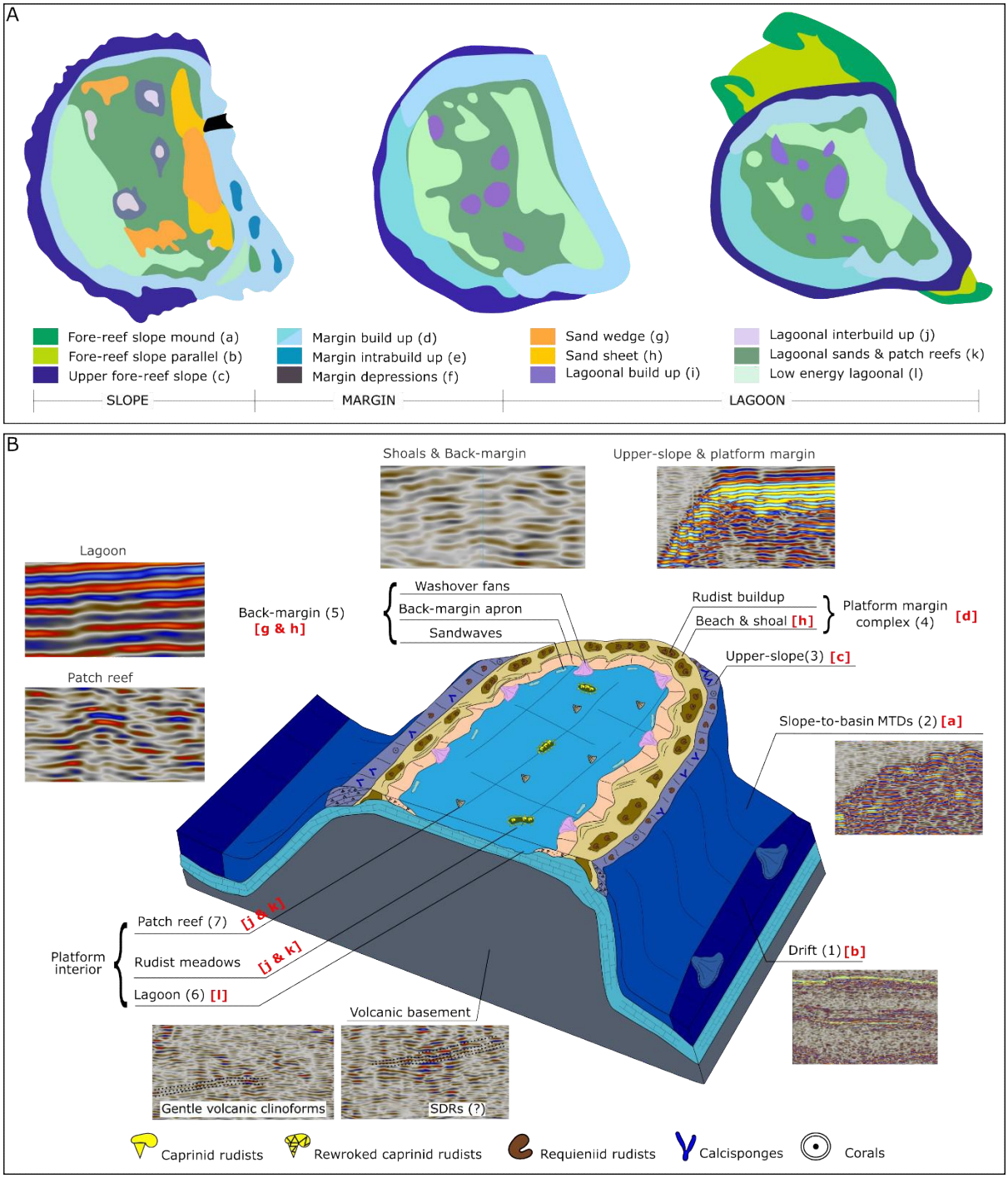


Figure 5.2 Comparison between (A) the sedimentological model of the isolated carbonate platform Dunquin South in Porcupine Basin, Ireland (modified after Gomez et al., 2022) and the 3D depositional model of Resolution Guyot carbonate atoll showing the palaeogeographic reconstruction of the different depositional environments and their corresponding seismic facies. The depositional model was generated by integrating the interpreted seismic facies with satellite images from the Glorieuses archipelago. Note that the legend of panel (A) is labelled from a to i which were used to link the highlight the similar facies in panel (B), appearing in red bold font.

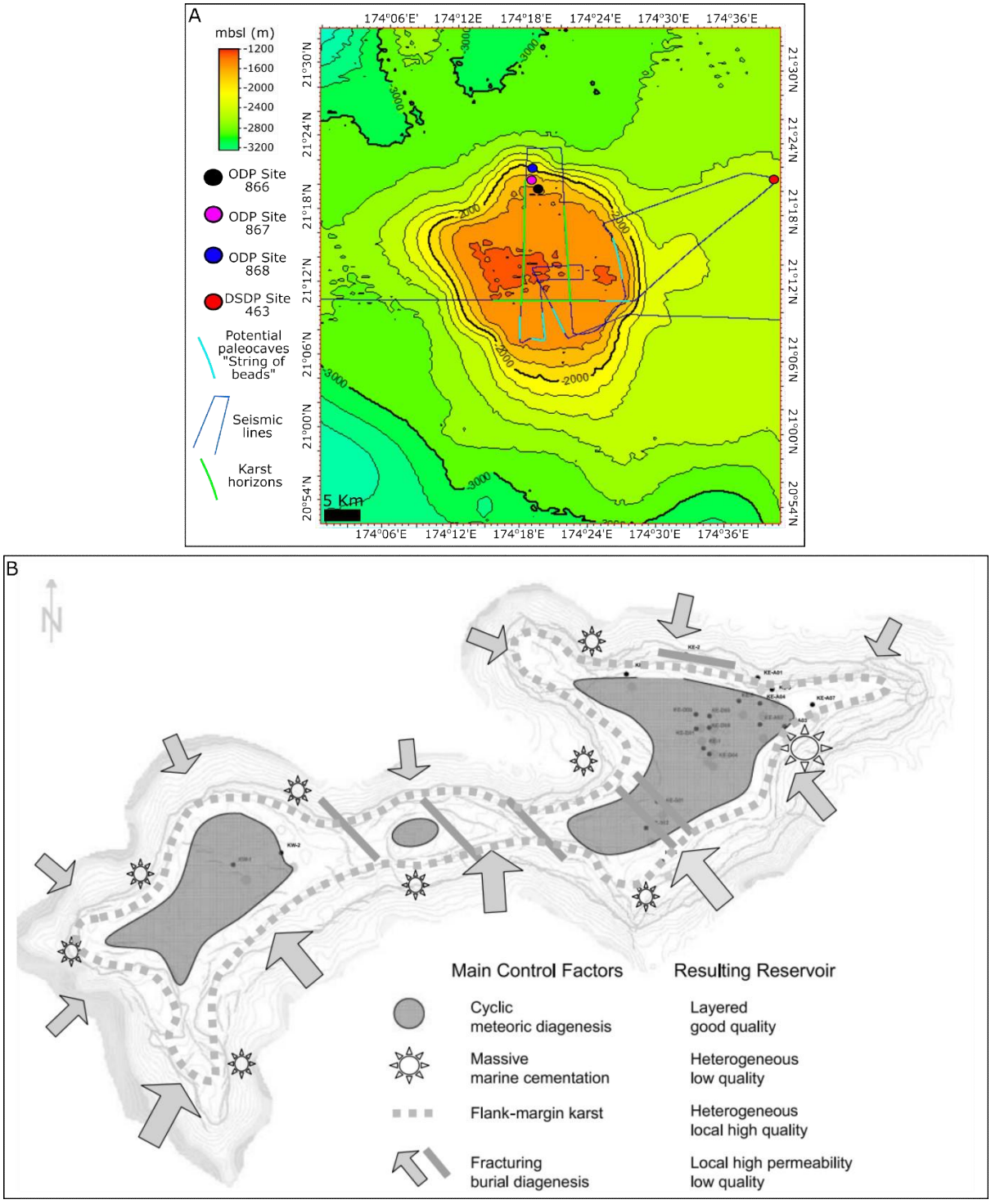


Figure 5.3 Map view of the isolated carbonate platforms of (A) Resolution Guyot and (B) Kashagan (adapted from Ronchi et al., 2010). The figure illustrates similarities in the distribution of different karstification geomorphologic features between the two platforms. In Resolution Guyot (A), laterally extensive karst horizons predominantly occur in the platform interior, matching the cyclic meteoric diagenesis zones observed in the Kashagan platform (B). The palaeocaves in Resolution Guyot are primarily located along the platform margin, influenced by flank margin fractures, a pattern closely resembling the distribution of flank-margin karst features in the Kashagan platform (B).

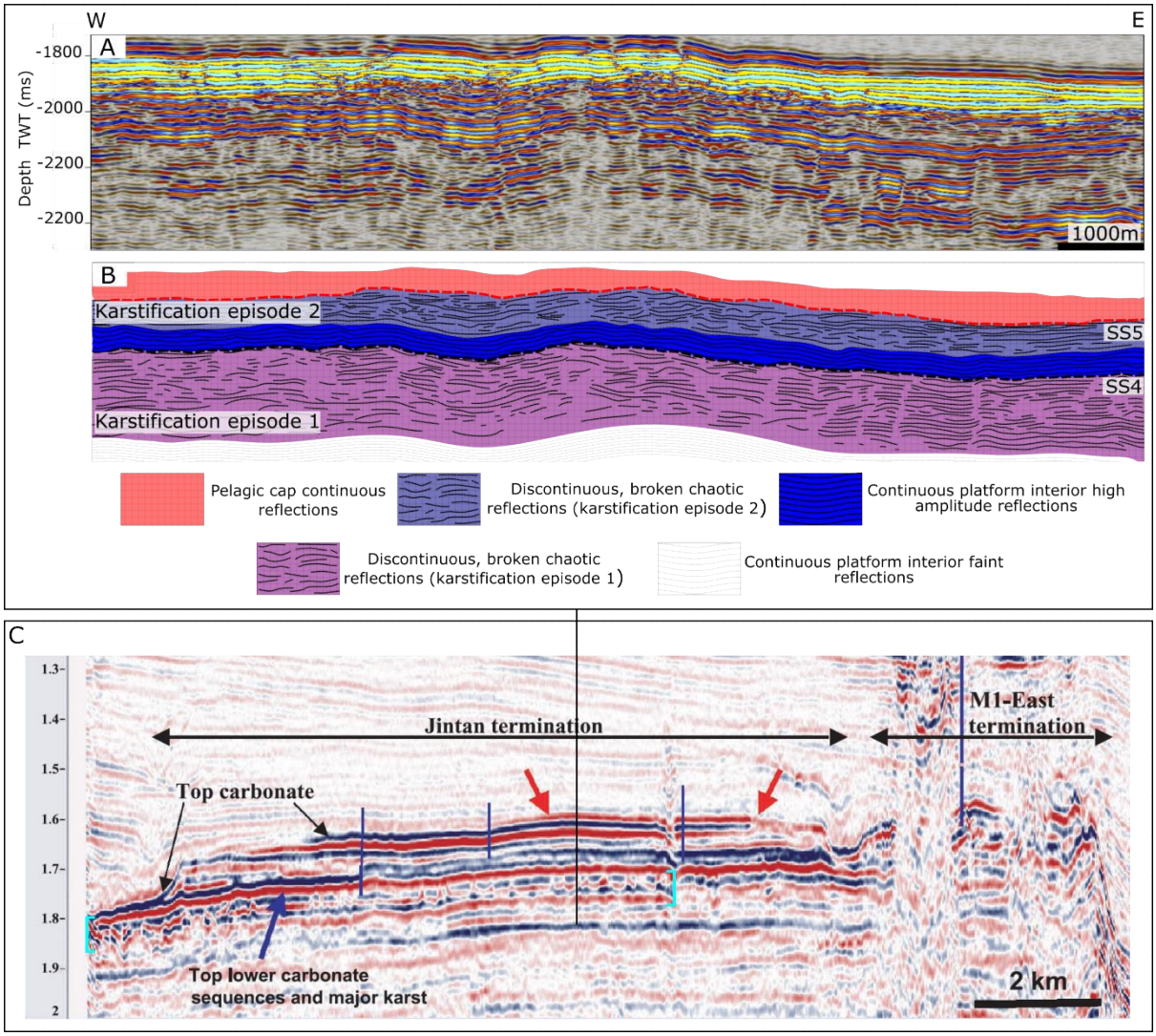


Figure 5.4 Seismic amplitude profiles from (A, B) Resolution Guyot and (C) the Middle Miocene Mega Platform, Luconia Province, Offshore Sarawak, Malaysia (modified after Vahrenkamp et al., 2004). The figure highlights the difference between the thicknesses of karstified intervals in Cretaceous isolated carbonate platforms (A, B) and Miocene counterparts (C; highlighted by cyan square bracket). The comparison reflects development of thicker karstified intervals in Cretaceous isolated carbonate platforms.

5.1.2 How did the scarce dolomitisation occur during the Cretaceous Calcitic ocean just in a few Pacific ICPs?

In Chapter 3, my compilation database of dolomitisation in Cretaceous and Cenozoic ICPs reveals significant differences in occurrence. Approximately 80% of Cenozoic ICPs produce dolostones from normal seawater, while only around 40% of Cretaceous counterparts are dolomitised, with about 11% attributed to normal seawater (Figure 3.1, Table B1). This database reinforces previous suggestions that during the Cretaceous, calcitic seas might have hindered extensive platform-scale dolomitisation in many carbonate successions. In my seismic stratigraphic interpretation of Allison and Resolution guyots, I identified magmatic intrusions and hydrothermal vent complexes affecting the lower sedimentary layers, where dolomitised units occur (Figure 3.5-3.8; Subsections 3.6.1 and 3.7.1). I integrated (a) my newly developed burial and thermal modelling of the dolomitised interval based on the age model developed in Chapter 2 and (b) my derived dolomitisation temperatures from $\delta^{18}O_{dol}$. I found that dolomitisation temperatures exceed the ambient temperature of the host-rock, indicating an external heat source (Figure 3.13). I derived the dolomitisation ages from the $^{87}Sr/^{86}Sr$ of dolomites which appear to be temporally overlapping with K/Ar and $^{40}Ar/^{39}Ar$ ages of the basement in Resolution Guyot (Subsections 3.6.3 and 3.7.2). Across the West Pacific Cretaceous ICPs, dolomites are exclusively associated with magmatic emplacements (i.e. Resolution and Allison guyots). The aforementioned points suggest a causal relationship between magmatic activities and dolomitisation in Resolution Guyot (Subsection 3.7.2). Thus, I proposed a new magmatically driven hydrothermal dolomitisation model for the Pacific Cretaceous ICPs (Figure 3.14). This model posits that magmatic activity enhanced dolomitisation by increasing heat flow and promoting vigorous seawater circulation (Subsection 3.7.2). Magmatism can increase the basal heat from background of ≤ 100 mW/m^2 to much higher heat flow anomalies that may reach >800–2000 mW/m^2 where magma ascends, and hydrothermal circulation is active. In addition, the widespread presence of the associated hydrothermal vents and fluid pipes means the presence of highly fractured rock masses across the atolls which are known to enhance the fluid flux across the atolls and so the dolomitisation reactivity (Subsection 3.7.2). I found that Fe-enriched dolomites are present atop the basaltic basement and considering the causal relationship between magmatic emplacements and dolomitisation, I propose that H_2O–CO_2–SO_2–HCl-rich magmatic-hydrothermal acidic fluids might have slightly mixed with seawater, leaching Mg and Fe from basaltic basement, and causing slight modification of the seawater (Subsection 3.7.2). Therefore, Cretaceous ICPs with active magmatism had greater potential for seawater dolomitisation due to increased heat flux and slight elevation in Mg:Ca ratio of dolomitising fluids.

The study (Chapter 3) shows wider implications. Firstly, it reveals that while other Pacific Cretaceous ICPs remained submerged under deep cold seawater below 1000 m for a prolonged period of approximately 20–56 Myr (Table B13), dolomites were only encountered in Resolution and Allison guyots (i.e. in association with magmatism; Subsection 3.7.3). This suggests that the presence of deep-seated island dolostones, in general, are not only be explained by the pumping of deep seawater below calcite saturation depth (e.g. Saller, 1986). Instead, I propose that magmatically driven hydrothermal dolomitisation, facilitated by sill emplacement, accounts for the depth of deep-seated dolomites in Resolution and potentially Allison guyots. This mechanism may also explain the presence of deep-seated dolomites in other atolls and islands during the Cretaceous and other periods characterised by significant magmatism. For example, in the Xisha Islands, Miocene-Pliocene magmatism(s) have been suggested to influence dolomitisation and dolomite transformation. Secondly, the absence of dolostones in other Pacific Cretaceous ICPs may raise doubts about the effectiveness of syndepositional and near-surface dolomitisation by circulation of Cretaceous normal unmodified seawater (Subsection 3.7.3). This may call into question some previous interpretations of Cretaceous normal seawater platform-scale massive dolomites, suggesting that modifications of Cretaceous seawater may be necessary. However, these modifications do not need to be significant. For example, dolomites in the Cretaceous Zebbag Formation in Southern Tunisia exhibit a chemical composition very close to normal seawater, with slightly more positive oxygen isotope signatures, slightly elevated concentrations of Sr, and a near-absence of evaporites, consistent with dolomitisation by reflux of mesohaline seawater (e.g., Newport et al., 2017). Therefore, considering the example mentioned previously and my study, I propose that the interpretations of these Cretaceous dolomites should consider additional factors such as geometry, geological settings, and dolomitisation age, as they may share characteristics with syndepositional and near-surface early-burial normal (unmodified) seawater dolomites.

5.1.3 What controlled the demise of the Cretaceous Pacific ICPs? Are they suitable analogues for thermal-stress intolerant or tolerant modern tropical atolls under the human-induced future climate changes?

I offer a new perspective on the demise of the Pacific Cretaceous ICPs. I started my work with questioning all the previously proposed hypotheses. In the death-by-emergence-and-submergence hypothesis, while fluctuations in relative sea level are proposed to have driven the submergence of these platforms, the underlying reasons for such fluctuations remain unclear. Additionally, the failure of carbonate platforms to re-establish after submergence remains unknown. In the death-in-the-tropics hypothesis, if equatorial upwelling of nutrients and CO_2 played a significant role in platform demise, the absence of corresponding organic-rich intervals atop the drowned platforms raises questions. Also, the fact that none of the Cretaceous Pacific ICPs were demised during any of the Cretaceous Oceanic Anoxic Events (OAEs) adds to the uncertainty. To test the death-by-excessively-warm-peri-equatorial-waters hypothesis, I compared the SSTs during atolls development and their drowning. The SSTs ranges were almost the same and they are overlapping with the optimal temperature range for rudist-bearing carbonate platforms during the Cretaceous. This challenges the notion that peri-equatorial warm waters caused atoll demise. The seismic interpretation I conducted on Resolution and Allison guyots unveiled for the first-time evidence of extensive magmatism during the late-Albian to early-Cenomanian, affecting their shallow-marine carbonate sedimentary successions while pelagic sediments unaffected (Figure 4.7-4.9). I therefore suggest the interpreted magmatism uplifted the platforms, leading to subaerial exposure and karstification, which explains the simultaneous cessation of shallow-marine carbonate sedimentation and karstification of their uppermost successions. (Figure 4.11 and 4.14; Subsection 4.7.1.1). To address why shallow-marine carbonate sedimentation didn't resume after submergence, the study used the latest palaeotectonic reconstruction of the Pacific Plate. This reconstruction revealed that between 98-95 Ma, the MPM Cretaceous ICPs migrated away from the Larson Melt Region (Figure 4.11; Subsection 4.7.1.2.1). This migration led to increased subsidence, which, combined with the Cenomanian eustatic rise, resulted in large rates of relative sea level rise. I test the possible ranges of the induced relative sea level rise from dynamic subsidence due to the migration off the hotspot swell and the Cenomanian eustatic rise. The potential ranges of relative sea-level rise exceed the maximum vertical carbonate production rates of different carbonate components but falls below the maximum vertical growth rates of rudists (Figure 4.12). However, rudists are susceptible to mechanical destruction by storms or migrating bioclastic bars, resulting in short-term sedimentation rates that cannot match vertical growth rates. Therefore, I combined the palaeogeographic reconstructions of the Pacific Cretaceous ICPs with

global palaeoclimatic modelling maps (Subsection 4.7.1.2.2) which showed that the MPM Cretaceous ICPs (~97 Ma) were exposed to equatorial hurricane belts, year-round tropical cyclones, and circumglobal equatorial currents. Rudists lack the ability to form reefal frameworks with topographic relief. Therefore, the platform tops of the MPM Cretaceous atolls were susceptible to disturbances caused by storms, hurricanes, and currents, resulting in sediment loss. This reduces the settling and vertical accumulation of newly produced sediments and grains, contributing to continuous negative feedback that supports relative sea-level rise outpacing carbonate accumulation (Subsection 4.7.1.2.2). As a result, the platform tops gradually deepened, eventually reaching depths beyond critical threshold for shallow-water carbonate producers, despite their maximum growth potential (Figure 4.14).

The proposed demise mechanism has two wider implications. First, the study adds to recent work suggesting that rapid subsidence resulting from islands migrating away from a mantle source of swell uplift (dynamic uplift) may provide a solution to the paradox of carbonate platform drowning (Huppert et al., 2020). The study suggests that previous explanations, such as rapid pulses of eustatic rise or paleoenvironmental changes in equatorial regions, may not be necessary (Huppert et al., 2020). Second, it indicates that the shallow-marine carbonate secreting organisms on the MPM Cretaceous atolls thrived under equatorial SSTs exceeding 30°C (30-34°C up to 35-≤36°C; Figure 5.5). Predictions show similar equatorial sea surface temperatures by 2100 under Representative Concentration Pathways (RCP) 8.5 (Figure 5.5). Species distribution models suggest that under RCP 8.5 scenario *Porites lobata* reefal islands will retain and gain habitat at and around the equator (Cacciapaglia and van Woesik, 2015). Given the overlapping equatorial SSTs between the Cretaceous and the simulations of year 2100 (Figure 5.5; Zhang et al., 2020b; Valdes et al., 2021), insights from the distribution of the Cretaceous tropical carbonates may aid in understanding the potential impact of climate change on modern counterparts. This is crucial for assessing extinction risks and identifying thermal-stress refugia for tropical islands. Consequently, I emphasise the need to examine similarities between the Pacific Cretaceous atolls' ecosystems and modern counterparts, considering the adaptability of Cretaceous organisms when evaluating the potential impacts of global warming on modern counterparts. However, we need first to understand how the ecological responses of the Cretaceous shallow-marine carbonate ecosystems can be applied to modern thermally resilient biota.

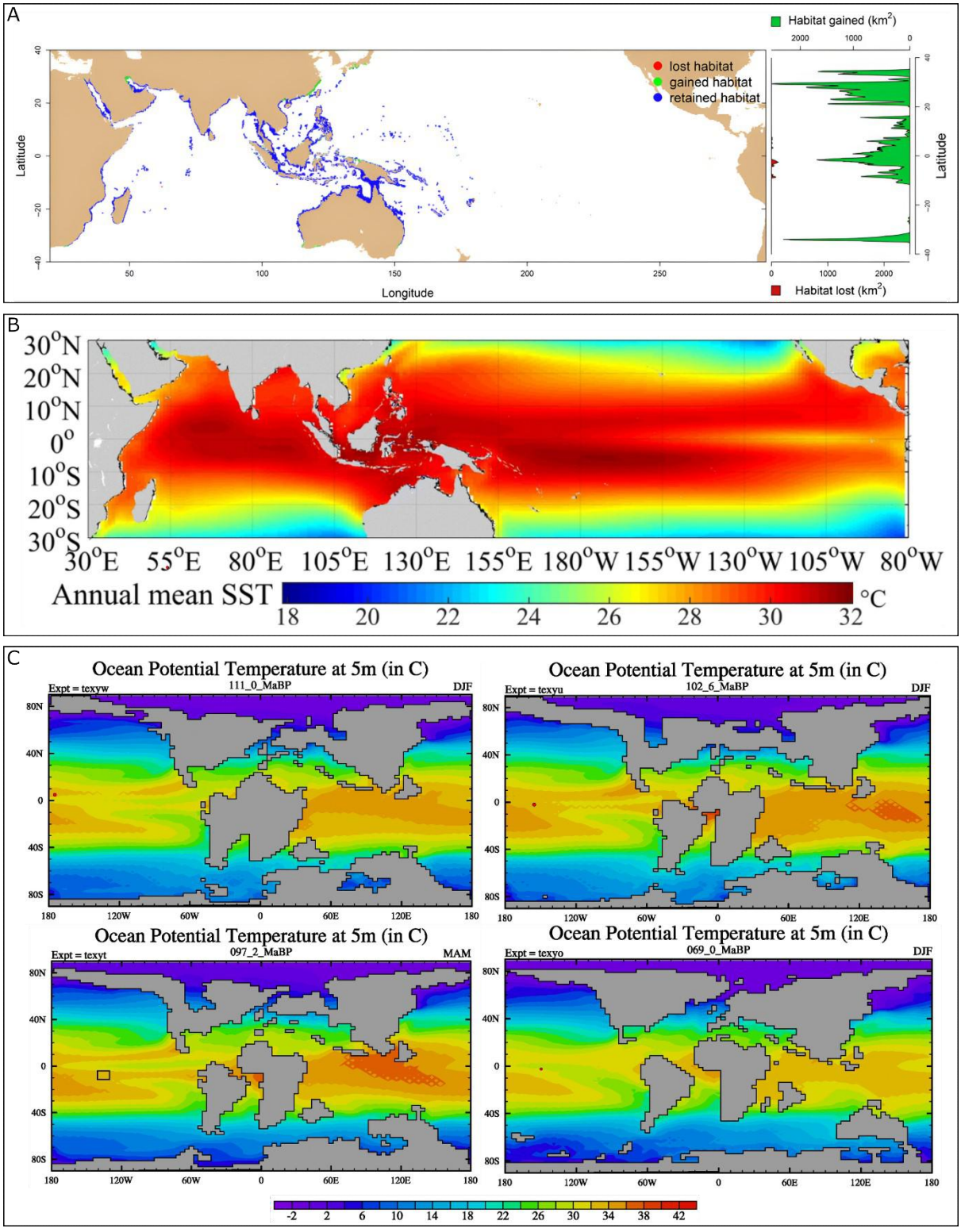


Figure 5.5 (A) The predicted global distribution of *Porites lobata* where red, green, and blue colours mean lost, gained and retained habitat, respectively under a 'business as usual' Representative Concentration Pathway 8.5 climate-change scenario in 2100 (Cacciapaglia and van Woesik, 2015). (B) The simulated annual sea surface temperature variability over Tropical Indo-Pacific region under RCP 8.5 conditions in year 2100 (Zhang et al., 2020b). (C) Modelled global sea surface temperatures during the Cretaceous (111, 102.6, 97.2, 69 Ma) at the locations of the Pacific Cretaceous isolated carbonate platforms (starting from the top left with Takuyo-Daisan then MIT then Resolution and Allison, and finally Wodejebato. Maps were retrieved using the Earth Systems Modelling Result website from the following URL https://www.paleo.bristol.ac.uk/ummodel/users/Valdes_et_al_2021/new2/; Valdes et al., 2021).

5.2 Future Work

My investigation using the challenging low-quality vintage seismic data from the MPM Cretaceous ICPs has revealed a profound complexity in their evolution from inception to demise. These platforms represent dynamic geological systems influenced by numerous factors, including magmatism, fluctuations in eustatic sea levels, variations in carbonate production rates, changes in subsidence patterns, hotspot migration dynamics, syndepositional and hydraulic fracturing, and hydrothermal fluid flow processes. Each of these factors contributes to a complex interplay of geological processes, resulting in a diverse range of potential effects and research inquiries. Despite the inherent limitations of the resolution in available seismic datasets, my research emphasises the critical importance of elucidating the spatial and temporal variabilities within the geological framework of these platforms, which cannot be adequately constrained using sparse well data as previously attempted. Findings from my Chapter 2 were used in justifying a proposal to return to these sites, including Resolution Guyot among other Pacific ICPs (Figure 5.6), for a comprehensive re-imaging seismic reflection campaign under The CARAPACE Project (Calcite-ARagonite transition Across Pacific Atolls from the Cretaceous to the Eocene). This great initiative aims to acquire higher quality seismic data, which will be crucial for deepening our understanding of the subtle subsurface characteristics and evolutionary processes in these geological formations.

My thesis has identified a number of possible future research opportunities:

5.2.1 Quantitative sequence stratigraphy and forward stratigraphic modelling

In Chapter 2, I elucidated the stratigraphic evolution of the MPM Cretaceous ICPs, identifying the qualitative interplay among fluctuations in eustatic sea levels, variations in carbonate production rates, changes in subsidence patterns, and magmatism. However, to quantitatively dissect the relative impact of each factor, forward stratigraphic modelling is essential. I plan to explore different scenarios with varying degrees of influence and control for each factor to discern the possible outcomes and the most plausible scenarios. The implications of this future plan are not going to be only specific to the Pacific Cretaceous ICPs, instead it would help in answering concerns of global impact including but not limited to (a) testing the plausibility of the different eustatic curves of the Cretaceous (Sahagian et al., 1996; Miller et al., 2004; Haq, 2014; van der Meer et al., 2022) and (b) understanding the impact of variations in carbonate production rates on depositional facies development and distribution, platform geometry, and stratigraphic architecture. Furthermore, the 3D forward stratigraphic model can be transferred into a 3D synthetic seismic model which can aid in comparison with vintage seismic data and offer valuable

insights for exploring new frontier areas or addressing challenges posed by low-quality seismic data, as encountered in my study.

5.2.2 Understanding dolomitisation during the Cretaceous calcitic sea through reactive transport modelling

In Chapter 3, I demonstrated the limited effectiveness of Cretaceous normal seawater in forming syndepositional and early-burial near-surface platform-scale dolomites. This finding aligns with existing research indicating that during the Cretaceous, factors such as global climate, calcitic seas, and high relative sea levels impeded extensive dolomitisation in many carbonate successions. The magmatically driven hydrothermal dolomitisation model that I proposed suggested that dolomitisation was promoted by providing high heat flow, boosting vigorous seawater circulation, and overcoming limited dolomitisation potential of Cretaceous seawater where the H_2O–CO_2–SO_2–HCl-rich magmatic-hydrothermal acidic fluids would slightly mix with seawater causing slight modification by leaching Mg and Fe from basaltic basement. It is important to test this model and other alternative dolomitisation models of normal seawater and ranges of derived brines through reactive transport modelling. Reactive transport modelling employs mathematical formulations to describe coupled transport and geochemical processes, which would enhance our understanding of the quantitative controls on dolomitisation in calcitic seas. This is of great importance because most reactive transport modelling studies (Table 5.1) have used normal seawaters (primarily modern seawater) and derived brines with high Mg:Ca ratios >2 and high Mg^{2+} concentration, resembling aragonitic seas. However, during the Cretaceous, Mg:Ca ratio was approximately 1, and Mg^{2+} concentrations were significantly lower.

5.2.3 Hydrothermal fluid flow vents: the history of intraplate volcanic activities in the Pacific and fluid flow pathways reutilisation in carbonate successions

In Chapter 3, I highlighted the significant impact of post-depositional magmatic emplacements and associated hydrothermal fluid flow vent complexes on the sedimentary successions of the MPM Cretaceous ICPs. This represents one of the few instances in the literature discussing the development of hydrothermal fluid flow vent complexes within shallow-marine carbonate successions, as most literature focuses on siliciclastic-dominated successions (Magee et al., 2015; Roelofse et al., 2020; Berndt et al., 2023; González-Escobar et al., 2023; Zhao et al., 2023). My interpretation revealed multiple volcanic activities affecting the sedimentary successions of the MPM Cretaceous ICPs. Therefore, further investigation involving the interpretation of the apparent ages of these activities through seismic stratigraphic relative dating of magmatic emplacements would be beneficial for (a) understanding the intraplate volcanic activities in the

MPM and its relationship with the passage of hotspots (Figure 5.7), and (b) testing the possibility of reutilisation of fluid flow pathways in carbonate successions (Figure 5.8). Regarding the latter, an interesting research topic would be integrating mechanical and reactive transport modelling to understand how hydrothermal fluid vents form in carbonate successions, which is different from siliciclastics. Additionally, it would be also important to investigate how the chemical reactivity of CO_2-rich hydrothermal fluids interacts with the host rock to influence the initiation and reutilisation of hydrothermal vents. This would have a direct impact in understanding the spatial distribution of induced diagenesis, for instance the potential distribution of hypogenic karst reservoirs.

5.2.4 Quantitative analyses of the factors controlling the demise of the Pacific Cretaceous isolated carbonate platforms

In Chapter 4, my study showed that after magmatism and subaerial exposure of Resolution and Allison ICPs, the demise of the MPM Cretaceous ICPs was suggested to be controlled by subsidence induced by the migration off the Larson Melt Region hotspot swell plus the Cenomanian eustatic sea level rise. In addition, palaeo-climatic factors such as equatorial hurricanes, year-round tropical cyclones, and circumglobal equatorial currents appear to be supporting the deepening of the platform top by concomitantly reducing the accumulation rate of sediments. Based on the main conclusion of Chapter 4, I propose two research ideas. First, the swell tail subsidence rate of the newly identified Larson Melt Region hotspot is yet unknown. Therefore, measuring swell length parallel to the plate motion would be important to provide the swell tail subsidence rate which should be tested with different eustatic curves using forward stratigraphic modelling to quantify their relative importance in the demise mechanism. Second, the proposed supportive factors should be also tested through forward stratigraphic modelling to quantify their relative importance in reducing sediment accumulation rates, which has been widely proposed recently as a potential drowning factor of shallow-marine carbonate platforms.

5.3 Conclusions

My comprehensive investigation into the Cretaceous Mid-Pacific guyots reveals unique insights into their geological evolution, subsequent diagenesis, and demise. The thesis collectively illuminated the complex interplay of geological processes and environmental factors that governed these ancient carbonate systems during a pivotal epoch in Earth's history.

1. The comprehensive integration of core, log, and seismic data has delineated the intricate carbonate system of the Cretaceous Mid-Pacific atolls. The proposed depositional model, encompassing various depositional environments such as deep shelf basin (including drift deposits), slope-to-basin (including MTDs), upper-slope (including sponge and requieniid rudists build-up and reworked material from the platform margin and interior), platform margin complex (including beaches, shoals, requieniid rudists build-up, and storm deposits), back-margin (including back-margin apron, washover fans, sandwaves and shoals) and platform interior (including lagoon deposits, patch reefs and rudist meadows), holds significant applicability to Cretaceous ICPs across diverse geological settings. This model may also serve as a valuable template for interpreting similar ICPs in frontier areas (e.g. the East Mediterranean and the Atlantic margins of Namibia and South Africa).
2. My detailed stratigraphic analyses unveiled the intricate relationship between eustasy, carbonate production rates, subsidence, ocean chemistry and magmatism, elucidating their profound influence on platform evolution. This adds to the growing work suggesting that T-factory carbonate stratigraphic evolution is a consequence of multiple controls, not just variations in accommodation.
3. My study highlights platform margins as key sites for karst reservoir development, demonstrating that meteoric dissolution preferentially targets syndepositional fractures along these margins, culminating in the formation of extensive stacked flank-margin caves with vertical extents of up to ~520-700 meters.
4. The Cretaceous Pacific atolls are affected by venting systems for cross-stratal fluids. This venting system, in conjunction with karstification features, likely facilitated the ventilation of seawater across the Mid-Pacific atolls. This observation answered why the geochemical analyses indicated active exchange between atoll pore-waters and surrounding seawater, notably in wells situated 4,000 to 6,000 metres away from the platform margin.
5. I unravelled a magmatically driven hydrothermal dolomitisation model for the Mid-Pacific atolls, wherein elevated heat flux from magmatic activity promotes dolomitisation by enhancing seawater circulation and overcoming inherent limitations of Cretaceous seawater.

The interaction of magmatic-hydrothermal acidic fluids with seawater further facilitates dolomite formation through slight mixing with seawater, leading to slight modification through slight leaching of Mg and Fe from the basaltic basement.

6. My findings support previous models of reduced effectiveness of massive dolomitisation by Cretaceous normal seawater, questioning interpretations of syndepositional and near-surface dolomitisation.
7. Deep-seated island dolostones do not exclusively signify dolomitisation by seawater circulation below calcite saturation depth. Instead, magmatism is a crucial factor in the dolomitisation processes of Cretaceous Pacific atolls and potentially other locations such as the Xisha Islands.
8. The life of the Mid-Pacific Mountains Cretaceous atolls came to an end through a complex history that has been puzzling for over 30 years. The cessation of carbonate sedimentation during the late Albian to early Cenomanian epoch is intricately linked to widespread volcanism in the Western Pacific which activity induced uplift, resulting in subaerial exposure that halted shallow-marine carbonate deposition on Mid-Pacific atolls. Upon re-submergence, these atolls migrated away from the Larson Melt Region Hotspot Swell. This migration, coupled with the Cenomanian eustatic rise, caused rapid relative sea level rise on the Mid-Pacific atolls. Following re-submergence, vertical accumulation rates at Mid-Pacific atolls were notably affected by off-bank sediment transport mechanisms (i.e. equatorial hurricanes, ocean-surface currents, production lag time, and the absence of true reefal bioconstructed margins). This convergence of factors facilitated a scenario where rapid relative sea-level rise outpaced the rate of carbonate accumulation, introducing continuous negative feedback. The study supports the hypothesis of "death-by-emergence-and-submergence," for the demise of Mid-Pacific atolls. It addresses the main uncertainties within the hypothesis previously challenged by other researchers; the cause of emergence and why shallow-water sediments didn't accumulate after re-submergence.
9. My study (a) contributes to recent research indicating that rapid subsidence caused by islands moving away from a mantle source of swell uplift (dynamic uplift) may offer an explanation for the paradox of carbonate platform drowning, and (b) challenges prevailing assumptions regarding the sensitivity of Cretaceous carbonate-secreting organisms to elevated sea surface temperatures (30-35°C), suggesting a degree of resilience that has implications as a more plausible analogue to modern heat-tolerant species.

In conclusion, my study underscores the importance of integrating multiple lines of evidence and adopting a holistic approach to unravelling the geological history of Cretaceous Mid-Pacific atolls. By elucidating the intricate interplay between geological processes and environmental variables,

my findings not only advance our understanding of ancient carbonate systems but also offer insights into the potential responses of modern reef ecosystems to future climate change.

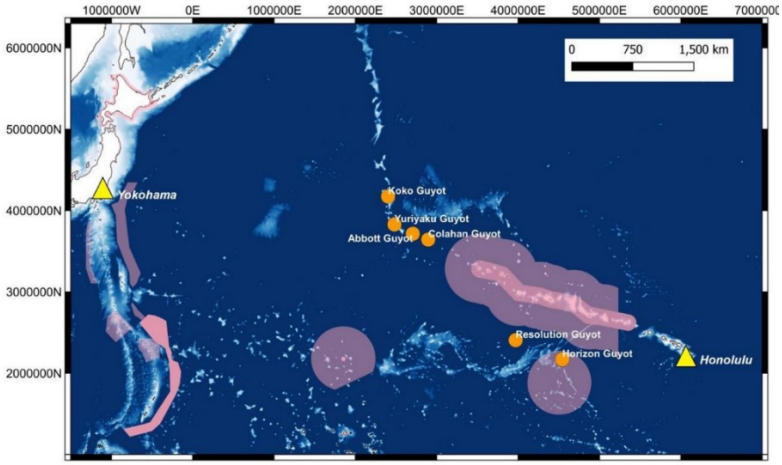


Figure 5.6 The Pacific Atolls to be investigated as part of the CARAPACE Project (Adapted from John et al., 2021).

References	Calcitic Seas	Aragonitic Seas	Hyperlinks
Frazer et al., 2023			https://onlinelibrary.wiley.com/doi/epdf/10.1002/dep2.234
Dong et al., 2021			https://doi.org/10.1016/j.marpetgeo.2020.104797
Zhang et al., 2021			https://doi.org/10.3390/min11121340
Gabellone et al., 2020			https://onepetro.org/IPTCONF/proceedings/20IPTC/3-20IPTC/D033S057R003/154693
Benjakul et al., 2020			https://se.copernicus.org/articles/11/2439/2020/se-11-2439-2020.pdf
Yapparova et al., 2017a			https://www.sciencedirect.com/science/article/pii/S0009254117304035?via%3Dihub
Yapparova et al., 2017b			https://link.springer.com/article/10.1007/s11242-017-0839-7
Abarca et al., 2016			https://www.sciencedirect.com/science/article/pii/S0009254119301159?via%3Dihub
Gabellone and Whitaker, 2016			https://onlinelibrary.wiley.com/doi/10.1111/sed.12259
Gabellone et al., 2016			https://www.sciencedirect.com/science/article/pii/S0037073816300823?via%3Dihub#s0035
Lu and Cantrell, 2015			https://onlinelibrary.wiley.com/doi/epdf/10.1111/sed.12241
Corbella et al., 2014			https://pubs.geoscienceworld.org/pg/article/20/1/41/383289/Insights-to-controls-on-dolomitization-by-means-of
AL-HELAL et al., 2012			https://pubs.geoscienceworld.org/sepm/jsedres/article-abstract/82/3/196/99453
Consonni et al., 2010			https://onlinelibrary.wiley.com/doi/epdf/10.1111/j.1365-3091.2009.01103.x
Whitaker and Xiao, 2010			https://pubs.geoscienceworld.org/aapgbull/article/94/6/889/133054/Reactive-transport-modeling-of-early-burial
SALAS et al., 2007			https://onlinelibrary.wiley.com/doi/epdf/10.1111/j.1468-8123.2006.00167.x
Xiao and Jones, 2007			https://onepetro.org/IPTCONF/proceedings/07IPTC/All-07IPTC/IPTC-11199-MS/30514
Jones and Xiao, 2005			https://pubs.geoscienceworld.org/aapgbull/article/89/5/577/40218/Dolomitization-anhydrite-cementation-and-porosity

Table 5.1 The number of reactive transport modelling studies on dolomitisation using chemical composition of calcitic seawater versus studies using chemical composition of aragonitic seawater. The literature review presented here was acquired by searching in the Scoups Database using the following search words "reactive transport model*" and "dolomit*" in article title, abstract, and keywords.

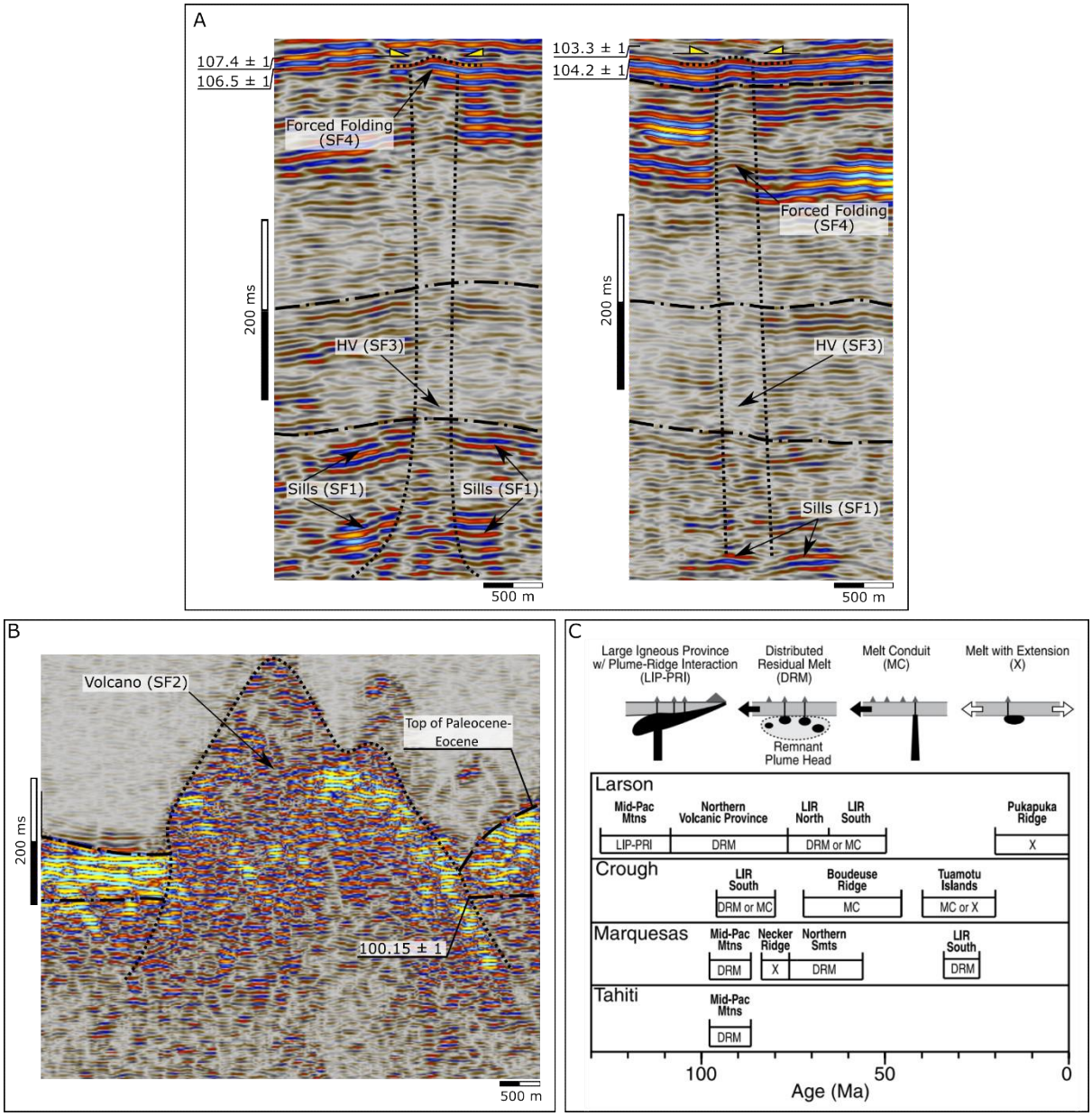


Figure 5.7 Seismic interpretation of multiple intraplate volcanisms in the Mid-Pacific Mountains Cretaceous isolated carbonate platforms. (A) Seismic amplitude profiles showing the apparent ages of multiple volcanisms in Resolution Guyot based on stratal terminations of the upper vent associated with the emplacement. (B) Seismic amplitude profiles showing the apparent age of intraplate volcanisms in Allison Guyot based on stratal terminations of the volcanic cone with the surrounding sediments. (C) Timelines of eruption timing and melt delivery style for each of melt sources and their effect on the Mid-Pacific Mountains (adapted from Pockalny et al., 2021).

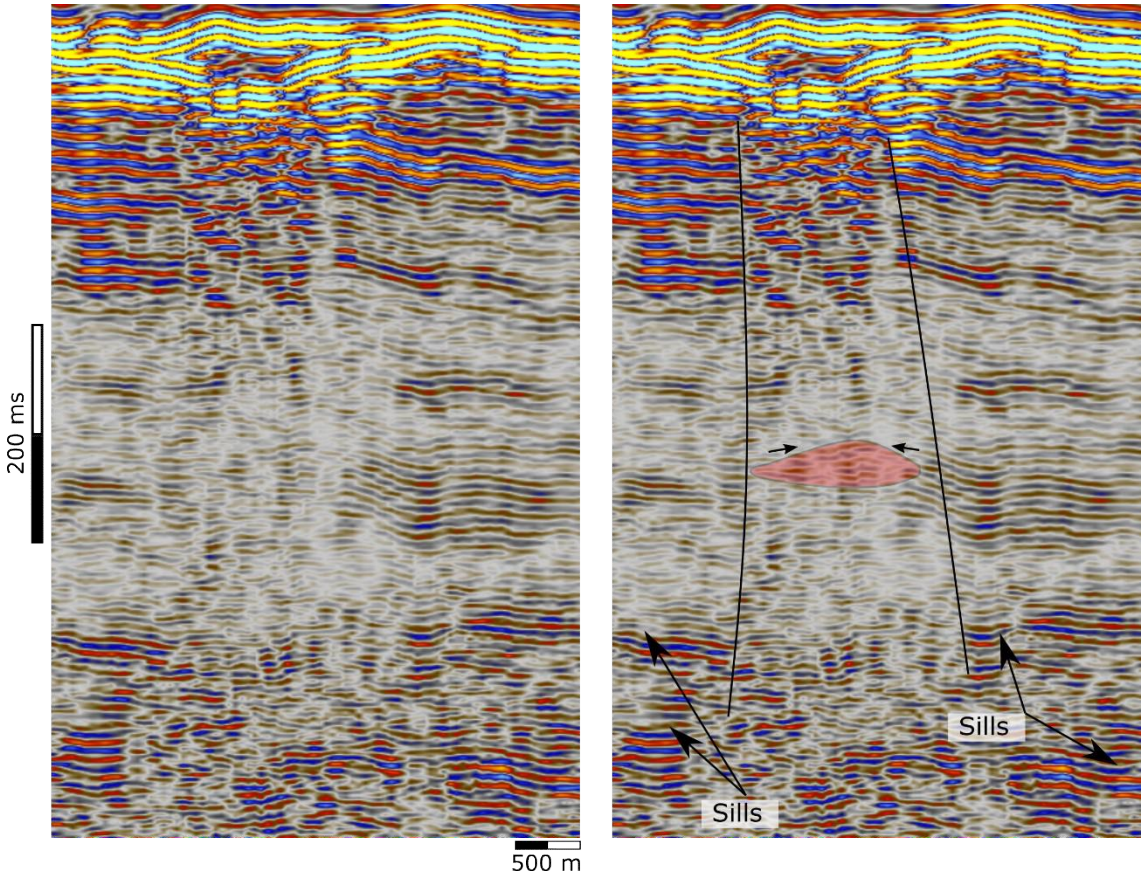


Figure 5.8 A preliminary seismic interpretation of a seismic amplitude profile from Resolution Guyot. The interpretation tentatively reveals a potential mounded structure situated in the middle of the hydrothermal vent, surrounded by amplitude anomalies. This observation may suggest the occurrence of multiple episodes of hydrothermal venting along the same fluid flow pathway, indicating a phenomenon known as hydrothermal vent reutilisation.

BIBLIOGRAPHY

Aarnes, I., Podladchikov, Y., & Svensen, H. (2012). Devolatilization-induced pressure build-up: Implications for reaction front movement and breccia pipe formation. Geofluids, 12(4), 265-279.

Abarca, E., Idiart, A., Grandia, F., Rodríguez-Morillas, N., Pellan, C., Zen, M., ... & Fontanelli, L. (2019). 3D reactive transport modeling of porosity evolution in a carbonate reservoir through dolomitization. Chemical Geology, 513, 184-199.

Agustsdottir, A. M., Barron, E. J., Bice, K. L., Colarusso, L. A., Cookman, J. L., Cosgrove, B. A., ... & White, T. S. (1999). Storm activity in ancient climates 1. Sensitivity of severe storms to climate forcing factors on geologic timescales. Journal of Geophysical Research Atmospheres, 104(D22), 27277-27293.

Aharon, P., Socki, R. A., & Chan, L. (1987). Dolomitization of atolls by sea water convection flow: test of a hypothesis at Niue, South Pacific. The Journal of Geology, 95(2), 187-203.

Al-Disi, Z. A., Bontognali, T. R., Jaoua, S., Attia, E., Al-Kuwari, H. A. S., & Zouari, N. (2019). Influence of temperature, salinity and Mg2+: Ca2+ ratio on microbially-mediated formation of Mg-rich carbonates by Virgibacillus strains isolated from a sabkha environment. Scientific Reports, 9(1), 1-12.

Al-Helal, A. B., Whitaker, F. F., & Xiao, Y. (2012). Reactive transport modeling of brine reflux: dolomitization, anhydrite precipitation, and porosity evolution. *Journal of Sedimentary Research*, *82*(3), 196-215.

Andrié, C., Jean-Baptiste, P., Pierre, C., Déjardin, P., Fichez, R., Poupeau, J. J., & Rougerie, F. (1998). Pore water geochemistry and mixing processes within the Tahiti barrier reef. Geochimica et Cosmochimica Acta, 62(16), 2809-2822.

Arnaud, H. M., Flood, P. G., & Strasser, A. (1995). Resolution Guyot (Hole 866A, Mid-Pacific Mountains): facies evolution and sequence stratigraphy: Northwest Pacific atolls and guyots. In Proceedings of the Ocean Drilling Program. Scientific results Vol. 143, 133-159.

Arnaud-Vanneau, A., Bergersen, D. D., Camoin, G. F., Ebren, P., & Haggerty, J. A. (1995). A model for depositional sequences and systems tracts on small, mid-ocean carbonate platforms: Examples from Wodejebato (sites 873-877) and Limalok (site 871) Guyots. In Proceedings of the Ocean Drilling Program. Scientific results Vol. 144, 819-840.

Arnaud-Vanneau, A., & Sliter, W. V. (1995). Early Cretaceous shallow-water benthic foraminifers and fecal pellets from Leg 143 compared with coeval faunas from the Pacific Basin, Central America, and the Tethys: Northwest Pacific atolls and guyots. In Proceedings of the Ocean Drilling Program. Scientific Results Vol. 144, pp. 537-564.

Arvidson, R. S., & Mackenzie, F. T. (1997). Tentative kinetic model for dolomite precipitation rate and its application to dolomite distribution. Aquatic Geochemistry, 2, 273-298.

Arvidson, R. S., & Mackenzie, F. T. (1999). The dolomite problem; control of precipitation kinetics by temperature and saturation state. American Journal of Science, 299(4), 257-288.

Arvidson, R. S., Guidry, M. W., & Mackenzie, F. T. (2011). Dolomite controls on Phanerozoic seawater chemistry. Aquatic Geochemistry, 17, 735-747.

Bachtel, S. L., Kissling, R. D., Martono, D., Rahardjanto, S. P., Dunn, P. A., & MacDonald, B. A. (2004). Seismic Stratigraphic Evolution of the Miocene Pliocene Segitiga Platform, East Natuna Sea, Indonesia: The Origin, Growth, and Demise of an Isolated Carbonate Platform. In: Seismic imaging of carbonate reservoirs and systems: AAPG Memoir 81, 309– 328.

Bai, Y., Gui, Z., Li, M., Dong, D., Wu, S., & Wang, Z. (2019). Crustal thickness over the NW Pacific and its tectonic implications. Journal of Asian Earth Sciences, 185, 104050.

Bąk, K., Fabiańska, M., Bąk, M., Misz-Kennan, M., Zielińska, M., Dulemba, P., ... & Naglik, B. (2016). Organic matter in upper Albian marine sediments in the High-Tatric units, central western Carpathians related to Oceanic Anoxic Event 1d—Geochemistry, microfacies and palynology. Palaeogeography, Palaeoclimatology, Palaeoecology, 454, 212-227.

Baker, P. E., Castillo, P. R., & Condliffe, E. (1995). Petrology and geochemistry of igneous rocks from Allison and Resolution guyots, Sites 865 and 866: Northwest Pacific atolls and guyots. In Proceedings of the Ocean Drilling Program. Scientific results Vol. 143, 245-261.

Basso, M., Kuroda, M. C., Afonso, L. C. S., & Vidal, A. C. (2018). Three-Dimensional Seismic Geomorphology of Paleokarst in the Cretaceous Macaé Group Carbonates, Campos Basin, Brazil. Journal of Petroleum Geology, 41(4), 513-526.

Baudin, F., Deconinck, J. F., Sachsenhofer, R. F., Strasser, A., & Arnaud, H. (1995). 12. Organic geochemistry and clay mineralogy of lower cretaceous sediments from allison and resolution guyots (sites 865 and 866), mid-pacific mountains1. In Proceedings of the Ocean Drilling Program, Scientific Results, (Vol. 143), pp. 173-196.

Behbehani, S., Hollis, C., Holland, G., Singh, P., & Edwards, K. (2019). A seismically controlled seal breach in a major hydrocarbon province: A study from the Mauddud Formation in the Bahrah field, Kuwait. Marine and Petroleum Geology, 107, 255-277.

Bell, B., & Butcher, H. (2002). On the emplacement of sill complexes: evidence from the Faroe–Shetland Basin. In: The North Atlantic Igneous Province: Stratigraphy, Tectonic, Volcanic and Magmatic Processes, 197, Geol. Soc. London. Spec. Publ., pp. 307-329.

Benjakul, R., Hollis, C., Robertson, H. A., Sonnenthal, E. L., & Whitaker, F. F. (2020). Understanding controls on hydrothermal dolomitisation: insights from 3D reactive transport modelling of geothermal convection. Solid Earth, 11(6), 2439-2461.

Berndt, C. (2005). Focused fluid flow in passive continental margins. Philosophical Transactions of the Royal Society A: Mathematical, Physical and Engineering Sciences, 363(1837), 2855-2871.

Berndt, C., Bünz, S., & Mienert, J. (2003). Polygonal fault systems on the mid-Norwegian margin: a long-term source for fluid flow. Geological Society, London, Special Publications, 216(1), 283-290.

Berndt, C., Planke, S., Alvarez Zarikian, C. A., Frieling, J., Jones, M. T., Millett, J. M., ... & Yager, S. L. (2023). Shallow-water hydrothermal venting linked to the Palaeocene–Eocene Thermal Maximum. Nature Geoscience, 16(9), 803-809.

Betzler, C., Brachert, T. C., & Kroon, D. (1995). Role of climate in partial drowning of the Queensland Plateau carbonate platform (northeastern Australia). Marine Geology, 123(1-2), 11-32.

Betzler, C., Lindhorst, S., Hübscher, C., Lüdmann, T., Fürstenau, J., & Reijmer, J. (2011). Giant pockmarks in a carbonate platform (Maldives, Indian Ocean). Marine Geology, 289(1-4), 1-16.

Betzler, C., Lindhorst, S., Lüdmann, T., Reijmer, J. J., Braga, J. C., Bialik, O. M., ... & Bissessur, D. (2021). Current and sea level control the demise of shallow carbonate production on a tropical bank (Saya de Malha Bank, Indian Ocean). Geology, 49(12), 1431-1435.

Betzler, C., Lindhorst, S., Lüdmann, T., Weiss, B., Wunsch, M., & Braga, J. C. (2015). The leaking bucket of a Maldives atoll: implications for the understanding of carbonate platform drowning. Marine Geology, 366, 16-33.

Betzler, C., Lindhorst, S., Reijmer, J. J., Braga, J. C., Lüdmann, T., Bialik, O. M., ... & Bissessur, D. (2023). Carbonate platform drowning caught in the act: The sedimentology of Saya de Malha Bank (Indian Ocean). Sedimentology, 70(1), 78-99.

Bi, D. J., Zhai, S. K., Zhang, D. J., Liu, X. F., Liu, X. Y., Jiang, L. J., & Zhang, A. B. (2018). Constraints of fluid inclusions and C, O isotopic compositions on the origin of the dolomites in the Xisha Islands, South China Sea. Chemical Geology, 493, 504-517.

Bialik, O. M., Samankassou, E., Meilijson, A., Waldmann, N. D., Steinberg, J., Karcz, K., & Makovsky, Y. (2021a). Short-lived early Cenomanian volcanic atolls of Mt. Carmel, northern Israel. Sedimentary Geology, 411, 105805.

Bialik, O. M., Zammit, R., & Micallef, A. (2021b). Architecture and sequence stratigraphy of the Upper Coralline Limestone formation, Malta—Implications for Eastern Mediterranean restriction prior to the Messinian Salinity Crisis. The Depositional Record. 1–15. https://doi.org/10.1002/dep2.138.

Bian, C., Chen, J., Jiang, C., Wu, Z., & Yao, Z. (2023). Threshold of motion of coral reef sediment under currents in flume experiments. Sedimentology, 70(6), 1723-1740.

Blanchon, P., Richards, S., Bernal, J. P., Cerdeira-Estrada, S., Ibarra, M. S., Corona-Martínez, L., & Martell-Dubois, R. (2017). Retrograde accretion of a Caribbean fringing reef controlled by hurricanes and sea-level rise. Frontiers in Earth Science, 5, 78.

Bodin, S., Meissner, P., Janssen, N. M., Steuber, T., & Mutterlose, J. (2015). Large igneous provinces and organic carbon burial: Controls on global temperature and continental weathering during the Early Cretaceous. Global and Planetary Change, 133, 238-253.

Bover-Arnal, T., Pascual-Cebrian, E., Skelton, P. W., Gili, E., & Salas, R. (2015). Patterns in the distribution of Aptian rudists and corals within a sequence-stratigraphic framework (Maestrat Basin, E Spain). Sedimentary Geology, 321, 86-104.

Braithwaite, C. J., Rizzi, G., & Darke, G. (2004). The geometry and petrogenesis of dolomite hydrocarbon reservoirs: introduction. Geological Society, London, Special Publications, 235(1), 1-6.

Breislin, C., Crowley, S., Banks, V. J., Marshall, J. D., Millar, I. L., Riding, J. B., & Hollis, C. (2020). Controls on dolomitization in extensional basins: An example from the Derbyshire Platform, UK. Journal of Sedimentary Research, 90(9), 1156-1174.

Brennan, S. T., Lowenstein, T. K., & Cendón, D. I. (2013). The major-ion composition of Cenozoic seawater: The past 36 million years from fluid inclusions in marine halite. American Journal of Science, 313(8), 713-775.

Broecker, W. S., & Takahashi, T. (1966). Calcium carbonate precipitation on the Bahama Banks. Journal of Geophysical Research, 71(6), 1575-1602.

Bromhead, A. D., van Buchem, F. S. P., Simmons, M. D., & Davies, R. B. (2022). Sequence Stratigraphy, Palaeogeography and Petroleum Plays of the Cenomanian–Turonian Succession of the Arabian Plate: AN Updated Synthesis. Journal of Petroleum Geology, 45(2), 119-161.

Bryers, O., Bulot, L. G., Duval-Arnould, A., Hollis, C., & Redfern, J. (2022). Kilometre-scale coral carpets on mixed carbonate-siliciclastic platforms; a sedimentological study from the Lower Cretaceous of northwestern Africa. Palaeogeography, Palaeoclimatology, Palaeoecology, 587, 110792.

Budd, D. A. (1997). Cenozoic dolomites of carbonate islands: their attributes and origin. Earth-Science Reviews, 42(1-2), p. 1-47.

Budd, D. A., Frost III, E. L., Huntington, K. W., & Allwardt, P. F. (2013). Syndepositional deformation features in high-relief carbonate platforms: long-lived conduits for diagenetic fluids. Journal of Sedimentary Research, 83(1), 12-36.

Burchette, T., Groves-Gidney, G., & Karcz, K. (2023). Seismic stratigraphy of the southern Eratosthenes High, eastern Mediterranean Sea: growth, demise and deformation of three superposed carbonate platforms (Mesozoic–Cenozoic). Petroleum Geoscience, 29(3), petgeo2023-017.

Burgess, P. M., & Prince, G. D. (2015). Non-unique stratal geometries: Implications for sequence stratigraphic interpretations. Basin Research, 27(3), 351-365.

Burgess, P. M., Winefield, P., Minzoni, M., & Elders, C. (2013). Methods for identification of isolated carbonate buildups from seismic reflection data. AAPG bulletin, 97(7), 1071-1098.

Burton, Z. F., McHargue, T., Kremer, C. H., Bloch, R. B., Gooley, J. T., Jaikla, C., ... & Graham, S. A. (2023). Peak Cenozoic warmth enabled deep-sea sand deposition. *Scientific Reports*, *13*(1), 1276.

Bush, A. B., & Philander, S. G. H. (1997). The late Cretaceous: Simulation with a coupled atmosphere-ocean general circulation model. Paleoceanography, 12(3), 495-516.

Cacciapaglia, C., & van Woesik, R. (2015). Reef-coral refugia in a rapidly changing ocean. Global Change Biology, 21(6), 2272-2282.

Camoin, G. F., Arnaud-Vanneau, A., Bergersen, D. D., Enos, P., & Ebren, P. (1998). Development and demise of mid-oceanic carbonate platforms, Wodejebato Guyot (NW Pacific). Reefs and carbonate platforms in the Pacific and Indian oceans, 39-67.

Carballo, J., Land, L. S., & Miser, D. E. (1987). Holocene dolomitization of supratidal sediments by active tidal pumping, Sugarloaf Key, Florida. Journal of Sedimentary Research, 57(1), 153-165.

Caress, D. W., McNutt, M. K., Detrick, R. S., & Mutter, J. C. (1995). Seismic imaging of hotspot-related crustal underplating beneath the Marquesas Islands. Nature, 373(6515), 600-603.

Carmichael, R. S. (1989). Practical handbook of physical properties of rocks and minerals. CRC Press, Boca Raton, FL.

Cartwright, J., & Santamarina, C. (2015). Seismic characteristics of fluid escape pipes in sedimentary basins: implications for pipe genesis. Marine and Petroleum Geology, 65, 126-140.

Cartwright, J., Huuse, M., & Aplin, A. (2007). Seal bypass systems. AAPG bulletin, 91(8), 1141-1166.

Caruso, S., Van Kranendonk, M. J., Baumgartner, R. J., Fiorentini, M. L., & Forster, M. A. (2021). The role of magmatic fluids in the~ 3.48 Ga Dresser Caldera, Pilbara Craton: New insights from the geochemical investigation of hydrothermal alteration. Precambrian Research, 362, 106299.

Charvis, P., Laesanpura, A., Gallart, J., Hirn, A., Lépine, J. C., de Voogd, B., ... & Pontoise, B. (1999). Spatial distribution of hotspot material added to the lithosphere under La Réunion, from wide-angle seismic data. Journal of Geophysical Research: Solid Earth, 104(B2), 2875-2893.

Chatalov, G. A. (1971). Schemes for the size of textural elements in carbonate rocks. Rev Bulg Geol Soc, 32, 374-377.

Chen, L., Chiang, H. T., Wu, J. N., Chiao, L. Y., Shyu, C. T., Liu, C. S., Wang, Y., Chen, S. C. (2020). The focus thermal study around the spreading centre of southwestern Okinawa trough. Tectonophysics, 796, 228649.

Chivas, A. R., Torgersen, T., & Polach, H. A. (1990). Growth rates and Holocene development of stromatolites from Shark Bay, Western Australia. Australian Journal of Earth Sciences, 37(2), 113-121.

Clague, D. A., Paduan, J. B., Dreyer, B. M., Chadwick Jr, W. W., Rubin, K. R., Perfit, M. R., & Fundis, A. T. (2018). Chemical variations in the 1998, 2011, and 2015 lava flows from Axial Seamount, Juan de Fuca Ridge: Cooling during ascent, lateral transport, and flow. Geochemistry, Geophysics, Geosystems, 19(9), 2915-2933.

Clark, R. W., Sager, W. W., & Zhang, J. (2018). Seismic stratigraphy of the Shatsky Rise sediment cap, northwest Pacific, and implications for pelagic sedimentation atop submarine plateaus. Marine Geology, 397, 43-59.

Clouard, V., & Bonneville, A. (2005). Ages of seamounts, islands, and plateaus on the Pacific plate. Special Papers-Plates, plumes,and paradigms, Boulder, Colorado: Geological Society of America, 388, 71-90.

Collignon, M., Schmid, D. W., Galerne, C., Lupi, M., & Mazzini, A. (2018). Modelling fluid flow in clastic eruptions: Application to the Lusi mud eruption. Marine and Petroleum Geology, 90, 173-190.

Consonni, A., Ronchi, P., Geloni, C., Battistelli, A., Grigo, D., Biagi, S., ... & Gianelli, G. (2010). Application of numerical modelling to a case of compaction-driven dolomitization: a Jurassic palaeohigh in the Po Plain, Italy. *Sedimentology*, *57*(1), 209-231.

Corbella, M., Gomez-Rivas, E., Martín-Martín, J. D., Stafford, S. L., Teixell, A., Griera, A., ... & Salas, R. (2014). Insights to controls on dolomitization by means of reactive transport models applied to the Benicàssim case study (Maestrat Basin, eastern Spain). *Petroleum Geoscience*, *20*(1), 41-54.

Corfield, R. I., Carmichael, S., Bennett, J., Akhter, S., Fatimi, M., & Craig, T. (2010). Variability in the crustal structure of the West Indian Continental Margin in the Northern Arabian Sea. Petroleum Geoscience, 16(3), 257-265.

Courgeon, S., Bourget, J., & Jorry, S. J. (2016a). A Pliocene–Quaternary analogue for ancient epeiric carbonate settings: The Malita intrashelf basin (Bonaparte Basin, northwest Australia). AAPG Bulletin, 100(4), 565-595.

Courgeon, S., Jorry, S. J., Camoin, G. F., BouDagher-Fadel, M. K., Jouet, G., Révillon, S., Bachèlery, P., Pelleter, E., Borgomano, J., Poli, E., & Droxler, A. W. (2016b). Growth and demise of Cenozoic isolated carbonate platforms: New insights from the Mozambique Channel seamounts (SW Indian Ocean). Marine Geology, 380, 90-105.

Courgeon, S., Jorry, S. J., Jouet, G., Camoin, G., BouDagher-Fadel, M. K., Bachèlery, P., Caline, B., Boichard, R., Révillon, S., Thomas, Y., Thereau, E., & Guérin, C. (2017). Impact of tectonic and volcanism on the Neogene evolution of isolated carbonate platforms (SW Indian Ocean). Sedimentary Geology, 355, 114-131.

Cozzi, A., Cascone, A., Bertelli, L., Bertello, F., Brandolese, S., Minervini, M., Ronchi, P., Ruspi, R. and Harby, H. (2018). Zohr Giant Gas Discovery – A Paradigm Shift in Nile Delta and East Mediterranean Exploration. Search and Discovery Article 20414. Am. Assoc. Petrol. Geol..

Cross, N. E., van Veen, L. J., Al-Enezi, A., Singh, S., & van Beusekom, G. (2021). Seismic geomorphology of karst in Cretaceous to Early Cenozoic carbonates of North Kuwait. Marine and Petroleum Geology, 128, 104947.

Crough, S. T. (1983). Hotspot swells. Annual Review of Earth and Planetary Sciences, 11(1), 165-193.

Dañobeitia, J. J., & Canales, J. P. (2000). Magmatic underplating in the Canary Archipelago. Journal of Volcanology and Geothermal Research, 103(1-4), 27-41.

Dasgupta, R., Jackson, M. G., & Lee, C. T. A. (2010). Major element chemistry of ocean island basalts—Conditions of mantle melting and heterogeneity of mantle source. Earth and Planetary Science Letters, 289(3-4), p. 377-392.

Davies, R., Bell, B. R., Cartwright, J. A., & Shoulders, S. (2002). Three-dimensional seismic imaging of Paleogene dike-fed submarine volcanoes from the northeast Atlantic margin. Geology, 30(3), 223-226.

Dechnik, B., Webster, J. M., Webb, G. E., Nothdurft, L., & Zhao, J. X. (2017). Successive phases of Holocene reef flat development: Evidence from the mid-to outer Great Barrier Reef. Palaeogeography, palaeoclimatology, palaeoecology, 466, 221-230.

Deer, W. A., Howie, R. A., & Zussman, J. (2013). An introduction to the rock-forming minerals. Mineralogical Society of Great Britain and Ireland, Longman, London (1966), p. 528.

Demicco, R. V., Lowenstein, T. K., Hardie, L. A., & Spencer, R. J. (2005). Model of seawater composition for the Phanerozoic. Geology, 33(11), 877-880.

DiCaprio, L., Müller, R. D., & Gurnis, M. (2010). A dynamic process for drowning carbonate reefs on the northeastern Australian margin. Geology, 38(1), 11-14.

Dickson, J. A. D., & Kenter, J. A. M. (2014). Diagenetic evolution of selected parasequences across a carbonate platform: Late Paleozoic, Tengiz Reservoir, Kazakhstan. Journal of Sedimentary Research, 84(8), p. 664-693.

Dong, Y., Duan, R., Li, Z., Lü, X., Cai, C., Liu, J., & Wang, L. (2021). Quantitative evaluation of hydrothermal fluids and their impact on diagenesis of deep carbonate reservoirs: Insights from geochemical modeling. Marine and Petroleum Geology, 124, 104797.

Drever, J.I., (1997). The Geochemistry of Natural Waters, Surface and Groundwater Environments. Englewood Cliffs, New Jersey (Prentice Hall), 436p.

Droste, H. J., Van Buchem, F. S. P., Al-Husseini, M. I., & Maurer, F. (2010). Sequence-stratigraphic framework of the Aptian Shu'aiba Formation in the Sultanate of Oman. Barremian-Aptian stratigraphy and hydrocarbon habitat of the eastern Arabian Plate. GeoArabia Special Publication, 4, 229-283.

Droxler, A. W., & Jorry, S. J. (2021). The Origin of Modern Atolls: Challenging Darwin's Deeply Ingrained Theory. Annual Review of Marine Science, 13, 537-573.

Dubicka, Z., Wierny, W., Bojanowski, M. J., Rakociński, M., Walaszczyk, I., & Thibault, N. (2024). Multi-proxy record of the mid-Maastrichtian event in the European Chalk Sea: Paleoceanographic implications. Gondwana Research, 129, 1-22.

Duncan, R. A., & Clague, D. A. (1985). Pacific plate motion recorded by linear volcanic chains. In The Ocean Basins and Margins: Volume 7A The Pacific Ocean (pp. 89-121). Boston, MA: Springer US.

Eberli GP, Massaferro JL, Sarg JF, editors. (2004b). Seismic Imaging of Carbonate Reservoir and Systems. American Association of Petroleum Geologists Memoir 88, 365pp.

Eberli, G. P., & Betzler, C. (2019). Characteristics of modern carbonate contourite drifts. Sedimentology, 66(4), 1163-1191.

Eberli, G. P., Anselmetti, F. S., Betzler, C., Van Konijnenburg, J. H., & Bernoulli, D. (2004a). Carbonate platform to basin transitions on seismic data and in outcrops: Great Bahama Bank and the Maiella platform margin, Italy. in Seismic imaging of carbonate reservoirs and systems: AAPG Memoir 81, p. 207– 250.

Eberli, G. P., Anselmetti, F. S., Isern, A. R., & Delius, H. E. I. K. E. (2010). Timing of changes in sea-level and currents along Miocene platforms on the Marion Plateau, Australia. In Cenozoic carbonate systems of Australasia Vol. 95, SEPM Society for Sedimentary Geology Special Publication, 219-242.

Elderfield, H. (2010). Seawater chemistry and climate. Science, 327(5969), 1092-1093.

El-Oribi, M.S., Salah, H. and Raslan, H. (2022). Is Al Thuraya another Mediterranean Giant Discovery Zohr Field? (identification of Al Thuraya reef build-up gas prospect, Offshore Nile Delta, Eastern Mediterranean, Egypt). SEG Technical Program Expanded Abstracts, 2022, 406–409.

El-Shazly, S., Košťák, M., Abdel-Gawad, G., Kloukčová, B., Saber, S. G., Salama, Y. F., ... & Žák, K. (2011). Carbon and oxygen stable isotopes of selected Cenomanian and Turonian rudists from Egypt and Czech Republic, and a note on changes in rudist diversity. Bulletin of Geosciences, 86(2), 209-226.

El-Yamani, M. S., John, C. M., & Bell, R. (2022). Stratigraphic evolution and karstification of a Cretaceous Mid-Pacific atoll (Resolution Guyot) resolved from core-log-seismic integration and comparison with modern and ancient analogues. Basin Research, 34(5), 1536-1566.

El-Yamani, M. S., John, C. M., & Bell, R. (2024). Mechanism of island dolostones formation in the Cretaceous Calcitic ocean: Insights from the Mid-Pacific Guyots. Marine and Petroleum Geology, 106741.

Enrique, L. J. (1976). Kinetics of continuous growth cultures using the logistic growth curve. Biotechnology and Bioengineering, 18(7), 1029-1032.

Erba, E., Channell, J. E., Claps, M., Jones, C., Larson, R., Opdyke, B., ... & Torricelli, S. (1999). Integrated stratigraphy of the Cismon Apticore (southern Alps, Italy); a" reference section" for the Barremian-Aptian interval at low latitudes. The Journal of Foraminiferal Research, 29(4), 371-391.

Erlich, R. N., Barrett, S. F., & Ju, G. B. (1990). Seismic and geologic characteristics of drowning events on carbonate platforms. AAPG bulletin, 74(10), 1523-1537.

Erlich, R. N., Longo Jr, A. P., & Hyare, S. (1993). Response of Carbonate Platform Margins to Drowning: Evidence of Environmental Collapse: Chapter 9. In R.G Loucks, J.F Sarg (Eds.), Carbonate Sequence Stratigraphy, American Association of Petroleum Geologists, Memoir, vol. 57 (1993), pp. 241-266.

Esestime, P., Hewitt, A., & Hodgson, N. (2016). Zohr–A newborn carbonate play in the Levantine Basin, East-Mediterranean. First Break, 34(2).

Evans, M. W., Snyder, S. W., & Hine, A. C. (1994). High-resolution seismic expression of karst evolution within the Upper Floridan aquifer system; Crooked Lake, Polk County, Florida. Journal of Sedimentary Research, 64(2b), 232-244.

Fairhurst, C., Brown, E. T., Detournay, E., Marsily, G. D., Nikolaevshiy, V., Pearson, J. R., ... & Berest, P. (1999). Underground Nuclear Testing in French Polynesia: Stability and Hydrology Issues.

Fallon, S. J., & Guilderson, T. P. (2005). Extracting growth rates from the nonlaminated coralline sponge Astrosclera willeyana using bomb radiocarbon. Limnology and Oceanography: Methods, 3(10), 455-461.

Feng, D., & Chen, D. (2015). Authigenic carbonates from an active cold seep of the northern South China Sea: new insights into fluid sources and past seepage activity. Deep sea research part II: topical studies in oceanography, 122, 74-83.

Fick, C., Puhl, E., & Toldo Jr, E. E. (2020). Threshold of motion of bivalve and gastropod shells under oscillatory flow in flume experiments. Sedimentology, 67(1), 627-648.

Fiordalisi, E., Marchegiano, M., John, C. M., Oxtoby, N., Rochelle-Bates, N., do Couto Pereira, G., Machado, V., Dixon, R., Sharp, I., & Schröder, S. (2021). Late Cretaceous volcanism and fluid circulation in the South Atlantic: Insights from continental carbonates in the onshore Namibe Basin (Angola). Marine and Petroleum Geology, 134, 105351.

Flood, P. G. (1998). Origin of White Sucrosic Dolomite within Shallow-Water Limestones, ODP Hole 866A, Resolution Guyot, Mid-Pacific Mountains: Strontium Isotopic Evidence for the Role of Sea Water in Dolomitization. Reefs and Carbonate Platforms in the Pacific and Indian Oceans, 137-144.

Flood, P. G., & Chivas, A. R. (1995). Origin of massive dolomite, Leg 143, Hole 866A, Resolution Guyot, Mid-Pacific Mountains: Northwest Pacific atolls and guyots. In Proceedings of the Ocean Drilling Program. Scientific results, Vol. 143, p. 161-169.

Flood, P. G., Fagerstrom, J. A., & Rougerie, F. (1996). Interpretation of the origin of massive replacive dolomite within atolls and submerged carbonate platforms: strontium isotopic signature ODP Hole 866A, Resolution Guyot, Mid-Pacific Mountains. Sedimentary Geology, 101(1-2), 9-13.

Flügel, E. (2010). Microfacies of carbonate rocks: Analysis, Interpretation and Application. Vol. 976, springer, Berlin

Föllmi, K. B. (2012). Early Cretaceous life, climate and anoxia. Cretaceous Research, 35, 230-257.

Foster, G. L., Hull, P., Lunt, D. J., & Zachos, J. C. (2018). Placing our current 'hyperthermal'in the context of rapid climate change in our geological past. Philosophical Transactions of the Royal Society A: Mathematical, Physical and Engineering Sciences, 376(2130), 20170086.

Fournier, F., Borgomano, J., & Montaggioni, L. F. (2005). Development patterns and controlling factors of Tertiary carbonate buildups: Insights from high-resolution 3D seismic and well data in the Malampaya gas field (Offshore Palawan, Philippines). Sedimentary Geology, 175(1-4), 189-215.

Fraschetti, S., Giangrande, A., Terlizzi, A., & Boero, F. (2002). Pre-and post-settlement events in benthic community dynamics. Oceanologica Acta, 25(6), 285-295.

Frazer, M., Hollis, C., & Whitaker, F. (2023). Dolomitisation of carbonate platform margins by fault-controlled geothermal convection: insights from coupling stratigraphic and reactive transport models. The Depositional Record.

French, S. W., & Romanowicz, B. (2015). Broad plumes rooted at the base of the Earth's mantle beneath major hotspots. Nature, 525(7567), 95-99.

Fritz, P., & Smith, D. G. W. (1970). The isotopic composition of secondary dolomites. Geochimica et Cosmochimica Acta, 34(11), 1161-1173.

Frost III, E. L., & Kerans, C. (2009). Platform-margin trajectory as a control on syndepositional fracture patterns, Canning Basin, Western Australia. Journal of Sedimentary Research, 79(2), 44-55.

Gabellone, T., & Whitaker, F. (2016). Secular variations in seawater chemistry controlling dolomitization in shallow reflux systems: insights from reactive transport modelling. Sedimentology, 63(5), 1233-1259.

Gabellone, T., Borromeo, O., Consonni, A., Geloni, C., Albertini, C., Bigoni, F., ... & Vercellino, A. (2020, January). A multistep reactive convection model for the prediction of the dolomite bodies distribution in the Karachaganak field-Kazakhstan. In International Petroleum Technology Conference (p. D033S057R003). IPTC.

Gabellone, T., Whitaker, F., Katz, D., Griffiths, G., & Sonnenfeld, M. (2016). Controls on reflux dolomitisation of epeiric-scale ramps: Insights from reactive transport simulations of the Mississippian Madison Formation (Montana and Wyoming). Sedimentary geology, 345, 85-102.

Gale, A. S., Bown, P., Caron, M., Crampton, J., Crowhurst, S. J., Kennedy, W. J., Petrizzo, M. R., & Wray, D. S. (2011). The uppermost Middle and Upper Albian succession at the Col de Palluel, Hautes-Alpes, France: An integrated study (ammonites, inoceramid bivalves, planktonic foraminifera, nannofossils, geochemistry, stable oxygen and carbon isotopes, cyclostratigraphy). Cretaceous Research, 32(2), 59-130.

Gale, A. S., Hardenbol, J., Hathway, B., Kennedy, W. J., Young, J. R., & Phansalkar, V. (2002). Global correlation of Cenomanian (Upper Cretaceous) sequences: Evidence for Milankovitch control on sea level. Geology, 30(4), 291-294.

Gamo, T., Okamura, K., Charlou, J. L., Urabe, T., Auzende, J. M., Ishibashi, J., ... & Chiba, H. (1997). Acidic and sulfate-rich hydrothermal fluids from the Manus back-arc basin, Papua New Guinea. Geology, 25(2), 139-142.

Gardner, T. A., Côté, I. M., Gill, J. A., Grant, A., & Watkinson, A. R. (2005). Hurricanes and Caribbean coral reefs: impacts, recovery patterns, and role in long-term decline. Ecology, 86(1), 174-184.

Garrabou, J., Coma, R., Bensoussan, N., Bally, M., Chevaldonné, P., Cigliano, M., ... & Cerrano, C. (2009). Mass mortality in Northwestern Mediterranean rocky benthic communities: effects of the 2003 heat wave. Global change biology, 15(5), 1090-1103.

Gartner, G. L. B., Schlager, W., & Adams, E. W. (2004). Seismic expression of the boundaries of a Miocene carbonate platform, Sarawak, Malaysia. In: Seismic Imaging of Carbonate Reservoirs and Systems (Eds G.P. Eberli, J.L. Masafero and J.F. Sarg), AAPG Mem., 81, pp. 351–365.

GATT, P. (2012). Carbonate facies, depositional sequences and tectonostratigraphy of the Palaeogene Malta Platform (Doctoral dissertation, Durham University).

Geng, M., Song, H., Guan, Y., Chen, J., Zhang, R., Zhang, B., & Zhang, X. (2020). Sill-related seafloor domes in the Zhongjiannan Basin, western South China Sea. Marine and Petroleum Geology, 122, 104669.

Geplan Consulting. (n.d.). Possible Analogues of The Eastern Mediterranean Cretaceous Isolated Carbonate Platforms. Available at: https://www.geplan.it/wp-content/uploads/2022/10/9_Cretaceous_2018-3.pdf.

Gertsch, B., Keller, G., Adatte, T., Berner, Z., Kassab, A. S., Tantawy, A. A. A., ... & Stueben, D. (2010). Cenomanian–Turonian transition in a shallow water sequence of the Sinai, Egypt. International Journal of Earth Sciences, 99, 165-182.

Ghalayini, R., Nader, F. H., Bou Daher, S., Hawie, N., & Chbat, W. E. (2018). Petroleum systems of Lebanon: An update and review. Journal of Petroleum Geology, 41(2), 189-214.

Gili, E., & Götz, S. (2018). Paleoecology of rudists. In: P. A. Selden (Ed.), Treatise online (Vol. 103, pp. 1– 29). University of Kansas, Paleontological Institute.

Gili, E., Masse, J. P., & Skelton, P. W. (1995). Rudists as gregarious sediment-dwellers, not reef-builders, on Cretaceous carbonate platforms. Palaeogeography, palaeoclimatology, palaeoecology, 118(3-4), 245-267.

Gischler, E. (2006). Sedimentation on rasdhoo and ari atolls, maldives, Indian ocean. Facies, 52(3), 341-360.

Gischler, E., Hudson, J. H., Eisenhauer, A., Parang, S., & Deveaux, M. (2023). 9000 years of change in coral community structure and accretion in Belize reefs, western Atlantic. Scientific Reports, 13(1), 11349.

Gischler, E., Storz, D., & Schmitt, D. (2014). Sizes, shapes, and patterns of coral reefs in the Maldives, Indian Ocean: the influence of wind, storms, and precipitation on a major tropical carbonate platform. Carbonates and Evaporites, 29(1), 73-87.

Gomez, M. G., Villacorta, R. L., Masip, J. D., & Pereira, A. D. F. (2022, June). Sedimentological Model of the Isolated Carbonate Platform Dunquin South in Porcupine Basin, Ireland. In 83rd EAGE Annual Conference & Exhibition (Vol. 2022, No. 1, pp. 1-5). European Association of Geoscientists & Engineers.

González-Escobar, M., Sánchez-Barra, A. C., Gallegos-Castillo, C. A., Ojeda, S. M. A., & Mastache-Román, E. A. (2023). Morphology of buried volcanic bodies in a sedimentary basin of the Pacific Continental Shelf (Gulf of California, Mexico). Journal of Volcanology and Geothermal Research, 107828.

Gordon, W. A. (1973). Marine life and ocean surface currents in the Cretaceous. The Journal of Geology, 81(3), 269-284.

Gradstein, F. M., Ogg, J. G., Schmitz, M. D., & Ogg, G. M. (Eds.). (2012). The geologic time scale 2012. elsevier.

Greenlee, S. M. and Lehmann, P. J. (1993). Stratigraphic framework of productive carbonate buildups. In: R. G. Loucks and J. F. Sarg (Eds.), Carbonate sequence stratigraphy: recent developments and advancements. AAPG Memoir 57, 43–62.

Gregg, J. M., & Sibley, D. F. (1984). Epigenetic dolomitization and the origin of xenotopic dolomite texture. Journal of Sedimentary Research, 54(3), 908-931.

Gregg, J. M., Bish, D. L., Kaczmarek, S. E., & Machel, H. G. (2015). Mineralogy, nucleation and growth of dolomite in the laboratory and sedimentary environment: a review. Sedimentology, 62(6), 1749-1769.

Gudbrandsson, S., Wolff-Boenisch, D., Gislason, S. R., & Oelkers, E. H. (2011). An experimental study of crystalline basalt dissolution from 2⩽ pH⩽ 11 and temperatures from 5 to 75 C. Geochimica et Cosmochimica Acta, 75(19), 5496-5509.

Guille, G. (1996). The atolls of Mururoa and fangataufa (French polynesia). I: Geology-Petrology-Hydrogeology from volcano to atoll. Musee oceanographique, Monaco.

Haggerty, J. A., & Silva, I. P. (1995). 53. Comparison of the origin and evolution of northwest pacific guyots drilled during leg 1441. In Proceedings of the Ocean Drilling Program, Scientific Results, Vol. 53, p. 935-949.

Hallam, A. (1984). Pre-Quaternary sea-level changes. Annual Review of Earth and Planetary Sciences, 12(1), 205-243.

Hallock, P., & Schlager, W. (1986). Nutrient excess and the demise of coral reefs and carbonate platforms. Palaios, 389-398.

Hamilton, E. L. (1956). Sunken islands of the mid-Pacific mountains (Vol. 64). Geological Society of America, 64, 1-92.

Handford, C. R., & Baria, L. R. (2007). Geometry and seismic geomorphology of carbonate shoreface clinoforms, Jurassic Smackover Formation, north Louisiana. Geological Society, London, Special Publications, 277(1), 171-185.

Hansen, D. M. (2006). The morphology of intrusion-related vent structures and their implications for constraining the timing of intrusive events along the NE Atlantic margin. Journal of the Geological Society, 163(5), 789-800.

Hansen, D. M., & Cartwright, J. (2006). Saucer-shaped sill with lobate morphology revealed by 3D seismic data: implications for resolving a shallow-level sill emplacement mechanism. Journal of the Geological Society, 163(3), 509-523.

Hansen, D. M., Redfern, J., Federici, F., Di Biase, D., & Bertozzi, G. (2008). Miocene igneous activity in the Northern Subbasin, offshore Senegal, NW Africa. Marine and Petroleum Geology, 25(1), 1-15.

Haq, B. U. (2014). Cretaceous eustasy revisited. Global and Planetary change, 113, 44-58.

Haq, B. U. (2018a). Triassic eustatic variations reexamined. GSA Today, 28(12), 4-9.

Haq, B. U. (2018b). Jurassic sea-level variations: a reappraisal. GSA Today, 28(1), 4-10.

Haq, B. U., & Al-Qahtani, A. M. (2005). Phanerozoic cycles of sea-level change on the Arabian Platform. GeoArabia, 10(2), 127-160.

Haq, B. U., & Schutter, S. R. (2008). A chronology of Paleozoic sea-level changes. Science, 322(5898), 64-68.

Haq, B. U., Hardenbol, J. A. N., & Vail, P. R. (1987). Chronology of fluctuating sea levels since the Triassic. Science, 235(4793), 1156-1167.

Hardie, L. A. (1996). Secular variation in seawater chemistry: An explanation for the coupled secular variation in the mineralogies of marine limestones and potash evaporites over the past 600 my. Geology, 24(3), 279-283.

Harnik, P. G., Lotze, H. K., Anderson, S. C., Finkel, Z. V., Finnegan, S., Lindberg, D. R., ... & Tittensor, D. P. (2012). Extinctions in ancient and modern seas. Trends in Ecology & Evolution, 27(11), 608-617.

Harris, P. M. (1979). Facies anatomy and diagenesis of a Bahamian ooid shoal. Sedimenta VII. University of Miami, 163 pp.

Harris, P. M., Purkis, S. J., Ellis, J., Swart, P. K., & Reijmer, J. J. (2015). Mapping bathymetry and depositional facies on Great Bahama Bank. Sedimentology, 62(2), 566-589.

Hart, S. R. (1984). A large-scale isotope anomaly in the Southern Hemisphere mantle. Nature, 309(5971), 753-757.

Hay, W. W. (2011). Can humans force a return to a 'Cretaceous' climate?. Sedimentary Geology, 235(1-2), 5-26.

Hay, W. W., and DeConto, R. M. (1999). A comparison of modern and Late Cretaceous meridional energy transport and oceanology. In: Barrera, E., Johnson, C. (Eds.), Evolution of the Cretaceous Ocean/Climate System. Special papers in Geological Society of America, 283-300.

Heezen, B. C., MacGregor, I.D., Foreman, H.P., Forristall, G., Hekel, H., Hesse, R., Hoskins, R.H., Jones, E.J.W., Kaneps, A., Krasheninnikov, V.A., Ruef, M.H. (1973). Tertiary pelagic ooze on Ita MaiTai guyot, equatorial Pacific: DSDP Sites 200 and 201. Initial Reports of the Deep-Sea Drilling Project, Vol. 20, 87-96.

Heiken, G. (1972). Morphology and petrography of volcanic ashes. Geological Society of America Bulletin, 83(7), 1961-1988.

Heinrich, C. A., & Candela, P. A. (2014). Fluids and ore formation in the Earth's crust. In Treatise on Geochemistry Second Edition, Vol. 13, pp. 1-28.

Hemley, J. J., Cygan, G. L., Fein, J. B., Robinson, G. R., & d'Angelo, W. M. (1992). Hydrothermal ore-forming processes in the light of studies in rock-buffered systems; I, Iron-copper-zinc-lead sulfide solubility relations. Economic Geology, 87(1), 1-22.

Henderson, L. J. (1985). Motion of the Pacific Plate relative to the hotspots since the Jurassic and model of oceanic plateaus of the Farallon plate [Ph. D. dissert.]. Northwestern Univ., Evanston, IL.

Hendry, J. P., Gregg, J. M., Shelton, K. L., Somerville, I. D., & Crowley, S. F. (2015). Origin, characteristics and distribution of fault-related and fracture-related dolomitization: Insights from Mississippian carbonates, Isle of Man. Sedimentology, 62(3), 717-752.

Hendry, J., Burgess, P., Hunt, D., Janson, X., & Zampetti, V. (2021). Seismic characterization of carbonate platforms and reservoirs: an introduction and review. In: Geological Society, London, Special Publications, 509, 1-28.

Henry, P., Guy, C., Cattin, R., Dudoignon, P., Sornein, J. F., & Caristan, Y. (1996). A convective model of water flow in Mururoa basalts. Geochimica et Cosmochimica Acta, 60(12), 2087-2109.

Herrle, J. O., Kößler, P., Friedrich, O., Erlenkeuser, H., & Hemleben, C. (2004). High-resolution carbon isotope records of the Aptian to Lower Albian from SE France and the Mazagan Plateau (DSDP Site 545): a stratigraphic tool for paleoceanographic and paleobiologic reconstruction. Earth and Planetary Science Letters, 218(1-2), 149-161.

Herrle, J. O., Schröder-Adams, C. J., Davis, W., Pugh, A. T., Galloway, J. M., & Fath, J. (2015). Mid-Cretaceous High Arctic stratigraphy, climate, and oceanic anoxic events. Geology, 43(5), 403-406.

Heubeck, C., C. Story, P. Peng, C. Sullivan, and S. Duff. (2004). An integrated reservoir study of the Liuhua 11-1 field using a high-resolution three-dimensional seismic data set, in G. P. Eberli, J. L. Masaferro, and J. F. Sarg, eds., Seismic imaging of carbonate reservoirs and systems: AAPG Memoir 81, 149–168.

Hirani, J., Bastesen, E., Boyce, A., Corlett, H., Gawthorpe, R., Hollis, C., ... & Whitaker, F. (2018). Controls on the formation of stratabound dolostone bodies, Hammam Faraun Fault block, Gulf of Suez. Sedimentology, 65(6), 1973-2002.

Hoffman, P. F., & Lamothe, K. G. (2019). Seawater-buffered diagenesis, destruction of carbon isotope excursions, and the composition of DIC in Neoproterozoic oceans. Proceedings of the National Academy of Sciences, 116(38), 18874-18879.

Holland, H. D. (2005). Sea level, sediments and the composition of seawater. American Journal of Science, 305(3), 220-239.

Homewood, P., Vahrenkamp, V., Mettraux, M., Mattner, J., Vlaswinkel, B., Droste, H., & Kwarteng, A. (2007). Bar Al Hikman: a modern carbonate and outcrop analogue in Oman for Middle East Cretaceous fields. First break, 25(11), 55-61.

Hönig, M. R., John, C. M., & Manning, C. (2017). Development of an equatorial carbonate platform across the Triassic-Jurassic boundary and links to global palaeoenvironmental changes (Musandam Peninsula, UAE/Oman). Gondwana Research, 45, 100-117.

Horita, J. (2014). Oxygen and carbon isotope fractionation in the system dolomite–water–CO_2 to elevated temperatures. Geochimica et Cosmochimica Acta, 129, 111-124.

Horita, J., Zimmermann, H., & Holland, H. D. (2002). Chemical evolution of seawater during the Phanerozoic: Implications from the record of marine evaporites. Geochimica et Cosmochimica Acta, 66(21), 3733-3756.

Hottinger, L. (1989). Conditions for generating carbonate platforms. Memorie della Società Geologica Italiana, 40, 265-271.

Howarth, V., & Alves, T. M. (2016). Fluid flow through carbonate platforms as evidence for deep-seated reservoirs in Northwest Australia. Marine Geology, 380, 17-43.

Huang, X., & Jokat, W. (2016). Sedimentation and potential venting on the rifted continental margin of Dronning Maud Land. Marine Geophysical Research, 37(4), 313-324.

Huang, X., Betzler, C., Wu, S., Bernhardt, A., Eagles, G., Han, X., & Hovland, M. (2020). First documentation of seismic stratigraphy and depositional signatures of Zhongsha atoll (Macclesfield Bank), South China Sea. Marine and Petroleum Geology, 117, 104349.

Huber, B. T., & Petrizzo, M. R. (2014). Evolution and taxonomic study of the Cretaceous planktic foraminiferal genus Helvetoglobotruncana Reiss, 1957. Journal of Foraminiferal Research, 44(1), 40-57.

Huck, S., Rameil, N., Korbar, T., Heimhofer, U., Wieczorek, T. D., & Immenhauser, A. (2010). Latitudinally different responses of Tethyan shoal-water carbonate systems to the Early Aptian oceanic anoxic event (OAE 1a). Sedimentology, 57(7), 1585-1614.

Hughes, G. W. (2000). Bioecostratigraphy of the Shu'aiba Formation, Shaybah field, Saudi Arabia. GeoArabia, 5(4), 545-578.

Huppert, K. L., Perron, J. T., & Royden, L. H. (2020). Hotspot swells and the lifespan of volcanic ocean islands. Science advances, 6(1), eaaw6906.

Huppert, K. L., Royden, L. H., & Perron, J. T. (2015). Dominant influence of volcanic loading on vertical motions of the Hawaiian Islands. Earth and Planetary Science Letters, 418, 149-171.

Hustoft, S., Mienert, J., Bünz, S., & Nouzé, H. (2007). High-resolution 3D-seismic data indicate focussed fluid migration pathways above polygonal fault systems of the mid-Norwegian margin. Marine Geology, 245(1-4), 89-106.

Huuse, M., Jackson, C. A. L., Van Rensbergen, P., Davies, R. J., Flemings, P. B., & Dixon, R. J. (2010). Subsurface sediment remobilization and fluid flow in sedimentary basins: an overview. Basin Research, 22(4), 342-360.

Iba, Y., & Sano, S. I. (2007). Mid-Cretaceous step-wise demise of the carbonate platform biota in the Northwest Pacific and establishment of the North Pacific biotic province. Palaeogeography, Palaeoclimatology, Palaeoecology, 245(3-4), 462-482.

Infante-Paez, L., & Marfurt, K. J. (2018). In-context interpretation: Avoiding pitfalls in misidentification of igneous bodies in seismic data. Interpretation, 6(4), SL29-SL42.

Intawong, A., Esestime, P., & Rodriguez, K. (2019). Observed link between folded Seaward Dipping Reflectors (SDRs) and large-scale morphology and architecture of the Early Cretaceous carbonate build-up and platform in the Orange Basin. First Break, 37(2), 63-68.

Iyer, K., Schmid, D. W., Planke, S., & Millett, J. (2017). Modelling hydrothermal venting in volcanic sedimentary basins: Impact on hydrocarbon maturation and paleoclimate. Earth and Planetary Science Letters, 467, 30-42.

Jackson, C. A., Schofield, N., & Golenkov, B. (2013). Geometry and controls on the development of igneous sill–related forced folds: A 2-D seismic reflection case study from offshore southern Australia. Bulletin, 125(11-12), 1874-1890.

Jacquemyn, C., El Desouky, H., Hunt, D., Casini, G., & Swennen, R. (2014). Dolomitization of the Latemar platform: fluid flow and dolomite evolution. Marine and Petroleum Geology, 55, 43-67.

Jahnert, R. J., & Collins, L. B. (2012). Characteristics, distribution and morphogenesis of subtidal microbial systems in Shark Bay, Australia. Marine Geology, 303, 115-136.

Jaillard, E., Kassab, W. H., Giraud, F., Robert, E., Masrour, M., Bouchaou, L., ... & Aly, M. F. (2019). Aptian–early Albian sedimentation in the Essaouira-Agadir basin, western Morocco. Cretaceous Research, 102, 59-80.

James, N. P., & Choquette, P. W. (1983). Diagenesis 6. Limestones—the sea floor diagenetic environment. Geoscience Canada.

James, N. P., & Jones, B. (2015). Origin of carbonate sedimentary rocks. John Wiley & Sons.

Jamtveit, B., Svensen, H., Podladchikov, Y. Y., & Planke, S. (2004). Hydrothermal vent complexes associated with sill intrusions in sedimentary basins. Physical Geology of High-Level Magmatic Systems. Geological Society, London, Special Publications, 234, 233-241.

Jean-Baptiste, P., & Leclerc, A. M. (2000). Self-limiting geothermal convection in marine carbonate platforms. Geophysical research letters, 27(6), 743-746.

Jeans, C. V., Wray, D. S., Williams, C. T., Bland, D. J., & Wood, C. J. (2021). Redox conditions, glacio-eustasy, and the status of the Cenomanian-Turonian Anoxic Event: new evidence from the Upper Cretaceous Chalk of England. Acta Geologica Polonica, 71(2).

Jenkyns, H. C. (1995). Carbon-isotope stratigraphy and paleoceanographic significance of the Lower Cretaceous shallow-water carbonates of Resolution Guyot, Mid-Pacific Mountains. In Proceedings of the Ocean Drilling Program, Scientific Results Vol. 143, pp. 99-104.

Jenkyns, H. C., & Wilson, P. A. (1999). Stratigraphy, paleoceanography, and evolution of Cretaceous Pacific guyots; relics from a greenhouse Earth. American Journal of Science, 299(5), 341-392.

Jenkyns, H. C., Paull, C. K., Cummins, D. I., & Fullagar, P. D. (1995). Strontium-isotope stratigraphy of Lower Cretaceous atoll carbonates in the Mid-Pacific Mountains. In Proceedings of the Ocean Drilling Program, Scientific Results Vol. 143, 89-97.

Jensen, K., Johansen, M. K., Lecomte, I., Janson, X., Tveranger, J., & Kaschwich, T. (2021). Paleokarst reservoirs: Efficient and flexible characterization using point-spread-function-based convolution modeling. Interpretation, 9(2), T331-T347.

John, C.M., Bell, R., Muxworthy, A., Robinson, S., Wilson, P., Mitchell, N., Rickaby, E.M., and Turchyn, A., 2021, CARAPACE: Calcite-Aragonite transition Across Pacific Atolls from the Cretaceous to the Eocene, UKRI UK IODP Site Survey Investigation 2021, Proposal # PA2243.

Johnson, C. C. (2002). The rise and fall of rudist reefs: reefs of the dinosaur era were dominated not by corals but by odd mollusks, which died off at the end of the Cretaceous from causes yet to be discovered. American Scientist, 90(2), 148-153.

Johnson, C. C., Barron, E. J., Kauffman, E. G., Arthur, M. A., Fawcett, P. J., & Yasuda, M. K. (1996). Middle Cretaceous reef collapse linked to ocean heat transport. Geology, 24(4), 376-380.

JOIDES Resolution Science Operator. (n.d.). International Ocean Discovery Program, Ocean Drilling Data of ODP Leg 143. https://web.iodp.tamu.edu/OVERVIEW/?&exp=143.

Jones, B. (1989). Calcite rafts, peloids, and micrite in cave deposits from Cayman Brae, British West Indies. Canadian Journal of Earth Sciences, 26(4), 654-664.

Jones, B. (2005). Dolomite crystal architecture: genetic implications for the origin of the Tertiary dolostones of the Cayman Islands. Journal of Sedimentary Research, 75(2), 177-189.

Jones, B., & Luth, R. W. (2002). Dolostones from Grand Cayman, British West Indies. Journal of Sedimentary Research, 72(4), 559-569.

Jones, B., Luth, R. W., & MacNEIL, A. J. (2001). Powder X-ray diffraction analysis of homogeneous and heterogeneous sedimentary dolostones. Journal of Sedimentary Research, 71(5), 790-799.

Jones, G. D., & Xiao, Y. (2005). Dolomitization, anhydrite cementation, and porosity evolution in a reflux system: Insights from reactive transport models. *AAPG bulletin*, *89*(5), 577-601.

Jones, G., Whitaker, F., Smart, P., & Sanford, W. (2000). Numerical modelling of geothermal and reflux circulation in Enewetak Atoll: implications for dolomitization. Journal of Geochemical Exploration, 69, 71-75.

Jones, N. S., Ridgwell, A., & Hendy, E. J. (2015). Evaluation of coral reef carbonate production models at a global scale. Biogeosciences, 12(5), 1339-1356.

Jorry, S.J., Camoin, G.F., Jouet, G., Le Roy, P., Vella, C., Courgeon, S., Prat, S., Paumard, V.,Boulle, J., Caline, B., Borgomano, J. (2016). Modern sediments and Pleistocene reefs from isolated carbonate platforms (Iles Eparses, SW Indian Ocean): a preliminary study. Acta oecologica, 72, 129-143.

Judd, A., & Hovland, M. (2007). Seabed fluid flow: the impact on geology, biology and the marine environment. Cambridge University Press, pp. 475.

Kaczmarek, S. E., & Sibley, D. F. (2011). On the evolution of dolomite stoichiometry and cation order during high-temperature synthesis experiments: an alternative model for the geochemical evolution of natural dolomites. Sedimentary Geology, 240(1-2), 30-40.

Karlsen, K. S., Domeier, M., Gaina, C., & Conrad, C. P. (2020). A tracer-based algorithm for automatic generation of seafloor age grids from plate tectonic reconstructions. Computers & geosciences, 140, 104508.

Keizer, P., Koppers, A., Staudigel, H., & Helly, J. (2001, December). The Seamount Catalog in EarthRef. org. In AGU Fall Meeting Abstracts (Vol. 2001, pp. OS11B-0358). https://earthref.org/SC/#top

Kemp, D. B., & Sadler, P. M. (2014). Climatic and eustatic signals in a global compilation of shallow marine carbonate accumulation rates. Sedimentology, 61(5), 1286-1297.

Kendall, C. G. S. C., Chiarenzelli, J., & Hassan, H. S. (2009, June). World source rock potential through geological time: A function of basin restriction, nutrient level, sedimentation rate, and sea-level rise. In Proceedings of the AAPG at the SEPM (Society for Sedimentary Petrology) AAPG Annual Meeting in Denver.

Kenter, J. A. M., Harris, P. M., Collins, J. F., Weber, L. J., Kuanysheva, G., & Fischer, D. J. (2006). Late Visean to Bashkirian platform cyclicity in the central Tengiz buildup, Precaspian Basin, Kazakhstan: Depositional evolution and reservoir development. in P. M. Harris and L. J. Weber, eds., Giant hydrocarbon reservoirs of the world: From rocks to reservoir characterization and modeling: AAPG Memoir 88/SEPM Special Publication, p. 7– 54.

Kenter, J. A., & Stafleu, J. (1994). 19. Synthetic seismograms at site 866: origin of reflections and implications for recognizing the limestone/basalt transition in Cretaceous Mid-Pacific Guyots. In Proceedings of the Ocean Drilling Program. Scientific results, Vol. 143, 305-315.

Kenter, J. M., & Ivanov, M. (1995). Parameters controlling acoustic properties of carbonate and volcaniclastic sediments at Sites 866 and 869: Northwest Pacific atolls and guyots. In Proceedings of the Ocean Drilling Program. Scientific results, Vol. 143, 287-303.

Kiessling, W. (2002). Secular variations in the Phanerozoic reef ecosystem. In Phanerozoic Reef Patterns (eds W Kiessling, E Flügel, J Golonka). SEPM Special Publication, 72, pp. 625–690.

Kiessling, W., Flügel, E., & Golonka, J. A. N. (2003). Patterns of Phanerozoic carbonate platform sedimentation. Lethaia, 36(3), 195-226.

Kim, W., Fouke, B. W., Petter, A. L., Quinn, T. M., Kerans, C., & Taylor, F. (2012). Sea-level rise, depth-dependent carbonate sedimentation and the paradox of drowned platforms. Sedimentology, 59(6), 1677-1694.

Kjoberg, S., Schmiedel, T., Planke, S., Svensen, H. H., Millett, J. M., Jerram, D. A., ... & Helsem, A. (2017). 3D structure and formation of hydrothermal vent complexes at the Paleocene-Eocene transition, the Møre Basin, mid-Norwegian margin. Interpretation, 5(3), SK65-SK81.

Klügel, A., Longpré, M. A., García-Cañada, L., & Stix, J. (2015). Deep intrusions, lateral magma transport and related uplift at ocean island volcanoes. Earth and Planetary Science Letters, 431, 140-149.

Knowlton, N., Brainard, R. E., Fisher, R., Moews, M., Plaisance, L., & Caley, M. J. (2010). Coral reef biodiversity. Life in the world's oceans: diversity distribution and abundance, 65-74.

Koeshidayatullah, A., Corlett, H., Stacey, J., Swart, P. K., Boyce, A., Robertson, H., ... & Hollis, C. (2020). Evaluating new fault-controlled hydrothermal dolomitization models: Insights from the Cambrian Dolomite, Western Canadian Sedimentary Basin. Sedimentology, 67(6), 2945-2973.

Kohout, F. A., Henry, H. R., Banks, J. E., Smith, K. L., & Griffin, G. M. (1977). Hydrogeology related to geothermal conditions of the Floridan Plateau. The geothermal nature of the Floridan Plateau, 21, 1-41.

Koppers, A. A., Staudigel, H., Christie, D. M., Dieu, J. J., & Pringle, M. S. (1995). Sr-Nd-Pb isotope geochemistry of leg 144 West Pacific guyouts: Implications for the geochemical evolution of the" SOPITA" mantle anomaly. In Proceedings of the Ocean Drilling Program, Initial Reports, 144, p. 535-545.

Koppers, A. A., Staudigel, H., Pringle, M. S., & Wijbrans, J. R. (2003). Short-lived and discontinuous intraplate volcanism in the South Pacific: Hot spots or extensional volcanism?. Geochemistry, Geophysics, Geosystems, 4(10).

Kump, Lee R., Timothy J. Bralower, and Andy Ridgwell. "Ocean acidification in deep time." Oceanography 22.4 (2009): 94-107.

Kurnosov, V. B., Zolotarev, B. P., & Artamonov, A. V. (2007). Sea water-basalt interaction in the Pacific seamounts: Low-temperature environments. In Water-Rock Interaction-Proceedings of the 12th International Symposium on Water-Rock Interaction, WRI-12 (pp. 135-138).

Kurnosov, V., Zolotarev, B., Eroshchev-Shak, V., Artamonov, A., & Kashinzev, G. (1995). Alteration of basalts from the West Pacific Guyots, Legs 143 and 144. In Proceedings of the Ocean Drilling Program: Scientific Results, Vol. 144, p. 475-491.

Ladant, J. B., Poulsen, C. J., Fluteau, F., Tabor, C. R., MacLeod, K. G., Martin, E. E., ... & Rostami, M. A. (2020). Paleogeographic controls on the evolution of Late Cretaceous ocean circulation. Climate of the Past, 16(3), 973-1006.

Lambregts, P., Pieter, H., & Sanne, D. (2014, March). Exploring for hydrocarbons in a deepwater boutique basin: Orange Basin. In South Africa: Geological Society Petroleum Group Conference Abstract Book: Petroleum Geoscience of the West Africa Margin, London, pp. 98-99.

Land, L. S. (1973). Contemporaneous dolomitization of Middle Pleistocene reefs by meteoric water, north Jamaica. Bull. Mar. Sci., 23, 64-90.

Land, L. S. (1985). The origin of massive dolomite. Journal of Geological Education, 33(2), 112-125.

Land, L. S. (1991). Dolomitization of the Hope Gate Formation (north Jamaica) by seawater: reassessment of mixing-zone dolomite. In Stable isotope geochemistry: a tribute to Samuel Epstein (Eds H.P. Taylor, J.R. O'Neil and I.R.Kaplan), Geochem. Soc. Spec. Publ.,3, 121-133.

Larson, R. L. (1991). Latest pulse of Earth: Evidence for a mid-Cretaceous superplume. Geology, 19(6), 547-550.

Larson, R. L., Erba, E., Nakanishi, M., Bergersen, D. D., & Lincoln, J. M. (1995). Stratigraphic, vertical subsidence, and paleolatitude histories of Leg 144 guyots. In Proceedings of the Ocean Drilling Program. Scientific results Vol. 144, p. 915-933.

Lau, K. V., & Hardisty, D. S. (2022). Modeling the impacts of diagenesis on carbonate paleoredox proxies. Geochimica et Cosmochimica Acta, 337, 123-139.

Laugié, M., Donnadieu, Y., Ladant, J. B., Green, J. A., Bopp, L., & Raisson, F. (2020). Stripping back the modern to reveal the Cenomanian–Turonian climate and temperature gradient underneath. Climate of the Past, 16(3), 953-971.

Lechler, M., von Strandmann, P. A. P., Jenkyns, H. C., Prosser, G., & Parente, M. (2015). Lithium-isotope evidence for enhanced silicate weathering during OAE 1a (Early Aptian Selli event). *Earth and Planetary Science Letters*, *432*, 210-222.

Leclerc, A. M., Jean-Baptiste, P., Texier, D., & Broc, D. (1999). Density-induced water circulations in atoll coral reefs: A numerical study. Limnology and Oceanography, 44(5), 1268-1281.

Lee, Y. I., & Friedman, G. M. (1987). Deep-burial dolomitization in the Ordovician Ellenburger Group carbonates, west Texas and southeastern New Mexico. Journal of Sedimentary Research, 57(3), 544-557.

Lehmann, J., Ifrim, C., Bulot, L., & Frau, C. (2015). Paleobiogeography of Early Cretaceous Ammonoids. Ammonoid Paleobiology: From macroevolution to paleogeography, 229-257.

Lenton, T. M., Daines, S. J., & Mills, B. J. (2018). COPSE reloaded: an improved model of biogeochemical cycling over Phanerozoic time. Earth-Science Reviews, 178, 1-28.

Leroy, S., Lucazeau, F., d'Acremont, E., Watremez, L., Autin, J., Rouzo, S., ... & Khanbari, K. (2010). Contrasted styles of rifting in the eastern Gulf of Aden: A combined wide-angle, multichannel seismic, and heat flow survey. Geochemistry, Geophysics, Geosystems, 11(7).

Li, R., Jones, B., Qiao, P., Cui, Y., Pei, J., Liu, X., & Shao, L. (2023a). Genesis of island dolostones during rapid island subsidence: Example from the Xisha (Paracel) islands, South China Sea. Sedimentology.

Li, X., Shi, Z., Han, L., & Hu, X. (2023b). Geochemical characteristics of hydrogen, oxygen, carbon isotopes and REE of cenozoic dolomites in Well Xike 1, Xisha Islands, South China sea and the significance for dolomitization in island-reef areas. Frontiers in Earth Science, 10, 1064808.

Lincoln, J. M., Pringle, M. S., & Silva, I. P. (1993). Early and Late Cretaceous volcanism and reef-building in the Marshall Islands. Washington DC American Geophysical Union Geophysical Monograph Series, 77, 279-305.

Ling, A., Eberli, G. P., Swart, P. K., Reolid, J., Stainbank, S., Rüggeberg, A., & Betzler, C. (2021). Middle Miocene platform drowning in the Maldives associated with monsoon-related intensification of currents. Palaeogeography, palaeoclimatology, palaeoecology, 567, 110275.

Liu, G., Wu, S., Gao, J., Zhang, H., Han, X., Qin, Y., ... & Huang, X. (2023). Seismic architecture of Yongle isolated carbonate platform in Xisha Archipelago, South China Sea. Frontiers in Earth Science, 11, 1100675.

Liu, Q., Tang, L., Chen, L., & Gao, P. (2022). 40Ar/39Ar ages and geochemistry of seamount basalts from the western Pacific province. Journal of Marine Science and Engineering, 10(1), 54.

Loma-Villacorta, R., Garcia-Gomez, M., & Diez-Masip, J. (2022, June). Controlling Factors on a Berriasian-Barremian Isolated Carbonate Platform in Central Porcupine Basin, Sw Ireland. In 83rd EAGE Annual Conference & Exhibition (Vol. 2022, No. 1, pp. 1-5). European Association of Geoscientists & Engineers.

Lottaroli, F., & Meciani, L. (2022). The rejuvenation of hydrocarbon exploration in the Eastern Mediterranean. Petroleum Geoscience, 28(1), petgeo2021-018.

Loucks, R. G. (1999). Paleocave carbonate reservoirs: Origins, burial-depth modifications, spatial complexity, and reservoir implications. AAPG bulletin, 83(11), 1795-1834.

Lu, P., & Cantrell, D. (2016). Reactive transport modelling of reflux dolomitization in the Arab-D reservoir, Ghawar field, Saudi Arabia. Sedimentology, 63(4), 865-892.

Lucia, F. J. (1995). Rock-fabric/petrophysical classification of carbonate pore space for reservoir characterization. AAPG bulletin, 79(9), 1275-1300.

Lüdmann, T., Kalvelage, C., Betzler, C., Fürstenau, J., & Hübscher, C. (2013). The Maldives, a giant isolated carbonate platform dominated by bottom currents. Marine and Petroleum Geology, 43, 326-340.

Ludwig, K. R., Szabo, B. J., Moore, J. G., & Simmons, K. R. (1991). Crustal subsidence rate off Hawaii determined from 234U/238U ages of drowned coral reefs. Geology, 19(2), 171-174.

Ma, B., Qin, Z., Wu, S., Cai, G., Li, X., Wang, B., Xueqin, L., Ain, Y., & Huang, X. (2021). High-resolution acoustic data revealing periplatform sedimentary characteristics in the Xisha Archipelago, South China Sea. Interpretation, 9(2), T533-T547.

Machel, H. G. (1999). Effects of groundwater flow on mineral diagenesis, with emphasis on carbonate aquifers. Hydrogeology Journal, 7, 94-107.

Machel, H. G. (2000a). Machel, H. G. (2000). Application of cathodoluminescence to carbonate diagenesis. In Cathodoluminescence in geosciences, pp. 271-301. Berlin, Heidelberg: Springer Berlin Heidelberg.

Machel, H. G. (2000b). Dolomite formation in Caribbean Islands: driven by plate tectonics?!. Journal of Sedimentary Research, 70(5), 977-984.

Machel, H. G., & Burton, E. A. (1991). Factors governing cathodoluminescence in calcite and dolomite, and their implications for studies of carbonate diagenesis. In: Luminescence Microscopy and Spectroscopy–Qualitative and Quantitative Applications (Eds.: C.E. Barker, O.C. Kopp), SEPM (Society for Sedimentary Geology) Short Course (1991), pp. 37-57

Machel, H. G., & Burton, E. A. (1994). Golden Grove dolomite, Barbados; origin from modified seawater. Journal of Sedimentary Research, 64(4a), 741-751.

Machel, H. G., & Lonnee, J. (2002). Hydrothermal dolomite—A product of poor definition and imagination. Sedimentary geology, 152(3-4), 163-171.

Macintyre, I. G., Glynn, P. W., & Toscano, M. A. (2007). The demise of a major Acropora palmata bank–barrier reef off the southeast coast of Barbados, West Indies. Coral Reefs, 26, 765-773.

Maclennan, J., & Lovell, B. (2002). Control of regional sea level by surface uplift and subsidence caused by magmatic underplating of Earth's crust. Geology, 30(8), 675-678.

MacNeil, A., & Jones, B. (2003). Dolomitization of the Pedro Castle Formation (Pliocene), Cayman Brac, British West Indies. Sedimentary Geology, 162(3-4), 219-238.

Madrigal, P., Gazel, E., Flores, K. E., Bizimis, M., & Jicha, B. (2016). Record of massive upwellings from the Pacific large low shear velocity province. Nature Communications, 7(1), 13309.

Maestrelli, D., Iacopini, D., Jihad, A. A., Bond, C. E., & Bonini, M. (2017). Seismic and structural characterization of fluid escape pipes using 3D and partial stack seismic from the Loyal Field (Scotland, UK): a multiphase and repeated intrusive mechanism. Marine and Petroleum Geology, 88, 489-510.

Magee, C., Jackson, C. A. L., Hardman, J. P., & Reeve, M. T. (2017). Decoding sill emplacement and forced fold growth in the Exmouth Sub-basin, offshore northwest Australia: Implications for hydrocarbon exploration. Interpretation, 5(3), SK11-SK22.

Magee, C., Jackson, C. L., & Schofield, N. (2014). Diachronous sub-volcanic intrusion along deep-water margins: Insights from the Irish Rockall Basin. Basin Research, 26(1), 85-105.

Magee, C., Maharaj, S. M., Wrona, T., & Jackson, C. A. L. (2015). Controls on the expression of igneous intrusions in seismic reflection data. Geosphere, 11(4), 1024-1041.

Magee, C., Muirhead, J. D., Karvelas, A., Holford, S. P., Jackson, C. A., Bastow, I. D., Schofield, N., Stevenson, C. T. E., McLean, C., McCarthy, W., & Shtukert, O. (2016). Lateral magma flow in mafic sill complexes. Geosphere, 12(3), 809-841.

Manche, C. J., & Kaczmarek, S. E. (2019). Evaluating reflux dolomitization using a novel high-resolution record of dolomite stoichiometry: a case study from the Cretaceous of central Texas, USA. Geology, 47(6), 586-590.

Manche, C. J., & Kaczmarek, S. E. (2021). A global study of dolomite stoichiometry and cation ordering through the Phanerozoic. Journal of Sedimentary Research, 91(5), 520-546.

Manton, B., Müller, P., Mazzini, A., Zastrozhnov, D., Jerram, D. A., Millett, J. M., ... & Planke, S. (2022). Characterizing ancient and modern hydrothermal venting systems. Marine Geology, 447, 106781.

Marcilly, C. M., Torsvik, T. H., & Conrad, C. P. (2022). Global Phanerozoic sea levels from paleogeographic flooding maps. Gondwana research, 110, 128-142.

Marine Geoscience Data System. (n.d.). RNDB10WT 1988 Seismic Reflection Data Processing Steps by the Institute for Geophysics at the University of Texas (UTIG). https://www.marine-geo.org/collections/#!/collection/Seismic.

Marques, F. O., Hildenbrand, A., Zeyen, H., Cunha, C., & Victória, S. S. (2020). The complex vertical motion of intraplate oceanic islands assessed in Santiago Island, Cape Verde. Geochemistry, Geophysics, Geosystems, 21(3), e2019GC008754.

Masaferro, J. L., Bourne, R., & Jauffred, J. C. (2004). Three-dimensional seismic visualization of carbonate reservoirs and structures. In G. P. Eberli, J. L. Masaferro, and J. F. Sarg, eds., Seismic imaging of carbonate reservoirs and systems: AAPG Memoir 81, 309– 328.

Masse, J. P., & Fenerci-Masse, M. (2006). Carbonate production by rudist bivalves. The record of Late Barremian requieniid communities from Provence (SE France). Palaeogeography, Palaeoclimatology, Palaeoecology, 234(2-4), 239-257.

Mathew, M., Makhankova, A., Menier, D., Sautter, B., Betzler, C., & Pierson, B. (2020). The emergence of Miocene reefs in South China Sea and its resilient adaptability under varying eustatic, climatic and oceanographic conditions. Scientific Reports, 10(1), 7141.

Matthews, A., & Katz, A. (1977). Oxygen isotope fractionation during the dolomitization of calcium carbonate. Geochimica et Cosmochimica Acta, 41(10), 1431-1438.

Matthews, J. L., Heezen, B. C., Catalano, R., Coogan, A., Tharp, M., Natland, J., & Rawson, M. (1974). Cretaceous drowning of reefs on Mid-Pacific and Japanese guyots. Science, 184(4135), 462-464.

Mazzullo, S. J. (1992). Geochemical and neomorphic alteration of dolomite: a review. Carbonates and evaporites, 7, 21-37.

McArthur J.M., Howarth R.J. and Shields G.A. (2012). Strontium isotope stratigraphy, Chapter 7, 127–144, in: Gradstein F.M., Ogg J.G., Schmitz M.D. and Ogg G.M. (2012). A Geologic Time Scale, Elsevier B.V., Vol 1 of 2, 1144 pp.

McDermott, K., Gillbard, E., & Clarke, N. (2015). From basalt to skeletons—The 200-million-year history of the Namibian margin uncovered by new seismic data. First Break, 33, 77–85.

McDonnell, A., Loucks, R. G., & Dooley, T. (2007). Quantifying the origin and geometry of circular sag structures in northern Fort Worth Basin, Texas: Paleocave collapse, pull-apart fault systems, or hydrothermal alteration?. AAPG bulletin, 91(9), 1295-1318.

McNutt, M. K., & Judge, A. V. (1990). The superswell and mantle dynamics beneath the South Pacific. Science, 248(4958), 969-975.

Meinshausen, M., Nicholls, Z. R., Lewis, J., Gidden, M. J., Vogel, E., Freund, M., ... & Wang, R. H. (2020). The shared socio-economic pathway (SSP) greenhouse gas concentrations and their extensions to 2500. Geoscientific Model Development, 13(8), 3571-3605.

Melim, L. A., Westphal, H., Swart, P. K., Eberli, G. P., & Munnecke, A. (2002). Questioning carbonate diagenetic paradigms: evidence from the Neogene of the Bahamas. Marine Geology, 185(1-2), 27-53.

Micallef, A., Paull, C. K., Saadatkhah, N., & Bialik, O. (2021a). The role of fluid seepage in the erosion of Mesozoic carbonate escarpments. Journal of Geophysical Research: Earth Surface, 126(11), e2021JF006387.

Micallef, A., Person, M., Berndt, C., Bertoni, C., Cohen, D., Dugan, B., Evans, R., Haroon, A., Hensen, C., Jegen, M., Key, K., Kooi, H., Liebetrau, V., Lofi, J., Mailloux, B. J., Martin-Nagle, R., Michael, H. A., Müller, T., Schmidt, M., Schwalenberg, K., Trembath-Reichert, E., Weymer, B., Zhang Y., & Thomas, A. T. (2021b). Offshore freshened groundwater in continental margins. Reviews of Geophysics, 59(1), e2020RG000706.

Michel, J., Laugié, M., Pohl, A., Lanteaume, C., Masse, J. P., Donnadieu, Y., & Borgomano, J. (2019). Marine carbonate factories: a global model of carbonate platform distribution. International Journal of Earth Sciences, 108, 1773-1792.

Miller, K. G., Browning, J. V., Schmelz, W. J., Kopp, R. E., Mountain, G. S., & Wright, J. D. (2020). Cenozoic sea-level and cryospheric evolution from deep-sea geochemical and continental margin records. *Science advances*, *6*(20), eaaz1346.

Miller, K. G., Kominz, M. A., Browning, J. V., Wright, J. D., Mountain, G. S., Katz, M. E., ... & Pekar, S. F. (2005). The Phanerozoic record of global sea-level change. science, 310(5752), 1293-1298.

Miller, K. G., Wright, J. D., & Browning, J. V. (2005). Visions of ice sheets in a greenhouse world. Marine Geology, 217(3-4), 215-231.

Mills, J. V., Gomes, M. L., Kristall, B., Sageman, B. B., Jacobson, A. D., & Hurtgen, M. T. (2017). Massive volcanism, evaporite deposition, and the chemical evolution of the Early Cretaceous Ocean. Geology, 45(5), p. 475-478.

Minzoni, M., Lehrmann, D. J., Dezoeten, E., Enos, P., Montgomery, P., Berry, A., ... & Payne, J. L. (2015). Drowning of the Triassic Yangtze Platform, South China, by tectonic subsidence into toxic deep waters of an anoxic basin. Journal of Sedimentary Research, 85(5), 419-444.

Mitchell, N. C., Simmons, H. L., & Lear, C. H. (2015). Modern and ancient hiatuses in the pelagic caps of Pacific guyots and seamounts and internal tides. Geosphere, 11(5), 1590-1606.

Mitchum, R. M. Jr, Vail, P. R., & Thompson, S. III (1977). Seismic stratigraphy and global changes of sea level; Part 2, The depositional sequence as a basic unit for stratigraphic analysis. In C. E. Payton (Ed.). Seismic stratigraphy; applications to hydrocarbon exploration (Vol. 26, pp. 53–62). AAPG Memoir.

Montaggioni, L. F. (2005). History of Indo-Pacific coral reef systems since the last glaciation: development patterns and controlling factors. Earth-Science Reviews, 71(1-2), 1-75.

Montaggioni, L. F., & Braithwaite, C. J. R. (2009). Chapter Seven Reef Hydrogeology. Developments in Marine Geology, 5, 271-321.

Montaggioni, L. F., Pons-Branchu, E., Fournier, F., Martin-Garin, B., Dapoigny, A., Marié, L., & Salvat, B. (2023). Revisiting the geodynamical history of the so-called uplifted atolls, north-west Tuamotu, French Polynesia, central South Pacific. Earth-Science Reviews, 104532.

Moss, J. L., & Cartwright, J. (2010). The spatial and temporal distribution of pipe formation, offshore Namibia. Marine and Petroleum Geology, 27(6), 1216-1234.

Müller, I. A., Rodriguez-Blanco, J. D., Storck, J. C., do Nascimento, G. S., Bontognali, T. R., Vasconcelos, C., ... & Bernasconi, S. M. (2019). Calibration of the oxygen and clumped isotope thermometers for (proto-) dolomite based on synthetic and natural carbonates. Chemical Geology, 525, 1-17.

Murdmaa, I., Kurnosov, V., & Vasilyeva, V. (1995). Clay mineralogy of the shallow-water deposits on Allison and Resolution guyots, sites 865 and 866. In Proceedings of the Ocean Drilling Program. Scientific results, Vol. 144, pp. 459-468.

Mylroie, J. E., & Carew, J. L. (1990). The flank margin model for dissolution cave development in carbonate platforms. Earth surface processes and landforms, 15(5), 413-424.

Mylroie, J. E., Carew, J. L., & Moore, A. I. (1995). Blue holes: definition and genesis. Carbonates and Evaporites, 10(2), 225-233.

Nader, F. H., Grohmann, S., Ghassal, B. I., El Atfy, H., Romero-Sarmiento, M. F., Daher, S. B., ... & Littke, R. (2023). A Review of the Offshore East Mediterranean Mesozoic-Cenozoic Petroleum Systems. The Phanerozoic Geology and Natural Resources of Egypt, 719-742.

Narr, W. & Flodin, E. (2012) Fractures in steep-rimmed carbonate platforms: comparison of Tengiz reservoir, Kazakhstan, and outcrops in Canning Basin, NW Australia. AAPG Search and Discovery Article, 20161, 1–31.

Netzeband, G. L., Krabbenhöft, A., Zillmer, M., Petersen, C. J., Papenberg, C., & Bialas, J. (2010). The structures beneath submarine methane seeps: seismic evidence from Opouawe Bank, Hikurangi Margin, New Zealand. Marine Geology, 272(1-4), 59-70.

Neuhaus, D., Borgomano, J., Jauffred, J. C., Mercadier, C., Olotu, S., & Grtsch, J. (2004). Quantitative seismic reservoir characterization of an Oligocene Miocene carbonate buildup: Malampaya field, Philippines. In: Seismic Imaging of Carbonate Reservoirs and Systems (Eds G.P. Eberli, J.L. Masafero and J.F. Sarg), AAPG Mem., 81, pp. 169–185.

Newport, R., Hollis, C., Bodin, S., & Redfern, J. (2017). Examining the interplay of climate and low amplitude sea-level change on the distribution and volume of massive dolomitization: Zebbag Formation, Cretaceous, Southern Tunisia. The Depositional Record, 3(1), 38-59.

Newport, R., Segura, M., Redfern, J., & Hollis, C. (2020). The interaction of tectonics, climate and eustasy in controlling dolomitization: A case study of Cenomanian–Turonian, shallow marine carbonates of the Iberian Basin. Sedimentology, 67(5), 2223-2247.

Niyazi, Y., Eruteya, O. E., Warne, M., & Ierodiaconou, D. (2021a). Discovery of large-scale buried volcanoes within the Cenozoic succession of the Prawn Platform, offshore Otway Basin, southeastern Australia. Marine and Petroleum Geology, 123, 104747.

Niyazi, Y., Warne, M., & Ierodiaconou, D. (2021b). Post-rift magmatism and hydrothermal activity in the central offshore Otway Basin and implications for igneous plumbing systems. Marine Geology, 438, 106538.

Nolting, A., & Fernández-Ibáñez, F. (2021). Stress states of isolated carbonate platforms: Implications for development and reactivation of natural fractures post burial. Marine and Petroleum Geology, 128, 105039.

Nolting, A., Zahm, C. K., Kerans, C., & Nikolinakou, M. A. (2018). Effect of carbonate platform morphology on syndepositional deformation: Insights from numerical modeling. Journal of Structural Geology, 115, 91-102.

Northrop, D. A., & Clayton, R. N. (1966). Oxygen-isotope fractionations in systems containing dolomite. The Journal of Geology, 74(2), 174-196.

Núñez-Useche, F., Barragán, R., Moreno-Bedmar, J. A., & Canet, C. (2015). Geochemical and paleoenvironmental record of the early to early late Aptian major episodes of accelerated change: Evidence from Sierra del Rosario, Northeast Mexico. Sedimentary Geology, 324, 47-66.

O'Brien, C. L., Robinson, S. A., Pancost, R. D., Damsté, J. S. S., Schouten, S., Lunt, D. J., ... & Wrobel, N. E. (2017). Cretaceous sea-surface temperature evolution: Constraints from TEX86 and planktonic foraminiferal oxygen isotopes. Earth-Science Reviews, 172, 224-247.

ODP Initial Reports. (1993a). Shipboard scientific party core description of Site 866. http://www-odp.tamu.edu/publications/143_IR/VOLUME/CHAPTERS/cor_0866.pdf

ODP Initial Reports. (1993b). Shipboard scientific party core description of Site 865. http://www-odp.tamu.edu/publications/143_IR/VOLUME/CHAPTERS/cor_0865.pdf

Ogg, J. G. (2012). Geomagnetic Polarity Time Scale. In The Geologic Time Scale 2012, 85-113. Elsevier.

Ogg, J. G., and Hinnov, L.A. (2012). The Cretaceous period. In The Geologic Time Scale 2012, 793-853. Elsevier.

Ogg, J. G., Camoin, G. F., & Arnaud Vanneau, A. (1995). Limalok Guyot: depositional history of the carbonate platform from downhole logs at Site 871 (lagoon). In Proceedings-Ocean Drilling Program Scientific Results, Vol. 144, pp. 233-254.

Omosanya, K. O., Eruteya, O. E., Siregar, E. S., Zieba, K. J., Johansen, S. E., Alves, T. M., & Waldmann, N. D. (2018). Three-dimensional (3-D) seismic imaging of conduits and radial faults associated with hydrothermal vent complexes (Vøring Basin, Offshore Norway). Marine Geology, 399, 115-134.

Omosanya, K. O., Johansen, S. E., Eruteya, O. E., & Waldmann, N. (2017). Forced folding and complex overburden deformation associated with magmatic intrusion in the Vøring Basin, offshore Norway. Tectonophysics, 706, 14-34.

O'Neil, J. R., & Epstein, S. (1966). Oxygen isotope fractionation in the system dolomite-calcite-carbon dioxide. Science, 152(3719), 198-201.

Özer, S., Güngör, T., Sarı, B., Sagular, E. K., Görmüş, M., & Özkar-Öngen, I. (2017). Cretaceous rudist-bearing platform carbonates from the Lycian Nappes (SW Turkey): Rudist associations and depositional setting. Cretaceous Research, 79, 122-145.

Pal, M., Taberner, C., & Tueckmantel, C. (2015). Simulation of end-member scenarios of density-driven flow: prediction of dolostone geobody dimensions using COMSOL. Geological Society, London, Special Publications, 406(1), 209-228.

Pandolfi, J. M., Connolly, S. R., Marshall, D. J., & Cohen, A. L. (2011). Projecting coral reef futures under global warming and ocean acidification. science, 333(6041), 418-422.

Papadimitriou, N., Gorini, C., Nader, F. H., Deschamps, R., Symeou, V., & Lecomte, J. C. (2018). Tectono-stratigraphic evolution of the western margin of the Levant Basin (offshore Cyprus). Marine and Petroleum Geology, 91, 683-705.

Paphitis, D., Collins, M. B., Nash, L. A., & Wallbridge, S. (2002). Settling velocities and entrainment thresholds of biogenic sands (shell fragments) under unidirectional flow. Sedimentology, 49(1), 211-225.

Parfitt, L., & Wilson, L. (2009). Fundamentals of physical volcanology. John Wiley & Sons.

Paull, C. K., Fullagar, P. D., Bralower, T. J., & Rohl, U. (1995). Seawater ventilation of mid-Pacific guyots drilled during Leg 143. In the Proceedings ofthe Ocean Drilling Program, Initial Reports, Vol. 143, p. 231-241.

Paumard, V., Zuckmeyer, E., Boichard, R., Jorry, S.J., Bourget, J., Borgomano, J., Maurin, T., Ferry, J.N (2017). Evolution of Late Oligocene-Early Miocene attached and isolated carbonate platforms in a volcanic ridge context (Maldives type), Yadana field, offshore Myanmar. Marine and Petroleum Geology, 81, 361-387.

Paytan, A., Kastner, M., Campbell, D., & Thiemens, M. H. (2004). Seawater sulfur isotope fluctuations in the Cretaceous. science, 304(5677), 1663-1665.

Pearson, P. N. (1995). Planktonic foraminifer biostratigraphy and the development of pelagic caps on guyots in the Marshall Islands group. In Proceedings-Ocean Drilling Program Scientific Results, Vo. 144, pp. 21-60.

Pearson-Grant, S. C., Miller, C. A., Carson, L. B., Bertrand, E. A., & Leonard, G. S. (2022). Influences on geothermal circulation in the Okataina Volcanic Centre, New Zealand. Journal of Volcanology and Geothermal Research, 432, 107705.

Petrovic, A., Lüdmann, T., Afifi, A. M., Saitz, Y., Betzler, C., & Vahrenkamp, V. (2023). Fragmentation, rafting, and drowning of a carbonate platform margin in a rift-basin setting. Geology, 51(3), 242-246.

Planavsky, N., & Ginsburg, R. N. (2009). Taphonomy of modern marine Bahamian microbialites. Palaios, 24(1), 5-17.

Planke, S., Rasmussen, T., Rey, S. S., & Myklebust, R. (2005). January, Seismic characteristics and distribution of volcanic intrusions and hydrothermal vent complexes in the Vøring and Møre basins. In Geological Society, London, Petroleum Geology Conference series of Geological Society of London, 6, p. 833-844.

Planke, S., Symonds, P. A., Alvestad, E., & Skogseid, J. (2000). Seismic volcanostratigraphy of large-volume basaltic extrusive complexes on rifted margins. Journal of Geophysical Research: Solid Earth, 105(B8), 19335-19351.

Pleydell, S. M., Jones, B., Longstaffe, F. J., & Baadsgaard, H. (1990). Dolomitization of the Oligocene–Miocene bluff formation on Grand Cayman, British West Indies. Canadian Journal of Earth Sciences, 27(8), 1098-1110.

Pockalny, R., Barth, G., Eakins, B., Kelley, K. A., & Wertman, C. (2021). Multiple melt source origin of the Line Islands (Pacific Ocean). Geology, 49(11), 1358-1362.

Pohl, A., Donnadieu, Y., Godderis, Y., Lanteaume, C., Hairabian, A., Frau, C., Michel, J., Laugie, M., Reijmer, J. J. G., Scotese, C. R., & Borgomano, J. (2020). Carbonate platform production during the Cretaceous. GSA Bulletin, 132(11-12), 2606-2610.

Pohl, A., Laugié, M., Borgomano, J., Michel, J., Lanteaume, C., Scotese, C. R., ... & Donnadieu, Y. (2019). Quantifying the paleogeographic driver of Cretaceous carbonate platform development using paleoecological niche modeling. Palaeogeography, palaeoclimatology, palaeoecology, 514, 222-232.

Pomar, L., Brandano, M., & Westphal, H. (2004). Environmental factors influencing skeletal grain sediment associations: a critical review of Miocene examples from the western Mediterranean. Sedimentology, 51(3), 627-651.

Poulsen, C. J., Barron, E. J., Peterson, W. H., & Wilson, P. A. (1999). A reinterpretation of Mid-Cretaceous shallow marine temperatures through model-data comparison. Paleoceanography, 14(6), 679-697.

Prager, E. J., Southard, J. B., & VIVONI-GALLART, E. R. (1996). Experiments on the entrainment threshold of well-sorted and poorly sorted carbonate sands. Sedimentology, 43(1), 33-40.

Prat, S., Jorry, S.J., Jouet, G., Camoin, G., Vella, C., Le Roy, P., Caline, B., Boichard, R. and Pastol, Y., (2016). Geomorphology and sedimentology of a modern isolated carbonate platform: The Glorieuses archipelago, SW Indian Ocean. Marine Geology, 380, 272-283.

Pratte, Z. A., Longo, G. O., Burns, A. S., Hay, M. E., & Stewart, F. J. (2018). Contact with turf algae alters the coral microbiome: contact versus systemic impacts. Coral Reefs, 37, 1-13.

Principaud, M., Mulder, T., Gillet, H., & Borgomano, J. (2015). Large-scale carbonate submarine mass-wasting along the northwestern slope of the Great Bahama Bank (Bahamas): Morphology, architecture, and mechanisms. Sedimentary Geology, 317, 27-42.

Pringle, M. S. (1993). Age progressive volcanism in the Musicians seamounts: a test of the hot spot hypothesis for the late Cretaceous Pacific. Washington DC American Geophysical Union Geophysical Monograph Series, 77, 187-215.

Pringle, M. S., & Duncan, R. A. (1995). Radiometric ages of basaltic lavas recovered at Sites 865, 866, and 869: Northwest Pacific atolls and guyots. In Proceedings of the Ocean Drilling Program. Scientific results Vol. 143, 277-283.

Pritchard, G. (2014). The Namibian Atlantic margin south of the Walvis Ridge: Piecing together the jigsaw of a potentially prospective new frontier: Petroleum Exploration Society of Great Britain PETEX Conference, London, November 18–20, 2014, MA-1.6, 32 p.

Puga-Bernabéu, A., Webster, J. M., Braga, J. C., Clague, D. A., Dutton, A., Eggins, S., ... & Potts, D. C. (2016). Morphology and evolution of drowned carbonate terraces during the last two interglacial cycles, off Hilo, NE Hawaii. Marine Geology, 371, 57-81.

Purkis, S., Casini, G., Hunt, D., & Colpaert, A. (2015). Morphometric patterns in Modern carbonate platforms can be applied to the ancient rock record: Similarities between Modern Alacranes Reef and Upper Palaeozoic platforms of the Barents Sea. Sedimentary Geology, 321, 49-69.

Rankey, E. C. (2016). On facies belts and facies mosaics: Holocene isolated platforms, South China Sea. Sedimentology, 63(7), 2190-2216.

Rankey, E. C. (2020). Eustatic, climatic, and oceanographic influences on geomorphology and architecture of isolated carbonate platforms: Miocene, Northwest Shelf, Australia. Lithosphere, 2020(1), 8844754.

Rankey, E. C. (2023). Introduction to Cenozoic Isolated Carbonate Platforms—Focus Southeast Asia. Chapter 1. In: Cenozoic isolated carbonate platforms: focus Southeast Asia. (Rankey, E. C., & Pöppelreiter, M.), SEPM Special Publication, 114, 5-19.

Rankey, E. C., Schlaich, M., Mokhtar, S., Ghon, G., Ali, S. H., & Poppelreiter, M. (2019). Seismic architecture of a Miocene isolated carbonate platform and associated off-platform strata (Central Luconia Province, offshore Malaysia). Marine and Petroleum Geology, 102, 477-495.

Read, J. F., Husinec, A., Cangialosi, M., Loehn, C. W., & Prtoljan, B. (2016). Climate controlled, fabric destructive, reflux dolomitization and stabilization via marine-and synorogenic mixed fluids: an example from a large Mesozoic, calcite-sea platform, Croatia. Palaeogeography, Palaeoclimatology, Palaeoecology, 449, 108-126.

Reddy, M. P. M. (2001). Descriptive physical oceanography. CRC Press. A.A Balkema Publishers, p. 445.

Reid, R. P., & Browne, K. M. (1991). Intertidal stromatolites in a fringing Holocene reef complex, Bahamas. Geology, 19(1), 15-18.

Ren, M., & Jones, B. (2016). Diagenesis in limestone-dolostone successions after 1 million years of rapid sea-level fluctuations: A case study from Grand Cayman, British West Indies. Sedimentary Geology, 342, 15-30.

Ren, M., & Jones, B. (2017). Spatial variations in the stoichiometry and geochemistry of Miocene dolomite from Grand Cayman: Implications for the origin of island dolostone. Sedimentary Geology, 348, 69-93.

Ren, M., & Jones, B. (2018). Genesis of island dolostones. Sedimentology, 65(6), 2003-2033.

Reolid, J., Betzler, C., Braga, J. C., Lüdmann, T., Ling, A., & Eberli, G. P. (2020). Facies and geometry of drowning steps in a Miocene carbonate platform (Maldives). Palaeogeography, palaeoclimatology, palaeoecology, 538, 109455.

Rivers, J. M. (2023). Warm acidified seawater: a dolomite solution. Journal of Sedimentary Research, 93(3), 187-201.

Rivers, J. M., Yousif, R., Kaczmarek, S. E., & Al-Shaikh, I. (2021). Cenozoic coastal carbonate deposits of Qatar: Evidence for dolomite preservation bias in highly-arid systems. Sedimentology, 68(2), 771-787.

Robbins, L. L., Tao, Y., & Evans, C. A. (1997). Temporal and spatial distribution of whitings on Great Bahama Bank and a new lime mud budget. Geology, 25(10), 947-950.

Robertson, H., Corlett, H., Hollis, C., Kibblewhite, T., & Whitaker, F. (2019). Listwanitization as a source of Mg for dolomitization: field evaluation in Atlin, British Columbia. In Barcelona, Goldschmidt Conference, August 2019.

Robinson, S. A. (2011). Shallow-water carbonate record of the Paleocene-Eocene Thermal Maximum from a Pacific Ocean guyot. Geology, 39(1), 51-54.

Rochelle-Bates, N., Calvès, G., Huuse, M., & Schröder, S. (2024). Carbonate platform or volcanic mound? Seismic characterization of a synrift buildup along the outer high of the Lüderitz Basin, Namibia. AAPG Bulletin, 108(2), 261-292.

Roelofse, C., Alves, T. M., & Kamal'deen, O. O. (2021). Reutilisation of hydrothermal vent complexes for focused fluid flow on continental margins (Modgunn Arch, Norwegian Sea). Basin Research, 33(2), 1111-1134.

Röhl, U., & Strasser, A. (1995). Diagenetic alterations and geochemical trends in Early Cretaceous shallow-water limestones of Allison and Resolution Guyots (Sites 865 to 868). In Proceedings of the Ocean Drilling Program. Scientific results Vol. 143, 197-229

Ronchi, P., Ortenzi, A., Borromeo, O., Claps, M., & Zempolich, W. G. (2010). Depositional setting and diagenetic processes and their impact on the reservoir quality in the late Visean–Bashkirian Kashagan carbonate platform (Pre-Caspian Basin, Kazakhstan). AAPG bulletin, 94(9), 1313-1348.

Rougerie, F., & Wauthy, B. (1993). The endo-upwelling concept: from geothermal convection to reef construction. Coral reefs, 12(1), 19-30.

Rougerie, F., Fichez, R., Déjardin, P., Vacher, H. L., & Quinn, T. (1997). Geomorphology and hydrogeology of selected islands of French Polynesia: Tikehau (atoll) and Tahiti (barrier reef). Geology and Hydrogeology of Carbonate Islands. Developments in sedimentology, 475-502.

Rusciadelli, G., & Shiner, P. (2018). Isolated carbonate platforms of the Mediterranean and their seismic expression—Searching for a paradigm. The Leading Edge, 37(7), 492-501.

Ryan, B. H., Kaczmarek, S. E., & Rivers, J. M. (2020). Early and pervasive dolomitization by near-normal marine fluids: New lessons from an Eocene evaporative setting in Qatar. Sedimentology, 67(6), 2917-2944.

Sager, W. W. (1995). Structural implications of gravity anomalies, Resolution and Heezen guyots, Mid-Pacific Mountains: Northwest Pacific atolls and guyots. In Proceedings of the Ocean Drilling Program. Scientific results (Vol. 143), pp. 419-429.

Sager, W. W., Haggerty, J. A., Winterer, E. L., Premoli-Silva, I., Firth, J., Palmer-Julson, A., ... & Francis, T. J. (1992). Ocean Drilling Program Legs 143 and 144 Scientific Prospectus Northwest Pacific Atolls and Guyots. PP 79.

Sager, W. W., Winterer, E. L., Firth, J. V., Arnaud, H., Baker, P. A., Baudin, F., Bralower, T. J., Castillo, P., Cooper, P., Flood, P. G., Golovchenko, X., Iryu, Y., Ivanov, M., Jenkyns, H. C., Kenter, J. A. M., Murdmaa, I., Mutterlose, J., Nogi, Y., Paull, C. K., … van Waasbergen, R. (1993a) Site 866. In Proceedings of the Ocean Drilling Program, Initial Reports (Vol. 143), pp. 181–271.

Sager, W. W., Winterer, E. L., Firth, J. V., Arnaud, H., Baker, P. A., Baudin, F., Bralower, T. J., Castillo, P., Cooper, P., Flood, P. G., Golovchenko, X., Iryu, Y., Ivanov, M., Jenkyns, H. C., Kenter, J. A. M., Murdmaa, I., Mutterlose, J., Nogi, Y., Paull, C. K., … van Waasbergen, R. (1993b) Site 867/868. In the Proceedings of the Ocean Drilling Program, Initial Reports (Vol. 143), pp. 273–296.

Sager, W. W., Winterer, E. L., Firth, J. V., Arnaud, H., Baker, P. A., Baudin, F., Bralower, T. J., Castillo, P., Cooper, P., Flood, P. G., Golovchenko, X., Iryu, Y., Ivanov, M., Jenkyns, H. C., Kenter, J. A. M., Murdmaa, I., Mutterlose, J., Nogi, Y., Paull, C. K., … van Waasbergen, R. (1993c) Site 865. In Proceedings of the Ocean Drilling Program, Initial Reports (Vol. 143), pp. 111–180.

Sahagian, D., Pinous, O., Olferiev, A., & Zakharov, V. (1996). Eustatic curve for the Middle Jurassic—Cretaceous based on Russian Platform and Siberian stratigraphy: Zonal resolution. AAPG bulletin, 80(9), 1433-1458.

Sahlström, F., Jonsson, E., Högdahl, K., Troll, V. R., Harris, C., Jolis, E. M., & Weis, F. (2019). Interaction between high-temperature magmatic fluids and limestone explains 'Bastnäs-type' REE deposits in central Sweden. Scientific reports, 9(1), 15203.

Salas, J., Taberner, C., Esteban, M., & Ayora, C. (2007). Hydrothermal dolomitization, mixing corrosion and deep burial porosity formation: numerical results from 1-D reactive transport models. Geofluids, 7(2), 99-111.

Saller, A. H. (1984). Petrologic and geochemical constraints on the origin of subsurface dolomite, Enewetak Atoll: An example of dolomitization by normal seawater. Geology, 12(4), 217-220.

Saller, A. H. (1986). Radiaxial calcite in lower Miocene strata, subsurface Enewetak Atoll. Journal of Sedimentary Research, 56(6), 743-762.

Saller, A. H., & Vijaya, S. (2002). Depositional and diagenetic history of the Kerendan carbonate platform, Oligocene, central Kalimantan, Indonesia. Journal of Petroleum Geology, 25(2), 123-149.

Saller, A. H., Lounsbury, K., & Birchard, M. (2001). Facies control on dolomitization and porosity in the Devonian Swan Hills Formation in the Rosevear area, west-central Alberta. Bulletin of Canadian Petroleum Geology, 49(4), 458-471.

Saller, A., & Winterbottom, C. (2022). Deep marine diagenesis, offshore Hawaii and Enewetak, with implications to older carbonates. The Depositional Record.

Sandwell, D. T., Müller, R. D., Smith, W. H., Garcia, E., & Francis, R. (2014). New global marine gravity model from CryoSat-2 and Jason-1 reveals buried tectonic structure. science, 346(6205), 65-67.

Saqab, M. M., Childs, C., Walsh, J., & Delogkos, E. (2021). Multiphase deformation history of the Porcupine Basin, offshore west Ireland. Basin Research, 33(3), 1776-1797.

Schlager, W. (1981). The paradox of drowned reefs and carbonate platforms. Geological Society of America Bulletin, 92(4), 197-211.

Schlager, W. (1991). Depositional bias and environmental change—important factors in sequence stratigraphy. Sedimentary Geology, 70(2-4), 109-130.

Schlager, W. (1999). Scaling of sedimentation rates and drowning of reefs and carbonate platforms. Geology, 27(2), 183-186.

Schlager, W. (2005). Carbonate sedimentology and sequence stratigraphy (No. 8). SEPM Society for Sedimentary Geology, 200p.

Schlanger, S. O., & Premoli Silva, I. (1986). Oligocene sea-level falls recorded in mid-Pacific atoll and archipelagic apron settings. Geology, 14(5), 392-395.

Schlanger, S. O., Graf, D. L., & Goldsmith, J. R. (1963). Subsurface geology of Eniwetok atoll. Geological Survey Professional. US Government Printing Office. Paper 260-BB, Washington, DC, 76 pp.

Schmidt, C., Titelboim, D., Brandt, J., Herut, B., Abramovich, S., Almogi-Labin, A., & Kucera, M. (2016). Extremely heat tolerant photo-symbiosis in a shallow marine benthic foraminifera. Scientific Reports, 6(1), 30930.

Schmitt, K. E., Huck, S., Krummacker, M., De Winter, N. J., Godet, A., Claeys, P., & Heimhofer, U. (2022). Radiolitid rudists: an underestimated archive for Cretaceous climate reconstruction?. Lethaia, 55(4), 1-21.

Scotese, C. R. (2015). Some thoughts on global climate change: the transition from icehouse to hothouse. Paleomap project, 21(2).

Scotese, C. R., & Wright, N. (2018). PALEOMAP paleodigital elevation models (PaleoDEMS) for the Phanerozoic PALEOMAP Project. Earth byte https://www.earthbyte.org/paleodem-resource-scotese-and-wright-2018.

Scott, G. A. J., & Rotondo, G. M. (1983). A model to explain the differences between Pacific plate island-atoll types. Coral Reefs, 1(3), 139-150.

Scott, R. W., Simo, J. T., & Masse, J. P. (1993). Economic Resources in Cretaceous Carbonate Platforms: An Overview: Chapter 2. In: Cretaceous carbonate platforms (Eds J.A.T. Simo, R.W. Scott and J.-P. Masse), AAPG Mem., 56, 15-24.

Seard, C., Borgomano, J., Granjeon, D., & Camoin, G. (2013). Impact of environmental parameters on coral reef development and drowning: Forward modelling of the last deglacial reefs from Tahiti (French Polynesia; IODP Expedition# 310). Sedimentology, 60(6), 1357-1388.

Seewald, J. S., Reeves, E. P., Bach, W., Saccocia, P. J., Craddock, P. R., Shanks III, W. C., ... & Walsh, E. (2015). Submarine venting of magmatic volatiles in the eastern Manus Basin, Papua New Guinea. Geochimica et Cosmochimica Acta, 163, p. 178-199.

Sena, C. M., & John, C. M. (2013). Impact of dynamic sedimentation on facies heterogeneities in Lower Cretaceous peritidal deposits of central east Oman. Sedimentology, 60(5), 1156-1183.

Seuront, L., Nicastro, K. R., Zardi, G. I., & Goberville, E. (2019). Decreased thermal tolerance under recurrent heat stress conditions explains summer mass mortality of the blue mussel Mytilus edulis. Scientific Reports, 9(1), 17498.

Seyyedi, M., Mahmud, H. K. B., Verrall, M., Giwelli, A., Esteban, L., Ghasemiziarani, M., & Clennell, B. (2020). Pore structure changes occur during CO2 injection into carbonate reservoirs. Scientific reports, 10(1), 3624.

Shahzad, K., Betzler, C., & Qayyum, F. (2019). Controls on the Paleogene carbonate platform growth under greenhouse climate conditions (Offshore Indus Basin). Marine and Petroleum Geology, 101, 519-539.

Shalev, N., Bontognali, T. R., Wheat, C. G., & Vance, D. (2019). New isotope constraints on the Mg oceanic budget point to cryptic modern dolomite formation. Nature communications, 10(1), 5646.

Sharp, W. D., & Renne, P. R. (2005). The 40Ar/39Ar dating of core recovered by the Hawaii Scientific Drilling Project (phase 2), Hilo, Hawaii. Geochemistry, Geophysics, Geosystems, 6(4).

Shea, J. J., Ezad, I. S., Foley, S. F., & Lanati, A. W. (2022). The Eastern Australian Volcanic Province, its primitive melts, constraints on melt sources and the influence of mantle metasomatism. Earth-Science Reviews, 104168.

Sheppard, S. M., & Schwarcz, H. P. (1970). Fractionation of carbon and oxygen isotopes and magnesium between coexisting metamorphic calcite and dolomite. Contributions to Mineralogy and Petrology, 26, 161-198.

Sibley, D. F. (1990). Unstable to stable transformations during dolomitization. The Journal of Geology, 98(5), 739-748.

Sibley, D. F., & Gregg, J. M. (1987). Classification of dolomite rock textures: Journal of Sedimentary Geology, v. 57. p. 967–975.

Sigurdsson, H., Leckie, R. M., Acton, G. D., Miller, C. M., & Maddox, E. M. (1997). Caribbean volcanism, Cretaceous/Tertiary impact, and ocean climate history: synthesis of Leg 165. In Proc. Ocean Drill. Program Initial Rep (Vol. 165, pp. 377-400).

Simo, J.A.T., Scott, R.W. and Masse, J.-P. (1993) Cretaceous carbonate platforms: an overview: Chapter 1. In: Cretaceous carbonate platforms (Eds J.A.T. Simo, R.W. Scott and J.-P. Masse), AAPG Mem., 56, 1–14.

Skelton, P. W., & Gili, E. (2012). Rudists and carbonate platforms in the Aptian: a case study on biotic interactions with ocean chemistry and climate. Sedimentology, 59(1), 81-117.

Skelton, P. W., Sano, S. I., & Masse, J. P. (2013). Rudist bivalves and the Pacific in the Late Jurassic and Early Cretaceous. Journal of the Geological Society, 170(3), 513-526.

Skelton, Peter W. (2003). Changing climate and biota: The marine record. In Peter W. Skelton, ed., The Cretaceous World. The Open University & Cambridge University Press Cambridge, 163–184.

Skogly, O. (1998). Seismic characterization and emplacement of intrusives in the Vøring Basin. Cand Scient thesis, Department of Geology, University of Oslo.

Smith, D. A., & Cheung, K. F. (2005). Transport rate of calcareous sand in unidirectional flow. Sedimentology, 52(5), 1009-1020.

Sliter, W. V., Winterer, E. L., Sager, W. W., Firth, J. V., & Sinton, J. M. (1995). Cretaceous planktonic foraminifers from Sites 865, 866, and 869: A synthesis of Cretaceous pelagic sedimentation in the central Pacific Ocean basin. In Proceedings of the Ocean Drilling Program, Initial Reports, 143, p. 15–30.

Śliwiński, M. G., Whalen, M. T., Meyer, F. J., & Majs, F. (2012). Constraining clastic input controls on magnetic susceptibility and trace element anomalies during the Late Devonian punctata Event in the Western Canada Sedimentary Basin. Terra Nova, 24(4), 301-309.

Smart, P. L., Dawans, J. M., & Whitaker, F. (1988). Carbonate dissolution in a modern mixing zone. Nature, 335(6193), 811-813.

Smith, D. A., & Cheung, K. F. (2005). Transport rate of calcareous sand in unidirectional flow. Sedimentology, 52(5), 1009-1020.

Song, H., Wignall, P. B., Chu, D., Tong, J., Sun, Y., Song, H., ... & Tian, L. (2014). Anoxia/high temperature double whammy during the Permian-Triassic marine crisis and its aftermath. Scientific reports, 4(1), 4132.

Stap, L. B., Van De Wal, R. S., De Boer, B., Bintanja, R., & Lourens, L. J. (2017). The influence of ice sheets on temperature during the past 38 million years inferred from a one-dimensional ice sheet–climate model. Climate of the Past, 13(9), 1243-1257.

Staudigel, H., & Clague, D. A. (2010). The geological history of deep-sea volcanoes: Biosphere, hydrosphere, and lithosphere interactions. Oceanography, 23(1), 58-71.

Staudigel, H., Park, K. H., Pringle, M., Rubenstone, J. L., Smith, W. H. F., & Zindler, A. (1991). The longevity of the South Pacific isotopic and thermal anomaly. Earth and Planetary Science Letters, 102(1), 24-44.

Stein, C. A., & Stein, S. (1992). A model for the global variation in oceanic depth and heat flow with lithospheric age. Nature, 359(6391), 123-129.

Steinig, S., Alexander, T., Lunt, D., Valdes, P., Duggan, Z., Lee, P., ... & Swann, M. (2022, May). " climatearchive. org": 540 million years of climate data at your fingertips. In EGU General Assembly Conference Abstracts (pp. EGU22-9361).

Steinmann, M., & Déjardin, P. (2004). The temporal evolution of fluid flow through the Tahiti barrier reef traced by Sr isotopes and pore water chemistry. Chemical geology, 203(1-2), 51-73.

Steuber, T. (2000). Skeletal growth rates of Upper Cretaceous rudist bivalves: implications for carbonate production and organism-environment feedbacks. Geological Society, London, Special Publications, 178(1), 21-32.

Steuber, T., & Rauch, M. (2005). Evolution of the Mg/Ca ratio of Cretaceous seawater: implications from the composition of biological low-Mg calcite. Marine Geology, 217(3-4), 199-213.

Steuber, T., Löser, H., Mutterlose, J., & Parente, M. (2023). Biogeodynamics of Cretaceous marine carbonate production. Earth-Science Reviews, 238, 104341.

Steuber, T., Rauch, M., Masse, J. P., Graaf, J., & Malkoč, M. (2005). Low-latitude seasonality of Cretaceous temperatures in warm and cold episodes. Nature, 437(7063), 1341-1344.

Steuber, T., Yilmaz, C., & Löser, H. (1998). Growth rates of early Campanian rudists in a siliciclastic-calcareous setting (Pontid MTS., North-Central Turkey). Geobios, 31, 385-401.

Stoessell, R. K., Coke, J. G., & Easley, D. H. (2002). Localized thermal anomalies in haloclines of coastal Yucatan sinkholes. Groundwater, 40(4), 416-424.

Stoner, D. S. (1990). Recruitment of a tropical colonial ascidian: Relative importance of pre-settlement vs. post-settlement processes. Ecology, 71(5), 1682-1690.

Stranghoener, M., Schippers, A., Dultz, S., & Behrens, H. (2018). Experimental microbial alteration and Fe mobilization from basaltic rocks of the ICDP HSDP2 drill core, Hilo, Hawaii. Frontiers in Microbiology, 9, 1252.

Strasser, A. (2015). Hiatuses and condensation: an estimation of time lost on a shallow carbonate platform. The Depositional Record, 1(2), 91-117.

Strasser, A. (2022). Shallow marine carbonates as recorders of orbitally induced past climate changes–example from the Oxfordian of the Swiss Jura Mountains. Climate of the Past, 18(9), 2117-2142.

Strasser, A., Arnaud, H., Baudin, F., & Röhl, U. (1995). Small-scale shallow-water carbonate sequences of Resolution Guyot (Sites 866, 867, and 868). In Proceedings of the Ocean Drilling Program, scientific results Vol. 143, 119-131.

Sun, Q., Cartwright, J., Wu, S., & Chen, D. (2013). 3D seismic interpretation of dissolution pipes in the South China Sea: Genesis by subsurface, fluid induced collapse. Marine Geology, 337, 171-181.

Sun, S. Q. (1994). A reappraisal of dolomite abundance and occurrence in the Phanerozoic. Journal of Sedimentary Research, 64(2a), 396-404.

Sun, S. Q., & Esteban, M. (1994). Paleoclimatic controls on sedimentation, diagenesis, and reservoir quality: lessons from Miocene carbonates. AAPG bulletin, 78(4), 519-543.

Suzuki, Y., Iryu, Y., Inagaki, S., Yamada, T., Aizawa, S., & Budd, D. A. (2006). Origin of atoll dolomites distinguished by geochemistry and crystal chemistry: Kita-daito-jima, northern Philippine Sea. Sedimentary Geology, 183(3-4), 181-202.

Swart, P. K., & Melim, L. A. (2000). The origin of dolomites in Tertiary sediments from the margin of Great Bahama Bank. Journal of Sedimentary Research, 70(3), 738-748.

Swartz, J.H. (1958). Geothermal measurements on Eniwetok and Bikini Atolls. U.S. Geological Survey, Professional Paper, 260-U, p. 711–741.

Szabó, N. P., Kilik, R., & Dobróka, M. (2023). Robust reservoir identification by multi-well cluster analysis of wireline logging data. Heliyon, 9(5).

Tarduno, J. A., Sager, W. W., & Nogi, Y. (1995). Early Cretaceous Magnetostratigraphy and Paleolatitudes from the Mid-Pacific Mountains: Preliminary Results Bearing on Guyot Formation and Pacific Plate Translation. In Proceedings of the Ocean Drilling Program, Scientific Results, Vol. 143, pp. 395-398.

Thiede, J., Dean, W. E., Rea, D. K., Vallier, T. L., & Adelseck, C. G. (1981). The geologic history of the Mid-Pacific Mountains in the central North Pacific Ocean: A synthesis of Deep-Sea Drilling studies. Initial Reports of the Deep-Sea Drilling Project, 62, 1073-1120.

Thorne, J. A. (1992). An Analysis of the Implicit Assumptions of the Methodology of Seismic Sequence Stratigraphy: Chapter 21: Sea-Level and Seismic Stratigraphic Studies. In Watkins J.S., Kenneth F.Z. & McMillen J. (eds) Geology Geophysical Continental Margins. American Association of Petroleum Geologists, Memoirs, 53, 375–394.

Tierney, J. E., Poulsen, C. J., Montañez, I. P., Bhattacharya, T., Feng, R., Ford, H. L., ... & Zhang, Y. G. (2020). Past climates inform our future. science, 370(6517), eaay3701.

Timofeeff, M. N., Lowenstein, T. K., Da Silva, M. A. M., & Harris, N. B. (2006). Secular variation in the major-ion chemistry of seawater: Evidence from fluid inclusions in Cretaceous halites. Geochimica et Cosmochimica Acta, 70(8), 1977-1994.

Timofeev, P. P., Renngarten, N. V., & Eremeev, V. V. (1981). Lithologic-genetic characteristics of sediments in a section at Site 463. Initial Reports of the Deep-Sea Drilling Project, vol. 62, 607-615.

Toomey, M. R., Curry, W. B., Donnelly, J. P., & van Hengstum, P. J. (2013). Reconstructing 7000 years of North Atlantic hurricane variability using deep-sea sediment cores from the western Great Bahama Bank. Paleoceanography, 28(1), 31-41.

Torres de la Cruz, F.J., Chacón-Baca, E., Chávez-Cabello, G., Hernández-Ocaña, I. (2020). Revisiting the Cupidito unit (Cupido Formation) along peritidal carbonates from northeastern Mexico. Revista mexicana de ciencias geológicas, 37(1), 9-25.

Torrieri, S., Volery, C., Bazalgette, L., & Strauss, C. G. (2021). From outcrop to subsurface model—Large-scale fractured zones in Apulian platform carbonates (Maiella Mountains, Central Apennines, Italy). AAPG Bulletin, 105(12), 2449-2476.

Torsvik, T. H., Van der Voo, R., Preeden, U., Mac Niocaill, C., Steinberger, B., Doubrovine, P. V., ... & Cocks, L. R. M. (2012). Phanerozoic polar wander, palaeogeography and dynamics. Earth-Science Reviews, 114(3-4), 325-368.

Trude, J., Cartwright, J., Davies, R. J., & Smallwood, J. (2003). New technique for dating igneous sills. Geology, 31(9), 813-816.

Trude, K. J. (2004). Kinematic indicators for shallow level igneous intrusions from 3D seismic data: evidence of flow firection and feeder location. Geological Society, London, Memoirs, 29(1), 209-218.

Turcotte, D. L., & Schubert, G. (2002). Geodynamics, second edition, Wiley, New York, 848pp.

Turner, D. L., & Jarrard, R. D. (1982). K-Ar dating of the Cook-Austral island chain: A test of the hot-spot hypothesis. Journal of volcanology and geothermal research, 12(3-4), 187-220.

Ulmishek, G. F., & Klemme, H. D. (1990). Depositional controls, distribution, and effectiveness of world's petroleum source rocks (No. 1931). US Geological Survey Bulletin, (59 pp.).

Utami, D. A., Reuning, L., & Cahyarini, S. Y. (2018). Satellite-and field-based facies mapping of isolated carbonate platforms from the Kepulauan Seribu Complex, I ndonesia. The Depositional Record, 4(2), 255-273.

Vahrenkamp, V. C., & Swart, P. K. (1994). Late Cenozoic dolomites of the Bahamas: metastable analogues for the genesis of ancient platform dolomites. Dolomites: A volume in honour of Dolomieu, 133-153.

Vahrenkamp, V. C., David, F., Duijndam, P., Newall, M., & Crevello, P. (2004). Growth architecture, faulting, and karstification of a middle Miocene carbonate platform, Luconia Province, offshore Sarawak, Malaysia. In: Seismic Imaging of Carbonate Reservoirs and Systems, 81, American Association of Petroleum Geologists Memoir, pp. 329-350.

Valdes, P. J., Scotese, C. R., & Lunt, D. J. (2021). Deep ocean temperatures through time. Climate of the Past Discussions, 2020, 1-37. https://www.paleo.bristol.ac.uk/ummodel/users/Valdes_et_al_2021/new2/.

Vallier, T.L., & Jefferson, W.S. (1981). Volcanogenic sediments from Hess Rise and the Mid-Pacific Mountains, Deep Sea Drilling Project Leg 62. In: Thiede, J., Vallier, T.L., et al. (Eds.), Initial Reports of the Deep Sea Drilling Project, 62. U.S. Government Printing Office, Washington, D.C., p. 545–557.

van der Meer, D. G., Scotese, C. R., Mills, B. J., Sluijs, A., & van de Weg, R. M. (2022). Long-term Phanerozoic global mean sea level: Insights from strontium isotope variations and estimates of continental glaciation. Gondwana Research, 111, 103-121.

Van der Meer, D. G., van Saparoea, A. V. D. B., Van Hinsbergen, D. J. J., Van de Weg, R. M. B., Godderis, Y., Le Hir, G., & Donnadieu, Y. (2017). Reconstructing first-order changes in sea level during the Phanerozoic and Neoproterozoic using strontium isotopes. *Gondwana Research*, *44*, 22-34.

van Hinsbergen, D. J., De Groot, L. V., van Schaik, S. J., Spakman, W., Bijl, P. K., Sluijs, A., ... & Brinkhuis, H. (2015). A paleolatitude calculator for paleoclimate studies. PloS one, 10(6), e0126946.

Van Tuyl, J., Alves, T. M., & Cherns, L. (2018). Geometric and depositional responses of carbonate build-ups to Miocene sea level and regional tectonics offshore northwest Australia. Marine and Petroleum Geology, 94, 144-165.

Van Tuyl, J., Alves, T., Cherns, L., Antonatos, G., Burgess, P., & Masiero, I. (2019). Geomorphological evidence of carbonate build-up demise on equatorial margins: A case study from offshore northwest Australia. Marine and Petroleum Geology, 104, 125-149.

Van Waasbergen, R. J., & Winterer, E. L. (1993). Summit geomorphology of western Pacific guyots. Washington DC American Geophysical Union Geophysical Monograph Series, The Mesozoic Pacific: Geology, Tectonics, and Volcanism, 77, 335-366.

van Waasbergen, R.J. (1995). Sediment facies and environments of deposition on Cretaceous pacific carbonate platforms: an overview of dredged rocks from western Pacific Guyots. In Proceedings of the ocean drilling program, scientific results. Vol 143, pp. 471-493.

Vasconcelos, C., McKenzie, J. A., Warthmann, R., & Bernasconi, S. M. (2005). Calibration of the δ18O paleothermometer for dolomite precipitated in microbial cultures and natural environments. Geology, 33(4), 317-320.

Veizer, J. (1983). Chemical diagenesis in carbonates: Theory and application of trace element technique, in Arthur, M.A., and Anderson, T.J., eds., Stable Isotopes in Sedimentary geology: Society of Economic Paleontologists and Mineralogists Short Course, no. 10, p. 3–100.

Vérard, C., Hochard, C., Baumgartner, P. O., Stampfli, G. M., & Liu, M. (2015). 3D palaeogeographic reconstructions of the Phanerozoic versus sea-level and Sr-ratio variations. Journal of Palaeogeography, 4(1), 64-84.

Vinci, F., Iannace, A., Parente, M., Pirmez, C., Torrieri, S., & Giorgioni, M. (2017). Early dolomitization in the Lower Cretaceous shallow-water carbonates of Southern Apennines (Italy): Clues about palaeoclimatic fluctuations in western Tethys. Sedimentary geology, 362, 17-36.

Vogt, P. R. (1989). Volcanogenic upwelling of anoxic, nutrient-rich water: a possible factor in carbonate-bank/reef demise and benthic faunal extinctions?. Geological Society of America Bulletin, 101(10), 1225-1245.

Voigt, S., Gale, A. S., & Voigt, T. (2006). Sea-level change, carbon cycling and palaeoclimate during the Late Cenomanian of northwest Europe; an integrated palaeoenvironmental analysis. Cretaceous Research, 27(6), 836-858.

Wall, M., Cartwright, J., Davies, R., & McGrandle, A. (2010). 3D seismic imaging of a Tertiary Dyke Swarm in the Southern North Sea, UK. Basin Research, 22(2), 181-194.

Walliser, E. O., & Schöne, B. R. (2020). Paleoceanography of the Late Cretaceous northwestern Tethys Ocean: Seasonal upwelling or steady thermocline? PLoS One, 15(8), 1-26.

Wang, H., Zhao, Q., Wu, S., Wang, D., & Wang, B. (2018b). Post-rifting magmatism and the drowned reefs in the Xisha Archipelago domain. Journal of Ocean University of China, 17, 195-208.

Wang, J., Wu, S., Kong, X., Ma, B., Li, W., Wang, D., Gao, J., & Chen, W. (2018a). Subsurface fluid flow at an active cold seep area in the Qiongdongnan Basin, northern South China Sea. Journal of Asian Earth Sciences, 168, 17-26.

WANG, L., SHI, X., REN, Z., PEI, J., YANG, X., SHEN, Y., ... & YAN, A. (2020). Tectono-thermal evolution features of the reef body developing area in the Liyue Basin, Southern South China Sea. Chinese Journal of Geophysics, 63(8), 3050-3062.

Wang, L., Sun, Z., Yang, J., Sun, Z., Zhu, J., Zhuo, H., & Stock, J. (2019b). Seismic characteristics and evolution of post-rift igneous complexes and hydrothermal vents in the Lingshui sag (Qiongdongnan basin), northwestern South China Sea. Marine Geology, 418, 106043.

Wang, R., Jones, B., & Yu, K. (2019a). Island dolostones: Genesis by time-transgressive or event dolomitization. Sedimentary Geology, 390, 15-30.

Wang, R., Xiao, Y., Yu, K., Jones, B., Wu, L., Liang, F., ... & Chang, B. (2022). Temperature regimes during formation of Miocene island dolostones as determined by clumped isotope thermometry: Xisha Islands, South China Sea. Sedimentary Geology, 429, 106079.

Wang, R., Yu, K., Jones, B., Wang, Y., Zhao, J., Feng, Y., ... & Zhang, Y. (2018c). Evolution and development of Miocene "island dolostones" on Xisha Islands, South China Sea. Marine Geology, 406, 142-158.

Warren, J. (2000). Dolomite: occurrence, evolution, and economically important associations. Earth-Science Reviews, 52(1-3), 1-81.

Watson, D., Schofield, N., Jolley, D., Archer, S., Finlay, A. J., Mark, N., Hardman, J., & Watton, T. (2017). Stratigraphic overview of Palaeogene tuffs in the Faroe–Shetland Basin, NE Atlantic margin. Journal of the Geological Society, 174(4), p. 627-645.

Watts, A. B., & Ten Brink, U. S. (1989). Crustal structure, flexure, and subsidence history of the Hawaiian Islands. Journal of Geophysical Research: Solid Earth, 94(B8), 10473-10500.

Watts, A. B., Ten Brink, U. S., Buhl, P., & Brocher, T. M. (1985). A multichannel seismic study of lithospheric flexure across the Hawaiian–Emperor seamount chain. Nature, 315(6015), 105-111.

Wei, X., Jia, C. Z., & Meng, W. G. (2008). Dolomitization characteristics of carbonate rock in Xisha Islands and its formation: A case study of Well Xichen-1. Journal of Jilin University (Earth Science Edition), 38(2), 217-224.

Wei, X., Zhu, Y., Xu, H., Zhao, G., Li, Y. (2006). Discussion on Neogene dolostone forming condition in Xisha Islands: evidences from isotope C and O and fluid inclosures. Acta Petrologica Sinica, 22(9), 2394-2404.

Weinmann, A. E., & Langer, M. R. (2017). Diverse thermotolerant assemblages of benthic foraminiferal biotas from tropical tide and rock pools of eastern Africa. Revue de Micropaléontologie, 60(4), 511-523.

Westphal, H., Riegl, B., & Eberli, G. P. (Eds.). (2010). Carbonate Depositional Systems: Assessing Dimensions and Controlling Parameters: The Bahamas, Belize and the Persian/Arabian Gulf. Springer Science & Business Media.

Wheeler, C. W., Aharon, P., & Ferrell, R. E. (1999). Successions of late Cenozoic platform dolomites distinguished by texture, geochemistry, and crystal chemistry; Niue, South Pacific. Journal of Sedimentary Research, 69(1), 239-255.

Whitaker, F. F., & Smart, P. L. (1997a). Geochemistry of meteoric waters and porosity generation in carbonate islands of the Bahamas. In Geofluids II, Second International Conference on Fluid Evolution, Migration and Interaction in Sedimentary Basins and Orogenic Belts, 415-418.

Whitaker, F. F., & Smart, P. L. (1997b). Climatic control of hydraulic conductivity of Bahamian limestones. Groundwater, 35(5), 859-868.

Whitaker, F. F., & Xiao, Y. (2010). Reactive transport modeling of early burial dolomitization of carbonate platforms by geothermal convection. AAPG bulletin, 94(6), 889-917.

Whitaker, F. F., Smart, P. L., Vahrenkamp, V. C., Nicholson, H., & Wogelius, R. A. (1994). Dolomitization by near-normal seawater? Field evidence from the Bahamas. Dolomites: A Volume in Honour of Dolomieu, 109-132.

White, R. H., Anderson, S., Booth, J. F., Braich, G., Draeger, C., Fei, C., ... & West, G. (2023). The unprecedented Pacific Northwest heatwave of June 2021. Nature Communications, 14(1), 727.

Wilckens, F. K., Reeves, E. P., Bach, W., Seewald, J. S., & Kasemann, S. A. (2019). Application of B, Mg, Li, and Sr isotopes in acid-sulfate vent fluids and volcanic rocks as tracers for fluid-rock interaction in back-arc hydrothermal systems. Geochemistry, Geophysics, Geosystems, 20(12), 5849-5866.

Wilson, A. M., Sanford, W., Whitaker, F., & Smart, P. (2001). Spatial patterns of diagenesis during geothermal circulation in carbonate platforms. American Journal of Science, 301(8), 727-752.

Wilson, E. N., Hardie, L. A., & Phillips, O. M. (1990). Dolomitization front geometry, fluid flow patterns, and the origin of massive dolomite; the Triassic Latemar buildup, northern Italy. American Journal of Science, 290(7), 741-796.

Wilson, P. A., Jenkyns, H. C., Elderfield, H., & Larson, R. L. (1998). The paradox of drowned carbonate platforms and the origin of Cretaceous Pacific guyots. Nature, 392(6679), 889-894.

Winterer, E. L. (1998). Cretaceous karst guyots: new evidence for inheritance of atoll morphology from subaerial erosional terrain. Geology, 26(1), 59-62.

Winterer, E. L., & Metzler, C. V. (1984). Origin and subsidence of guyots in Mid-Pacific Mountains. Journal of Geophysical Research: Solid Earth, 89(B12), 9969-9979.

Winterer, E. L., & Sager, W. W. (1995). Synthesis of Drilling Results from the Mid-Pacific Mountains: Regional Context and Implications. In Proceedings of the Ocean Drilling Program, scientific results, 143, p. 497-535.

Winterer, E. L., Natland, J. H., Van Waasbergen, R. J., Duncan, R. A., Mcnutt, M. K., Wolfe, C. J., ... & Sliter, W. V. (1993). Cretaceous guyots in the northwest Pacific: An overview of their geology and geophysics. The Mesozoic Pacific: Geology, Tectonics, and Volcanism, 77, 307-334.

Winterer, E. L., Van Waasbergen, R., Mammerickx, J., & Stuart, S. (1995). Karst morphology and diagenesis of the top of Albian limestone platforms, Mid-Pacific Mountains: Northwest Pacific atolls and guyots. In Proceedings of the Ocean Drilling Program. Scientific results, Vol. 143, pp. 433–470.

Winterer, E.L., Ewing, J.I., Douglas, R.G., Jarrard, R.D., Lancelot, Y., Moberly, R.M., Moore Jr., T.C., Peter, H.R., and Schlanger S.O. (1973). Site 171. In the initial Reports of the Deep-Sea Drilling Project, Vol. 17, pp. 283-334.

Wohlwend, S., Hart, M., & Weissert, H. (2016). Chemostratigraphy of the Upper Albian to mid-Turonian Natih Formation (Oman)–how authigenic carbonate changes a global pattern. The Depositional Record, 2(1), 97-117.

Woronick, R. E., & Land, L. S. (1985). Late burial diagenesis, lower Cretaceous Pearsall and lower Glen Rose formations, South Texas. In: N. Schneiderman and P.M. Harris (Editors), Carbonate Cements. Soc. Econ. Paleontol. Mineral., Spec. Publ. 36: 265-275.

Wright, N. M., Seton, M., Williams, S. E., Whittaker, J. M., & Müller, R. D. (2020). Sea-level fluctuations driven by changes in global ocean basin volume following supercontinent break-up. Earth-Science Reviews, 208, 103293.

Wright, V. P., & Burgess, P. M. (2005). The carbonate factory continuum, facies mosaics and microfacies: an appraisal of some of the key concepts underpinning carbonate sedimentology. Facies, 51, 17-23.

Wu, S., Chen, W., Huang, X., Liu, G., Li, X., & Betzler, C. (2020). Facies model on the modern isolated carbonate platform in the Xisha Archipelago, South China Sea. Marine Geology, 425, 106203.

Wunsch, M., Betzler, C., Eberli, G. P., Lindhorst, S., Lüdmann, T., & Reijmer, J. J. (2018). Sedimentary dynamics and high-frequency sequence stratigraphy of the southwestern slope of Great Bahama Bank. Sedimentary geology, 363, 96-117.

Xiao, J., & Waltham, D. (2019). Non-uniqueness and symmetry in stratigraphic interpretations: A quantitative approach for determining stratal controls. Sedimentology, 66(5), 1700-1715.

Xiao, Y., & Jones, G. D. (2007, December). Reactive transport models of limestone-dolomite transitions: implications for reservoir connectivity. In *IPTC 2007: International Petroleum Technology Conference* (pp. cp-147). European Association of Geoscientists & Engineers.

Yang, P., Sun, S. Z., Liu, Y., Li, H., Dan, G., & Jia, H. (2012). Origin and architecture of fractured-cavernous carbonate reservoirs and their influences on seismic amplitudes. The Leading Edge, 31(2), 140-150.

Yang, W., Gong, X., & Li, W. (2018). Geological origins of seismic bright spot reflections in the Ordovician strata in the Halahatang area of the Tarim Basin, western China. Canadian Journal of Earth Sciences, 55(12), 1297-1311.

Yapparova, A., Gabellone, T., Whitaker, F., Kulik, D. A., & Matthäi, S. K. (2017a). Reactive transport modelling of hydrothermal dolomitisation using the CSMP++ GEM coupled code: Effects of temperature and geological heterogeneity. Chemical Geology, 466, 562-574.

Yapparova, A., Gabellone, T., Whitaker, F., Kulik, D. A., & Matthäi, S. K. (2017b). Reactive transport modelling of dolomitisation using the new csmp++ gem coupled code: Governing equations, solution method and benchmarking results. Transport in Porous Media, 117(3), 385-413.

Yordanova, E. K., & Hohenegger, J. (2007). Studies on settling, traction and entrainment of larger benthic foraminiferal tests: implications for accumulation in shallow marine sediments. Sedimentology, 54(6), 1273-1306.

Yose, L. A., Ruf, A. S., Strohmenger, C. J., Schuelke, J. S., Gombos, A., Al-Hosani, I., Al-Maskary, S., Bloch, G., Al-Mehairi, Y., & Johnson, I. G. (2006). Three-dimensional characterization of a heterogeneous carbonate reservoir, Lower Cretaceous, Abu Dhabi (United Arab Emirates). In: Harris, P. M. & Weber, L. J. (eds) Giant Hydrocarbon Reservoirs of the World: From Rocks to Reservoir Characterization and Modelling. American Association of Petroleum Geologists Memoir 88, 173– 212.

Young, A., Flament, N., Williams, S. E., Merdith, A., Cao, X., & Müller, R. D. (2022). Long-term Phanerozoic sea level change from solid Earth processes. Earth and Planetary Science Letters, 584, 117451.

Yu, J., Li, Z., & Yang, L. (2016). Fault system impact on paleokarst distribution in the Ordovician Yingshan Formation in the central Tarim basin, northwest China. Marine and Petroleum Geology, 71, 105-118.

Zampetti, V., Schlager, W., van Konijnenburg, J. H., & Everts, A. J. (2004). Architecture and growth history of a Miocene carbonate platform from 3D seismic reflection data; Luconia province, offshore Sarawak, Malaysia. Marine and petroleum geology, 21(5), 517-534.

Zeng, C., Li, Z., Wang, Y., & Li, H. (2020). Early paleozoic tropical paleokarst geomorphology predating terrestrial plant growth in the tahe oilfield, Northwest China. Marine and Petroleum Geology, 122, 104653.

Zenger, D. H. (1968). Determination of calcite and dolomite composition using the air comparison pycnometer. Journal of Sedimentary Research, 38(2), 373-377.

Zenger, D. H., Dunham, J. B., & Ethington, R. L. (1980). Concepts and models of dolomitization. SEPM Special Publication 28, 320 p.

Zhang, M., Lin, C., Sun, Y., Liu, J., Li, H., Wang, Q., & Wang, Y. (2020a). Sequence framework, depositional evolution and controlling processes, the Early Carboniferous carbonate system, Chu-Sarysu Basin, southern Kazakhstan. Marine and Petroleum Geology, 111, 544-556.

Zhang, W., Wang, G., & Cao, Z. (2021). Reactive Transport Modeling of Reflux Dolomitization of Carbonate Platforms: Enlightenment from Yingshan Formation in Shunnan Area, Tarim Basin. Minerals, 11(12), 1340.

Zhang, X., Liu, L., & Song, Y. (2020b). Seasonal Sea Surface Temperature Variability over Tropical Indo-Pacific Region Simulated by FIO-ESM Model Under Global Warming. Pure and Applied Geophysics, 177, 4045-4056.

Zhao, H., & Jones, B. (2012a). Genesis of fabric-destructive dolostones: a case study of the Brac Formation (Oligocene), Cayman Brac, British West Indies. Sedimentary Geology, 267, 36-54.

Zhao, H., & Jones, B. (2012b). Origin of "island dolostones": a case study from the Cayman formation (Miocene), Cayman Brac, British West Indies. Sedimentary Geology, 243, 191-206.

Zhao, W., Shen, A., Qiao, Z., Zheng, J., & Wang, X. (2014). Carbonate karst reservoirs of the Tarim Basin, northwest China: Types, features, origins, and implications for hydrocarbon exploration. Interpretation, 2(3), SF65-SF90.

Zhou, J., Poulsen, C. J., Pollard, D., & White, T. S. (2008). Simulation of modern and middle Cretaceous marine δ18O with an ocean-atmosphere general circulation model. Paleoceanography, 23(3).

Zhu, H., Zhu, X., & Chen, H. (2017). Seismic characterization of hypogenic karst systems associated with deep hydrothermal fluids in the Middle-Lower Ordovician Yingshan Formation of the Shunnan Area, Tarim Basin, NW China. Geofluids, (V. 2017), 8094125, 13 p.

APPENDIX A: *SUPPLEMENT* TO STRATIGRAPHIC EVOLUTION AND KARSTIFICATION OF A CRETACEOUS MID-PACIFIC ATOLL (RESOLUTION GUYOT) RESOLVED FROM CORE-LOG-SEISMIC INTEGRATION AND COMPARISON WITH MODERN AND ANCIENT ANALOGUES[1]

Contents:

Table A1: Correlation and tie-points between the $^{87}Sr/^{86}Sr$ and $\delta^{13}C_{carb}$ data from Resolution Guyot (ODP Site 866) and reference curves; the low-latitude calibrated composite $\delta^{13}C_{carb}$ curve (reproduced from Herrle et al., 2015, using published data from Tethyan sections of Erba et al., 1999; Herrle et al., 2004; Gale et al., 2011, and calibrated using Gradstein et al., 2012; GTS2012) and global $^{87}Sr/^{86}Sr$ curve (McArthur et al., 2012, version 5B).

Table A2: Seismic to well tie at Site 866.

[1] A version of this appendix is published in ***Basin Research*** as Supplementary Information to:

El-Yamani, M. S., John, C. M., & Bell, R. (2022). Stratigraphic evolution and karstification of a Cretaceous Mid-Pacific atoll (Resolution Guyot) resolved from core-log-seismic integration and comparison with modern and ancient analogues. ***Basin Research***, 34(5), 1536-1566.

Table A1: Depositional Age Dating Methodology at Site 866

- Correlation and tie-points between the data from Resolution Guyot (ODP Site 866) and Reference curve (reproduced from Herrle et al., 2015, using published data from Tethyan sections of Erba et al., 1999; Herrle et al., 2004; Gale et al., 2011, and calibrated using Gradstein et al., 2012; GTS2012) were determined based on the following criteria (Figure A1-1):

1) points of similar excursion between the data points and the reference curves (these points share similar carbon isotopic value with the reference curve). These points are tied by correlation lines.

2) the data between the excursion points in the study area and the reference curve share similar trends of positive and negative excursion. Therefore, they are correlative intervals highlighted by alternating dark and light blue shaded areas.

- Tie-points and strontium isotope stratigraphy for Resolution Guyot using reference curves of McArthur et al. (2012, version 5B) and Bodin et al. (2015)

- In order to make age model using the strontium isotope values, tie-points (highlighted by circles) between our data and reference curves (McArthur et al., 2012; Bodin et al., 2015) should be identified first. Tie-points were determined based on the following criteria (Figure A1-2):

1) Points that represent easily detectable inflection from decreasing to increasing trend or vice versa.

2) points that represent constant trend with no change like in middle to late Albian strata.

Some of the points have values different than their tie-points in the reference curve(s). These points were selected as they show similar trend in the values before and after it. Regardless of this shift in the values of some points, the plotted data points with depth have similar trends (highlighted by arrows) to the reference curves (McArthur et al., 2012; Bodin et al., 2015).

3) Age-depth model was achieved based on integrating the tying points of the strontium isotope stratigraphy and the carbon isotope stratigraphy (Table A1-1).

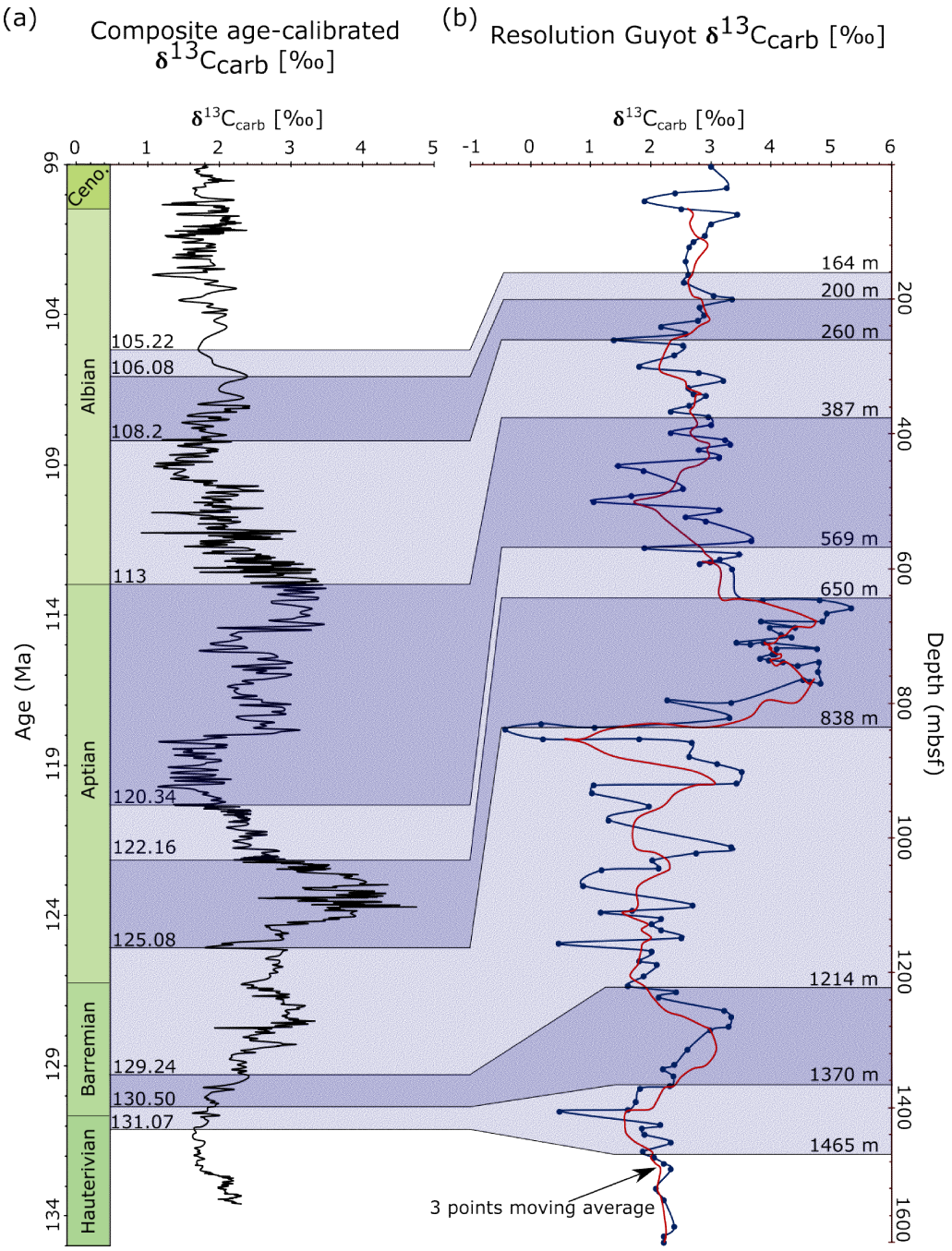


Figure A1.1 Correlation and tie-points between the data from Resolution Guyot (ODP Site 866) and Reference curve (reproduced from Herrle et al., 2015, using published data from Tethyan sections of Erba et al., 1999; Herrle et al., 2004; Gale et al., 2011, and calibrated using Gradstein et al., 2012; GTS2012).

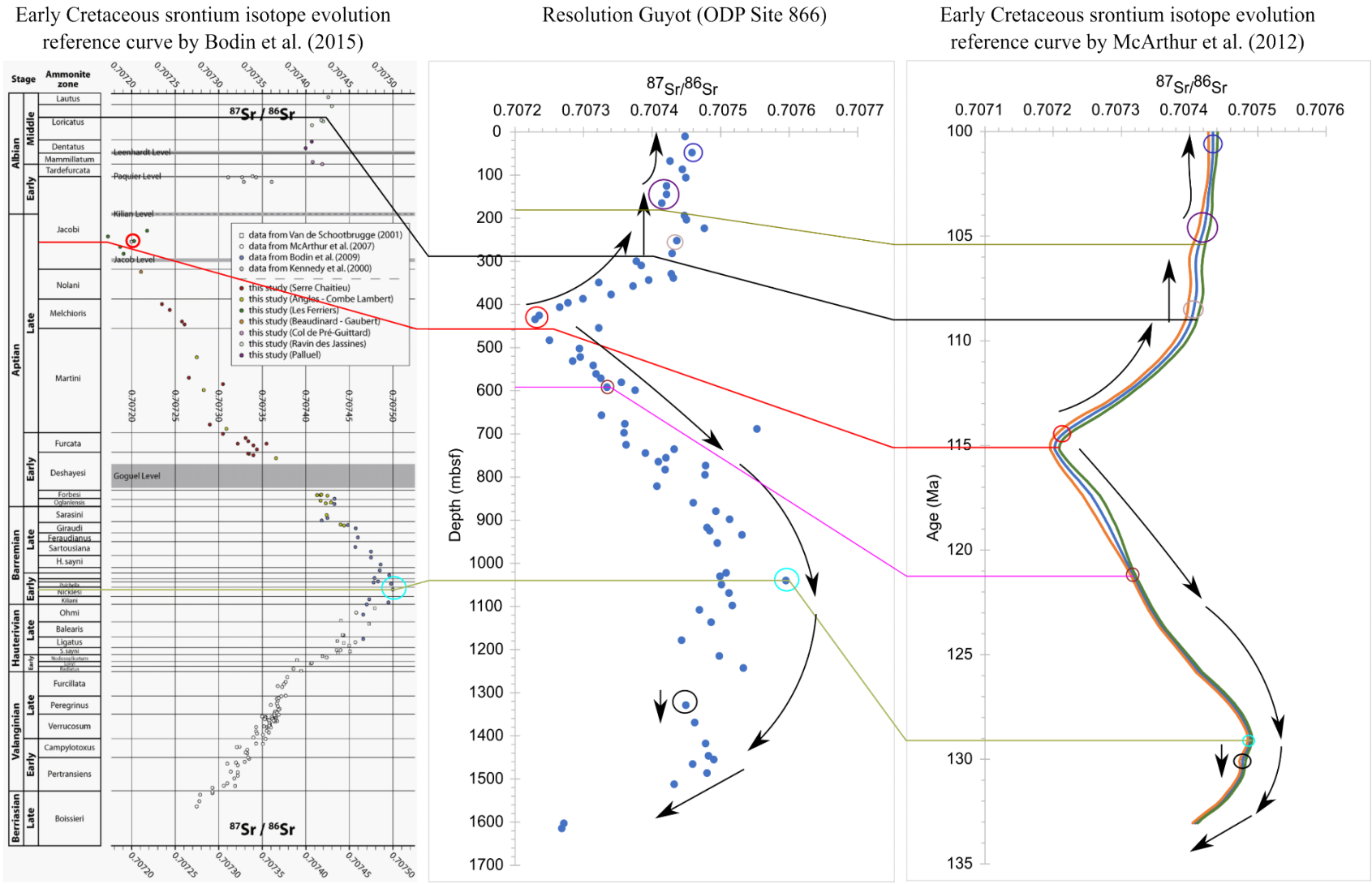


Figure A1.2 Tie-points and strontium isotope stratigraphy for Resolution Guyot using reference curves of McArthur et al. (2012, version 5B) and Bodin et al. (2015). Some of the points have values different than their tie-points in the reference curve(s). These points were selected as they show similar trend in the values before and after it. Regardless this shift in the values of some points, the plotted data points with depth has similar trends (highlighted by arrows) to the reference curves (McArthur et al., 2012; Bodin et al., 2015).

Depth (mbsf)	Strontium isotope ratio	error value	calculated age (Ma)	approx. age (Ma)	approx. age +1 (Ma)	approx. age -1 (Ma)
10.21	0.707448	0.000020				
47.94	0.707458	0.000024	101.30	101.3	102.3	100.3
67.22	0.707426	0.000020	101.87	101.9	102.9	100.9
86.59	0.707444	0.000020	102.45	102.5	103.5	101.5
105.83	0.707449	0.000020	103.02	103.0	104.0	102.0
125.02	0.707421	0.000020	103.60	103.6	104.6	102.6
144.42	0.707421	0.000021	104.40	104.4	105.4	103.4
164.87	0.707414	0.000020	105.15	105.2	106.2	104.2
193.88	0.707447	0.000024	106.01	106.0	107.0	105.0
203.43	0.707450	0.000030	106.29	106.3	107.3	105.3
223.31	0.707476	0.000022	106.89	106.9	107.9	105.9
251.69	0.707436	0.000031	107.75	107.8	108.8	106.8
281.41	0.707429	0.000020	108.90	108.9	109.9	107.9
299.62	0.707377	0.000020	109.61	109.6	110.6	108.6
309.24	0.707384	0.000022	109.98	110.0	111.0	109.0
328.77	0.707428	0.000020	110.73	110.7	111.7	109.7
338.24	0.707431	0.000020	111.10	111.1	112.1	110.1
343.23	0.707395	0.000020	111.29	111.3	112.3	110.3
349.00	0.707322	0.000020	111.51	111.5	112.5	110.5
357.31	0.707372	0.000020	111.83	111.8	112.8	110.8
376.67	0.707340	0.000020	112.58	112.6	113.6	111.6
386.51	0.707299	0.000025	112.96	113.0	114.0	112.0
395.97	0.707277	0.000020	113.32	113.3	114.3	112.3
405.98	0.707265	0.000020	113.71	113.7	114.7	112.7
425.30	0.707235	0.000020	114.46	114.5	115.5	113.5
434.43	0.707229	0.000020	114.80	114.8	115.8	113.8
454.12	0.707322	0.000020	115.61	115.6	116.6	114.6
482.71	0.707250	0.000023	116.81	116.8	117.8	115.8

483.11	0.707301	0.000020	116.83	116.8	117.8	115.8
502.08	0.707294	0.000024	117.62	117.6	118.6	116.6
521.52	0.707295	0.000020	118.44	118.4	119.4	117.4
531.12	0.707284	0.000020	118.84	118.8	119.8	117.8
541.14	0.707314	0.000020	119.26	119.3	120.3	118.3
560.58	0.707318	0.000021	120.08	120.1	121.1	119.1
570.80	0.707325	0.000020	120.51	120.5	121.5	119.5
580.12	0.707355	0.000021	120.90	120.9	121.9	119.9
591.43	0.707334	0.000020	121.40	121.4	122.4	120.4
598.63	0.707375	0.000024	121.54	121.5	122.5	120.5
648.47	0.707373	0.000020	122.39	122.4	123.4	121.4
656.50	0.707347	0.000020	122.53	122.5	123.5	121.5
656.60	0.707326	0.000020	122.53	122.5	123.5	121.5
676.52	0.707360	0.000020	122.87	122.9	123.9	121.9
688.47	0.707553	0.000020	123.07	123.1	124.1	122.1
697.19	0.707359	0.000020	123.22	123.2	124.2	122.2
705.21	0.707396	0.000020	123.36	123.4	124.4	122.4
725.09	0.707362	0.000020	123.70	123.7	124.7	122.7
726.54	0.707413	0.000020	123.72	123.7	124.7	122.7
735.21	0.707432	0.000020	123.87	123.9	124.9	122.9
744.40	0.707390	0.000020	124.03	124.0	125.0	123.0
755.38	0.707420	0.000021	124.22	124.2	125.2	123.2
764.13	0.707409	0.000020	124.37	124.4	125.4	123.4
773.31	0.707478	0.000020	124.52	124.5	125.5	123.5
782.78	0.707419	0.000020	124.69	124.7	125.7	123.7
794.88	0.707477	0.000020	124.89	124.9	125.9	123.9
820.98	0.707407	0.000020	125.34	125.3	126.3	124.3
832.48	0.707525	0.000020	125.54	125.5	126.5	124.5
850.54	0.707504	0.000020	125.84	125.8	126.8	124.8
859.42	0.707460	0.000020	126.00	126.0	127.0	125.0
878.97	0.707493	0.000020	126.33	126.3	127.3	125.3
897.81	0.707513	0.000020	126.65	126.7	127.7	125.7

907.73	0.707497	0.000020	126.82	126.8	127.8	125.8
917.20	0.707480	0.000020	126.98	127.0	128.0	126.0
924.36	0.707484	0.000020	127.11	127.1	128.1	126.1
933.91	0.707531	0.000020	127.27	127.3	128.3	126.3
952.86	0.707495	0.000020	127.59	127.6	128.6	126.6
1021.93	0.707508	0.000020	128.78	128.8	129.8	127.8
1030.05	0.707499	0.000021	128.91	128.9	129.9	127.9
1039.60	0.707595	0.000020	129.05	129.1	130.1	128.1
1049.09	0.707501	0.000022	129.09	129.1	130.1	128.1
1068.79	0.707512	0.000020	129.18	129.2	130.2	128.2
1097.50	0.707517	0.000020	129.33	129.3	130.3	128.3
1107.74	0.707469	0.000020	129.38	129.4	130.4	128.4
1136.43	0.707486	0.000020	129.52	129.5	130.5	128.5
1178.09	0.707443	0.000020	129.73	129.7	130.7	128.7
1214.53	0.707498	0.000022	129.91	129.9	130.9	128.9
1242.41	0.707533	0.000020	130.05	130.1	131.1	129.1
1328.74	0.707449	0.000033	130.50	130.5	131.5	129.5
1368.91	0.707462	0.000020	130.68	130.7	131.7	129.7
1417.66	0.707478	0.000020	130.93	130.9	131.9	129.9
1446.06	0.707482	0.000020	131.07	131.1	132.1	130.1
1454.90	0.707490	0.000020	131.11	131.1	132.1	130.1
1465.49	0.707459	0.000020	131.17	131.2	132.2	130.2
1486.17	0.707480	0.000020	131.27	131.3	132.3	130.3
1511.85	0.707432	0.000020	131.40	131.4	132.4	130.4
1602.52	0.707271	0.000020	131.85	131.9	132.9	130.9
1614.40	0.707268	0.000020	131.91	131.9	132.9	130.9

Table A1.1. Age-depth correlation at Site 866 derived from the strontium isotope data tying points.

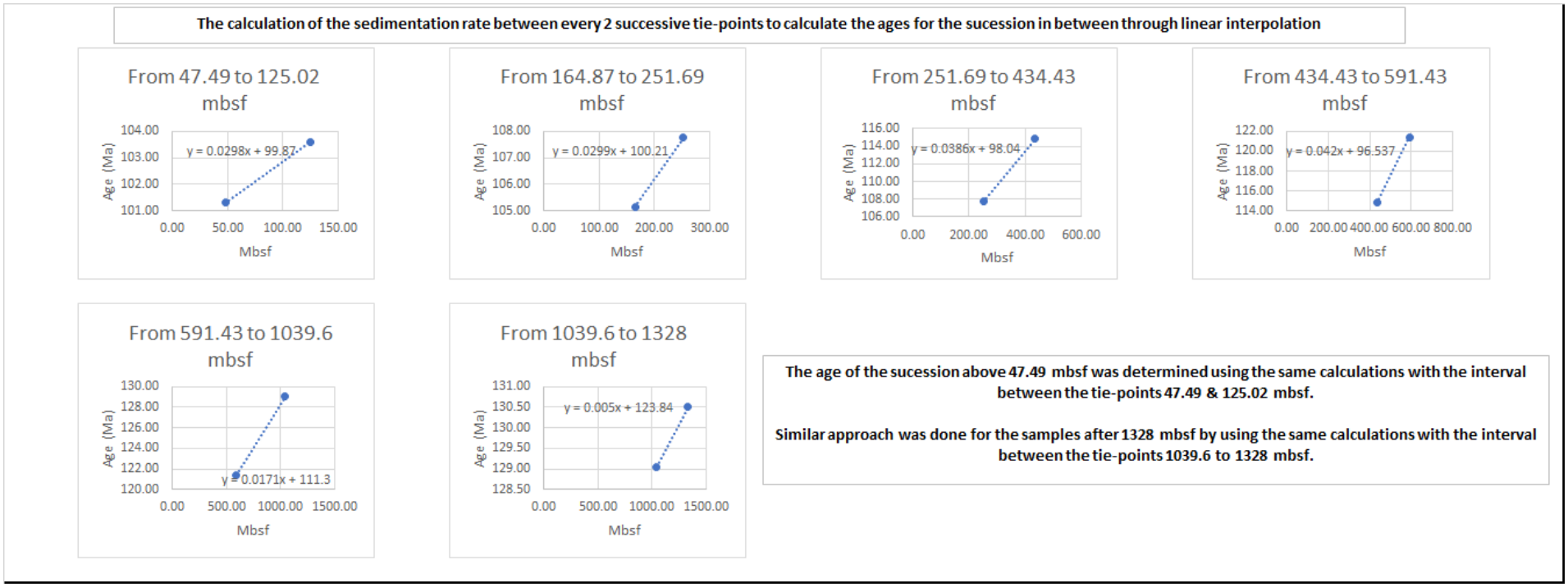


Figure A1.3 The calculation of the sedimentation rate between every 2 successive tie-points to calculate the ages for the succession in between through linear interpolation.

Table A2: Time-Depth Relationship at Site 866 (Resolution Guyot)

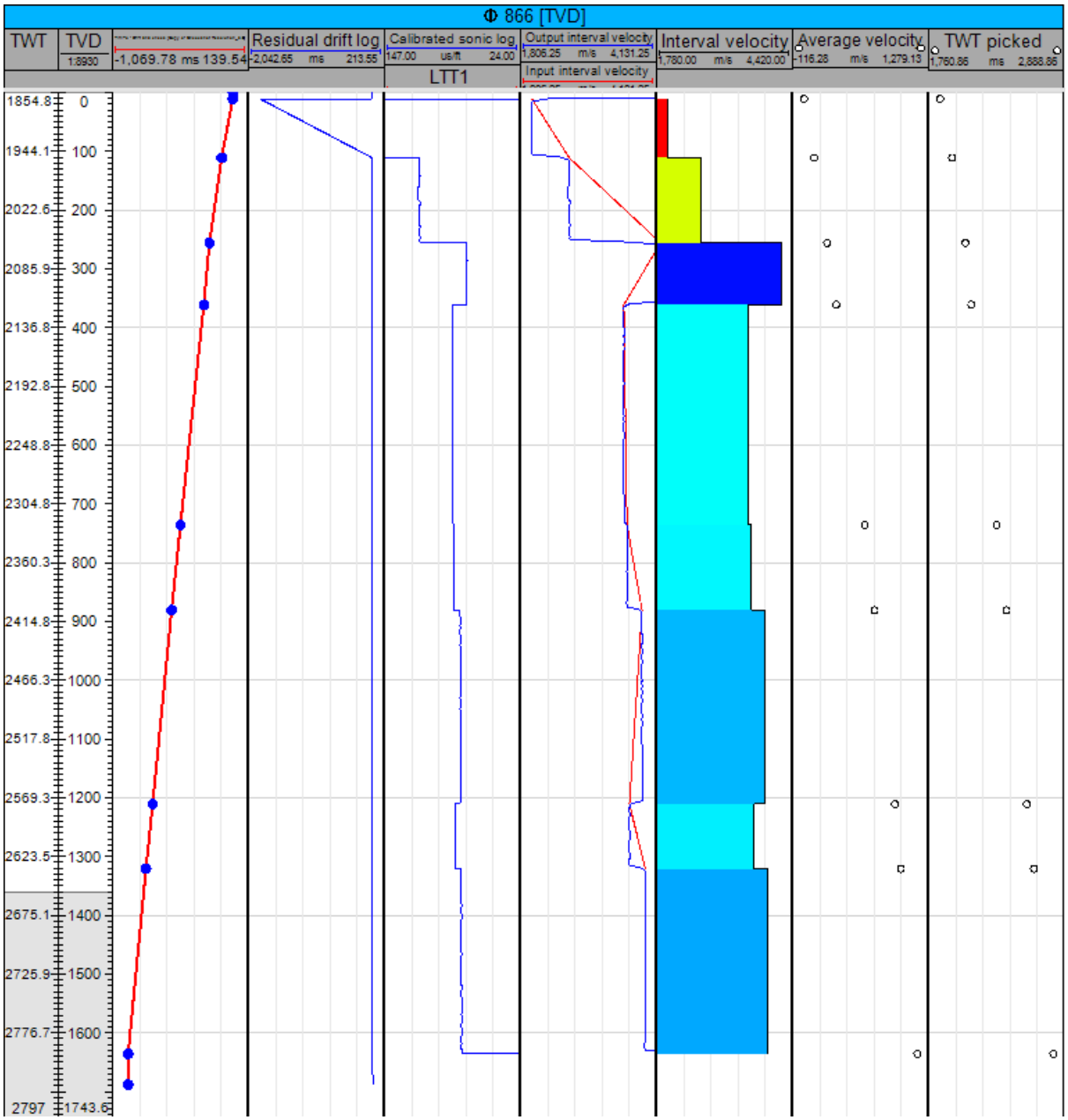
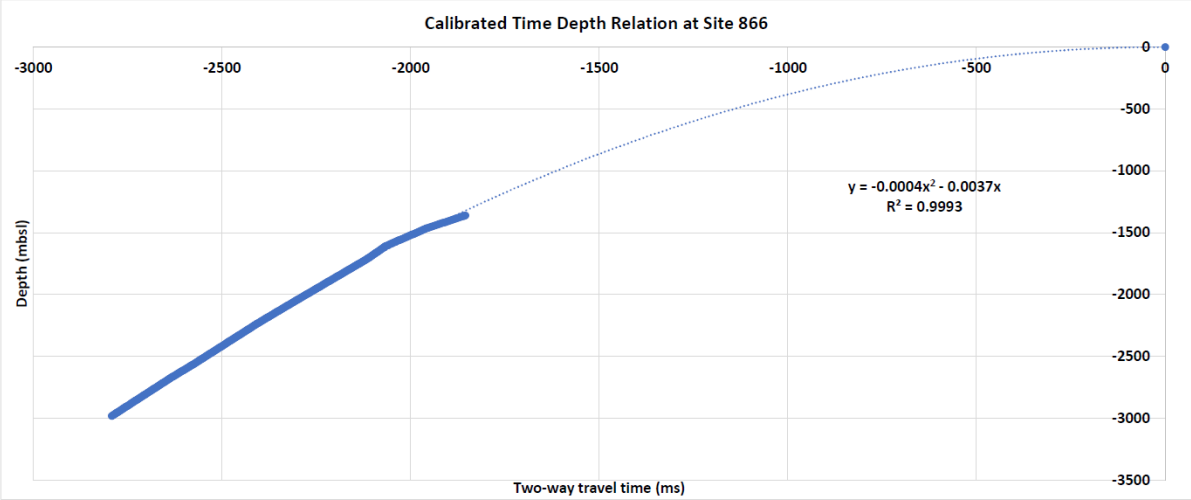


Figure A2.1 Sonic calibration and seismic to well tie at Site 866 using the principal reflectors beneath the pelagic cap suggested by Sager et al. (1993a), sonic and density wireline logs.



The first 100 of meters at Site 866 seem to have an average interval velocity ~ 2000 m/s. Therefore, this value is applied to Site 867 and 868 where their penetration depths are below 100m

Figure A2.2 Time-depth relationship for depth conversion at Site 866 in Resolution Guyot

APPENDIX B: *SUPPLEMENT* TO MECHANISM OF ISLAND DOLOSTONES FORMATION IN THE CRETACEOUS CALCITIC OCEAN: INSIGHTS FROM THE MID-PACIFIC GUYOTS[2]

Contents:

Material B1: Dolomite age determination using the $^{87}Sr/^{86}Sr$ data of the dolomites at Site 866.

Material B2: The fractionation temperature of the dolomite using the dolomite oxygen isotope data.

Material B3: Host rock burial and thermal history modelling calculations.

Table B4: Cenozoic island dolostones geo-database.

Table B5: Cretaceous island dolostones geo-database.

Table B6: Logging data at Site 866.

Table B7: Dolomite isotope data at Site 866.

Table B8: Major, minor, and trace elements of limestones and dolomites at Site 866.

Table B9: XRF data at Site 866.

Table B10: Time-Depth relation at Resolution Guyot.

Table B11: Dolomite content (%) at Site 866.

Table B12: Sea surface temperature and palaeo-$\delta^{18}O_{sw}$ during dolomitisation.

Table B13: Age-Depth relationship at Resolution Guyot.

Table B14: Geotherm Gradient Eniwetok.

Table B15: The fractionation temperature of the dolomite using the dolomite oxygen isotope data and different fractionation equations.

Table B16: Time spent by Cretaceous Pacific atolls below 1000 mbsl.

Table B17: Estimated permeabilities at Site 866.

[2] A version of this appendix is published in ***Marine and Petroleum Geology*** as Supplementary Information to:

El-Yamani, M. S., John, C. M., & Bell, R. (2024). Mechanism of island dolostones formation in the Cretaceous calcitic ocean: Insights from the Mid-Pacific Guyots. ***Marine and Petroleum Geology***, 106741.

Table B1: Cenozoic Island Dolostone Database

Number of references	Rock Unit & Island	References	
1	Cayman Formation, Grand Cayman	Jones, B. (1989). Syntaxial overgrowths on dolomite crystals in the Bluff Formation, Grand Cayman, British West Indies. Journal of Sedimentary Research, 59(5), 839-847. Jones, B., & Luth, R. W. (2002). Dolostones from Grand Cayman, British West Indies. Journal of Sedimentary Research, 72(4), 559-569. Jones, B., & Luth, R. W. (2003). Petrography of finely crystalline Cenozoic dolostones as revealed by backscatter electron imaging: case study of the Cayman Formation (Miocene), Grand Cayman, British West Indies. Journal of sedimentary research, 73(6), 1022-1035. Jones, B., & Luth, R. W. (2003). Temporal evolution of Tertiary dolostones on Grand Cayman as determined by 87Sr/86Sr. Journal of Sedimentary Research, 73(2), 187-205. Pleydell, SM, Jones, B., Longstaffe, FJ, & Baadsgaard, H. (1990). Dolomitization of the oligocene–miocene bluff formation on Grand Cayman, British West Indies. Canadian Journal of Earth Sciences , 27 (8), 1098-1110. Ren, M., & Jones, B. (2016). Diagenesis in limestone-dolostone successions after 1 million years of rapid sea-level fluctuations: A case study from Grand Cayman, British West Indies. Sedimentary Geology, 342, 15-30. Ren, M., & Jones, B. (2017). Spatial variations in the stoichiometry and geochemistry of Miocene dolomite from Grand Cayman: Implications for the origin of island dolostone. Sedimentary Geology, 348, 69-93.	DOLOMITISED
2	Cayman Formation, Cayman Brac	Zhao, H., & Jones, B. (2012). Genesis of fabric-destructive dolostones: a case study of the Brac Formation (Oligocene), Cayman Brac, British West Indies. Sedimentary Geology, 267, 36-54. Zhao, H., & Jones, B. (2012). Origin of "island dolostones": a case study from the Cayman formation (Miocene), Cayman Brac, British West Indies. Sedimentary Geology, 243, 191-206.	
3	Little Bahama Bank Lower and Upper Dolomite	Vahrenkamp, V. C., Swart, P. K., & Ruiz, J. (1991). Episodic dolomitization of late Cenozoic carbonates in the Bahamas; evidence from strontium isotopes. Journal of Sedimentary Research, 61(6), 1002-1014. Vahrenkamp, V. C., & Swart, P. K. (1994). Late Cenozoic dolomites of the Bahamas: metastable analogues for the genesis of ancient platform dolomites. Dolomites: A volume in honour of Dolomieu, 133-153.	
4	Mururoa	Chevalier, J. P. (1973). Geomorphology and geology of coral reefs in French Polynesia. In: Jones, O.A., Endean, R. (Eds.), Biology and Geology of Coral Reefs. Academic Press, pp. 113-141. Aissaoui, D. M., Buigues, D., & Purser, B. H. (1986). Model of reef diagenesis: Mururoa atoll, French Polynesia. Reef diagenesis, 27-52.	
5	Kita-daito-jima Daito Formation	Ohde, S., & Elderfield, H. (1992). Strontium isotope stratigraphy of Kita-daito-jima Atoll, North Philippine Sea: implications for Neogene sea-level change and tectonic history. Earth and Planetary Science Letters, 113(4), 473-486. Suzuki, Y., Iryu, Y., Inagaki, S., Yamada, T., Aizawa, S., & Budd, D. A. (2006). Origin of atoll dolomites distinguished by geochemistry and crystal chemistry: Kita-daito-jima, northern Philippine Sea. Sedimentary Geology, 183(3-4), 181-202. Berner, R. A. (1965). Dolomitization of the mid-Pacific atolls. Science, 147(3663), 1297-1299. Schlanger, S. O., Graf, D. L., & Goldsmith, J. R. (1963). Subsurface geology of Eniwetok atoll. US Government Printing Office.	
6	San Salvador	Supko, P. R. (1977). Subsurface dolomites, San Salvador, Bahamas. Journal of Sedimentary Research, 47(3), 1063-1077. Swart, P. K., Ruiz, J., & Holmes, C. W. (1987). Use of strontium isotopes to constrain the	

		timing and mode of dolomitization of upper Cenozoic sediments in a core from San Salvador, Bahamas. Geology, 15(3), 262-265. Dawans, J. M., & Swart, P. K. (1988). Textural and geochemical alternations in Late Cenozoic Bahamian dolomites. Sedimentology, 35(3), 385-403.	
7	Funafuti	Berner, R. A. (1965). Dolomitization of the mid-Pacific atolls. Science, 147(3663), 1297-1299. Schlanger, S. O., Graf, D. L., & Goldsmith, J. R. (1963). Subsurface geology of Eniwetok atoll. US Government Printing Office.	
8	Xisha Islands	Bi, D. J., Zhai, S. K., Zhang, D. J., Liu, X. F., Liu, X. Y., Jiang, L. J., & Zhang, A. B. (2018). Constraints of fluid inclusions and C, O isotopic compositions on the origin of the dolomites in the Xisha Islands, South China Sea. Chemical Geology, 493, 504-517. Wang, R., Xiao, Y., Yu, K., Jones, B., Wu, L., Liang, F., ... & Chang, B. (2022). Temperature regimes during formation of Miocene island dolostones as determined by clumped isotope thermometry: Xisha Islands, South China Sea. Sedimentary Geology, 429, 106079. Xi, W., Yonglun, Z., Hong, X., GuoChun, Z., & YuXi, L. (2006). Discussion on Neogene dolostone forming condition in Xisha Islands: evidences from isotope C and O and fluid inclosures. Acta Petrologica Sinica, 22(9), 2394-2404. Wei, X., Jia, C. Z., & Meng, W. G. (2008). Dolomitization characteristics of carbonate rock in Xisha Islands and its formation: A case study of Well Xichen-1. Journal of Jilin University (Earth Science Edition), 38(2), 217-224.	
9	Bonaire Seroe Domi Formation	Deffeyes, K. S., Lucia, F. J., & Weyl, P. K. (1965). Dolomitizanon of Recent and Plio-Pleistocene sediments by marine evaporite waters on Bonaire Netherlands Antilles.In: Pray, L.C., Murray, R.C. (Eds.), Dolomitization and Limestone Diagenesis. SEPM Special Publication 13, pp. 71-88. Bandoian, C. A., & Murray, R. C. (1974). Pliocene-pleistocene carbonate rocks of Bonaire, Netherlands Antilles. Geological Society of America Bulletin, 85(8), 1243-1252. Sibley, D. F. (1980). Climatic control of dolomitization, Seroe Domi Formation (Pliocene), Bonaire, NA. in D.H Zenfger, J.B Dunham, R.L Ethington (Eds.), Concepts and Models of Dolomitization, Spec. Publ.-SEPM, vol. 28 (1980), pp. 247-258. Sibley, D. F. (1982). The origin of common dolomite fabrics; clues from the Pliocene. Journal of Sedimentary Research, 52(4), 1087-1110. Lucia, F. J., & Major, R. P. (1994). Porosity evolution through hypersaline reflux dolomitization. Dolomites: A volume in honour of Dolomieu, 325-341.	
10	Curacao Seroe Domi Formation	Fouke, B. W. (1994). Deposition, diagenesis and dolomitization of Neogene Seroe Domi Formation coral reef limestones on Curaçao, Netherlands Antilles (No. 134). Publications Foundation for scientific research in the Caribbean region.	
11	Great Bahama Bank	Beach, D. K. (1993). Submarine cementation of subsurface Pliocene carbonates from the interior of Great Bahama Bank. Journal of Sedimentary Research, 63(6), 1059-1069. Beach, D. K. (1995). Controls and effects of subaerial exposure on cementation and development of secondary porosity in the subsurface of Great Bahama Bank. In: Budd, D.A., Saller, A.H., Harris, P.M. (Eds.), Unconformities and Porosity in Carbonate Strata. American Association of Petroleum Geologists Memoir 63, pp. 1-33. Swart, P. K., & Melim, L. A. (2000). The origin of dolomites in Tertiary sediments from the margin of Great Bahama Bank. Journal of Sedimentary Research, 70(3), 738-748. Melim, L. A., Westphal, H., Swart, P. K., Eberli, G. P., & Munnecke, A. (2002). Questioning carbonate diagenetic paradigms: evidence from the Neogene of the Bahamas. Marine Geology, 185(1-2), 27-53.	
12	Cayman Brac Brac Formation		

		Zhao, H., & Jones, B. (2012). Genesis of fabric-destructive dolostones: a case study of the Brac Formation (Oligocene), Cayman Brac, British West Indies. Sedimentary Geology, 267, 36-54.	
13	Cayman Islands Pedro Castle Formation	MacNeil, A., & Jones, B. (2003). Dolomitization of the Pedro Castle Formation (Pliocene), Cayman Brac, British West Indies. Sedimentary Geology, 162(3-4), 219-238. Jones, B., & Luth, R. W. (2002). Dolostones from Grand Cayman, British West Indies. Journal of Sedimentary Research, 72(4), 559-569.	
14	Niue	Rodgers, K. A., Easton, A. J., & Downes, C. J. (1982). The chemistry of carbonate rocks of Niue Island, South Pacific. The Journal of Geology, 90(6), 645-662. Aharon, P., Socki, R. A., & Chan, L. (1987). Dolomitization of atolls by sea water convection flow: test of a hypothesis at Niue, South Pacific. The Journal of Geology, 95(2), 187-203.	
15	Niue Upper Dolomite	Wheeler, C. W., Aharon, P., & Ferrell, R. E. (1999). Successions of late Cenozoic platform dolomites distinguished by texture, geochemistry, and crystal chemistry; Niue, South Pacific. Journal of Sedimentary Research, 69(1), 239-255.	
16	Jamaica Hope Gate Formation	Land, L. S. (1973). Holocene meteoric dolomitization of Pleistocene limestones, North Jamaica. Sedimentology, 20(3), 411-424. LAND, L. S. (1991). Dolomitization of the Hope Gate Formation (north Jamaica) by seawater: reassessment of mixing-zone dolomite. In: Taylor, H.P., O'Neil, J.R., Kaplan, I.R. (Eds.), Stable Isotope Geochemistry: A Tribute to Samuel Epstein. Geochemical Society Special Publication 3, pp. 121-130.	
17	Yucatan	Ward, W. C., & Halley, R. B. (1985). Dolomitization in a mixing zone of near-seawater composition, late Pleistocene, northeastern Yucatan Peninsula. Journal of Sedimentary Research, 55(3), 407-420.	
18	Enewetak	Berner, R. A. (1965). Dolomitization of the mid-Pacific atolls. Science, 147(3663), 1297-1299. Schlanger, S. O., Graf, D. L., & Goldsmith, J. R. (1963). Subsurface geology of Eniwetok atoll. US Government Printing Office. Saller, A. H. (1984). Petrologic and geochemical constraints on the origin of subsurface dolomite, Enewetak Atoll: an example of dolomitization by normal seawater. Geology, 12(4), 217-220.	
19	Midway	Ladd, H. S., Tracey, J. I., & Gross, M. G. (1970). Deep drilling on Midway atoll (No. 680). US Government Printing Office.	
20	Niue Lower Dolomite	Wheeler, C. W., Aharon, P., & Ferrell, R. E. (1999). Successions of late Cenozoic platform dolomites distinguished by texture, geochemistry, and crystal chemistry; Niue, South Pacific. Journal of Sedimentary Research, 69(1), 239-255.	
21	Aitutaki	Hein, J. R., Gray, S. C., Richmond, B. M., & White, L. D. (1992). Dolomitization of quaternary reef limestone, Aitutaki, Cook Islands. Sedimentology, 39(4), 645-661.	

22	Barbados	Humphrey, J. D. (1988). Late Pleistocene mixing zone dolomitization, southeastern Barbados, West Indies. Sedimentology, 35(2), 327-348. Humphrey, J. D. (2000). New geochemical support for mixing-zone dolomitization at Golden Grove, Barbados. Journal of Sedimentary Research, 70(5), 1160-1170. Humphrey, J. D., & Radjef, E. M. (1991). Dolomite stoichiometric variability resulting from changing aquifer conditions, Barbados, West Indies. Sedimentary geology, 71(3-4), 129-136. Machel, H. G., & Burton, E. A. (1994). Golden Grove dolomite, Barbados; origin from modified seawater. Journal of Sedimentary Research, 64(4a), 741-751.	
23	St. Croix	Gill, I. P., Moore, C. H., & Aharon, P. (1995). Evaporitic mixed-water dolomitization on St. Croix, USVI. Journal of Sedimentary research, 65(4a), 591-604.	
24	Puerto Rico	González, L. A., & Ruiz, H. M. (1991). Diagenesis of middle tertiary carbonates in the Toa Baja well, Puerto Rico. Geophysical Research Letters, 18(3), 513-516.	
1	Woodlark Island	Lindley, I. D. (2021). Cenozoic volcanism, tectonics and mineralisation of Woodlark Island (Muyuw), eastern Papua. Australian Journal of Earth Sciences, 68(5), 609-627.	NOT DOLOMITISED
2	Maldives	Betzler, C., Fürstenau, J., Lüdmann, T., Hübscher, C., Lindhorst, S., Paul, A., ... & Droxler, A. W. (2013). Sea-level and ocean-current control on carbonate-platform growth, M aldives, I ndian O cean. Basin Research, 25(2), 172-196.	
3	La Désirade island (Guadeloupe archipelago) Lesser Antilles forearc	CORNÉE, J. J., LÉTICÉE, J. L., Muench, P., Quillevere, F., LEBRUN, J. F., Moissette, P., ... & Randrianasolo, A. (2012). Sedimentology, palaeoenvironments and biostratigraphy of the Pliocene–Pleistocene carbonate platform of Grande-Terre (Guadeloupe, Lesser Antilles forearc). Sedimentology, 59(5), 1426-1451. Münch, P., Cornee, J. J., Lebrun, J. F., Quillevere, F., Verati, C., Melinte-Dobrinescu, M., ... & Randrianasolo, A. (2014). Pliocene to Pleistocene vertical movements in the forearc of the Lesser Antilles subduction: insights from chronostratigraphy of shallow-water carbonate platforms (Guadeloupe archipelago). Journal of the Geological Society, 171(3), 329-341. Münch, P., Lebrun, J. F., Cornée, J. J., Thinon, I., Guennoc, P., Marcaillou, B. J., ... & Randrianasolo, A. (2013). Pliocene to Pleistocene carbonate systems of the Guadeloupe archipelago, French Lesser Antilles: a land and sea study (the KaShallow project). Bulletin de la Société géologique de France, 184(1-2), 99-110.	
4	Padthaway Ridge Archipelago (South Australia)	Riordan, N. K., James, N. P., & Bone, Y. (2012). Oligo–Miocene seagrass-influenced carbonate sedimentation along a temperate marine palaeoarchipelago, Padthaway Ridge, South Australia. Sedimentology, 59(2), 393-418.	
5	Chatham Islands	Campbell, H. J., Andrews, P. B., Beu, A. G., Edwards, A. R., Hornibrook, N. D., Laird, M. G., ... & Watters, W. A. (1988). Cretaceous-Cenozoic lithostratigraphy of the Chatham Islands. Journal of the Royal Society of New Zealand, 18(3), 285-308.	

6	Mallorca Baleraic Islands	Mas, G., & Fornós, J. J. (2006). Aportacions al coneixement del Neogen postorogènic de la cubeta sedimentària de Campos (Mallorca, Illes Balears, Mediterrània occidental). Bolletí de la Societat d'Història Natural de les Balears, 2006, vol. 49, p. 67-81.	

Table B2: Cretaceous Island Dolostone Database

	Rock Unit & Island	References	
1	MIT Guyot	Shipboard Scientific Party, 1993. Site 878. In: Premoli Silva, I., Haggerty, J., Rack, F., et al., Proceedings of the Ocean Drilling Program, Initial Reports 144, Ocean Drilling Program, College Station, TX, pp. 331-412. Haggerty, J. A., & Van Waasbergen, R. J. (1995). Geochemistry of MIT and Takuyo-Daisan carbonate platforms compared with other northwest Pacific guyots drilled during Leg 144: implications for their diagenetic history. In Proceedings of the Ocean Drilling Program. Scientific results (Vol. 144, pp. 841-871).	NOT DOLOMITISED
2	Wodejebato Guyot	Shipboard Scientific Party, 1993. Site 873. In: Premoli Silva, I., Haggerty, J., Rack, F., et al., Proceedings of the Ocean Drilling Program, Initial Reports 144, Ocean Drilling Program, College Station, TX, pp. 145-207. Shipboard Scientific Party, 1993. Site 874. In: Premoli Silva, I., Haggerty, J., Rack, F., et al., Proceedings of the Ocean Drilling Program, Initial Reports 144, Ocean Drilling Program, College Station, TX, pp. 209-253. Enos, P., Camoin, G. F., Wilson, P. A., Opdyke, B. N., Lincoln, J. M., & Wyatt, J. L. (1995). Diagenesis of platform carbonates, Wodejebato Guyot, Marshall Islands. In Proceedings of the Ocean Drilling Program. Scientific results (Vol. 144, pp. 789-817).	
3	Takuyo-Daisan Guyot	Haggerty, J. A., & Van Waasbergen, R. J. (1995). Geochemistry of MIT and Takuyo-Daisan carbonate platforms compared with other northwest Pacific guyots drilled during Leg 144: implications for their diagenetic history. In Proceedings of the Ocean Drilling Program. Scientific results (Vol. 144, pp. 841-871). Shipboard Scientific Party, 1993. Site 879. In: Premoli Silva, I., Haggerty, J., Rack, F., et al., Proceedings of the Ocean Drilling Program, Initial Reports 144, Ocean Drilling Program, College Station, TX, pp. 413-441.	
4	Mt. Carmel	Bialik, O. M., Samankassou, E., Meilijson, A., Waldmann, N. D., Steinberg, J., Karcz, K., & Makovsky, Y. (2021). Short-lived early Cenomanian volcanic atolls of Mt. Carmel, northern Israel. Sedimentary Geology, 411, 105805.	
5	Ita Mai Tai Guyot	Mel'nikov, M., Pletnev, S., Sedysheva, T., Punina, T., & Khudik, V. (2012). New data on the structure of the sedimentary section on the Ita Mai Tai Guyot (Magellan Seamounts, Pacific Ocean). Russian Journal of Pacific Geology, 6(3). Zhao, B., Yang, Y., Zhang, X., He, G., Lü, W., Liu, Y., ... & Huang, N. (2020). Sedimentary characteristics based on sub-bottom profiling and the implications for mineralization of cobalt-rich ferromanganese crusts at Weijia Guyot, western	

		Pacific Ocean. Deep Sea Research Part I: Oceanographic Research Papers, 158, 103223.	
6	Eratosthenes Seamount	Sakamoto, T., Janecek, T., & Emeis, K. C. (1998). Continuous sedimentary sequences from the eastern Mediterranean Sea: composite depth sections. In Proceedings of the Ocean Drilling Program. Scientific results (Vol. 160, pp. 37-59). Gao, H., Tong, X., Wen, Z., & Wang, Z. (2019). The tectonic evolution of the eastern Mediterranean basin and its control on hydrocarbon distribution. Journal of Petroleum Science and Engineering, 178, 389-407. Papadimitriou, N., Gorini, C., Nader, F. H., Deschamps, R., Symeou, V., & Lecomte, J. C. (2018). Tectono-stratigraphic evolution of the western margin of the Levant Basin (offshore Cyprus). Marine and Petroleum Geology, 91, 683-705.	
7	Japanees Islands Northwest Pacific (Japan and Sakhalin Island)	Ohga, H., Kolodziej, B., Nose, M., Schmid, D. U., Takayanagi, H., & Iryu, Y. (2013). Sedimentary facies and biofacies of the Torinosu Limestone in the Torinosu area, K ochi Prefecture, Japan. Island Arc, 22(2), 150-169. Sakai, S., Hirano, N., Dilek, Y., Machida, S., Yasukawa, K., & Kato, Y. (2021). Tokoro Belt (NE Hokkaido): an exhumed, Jurassic–Early Cretaceous seamount in the Late Cretaceous accretionary prism of northern Japan. Geological Magazine, 158(1), 72-83. Sano, S. I. (1995). Litho-and biofacies of Early Cretaceous rudist-bearing carbonate sediments in northeastern Japan. Sedimentary Geology, 99(3-4), 179-189. Iba, Y., & Sano, S. I. (2007). Mid-Cretaceous step-wise demise of the carbonate platform biota in the Northwest Pacific and establishment of the North Pacific biotic province. Palaeogeography, Palaeoclimatology, Palaeoecology, 245(3-4), 462-482.	
8	Cebu Island, Philippines	Rodrigo, J., & Schlagintweit, F. (2022). The Lower Cretaceous Tuburan Limestone of Cebu Island, Philippines: Microfacies, micropalaeontology, biostratigraphy, and palaeogeographic perspectives. Carnets Geol., 22(14), 661-679.	
9	Horizon Guyot	Shipboard Scientific Party, 1973. Site 171. In Winterer, E.L., Ewing, J.I., et al., Init. Repts. DSDP, 17: Washington (U.S. Govt. Printing Office), 283-334.	
10	Hispaniola Island (Dominican Republic and Haiti)	Gorosabel-Araus, J. M., Granja-Bruña, J. L., Gallego-Mingo, A., de la Peña, L. G., Rodríguez-Zurrunero, A., Mas, R., ... & Navarro-Comet, J. (2021). New constraints on the tectonosedimentary evolution of the offshore San Pedro Basin (southeastern Dominican Republic): implications for its hydrocarbon potential. Nelson, C., Polanco, J., Macassi, A., Dominguez, H., Proenza, J. A., Torró, L., ... & Iturralde-Vinent, M. (2020). The Hatillo Limestone, Pueblo Viejo district, Dominican Republic: Marginal reef or impermeable cap?. Wessels, R. J., Ellouz-Zimmermann, N., Bellahsen, N., Hamon, Y., Rosenberg, C., Deschamps, R., ... & Leroy, S. (2019). Polyphase tectonic history of the Southern Peninsula, Haiti: from folding-and-thrusting to transpressive strike-slip. Tectonophysics, 751, 125-149. Boletín de la Sociedad Geológica Mexicana, 72(3). Bonilla-Rodríguez, A. J., González, L. A., Walker, J. D., & Santos, H. (2014). Strontium isotope (87Sr/86Sr) stratigraphy	

		from the Coalcomana–Caprinuloidea rudist assemblage in the Greater Antilles (Puerto Rico, Dominican Republic and Jamaica). Cretaceous Research, 50, 97-109. MYCZYN, R., & ITURRALDE-VINENT, M. A. N. U. E. L. (2005). The Late Lower Albian Invertebrate Fauna of the Río Hatillo Formation of Pueblo Viejo, Dominican Republic. Caribbean Journal of Science, 41(4), 782-796.	
11	Qeshm Island (Southern Iran)	Mansouri-Daneshvar, P., Moussavi-Harami, R., Mahboubi, A., Gharaie, M. H. M., & Feizie, A. (2015). Sequence stratigraphy of the petroliferous Dariyan Formation (Aptian) in Qeshm Island and offshore (southern Iran). Petroleum Science, 12, 232-251. Piryaei, A., Reijmer, J. J. G., Borgomano, J., & Van Buchem, F. S. P. (2011). Late Cretaceous tectonic and sedimentary evolution of the Bandar Abbas area, Fars region, southern Iran. Journal of Petroleum Geology, 34(2), 157.	
12	Bonaire Island	Teoh, C. P., & Laya, J. C. (2021). Preferential dolomitization in Mio–Pliocene bioclastic clinoforms, Bonaire Island, South Caribbean: insights from petrographic and geochemical analyses. Facies, 67(4), 30. Laya, J. C., Teoh, C. P., Whitaker, F., Manche, C., Kaczmarek, S., Tucker, M., ... & Hasiuk, F. (2021). Dolomitization of a Miocene-Pliocene progradational carbonate platform by mesohaline brines: Re-examination of the reflux model on Bonaire Island. Marine and Petroleum Geology, 126, 104895.	
13	PUERTO RICO Puerto Rico and the U.S. Virgin Islands & St Croxi, St John & St thomas	Jolly, W. T. (1998). Volcanism, tectonics, and stratigraphic correlations in Puerto Rico. Tectonics and geochemistry of the Northeast Caribbean. Renken, R. A., Ward, W. C., Gill, I. P., Gómez-Gómez, F., & Rodríguez-Martínez, J. (2002). Geology and hydrogeology of the Caribbean islands aquifer system of the commonwealth of Puerto Rico and the US Virgin Islands (No. 1419). US Geological Survey. Lidz, B. H. (1988). Upper Cretaceous (Campanian) and Cenozoic stratigraphic sequence, northeast Caribbean (St. Croix, US Virgin Islands). Geological Society of America Bulletin, 100(2), 282-298.	
1	Resolution Guyot	Sager, W. W., Winterer, E. L., Firth, J. V., Arnaud, H., Baker, P. A., Baudin, F., Bralower, T. J., Castillo, P., Cooper, P., Flood, P. G., Golovchenko, X., Iryu, Y., Ivanov, M., Jenkyns, H. C., Kenter, J. A. M., Murdmaa, I., Mutterlose, J., Nogi, Y., Paull, C. K., ... van Waasbergen, R. (1993) Site 866. In Proceedings of the Ocean Drilling Program, Initial Reports (Vol. 143, pp. 181– 271). Winterer, E. L., & Sager, W. W. (1995). Synthesis of drilling results from the mid- pacific mountains: Regional context and implications. In Proceedings of the Ocean Drilling Program, Scientific Results (Vol. 143, pp. 497– 535). Flood, P. G., Fagerstrom, J. A., & Rougerie, F. (1996). Interpretation of the origin of massive replacive dolomite within atolls and submerged carbonate platforms: strontium isotopic signature ODP Hole 866A, Resolution Guyot, Mid-Pacific Mountains. Sedimentary Geology, 101(1-2), 9-13. Flood, P. G., & Chivas, A. R. (1995). Origin of massive dolomite, Leg 143, Hole 866A, Resolution Guyot, Mid- Pacific Mountains: Northwest Pacific atolls and guyots. In Proceedings of the Ocean Drilling Program. Scientific results (Vol. 143, pp. 161– 169).	MARINE DOLOMITISED &/OR SEASONALLY EVAPORATIVE PUMPING
2	Allison Guyot	Sager, W. W., Winterer, E. L., Firth, J. V., Arnaud, H., Baker, P. A., Baudin, F., Bralower, T. J., Castillo, P., Cooper, P., Flood, P. G., Golovchenko, X., Iryu, Y., Ivanov, M., Jenkyns, H. C., Kenter, J. A. M., Murdmaa, I., Mutterlose, J.,	

		Nogi, Y., Paull, C. K., ... van Waasbergen, R. (1993) Site 867/868. In the Proceedings of the Ocean Drilling Program, Initial Reports (Vol. 143, pp. 273– 296). Winterer, E. L., & Sager, W. W. (1995). Synthesis of drilling results from the mid- pacific mountains: Regional context and implications. In Proceedings of the Ocean Drilling Program, Scientific Results (Vol. 143, pp. 497– 535).	
1	Malta Isolated Carbonate Platform	Gatt, P. (2022). Facies, depositional environments and drowning of Tethyan isolated carbonate platforms: the Paleogene carbonates of Malta. Facies, 68(3), 9. GATT, P. (2012). Carbonate facies, depositional sequences and tectonostratigraphy of the Palaeogene Malta Platform (Doctoral dissertation, Durham University).	SEEPAGE REFLUX DOLOMITISED
2	Adriatic platform	Read, J. F., Husinec, A., Cangialosi, M., Loehn, C. W., & Prtoljan, B. (2016). Climate controlled, fabric destructive, reflux dolomitization and stabilization via marine-and synorogenic mixed fluids: an example from a large Mesozoic, calcite-sea platform, Croatia. Palaeogeography, Palaeoclimatology, Palaeoecology, 449, 108-126.	
3	Apenninic Platform	Vinci, F., Iannace, A., Parente, M., Pirmez, C., Torrieri, S., & Giorgioni, M. (2017). Early dolomitization in the Lower Cretaceous shallow-water carbonates of Southern Apennines (Italy): Clues about palaeoclimatic fluctuations in western Tethys. Sedimentary geology, 362, 17-36.	
4	Apulian platform	Torrieri, S., Volery, C., Bazalgette, L., & Strauss, C. G. (2021). From outcrop to subsurface model—Large-scale fractured zones in Apulian platform carbonates (Maiella Mountains, Central Apennines, Italy). AAPG Bulletin, 105(12), 2449-2476. Heba, G., Prichonnet, G., & El, A. A. (2009). Meteoric diagenesis of Upper Cretaceous and Paleocene-Eocene shallow-water carbonates in the Kruja Platform (Albania): geochemical evidence. Geologica carpathica, 60(2), 165.	
1	Cuba	Hempton, M. R., & Barros, J. A. (1993). Mesozoic stratigraphy of Cuba: Depositional architecture of a southeast facing continental margin.	DOLOMITISED (UNKNOWN DOLOMITISIATION MECHANISM)
2	Jamaica	Mitchell, S. F. (2021). Cretaceous geology and tectonic assembly of Jamaica.Rodrigues, K. (1991). Organic geochemistry and petroleum potential of Jamaica. Journal of Petroleum Geology, 14(2), 309-322.	
3	island of Ibiza	de Neira, J. A. D., & Gil-Gil, J. (2013). Ascription of the island of Ibiza to the Prebetic of Alicante (Betic Range, Spain) after correlation of Lower Cretaceous sedimentary successions. Cretaceous Research, 41, 194-209.	

Table B3: Logging Data at Site 866

Logging data (RHOB, gm/cm3; DTLN, us/ft; DTLF, us/ft; NPHI, %; PEF, b/e) can be accessed from the Division of Marine and Large Programs (Lamon-Doherty Earth Observatory, Columbia University). https://mlp.ldeo.columbia.edu/logdb/scientific_ocean_drilling/

Table B4: Dolomite Isotope Data at Site 866

Sample #	depth	$\delta^{18}O_{dol}$	$\delta^{13}C_{dol}$	Mean $^{87}Sr/^{86}Sr$	Max $^{87}Sr/^{86}Sr$	Mini $^{87}Sr/^{86}Sr$
130R-2,17-19 cm	1224	0.7	2.4	0.707394	0.707409	0.707379
148R-1,44-^6	1396	-0.4	2.1	0.707363	0.707379	0.707347
159R-3, 82-84	1505	-0.6	2.4	0.707337	0.707347	0.707327
160R-1,70-73	1512	-0.7	2.2	0.707397	0.707407	0.707387
162R-2,139-141	1534	-0.6	2.5	0.707288	0.707303	0.707273
162R-3,0-3	1535	-1.1	2.3	0.70731	0.707326	0.707294
163R-1,16-17	1540	-1	2.1	0.70735	0.707366	0.707334
164R-1,94-96	1554	-1	2.8	0.707383	0.707395	0.707371
166R-2,109-122	1572	-1.6	2.4	0.707323	0.707339	0.707307

Table B5: Elemental Composition at Site 866, 867, & 868

Sample (Core, Section, Interval)	Depth	Fe (ppm)	Mn (ppm)
125R-1,42-^7	1175	122	6
139R-1, 32-34	1310	132	5
144R-3,50-52	1361	121	6
146R-1,111-113	1377	579	25
148R-3,12-14	1398	2051	49
154R-2,112-113	1456	92	6
159R-1, 87-89	1502	70	15
162R-3,0-3	1534	110	11
163R-1,75-78	1541	3,172	44
164R-2, 104-107	1554	268	7
168R-3, 78-79	1594	2055	2
170R-2,52-53	1611	1536	27

SITES	Sample (Core, Section, Interval)	Depth	Fe (ppm)	Mn (ppm)
SITE 868	3R-2, 34-36	12.76	40	2
SITE 867	2R-2, 28-30	9.88	207	12
	7R-1, 37-39	43.57	60	9
	8R-2, 44-^6	54.44	122	4
SITE 866	8R-CC, 3-5	57.33	104	8
	46R-1, 108-110	416.38	29	1
	88R-1,22-25	821.12	143	18
	103R-1,60-62	963	13	11
	105R-1, 82-84	982.12	9	11
	146R-2, 33-35	1378.23	24	24
	159R-1, 87-89	1501.77	61	10
	168R-3, 78-79	1593.82	388	28
	163R-1,75-78	1541.05	163	9

SITES	Sample (Core, Section, Interval)	Depth	Sr (ppm)	Type of Samples
SITE 866	133R-1, 129-121	1252.79	135	Dolomite Samples
	134R-2, 26-28	1262.96	125	
	159R-1, 87-89	1501.77	132	
	168R-3, 78-79	1593.82	239	
	163R-1,75-78	1541.05	151	
	162R-01,0-3	1531	106	
SITE 867	2R-2, 28-30	9.88	260	Limestone Samples
SITE 868	3R-2, 34-36	12.76	262	
SITE 867	7R-1, 37-39	43.57	188	
	8R-2, 44-^6	54.44	72	
SITE 866	8R-CC, 3-5	57.33	263	
	46R-1, 108-110	416.38	72	

	88R-1,22-25	821.12	129	
	103R-1,60-62	963	56	
	105R-1, 82-84	982.12	77	
	146R-2, 33-35	1378.23	58	
	159R-1, 87-89	1501.77	286	
	168R-3, 78-79	1593.82	368	
	163R-1,75-78	1541.05	348	

Table B6: XRF major, minor, and trace elements at Site 866

Samples	Depth	SiO_2%	TiO_2%	Al_2O_3%	Fe_2O_3%	Cr ppm	MgO%
6R-CC, 2-3	38.42	0.78	0.013	0.27	0.17	1	0.64
8R-CC, 3-5	57.33	0.46	0.006	0.15	0.06	12	0.54
10R-CC4-5	76.94	0.68	0.007	0.17	0.06	11	0.51
19R-CC, 3 ^	164.83	0.34	0.01	0.16	0.06	1	0.5
25R-1,53-55	223.23	0.22	0.005	0.08	0.04	1	0.58
31R-1, 56-58	281.16	0.18	0.008	0.11	0.06	1	0.54
35R-1,33-35	319.23	0.11	0.005	0.08	0.04	1	0.5
35R-1, 33-35	319.23	0.39	0.012	0.2	0.06	7	0.44
36R-1,21-23	328.71	0.21	0.007	0.12	0.05	8	0.57
40R-CC, 36-38	357.66	0.26	0.01	0.16	0.05	1	0.52
39R-1,35-36	348.05	0.15	0.007	0.1	0.05	1	0.49
46R-2, 46-48	417.26	0.42	0.027	0.34	0.07	13	0.45
48R-1,30-32	434.7	0.19	0.009	0.13	0.2	12	0.54
52R-CC, 18-19	473.18	0.38	0.014	0.2	0.1	1	0.71
55R-CC, 30-31	502.2	0.18	0.008	0.12	0.09	1	0.52
58R-1,72-75	531.72	0.12	0.006	0.08	0.05	1	0.56
61R-1, 103-10	560.93	0.24	0.009	0.13	0.07	1	0.66
62R-2, 21-23	571.31	0.41	0.018	0.19	0.12	8	0.73
64R-1,69-71	589.69	0.28	0.01	0.15	0.08	1	0.71
65R-1,57-60	599.17	0.16	0.008	0.1	0.06	11	0.69
70R-1, 1-3	646.91	2.84	0.149	0.97	0.79	27	0.8
71R-1, 64-67	657.14	0.38	0.012	0.16	0.13	8	0.67
71R-2,71-72	658.49	37.59	0.971	14.28	8.12	151	3.45
74R-2, 94-97	687.72	0.05	0.005	0.06	0.04	1	0.64
75R-3, 67-69	698.21	0.05	0.006	0.06	0.05	1	0.72
76R-2, 26-29	706.46	2.1	0.069	1.06	0.29	15	0.95
77R-1,59-60	715.09	0.05	0.005	0.02	0.05	1	0.59

78R-2, 85-87	726.34	0.05	0.005	0.06	0.04	1	0.69
79R-2, 104-10	736.34	0.05	0.004	0.06	0.04	1	0.63
80R-1,32-34	743.82	0.05	0.005	0.05	0.04	1	0.64
82R-2,45^18	764.63	0.05	0.005	0.06	0.04	1	0.6
85R-2, 140-14	794.65	0.05	0.005	0.06	0.04	1	0.74
86R-2, 72-74	803.72	0.22	0.008	0.12	0.07	1	0.72
89R-1,39-40	830.99	0.59	0.013	0.25	0.13	1	0.84
91R-1, 50-51	850	0.8	0.023	0.34	0.18	1	0.95
95R-1,21-24	888.21	0.05	0.004	0.05	0.03	1	0.71
97R-1, 16-18	907.56	0.21	0.009	0.11	0.09	1	0.99
98R-1, 108-110	918.08	5.7	0.226	2.08	1.18	12	1.17
100R-1,31-33	933.71	1.89	0.045	0.71	0.31	1	1.05
105R-1,82-84	982.12	0.14	0.008	0.09	0.05	1	0.83
103 R-1,60-62	963	0.22	0.009	0.13	0.07	1	0.79
108R-1,55-57	1010.8	0.05	0.006	0.07	0.05	1	0.8
111R-1, 49-50	1039.8	0.57	0.015	0.24	0.11	1	1.01
115R-1,22-26	1078.1	68.95	0.007	0.05	0.05	1	0.27
117R-1,44-47	1097.5	0.32	0.011	0.12	0.07	1	1.11
118R-1, 144-146	1108.2	2.59	0.058	0.93	0.47	1	1.22
121R-1, 56-58	1136.3	1.42	0.022	0.5	0.36	14	13.19
123R-1,55-57	1155.7	0.16	0.006	0.07	0.05	1	8.61
126R-2, 32-33	1185.6	0.05	0.005	0.06	0.05	1	0.9
129R-1,77-78	1213.7	2.03	0.127	0.76	0.67	10	10.8
131R-1, 12-14	1232.3	1.6	0.067	0.55	0.34	7	15.23
132R-1,40-41	1242.3	2.08	0.069	0.78	0.41	1	17.41
133R-2, 108-1	1254.2	0.05	0.006	0.02	0.04	1	18.14
137R-2,43^15	1291.6	0.05	0.006	0.02	0.04	1	17.27
139R-1,45-47	1309.7	0.05	0.005	0.06	0.04	1	1.08
141R-CC, 18-19	1328.8	0.05	0.006	0.02	0.04	1	16.77
143R-1,70-72	1348.6	0.05	0.004	0.02	0.04	1	1.7
145R-1, 82-84	1367.6	3.64	0.013	0.08	0.08	1	17.51
147R-1, 1-3	1386.1	0.35	0.015	0.16	0.12	8	1.42
147R-1, 21-22	1386.3	0.65	0.036	0.26	0.29	8	1.49
147R-1,41-43	1386.5	0.41	0.025	0.16	0.14	1	1.04
147R-1,49-52	1386.6	0.17	0.008	0.09	0.07	8	1.63
147R-1,59-64	1386.7	0.29	0.019	0.13	0.1	1	1.77
147R-1,75-78	1386.9	0.31	0.02	0.15	0.11	1	1.54
147R-1, 88-91	1387	2.55	0.087	0.98	0.53	1	2.54
147R-1,95-98	1387.1	0.28	0.014	0.13	0.09	1	0.88
148R-4, 35-37	1399.7	3.04	0.143	1.21	0.59	8	0.83
150R-1, 9-11	1415.2	0.05	0.006	0.06	0.05	1	5.11

152R-2, 93-95	1436.9	0.16	0.012	0.09	0.07	1	0.92
155R-3, 9-11	1466.4	0.05	0.007	0.05	0.04	10	0.95
157R-2, 52-54	1484.8	0.15	0.016	0.08	0.06	1	0.98
159R-2, 65-67	1503.1	0.05	0.008	0.07	0.05	1	1.72
159R-1, 87-89	1501.8	0.05	0.009	0.02	0.05	1	13.79
162R-2, 74-78	1533.2	0.17	0.012	0.08	0.09	1	18.1
164R-2, 140-42	1552.6	1.16	0.041	0.23	0.21	14	8.21
166R-1,50-54	1569.8	0.18	0.011	0.09	0.06	1	5.83
168R-1, 108-10	1591.2	0.11	0.014	0.07	0.07	1	13.7

Table B7: Time-Depth Relationship at Site 866 (Resolution Guyot)

Please refer to *APPENDIX A*, Table A2.

Table B8: Summary of Index Properties at Site 866

Summary of index properties for rock specimens from Site 866 (Kenter and Ivanov, 1995) and our calculations of the dolomite%.

Depth (mbsf)	Grain density (g/cm³)	Dolomite (%)
348.15	2.71	0.00
434.88	2.71	0.00
531.69	2.6	0.00
571.16	2.71	0.00
685.76	2.71	0.00
698.59	2.77	0.00
708.09	2.73	0.00
716.9	2.7	0.00
738.15	2.72	1.35
764.83	2.72	1.35
793.81	2.71	0.00
849.57	2.71	0.00
868.95	2.73	0.00
953.49	2.71	0.00
1021.51	2.72	1.35
1030.14	2.73	8.11
1069.02	2.74	14.86
1078.67	2.74	14.86
1088	2.73	8.11
1136.03	2.79	48.65
1165.22	2.76	28.38
1184.55	2.73	8.11
1204.75	2.86	95.95

1213.15	2.85	89.19
1224.33	2.75	21.62
1253.66	2.83	75.68
1263.39	2.84	82.43
1272.05	2.84	82.43
1292.1	2.84	82.43
1339.1	2.865	99.32
1359.55	2.71	0.00
1368.13	2.79	48.65
1377.2	2.72	1.35
1388.52	2.72	1.35
1396.27	2.86	95.95
1401.17	2.76	28.38
1454.47	2.73	8.11
1464.45	2.76	28.38
1475.28	2.72	1.35
1501.9	2.77	35.14
1532.53	2.83	75.68
1561.83	2.82	68.92
1574.67	2.77	35.14
1584.42	2.85	89.19
1591.41	2.81	62.16
1610.55	2.74	14.86

Summary of the dolomite occurrence and abundance in Site 866 based on the core descriptions and integrating the core images (0: Not dolomitised, 1: patchy dolomitised, 2: partially dolomitised, 3: intensively dolomitised).

Depth (mbsf)	Dolomite abundance
0	0
10.2	0
38.4	0
47.8	0
57.3	0
67.2	0
76.9	0
86.5	0
96.1	0
105.8	0
115.4	0
125	0
134.7	0
144.4	0
155.1	0
164.8	0

174.5	0
184.2	0
193.8	0
203.4	0
213.1	0
222.7	0
232.4	0
242	0
251.6	0
261.3	0
271	0
280.6	0
289.9	0
299.5	0
309.2	0
318.9	0
328.5	0
338	0
342.7	0
347.7	0
357.3	0
367	0
376.6	0
386.3	0
395.9	0
405.6	0
415.3	0
424.7	0
434.4	0
444	0
453.7	0
463.4	0
473	0
482.7	0
492.3	0
501.9	0
511.6	0
521.3	0
531	0
540.7	0
550.3	0
559.9	0
569.6	0
579.3	0

589	0
598.6	0
608.3	0
618	0
627.7	0
637.2	0
646.9	0
656.5	0
666.2	0
675.8	0
685.5	0
695.1	0
704.7	0
714.5	0
724.1	0
733.8	0
743.5	0
753.1	0
762.8	0
772.5	0
782.2	0
791.8	0
801.5	0
811.2	0
820.9	0
830.6	0
839.9	0
849.5	0
859.2	0
868.7	0
878.4	0
888	0
897.7	0
907.4	0
917	0
923.9	0
933.4	0
943.1	0
952.7	0
962.4	0
971.7	0
981.3	0
990.9	0
1000.5	0

1010.2	0
1019.9	0
1029.6	0
1039.3	0
1048.9	0
1058.5	0
1068.2	0
1077.9	0
1087.5	0
1097.1	1
1106.8	1
1116.5	1
1126.1	1
1135.7	1
1145.4	1
1155.1	2
1164.8	1
1174.4	1
1184	0
1193.5	2
1203.2	3
1212.9	2
1222.6	3
1232.2	3
1241.9	3
1251.6	3
1261.2	3
1270.9	3
1280.2	2
1289.8	3
1299.5	2
1309.2	1
1318.9	3
1328.6	3
1338.2	3
1347.9	1
1357.5	0
1366.8	2
1376.4	0
1386.1	2
1395.7	2
1405.4	0
1415.1	0
1424.8	0

1434.5	2
1444.1	2
1453.8	2
1463.5	1
1473.2	1
1482.8	1
1492.5	2
1500.9	3
1511.7	3
1521.3	3
1531	3
1540.3	3
1549.9	3
1559.6	3
1569.3	3
1580.4	3
1590.1	3
1599.8	2
1609.4	2
1619.1	2

Summary of Grain Density and Porosity of the sedimentary successions at Site 866 (Sager et al., 1993a). In addition, we show our calculations of the dolomite% using grain density as a proxy for mineralogy in Zenger (1968) equation.

Porosity %	Depth (mbsf)	Grain Density	Dol %
13.86	125.12	2.72	0
15.02	193.96	2.72	0
1.24	281.81	2.7	0
7.97	290.05	2.69	0
10.88	319.7	2.72	0
3.32	328.89	2.69	0
7.55	338.15	2.69	0
5.24	343.35	2.69	0
13.79	367.27	2.7	0
0.79	405.9	2.65	0
0.66	415.5	2.71	0
0.45	425.27	2.69	0
21.42	434.81	2.72	0
25.39	453.9	2.72	0
20.51	463.59	2.71	0
21.73	483.38	2.71	0
25.3	493.05	2.72	0
29	511.73	2.71	0

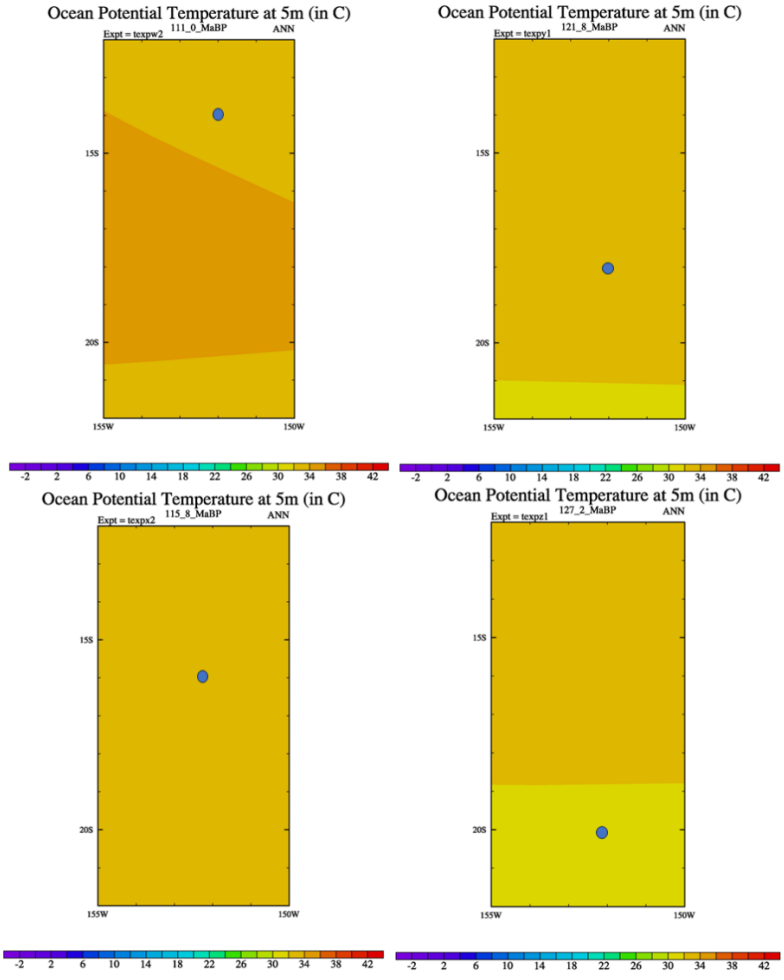
33.51	531.51	2.71	0
29.71	540.24	2.76	0
32.46	550.33	2.71	0
24.7	560.78	2.72	0
28.81	570.61	2.7	0
33.71	579.57	2.74	0
25.02	581.45	2.73	0
31.37	589.75	2.73	0
28.26	590.91	2.68	0
22.38	609.28	2.69	0
22.42	618.16	2.72	0
21.22	647.64	2.72	0
18.1	657.05	2.69	0
19.63	658.22	2.71	0
25.09	666.94	2.71	0
25.7	686.22	2.74	0
27.07	698.68	2.74	0
17.74	708.27	2.73	0
22.18	735.04	2.73	0
28.49	744.34	2.73	0
26.29	754.41	2.72	0
21.88	764.89	2.73	0
27.88	773.02	2.73	0
22.76	802.15	2.7	0
20.66	812.21	2.72	0
24.1	822.12	2.73	0
25.77	831.79	2.81	0
26.77	832.27	2.85	0
23.1	849.97	2.79	0
28.47	917.38	2.72	0
26.19	924.65	2.68	0
17.92	933.69	2.72	0
17.59	943.42	2.72	0
28.39	953.62	2.72	0
21.52	954.54	2.67	0
18.63	971.89	2.73	0
32.08	981.78	2.75	0
27.38	991.12	2.74	0
23.22	1010.33	2.73	13.51351351
10.87	1020.69	2.72	6.756756757
24.23	1021.84	2.71	0
14.69	1031.53	2.73	0
25.09	1049.26	2.73	0
26.25	1049.82	2.69	0

21.63	1069.19	2.69	0
19.73	1078.25	2.74	20.27027027
24.85	1088.18	2.72	6.756756757
22.37	1107.52	2.72	6.756756757
25.82	1116.94	2.74	20.27027027
17.66	1126.41	2.74	20.27027027
11.58	1135.79	2.77	40.54054054
23.31	1145.69	2.74	20.27027027
16.15	1155.28	2.81	67.56756757
16.8	1164.94	2.75	27.02702703
7.83	1176.45	2.71	0
4.92	1184.49	2.69	-13.51351351
11.87	1185.91	2.73	13.51351351
2.03	1204.25	2.78	47.2972973
19.99	1214.22	2.72	6.756756757
34.32	1222.65	2.75	27.02702703
12.7	1233.4	2.85	94.59459459
5.71	1242.74	2.79	54.05405405
6	1255.07	2.84	87.83783784
7.05	1263.34	2.84	87.83783784
13.08	1272	2.84	87.83783784
24.47	1280.22	2.74	20.27027027
8.03	1290.08	2.84	87.83783784
23.57	1300.46	2.71	0
23	1309.49	2.72	6.756756757
23.43	1339.37	2.78	47.2972973
23.59	1347.92	2.75	27.02702703
25.23	1348.72	2.8	60.81081081
13.18	1358.34	2.73	13.51351351
26.58	1366.93	2.74	20.27027027
3.08	1368.1	2.81	67.56756757
8.44	1377.64	2.77	40.54054054
5.63	1386.19	2.76	33.78378378
4.18	1396.22	2.71	0
6.1	1397.7	2.72	6.756756757
17.05	1401.13	2.73	13.51351351
21.56	1416.26	2.74	20.27027027
33.69	1434.76	2.75	27.02702703
29.33	1454.39	2.74	20.27027027
26.38	1455.7	2.71	0
22.54	1464.5	2.74	20.27027027
20.85	1474.55	2.75	27.02702703
20.25	1475.52	2.73	13.51351351
21.13	1503.41	2.74	20.27027027

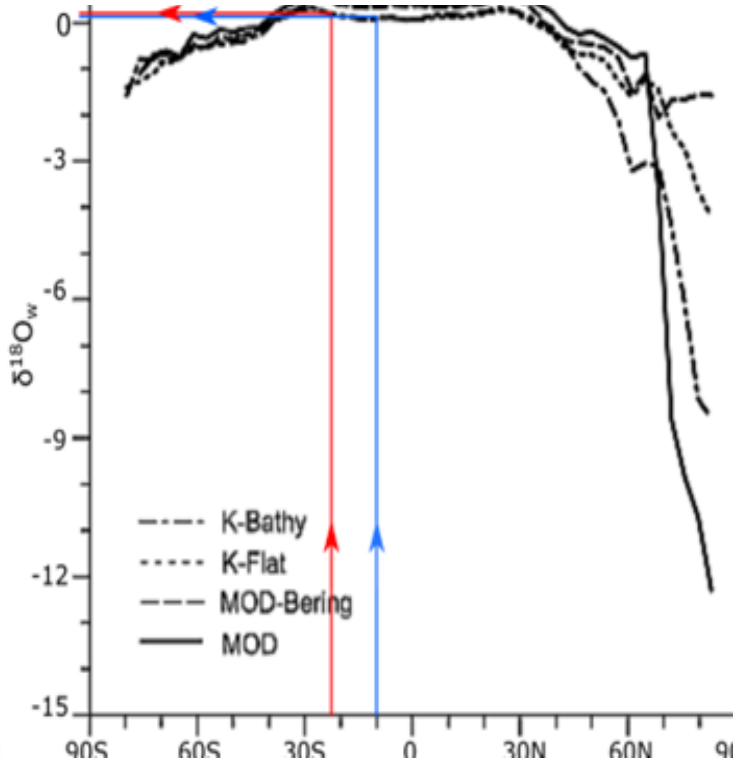
6.57	1503.97	2.84	87.83783784
6.95	1512.42	2.84	87.83783784
3.17	1532.03	2.82	74.32432432
4.38	1540.73	2.72	6.756756757
6.45	1552.93	2.83	81.08108108
5.86	1561.38	2.79	54.05405405
17.33	1570.11	2.75	27.02702703
9.11	1581.32	2.74	20.27027027
3.27	1584.22	2.84	87.83783784
6.83	1592.55	2.79	54.05405405
9.01	1592.47	2.8	60.81081081
15.21	1601.08	2.76	33.78378378
17.47	1602.19	2.73	13.51351351
19.4	1610.54	2.73	13.51351351

Table B9: Palaeoclimate Maps of Mid-Pacific Atolls During Dolomitisation

Location of Resolution Guyot highlighted by blue circle in the attached maps using Palaeogeographic reconstruction by Scotese and Wright (2018). Global maps of the palaeoclimatological condition were retrieved from Bridge website of Valdes et al. (2021).



The corresponding Mid-cretaceous seawater oxygen isotope (Zhou et al., 2008) at the latitudes of Resolution Guyot. The plot suggests value of Mid-cretaceous seawater oxygen isotope at these latitudes of ~0.2‰ VSMOW. The $\delta^{18}O_{sw}$ value of −1.0‰ VSMOW (Vienna Standard Mean Ocean Water) is commonly used in the literature to represent the average isotopic composition of seawater during the non-glacial Cretaceous period. However, I chose to use the data from Zhou et al. (2008), as it accounts for palaeolatitudinal variations in seawater isotopic composition, reflecting conditions similar to the modern surface ocean, where $\delta^{18}O_{sw}$ varies significantly (−0.5 to +1.25‰). Even if I had used $\delta^{18}O_{sw}$ of −1.0‰, the calculated dolomitisation temperatures (25–35°C) would still exceed the temperatures of the contemporaneous host rock by approximately 9–20°C. While this would alter the absolute temperature differences, it would not change the conclusion that dolomitisation occurred at higher temperatures than those of the host rock.



Material B1: Dolomitisation Age Determination Methodology

To calculate the "possible" ages of the dolomites, the $^{87}Sr/^{86}Sr$ data of the dolomites at Site 866 (Flood and Chivas, 1995) were compared with the lookup table of the global seawater strontium isotope stratigraphy of McArthur et al. (2012).

The table below (Table B1-1) shows two different ranges of the calculated ages. The age range of the dolomite is 125 ± 0.5 to 119.3 ± 1 Ma and/or 112.9 ± 0.35 to 109.5 ± 1.1 Ma which yields a possible duration for the dolomitisation process of 9 Myr. This is because the values of the strontium isotope of the dolomites cover two overlapping segments of the global strontium isotope stratigraphy of McArthur et al. (2012).

Graphical display of the possible ages of the dolomites is provided below (Figure B1-1).

Sample #	Depth (m)	$\delta^{18}O_{dol}$ (VPDB)	$\delta^{13}C_{dol}$ (VPDB)	Mean $^{87}Sr/^{86}Sr$	Age (Ma)	Max $^{87}Sr/^{86}Sr$	Age (Ma)	Mini $^{87}Sr/^{86}Sr$	Age (Ma)
130R-2,17-19 cm	1224	0.7	2.4	0.707394	125.0	0.707409	125.6	0.707379	124.6
148R-1,44-^6	1396	-0.4	2.1	0.707363	123.8	0.707379	124.6	0.707347	123.0
159R-3, 82-84	1505	-0.6	2.4	0.707337	122.5	0.707347	123.5	0.707327	121.9
160R-1,70-73	1512	-0.7	2.2	0.707397	125.2	0.707407	125.5	0.707387	124.8
162R-2,139-141	1534	-0.6	2.5	0.707288	119.3	0.707303	120.3	0.707273	118.3
162R-3,0-3	1535	-1.1	2.3	0.707310	120.6	0.707326	121.8	0.707294	119.5
163R-1,16-17	1540	-1	2.1	0.707350	123.5	0.707366	124.0	0.707334	122.3
164R-1,94-96	1554	-1	2.8	0.707383	124.6	0.707395	125.0	0.707371	124.1
166R-2,109-122	1572	-1.6	2.4	0.707323	121.6	0.707339	122.6	0.707307	120.5
Sample #	depth	$\delta^{18}O_{dol}$ (VPDB)	$\delta^{13}C_{dol}$ (VPDB)	Mean $^{87}Sr/^{86}Sr$	Age (Ma)	Max $^{87}Sr/^{86}Sr$	Age (Ma)	Mini $^{87}Sr/^{86}Sr$	Age (Ma)
130R-2,17-19 cm	1224	0.7	2.4	0.707394	109.5	0.707409	107.5	0.707379	110.3
148R-1,44-^6	1396	-0.4	2.1	0.707363	111.0	0.707379	110.3	0.707347	111.4
159R-3, 82-84	1505	-0.6	2.4	0.707337	111.7	0.707347	111.4	0.707327	112.0
160R-1,70-73	1512	-0.7	2.2	0.707397	109.3	0.707407	107.7	0.707387	110.0
162R-2,139-141	1534	-0.6	2.5	0.707288	112.9	0.707303	112.6	0.707273	113.3
162R-3,0-3	1535	-1.1	2.3	0.707310	112.7	0.707326	112	0.707294	112.8
163R-1,16-17	1540	-1	2.1	0.707350	111.3	0.707366	110.8	0.707334	111.8
164R-1,94-96	1554	-1	2.8	0.707383	110.2	0.707395	109.5	0.707371	110.6
166R-2,109-122	1572	-1.6	2.4	0.707323	112.1	0.707339	111.6	0.707307	112.5

Table B1-1. Geochemical data for dolomites at Site 866 including $^{87}Sr/^{86}Sr$, $\delta^{18}O_{dol}$, $\delta^{13}C_{dol}$ (data Flood and Chivas, 1995). The table shows the ages using $^{87}Sr/^{86}Sr$.

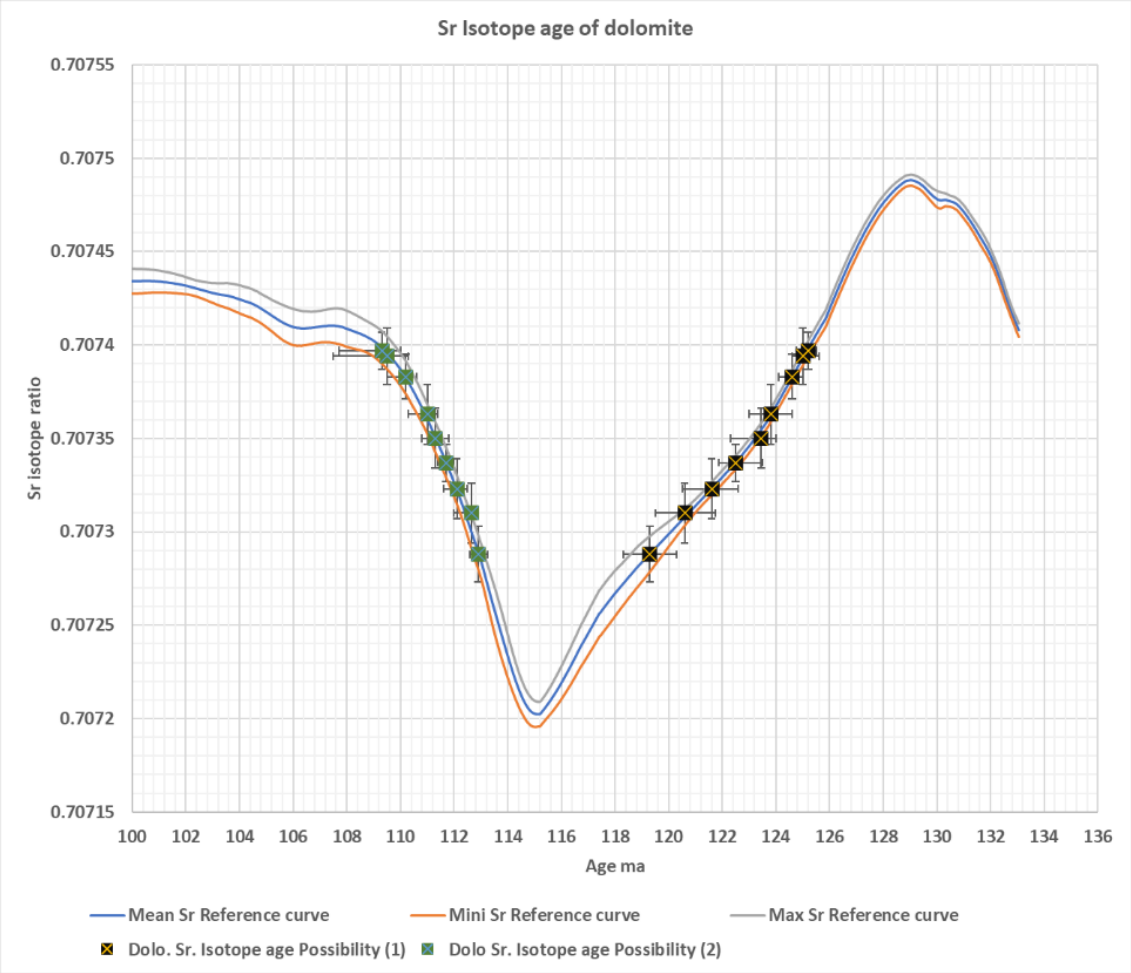


Figure B.1 Possible ages of the dolomites spanning from ~125.6 Ma to ~107.5 Ma.

Material B2: Dolomitisation Temperature Calculation Methodology

To calculate the fractionation temperature of the dolomite, we used Flood and Chavis' (1995) dolomite oxygen isotope data, Horita (2014) fractionation equation, and considering $\delta^{18}O_{sw}$ value of 0.2‰ standard mean ocean water (VSMOW) for the modelled isotopic composition of the Mid-Cretaceous seawater at the paleogeographic location of the Mid-Pacific Mountains during the dolomitisation age (Zhou et al., 2008).

Horita equation: $10^3 \ln \alpha_{dolomite-water} = 3.140(\pm 0.022) \times (10^6/T^2) - 3.14(\pm 0.11)$

The table below (Table B2-1) show temperature range from 30.4 °C to 41.2 °C.

$\delta^{18}O_{dol}$ [VPDB]	$\delta^{18}O_{dol}$ [VSMOW]	$\delta^{18}O_{sw}$ [VSMOW]	αdol-wat	1000ln	1000ln+3.14	T^2	T °K	T °C
0.7	31.63	0.2	1.031425	30.94	34.08	92131.6	303.5319	30.38
-0.4	30.49	0.2	1.030292	29.84	32.98	95203.89	308.5513	35.40
-0.6	30.29	0.2	1.030085	29.64	32.78	95785.01	309.4915	36.34
-0.7	30.18	0.2	1.029982	29.54	32.68	96078.29	309.965	36.8
-0.6	30.29	0.2	1.030085	29.64	32.78	95785.01	309.4915	36.34
-1.1	29.77	0.2	1.02957	29.14	32.28	97269.87	311.8812	38.73
-1	29.87	0.2	1.029673	29.24	32.38	96969.17	311.3987	38.24
-1	29.87	0.2	1.029673	29.24	32.38	96969.17	311.3987	38.24
-1.6	29.26	0.2	1.029055	28.64	31.78	98802.27	314.3283	41.17

Table B2-1. Calculated formation temperatures of the dolomites.

Material B3: Burial & Thermal History Modelling Methodology

To compare the apparent formation temperature of the dolomite and thermal history of the host rock, reconstruction of the thermal history of Resolution Guyot was performed taking in consideration the active exchange between the atoll pore-waters and surrounding seawater (Paull et al., 1995) and worldwide examples of negative geothermal gradients in atolls and banks (Eniwetok, Bikini, and Mururoa atolls and Reed Bank; Swartz, 1958; Henry et al., 1996; Leclerc et al., 1999 and 2000; Wang et al., 2020)

Steps to predict the thermal history:

1. Using the depositional age model from El-Yamani et al. (2022), we predict the overburden thicknesses and changes every 1 Ma.
2. The values of the overburden thicknesses multiplied by the corresponding geothermal gradient using the values from Swartz (1958) in Enewetak atoll.
3. The sea surface temperature (i.e. 0-5 m depth) was set at 33 °C using the modelled tropical sea surface temperatures of the Mid-Cretaceous at the paleogeographic location of the Mid-Pacific Mountains between 125-110 Ma (i.e. dolomitisation age) (Valdes et al., 2021).
4. Two burial and thermal history modelling of the host rock were performed:
    a. One is for the host rock of the dolomite sample 166R-2 at 1572 mbsf (Table B3-1).
    b. The second one is for the host rock of the dolomite sample 130R-2 at 1227 mbsf (Table B3-2).

Depth (mbsf) at Site 866	Age (Ma)	Cumulative overburden thickness	Overburden thickness every 1 Ma	Paleotemperature °C of the host rock at 1572 mbsf
1572.0	131.7	0.0	0.0	33.0
1368.0	130.7	204.0	204.0	23.1
1178.0	129.7	394.0	190.0	15.7
1017.5	128.7	555.0	161.0	13.5
959.0	127.7	613.0	58.0	13.1
900.0	126.7	672.0	59.0	12.7
842.0	125.7	730.0	58.0	12.3
801.0	125.0	771.0	41.0	12.0
743.0	124.0	829.0	58.0	11.6
684.0	123.0	888.0	59.0	11.2
626.0	122.0	946.0	58.0	11.0
582.0	121.0	990.0	44.0	10.9

558.6	120.0	1013.4	23.4	10.8
534.8	119.0	1037.2	23.8	10.9
511.0	118.0	1061.0	23.8	11.3
487.0	117.0	1085.0	24.0	11.7
465.0	116.0	1107.0	22.0	12.0
439.0	115.0	1133.0	26.0	12.4
413.0	114.0	1159.0	26.0	12.9
388.0	113.0	1184.0	25.0	13.3
362.0	112.0	1210.0	26.0	13.7
336.0	111.0	1236.0	26.0	14.1
310.0	110.0	1262.0	26.0	14.5

Table B3-1. Thermal history calculations of the host rock at depth 1572 mbsf from initial deposition to 110 Ma. The corresponding host rock ambient temperatures at the potential age range are highlighted in yellow.

Depth (mbsf) at Site 866 age model	Age (Ma)	Cumulative overburden thickness	Overburden thickness	Temperature °C of the host rock at 1224 mbsf
1224.0	130.0	0.0	0.0	33.0
1035.0	129.0	189.0	189.0	23.7
977.0	128.0	247.0	58.0	21.4
918.0	127.0	306.0	59.0	19.1
859.0	126.0	365.0	59.0	16.8
801.0	125.0	423.0	58.0	14.6
743.0	124.0	481.0	58.0	14.0
684.0	123.0	540.0	59.0	13.6
626.0	122.0	598.0	58.0	13.2
582.0	121.0	642.0	44.0	12.9
558.6	120.0	665.4	23.4	12.7
534.8	119.0	689.2	23.8	12.6
511.0	118.0	713.0	23.8	12.4
487.0	117.0	737.0	24.0	12.2
465.0	116.0	759.0	22.0	12.1
439.0	115.0	785.0	26.0	11.9
413.0	114.0	811.0	26.0	11.7

388.0	113.0	836.0	25.0	11.5
362.0	112.0	862.0	26.0	11.4
336.0	111.0	888.0	26.0	11.2
310.0	110.0	914.0	26.0	11.0

Table B3-2. Thermal history calculations of the host rock at depth 1224 mbsf from initial deposition to 110 Ma. The corresponding host rock ambient temperatures at the potential age range are highlighted in yellow.

Table B10: Depositional Age Dating Methodology at Site 866

Please refer to *APPENDIX A*, Table A1.

Table B11: Geothermal Gradient of Enwetak Atoll

Geothermal gradients zones (°C/m) vs depth (Swartz, 1956)

Interval (m)	Geothermal gradient (°C/m)
0 to 9	-0.09
9 to 39	-0.068
39 to 69	-0.039
69 to 100	-0.059
100 to 427	-0.039
427 to 908	-0.007
908 to 1030	-0.002
1030 to 1213	0.016

Table B12: Dolomitisation Temperature Calculation Results Using Nine Different Fractionation Equation

Sample #	depth	$\delta^{18}O_{SW}$	$\delta^{18}O_{dol}$	Temperature °C								
				Northrop and Clayton, 1966	O'Neil and Epstein, 1966	Fritz and Smith, 1970	Sheppard and Schwarcz, 1970	Matthews and Katz, 1977	Land, 1985	Woronick and Land, 1985	Vasconcelos et al., 2005	Müller et al., 2019
130R-2,17-19 cm	1224	0.2	0.7	40.92	38.98	27.13	32.55	26.05	22.89	32.55	25.14	26.61
148R-1,44-^6	1396	0.2	-0.4	46.38	44.12	32.63	37.58	30.98	28.32	37.58	30.64	31.69
159R-3, 82-84	1505	0.2	-0.6	47.41	45.08	33.67	38.52	31.91	29.34	38.52	31.67	32.64
160R-1,70-73	1512	0.2	-0.7	47.92	45.56	34.19	39.00	32.37	29.86	39.00	32.19	33.12
162R-2,139-141	1534	0.2	-0.6	47.41	45.08	33.67	38.52	31.91	29.34	38.52	31.67	32.64
162R-3,0-3	1535	0.2	-1.1	50.01	47.52	36.30	40.92	34.26	31.94	40.92	34.30	35.06
163R-1,16-17	1540	0.2	-1	49.49	47.03	35.77	40.44	33.78	31.42	40.44	33.77	34.57
164R-1,94-96	1554	0.2	-1	49.49	47.03	35.77	40.44	33.78	31.42	40.44	33.77	34.57
166R-2,109-122	1572	0.2	-1.6	52.69	50.02	39.00	43.37	36.66	34.61	43.37	37.00	37.54

Table B13: Calculation of Estimated Duration Spent by the Shallow Marine Carbonates of the Cretaceous Pacific Atolls Below 1000 m

Atoll	Age of the oldest pelagic cap	current depth of the platform	linear subsidence rate m/million year	estimated duration spent by shallow marine carbonates below 1000 m
Wodejebato	Based on Pearson (1995) the age of oldest pelagic cap was 20 Ma and deposited at depth ~1000-1100 mbsl			20 Million Years
Allison	Turonian (94 Ma; Sliter, 1995)	1518 mbsl	14.02	37 Million Years
Resolution	Maastrichtian (72 Ma; Sager et al., 1993)	1362 mbsl	16.13	22.4 Million Years
Ita Mai Tai	Early Eocene (55.8 Ma; Heezen et al., 1973)	1500 mbsl	23.3	21.5 Million Years
Horizon	Turonian (94 Ma; Winterer et al. (1973)	2200 mbsl	21.3	56.4 Million Years
MIT	Latest Albian (~100 Ma; Larson et al., 1995)	1323 mbsl	11.23	28.8 Million Years

Table B14: Summary of Interparticle Porosities at Site 866

Sample Number	Depth (mbsf)	Rock Texture	Porosity %	Estimated Perm (md)
109R-2, 10-12	1021	Packstone	26.12	388.9725989
110R-1, 53-55	1030	Packstone	25.37	322.9942182
114R-1,85-87	1069	Packstone	17.53	30.54631262
115R-1,76-78	1078	Wackestone	12.52	0.400178509
116R-1,49-51	1088	Packstone	25.19	308.649712
129R-2, 23-26	1213	Grainstone	22.62	13992.02662
144R-2, 51-59	1359	Grainstone	16.59	991.758403
146R-1,79-81	1377	Mudstone	8.51	0.076814662
147R-2, 91-93	1388	Packstone	4.43	0.004717218
148R-4, 95-98	1401	Grainstone	17.6	1642.551278
154R-1,63-70	1454	Grainstone	27.22	67954.33694
155R-1,91-98	1464	Grainstone	22.12	11561.33228
159R-1, 99-101	1501	Packstone	17.37	28.81064685
170R-1, 109-118	1610	Grainstone	18.83	2923.980509

APPENDIX C: *SUPPLEMENT* TO BEYOND THERMAL STRESSES: MAGMATISM, KARSTIFICATION, AND HOTSPOT MIGRATION DICTATED DEMISE OF THE MID-PACIFIC CRETACEOUS ATOLLS

Contents:

Figure C1: Potential areal extent of the interpreted sills at Allison Guyot.

Figure C2: Potential areal extent of the interpreted sills at Resolution Guyot.

Figure C3: Hurricane Index at the Mid-Pacific Mountains (highlighted by red box) at 97 Ma (**https://www.paleo.bristol.ac.uk/ummodel/users/Valdes_et_al_2021/new2/**).

Figure C4: Tropical cyclogenesis (dark shade) during the Mid-Cretaceous (Agustsdottir et al., 1999) and the corresponding location of the Mid-Pacific Mountains (highlighted by red box).

Figure C5: Ocean surface currents at the Mid-Pacific Mountains (highlighted by red box) at 97 Ma (**https://www.paleo.bristol.ac.uk/ummodel/users/Valdes_et_al_2021/new2/**).

Figure C6: ocean surface current at Wodejebato Guyot (highlighted by red dot) at demise age (**https://www.paleo.bristol.ac.uk/ummodel/users/Valdes_et_al_2021/new2/**).

Figure C7: ocean surface current at MIT Guyot (highlighted by red dot) at demise age (**https://www.paleo.bristol.ac.uk/ummodel/users/Valdes_et_al_2021/new2/**).

Figure C8: The age progression track of the Japanese Seamount Trail (highlighted by transparent red box and an arrow of the hotspot migration direction) revealing a singular hotspot origin (Modified after Koppers et al., 2003).

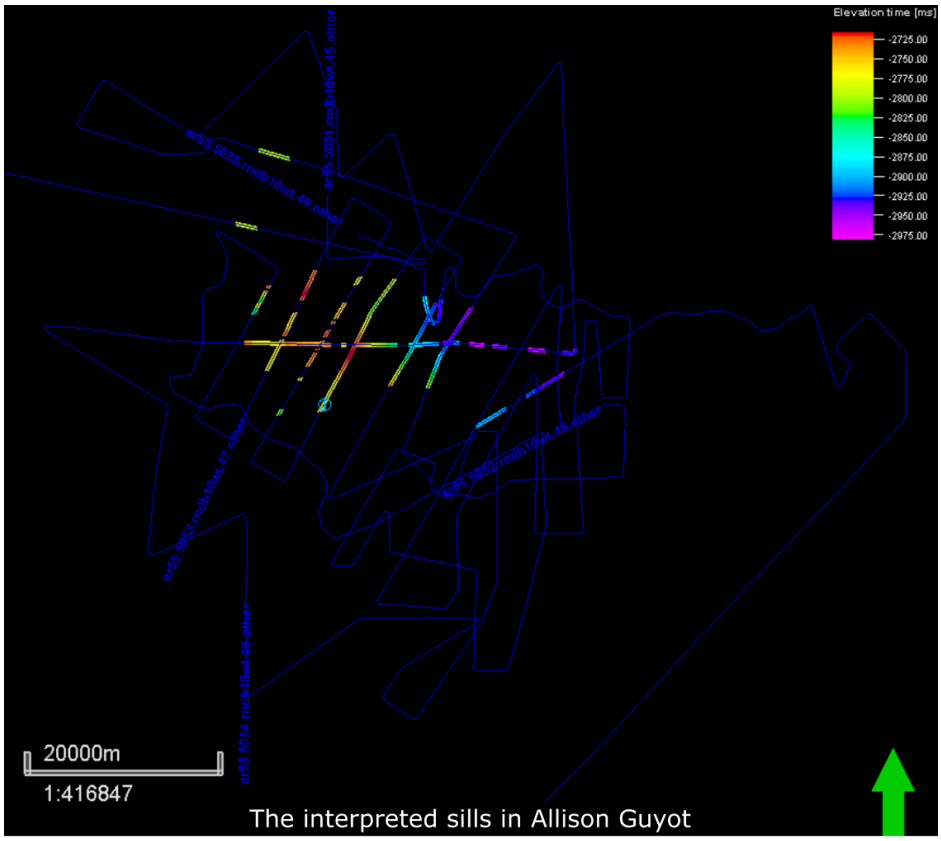
Figure C9: Sea surface temperature at the Mid-Pacific Mountains (highlighted by red box) at 97 Ma (**https://www.paleo.bristol.ac.uk/ummodel/users/Valdes_et_al_2021/new2/**).

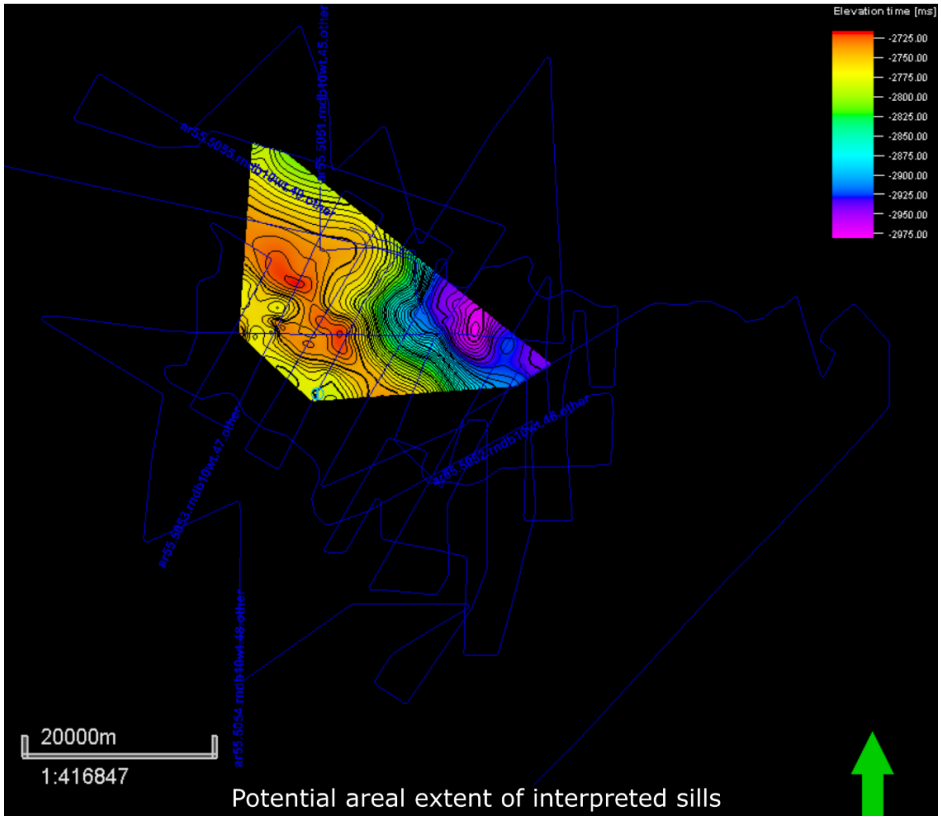
Figure C10: Sea surface temperature at Takuyo-Daisan Guyot (highlighted by red dot) at 111 Ma (**https://www.paleo.bristol.ac.uk/ummodel/users/Valdes_et_al_2021/new2/**).

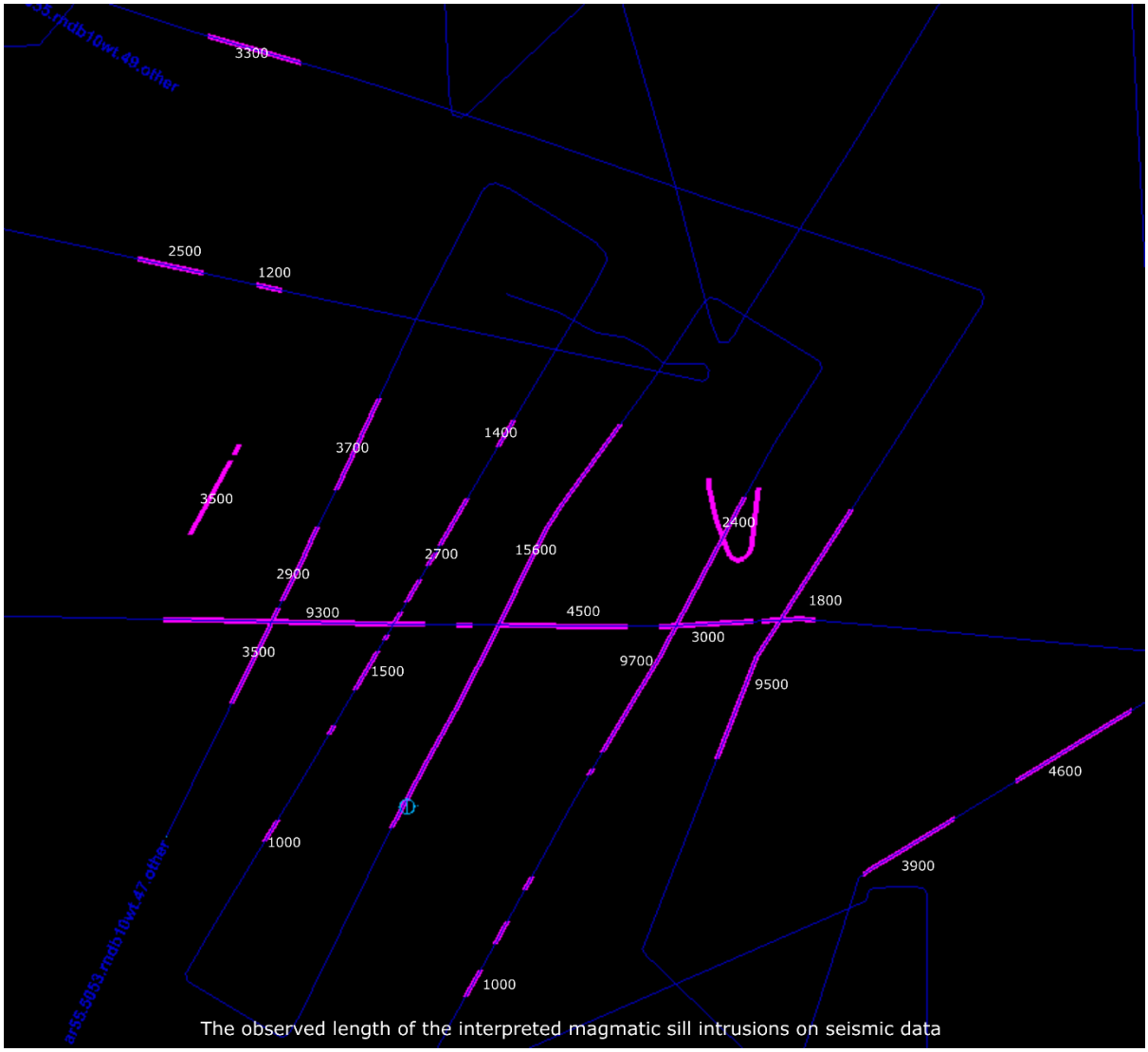
Figure C11: Sea surface temperature at MIT Guyot (highlighted by red dot) at 102.6 Ma (**https://www.paleo.bristol.ac.uk/ummodel/users/Valdes_et_al_2021/new2/**).

Figure C12: Sea surface temperature at Wodejebato Guyot (highlighted by red dot) at 69 Ma (**https://www.paleo.bristol.ac.uk/ummodel/users/Valdes_et_al_2021/new2/**).

Figure C1: Potential Areal Extent and Diameters of the Interpreted Sills at Allison Guyot







The observed length of the interpreted magmatic sill intrusions on seismic data

Figure C2: Potential Areal Extent and Diameters of the Interpreted Sills At Resolution Guyot

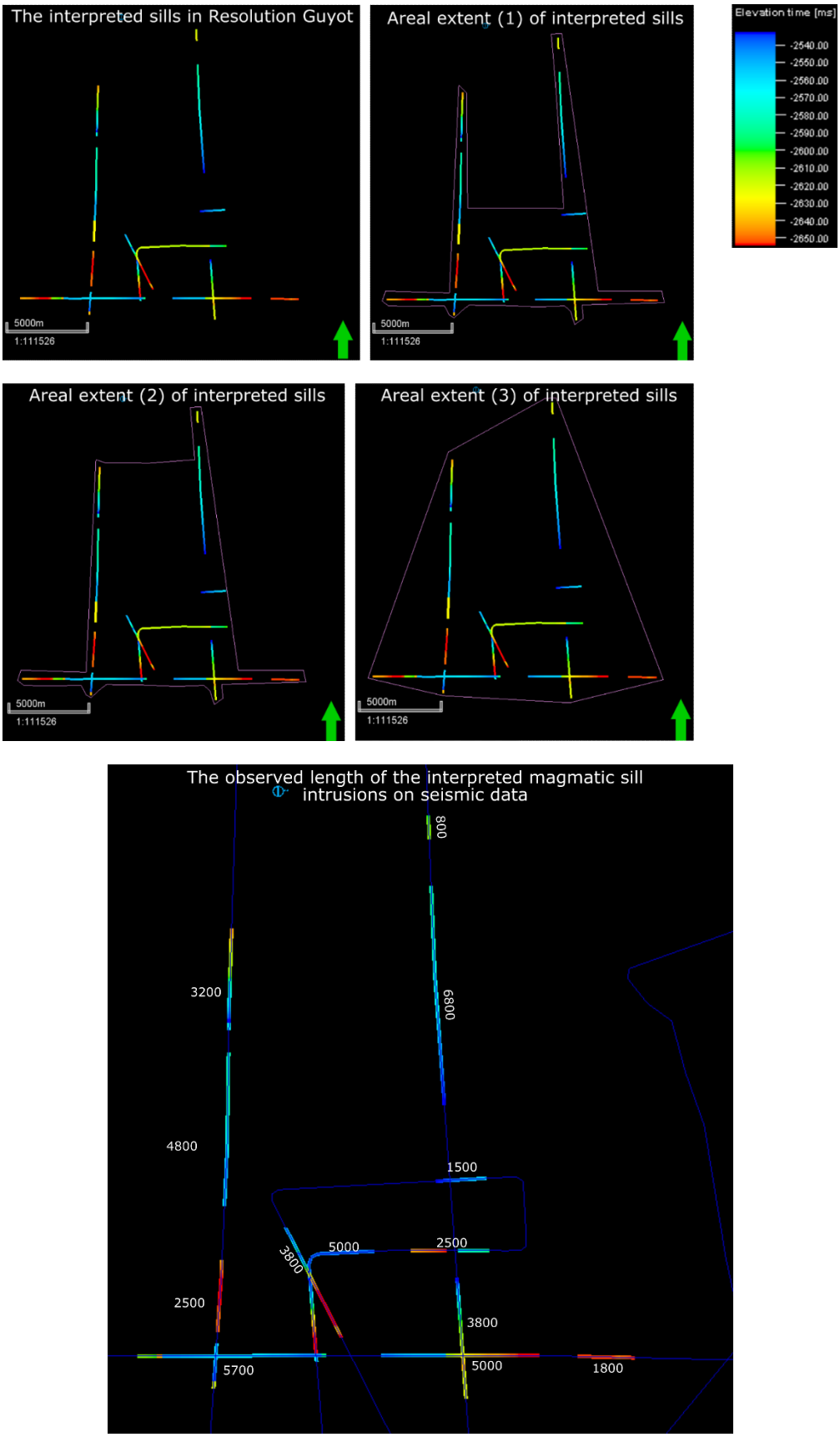


Figure C3: Hurricane Index at the Mid-Pacific Mountains (highlighted by red box) at 97 Ma (Valdes et al., 2021)

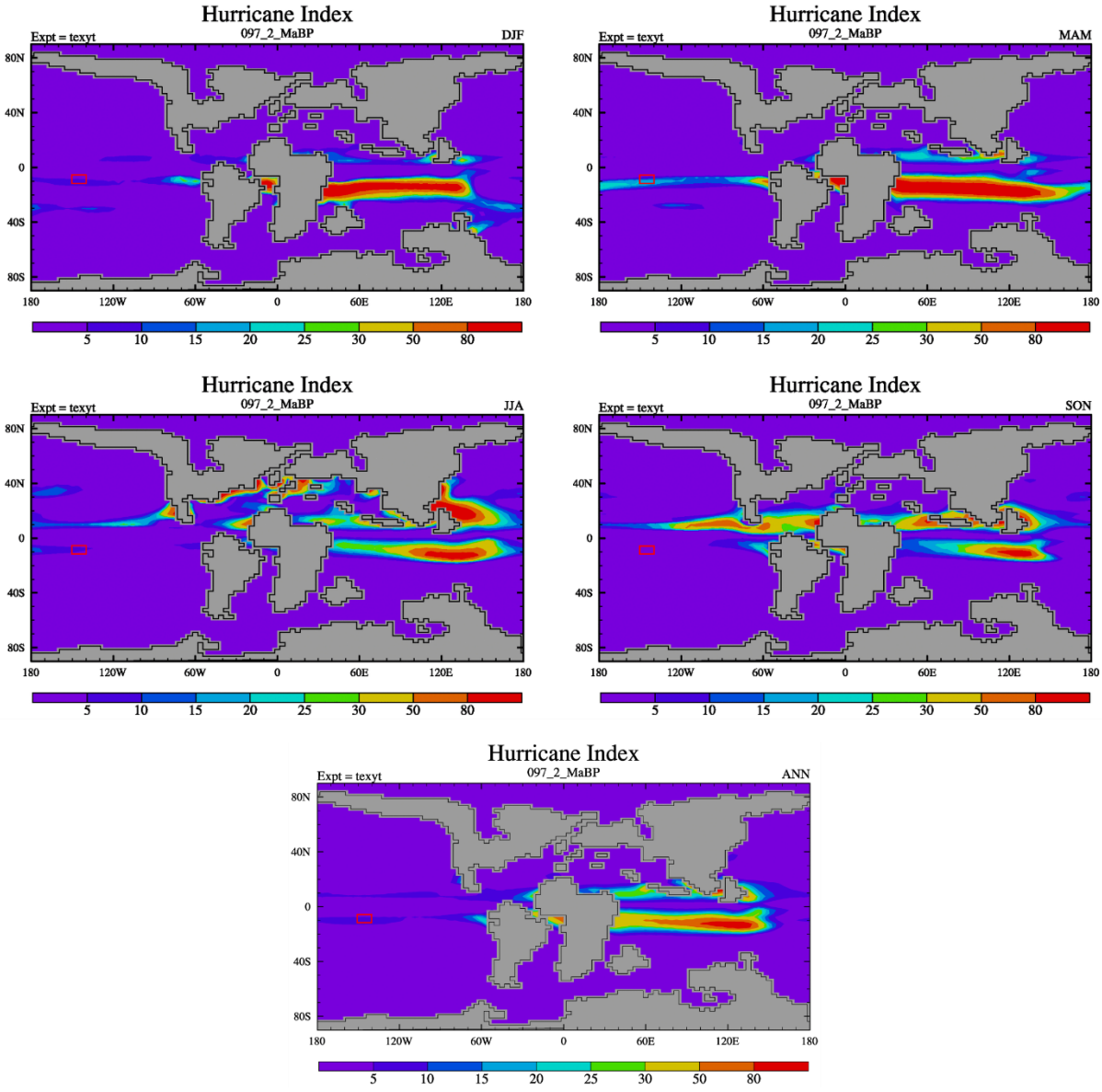


Figure C4: Tropical cyclogenesis (dark shade) during the Mid-Cretaceous (Agustsdottir et al., 1999) and the corresponding location of the Mid-Pacific Mountains (highlighted by red box)

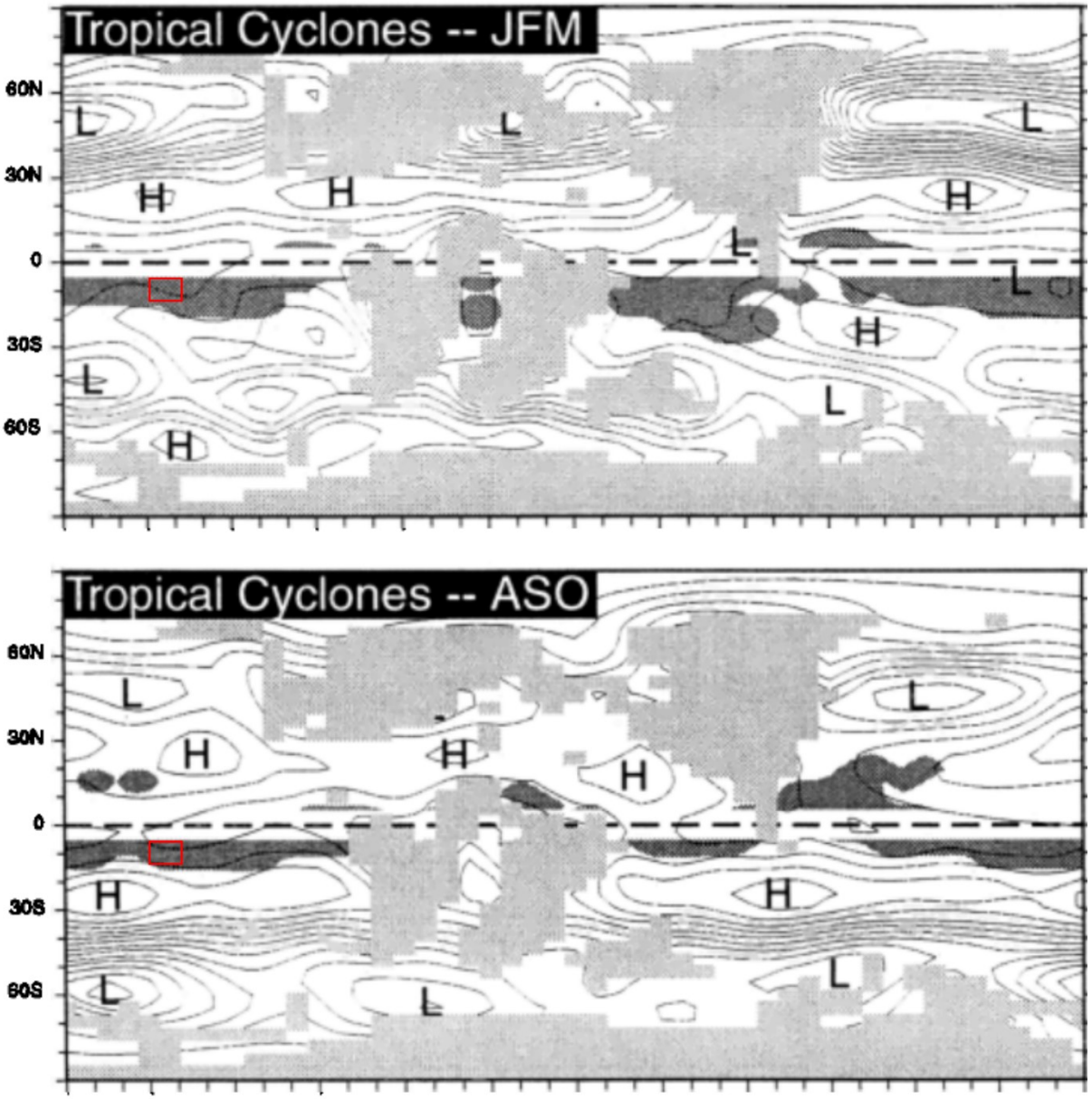


Figure C5: Ocean surface currents at the Mid-Pacific Mountains (highlighted by red box) at 97 Ma (Valdes et al., 2021)

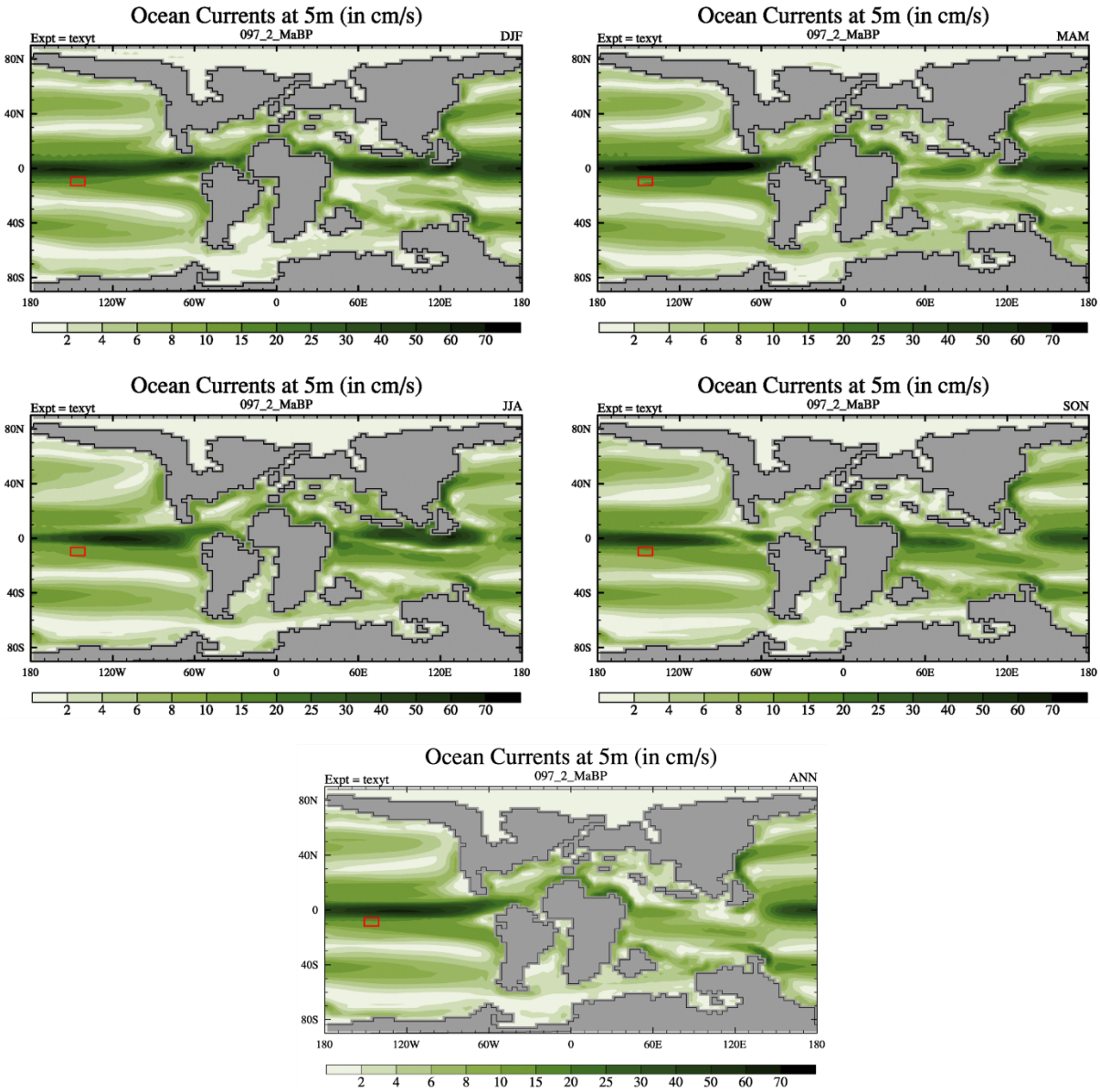


Figure C6: Ocean surface current at Wodejebato Guyot (highlighted by red star) at demise age (Valdes et al., 2021)

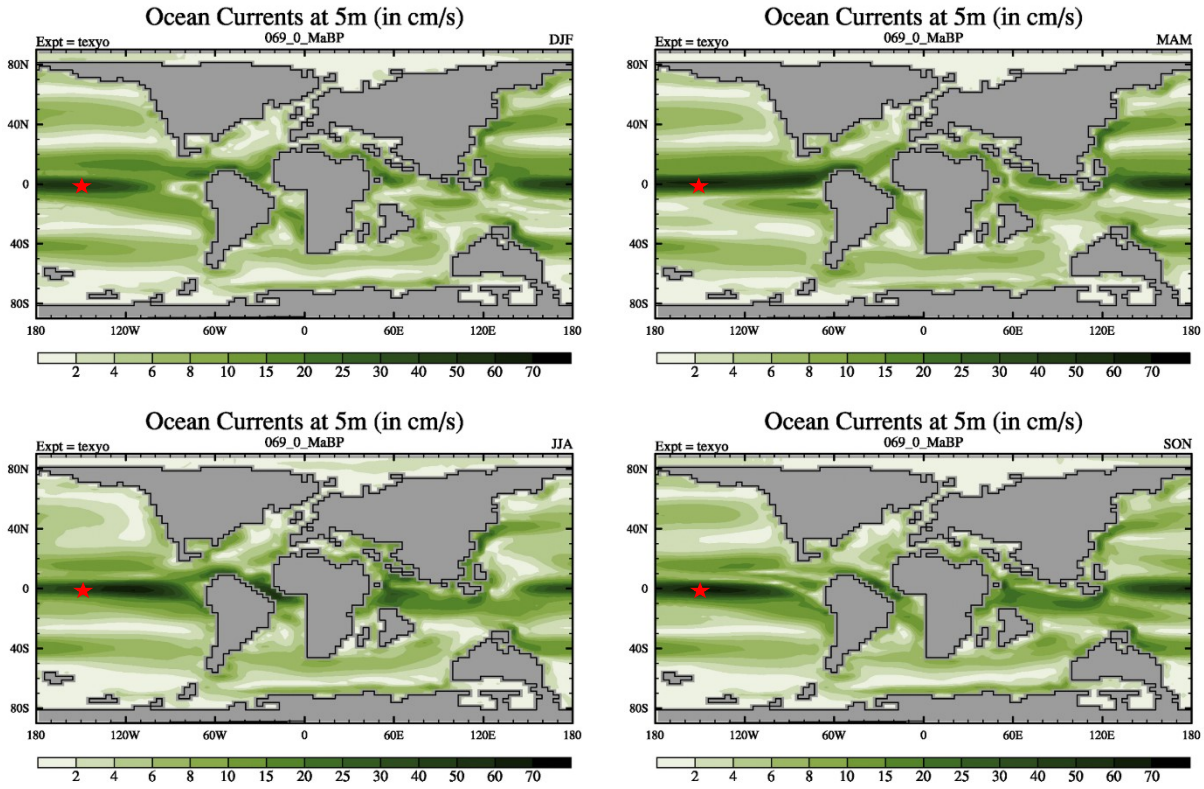


Figure C7: Ocean temperature and ocean surface current at MIT Guyot (highlighted by red star) at demise age (Valdes et al., 2021)

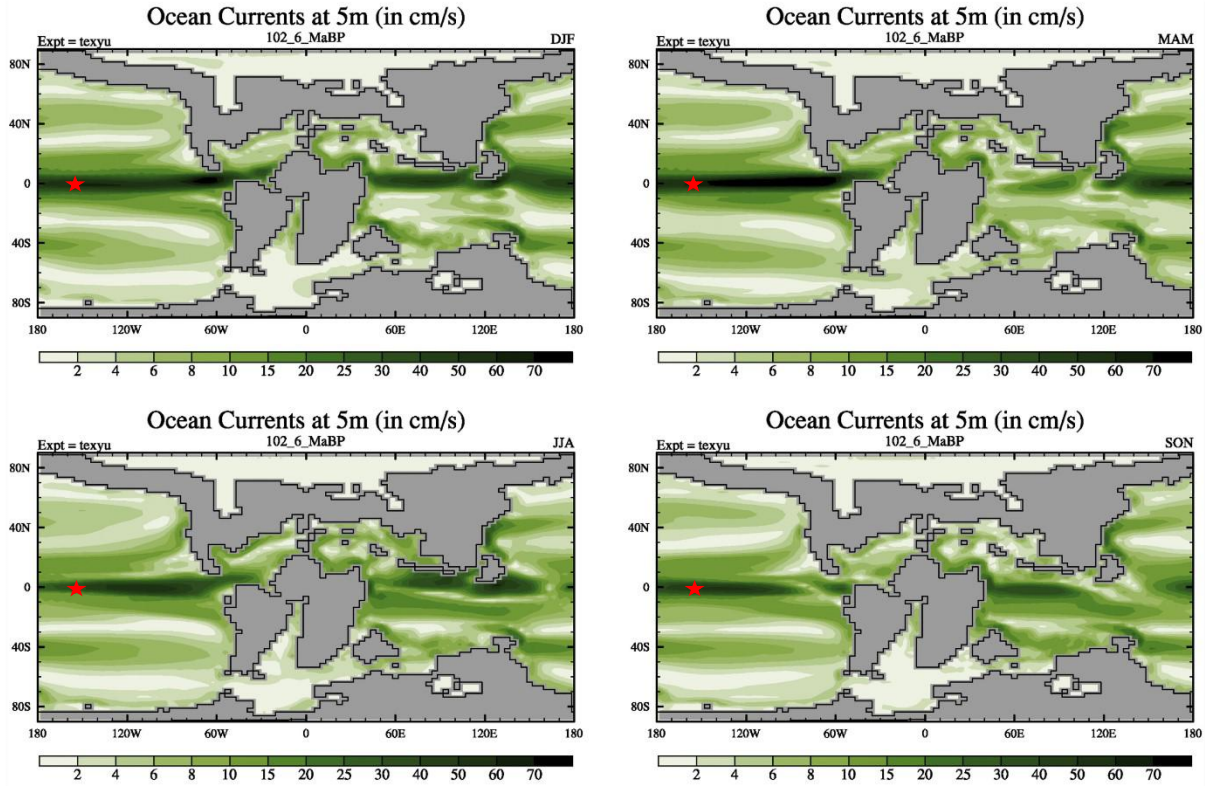


Figure C8: The age progression track of the Japanese Seamount Trail (highlighted by transparent red box and an arrow of the hotspot migration direction) revealing a singular hotspot origin (Modified after Koppers et al., 2003)

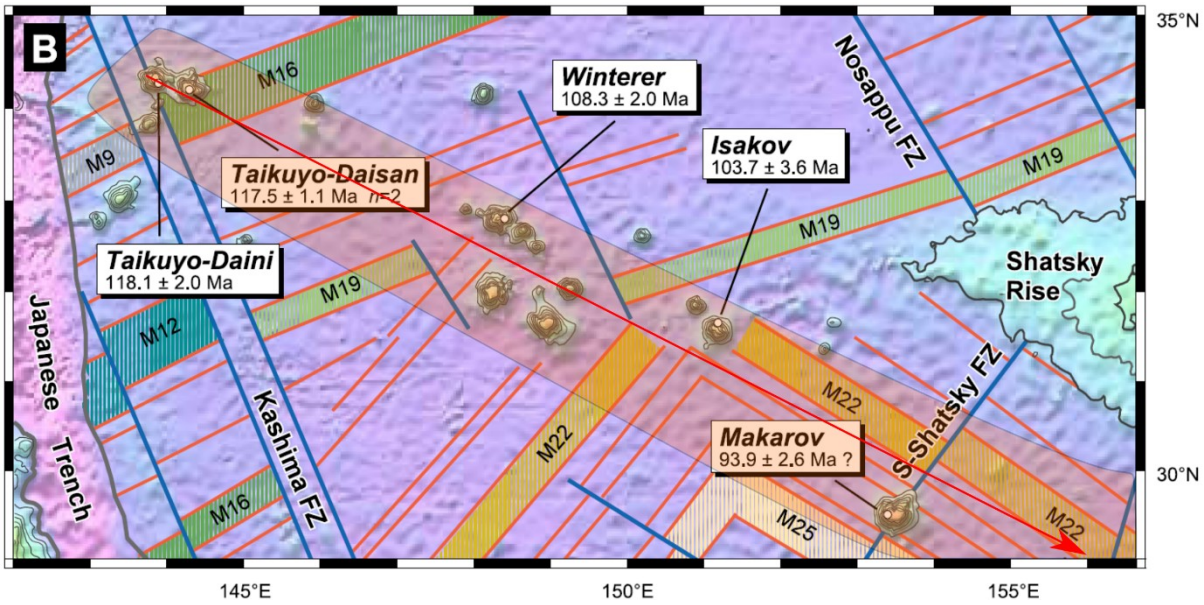


Figure C9: Ocean surface temperature at the Mid-Pacific Mountains (highlighted by red box) at 97 Ma (Valdes et al., 2021)

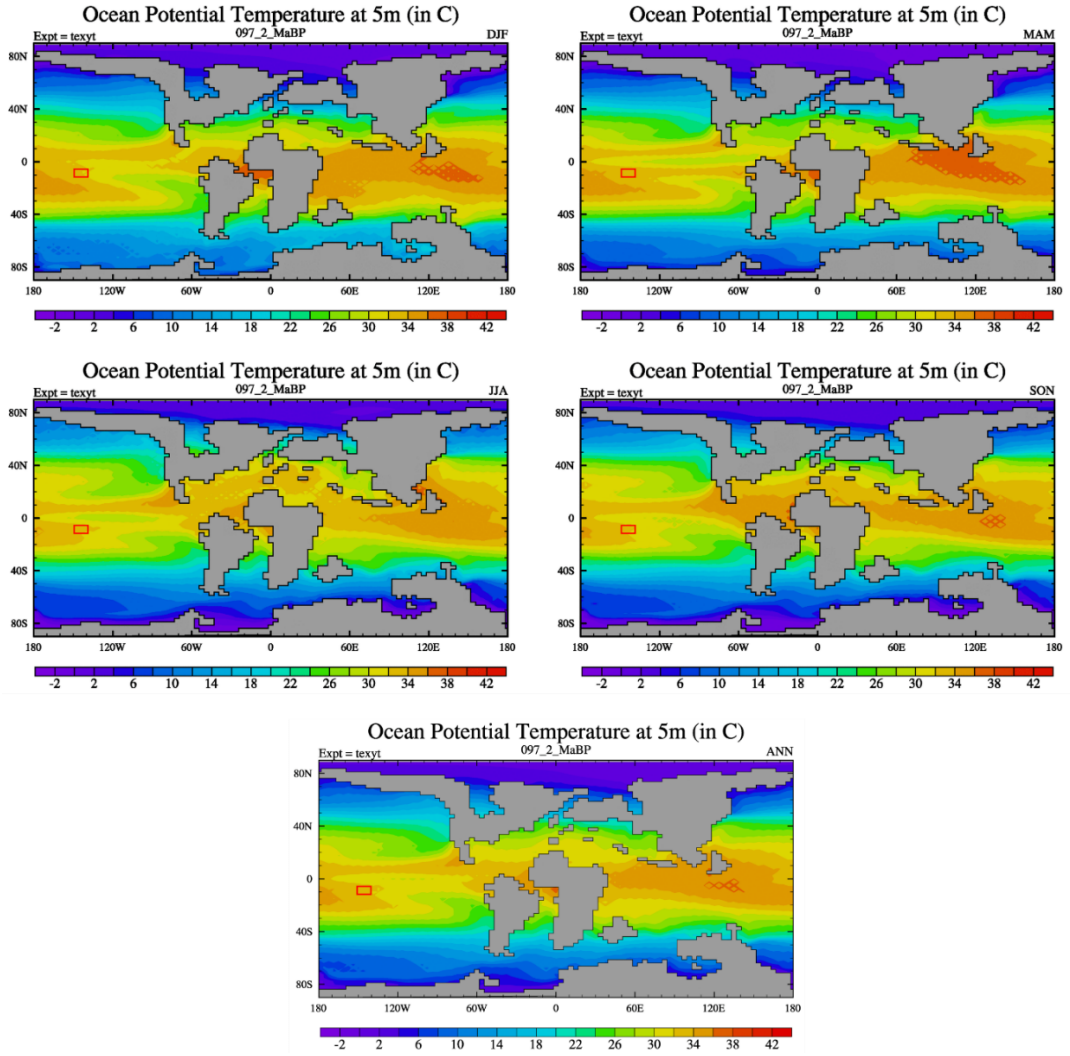


Figure C10: Ocean surface temperature at Takuyo-Daisan Guyot (highlighted by red star) at 111 Ma (Valdes et al., 2021)

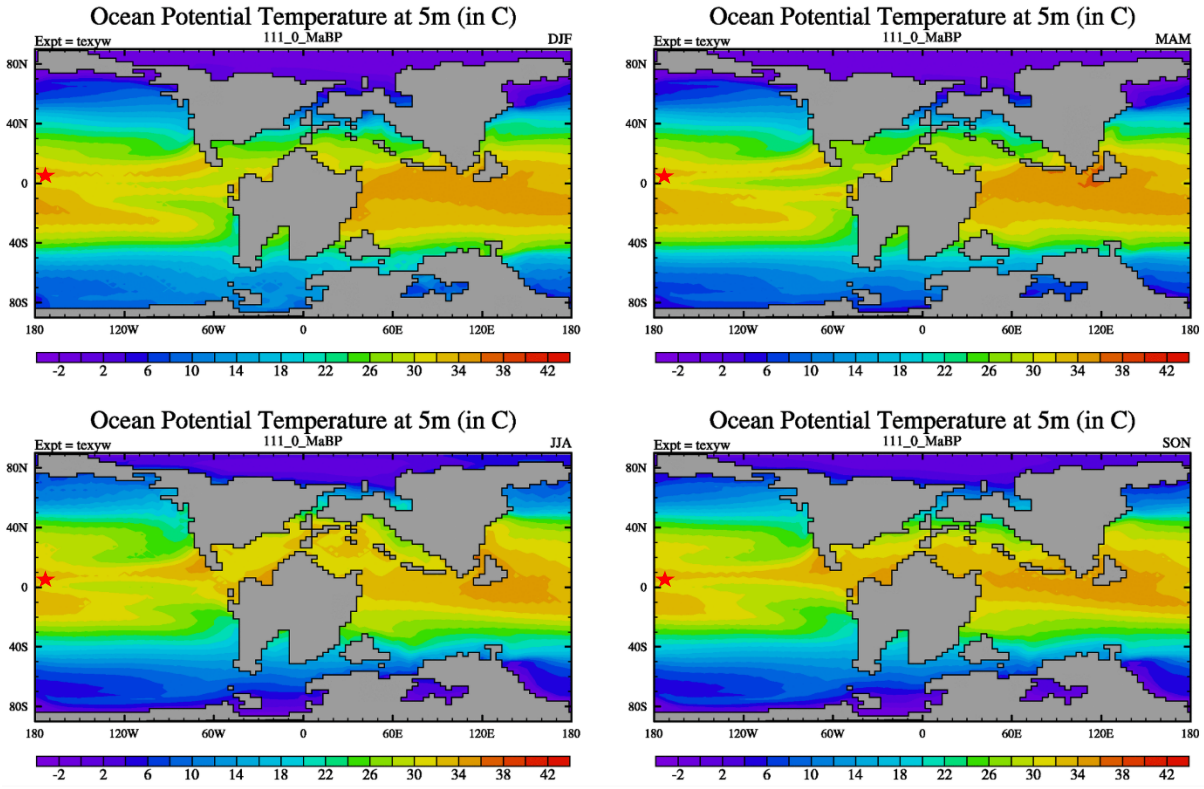


Figure C11: Sea surface temperature at MIT Guyot (highlighted by red star) at 102.6 Ma (Valdes et al., 2021)

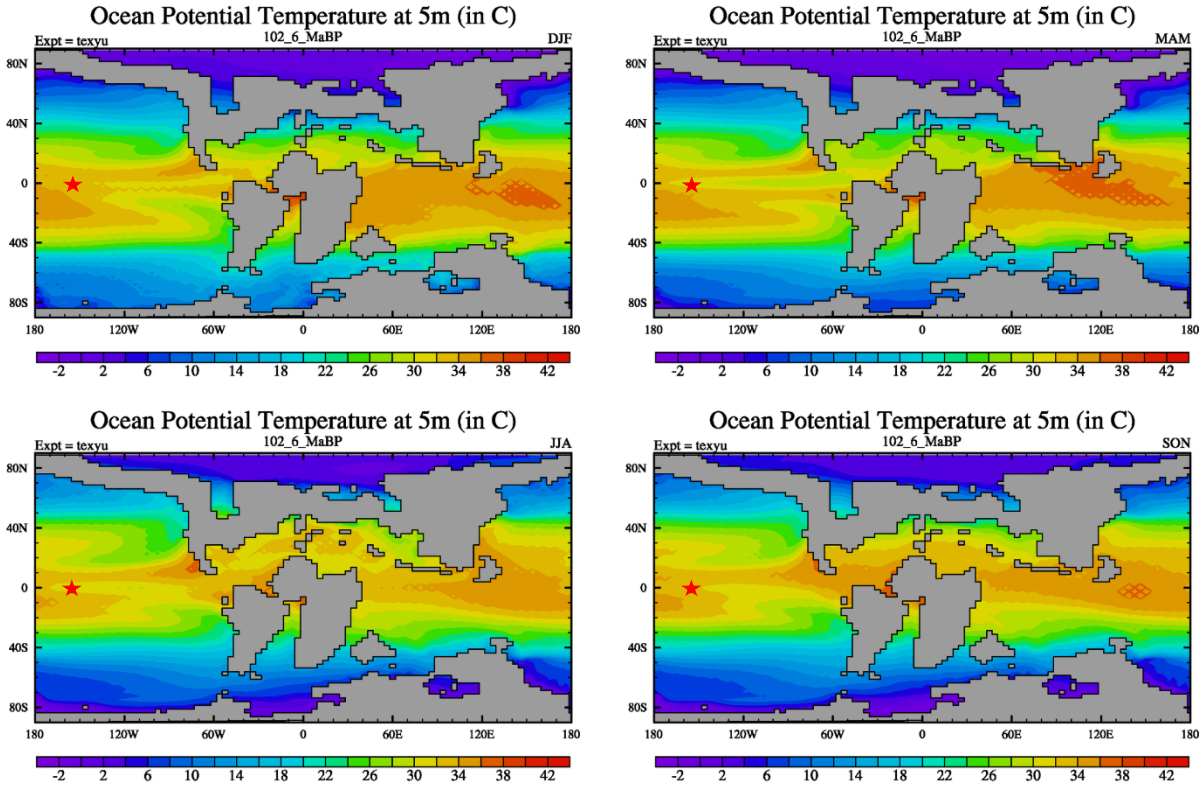


Figure C12: Ocean surface temperature at Wodejebato Guyot (highlighted by red star) at 69 Ma (Valdes et al., 2021)

